Hydrogen Bonded Structures and Polymorphism in Agrochemicals

Antonietta Di Pumpo

A thesis submitted for the degree of Doctor of Philosophy

University of Bath

Department of Chemistry

October 2016

Table of Contents

Additional material Crystallographic information files (***.cif***) on CD-ROM on thesis rear cover

List of Figures

List of Tables

Acknowledgements

First I want to thank my supervisors, Prof. Mark Weller at the University of Bath, and Dr. Sax Mason at ILL, for all the support, patience and fruitful discussions, concerning both work and everyday life.

I also want to thank everybody in the Weller group, old members and new additions, for the good times shared in the lab, hoping and waiting for something to happen.

Special thanks to the friends in Bath, Dom, Karen, Louise and Lauren, and so many others. I enjoyed every minute spent in your company.

A big thank you to the great IT guys that had the misfortune to work with me, both in Bath and at ILL. I am very grateful for all the help you gave me.

Thank you to my wonderful family for all the help and support throughout my PhD, especially during writing up. It does not matter what happens, you are always there and I am forever grateful.

And finally, a huge thank you to Beppe for the infinite patience and for keeping up with my frequent mood swings, especially during my PhD. I couldn't have done it without you.

Abstract

Characterisation of the phenomenon of polymorphism in organic active materials used as pesticides, herbicides and fungicides can allow the identification of possible modifications of the same compound exhibiting different physical properties, such as solubility and dissolution rates, enabling control over potentially contaminated areas by this type of materials and providing a tool for their stability upon storage. These ambitious goals can be achieved through a thorough study of the intra- and intermolecular interactions that are responsible for the formation of different polymorphs of the same compound, using a combination of single-crystal and powder X-ray diffraction (SXD and PXD) for the definition of the atomic coordinates and thermal vibration of all non-hydrogen atoms, and of single-crystal and powder neutron diffraction (SND and PND) to investigate the behaviour of hydrogen atoms, which can introduce temperature-dependent proton effect, for example proton transfer and proton migration, in the compounds understudy.

Chapter 3 of this thesis describes intramolecular H-bonded herbicides, such as pendimethalin (PDM), in which a variation of the planarity of the intramolecular hydrogen bond leads to the formation of two polymorphs showing different delocalisation of the electrons on the aromatic ring of PDM causing a change of colour between the two forms.

Interesting effects of the presence of hydrogen bonding networks in intermolecular H-bonded systems are shown in Chapters 4 and 5. Responses of a crystal structure undergoing a controlled temperature program were studied by variable-temperature (VT) PND measurements, which showed a direct correlation between the variation of the unit cell parameters and changes in the hydrogen bonding network. For example, the VT-PND data collected on a sample of the herbicide glyphosate (GLY) suggest that changes of the characteristics of the hydrogen bond aligned along the ***a***-axis are the reason behind the initial decrease of the unit cell parameter ***a*** from 4K to 200K, indicating that the hydrogen bonding network of GLY is not rigid but flexible, allowing the molecules inside the crystal structure to slightly vary their relative position and preventing disruptions in the long-range order of the crystal.

The arise of polymorphism in the fungicide cyprodinil (CYP) causes the formation of two crystal structures that exhibit different types of intermolecular interaction: linear hydrogen bonds between three molecules of cyprodinil in form A, while form B displays the organisation of the molecules in dimers forming a hydrogen bonded 8-membered ring. VT-PND experiments allowed the identification of the phase transition from the stable form A to the metastable form B, which occurs around 350K, and the re-crystallisation, upon cooling of the same sample, of the metastable form B around 310K. Crystallisation of form A was followed by ***in situ*** PND measurements on a saturated solution of CYP in deuterated-ethanol.

The polymorphic transformation in CYP poses critical problems in the application of the fungicide on crop fields because it causes the formation of particle aggregates, which can obstruct the nozzle

of delivery equipments. These inconveniences were addressed using the hydrogen bond as a tool for the design of molecular complexes of cyprodinil, which might increase the stability and the melting point of the fungicide, preventing the occurrence of the polymorphic conversion. The co-formers that were used for the co-crystallisation work, such as 2-aminopyrimidine, maleimide and benzoic acid (described in Chapter 6), and differently substituted benzoic acids (discussed in Chapter 7), show encouraging results in the stabilisation of the crystal structure of cyprodinil: in fact, in most cases the fusion temperature of the co-crystal is higher than that of both pure forms of cyprodinil. All co-crystals are characterised by the organisation of the molecules in heterogeneous dimers, which are stabilised by the formation of circular hydrogen bonds. Furthermore, the different values of the $\boldsymbol{pK_a}$ exhibited by the various substituted benzoic acids used as co-formers introduce interesting proton effect in the structure of the hydrogen bond of these materials. For example, the higher acidity of 2-nitro and 2-chlorobenzoic acids causes the transfer of a proton from the carboxylic group of the acid to the nitrogen atom of the pyrimidine ring of cyprodinil, while migration of the hydrogen atom involved in an intermolecular interaction between a molecule of CYP and one of 3-chlorobenzoic acid can be observed. VT-SND experiments showed that the degree of migration is tunable by temperature: at 30K the proton is modelled close to the nitrogen atom of a molecule of cyprodinil, while at 300K the bond connectivity changes and the hydroxyl group of the acid is restored.

Chapter 1

1. Introduction

1.1 Preface

Polymorphism in crystals and control of crystal habit and crystal growth are important parameters that must be controlled for any commercial crystallisation processes. Dissimilar crystal structures of active molecules exhibit different solubilities which affect biological efficacy, for example through differing dissolution rates, reaction pathways, toxicity and side effects. As a consequence, the rational design of chemical crystallisation procedures and use of additives for the control of crystal habit and crystal growth for functional organic compounds in biological applications is a highly important area. While such a rationale has been widely applied for many decades to the pharmaceutical industry, for example on the study of carbamazepine[1], chloroamphenicol[2] and cisplatin[3], it has not been applied systematically or substantially to agrochemicals. Given the importance and value of agrochemicals worldwide, around US$ 3.5 B annually, the understanding and control of agrochemical crystallisation and dissolution is of massive importance.

All agrochemicals taken into consideration during the work of this thesis are organic molecules, constituted mostly by light elements, such as hydrogen, carbon, nitrogen and oxygen, resulting in crystal structures that are governed by interactions that are classified as weak, for example π-π interactions, and hydrogen bonds. Since the phenomenon of polymorphism affects the molecular arrangement in different modifications, an exhaustive understanding of the nature and characteristics of the hydrogen bonding network responsible of the crystal packing of these compounds is pivotal for the design of materials exhibiting desired physical properties.

1.2 Polymorphysm

1.2.1 Historic background

To this day, a satisfying definition for polymorphism has not been found. Literally, the word polymorphism means “that shows many forms”: a compound exhibits polymorphism if it exists in at least two different structural arrangements.

The phenomenon of polymorphism was known since 1796, when the chemist Smithson Tennant (1761-1815) proved that diamond “consists entirely of charcoal, differing from the usual state of that substance only by its crystallized form”. This discovery was not very successful among scientists at that time. Very sceptical was the chemist Humphry Davy (1778-1829), who thought

impossible the idea of two compounds exactly the same in composition and chemical nature, but totally different in their physical properties. With time, however, Davy completely supported Tennant's interpretation, after testing for himself the physical properties of diamond and observing the significant differences compared to those exhibited by charcoal.

E. Mitscherlich (1794-1863) is recognized to be the first to acknowledge the general nature of polymorphism, after exhaustive studies on phosphate and arsenate salts, in particular on the pairs $NaH_2PO_4 \cdot H_2O$/ $NaH_2AsO_4 \cdot H_2O$ and $NaH_2PO_4 \cdot H_2O$/$NaH_2AsO_4 \cdot H_2O$. He noted that phosphates and arsenates can sometimes crystallise in the same form. He named this phenomenon isomorphism. A few years later he recognised the phenomenon of isomorphism also in sulphur, which constitutes a dimorphic system. Various studies, mostly carried out through simple observation of the crystal with a microscope, led to an increase in the interest towards the phenomenon of polymorphism and towards its clear definition.

As a result of deep analyses on mercuric iodide, in 1839 M. L. Frankeheim (1801-1869) was able to define some main principles of polymorphism, some of which are still considered fundamentals[4]:

i. different polymorphs exhibit different melting and boiling points (*sic!*) and their vapours show different densities;
ii. the transition from one form A, stable at low temperature, to a form B, stable at high temperature, is characterized by a specific transition temperature;
iii. form A cannot exist at a temperature higher than the transition point, while form B can exist as a metastable form below the transition temperature;
iv. at temperatures below the transition, form B converts into form A, by simple contact with form A;
v. in some cases, form B can convert into form A without coming into contact with it, but by mechanical shock or by friction;
vi. heat is absorbed during the transformation from form A to form B.

Frankenheim focused his attention on the forces responsible for each different aggregation state; he suggested that the formation of different solid states was due to the presence of different attractive forces, characterised by different symmetry relations.

A milestone in the history of polymorphism is the work by McCrone (1965), whose studies are considered fundamental for a true understanding of polymorphism. McCrone pointed out clearly how the concept of polymorphism in itself was complicated and rich of meaning. Along with the polymorphism interpreted as a different structural arrangement in the solid state, he introduced the concept of CONFORMATIONAL polymorphism, in which were classified all those molecules capable of adopting different conformations in different crystal structures; isomerism and tautomerism are not considered examples of conformational polymorphism, because they lead to the formation of different molecules. Indeed, the main feature of polymorphism is the fact that

different crystal structures of the same molecule exhibit the same liquid and vapour states. Two isomers, as two polymorphs, melt at different temperatures; however, the chemical composition of the melt isomers is different. On the other hand, the melt derived from two polymorphs is the same. It is important, however, not to forget that isomers can reach a temperature dependent equilibrium state after a certain time. This means that two isomers, which are rapidly converted the one into the other, can be considered as a polymorphic system. However, a distinction between a polymorphic system and one that is not polymorphic cannot be reached, because the time ranges, which can label a compound, or an isomer, as a polymorph, have not been clearly defined, yet.

The conformational polymorphism is just one of the many branches of the concept of polymorphism. McCrone himself created the term of PSEUDOPOLYMORPHISM, in which he gathered lots of phenomena related to polymorphism, as desolvatation, second order transitions, isomerism, mesomorphism and recrystallization in the solid state.

1.2.2. Stability and conversion

Thermodynamics state that only one polymorph at a time can be the stable form under defined conditions of temperature and pressure. The Gibbs free energy is the driving force in a polymorphic transformation at constant temperature and pressure. This energy can be written as follows:

$$G = H - TS$$

where *H* is the enthalpy, *T* is the temperature and *S* is the entropy. This means that the total energy of a system is defined by the enthalpy at a constant pressure and by the energy linked to the disorder of the molecules, indicated by the term *TS* in the previous equation. The stable form has the lowest value of the Gibbs free energy and, consequently, has the lowest vapour pressure, thermodynamic activity and solubility.

Regarding the thermodynamics, in the end of the XIX century, D. Lehmann suggested a classification of the phenomenon of polymorphism into two categories: **monotropism** and **enantiotropism**. Monotropic polymorphism is characterized by the irreversible conversion between two polymorphs, while two polymorphs are enantiotropically related when they can convert reversibly into one another.

Also the chemist E. W. Jenkins, in his book *The Polymorphism of Elements and Compounds* pointed out the differences between monotropic and enantiotropic polymorphism[5].

He defined the monotropic polymorphism as the presence of only one stable form below the melting temperature; in this case, the transition from one polymorph to another is an irreversible process in the solid state. Phosphorus is an example of monotropic polymorphism: starting from its white form, it can convert into its red form, after heating in an airless environment. However, it has been proved that the red phosphorus cannot convert back into white phosphorus without leaving the solid state. This means that white phosphorus is a metastable form under the normal reaction

conditions. There are, then, substances which can undergo a reversible transformation into another form. These substances were classified by Jenkins under the concept of enantiotropic polymorphs. An example is sulphur, which can convert from its rhombic form to its monoclinic modification reversibly, under appropriate equilibrium conditions. The temperature of the equilibrium between two enantiotropic forms is called **transition point** and is measured at air pressure.

A rigorous representation of the differences between entantiotropism and monotropism is reported by McCrone, who proposed to monitor the free energy (F) profile as a function of temperature (T), as shown in Figure 1.1.

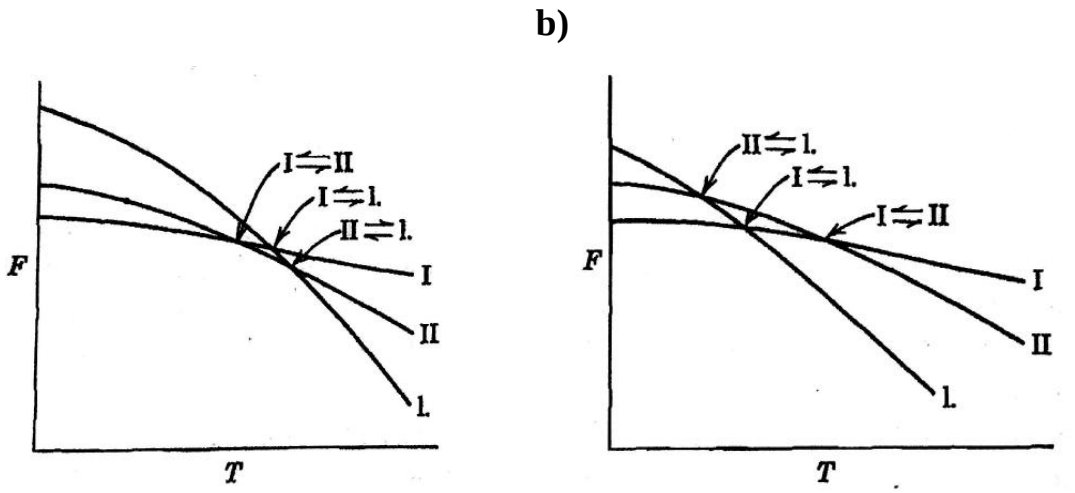

Figure 1.1. *Free energy-temperature curves for a) enantiotropic and b) monotropic systems. I and II represent two polymorphs of a compound, while l. is the liquid curve*[6].

In the case of two polymorphs enantiotropically related, the thermodynamic stability between the two is a function of temperature and pressure; there is a temperature of transition (T_t) and the transition is reversible. Thermodynamically, polymorph I is the stable form below the transition temperature, while, above that temperature, form II is the stable one. The transition point can be measured by thermal analyses, solubility or a combination of solubility measurements and enthalpies of fusion.

For the case of monotropic polymorphism, only one polymorph is stable at all temperatures below its melting point. As can be seen in Figure 1.1.b, the free energy curves of the two forms do not cross, making a reversible transition before the temperature of fusion an impossible process.

There are cases in which a polymorph can be monotropically related to a second polymorph, but enantiotropically related with a third, as occur in the case of flufenamic acid. This can be an undesirable effect because one form, thermodynamically more stable, could be hidden by kinetic conditions. The existence of enantiotropism between polymorphs indicates that the relative stabilities between one form and the other are very similar, so that to foresee polymorphism is a difficult matter.

A summary of the main differences between enantiotropy and monotropy is given in Table 1.1.

Enantiotropy	Monotropy
Transition point lies below the melting point.	Transition point lies above the melting point.
Transition point is reached under ordinary (atmospheric) pressure.	Transition point is not reached under ordinary pressure.
Each polymorphic variety is stable over a given range of temperature and pressure.	One variety is always metastable with respect to the other.
The polymorphic change is reversible in the solid state.	The change is irreversible in the solid state.
If the first variety is heated, it changes into the second at the transition point. This second variety then melts at a higher temperature.	On heating gently, the metastable polymorph will melt and then solidify to give the stable variety which melts at a higher temperature.

Table 1.1. *Summary of the main differences between entatiotropic and monotropic systems.*

From a thermodynamic point of view, only one polymorph can be the stable form under specific experimental conditions. It is important to remember that kinetic processes also play a significant role in the definition of the various polymorphs. Hence, metastable forms can exist or co-exist with more stable ones. However, depending on various conditions, such as temperature, pressure and humidity, a metastable form can convert into a thermodynamically more stable modification and an anhydrous crystal can transform into a hydrated form, due to the absorption of vapour from the environment. In most cases, the last obtained crystalline form has different properties than the crystal with which the process has started.

1.2.3. Applications of polymorphism

The importance given to the phenomenon of polymorphism is due to the fact that crystalline or amorphous phases, although formed by the same molecules, can exhibit different chemical, physical and mechanic properties, leading, sometimes, to huge modification in their performances and, consequently, in their use and behaviour. Some of the properties that can change with a polymorphic transformation are: physical and thermodynamic properties, such as density, refraction index, thermal and electric conductivity, melting point, chemical potential, free energy, thermal capacity, vapour pressure, solubility and thermal stability; spectroscopic properties, such as vibrating and rotating electronic properties, nuclear magnetic resonance and spectrum characteristics; kinetic properties, such as rates of dissolution, kinetic characteristic of solid state reactions, stability; mechanic properties, such as hardness, thermal expansion; chemical properties, such as chemical and photochemical reactivity.

This change in a wide range of properties with the conversion of one polymorph to another has extensive implications both from a scientific and an industrial point of view. It is well known that

the phenomenon of polymorphism can be observed in many application fields, for example in the case of explosives, pharmaceuticals, food, pigments, and agrochemicals.

The main objective of an industry is to provide the customer with a product with well known behaviour and properties, and stability over time. In this context, the exhibition of polymorphism can be a huge disadvantage: if a polymorphic transformation occurs, the product in question might lose the characteristics for which it was prepared.

In the industry of explosives, polymorphism is of high importance, since by varying the crystal form, the sensibility to detonation, for example, may also vary. The well known explosive 2,4,6-trinitrotoluene constitutes evidence of the risks that polymorphism can cause.

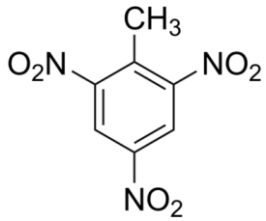

Figure 1.2. *Molecular structure of 2,4,6-trinitrotoluene (TNT).*

2,4,6-trinitrotoluene, TNT, is one of the most used explosives worldwide; in respect to spontaneous detonation, it is stable under a wide range of temperature, meaning that its manipulation is relatively safe. However, it can be a problematic material in relation to its polymorphic behaviour. It exists in two forms, structurally very similar: the metastable orthorhombic form (Figure 1.3.a) converts into the stable monoclinic modification (Figure 1.3.b) during time.

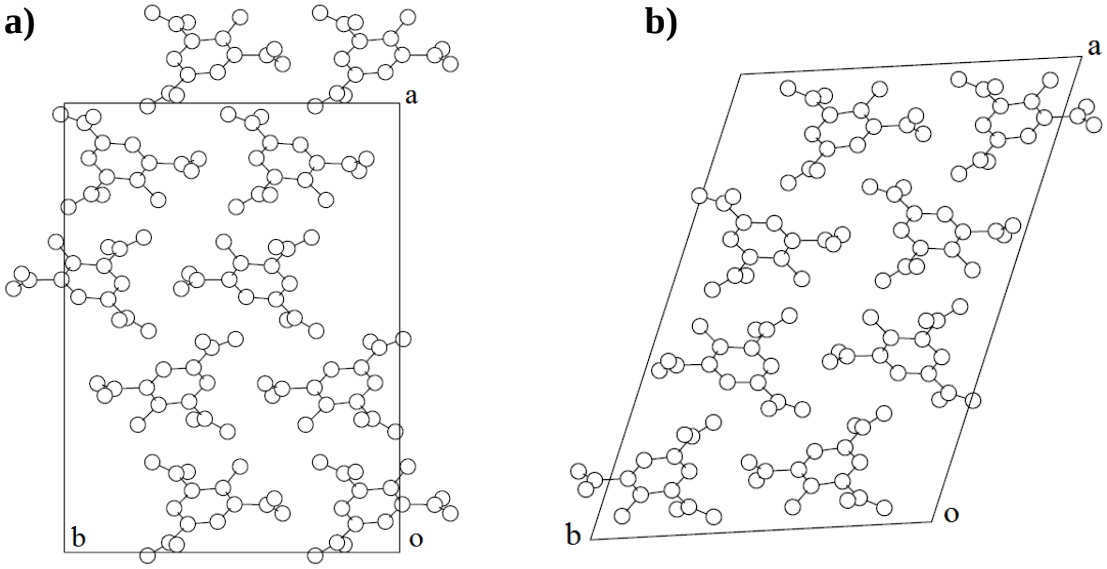

Figure 1.3. *Crystal packing in (a) orthorhombic and (b) monoclinic modifications of TNT*[4].

This transformation in the solid state causes macroscopic defects such as cracks and holes in the form obtained after the conversion, increasing the sensibility of the material to detonation and making it more difficult to work with, especially in a controlled situation, like demolition in confined places.

Another field in which the phenomenon of polymorphism can represent a disadvantage is in pharmaceuticals. In this case different crystalline forms can cause changes in the bio-availability, absorption and solubility of the active compound. Among all the parameters that might change with a polymorphic transition, surely the most important is the bio-availability. This property is defined in terms of velocity and quantity with which the drug reaches the whole body. Generally, the aim is to produce a form with fast and complete absorption, especially when used against pain, allergy, insomnia and those cases in which a prompt action is required. A clear example of the consequence that polymorphism can have on a substance is represented by the drug *Ritonavir (Norvir)*, used for the cure of the HIV virus (HIV-protease). The unexpected appearance of a more stable and less soluble form forced the manufacturer *Abbott* to pull back the drug from the market for a long period of time and to replace the solid form with a suspension, with consequent problems related to its stability other than economic and marketing damages. Another example proving the problem associated with polymorphism is the case of the drug *Novobiocin*, whose molecular structure is reported in Figure 1.4.

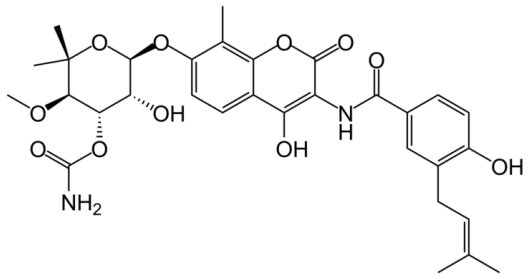

Figure 1.4. *Molecular structure of Novobicin.*

It is an antibiotic with an action similar to that of penicillin; it is used for the treatment of infection due to germs resistant to penicillin or for patients that show an allergic reaction to penicillin. Generally, it is prepared in crystalline form, as sodium or calcium salts, or in its amorphous state, which lacks the long-range order of crystals and the molecules are not related by symmetry relations, increasing its solubility. Comparative studies between the sodium salt and the crystalline and amorphous forms proved that the amorphous state is ten times more soluble than the crystalline form and has an efficacy comparable to that of the sodium salt with the advantage of a higher solubility. However, the amorphous state is a metastable form and it undergoes a polymorphic transformation leading to the stable crystalline form. In the case of Novobiocin this transformation

can occur in a few months, reducing the lifetime of the drug. There are many ways with which this process can be slow down: for example, substances that thicken the formulation can be used, increasing the viscosity and, consequently, the solubility.

The phenomenon of polymorphism also affects the food industry: it is known that the behaviour of fats, sugars and polysaccharides can vary during manipulation, packaging and storage, depending on the polymorph, leading to the deterioration of the product. Chocolate[7] can be taken as an example: it can easily happen in tasting a chocolate bar that, instead of being soft and foamy, it is hard and grainy. This is due to a polymorphic transformation of the cocoa butter from a polymorph with a melting temperature similar to the temperature inside the mouth to a more stable form with a higher melting temperature.

It is interesting to notice how polymorphism affects the behaviour of pigments. When thet are used as dyes, their solubility and dissolution rates are key features for their application, but pigments also play a crucial role in the chemistry of photographic processes and in the development of new technologies. They are classified in the *Color Index*, where each pigment is denominated with a number. Since pigments are used as solid formulation, the chemistry of their solid state, their properties and the crystalline structure are aspects of high importance. A typical physical property that can highly affect the behaviour of this kind of material is their size distribution. It is known that, due to reasons related with the surface energy, smaller pigment particles are more inclined to form conglomerates, changing the behaviour of the solid state. A certain number of physical properties define the use of a material as a pigment and these properties can vary by varying the polymorph. An example is the *tinctorial strength*, a measurement of the pigment ability to absorb and disperse light, linked with the maximum molar extinction coefficient, ε_{max}. This coefficient essentially derives from molecular properties which follow perturbations due to different correlation between the molecules in the solid; this means that different polymorphs can produce different perturbations and, consequently, different properties. Other properties that highly determine the behaviour of a pigment are its solubility; its *lightfastness* and *weatherfastness* that indicate the strength against degradation after exposure to light and weather conditions, respectively; the specific surface area, measured as surface area per weight unit; the inclination to form conglomerates, which defines how much the pigment can be dispersed into a buffer; and, finally, its crystalline state, which will determine its ultimate application. All these factors change within different polymorphs. An exhaustive example of polymorphism in pigments is the case of the copper phthalocyanine (CuPc), which shows a range in colour that can vary from a greenish-blue shade to a reddish-blue one. The molecular structure of CuPc is reported in Figure 1.5.

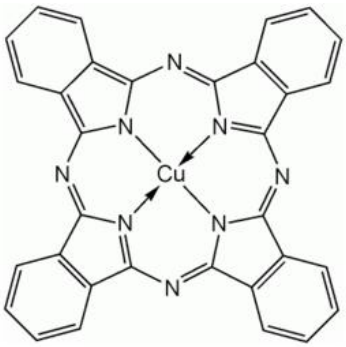

Figure 1.5. *Molecular structure of the CuPc.*

CuPc can crystallize in five polymorphs, named with the letters of the Greek alphabet, α, β, γ, δ and ε; but four other forms are present in the literature, 'R', 'π', 'X' and 'ρ', although it is not yet clear whether these forms are real or are just a misunderstanding in the nomenclature. Proof for the existence of the different polymorphs of CuPc was provided in 1997 by Herbst and Hunger[8], who reported a comparison of X-ray powder diffraction patterns of the five modifications, which are shown in Figure 1.6.

Figure 1.6. *X-ray powder diffraction patterns of the five polymorphs of CuPc*[4].

In 1974 Horn and Honningam[9] determined the stability of the five forms, based on studies on the solubility of each form in benzene. The results are as follows, $\alpha = \gamma < \delta < \varepsilon < \beta$, from which it can be seen that the most stable form is the β modification.

The crystal packing of all forms is governed by the stacking of the molecules into parallel lines, differing by the orientation exhibited by the phthalocyanine ring. In Figure 1.7, a comparison between the crystal packing of α and β modifications is reported.

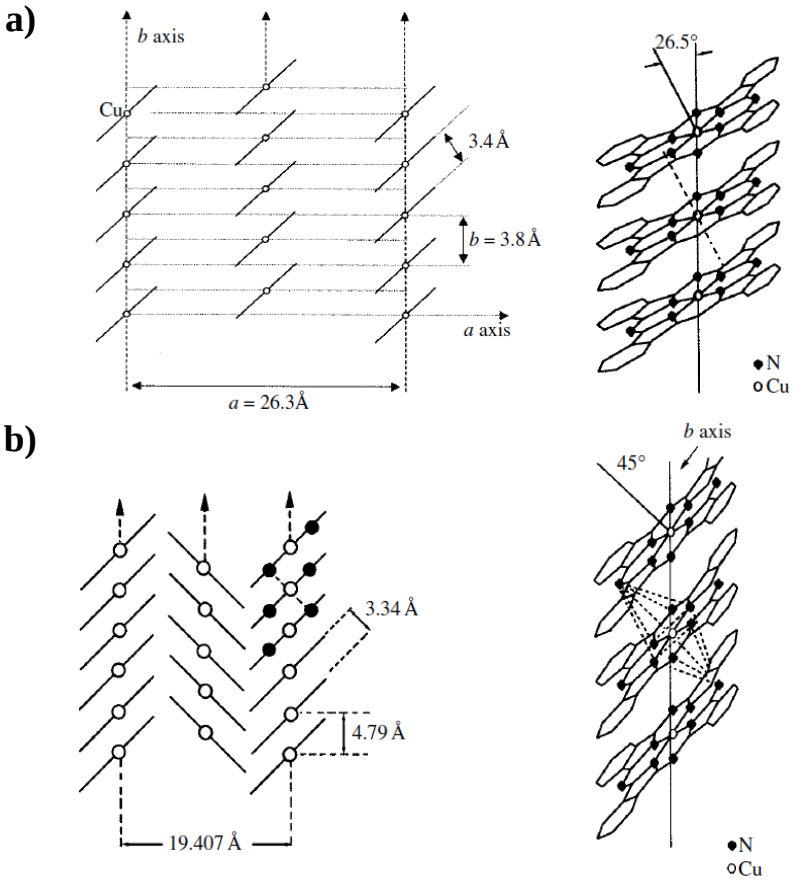

Figure 1.7. *Crystal packing for (a) triclinic α-CuPc and (b) monoclinic β-CuPc*[4].

All the structural differences in the arrangement of CuPc molecules cause the different colour shades for the five modifications: the β-form has a greenish-blue shade, while, at the opposite, ε-form has strong reddish-blue shade.

A well known example of the expression of polymorphism in agrochemicals is the herbicide *Methazachlor (MTZC)*, 2-chloro-N-(2,6-dimethylphenyl)-N-(pyrazol-1-ylmethyl)-acetamide, trade and chemical name, respectively, whose molecular structure is reported in Figure 8, produced by BASF in 1976. It is a chloroacetanilide derivative and one of the most widely applied herbicides against weeds in potato, rape, soybean and tobacco crops; it is usually formulated and marketed as an aqueous suspension.

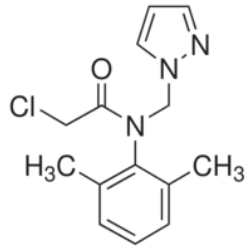

Figure 1.8. *Molecular structure of Metazachlor (MTZC).*

From the literature[10] it is known that this herbicide crystallizes in five different polymorphs, named following the Kofler notation, with Roman numerals in the order of the melting points, from the highest to the lowest. A summary of the melting temperature for all modifications is reported in Table 1.2.

Modification	Melting temperature
I	83˚C
II	80˚C
III	76˚C
IV	72˚-74˚C
V	65˚C

Table 1.2. *Melting point for the five polymorphs of Metazachlor.*

Among the polymorphs, form III is the most stable form, the one usually present in commercial samples. Form I is stable at high temperatures and it can be obtained by crystallisation from aqueous solution at 66˚C, starting from form III or II. It can also crystallise from ethanol, but a slow cooling of the solution is necessary. A transition III → II or I → II can be achieved in water at 61˚C, but modification II can also crystallise from organic solvents, such as n-hexane, acetone, methanol and ethanol. Polymorphs IV and V can only be produced by melting the stable form III. Unfortunately, they are highly unstable and can convert back to form III by simple exposure to air, since humidity seems to induce the transformation.

X-ray powder diffraction is the technique that allows the best discrimination between the modifications, as shown in Figure 1.9. Unfortunately, in the literature the powder patterns for forms IV and V are not reported.

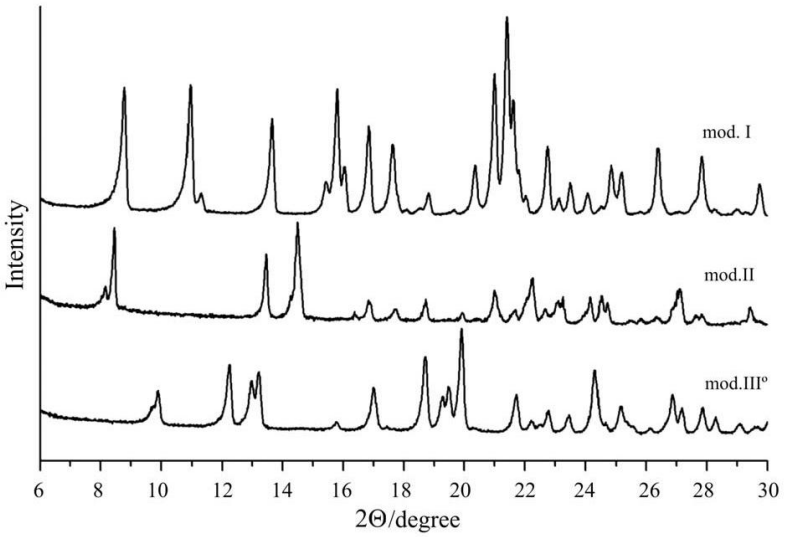

Figure 1.9. *X-ray powder diffraction patterns for modifications I, II and III of Metazachlor*[10].

Studies on the thermodynamics, performed by Griesser[10] and collegues, of the five polymorphs of MTZC conclude that forms IV and V are too unstable to be isolated and analysed, while form I is stable at temperatures higher than 60˚C, form III is stable at temperatures below 55˚C and form II is stable in the narrow range of temperatures between the other forms. Moreover, the metastable forms I and II are kinetically more stable, can crystallize from solvents and be present in commercial samples. Since metazachlor is used as an aqueous suspension, the presence of metastable forms in the formulation can represent a problem if a conversion to the more stable form occurs, because this might lead to a modification in the particle size distribution and to the formation of large particles that might obstruct spray-nozzles when the product is used on the crop field.

Contrary to what discussed above for pharmaceuticals, it is important to clarify that high stability of an agrochemical compound is not always a valuable property. Due to the massive production and usage of pesticides and herbicides, release of these substances in waters or soil is common, increasing contamination effects, which are caused by the intrinsic toxicity of some agrochemicals, and consequent accumulation of the chemical materials. Detoxication, through mineralisation or biodegradation processes, can be achieved in soil thanks to non-enzymatic or enzymatic reactions undertaken by microorganisms present in the ecosystem. The conversion of organic compounds in inorganic products by microbial activity is correlated to an increase in the microbial population, because the organisms responsible for this transformation can use the carbon present in the substrate and convert it to cell constituents, acquiring energy for the biosynthesis. It follows that the mineralisation process is connected to a growth of the microbial population. However, it has been noted that some chemicals do not abide to this behaviour, meaning that the degradation of the organic molecule is not associated to an increase in the number of the microorganisms present in the ecosystem[11]. The mineralisation of the toxic chemical is still undertaken by microbial

populations, as confirmed by the transformation of the compound in non sterile products, but these populations are not capable of using the substrate as an energy source. This different mineralisation process is known as cometabolism. Examples of chemicals that cometabolise are DDT and many chlorinated and non-chlorinated molecules. A characteristic of cometabolism is the slow process of biodegradation of the organic molecules by bacteria, since the latter need to find alternative sources of energy. The main consequence is that often cometabolism causes only small changes in the molecule and does not affect those functional groups responsible for the toxicity, leading to accumulation of the chemical in the soil for longer periods of time.

Thus, the design of agrochemicals always requires extensive knowledge on the behaviour of the compound in the solid state in order to be able to balance the need for stability upon storage or formulation to successful detoxication processes.

1.2.4. Formation of polymorphs

The screening of new polymorphs of one compound can be achieved by several methods, which involve crystallisation processes from saturated solution using different solvents or by mechano-chemical reactions.

Crystallisation is a multi-step mechanism, involving nucleation and crystal growth; these two steps can determine the nature of the polymorph which will grow from a certain solution. In most cases nucleation is the critical part of the process. Two different kinds of nucleation can be outlined:

i. primary nucleation, which defines the formation of nuclei of growth inside the solution. It is called homogeneous primary nucleation if the formation of the nuclei is spontaneous in the bulk; otherwise, if the nucleation occurs on interfaces or is induced by unrelated particles the process is called heterogeneous primary nucleation;
ii. secondary nucleation, in which small crystals of the material to be crystallised are already present in the solution (seeding process). Of course, in this case, the solution must be already saturated in order to avoid dissolution of the seed crystal. Secondary nucleation is usually applied in growing crystals of a particular modification.

The selectivity in growing polymorphs can be achieved by varying different parameters, which affect the arrangement of the molecules in the solid state: temperature and rates of cooling; concentration of the solution and, consequently, saturation; solvent used, so to find the right solute-solvent interaction that might play a role in determining the crystal packing of a material; rates of nucleation; altering the pH of the solution; addition of additives. Over the years, experience has shown how important the choice of the right solvent is. The solubility of a particular compound in the chosen solvent must be between 5 and 200 mg/ml at room temperature. This is due to the fact

that high solubility implies high viscosity, leading to the formation of amorphous forms, while high boiling solvents can promote the crystallisation of metastable forms.

The rate of nucleation plays also a key role in the formation of a polymorph over another. This rate can be affected by different factors, such as stirring rate, level of supersaturation, seeding, impurities and temperature. The same considerations can be extended to the rate of growth, which can be affected by temperature, stirring, density and viscosity of the solvent. In most cases the optimal temperature for the nucleation is not the same as the one for the crystal growth; consequently, a balance between the two must be achieved. For example, for a compound that can crystallise in two different modifications, these forms will have different solubility curves, and the formation of one form rather than the other depends on which conditions of temperature and concentration are chosen. Figure 1.10 shows the solubility diagram for a dimorphic system, in which the arrow indicates a possible crystallisation pathway at constant temperature.

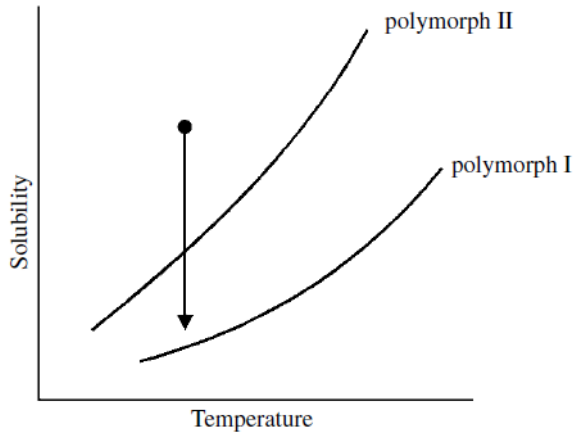

Figure 1.10. *Schematic solubility diagram for a dimorphic system*[4].

Although many studies have been carried out over the years regarding the subject of polymorphism, control over nucleation, crystallisation and composition of the crystalline phases are still a scientific challenge. It is difficult to predict if a compound will crystallise in one or more crystalline forms, or if it will interact with the solvent or with other molecules in the solution, forming stable materials. This uncertainty and unpredictability are considered by most scientists to be an inevitable limit in the design and building of desired materials.

Other than crystallization from solution, the conversion of one polymorph into another can be induced by mechano-chemical stresses on the material. It is usually forgotten that the efficiency of chemical reactions in the solid state is comparable to those occurring in solution. Advantages of reactions carried out in the solid state are multiple, such as decrease of pollution, since solvents are no longer required; decrease in cost of production, because the use for solvents it is not necessary and, usually, solid state reactions show high yields; and increase in the simplicity of the process,

due to the fact that the only process to take place is the grinding process. The limitations of this technique lie in the fact that crystals obtained by this method are not always of sufficient quality for single crystal X-ray diffraction experiments.

Analogous to the grinding, the kneading, also called solvent-drop grinding, is especially used for the synthesis of co-crystals. In this method one or more components are ground with the addition of a catalytic amount of solvent. This accelerates the reaction, leading to higher yields and, in some cases, offers the opportunity of controlling polymorphism, inducing the formation of one form rather than another. This is, for example, the case of a co-crystal of caffeine and glutaric acid[12], which shows polymorphism. The different polymorphs can be obtained by using different solvents during the kneading process.

1.2.5. Characterisation of polymorphs

It is known how different crystalline forms of the same compound show different properties, as colour, solubility, density, melting point and electric or thermal conductivity. However, exhaustive studies proved that the simple observation of these different properties does not necessarily imply the presence of polymorphism. If it is correct to state that the change in behaviour of a polymorph is caused by the different arrangement of atoms, molecules and ions inside the crystal structure, it follows that the only way to prove the presence of polymorphism is the structural analysis of a material. Various spectroscopic techniques, such as infrared and Raman spectroscopy or NMR, can be used for that purpose. Nevertheless, X-ray and neutron diffraction are the most appropriate methods for this study. Indeed, the diffraction techniques are based on the type of spatial arrangement displayed by atoms, molecules and ions inside the crystal structure: different arrangements exhibit different diffraction images. There are two methods usually employed: single crystal diffraction and powder diffraction. The advantage in using powder diffraction is the fact that is not necessary to determine the lattice dimensions; the diffraction pattern itself can distinguish between true polymorphs. For more in depth studies, in order to understand the reasons behind the formation of polymorphs, it is necessary to characterize each polymorph by single crystal diffraction, which allows obtaining atomic coordinates and thermal vibrations.

Powder diffraction gives information about the crystal structure of a solid through the formation of a diffraction image. The diffraction image of a solid can be plotted in an intensity of diffraction I vs. 2θ value graph and can be considered as the fingerprint of a crystalline solid. The value of the distance between crystallographic planes reflects the dimensions of the unit cell, while the intensity of diffraction is due to the kind of atoms or molecules contained in the lattice and to their arrangement. Since the various crystalline forms of a solid are characterised by different cell parameters and, especially, by different arrangements, they will give different diffraction patterns; this explains the benefit given by X-ray diffraction in the study of polymorphism.

As said previously, when applying diffraction techniques to the study of molecular solid, in general, and to polymorphic systems, in particular, it is necessary to distinguish between two methodologies: powder diffraction and single crystal diffraction. Generally, the former is used for a qualitative and quantitative identification of polymorphs, while the latter allows achieving a detailed determination of the molecular and crystal structure of a solid. In particular, single crystal diffraction gives information about thermal vibration of the atoms inside the unit cell. The use of both methods allows reaching more detailed and more precise crystallographic studies.

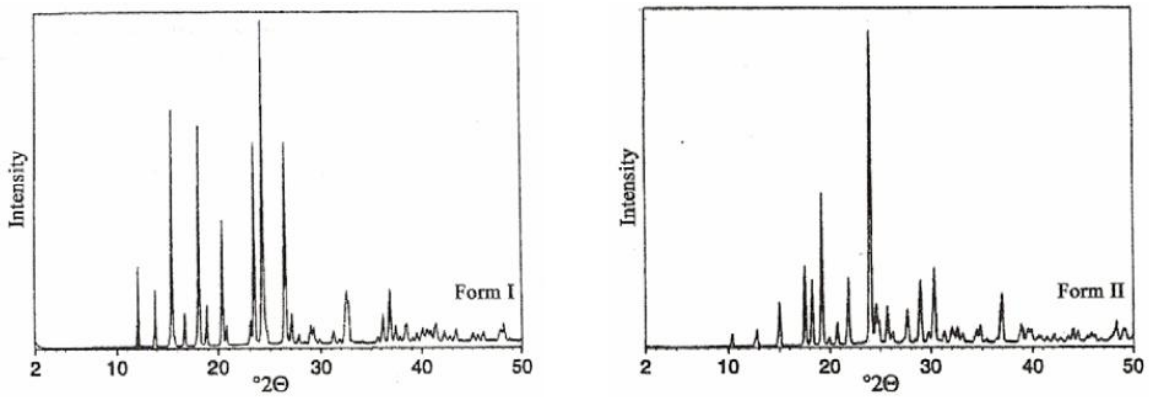

Figure 1.11. *Powder patterns (I/2θ) of two polymorphs of paracetamol*[4].

By simple observation of the two powder patterns reported in Figure 1.11, it is possible to recognize distinct differences in the diffraction patterns of paracetamol, indicating the presence of two polymorphs of the material.

However, in the literature there are cases of polymorphs of the same compound, showing very similar diffraction patterns. An example is represented by two modifications of terephthalic acid, whose powder diffraction patterns are reported in Figure 1.12.

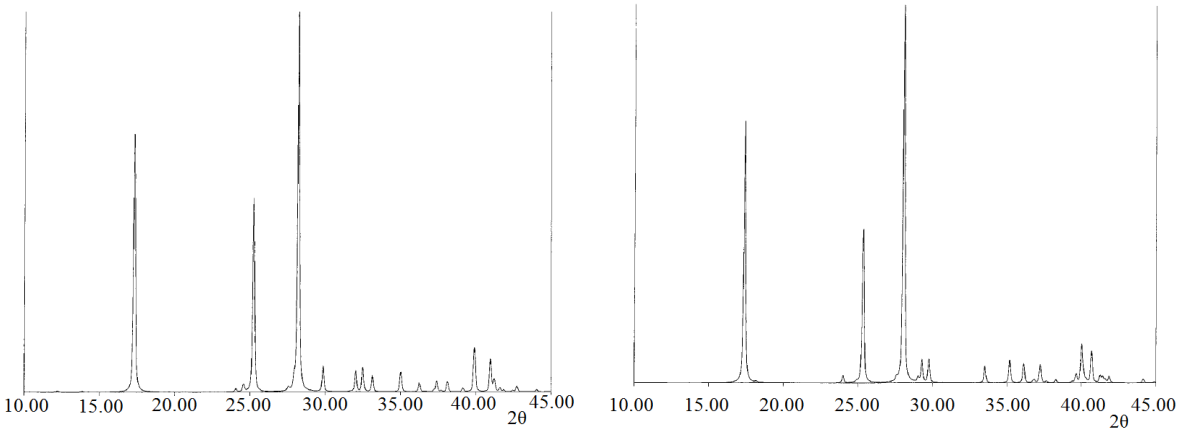

Figure 1.12. *Powder patterns of the two polymorphs of terephthalic acid*[4].

Differences between the two patterns can be found in the region of $2\theta > 30^{\circ}$. The existence of these kinds of pattern is justified by considering the structure of the two forms. According to Berkovitch-Yellin and Leiserowitz (1982) and Davey[13] in both structures there are infinite chains of hydrogen bonds. These chains are organized in two bi-dimensional planes and the distance between neighbouring planes is the main difference between the two crystal structures, which are depicted in Figure 1.13.

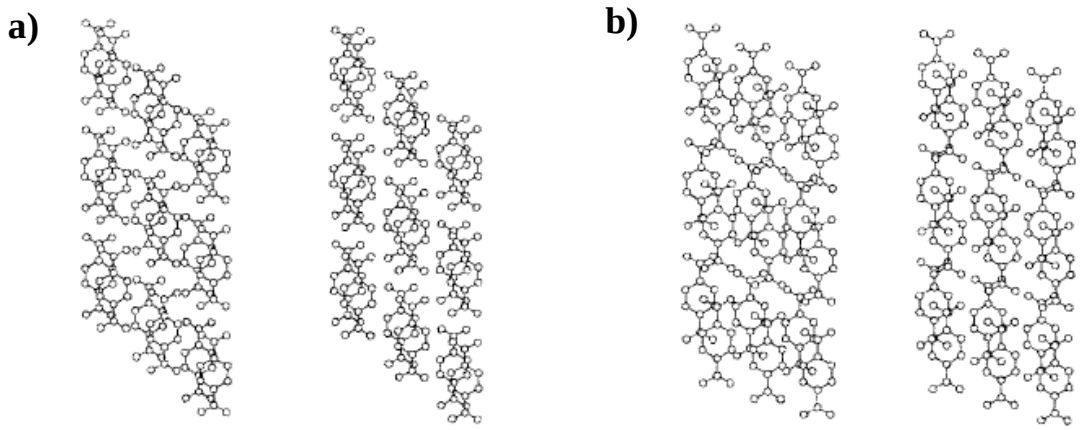

Figure 1.13. *Stereographic representations of the structures of the two polymorphs of terephthalic acid; a) form I; b) form II*[4].

Both polymorphs crystallise in the triclinic system, space group $\boldsymbol{P\bar{1}}$, and are made of planes, linked together by hydrogen bonds. The main difference between the structures is the different orientation adopted by the planes.

The preparation of the sample for the diffraction experiment could induce changes and disagreements during the measurement of the sample itself. Jenkins and Snyder[14] describe possible causes on variation of the composition of a sample prepared for the analysis: grinding the sample can cause amorphism; a distortion of the particles which form the solid can occur; decomposition of the sample; solid state reactions or contamination. Furthermore, the radiation used during the diffraction experiment can cause changes inside the material, for instance, polymerization, decomposition or transformation into an amorphous state. Finally, working conditions, such as humidity and temperature, which can lead to addition or loss of solvent, play a very important role in the outcome of a diffraction experiment. All these factors need to be taken into account during the interpretation of diffraction patterns.

Jenkins and Snyder pointed out one problem in particular, which they defined as the most responsible factor in sample variations: a preferred orientation of the crystallites, an example of which is reported in Figure 1.14. Preferred orientation is especially present in crystallites that have a non-spherical habit. These crystallites show a tendency to orient along one direction, for example

the longer axis for needle-shaped crystallites, in order to occupy the minimum volume possible. This can cause decrease in intensity of those Bragg reflections that cannot be in diffracting conditions due to the preferred orientation. The effect of preferred orientation can be reduced by grinding the sample before the experiment or by spinning it.

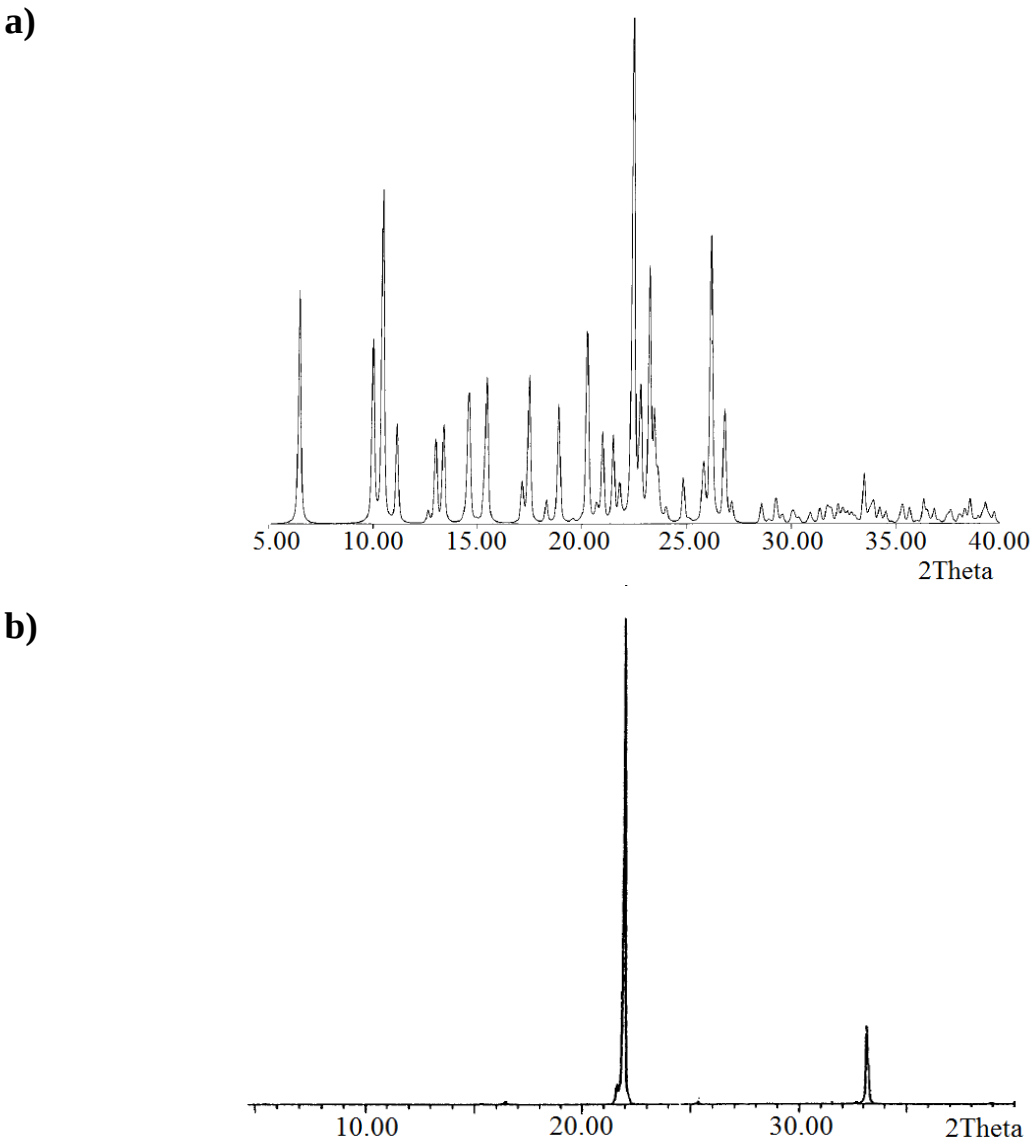

Figure 1.14. *Influence of the preferred orientation of the crystallites in the form III of sulphathiazole: a) calculated and b) experimental powder pattern*[4].

In the case of sulphathiazole, the two authors suggested a useful way to avoid this phenomenon was to prepare the sample by spray-drying. However, a side-effect of this solution was the possible loss of the polymorph. It is, now, necessary distinguishing between polymorphic identity and polymorphic purity: the former is a qualitative determination; substantially, the question is whether or not a polymorph is present inside a sample. The latter is a quantitative analysis and leads to the assumption of having a chemically pure sample, containing only polymorphs.

The chemists Zevin and Kimmel[15] and Stephenson[16] summed up the various techniques for a quantitative analysis using X-ray diffraction. All these techniques assume that the integration of a diffraction peak is proportional to the amount of polymorph present in the sample. However, a diffraction peak can be affected by different phenomena, such as absorption of the incident radiation or overlapping of neighbouring peaks so that appropriate corrections might become necessary.

Resourceful methodologies in the screening and characterisation of polymorphs are thermal analyses, in particular the differential scanning calorimetry (DSC). This technique is based on the principle that any variation in the structure of a sample is accompanied by emission or absorption of heat, indicating exothermic and endothermic processes, respectively. An example of the information that can be gained through a DSC analysis is represented by sulphapyridine[17].

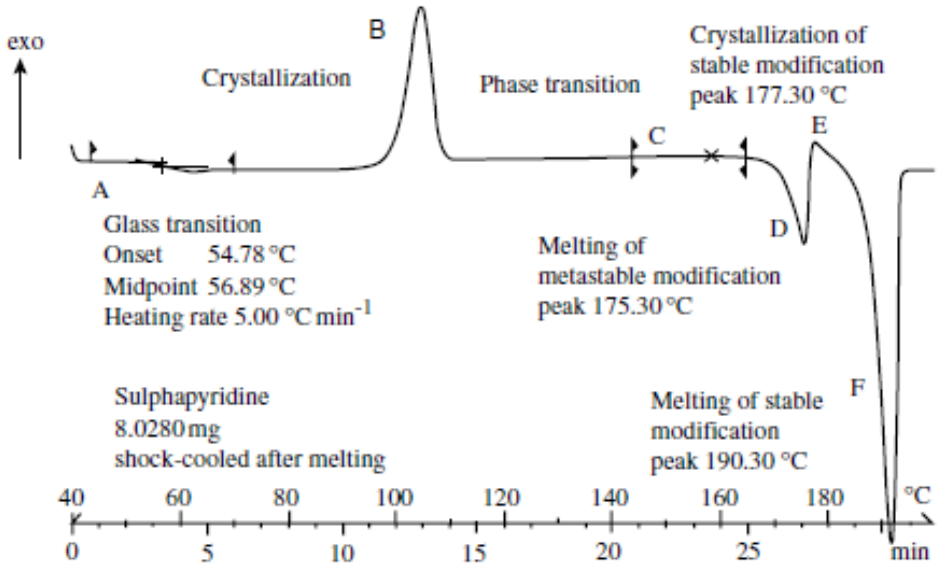

Figure 1.15. *DSC profile for sulphapyridine*[4].

As displayed in Figure 1.15, the DSC profile of sulphapyridine shows all structural variations that occur with increasing temperature. The starting material is the amorphous phase of sulphapyridine, which is obtained by rapid cooling of the molten substance. The first thermal event at 56.89˚C is a glass transition (A) indicating the formation of an unstable supercooled liquid, which crystallises around 110˚C (exothermic event B). After reaching a temperature of 145˚C, a monotropic phase transition (C) occurs, leading to the formation of a metastable phase (D) that melts at 175.30˚C. Finally, it follows the re-crystallisation of the stable polymorph (E), which has a temperature of fusion of 190.30˚C (F).

An additional advantage of the DSC method lies in the possibility of discriminating between monotropic or enantiotropic polymorphism, although the kinetic properties of the phase transition

must be considered. Figures 1.16 and 1.17 report the DSC profile for a dimorphic system for the monotropic and enantiotropic cases, respectively.

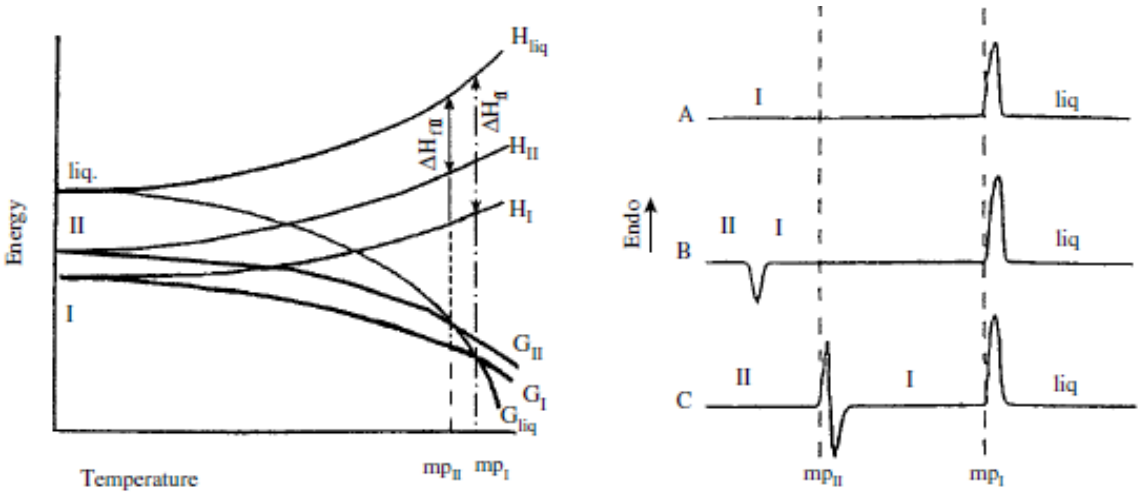

Figure 1.16. *Free energy-temperature plot (on the left) and DSC profiles (on the right) for a monotropic dimorphic system. Form I is the stable form at temperatures below the melting point*[4].

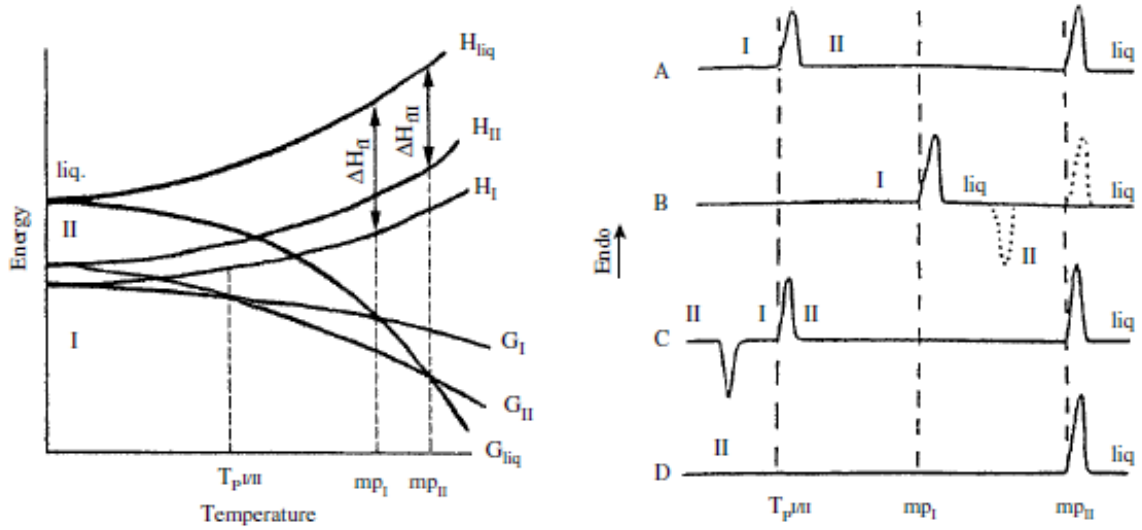

Figure 1.17. *Free energy-temperature plot (on the left) and DSC profiles (on the right) for an enantiotropic dimorphic system. Form I is the stable form at temperatures below the melting point*[4].

Considering the monotropic system, trace A of the DSC results shows only the endothermic event corresponding to the melting of the thermodynamically stable form I. Traces B and C display the metastable form II as starting material: in the former it is possible to notice the monotropic phase transition from form II to form I and the consequent melting of form I, while the latter displays the melting of the metastable form followed by the re-crystallisation of the stable form I and its melting.

In the case of a dimorphic enantiotropic system, starting with stable form I and depending on the kinetic characteristics of the transition, two DSC profiles can be obtained: one (trace A) shows the conversion of form I into form II at the transition temperature $T_{pI/II}$, after which the melting of the metastable form II occurs (mp_{II}); a second (trace B) displays the fusion of form I, a re-crystallisation of form II and the final fusion of form II (form II is indicated by the dotted line). When the starting material is the metastable modification, depending on the experimental conditions, either the metastable form II only shows the melting event (trace D), or it can first crystallise exothermically into the stable form I, which, in turn, at the transition temperature convert back to form II (trace C).

1.3. Hydrogen bond

1.3.1. Historic background

The hypothesis of molecular association through attractive or repulsive interactions began in the second half of the nineteenth century when chemists started to notice that some substances, such as alcohols and phenols, were more likely to show associated complexes than others, for example hydrocarbons. In 1902 Alfred Werner[18] in his studies of ammonium salts suggested that in their association the ammonia molecules and anions shared a proton, which lied between the two; he symbolised this concept by the notation $(H_3N\cdots H)X$. Years later Moore and Winmill[19] agreed with Werner's findings in the study of trimethyl ammonium hydroxide, to which they assigned the structure Me_3N-H-OH that was held responsible for the slight dissociation of the compound compared to tetramethyl ammonium hydroxide. Just a few years after Werner's theories, an intramolecular interaction involving hydrogen atoms was detected in some azo derivatives of eugenol by Oddo and Puxeddu[20] and in 1913 Pfeiffer[21] *et al.* found a similar intramolecular link between the hydroxyl and carbonyl groups of a molecule of 1-hydroxy-anthraquinone. In 1920 revolutionary was the work of Latimer and Rodenbush[22] who identified the hydrogen bond as the cause for the unique chemical and physical properties of water by saying: "*Water ... shows tendencies both to add and give up hydrogen, which are nearly balanced. Then ... a free pair of electron on one water molecule might be able to exert sufficient force on a hydrogen held by a pair of electrons on another water molecule to bind the two molecules together ... Indeed the liquid may be made up of large aggregates of molecules, continually breaking up and reforming under the influence of thermal agitation. Such an explanation amounts to saying that the hydrogen nucleus held between 2 octets constitutes a weak bond*". The term hydrogen bond is attributed to Pauling[23], who used it during the study and investigation of the structure of $[F:H:F]^-$ ions in 1931. Successively, Pimentel and McClellan dedicated an entire book to the phenomenon of the hydrogen bond[24].

Due to the extensive work carried out on the concept of hydrogen bond over the years by many members of the scientific community, it is not simple to find a unique definition for the phenomenon, although all can be connected to either purely empirical considerations or to a more general theory of the hydrogen bond: the former is ascribed to Pimentel an McClellan, who stated that "*a H bond [A-H···B] exists between a functional group A-H and an atom or a group of atoms B in the same or a different molecule when (a) there is evidence of bond formation (association or chelation) and (b) there is evidence that this new bond linking A-H and B specifically involves the hydrogen atom already bonded to A*"; the latter, originally proposed by Latimer and Rodenbush, was suggested by Vinogradov and Linnell[25] in their book *Hydrogen Bonding* and can be reported as "*hydrogen bonding occurs between a proton-donor group A-H and a proton-acceptor group B, where A is an electronegative atom, O, N, S, X (F, Cl, Br, I) or C, and the acceptor group is a lone pair of an electronegative atom or a π bond of a multiple bond (unsaturated) system. Generally, a H-bond can be characterised as a proton shared by two lone electron pairs*". Although the first definition is based on empirical evidence that can be due to the formation of a hydrogen bond and the second lies upon the electronic structure of the interacting molecules, thus being able to predict the formation of hydrogen bonds, the main difference between the two can be found in the fact that according to Pimentel and McClellan all interactions involving hydrogen atoms can be classified as H-bonds, as, for example, the B-H-B bond in boranes. In addition, the second definition highlights the polarity exhibited by a hydrogen bond, which can be represented as $A^{\delta-}$-$H^{\delta+}$···$B^{\delta-}$, excluding, for example, agostic interactions that show an inverted polarity.

1.3.2. Classification of the hydrogen bond

Since its discovery and recognition, the definition of the strength of the hydrogen bond has been based on the electronegativity of the atoms acting as H-bond donors and acceptors. It follows that a first classification divides the hydrogen bonds in four main groups: (1) *conventional H-bonds*, which are characterised by the presence of strongly electronegative atoms, leading to the formation of strong H-bonds; (2) *weak H-bond donors*, which includes all those donors that exhibit low values of electronegativity; (3) *weak H-bond acceptors* and (4) *weak H-bond π-acceptors*, in which the acceptor shows poor affinity for the proton either because it has lower electronegativity than the hydrogen atom or because is already part of an unsaturated system.

In their classification of the *conventional H-bonds*, Gilli G. and Gilli P.[26] outline six subgroups, called *chemical leifmotifs* (*CLs*) for the understanding of the wide variety of hydrogen bond strength and behaviour. A summary of the six *CLs* is reported in Table 1.3.

CL	Name	Acronym	Strength
1	Ordinary H-bond	OHB	Weak
2	Double charged-assisted H-bond	(±) CAHB	Strong
3	Negative charge-assisted H-bond	(-) CAHB	Strong
4	Positive charge-assisted H-bond	(+) CAHB	Strong
5	Resonance-assisted H-bond (π-bond cooperative H-bond)	RAHB	Strong
6	Polarisation-assisted H-bond (σ-bond cooperative H-bond)	PAHB	Moderate

Table 1.3. *Six chemical leifmotifs (CLs) for the definition of conventional H-bonds*[26].

The first class of *CL*, the ordinary H-bond, includes all those hydrogen bonds that do not belong to any other *chemical leifmotifs* and that lead to the formation of weak interactions; their importance resides in the wide occurrence of this type of hydrogen bond in nature. In the second class of *CL* are classified strong hydrogen bonds in which the pK_a values of donor and acceptor are similar, as in the molecular complex pyridine-N-oxide/trichloroacetic acid. Negative or positive charged-assisted H-bonds indicate the formation of strong hydrogen bonds, which can be described with the notations $[X\cdots H\cdots X]^-$ and $[X\cdots H\cdots X]^+$, respectively. The *CL* class of resonance-assisted H-bonds refers to the case in which both donor and acceptor groups are on the same molecule and are placed at the ends of a π-conjugated molecular fragment, for example the dibenzoylmethane enol. Finally, the polarisation-assisted H-bonds, first proposed by Jeffrey and Saenger[27] in 1991, indicates those bonds that organise in chains such as ···O-H···O-H, leading to the formation of moderately strong hydrogen bonds, examples of which can be find in the association of phenol molecules.

A second type of classification of the hydrogen bond can be done considering exclusively the physical properties of an H-bonded system that can be measured experimentally. This classification simply distinguishes among weak, moderate and strong hydrogen bonds and it was first suggested by Jeffrey[28] in 1997. In Table 1.4 a summary of this classification is reported.

H-bond	Weak H-bond	Moderate H-bond	Strong H-bond
D-H···A bond	Electrostatic	Electrostatic-covalent	Mostly covalent
Bond Lengths	D-H ≪ H···A	D-H < H···A	D-H ≈ H···A
H···A (Å)	3.2-2.2	2.2-1.5	1.5-1.2
D···A (Å)	4.0-3.2	3.2-2.5	2.5-2.2
D-H-A angle (˚)	90-150	130-180	165-180
Bond Energy, E_{HB} (kcal mol^{-1})	1-4	4-15	15-45

Table 1.4. *Physicochemical properties of weak, moderate and strong H-bond*[26]*. D-H represents the H-donor, while A is the H-acceptor.*

All properties listed in Table 4 can be measured experimentally either by single crystal X-ray and neutron diffraction for the derivation of the exact atomic positions and investigation of the electron density and atomic mass distribution in H-bonded structures or by thermal analyses and IR and Raman spectroscopies for the characterisation of the bond energies.

Computational methods represent an important tool in the study of the nature and characteristics of the hydrogen bond as they can assess its strength by the production of PT (proton transfer) pathways, which are reported in Figure 1.18 for weak, moderate, strong and very strong H-bonds.

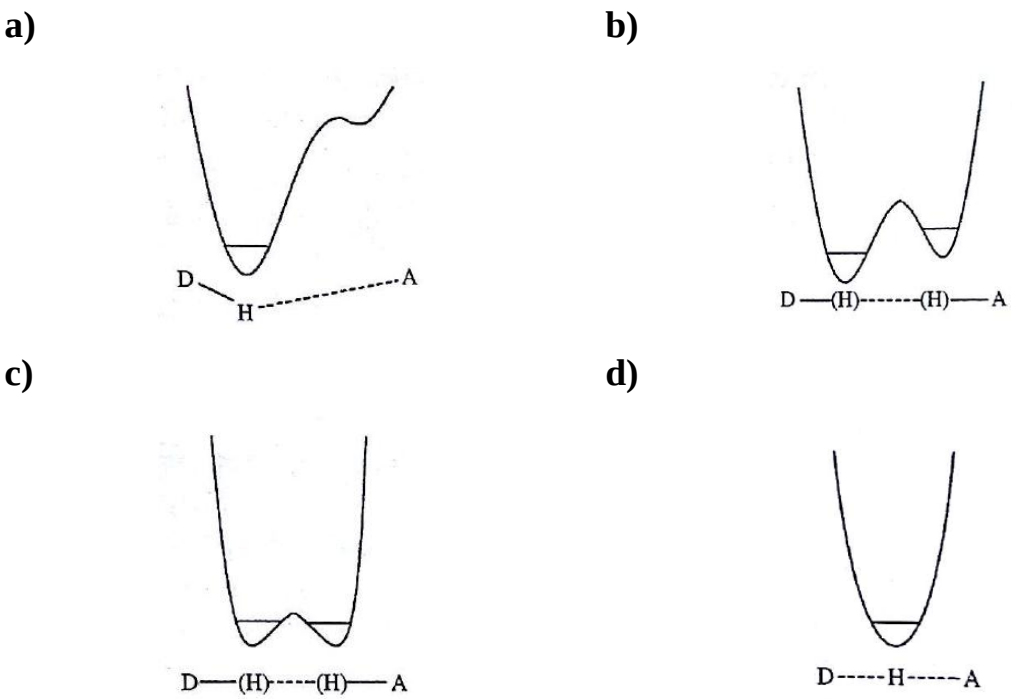

Figure 1.18. *PT pathways for a) weak, b) moderate, c) strong and d) very strong hydrogen bond*[26].

The different shape of the potential energy of the H-bond outlines four cases (Figure 18). Case a) indicates a weak hydrogen bond, in which the proton is bonded to the donor, as the PT barrier to overcome so that a proton transfer may occur is very large; this type of weak H-bond are long, strongly dissymmetric and of electrostatic nature. The PT pathways of b) and c) refer to a moderate and a strong H-bond, respectively. They both formalise the possibility of two sites for the hydrogen atom, indicating the presence of proton disorder. The higher energy barrier in the case of moderate H-bonds entails that disorder can be detected only in crystals, while for strong H-bonds dynamic disorder can be present both in crystals and in solution. The last situation (case d) describes a very strong H-bond, in which the complete absence of the energy barrier allows the proton to be centred between the donor and acceptor groups. These hydrogen bonds are short, symmetric, linear and essentially covalent in character.

For the purpose of this thesis the second classification made by Jeffrey[28] will be the one used for the definition and characterisation of the hydrogen bond.

1.3.3. Proton transfer, migration and disorder

Proton transfer, proton migration and proton disorder all refer to the movement of a hydrogen atom along the H-bond in which it is involved. Their identification is based on the shape of the PT pathway of the interaction and they represent a useful and important tool for the design of materials with specific physical properties because the degree of movement is temperature dependent.

Since proton transfer, which can occur in moderate and strong H-bonds, leads to the formation of charged species, in the same manner as an acid-base reaction, predictions on the appearance of this phenomenon in a specific material, and sometimes even its introduction in a molecular system, can be made considering the pK_a values of the functional groups involved in the interaction. It has been reported[29,30] that when the difference between pK_a values of the H-acceptor (base) and H-donor (acid) is around 3 a proton transfer occurs, leading to the formation of a salt, while for values below zero the result will be a neutral co-crystal. However, cases falling into the range between zero and 3 show inconclusive results, leading to the formation of either a salt or a co-crystal. Evidence of proton transfer were found in the 1 : 1 adduct of diprotic squaric acid and 4,4'-bipyridine (SQBP). In their paper[31] the authors reported two polymorphs of the adduct SQBP: yellow form-I, stable at room temperature, crystallises in the monoclinic system, space group $P2_1/n$, but it converts through a single-crystal to single-crystal transition at around 453K into red form-II, belonging to space group ***C2/c***. Form-I displays only one proton transfer from the acid to the bipyridine molecule, while in form-II the interacting species are present as $[BPH_2]^{2+}$ and $[SQ]^{2-}$. The crystal packing is similar in both modifications and it is governed by the formation of chains of H-bonds of two types, N-H···O and O-H···N. The interatomic distances are N···O = 2.6058(18) Å for the first type of interaction and O···N = 2.6291(18) Å for the second type. Powder neutron diffraction on a deuterated sample confirmed the conversion from form-I to form-II, but highlighted a transition temperature of 488K, which is significantly higher than the non-deuterated adduct, indicating that, indeed, the phase transition involves the proton transfer.

Proton migration indicates a dynamic movement of the proton along the direction of the hydrogen bond due to the fact that its PT pathway is a symmetric single-well with no-barrier (case d in Figure 18). An important characteristic of this type of effect in H-bond resides in the possibility to control the migration by varying the temperature. An example of this type of proton behaviour was reported in the adduct between 4-methylpyridine (4-MePy) and pentachlorophenol (PCP)[32]. In this study a variable temperature (VT) single crystal neutron diffraction (SND) experiment was undertaken to investigate the migration of the hydrogen atom of PCP as a function of temperature.

a) **b)**

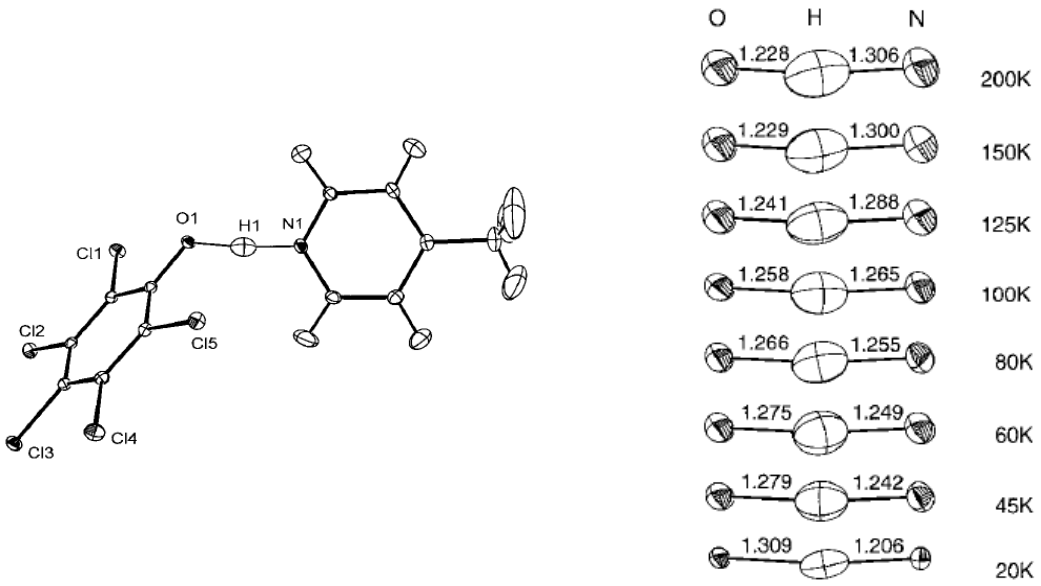

Figure 1.19. *a) Interacting molecules in the adduct 4-MePy/PCP collected by SND at 100K. b) Particular of the hydrogen bond at all temperatures of the VT-SND experiment*[31].

As displayed in Figure 1.19, in the structure at 20K the hydrogen atom is closer to the pyridine nitrogen, while at 200K it is placed closer to oxygen of the PCP molecule.; presumably, it is centred in respect to the O···N distance around 90K. An explanation for this type of behaviour can be found in a slightly asymmetrical potential energy of the hydrogen bond, whose minimum is subjected to a shift that may be due to changes in the crystal packing environment with the varying temperature or to a major contribution of the molecular thermal motion.

The PT pathway describing proton disorder is a symmetrical double-wave with a low energy barrier so that the hydrogen atom can access both proton sites with small costs in energy; it is a proton effect usually detected in strong H-bonds. It is well known that benzoic acid[33,34,35] shows proton disorder in the position of the hydrogen atoms involved in intermolecular interactions between the acid molecules, which organise in dimers, leading to the formation of cyclic H-bonds. Worth of notice are studies on carboxylic acid derivatives, such as 2,4,6-trimethylbenzoic acid (TMBA) and β-9-anthracene carboxylic acid (β-9AC), which retain the positional disorder of the proton involved in an intermolecular H-bond. Variable temperature (VT) single crystal X-ray diffraction (SXD) data were collected on TMBA[36] between 100K and 290K. The investigation of Fourier difference maps for the cyclic hydrogen bond that is formed between two interacting TMBA molecules allows identification of a second site for the proton, which becomes more occupied with increasing temperature. Figure 1.20 reports the electron-density maps for the carboxylic group at the collection temperatures.

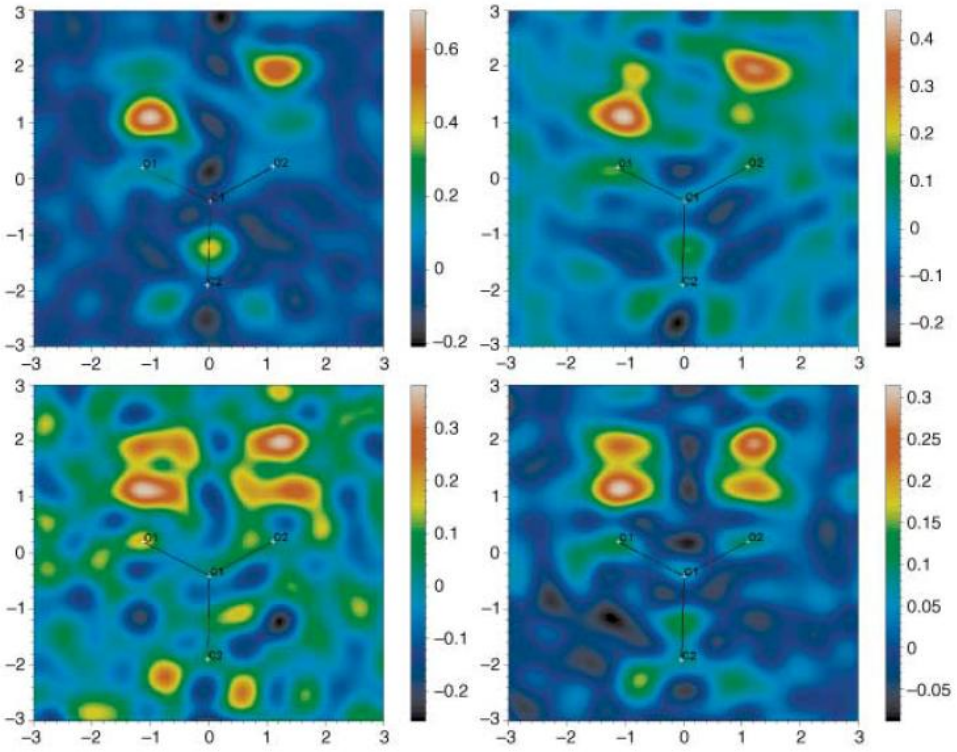

Figure 1.20. *X-ray difference Fourier maps in the region of the carboxylic group in 2,4,6-trimethylbenzoic acid at 100K (top left), 170K (top right), 240K (bottom left), and 290K (bottom right)*[36].

Although the site occupancy factors (***s.o.f.***) cannot be determined accurately due to bonding effects and correlation of ***s.o.f.*** with thermal parameters, the Fourier difference maps clearly indicate the appearance of a second site for the hydrogen atom tuneable by varying the temperature. The presence of disorder is additionally confirmed by the variation in the bond lengths C-O and C=O in the carboxyl group: a shortening for the former and a stretching for the latter.

A similar situation is described in monoclinic crystals of β-9AC[37], where the acid molecules are organised in dimers, interacting via cyclic hydrogen bonds. Investigation of the electron density of the hydrogen atoms involved in the formation of the dimer shows disorder of the protons depending on the temperature of collection.

a) **b)**

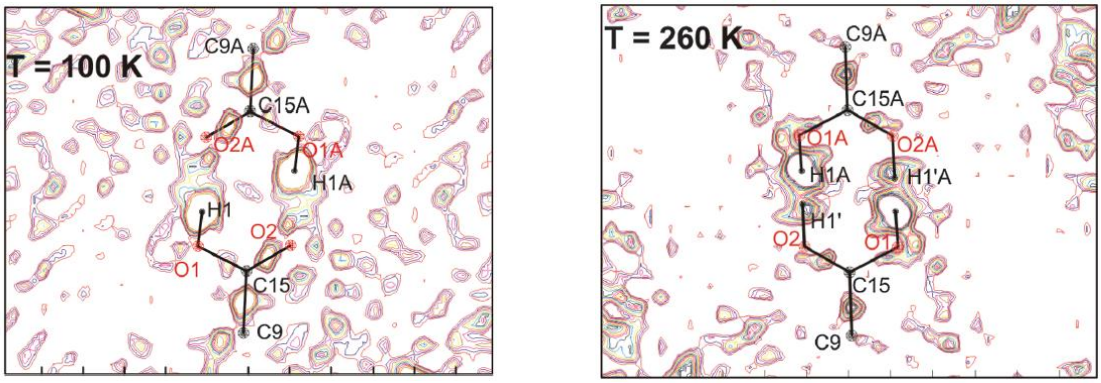

Figure 1.21. *Fourier difference maps for the interacting carboxyl groups in β-9AC monoclinic crystals at a) 100 and b) 260K*[37].

As shown in Figure 1.21, the structure at 260K displays a second site for the hydrogen atom of the hydroxyl on the carboxylic group. The proton disorder is accompanied by a shortening of the single bond C-O and a lengthening of the double bond C=O of the carboxylic group with the increase of disorder, heating from 100K to 260K.

1.3.4. Importance of the hydrogen bond

Numerous are the fields in which the hydrogen bond plays a pivotal role: chemistry and biology in the first place, but surely also material science highly benefits from the many advantages provided by H-bonded systems. In chemistry, for example, resonance-assisted H-bonds participate in the activation of the carbon atom positioned in α with respect to a carbonyl group, which occurs through the formation of an enolate-ion intermediate, but proceeds slowly due to the low acidity ($\boldsymbol{pK_a}$ ≈ 19-21) of the α-carbon, unless a strong base is used. This reaction results to be facilitated, even in absence of a strong base, in the case of β-dicarbonyl derivatives in which the α-carbon becomes a so-called *active methylene*, which highly increases the acidity, exhibiting a $\boldsymbol{pK_a}$ value that is 11-13 times smaller than the simple enolate-ion, as reported in Figure 1.22, depending on the β-dicarbonyl derivative taken into consideration.

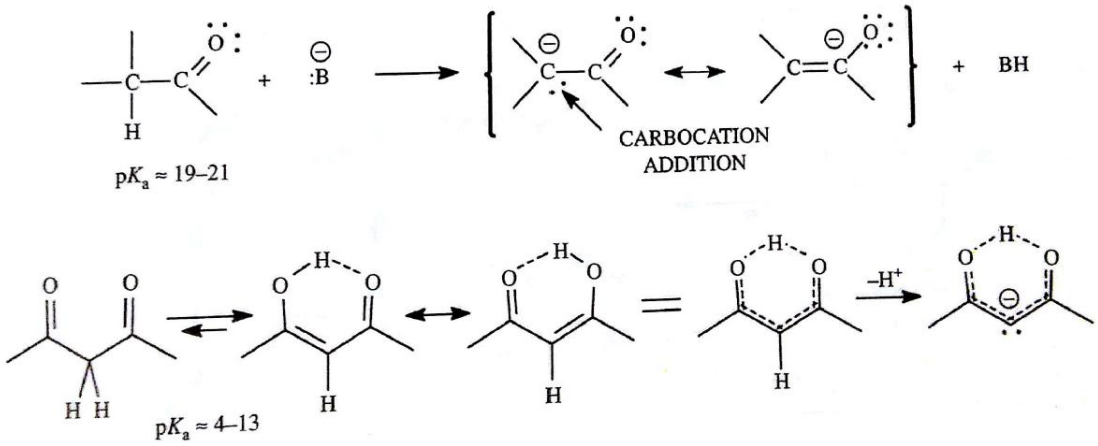

Figure 1.22. *Activation of the carbon in α to a carbonyl group. On the bottom, the reaction is accelerated by a resonance-assisted H-bond*[26].

As shown Figure 1.22, although the enolisation process is assisted by electronic factors, the presence of the H-bond increases the acidity of the α-carbon by stabilising the negative charge of the carbanion, allowing delocalisation on the H-bonded ring.

Considering the field of material science, H-bonded structures are often used for the design of functional materials, which are molecular systems exhibiting very specific functions that find application in electronics, memory storage, signal transmission and amplification, and sensors. In these functional materials the hydrogen bond, especially the strong type, displays a structural and a functional role. The structural role resides on the fact that H-bonds are essential for the molecular recognition and the crystal packing, allowing the rational design of molecular and crystal architectures. In order to understand the functional role displayed by functional materials is important to define them as "*assemblies of nanoscale molecular machines (gadget, devices) based on two states, or bistable, molecular systems that produce their specific effects by cyclically switching between two different stability points*"[26]. In the case of H-bonded systems three effects can cause the switching process between the two stabilities: energy transfer, charge or electron transfer, and proton transfer (PT). It follows that H-bonded functional materials must be designed with systems that shows strong hydrogen bonds, whose energy potential is described by a double-well PT pathway with a small PT barrier so that the proton transfer can occur with contained costs in energy.

Those are only few examples of the importance of the hydrogen bonds, which was elegantly described by Pimentel and McClellan as follows: "*In fact, man himself is fabricated of H bonding substances. We feed, clothe, and house ourselves in H bonded materials. What is the key to the catholic importance of this chemical interaction in our environment? It is, no doubt, to be found in the H bonding properties of water since all of the physical and chemical properties of water are determined or influenced by H bonding. And this interaction pervades our chemistry simply because all living things evolved from and exist in an aqueous environment. It is hardly an*

exaggeration to say that in the chemistry of living systems the H bond is as important as the carbon-carbon bond"[24].

1.4. π-π interactions

Although they are classified as weak, π-π interactions can play an important role in the molecular arrangement of a crystalline structure. They are considered to be electrostatic interactions involving a π- or delocalised-electron system and a donor atom or another π-system, which can be an aromatic compound as well as alkene or alkyne moieties. Because of their electrostatic nature these attractive interactions are believed to form between negative charged areas of one molecule and a positive charged region of a neighbouring molecule. For π-systems a negative charge is usually formalised, indicating their tendency to interact with electron-deficient moieties. Due to their planar geometry, aromatic π-systems are characterised by a large surface-to-volume ratio, which may indicate that the best packing for these materials is achieved when the aromatic rings are stacked one on top of the other, maximising the π-overlap. Experimentally, however, this arrangement is rarely detected and an offset of the parallel stacking of aromatic molecules is preferred. This type of crystal packing was explained by Hunter and Sanders[38], who described the molecular structure of an aromatic π-system as constituted by "*a positively charged σ-framework sandwiched between the two negatively charged π-electron clouds*"[38]. A schematic representation of this π-system is reported in Figure 1.23.

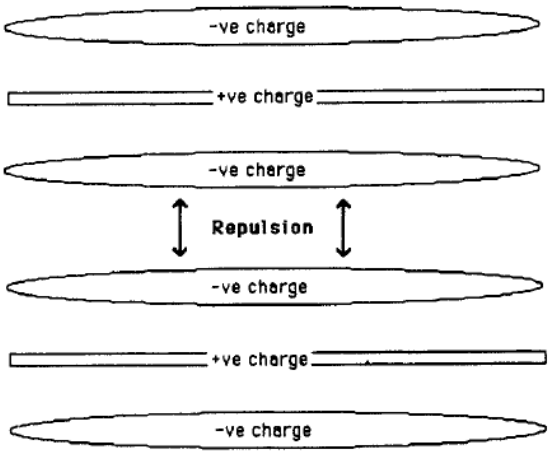

Figure 1.23. *The interaction between two face-to-face π-systems*[38]

The presence of negative and positive charges on a π-system allows the formation of three types of geometries, shown in Figure 1.24, for π-π interactions: *face-to-face*, or eclipsed face-to-face, stacking; *offset face-to-face*, or slipped or skewed, stacking; and *edge-to-face*, or T-shaped or edge-on, stacking. Usually, the interplanar distance in face-to-face and offset face-to-face interactions is

between 3.3 – 3.8 Å, whereas the distances between centroids in the edge-to-face geometry are no greater than 5 Å[39].

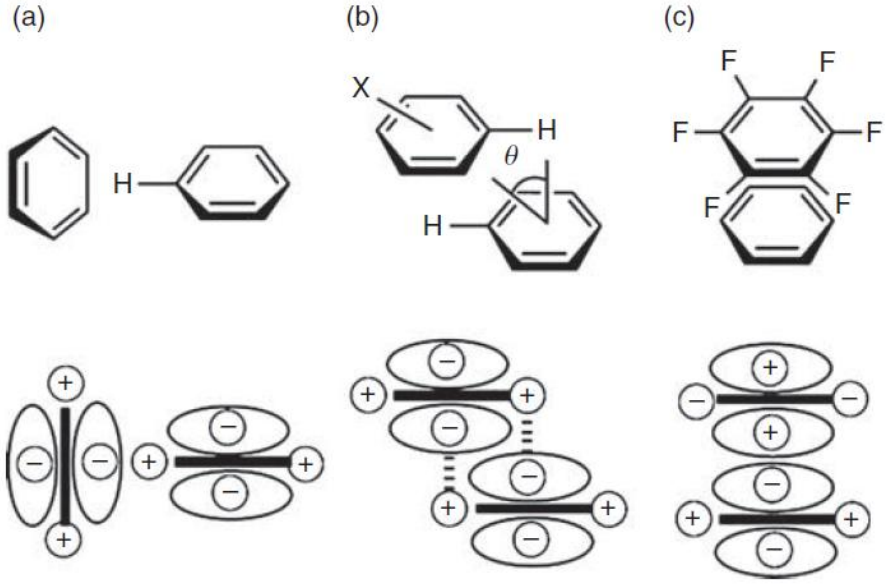

Figure 1.24. *Geometries of aromatic π-π interactions: (a) edge-to-face stacking; (b) offset face-to-face stacking; and (c) face-to-face stacking*[39].

Starting from their study on porphyrins[38], Hunter and Sanders formalised three rules for the arrangement of aromatic π-systems: "*rule 1, π-π repulsion dominates in a face-to-face π-stacked geometry; rule 2, π-σ attraction dominates in an edge-on or T-shaped geometry; and rule 3, π-σ attraction dominates in and offset π-stacked geometry*"[38]. Following considerations regarding polarisation effects due to heteroatoms in the aromatic π-system, they proposed other three additional rules, explaining the changes induced by polarisation in the π-π geometries usually observed: "*rule 4, for interactions between highly charged atoms, charge-charge interactions dominates. Rule 5, a favourable interaction with a neutral or weakly polarised site requires the following π-polarisation: (a) a π-deficient atom in a face-to-face geometry, (b) a π-deficient atom in the vertical T-group in the edge-on geometry, and (c) a π-rich atom in the horizontal T-group in the edge-on geometry. Rule 6, a favourable interaction with a neutral or weakly polarised site requires the following σ-polarisation: (a) a positively charged atom in a face-to-face geometry, (b) a positively charged atom in the vertical T-group in the edge-on geometry, and (c) a negatively charged atom in the horizontal T-group in the edge-on geometry*"[38].

Based on these geometries of interactions between π-systems, Desiraju and Gavezzotti[40] were able to predict the molecular arrangement of 32 polynuclear aromatic hydrocarbons (PAHs). In particular, they showed that the PAHs understudy displayed one of four possible packing arrangements, depending on the length of the shortest crystallographic axis, and that the choice amongst these packings was driven by the contribution of carbon and hydrogen atoms to the

molecular surface area. The four packing arrangements include (*i*) a herringbone structure, in which neighbouring molecules are nonparallel and the value of the shortest axis falls in the range 5.4 – 8.0 Å, (*ii*) a sandwich-herringbone structure, where the motif is made by diads and the shortest axis is greater than 8.0 Å, (*iii*) a γ-structure, in which the interaction involves parallel translated molecules and the length of the shortest axis is between 4.6 – 5.4 Å, and (*iv*) a β-structure, described as similar to graphitic planes, the value of the shortest axis being smaller than 4.2 Å. The four packing arrangements are summarised in Figure 1.25.

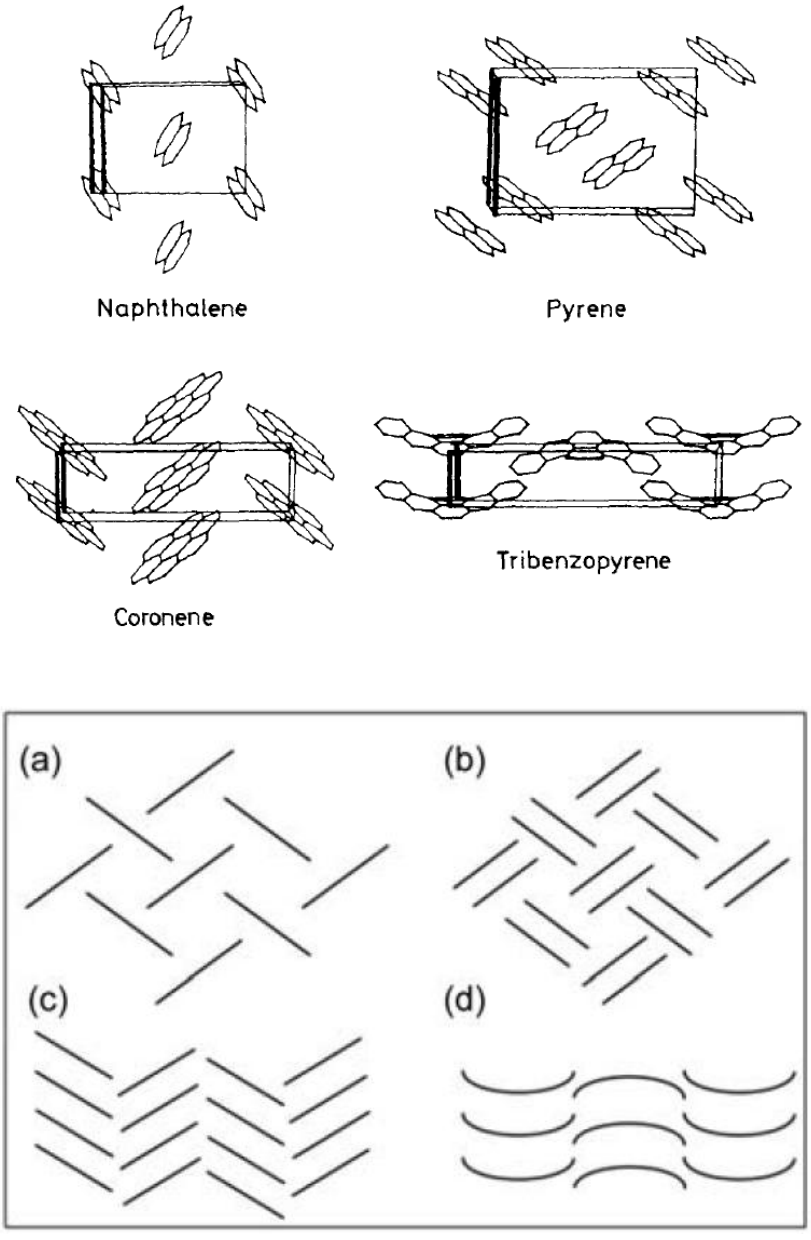

Figure 1.25. *On top, the four basic aromatic crystal packings: naphthalene (herringbone), pyrene (sandwich-herringbone), corronene (γ-structure), and tribenzopyrene (β-structure)*[40]*. On bottom, diagrammatic representation of the (a) herringbone, (b) sandwich-herringbone, (c) γ- and (d) β-structures*[39]*.*

In their work[40] Desiraju and Gavezzotti pointed out that the molecular and crystal structures of these PAHs were strongly correlated to the ability of the molecule in forming C···C and C···H interactions, asserting that optimisation of C···C interactions is achieved in molecules stacked in parallel lines, while C···H interactions are stronger between inclined molecules. It follows that the former are important in γ- and β-structures, while the latter are pivotal in a herringbone packing. For the prediction of the crystal structures of the 32 PAHs, Desiraju and Gavezzotti considered the molecular surface of these materials to be formed by two areas: a stack-promoting region and a glide-promoting one; core atoms and 50% of the rim carbon atoms of an aromatic molecule have a major contribution to the stacking, while the other 50% of rim carbon atoms and the hydrogen atoms encourage a glide-packing. By considering the glide-to-stack ratio as a function of the total molecular surface it is possible to predict the crystal packing from the molecular structure.

1.5. Supramolecular chemistry and crystal engneering

The concept of *supramolecular chemistry* was firstly proposed by Lehn, who suggested that "*supermolecules are to molecules and intermolecular bond what molecules are to atoms and the covalent bond*"[41]. In this context the concept of supramolecular systems distances from the classical theory, in which they were considered as simple molecular aggregates exhibiting the same chemical and physical properties of the constituting molecules, and gains a proper valence becoming systems characterised by defined structure and properties. From this consideration it follows that the long-range order of a crystal can be considered as a supramolecular system, as stated by Dunitz, who defined a crystal as "*a supermolecule par excellence, an assembly of literally millions of molecules self-crafted by mutual recognition at an amazing level of precision*"[42]. Since crystals are ordered supramolecular systems, it is possible to compare the process of crystallisation to the supramolecular assembly. The consequent attempt to find reliable connections on the base of intermolecular interactions between molecular and supramolecular structures is the ultimate aim of the **crystal engineering**, which tries to understand the intermolecular interactions in order to identify those building blocks, called *synthons*, which allow the design of materials with desired and specific chemical and physical properties. The first appearance of the term *synthons* was reported in 1967 by Corey in his paper entitled "*General methods for the construction of complex molecules*". With this terminology Corey identified all "*structural units within molecules which can be formed and/or assembled by known or conceivable synthetic operations*"[43]. In his definition, Corey does not pose limitation on the dimension of the building block: it can be as large as a molecule or as small as a hydrogen atom; moreover, the same atoms that form a specific molecule can lead to the formation of different *synthons*. The high generality of Corey's definition of *synthons* allows using them for the description of supramolecular systems: thus, "*supramolecular synthons are structural units within supermolecules which can be formed and/or assembled by*

known or conceivable synthetic operations involving intermolecular interactions"[44]. However, over the years the term *synthon* was partially abandoned and it was used in retrosynthetic organic chemistry, where it indicates an idealised representation of a retrosynthesis product, highlighting the required reactivity for the synthetic process. In 1995 G. R. Desiraju re-introduced the term *synthon* in a paper entitled "*Supramolecular synthons in crystal engineering – A new organic synthesis*"[44], in which he defines a supramolecular *synthon* as an identifiable element of design. In Figure 1.26 a summary of the most common supramolecular *synthons* is reported.

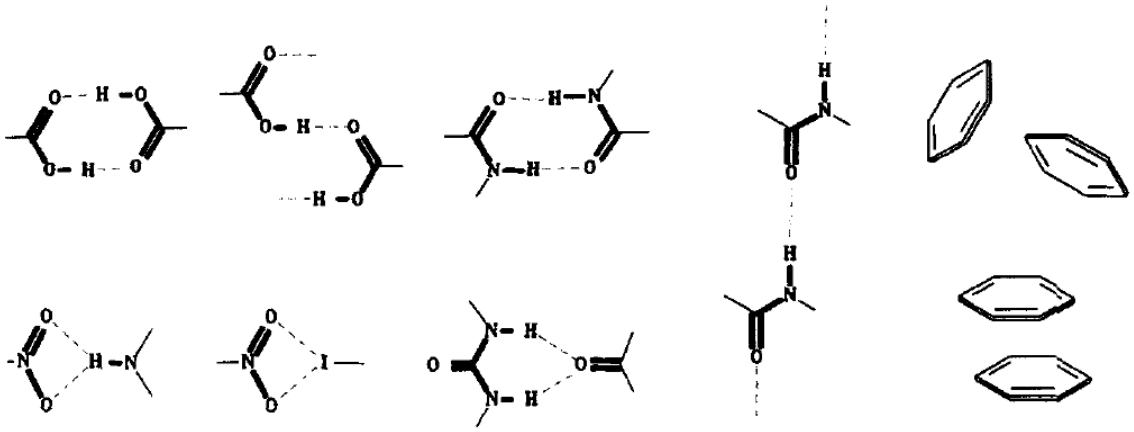

Figure 1.26. *Most common supramolecular synthons used for the design of materials by the crystal engineering*[44].

It is, however, important to underline that, although supramolecular *synthons* originate from combinations of intermolecular interactions, they do not represent intermolecular interactions. It is a subtle but important and real distinction, because supramolecular *synthons* combine both chemical and geometric characteristics of the constituting molecular fragments.

As reported in Figure 1.23, numerous are the possible combinations of intermolecular interactions, such as halogen bonding or weaker π-interactions, which can lead to the formation of *synthons.* Amongst those a relevant role is played by the hydrogen bond. In 1990 Etter considered the possibility to predict hydrogen bonding patterns and, consequently, to direct the crystallisation process towards a particular and desired network. In her paper entitled "*Encoding and decoding hydrogen-bond patterns of organic compounds*"[45], she suggested three general rules to be considered when H-bond is used as a designing tool: *(i)* all good proton donors and acceptors are used in hydrogen bonding; *(ii)* six-membered-ring intramolecular hydrogen bonds form in preference to intermolecular hydrogen bonds; *(iii)* the best proton donors and acceptors remaining after intramolecular hydrogen-bond formation form intermolecular hydrogen bonds to one another. Identification and classification of the various supramolecular *synthons* formed by different hydrogen bonding network can be achieved using the graph-set notation, which recognises four main motifs in the organisation of hydrogen bonds: chains, indicated by the letter C; rings, denoted

by the letter R; dimers or other finite sets, which are represented by the letter D; and, finally S, which refers to intramolecular hydrogen bonds. Each letters is accompanied by a subscript, a superscript and it is followed by a number in parentheses. The subscript and superscript indicate the number of donors and acceptors, respectively, that are present, while the number in parentheses refers to the number of atoms involved in the interaction. For example, the graph-set for the H-bond in benzoic acid dimers can be written as $R_2^2(8)$, which represents a cyclic hydrogen bond that counts two H-donors, two H-acceptors and a total of eight atoms involved in the ring.

Well known examples of materials designed by hydrogen bong patterns are molecular complexes of carboxylic acids with 2-aminopyridine derivates[46,47,48,49]. An interesting study took into consideration co-crystals formed by 2-aminopyrimidine and diols. This study[50] describes the crystal structures of two co-crystals of 2-aminopyrimidine (APY), one with hydroquinone (HQ) and another with 1,4-benzenedimethanol BMD. In the first co-crystal, APY/HQ, the interacting molecules form a $R_3^3(10)$ hydrogen bonding pattern between two molecules of APY and one of HQ (Figure 1.27).

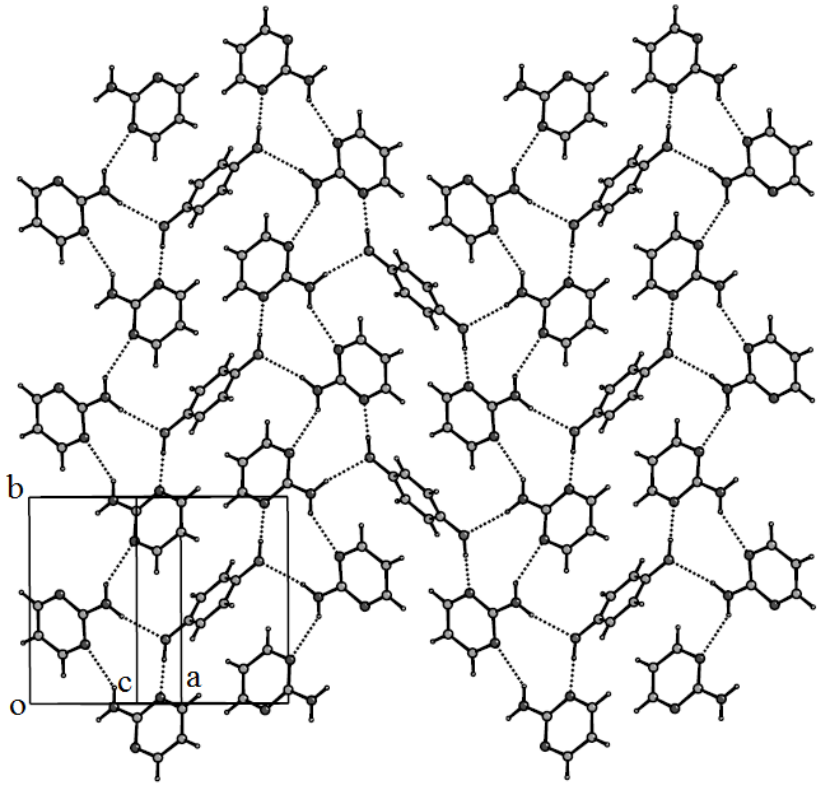

Figure 1.27. *Crystal packing of the molecular complex APY/HQ[50].*

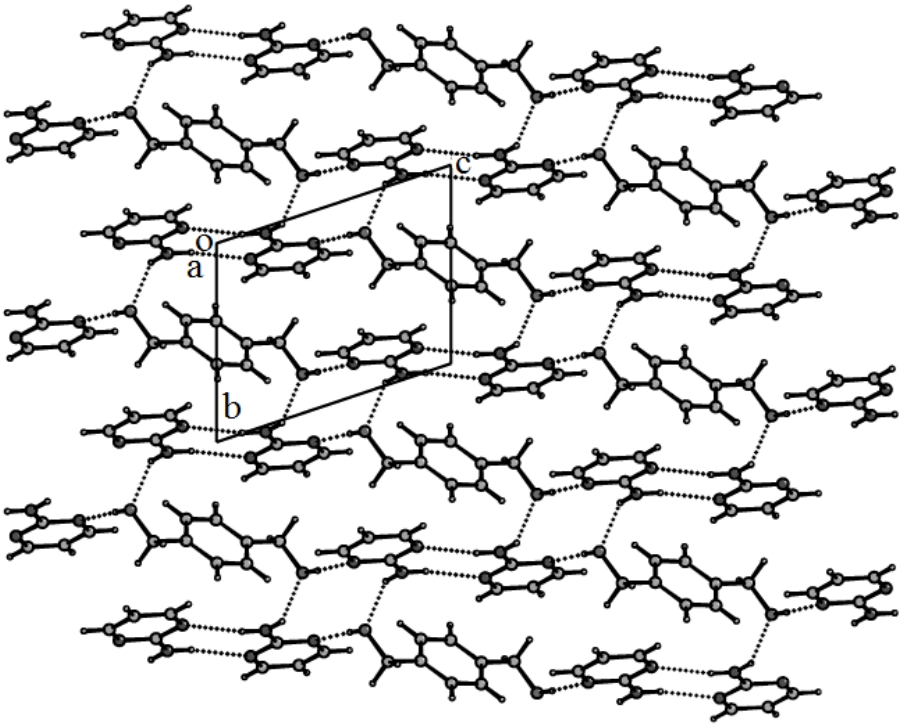

Figure 1.28. *Crystal packing of the molecular complex APY/BMD*[50].

The arrangement of the molecules in crystals of APY/BMD shows two hydrogen bonding networks: one involving the amino substituents on two APY molecules and a second, described by the graph-set notation $R_4^4(12)$, between two molecules of APY and two molecules of BMD, as shown in Figure 1.28.

1.6. Aim of the work

Agrochemicals investigated in the work described in this thesis, present issues either related to their potential environmental toxicity (as with isoproturon and glyphosate) or to practical problems regarding formulations and stability during transport or storage for long periods of time (pendimethalin and cyprodinil). Due to their relative low solubility in water, these agrochemicals are often formulated as wettable suspensions or emulsions to be sprayed directly on the leaves of plants, where they are usually absorbed. However, suspension formulations are typically stable over a narrow range of particle size, meaning that all those processes capable of modifying the particle size distribution of the compound, such as a polymorphic transformation, can alter the product, affecting its performance as a herbicide or fungicide. For the cases of pendimethalin and cyprodinil, which are both dimorphic systems with melting temperatures for each form below 80˚C, a polymorphic transformation can occur during transport, where the temperature can reach the respective phase transition points of the two systems. The result is the formation of a different crystalline form, which may not exhibit the role for which it was produced. During this work this

problem was addressed through the design of co-crystals, where the active molecule, for example the molecule of cyprodinil, is involved in intermolecular interactions with a co-former in order to increase the stability over a wider range of temperature. The successful co-crystallisation of cyprodinil with differently substituted benzoic acids is proof that the rational design of co-crystals can represent a solution to storage and formulation issues.

Structural studies concerning both crystal structure and crystal morphology were undertaken also to address the environmental toxicity of herbicides, such as isoproturon and glyphosate. These two agrochemicals can be washed off by rain before they are absorbed by a plant, causing contamination and accumulation of these substances in ground waters and the soil. One method of addressing this problem would be to discover different crystal structures that would be more effectively absorbed by the plant; for example by altering the crystal morphology to obtain flat shape, thereby increasing the strength of the contact between plant and herbicide crystal. This would reduce wash-off of the active organic compound and the potential environmental contamination.

Chapter 2

2. Experimental techniques

The work undertaken in this thesis focused on the investigation and characterisation of those phenomena responsible for the molecular self-assembly of crystalline organic compounds, as hydrogen bonds and intermolecular interactions. The best method for the definition of the crystal structure of a material is represented by single crystal and powder diffraction techniques, which allow the determination of the atomic positions and the characterisation of the atomic displacement parameters for a better understanding of the atomic thermal motion. The bases of these techniques are described in this chapter.

Since their discovery in 1896 by Willhelm Röntgen, the first person to recognise the value of X-rays in the study of solid matter was Max von Laue, who was able to demonstrate that a X-ray beam can be diffracted by a crystalline material. Following Laue's studies and experiments, William Henry Bragg and William Lawrence Bragg, father and son, developed a rigorous representation of the diffraction phenomenon.

2.1. X-ray and neutron diffraction

2.1.1. Theory of diffraction

Crystals are solid materials with a long-range order and a periodic structure. The whole crystal is generated by the repetition in the three dimensions of a basic structure, called motif, which can be as chemically complex as an entire protein, or as simple as a single atom. The mathematic set of points, which defines all the geometric relations between the motifs, is called the lattice. The characteristic of long-range order allows for the definition of the smallest fraction of the three-dimensional lattice, containing the motif and the information about the symmetry relations: the unit cell. The unit cell is defined by the lattice parameters: three sides, a, b and c, and three angles, α, β and γ.

In a three-dimensional lattice the direction and amplitude of the translating vectors depend on the symmetry elements ruling the order in the unit cell. The combination of different types of lattice with compatible point groups gives rise to seven crystal systems, further divided in the 14 Bravais lattices, which describe infinite arrays of discrete points generated by a set of discrete translating operations. The action of centring translating vectors produces four classes of lattice: PRIMITIVE (***P***), with 1 lattice point, only in the corners of the unit cell; BODY-CENTRED (***I***), with an additional point at the centre of the cell (2 lattice points); FACE-CENTRED (***F***), with an additional

lattice point at the centre of each face of the cell (4 lattice points); and BASE-CENTRED (***C***), with an additional lattice point at the centre of one pair of cell faces (2 lattice points). A summary is reported in Table 2.1.

Crystal system	Lattice parameters	Bravais lattice	Point groups
Triclinic	a≠b≠c; α≠β≠γ≠90°	*P*	$1,\ \bar{1}$
Monoclinic	a≠b≠c; α=γ=90°, β≠90°	*P, C*	$2, m, 2/m$
Orthorhombic	a≠b≠c; α=β=γ=90°	*P, C, I, F*	$222, mm2, mmm$
Tetragonal	a=b≠c; α=β=γ=90°	*P, I*	$4, \bar{4}, 4/m, 422, 4mm, \bar{4}2m, 4/mmm$
Hexagonal	a=b≠c; α=β=90°, γ=120°	*P*	$3, \bar{3}, 6/m, 622, 6mm, \bar{6}m2, 6/mmm$
Trigonal/Rhombohedral	a=b=c; α=β=γ≠90°	*P*	$23, m\bar{3}, 432, \bar{4}3m, m\bar{3}m$
Cubic	a=b=c; α=β=γ=90°	*P, I, F*	$23, m\bar{3}, 432, \bar{4}3m, m\bar{3}m$

Table 2.1. *Summary of the crystal systems, Bravais lattices and respective point groups.*

When electromagnetic radiation goes through a crystalline material, the electric and magnetic fields associated with the radiation will interact with the material, causing the oscillation of the atoms inside it. As a result the atoms become sources of electromagnetic radiation, with the same frequency as the incident beam. This phenomenon is called *scattering* and the atoms are called *scattering centres*.

In a crystal lattice atoms are placed on ordered arrays of planes, which are refered to with the Miller indices, *h*, *k* and *l*, representing the reciprocal fractional intersections between a lattice plane and the unit cell axes, *a*, *b* and *c*, respectively. Another important factor in the characterisation of a crystal lattice is the distance between the lattice planes, d_{hkl}.

When an X-ray beam impacts on a crystalline material, interference between beams scattered by all atoms occurs: a constructive interference, leading to the observation of a peak, is produced only if the beams are in phase. Considering a single array of atoms (Figure 2.1), the distance between two of these atoms, A_1 and A_2 is shown in eq. 2.1.

$$\vec{r} = u\overrightarrow{\tau_1} + v\overrightarrow{\tau_2} + w\overrightarrow{\tau_3} \qquad 2.1$$

where $\overrightarrow{\tau_1}$, $\overrightarrow{\tau_2}$ and $\overrightarrow{\tau_3}$ are the unit vectors, and *u*, *v* and *w* are integers, including zero.

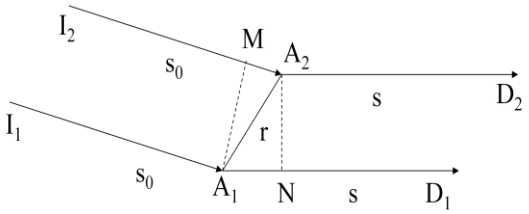

Figure 2.1. *Interaction of X-ray beams with a single array of atoms.*

$\overrightarrow{s_0}$ represents the direction of the incident X-ray beam, and is a unit vector, while $\vec{s}$ determines the direction of the diffracted beam. For a constructive interference to be observed, the difference in the pathways of the beams diffracted by the two atoms, $\overline{A_1N} - \overline{MA_2}$, needs to be an integer number of wavelengths (eq. 2.2)

$$\overline{A_1N} - \overline{MA_2} = \vec{r} \times \vec{s} - \vec{r} \times \overrightarrow{s_0} = n\lambda \qquad 2.2$$

which, by replacing $\vec{S} = \vec{s} - \overrightarrow{s_0}$, can be written as

$$\vec{r} \times \vec{S} = n\lambda \qquad 2.3$$

The introduction of eq. 2.1 in eq. 2.3 gives the Laue's equations (2.4).

$$\overrightarrow{\tau_1} \times \vec{S}/_{\lambda} = h \qquad \overrightarrow{\tau_2} \times \vec{S}/_{\lambda} = k \qquad \overrightarrow{\tau_3} \times \vec{S}/_{\lambda} = l \qquad 2.4$$

where *h*, *k* and *l* are integer numbers, zero included.
Considering μ_1, μ_2, μ_3 and ν_1, ν_2, ν_3 as the angles of the incident and the diffracted beams, respectively, Laue's equations can be re-written as:

$$\begin{cases} \tau_1(cos\nu_1 - cos\mu_1) = h\lambda \\ \tau_2(cos\nu_2 - cos\mu_2) = k\lambda \\ \tau_3(cos\nu_3 - cos\mu_3) = l\lambda \end{cases} \qquad 2.5$$

In order to observe a diffracted beam with wavelength λ, all three equations must be satisfied simultaneously. William Henry and William Lawrence Bragg confirmed Laue's theory of diffraction by making the assumption that crystalline planes can reflect X-rays.

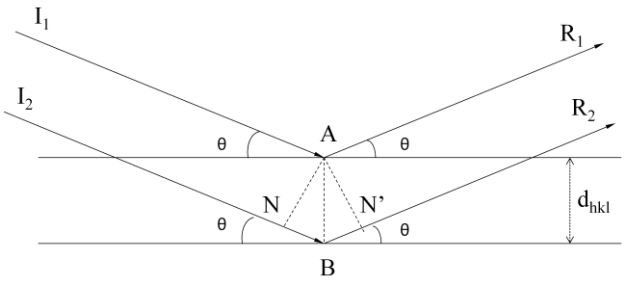

Figure 2.2. *Schematic representation of the Bragg's law.*

Figure 2.2 reports a schematic representation of Bragg's theory. Upon impact of a monochromatic X-ray beam on a family of crystallographic planes with an angle θ, the resulting diffracted beam is reflected by the same angle θ. Constructive interference, and consequent observation of a diffraction spot, can occur only when the difference in pathlength $\overline{NB} + \overline{BN'}$ between the two incident beams, I_1 and I_2, is equal to an integer number n of wavelength. By the geometrical construction of Figure 2.2, the two segments $\overline{NB}$ and $\overline{BN'}$ can be written as a function of the d-spacing between lattice planes $\overline{NB} = \overline{BN'} = d_{hkl} sin\theta$, which reveal the Bragg's law (eq. 2.6).

$$n\lambda = 2d_{hkl} sin\theta \qquad 2.6$$

Bragg's law, which determines the conditions needed for the observation of a diffracted beam, can be visualised geometrically by using the *reciprocal lattice* that represents the space investigated during a diffraction experiment. The reciprocal lattice is formed by spots, which correspond to families of planes in real space. The position of each spot is determined by the inverse of the lattice spacing, $1/d_{hkl}$, and the direction of the perpendicular of the lattice plane.

A unit cell in reciprocal space is defined by three axes, a^*, b^* and c^*:

- a^* is perpendicular to the *(bc)* plane in real space, $a^* = 1/d_{100}$;
- b^* is perpendicular to the *(ac)* plane in real space, $b^* = 1/d_{010}$;
- c^* is perpendicular to the (ab) plane in real space, $c^* = 1/d_{001}$.

While in real space the Miller indices, *hkl*, represent a family of parallel planes, in reciprocal space they represent the components of the vector d^*_{hkl}. The advantage of this construction is that it highlights the relations between families of lattice planes, the Bragg's law, and the geometry and direction of the beams diffracted by the crystal.

The reciprocal lattice is used in the construction of the *Ewald's sphere*, a powerful tool for the characterisation of the entire crystal structure. The Ewald's sphere allows for the geometrical representation of the conditions needed for diffraction to be defined. For its construction, a crystal

is placed at the centre of a sphere with radius $^1/_\lambda$ and a X-ray beam is directed at it. The part of X-ray radiation that does not interact with the crystal, passing through it, will form the lattice point (000), which is taken as the origin of the reciprocal space. The remaining part of the incident radiation will interact with the crystallographic planes, producing diffraction events upon satisfaction of the Bragg's law. This happens when a diffraction spot lies on the surface of the sphere. In Figure 2.3 a schematic representation of the Ewald's sphere, in two dimensions, is reported.

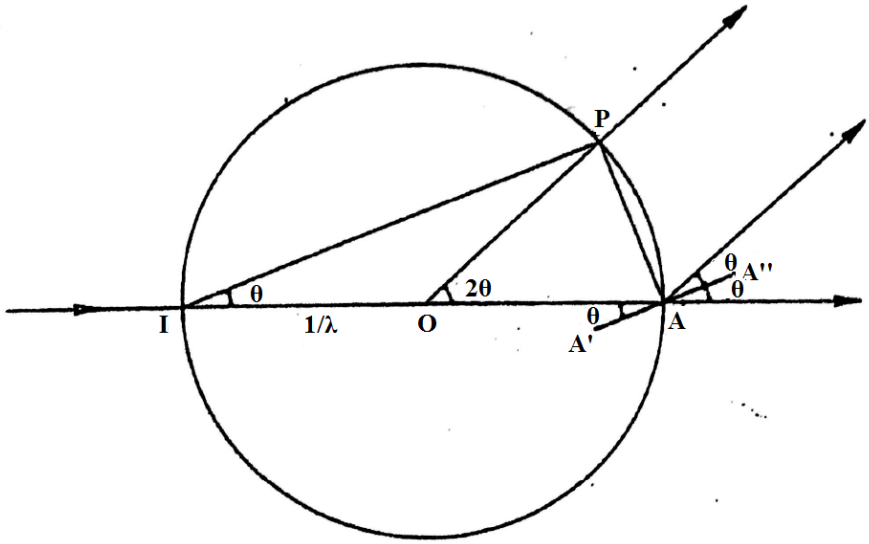

Figure 2.3. *Schematic representation in two dimensions of the Ewald's sphere*[51].

IA is the direction of the X-ray beam impacting, with an angle θ, on the family of planes $A'A''$, with Miller indices *hkl*. *A* is the origin of the reciprocal space and *P* represents one of its points, corresponding to the family of planes, characterised by indices *hkl* and lattice spacing d_{hkl}. The definition of reciprocal lattice allows writing:

$$\overline{AP} = d^* = {}^1/_{d_{hkl}} \qquad 2.7$$

Considering the triangle IAP, it is possible to write

$$\overline{AP} = \overline{IA}\sin\theta \qquad 2.8$$

Since the radius of the circle is $^1/_\lambda$, it is possible to re-arrange the previous equation as

$${}^1/_{d_{hkl}} = {}^2/_\lambda \sin\theta \qquad \rightarrow \qquad \lambda = 2d_{hkl}\sin\theta \qquad 2.9$$

which is Bragg's law: in order for a crystallographic plane *hkl* to diffract, the correspondent vector in reciprocal space needs to lie upon the Ewald's sphere. By changing the orientation of the crystal at the centre of the sphere, other points of the reciprocal space find themselves in conditions to diffract, allowing collection of a set of data, which contains all information about the crystal structure under study.

The Laue equations and the Bragg's law, which determine the diffraction maxima corresponding to *hkl* reflections, have been derived under the assumption that the beams diffracted by all the atoms in a lattice were in phase. It is well known that in a crystal there are as many permeated and parallel primitive lattices as the atoms in the unit cell. Since all the lattices are identical to each other, the directions of the diffraction maxima do not depend on the atoms present in the structure.

Based on the nature and the positions of the atoms in the unit cell, it is possible to calculate the intensity of the reflections, *hkl*, by putting together, in the direction of reflection, all beams diffracted by the atoms. Considering f_1, f_2, ..., and φ_1, φ_2, ..., as the amplitudes and the phases, respectively, of the diffracted beams, the amplitude and the phase of the resulting wave are given by the modulus and argument of the complex number *F*, that is the sum of $f_1 e^{i\varphi_1} + f_2 e^{i\varphi_2} + \cdots$

The amplitudes f_1, f_2, ..., correspond to the atomic *scattering factors* for the various atoms. The scattering factor is proportional to the atomic number: *f* is equal to the number of electrons of an atom when the angle 2θ between the direction of the incident beam and the direction of the diffracted beam is equal to zero. When the value of 2θ increases the scattering factor *f* rapidly decreases, due to interferences between beams diffracted by all the electrons of the same atom, as shown in Figure. 2.4.

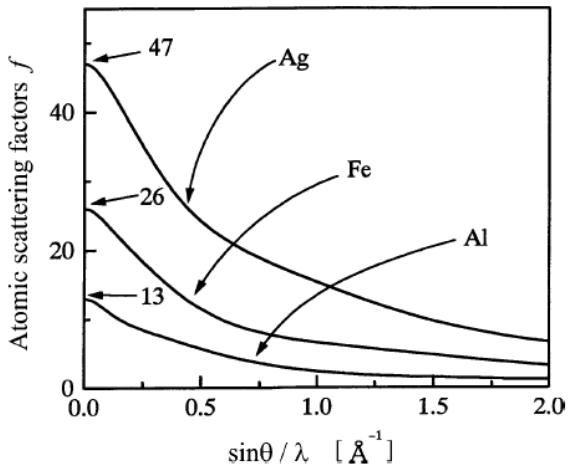

Figure 2.4. *Dependence of atomic scattering factors of Al, Fe and Ag on* $\boldsymbol{\sin\theta/\lambda}$ [52].

The phases φ_1, φ_2, ..., of the diffracted beams depend on the position of the atoms inside the unit cell and are calculated considering the difference in the path between the beam diffracted by the n-

th atom and the beam diffracted by the origin. The Laue equations, which consider the direction of a maximum of interference, allow writing:

$$\varphi_n = 2\pi(hx_n + ky_n + lz_n) \qquad 2.10$$

where x_n, y_n and z_n are the coordinates of the n-th atom inside the unit cell.
The previous equation allows writing the expression of the diffracted beam as:

$$f_n e^{2\pi i(hx_n+ky_n+lz_n)} \qquad 2.11$$

All N atoms present in the unit cell contribute to a *hkl* reflection, leading to the definition of the *structure factor*, F_{hkl} (eq. 2.12):

$$F_{hkl} = \sum_{1}^{N} f_n e^{2\pi i(hx_n+ky_n+lz_n)} \qquad 2.12$$

The structure factor represents the amplitude and the phase of the beam diffracted by the unit cell for an *hkl* reflection; its value depends on the indices *h*, *k*, and *l* and on the nature and arrangement of the atoms inside the unit cell. The intensity of the reflection, I_{hkl}, is proportional to $|F_{hkl}|^2$.
For a diffraction experiment it is useful to consider the crystal structure not as a discrete and ordered set of atoms, but rather as a continuous function, $\rho(x, y, z)$, which represents the *electron density* in the unit cell. The electron density is defined by a *Fourier transform* as:

$$\rho(x, y, z) = \sum_{m}\sum_{n}\sum_{p} C(m, n, p)\, e^{2\pi i(mx+ny+pz)} \qquad 2.13$$

where $C(m, n, p)$ is the Fourier coefficient and *m*, *n*, *p* are integer numbers, and the sums are calculated in $\pm\infty$. Replacing eq. 2.13 in the expression for the structure factor (eq. 2.12) gives:

$$F_{hkl} = \iiint \sum_{m}\sum_{n}\sum_{p} C(m, n, p)\, e^{2\pi i(mx+ny+pz)}\, e^{2\pi i(hx_n+ky_n+lz_n)}\, V\, dxdydz \qquad 2.14$$

This integral is equal to zero unless $m = -h$, $n = -k$, $p = -l$, which allows to write:

$$F_{hkl} = C(\bar{h}, \bar{k}, \bar{l})\, V \qquad 2.15$$

and

$$\rho(x,y,z) = \frac{1}{V}\sum_{h}\sum_{k}\sum_{l} F_{hkl} e^{-2\pi i(hx+ky+lz)} \qquad 2.16$$

A sufficient number of F_{hkl} allows calculating the values of $\rho(x,y,z)$ for the unit cell, producing a *Fourier synthesis*: the maximum values of $\rho(x,y,z)$ represent the atoms positions. For a direct determination of a crystal structure using a Fourier synthesis, it is necessary to know the structure factors, F_{hkl}, which are complex numbers defined by an amplitude and a phase. However, during a diffraction experiment, only the intensity of a reflection, that is $I_{hkl} \propto |F_{hkl}|^2$, is recorded and the information about the phase is lost, giving rise to the so-called *phase problem*.

There are two main methods for bypassing the phase problem: the *Patterson method* and *direct methods*.

The *Patterson method* introduces some modification into the electron density function, so that the structure factors, represented by their amplitudes and phases, are replaced by the square amplitudes, whose values are proportional to the diffracted intensity. For a generic point of coordinates (u,v,w) the value of the Patterson function is given by the product of the auto-convolution of the electron density:

$$\rho(u,v,w) = \iiint_{o}^{1} \rho(u,v,w) * \rho(x+u, y+v, z+w)dV \qquad 2.17$$

By inspecting the unit cell with a vector of generic components(u,v,w), three different situations can be outlined: the vector does not detect any atom at its ends; the vector detects one atom at one end; the vector detects one atom at each ends. The result of the product of the electron densities at the two ends of the vector is different from zero only in the third case.

The Patterson function can be written as:

$$P(x,y,z) = \frac{1}{V}\sum_{h,k,l} |F_{hkl}|^2 \, e^{-2\pi i(hx+ky+lz)} \qquad 2.18$$

All terms in the function are known, so that it is possible to solve the equation. The Patterson function produces a map where peaks represent vectors between atoms, rather than an electron density map. The peaks are characterised by amplitude, due to the fact that atoms possess an electronic distribution, with only heavy atoms producing obvious peaks. This means that for a complex molecule the Patterson map can present overlap of the peaks, especially if the structure contains atoms with similar atomic number, making its interpretation difficult to achieve.

The approach used by *direct methods* in solving the phase problem is based on considerations of the direct relationships existing between the amplitudes of the structure factors. They were developed in 1950s by combining statistical analyses on the intensities of the reflections. They constitute a series of mathematical steps on the experimental data, without considering any chemical knowledge.

Generally, the amplitude and the phase of a wave are independent from one another. In order to understand why this concept is not always satisfied in the case of X-ray diffraction, it is essential to remember that the final purpose of a diffraction experiment is the construction of an electron density map, $\rho(r)$. Disregarding its complexity, direct methods require $\rho(r)$ to satisfy two general criteria: it must be either positive or equal to zero everywhere, and it must be concentrated in small areas (principle of atomicity). The main consequence of these two properties is the fact that structure factors are no longer affected by the atomic size, as stated by the principle of atomicity, allowing to covert the structure factors, whose expected intensity is expressed by eq. 2.19, into normalised structure factors *E* (eq. 2.20).

$$\langle |F|^2 \rangle_\theta = \sum_{j=1}^{N} f_j^2(\theta) \qquad 2.189$$

$$|E_{hkl}|^2 = \frac{|F_{hkl}|^2}{\sum_{j=1}^{N} f_j^2} \qquad 2.20$$

The normalised structure factors help in the selection of the space group by discriminating between non-centrosymmetric and centrosymmetric space groups: the mean value $(E^2 - 1)$ is 0.74 and 0.97 for non-centrosymmetric and centrosymmetric structures, respectively.

To solve a crystal structure direct methods use a "trial-and-error" approach, starting by considering the reflections, and thus the normalised structure factors, that give the major contribution to the Fourier transform, and calculating their probable phase relationship. After calculation of different combinations of phases and their comparison to the probable phase relationships, the most promising combination of phases is used in a reverse Fourier transform with the observed amplitudes $|F_o|$ and the calculated phases $e^{i\varphi_c}$. This cycle is repeated until all non-H atoms are found, allowing the construction of an initial model of the structure. This model is then refined with least squares methods, which minimises eq. 2.21 in order to obtain an optimal representation of the crystal structure in terms of both atomic positions and anisotropic temperature factors.

$$D = \sum w(|F_o| - |F_c|)^2 \qquad 2.21$$

where *w* is a weight assigned to each reflection, indicating the importance that a specific reflection makes to the sum, taken over all measured reflections. The weight *w* is expressed as:

$$w = \frac{1}{\sigma^2 F_o^2 + (aP)^2 + bP} \qquad 2.22$$

where $P = [2F_c^2 + Max(F_o^2, 0)]/3$; σ is the standard deviation; and *a* and *b* are constants.

If the initial model is not complete, a *F-obs Fourier synthesis* can be performed. Usually used in earlier stage of the refinement procedure, the F-obs Fourier synthesis produces an electron density map calculated by using eq. 2.23.

$$\rho(xyz) = \sum_{hkl} |F_{hkl}^o| e^{-2\pi i(hx+ky+lz)+\alpha_{hkl}^c} \qquad 2.23$$

The combination of the best calculated phases and observed structure factors gives rise to the appearance in the electron density map of peaks, corresponding to the missing atoms.
When only a small part of the asymmetric unit is missing, a difference Fourier map can be calculated. This map, reported in eq. 2.24, shows the difference between the observed and calculated structure factors, $|F_{hkl}^o| - |F_{hkl}^c|$, revealing the aspects of the scattering density contained in F_{hkl}^o.

$$\Delta\rho(xyz) = \sum_{hkl} (|F_{hkl}^o| - |F_{hkl}^c|) e^{-2\pi i(hx+ky+lz)+\alpha_{hkl}^c} \qquad 2.24$$

Difference Fourier maps are largely used for the identification of hydrogen atoms during the refinement of neutron data and for the investigation of the electron density around specific atoms or bonds.

Once a complete model of the motif has been achieved, the whole structure is improved by consecutive refinement cycles. Structural refinement is carried out through least squares procedures, which allow for the variation of different parameters simultaneously, in particular coordinates and thermal parameters for each atom and other parameters such as scale factor, absorption and extinction corrections. The refinement is considered complete when the minimisation of the difference between the observed diffraction intensities and the ones calculated from the structural model is achieved, as indicated by the crystallographic R-factors:

$$R(F) = \frac{\sum \left| |F_{hkl}^{o}| - |F_{hkl}^{c}| \right|}{\sum |F_{hkl}^{o}|} \quad 2.25$$

$$R_w(F^2) = \left\{ \frac{\sum \left[w\left({F_{hkl}^{o}}^2 - {F_{hkl}^{c}}^2 \right)^2 \right]}{\sum \left[w\left({F_{hkl}^{o}}^2 \right)^2 \right]} \right\}^{1/2} \quad 2.26$$

and the Goodness-of-Fit (GooF):

$$S = \left\{ \frac{\sum \left[w\left({F_{hkl}^{o}}^2 - {F_{hkl}^{c}}^2 \right)^2 \right]}{n - p} \right\}^{1/2} \quad 2.27$$

where *n* is the number of reflections, *p* is the number of refined parameters, and the weight *w* has the general form $w = 1/\sigma^2\left({F_{hkl}^{o}}^2\right)$. A structural refinement is considered of publishable quality for values of R in the interval *2-7%* and GooF as close to unity as possible. Although $R_w(F^2)$ is always greater than $R(F)$, since it is calculated on F^2, its value is more significant because it takes into consideration the contribution of each reflection, describing a more reliable structural model.

2.1.2. X-ray generation

X-rays are a part of the electromagnetic radiation with a range in wavelength varying from 0.1 to 100 Å.

For their use in laboratory experiments they are produced in X-ray tubes, which are formed by a cathode, which is generally constituted by a tungsten filament, and an anode, which is represented by a metal target. A difference in the electric potential is applied to the cathode, so that a current can pass through the cathode itself, causing heating of the filament and rising of the temperature. When a metal is heated, the process of thermoionic emission can occur, leading to spontaneous emission of electrons by the metal. The number of emitted electrons per second as a result of the thermoionic emission is highly dependent on the temperature; for this reason, the filament is heated slightly below its melting point. Once the electrons are produced, they are accelerated by an electric field and they impact on the metallic anode, usually copper or molybdenum. If the energy of the electron beam is sufficiently high, the collision with the atoms of the target causes the expulsion of an electron by the metal. The vacancy can be filled by an electron from higher energy orbitals. The decay from a higher energy orbital to the core level causes the emission of a photon.

When the difference in energy between the two states is sufficiently high, the emitted radiation is X-ray radiation. This means that X-rays are produced only if the vacancy is in a core level.

The spectrum derived from the X-ray generation method just described shows a continuous radiation (braking radiation), with some intense peaks, which correspond to the electronic decays from high energy orbitals to the core state. K_{α_1} and K_{α_2} refer to transitions from the *2p* and *2s* orbitals to the *1s* orbital, respectively, whereas K_{β_1} indicates a transition from the *3p* orbital to the core state. The K_{β_1} peak is weaker that the doublet formed by K_{α_1} and K_{α_2}, with a ratio between K_{α_1} and K_{α_2} of 2 : 1.

The wavelengths of each peak, $\lambda(K_{\alpha_1})$, $\lambda(K_{\alpha_2})$, $\lambda(K_{\beta_1})$, are characteristic of the metal chosen as anode: for example, for copper $\lambda(K_{\alpha_1})$ = 1.54060 Å, $\lambda(K_{\alpha_2})$ = 1.54443 Å, and $\lambda(K_{\beta_1})$ = 1.39225 Å; for molybdenum $\lambda(K_{\alpha_1})$ = 0.70932 Å, $\lambda(K_{\alpha_2})$ = 0.71361 Å, and $\lambda(K_{\beta_1})$ = 0.63230 Å.

The K_β wavelength can be significantly reduced using β-filters made of a chemical element with atomic number one or two below the one of the metal target. Typical filters for Cu and Mo radiations are Ni and Zr, respectively. It is, however, important to remember that these kinds of filters cannot remove the K_{α_2} component of the K_α radiation. This is done by using a monochromator.

Another way to obtain a monochromatic X-ray beam is with the use of a monochromator. This piece of equipment is constituted by a single crystal made out of little crystal, which are oriented to form a mosaic. Depending on the distribution of the alignement, it is possible to observe different *mosaic spread* of the crystal, leading to two types of monochromator: broad band and narrow band ($\Delta\lambda/\lambda$) monochromators. The former are characterised by a relatively broad mosaic spread when compared to the latter, in which the alignement of the mosaic blocks is almost perfect, meaning that both components of the K_α radiation can be diffracted, but not the K_β. Examples of broad band and narrow band monochromators are pyrolytic graphite and silicon. The monochromatic radiation derived from monochromators is characterised by a low signal to noise ratio and very narrow peaks ($\Delta\lambda$); this allows for high discrimination between all the diffraction events, which would otherwise overlap in the braking radiation.

2.1.3. Single crystal X-ray diffraction

Single crystal X-ray diffraction (SXD) was the main technique used in this work.

For the determination of a crystal structure from a SXD experiment the first things to identify are the space group and the cell parameters. The instrument used is a diffractometer (Figure 2.5) equipped with a four-circle goniometer, also known as *Eurelian cradle*, at the centre of which a suitable crystal is mounted.

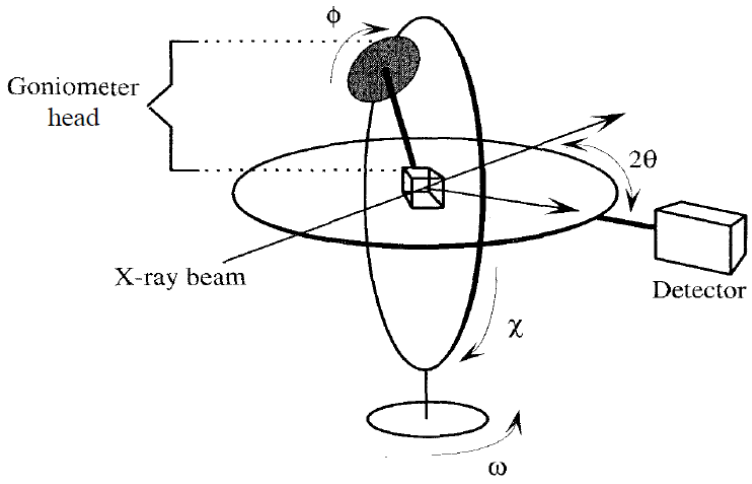

Figure 2.5. *Schematic representation of a four-circle diffractometer*[53].

During a data collection the crystal is rotated along four directions: the vertical axis χ, the axis φ perpendicular to χ, the rotation axis 2θ parallel to the equatorial plane, containing the detector, and the axis ω also parallel to the equatorial plane, but independent from 2θ. After centring the crystal in the X-ray beam, so that rotations along $\chi, \varphi, 2\theta, \omega$ do not cause translation of the crystal, the first step is the determination of the unit cell parameters and the orientation of the crystal axes. This can be accomplished in two ways: either collecting a set of data upon rotation around the axis φ, which, by inspecting the diffraction spots, give the coordinates φ, χ and θ for each reflection; or by the investigation of the reciprocal lattice through a list of values for φ, χ and θ, obtaining the φ, χ, θ coordinates for every point of the reciprocal lattice in diffracting conditions. By knowing the coordinates φ, χ, θ of a small number of reflections, it is possible to recreate the lattice, allowing the definition of the crystal system, the unit cell parameters and the orientation matrix.

It is well known that all structural information about a crystal is contained in the intensities recorded on a diffraction image. However, for the determination of the space group of a crystal lattice is very helpful to look for those reflections that are not visible because of the symmetry of the unit cell.

The elements of symmetry dictate the relations between the coordinates of the atoms inside the unit cell and affect the expression of the structure factors, since the structure factor depends on the atomic coordinates. For example, considering an atom of general coordinates (x, y, z), the presence of an inversion centre, $\bar{\imath}$, taken as the origin of the axes, produces another atom of coordinates $(\bar{x}, \bar{y}, \bar{z})$. The expression of the structure factor for an *hkl* reflection can be written as:

$$F_{hkl} = \sum_{n=1}^{N/2} f_n \left\{ e^{2\pi i(hx_n + ky_n + lz_n)} + e^{-2\pi i(hx_n + ky_n + lz_n)} \right\} \qquad 2.28$$

which, by replacing $e^{i\varphi} + e^{-i\varphi} = 2cos\varphi$, can be rearranged in:

$$F_{hkl} = 2\sum_{n=1}^{N/2} f_n cos2\pi(hx_n + ky_n + lz_n) \qquad 2.29$$

The expressions of the structure factor modified for other elements of symmetry can be derived similarly.

It is interesting to notice that in the presence of elements of symmetry with a translational component certain types of *hkl* reflections show no intensity, being $F_{hkl} = 0$: these reflections are called *systematic absences*.

Systematic absences are of great value in the determination of the space group of the crystalline material taken under study. In a face-centred lattice, C, there will be a lattice plane shifted by $^1/_2$ in *x* and *y*, modifying the expression of the structure factor in:

$$F_{hkl} = \sum_{n=1}^{N/2} f_n \left\{ e^{2\pi i(hx_n + ky_n + lz_n)} + e^{2\pi i(hx_n + ky_n + lz_n + \frac{1}{2}h + \frac{1}{2}k} \right\} \qquad 2.30$$

which can be rearranged as:

$$F_{hkl} = \sum_{n=1}^{N/2} f_n \left\{ e^{2\pi i(hx_n + ky_n + lz_n)} \left[1 + e^{2\pi i(\frac{h+k}{2})} \right] \right\} \qquad 2.31$$

In eq. 2.30 the term $\left[1 + e^{2\pi i(\frac{h+k}{2})}\right]$ is different from zero when the sum $(h + k)$ is even, or equal to zero when the sum $(h + k)$ is odd. In the latter case, the structure factor F_{hkl} will have no intensity for any value of x_n, y_n, z_n. It follows that in a C lattice there will be observation of only those hkl reflections for which the sum $(h + k)$ is an even number. In Table 2.2 the conditions in which there are observed reflections in different lattices are listed.

Lattice	Reflection	Conditions for reflection
A	*hkl*	$k + l = 2n$
B	*hkl*	$h + l = 2n$
C	*hkl*	$h + k = 2n$
F	*hkl*	h, k, l *all even or all odd*
I	*hkl*	$h + k + l = 2n$
R	*hkl*	$-h + k + l = 3n$

Table 2.2. *Conditions for the observation of hkl reflections in different lattices.*

For a complete characterisation of a crystal structure all atom positions and their thermal parameters must be defined. This is done considering the structure factors, whose amplitudes are linked to the recorded intensities by equation 2.32.

$$I_{hkl} = K \cdot T \cdot p \cdot L \cdot m \cdot |F_{hkl}|^2 \qquad 2.32$$

which shows how the intensity of a reflection depends on physical and geometric factors:

K is a constant;

T is a *transmission factor* and depends on the X-ray absorption coefficients of the various atoms and on the size and morphology of the crystal;

$p = \frac{(1+cos^2 2\theta)}{2}$ is a *polarisation factor* and expresses the degree of polarisation of the reflected beam;

L represents the *Lorentz factor*, which depends on the experimental method used to obtain the reflection;

m is a *multiplicity factor* and indicates the number of *hkl* planes that contribute to the same reflection;

and F_{hkl} is the structure factor.

Many factors can affect the intensity of a diffraction peak; one of them is thermal motion. It is well known that in a solid material atoms are not fixed is a certain position, but they oscillate around a position of equilibrium. The oscillation depends on the thermal energy received from the environment and is expressed by the difference between the maximum displacement r_j' and the position of equilibrium, r_j: $u_j = r_j' - r_j$. The size of the oscillation is dependent on the atomic mass and on the strength of the bonds formed by the atom. Since the thermal vibration causes an atom j with scattering power f_j to occupy a larger volume, a decrease of the scattering power is observed with an increase in temperature. In the case of an isotropic thermal motion, the size of the oscillation $\boldsymbol{u}$ can be introduced in the structure factor as shown in equation 2.33.

$$F_{hkl} = \sum f_j e^{2\pi i \boldsymbol{S}\cdot(\boldsymbol{r_j}+\boldsymbol{u})} = e^{2\pi i \boldsymbol{S}\cdot\boldsymbol{u}} \sum f_j e^{2\pi i \boldsymbol{S}\cdot\boldsymbol{r_j}} \quad 2.33$$

where *S* is the scattering vector.

The use of a power series for the term $e^{2\pi i \boldsymbol{S}\cdot\boldsymbol{u}}$ containing the mean value of the amplitude of the oscillation, allows writing the structure factor in the form:

$$F_{hkl} = \sum f_j e^{-\left(B\sin^2\theta/\lambda^2\right)}\ e^{2\pi \boldsymbol{S}\cdot\boldsymbol{r_j}} \quad 2.34$$

B is the *Debye-Waller factor* also called *temperature factor*, and can be expressed through the mean square value of the amplitude of the oscillation $U = \langle u^2 \rangle$ as:

$$B = 8\pi^2 \langle u^2 \rangle = 8\pi^2 U \quad 2.35$$

In a crystal structure refinement all non-H atoms are refined anisotropically; consequently, the term U_{iso} for the isotropic case is replaced by six coefficients, U_{ij}, describing the dimensions and the orientation of an ellipsoid.

Amongst the other factors affecting the intensity of a diffraction peak, an important role is constituted by absorption effects and primary and secondary extinction.

Depending on the radiation used and on the nature and composition of the crystal, the incident and the outgoing beams suffer from absorption by the material. The extent of this absorption is a function of the path that the radiation covers inside the crystal and it will vary with the Bragg angle θ and the crystal morphology. Absorption corrections can be made on the set of diffraction data in order to recover part of the intensity and, accordingly, more information regarding the crystal structure of the material under study.

Primary and secondary extinction effects arise from the fact that a diffraction experiment is carried out on a *real crystal*. Opposed to *ideal crystals*, where the crystal lattice is constituted by an ordered array of atoms or molecules without any impurities or defects, the structure of a real crystal displays various small ordered domains, which are slightly displaced in respect to one another; the amount of displacement is indicated by the *degree of mosaicity*. As shown in Figure 2.6, the incident beam *AB* is partly reflected of an angle θ by the *PP'* plane along the *BC* direction.

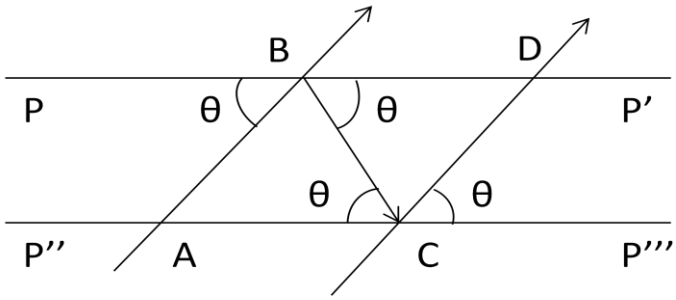

Figure 2.6. *Schematic representation of the effect of primary extinction.*

The diffracted *BC* beam impacts with the same angle θ on the *P''P'''* plane, causing reflection of the *CD* beam, parallel to the incident beam *AB*. The beam diffracted firstly along *BC* and then along *CD* is not in phase with the primary beam *AB*, having a displacement of $\pi/2$. The result is a destructive interference between the two beams, *AB* and *CD*, causing a decrease of the intensity of the outgoing diffracted beam. This effect is known as *primary extinction* and can be minimised using crystals with high mosaicity: the different domains diffract the incoming radiation at slightly different θ values, confining the primary extinction effect inside a single domain.
Secondary extinction arises with the penetration of the incident radiation inside the crystal: the incoming beam will lose part of its original intensity, due to diffracting effects along the path. This phenomenon affects especially intense reflections and it is comparable to the absorption effect. As for the case of primary extinction, it can be minimised using crystals with high mosaicity.

2.1.4. Single crystal X-ray instrumentation

Single crystal X-ray diffraction experiments were performed at the University of Bath, UK, on three diffractometers, depending on the crystals dimensions: an Agilent Technologies Gemini A Ultra CCD diffractometer, an Agilent Technologies Xcalibur diffractometer, both used for reasonably large crystals, and an Agilent Technologies SuperNova Dualwavelength diffractometer for the study of very small crystals. The Xcalibur diffractometer uses a monochromatic Mo-K_α radiation (λ = 0.71073 Å), while the Gemini and SuperNova diffractometers display two micro-focus X-ray sources, one with a molybdenum target and the other with copper Cu-K_α (λ = 1.5418 Å). All three diffractometers are equipped with Oxford Cryosystems, a Cryojet apparatus for the Gemini and a Cryostream for the Xcalibur and SuperNova, to ensure a standard temperature collection of 150K, with the possibility of reaching 100K for variable temperature studies. They all have a four-circle kappa goniometer, which allows easy crystal loading and alignment. Data collection and data reduction were performed with the software CrysAlisPro version 1.171.36.21. In Figure 2.7 a picture of the SuperNova apparatus is reported.

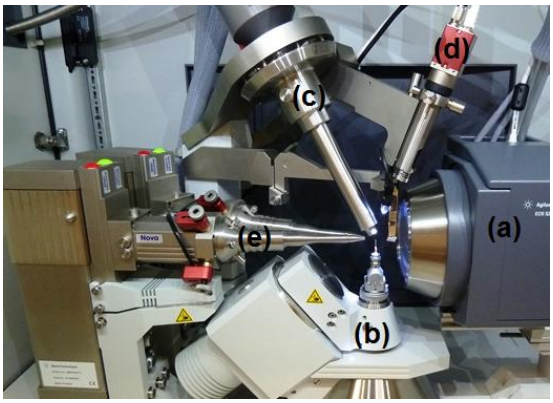

Figure 2.7. *Agilent Technologies SuperNova DualWavelength diffractometer. (a) CCD detector; (b) four-circle goniometer; (c) cryostream; (d) positioning camera; (e) X-ray beam exits.*

After mounting of a suitable crystal and its centring in the X-ray beam, an initial screening is performed to assess the quality of the single crystal. A default of 10 diffraction images is recorded and the unit cell parameters are suggested. Additional information is also given at this stage: the number of peaks that fit the proposed unit cell and estimations of the I/σ for various resolution values, along with the diffraction limit and the mosaicity of the sample. If the quality of the crystal is judged adequate, a pre-experiment is launched to better determine the unit cell parameters and diffraction symmetry. Usually 15 frames are recorded when the pre-experiment is carried out using the Mo source, while a total of 30 frames are collected for the Cu radiation, half low-angle and the other at high angles. At this stage is possible to change the exposure time to the X-ray beam to enhance the scattering by the crystal. At the end of the pre-experiment a data collection strategy is calculated, but changes can be made manually, especially regarding the portion of reciprocal space to be investigated, by selecting the Laue symmetry, and the exposure time, which should be longer at high angles when working with Cu radiation. Data reduction starts automatically after the whole experiment is complete, but also in this case, a manual re-process of the data can be done.

The final data sets are given as a list of *hkl* values with the corresponding F_o^2 and $\sigma(F_o^2)$ and are studied with the use of the WinGX[54] package, with XPREP[55] for the initial setup, SHELXS-97[56] for solving the structure and SHELXL-97[57] for the structural refinement and the production of a *crystallographic information file* (***.cif***), which contains coordinates and thermal parameters for all atoms. All ***.cif*** files relative to the crystals studied in this work are reported on a CD-ROM attached to the back cover of the thesis.

2.1.5. Powder diffraction

All the principles of diffraction described above for single crystals also apply to powder samples. The main advantage in using powder diffraction over single crystal diffraction is the simplicity in

the preparation of the sample, which must be in the form of a fine powder, highly reducing time and effort during the preparation process. Powder diffraction is highly used by mineralogists and geologists for the investigation of the various phases contained in a mineral or for studies on the composition of a soil. In addition, powder diffraction is a useful technique for material science studies, where the presence of different phases can affect the behaviour of a material. It plays a crucial role in *in situ* experiments, allowing monitoring of a reaction while it takes place, or studying of changes in the crystal structure upon variation of temperature or pressure.

A powder sample contains a large amount of microcrystallites, with random orientations. An incident radiation, X-rays or neutrons, impacting on the surface of the powder, causes diffraction by those microcrystallites, whose orientation satisfy Bragg's law, $\lambda = 2d_{hkl}sin\theta$. Since diffraction occurs in every possible direction, the result is a cone with angular aperture of 4θ. For each family of lattice planes different cones with different angular aperture are generated. The formation of these cones can be explained using the reciprocal lattice: since there are a large number of crystallites, orientated in every possible direction, the points of the reciprocal lattice lie on the surface of the various spheres with radius $d^*_{hkl} = {}^1/_{d_{hkl}}$. The intersections of these spheres with the Ewald's sphere originate rings, which are perpendicular to the incoming beam and whose centres lie on the direction of the incident radiation, *IO* (Figure 2.8).

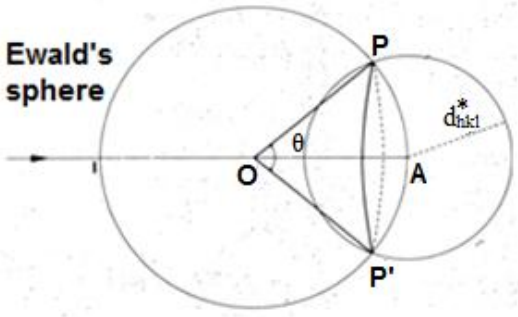

Figure 2.8. *Schematic representation of the formation of cones with angular aperture* $\mathbf{4\theta}$[51].

The diffraction cones are concentric and each one of them is characterised by a different value of d_{hkl}. The greatest problem of powder diffraction arises at this point: similar values of d-spacing can cause the diffraction cones to overlap with one another, leading to incorrect results. The resulting mono-dimensional powder pattern is usually given as *I vs. 2θ* plot. Knowing the wavelength of the incident beam and replacing the values for θ into the Bragg's law, $\lambda = 2d_{hkl}sin\theta$, the d-spacing values for each family of *hkl* planes are calculated, allowing, after indexing of the peaks, all lattice parameters, *a, b, c, α, β, γ*, to be defined by the relationships shown in Table 2.3. The lower the symmetry of the sample, the more complicated it is to calculate the lattice parameters.

Crystal system	Equation for d_{hkl}
Cubic	$\frac{1}{d_{hkl}^2} = \frac{h^2+k^2+l^2}{a^2}$
Tetragonal	$\frac{1}{d_{hkl}^2} = \frac{h^2+k^2}{a^2} + \frac{l^2}{c^2}$
Orthorhombic	$\frac{1}{d_{hkl}^2} = \frac{h^2}{a^2} + \frac{k^2}{b^2} + \frac{l^2}{c^2}$
Hexagonal	$\frac{1}{d_{hkl}^2} = \frac{4}{3}\left(\frac{h^2+hk+k^2}{a^2}\right) + \frac{l^2}{c^2}$
Monoclinic	$\frac{1}{d_{hkl}^2} = \frac{1}{sin^2\beta}\left(\frac{h^2}{a^2} + \frac{k^2 sin^2\beta}{b^2} + \frac{l^2}{c^2} - \frac{2hlcos\beta}{ac}\right)$
Triclinic	$\frac{1}{d_{hkl}^2} = \frac{1}{V^2}\begin{pmatrix} h^2b^2c^2sin^2\alpha + k^2a^2c^2sin^2\beta + l^2a^2b^2sin^2\gamma \\ +2hkabc^2(cos\alpha cos\beta - cos\gamma) \\ +2kla^2bc(cos\beta cos\gamma - cos\alpha) \\ +2hlab^2c(cos\alpha cos\gamma - cos\beta) \end{pmatrix}$
	$V = abc(1 - cos^2\alpha - cos^2\beta - cos^2\gamma + 2cos\alpha cos\beta cos\gamma)^{1/2}$

Table 2.3. *Summary of the equations allowing calculating unit cell parameters from a set of powder data*[58].

Even though there are a fewer number of factors to be taken into account in the preparation of a powder sample compared to a single crystal, experimental problems can emerge if a complete statistical distribution of the microcrystallites inside the powder is not achieved. This situation is present when the morphologies of the crystallites are not close to a sphere, but rather are elongated, similar to needles or thin plates. The consequence is a *preferred orientation* of the crystallites inside the sample: the intensities of the diffraction peaks are affected by the contribution of all the families of *hkl* planes that favour a particular orientation in order to satisfy the Bragg's law. By knowing which orientations are the preferred ones in a powder sample, it is possible to correct the powder pattern, removing the false contributions to a specific diffraction peak. Complete removal of the effects caused by preferred orientation can be achieved by the simultaneous rotation of the powder along two directions.

2.1.6. Powder diffration geometries

After Laue's discovery of diffraction by crystals, powder diffraction experiments were perfomed using the so-called Debye-Scherrer method, where the powder sample is contained in a thin cylindrical capillary mounted on a rotable sample holder and diffraction events are recorded on a film. This method allowed for the simultaneous collection of all reflections in one single exposure.

Although Debye-Scherrer cameras are very reliable devices equipped with highly precise optical instrumentations, their usage has decreased over the years in favour of modern powder diffractometers. A high resolution powder diffractometer can be constructed using different self-focusing geometries because the beam produced by a laboratory X-ray source is divergent. In Figure 2.9 the optical focusing instrumentation is reported.

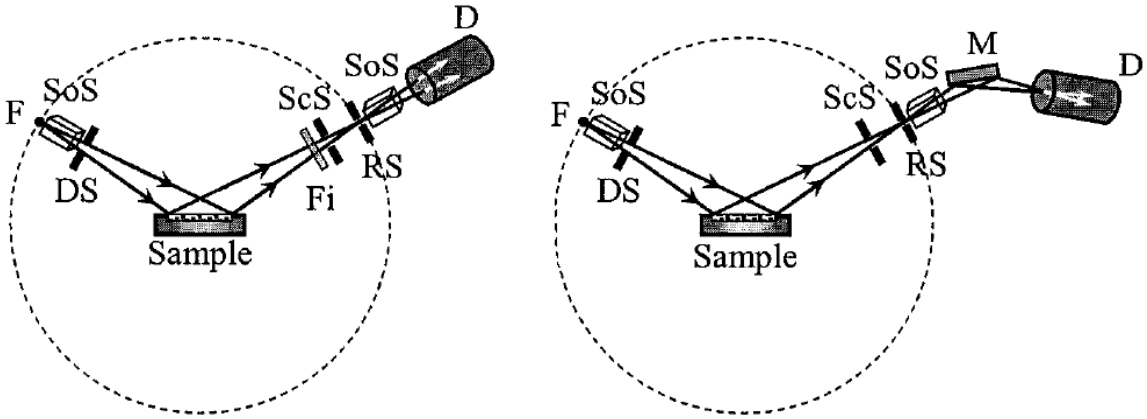

Figure 2.9. *Typical focusing optics employed in modern powder diffractometry: without (left) and with (right) the diffracted beam monochromator. F is the focus of the X-ray source; SoS are the Soller slits; DS is the divergence slit; Fi is the β-filter; ScS is the scatter slit; RS is the receiving slit; M is the monochromator; and D is the detecto*[53].

After passing through the Soller slits, which aim to restrict the divergence of the beam, the incident beam irradiates the sample and the diffracted beam self-focuses at the receiving slit. The diffracted beam can be monochromatised using a β-filter or a crystal monochromator. A monochromator placed after the diffracted beam is generated allows reaching a reduction of the background.

The most common geometry used for powder diffraction experiments is the Bragg-Brentano geometry in reflection mode, which indicates that the scattered intensity is registered on the detector after reflection from the sample. This geometry is displayed in Figure 2.10.

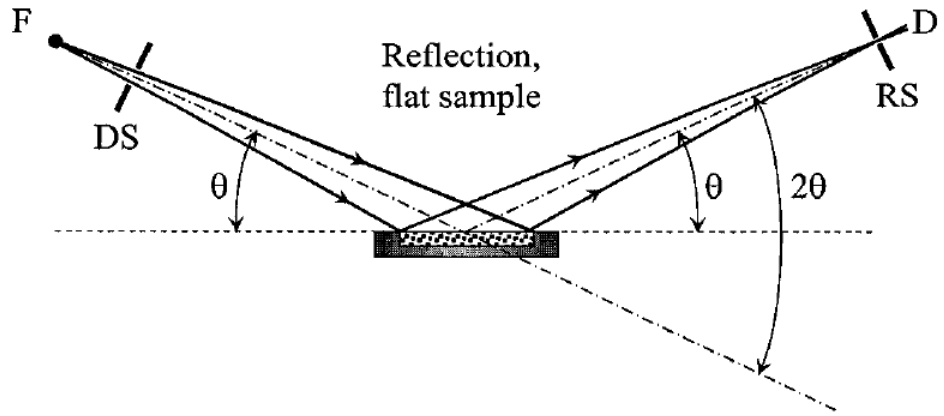

Figure 2.10. *Schematic representation of the Bragg-Brentano geometry in reflection mode. F is the focus of the X-ray source; DS is the divergence slit; RS is the receiving slit; and D is the detector*[58].

Usually, in a powder diffraction experiment with this kind of set-up the position of the X-ray source is fixed, while sample and detector are allowed to rotate along the goniometer axis by the angles θ and 2θ, respectively, where θ is the angle that both incident and diffracted beams form with the sample, while 2θ is the angle between diffracted and incident beam. The main advantage offered by the reflection geometry is constituted by the self-focusing of the diffracted beam, leading to high resolution and high diffracted intensity.

In addition to the reflection mode, powder data in a Bragg-Brantano configuration can be colleted using the transmission geometry. In this case the diffracted intensities are recorded on the detector after transmission of the incident radiation through the sample. A schematic representation of this geometry is reported in Figure 2.11.

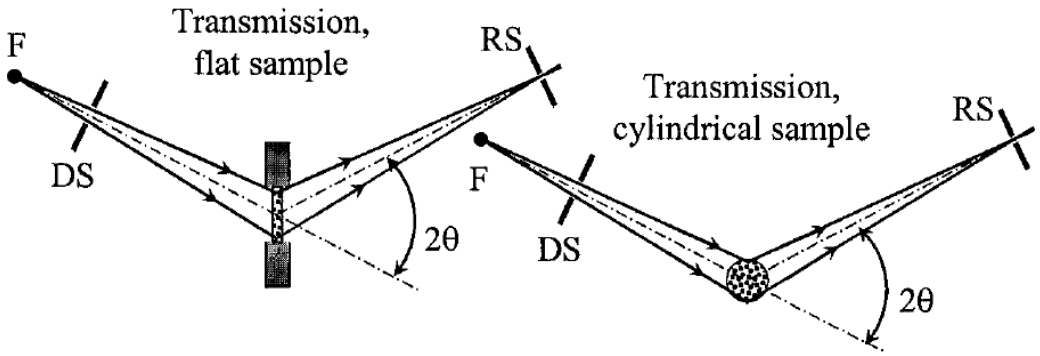

Figure 2.11. *Representation of the transmission geometry for a flat (left) and a cylindrical (right) sample. F is the focus of the X-ray source; DS is the divergence slit; RS is the receiving slit; and θ is the Bragg's angle*[58].

As shown in Figure 2.11, the sample can be placed either on a flat support or in a cylindrical capillary. The latter offers an easier sample preparation, since it may be difficult to obtain a

uniformerly dense sample for the flat configuration, and it is less affected by preferred orientation. The reduced self-focusing ability of a diffracted beam in the transmission geometry causes a lower resolution when compared to data collected in reflection mode.

2.1.7. Powder data refinement

One of the best methods used for structural refinement from powder data was developed in 1967 by Hugo M. Rietveld[58], after whom the method was named.

The success of the Rietveld method is based on the refinement of structural and instrumental parameters without extracting either the intensity of each diffraction event or their structure factors, thus bypassing the problem of overlapping peaks in the one-dimensional powder diffraction pattern. The major limitation of the Rietveld method is the need of a good structural model as a starting point. It is a method used only for structure refinement, since it cannot perform a structure determination of an unknown material.

The Rietveld refinement is based on the minimisation of the difference (eq 2.36) between the experimental data and the profile calculated from the initial model by non-linear least squares procedures.

$$S_y = \sum_i w_i \left(y_i^{obs} - y_i^{calc}\right)^2 \qquad 2.36$$

where y_i^{obs} is the observed intensity at point *i*, y_i^{calc} is the calculated intensity at the same point *i*, and w_i is a weight factor, calculated as $w_i = {}^{1}/_{y_i^{obs}}$.

The calculated profile for a single phase sample is given by eq 2.37.

$$y_i^{calc} = s \sum_H L M_H |F_H|^2 \varphi(2\theta_i - 2\theta_H) P_H A + y_i^{bkg} \qquad 2.37$$

in which *s* is the overall scale factor; *H* refers to the Miller indices of a Bragg reflection; *L* contains the Lorentz and polarisation factors; M_H is the multiplicity; F_H is the structure factor for the H^{th} Bragg reflection; $\varphi(2\theta_i - 2\theta_H)$ is a profile function, where $2\theta_i$ is corrected for the 2θ zero error; P_H represents the preferred orientation function, which was not applied in the current work, due to neutron powder diffraction being less sensitive to preferred orientation than X-ray techniques; *A* is the absorption factor; and y_i^{bkg} is the intensity of the background at point *i*.

A structural refinement obtained with the Rietveld method is successful if a very accurate model for the peak shape function is achieved. The peak shape $\varphi(\Delta\theta_{ik})$ can be affected by several factors, both instrumental and from the sample. Amongst the instrumental contributions to the peak shape

function there are the radiation source, especially for sealed tube or rotating anode sources; the monochromator; slit systems, which usually contribute to broaden the peak profile; axial divergence, which adds asymmetry to low angle peaks; and misalignment of the sample, which may give erroneous peak positions. Contributions by the sample consist in its degree of mosaicity; absorption effects, which vary for different setup geometries and cause broadening of the peaks and a shift of the profile towards lower 2θ angles; crystallites size effects, producing a broadening β in radians defined by the Scherrer equation $\beta = k\,\lambda/(T cos\theta)$, where T is the thickness of the sample; and strain broadening.

$\varphi(\Delta\theta_{ik})$ is usually defined by a pseudo-Voigt function, which arises by combining Gaussian (G) and Lorentzian (L) components, as shown in eqs 2.38, 2.39, 2.40, respectively.

$$\varphi(\Delta\theta_{ik}) \approx \eta L + (1-\eta)G \tag{2.38}$$

$$G = \frac{2\sqrt{ln2}}{\sqrt{\pi}H_k} exp\left[-4ln2\left(\frac{\Delta\theta_{ik}}{H_k}\right)^2\right] \tag{2.39}$$

$$L = \frac{2}{\pi H_k}\left(1 + 4\left(\frac{\Delta\theta_{ik}}{H_k}\right)^2\right)^{-1} \tag{2.40}$$

where H_k represents the full-width-at-half-maximum (FWHM) of the k^{th} peak and η is a refinable mixing parameter allowed to vary in the interval $0 \leq \eta \leq 1$: when $\eta = 0$, the pseudo-Voigt function is reduced to a pure Lorentzian function, opposed to the case $\eta = 1$, which defines a pure Gaussian.

The FWHM is known to vary with the 2θ angle, as shown in eq 2.41 for the Gaussian component and in eq 2.42 for the Lorentzian contribution.

$$H_k^2 = U\,tan^2\theta_k + V\,tan\theta_k + W \tag{2.41}$$

$$H_k = X\,tan\theta_k + \frac{Y}{cos\theta_k} \tag{2.42}$$

U, V, W, X and Y are refinable parameters used to describe the peak broadening due to particle size effects. Asymmetry of peaks at low scattering angles and the shift of peak maxima to lower 2θ angles can be corrected by the semi-empirical factor k' (eq. 2.43).

$$k' = 1 - sP\frac{(\Delta\theta_k)^2}{tan\theta_k} \tag{2.43}$$

where *P* represents the asymmetry parameter and *s* can assume the values -1, 0, +1 when $\Delta\theta_k$ is negative, zero or positive, respectively.

As stated before, the Rietveld refinement is carried out by non-linear least squares procedures, which, after consecutive refinement cycles, find the best set of increments that, once added to free variables selected for the initial model, minimise the corresponding function, leading to the best fit between observed and calculated data. Since both the data and the computations are of finite accuracy, it cannot be expected to reach a situation in which every refined parameter has become zero. Four important figures of merit (FOM) help the powder crystallographer to recognise the right time to end a structural refinement: $R_{profile}$ (eq 2.44), $R_{weighted\ profile}$ (eq 2.45), $R_{expected}$ (eq 2.46), and the goodness-of-fit χ^2 (eq 2.47).

$$R_{profile} = R_p = 100 \left[\frac{\sum_i \left|y_i^{obs} - y_i^{calc}\right|}{\sum_i y_i^{obs}}\right] \qquad 2.44$$

$$R_{weighted\ profile} = R_{wp} = 100 \left[\frac{\sum_i w_i \left(y_i^{obs} - y_i^{calc}\right)^2}{\sum_i w_i \left(y_i^{obs}\right)^2}\right]^{1/2} \qquad 2.45$$

$$R_{expected} = R_{exp} = 100 \left[\frac{N - P + C}{\sum_i w_i \left(y_i^{obs}\right)^2}\right]^{1/2} \qquad 2.46$$

where *N* represents the number of total observations; *P* is the number of refined parameters; and *C* the number of constraints.

As shown in the equations above, all R-values have the total area of the powder patter as denominator, indicating the important role played by the background in a Rietveld refinement. Only in the case of a properly modelled background, the refinement is successful, displaying low R-values.

R_{exp} is a purely statistical value and it represents the smallest value for R_{wp} that is reached when in the model there are only random errors. This concept is better described by the goodness-of-fit χ^2:

$$\chi^2 = \left[\frac{1}{N - P + C}\right]^2 \sum_i w_i \left|y_i^{obs} - y_i^{calc}\right|^2 = \left[\frac{R_{wp}}{R_{exp}}\right]^2 \qquad 2.47$$

As the refinement progresses, the two values, R_{wp} and R_{exp}, should become similar, leading to an ideal χ^2 value of 1.

Although the R-values represent a valuable tool for recognising the quality of a refinement, it is important to remember that a residual value gives only a measure of the average residual, leading to the possibility of finding a local minimum in S_y, instead of a global one. The only effective way to avoid misinterpretation of a set of powder data during a Rietveld refinement is to plot on the same scale the observed and calculated profiles together with the difference between the two. By studying the difference profile it is possible to identify the parameters responsible for the local minimum: a shift between the observed and calculated data indicates a wrong value for the 2θ zero error, while discrepancies in the peak intensities are due to incorrect or incomplete refinement of structural parameters, such as unit cell parameters and contents.

The powder data obtained during the course of this thesis were analysed with the Generalised Structural Analysis Suite, GSAS[59], and its graphical interface EXPGUI. These programs analyse powder data performing a Rietveld refinement, whose principles are described above.
As for the case of single crystal data, the refinement process of power data is done in consecutive steps, each allowing one more parameter to be refined. After uploading into the program the best starting model available for the structure under study, the first parameter to be refined is the overall scale factor, which depends on beam intensity, phase volume fraction and phase cell volume, followed by the 2θ zero error correction, which should eliminate any difference in the position of the same peak in the calculated and measured patterns. The next step begins refining the background function, which consists in a cosine Fourier series, formed by a total of 36 parameters; usually, at this early stage only 5 terms for the background are allowed to be refined. At this point the lattice parameters are refined, followed by the introduction of the Gaussian coefficients U, V and W for the optimisation of the peak shapes; the Lorenztian components X and Y are usually not refined for neutron powder data, due to their lower effect on the overall peak shape function. Remaining differences in peak shape and intensity of the peaks can be minimised by refining the x, y, z coordinates and the isotropic temperature factors for each atom present in the unit cell.
If any atom is missing from the initial model, as is usually the case for H-atoms, a difference-Fourier map can be calculated. This option was not used during the refinement processes for the current thesis because the initial structural information was obtained by single crystal neutron diffraction experiments.

2.1.8. Powder X-ray instrumentation

For the purposes of this thesis, powder X-ray diffraction (PXD) measurements were undertaken to discriminate between polymorphs and to assess whether a new crystal structure had formed, by comparing the powder pattern of the unknown product to those of the starting materials. All PXD

analyses were performed on a Siemens D5000 diffractometer, a representation of which is reported in Figure 2.12.

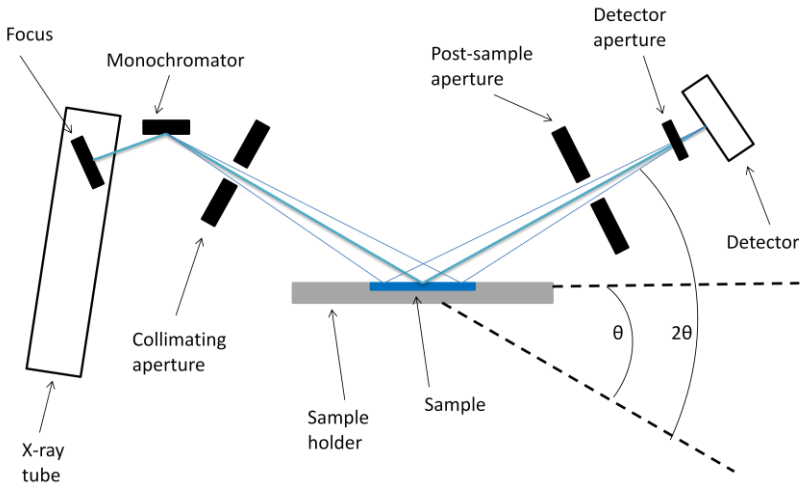

Figure 2.12. *Schematic representation of the D5000 powder diffractometer.*

This powder diffractometer is constituted by a copper source and a Ge(111) monochromator, which garantees a monochromatic X-ray beam of $Cu_{K_{\alpha 1}}$ with wavelength of λ = 1.5406 Å. It is configured in the Bragg-Brentano geometry with the sample rotating at half the rate of the detector in order to have a constant $\theta/2\theta$ relationship. The two slits with aperture of 2mm, which are placed before and after interaction with the sample, provide collimation of both incident and diffracted beams, respectively. The diffracted beam passes through an additional aperture of 0.2 mm and it is, finally, recorded on the detector.

All crystalline samples analysed by PXD were manually ground into a fine powder and placed on Perspex sample holders. Data were collected between 3˚ and 40˚ in 2θ in step increments of 0.02˚ with Cu radiation, λ = 1.5406 Å.

2.2. Neutrons

After a short period of time since their discovery by Chadwick in 1932, the wave-like behaviour of neutrons was recognised. The first experimental proof of this hypothesis, predicted by Elsasser (1936)[60], was carried out by Halban and Preiwerk (1936)[61] on a powder sample; a few months later, Mitchell and Powers (1936)[62] demonstrated that neutron diffraction was also possible from a single crystal. The experiments used radioactive beryllium sources; the outgoing neutrons were neither monochromatic nor constant and, although sufficient to prove the diffraction of neutrons by crystalline materials, could not give any quantitative results. With the development of nuclear reactors it has been possible to produce a sufficient amount of neutrons in order to allow the

collimation in beams and their limitation in energy in sufficiently narrow peaks. In this way neutrons can be used like X-rays for crystallographic experiments.

For the investigation of the arrangement of atoms in crystals, the wavelength of neutrons, or any other particle beam with oscillating properties, must be of the same order of magnitude as the distance between atoms. In the case of neutrons λ, based on the oscillatory theory, is given by the *de Broglie* eq. 2.48:

$$\lambda = {}^{h}/_{mv} \qquad 2.48$$

where h is Planck's constant, m is the neutron mass and v is its velocity.

In a nuclear reactor at a given temperature T neutrons come out of its core, after going through several collisions. The averaged squared velocity, which is dependent on the temperature, needs to be considered, as in eq. 2.49:

$${}^{1}/_{2}\, mv^2 = {}^{3}/_{2}\, kT \qquad 2.49$$

where k is the Boltzmann constant.

The combination of eqs. 2.48 and 2.49 in:

$$\lambda^2 = {}^{h^2}/_{3mkT} \qquad 2.50$$

allows for the calculation of the wavelength of the neutrons depending on their temperature.

The final neutron beam is obtained by adding a collimator on the reactor walls.

As shown in paragraph 2.1, with X-rays the scattering factor of an atom is dependent from the square of its atomic number, Z^2, and it decreases rapidly for high values of ${}^{sin\theta}/_{\lambda}$, leading to a loss in peak intensity at high angles. The consequent problems arise: since X-rays are scattered by the electron clouds surrounding the atom, it is difficult to distinguish between neighbouring elements in the periodic table and, at times, absolutely impossible to detect light atoms, especially H atoms, in the presence of heavier ones. These inconveniences can be overcome using a neutron beam, instead of X-rays, for the study of a crystal structure. The main difference between X-rays and neutrons is the fact that the latter are scattered by the nucleus of an atom, rather than by its electron cloud. As direct consequence of this characteristic, the scattering power of neutrons depends on the properties of the nucleus itself, causing the lack of a fall-off of scattering power as a function of scattering angle, allowing data collection at high angle and, consequently, the study of structures at very high resolution.

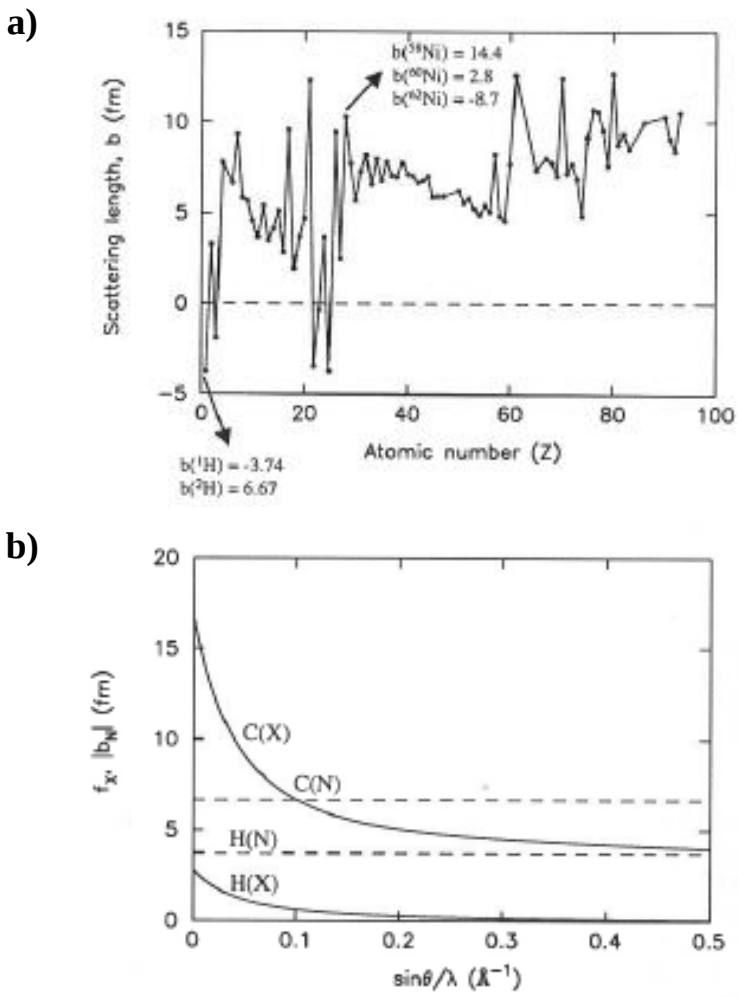

Figure 2.13. *a) Neutron scattering length values for increasing atomic number[63]. b) Comparison between X-ray scattering factors (solid lines) and neutron scattering lengths (dashed lines) for carbon and hydrogen atoms[63].*

As shown in Figure 2.13a not only isotopes of an atom have very different scattering lengths, as the case of Ni, but some of those values are negative, a fact that increases the contrast between different elements. This intrinsic property of the nucleus represents a valuable advantage in all those cases involving light atoms, such as hydrogen atoms, which are very difficult to detect with X-rays because of the presence of just one electron in their electronic configuration. The scattering length for the hydrogen atom is $b = -3.74\ fm$, a very different value compared to those of non-metallic elements as carbon, nitrogen, oxygen, etc. In Table 2.4 some scattering length values for some elements are reported.

Z	Nucleus	b *(fm)*	Z	Nucleus	b *(fm)*
1	^{1}H	-3.74	15	*P*	5.13
1	^{2}H	6.67	16	*S*	2.80
4	*Be*	7.79	25	*Mn*	-3.73
6	^{12}C	6.65	26	*Fe*	9.45
8	^{16}O	5.80	29	*Cu*	7.72
12	*Mg*	5.37	30	*Zn*	5.68
13	*Al*	3.45	82	*Pb*	9.40
14	*Si*	4.15	92	*U*	8.42

Table 2.4. *Neutron scattering length values for different element in the periodic table*[64].

The properties of neutrons can be summarised as follow:

- neutrons can easily detect light atom, as hydrogen, in the presence of heavier ones. For example, in the presence of relatively heavier carbon atoms, hydrogen atoms contribute only by $^{1}/_{36}$, less than 0.03, of the X-ray scattering intensity from a carbon atom. The equivalent ratio for neutrons is around 0.32, meaning that hydrogen atoms are determined almost 12 times more accurately with neutrons than X-rays, in the presence of carbon atoms. This factor generally increase for heavier atoms, reaching 41 for hydrogen in the presence of oxygen and almost 1100 for hydrogen and lead;
- neighbouring elements in the periodic table have substantially different scattering cross-sections;
- the dependence of the scattering power on the nucleus allows for different scattering length values for isotopes, thus allowing the technique of isotopic substitution to be used to understand structural and dynamical details. In the field of organic molecular structure, the most relevant isotopic substitution is that of deuterium, D, $b = 6.67\ fm$, for hydrogen, H, $b = -3.74\ fm$. This also allows for the use of contrast variation, where the scattering density of different parts of a molecule or of a $H_2O - D_2O$ system is altered;
- the lack of a fall-off in scattering power as a function of scattering angle gives neutron diffraction the ability to study structures to very high resolution, even though also for neutrons there will be a fall-off in scattered intensity caused by thermal effects.

2.2.1. Neutron generation

The production of neutrons suitable for research experiments is achieved in two different facilities: spallation sources and nuclear reactors.

The spallation process is a dynamic mechanism based on the acceleration of protons, which impact on a heavy metal target. An example of such a source is the ISIS facility at the Rutherford

Appleton Laboratory in Oxfordshire, UK. In this case, three steps can be identified during the production of neutrons. The first is the generation of H^- ions, which are accelerated in a pre-injection column. The second step is an additional acceleration through four accelerating radio frequency cavities. Finally, the beam of accelerated H^- ions is injected into a synchrotron, where it reaches a thin alumina foil. This foil has the purpose of pulling out the electrons, producing a circulating beam of protons, which can be directed onto the metallic target. This process is repeated 50 times per second.

Neutrons are produced when the 160 kW proton beam from the accelerator hits a metal target, roughly the size of a house brick, which is made of a series of thick tungsten plates, clad with tantalum to prevent corrosion, and housed in a pressured vessel. Water cooling channels remove around 90 kW of heat generated in the target. Moderators surround the target, so that the outgoing neutron beam can be thermalised. There are three moderators in use at ISIS: water at ambient temperature; liquid methane at 105K; and a cold moderator of liquid H_2 at 25K. A beryllium reflector, which concentrates the fast neutron flux into the area occupied by the moderators, surrounds the whole target. Cadmium or boron decouplers are wrapped around the wall of the moderator facing the reflector. This restricts the incoming neutrons to the high energy part of the spectrum and prevents the pulse width to be degraded by slow neutrons, which have been moderated in the beryllium reflector itself. The slow neutrons emitted by the front face of the moderator pass through collimators, 2 m long, to reach the beamlines and the instruments.

In a nuclear reactor neutrons are produced by a fission reaction. Typically, the fuel core is made by highly enriched uranium ^{235}U, surrounded by a moderating region, usually light or heavy water, which also provide the reactor with a cooling system. A reflection region, constituted by beryllium and water, embraces the cooling area, increasing the effective flux by reflecting back fast neutrons, which will induce further fission processes. The whole reaction vessel is placed at the centre of a so-called *swimming pool*, which provides the first biological shielding. The beam coming out of the reflection area is highly energetic, of the order of the MeV, too high for an experiment on condensed matter. In order to decrease the energy and slow down the neutron beam, moderators are used. The role of a moderator is to slow down neutrons by exploiting their large collision cross-section associated with the hydrogen atom. Since hydrogen is the most abundant element, neutron moderators can be built from common materials, as water, methane, hydrocarbons and hydrogen itself. The neutron beam passes through the moderator, where it is subjected to multiple collisions with the hydrogen atoms of the moderator itself. The fact that fast neutrons are at much higher temperature than the molecules in the moderator makes the loss of energy from neutrons higher than the gain of energy they can get during the collisions. There are two factors affecting the action of a moderator: its temperature and the number of collisions; the latter is determined by the size and shape of the moderator. When the thermalised white beam comes out of the moderator, it

reaches a monochromator, usually a crystal or a diffracting grating abiding to Bragg's law, giving a very narrow range in wavelength. At this point the neutron beam is ready to be used in an experiment.

A high flux neutron reactor is located at the Institut Laue-Langevin (ILL), in Grenoble, France. A schematic representation of the ILL reactor is reported in Figure 2.14.

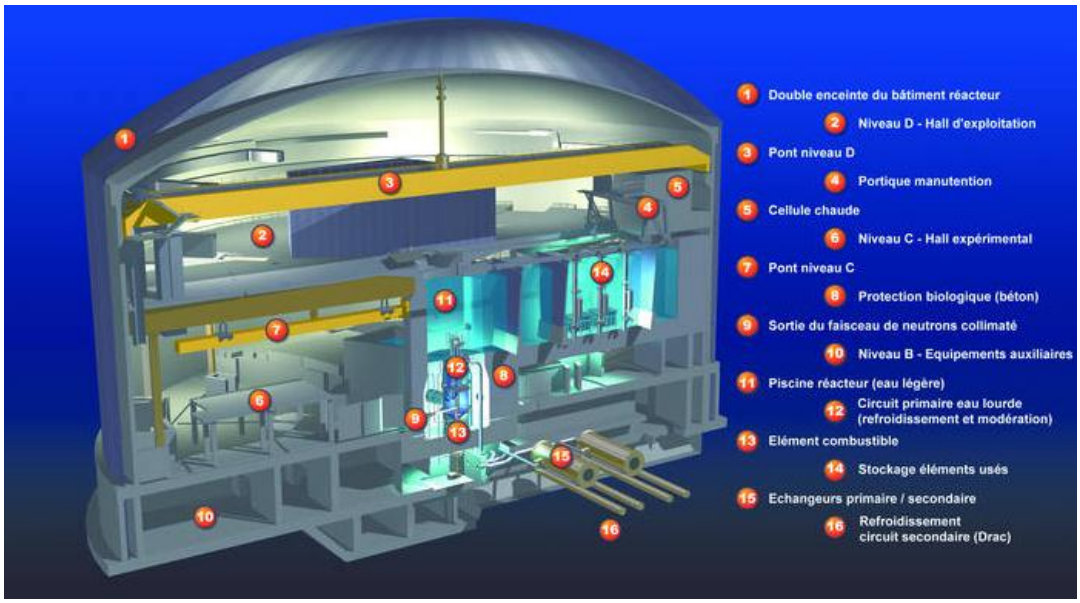

Figure 2.14. *Representation of the nuclear reactor at ILL, Grenoble, France*[65].

The ILL high flux reactor is devoted exclusively to research and it operates continuously in 50-day cycles. Its core is constituted by a single highly enriched uranium, ^{235}U, fuel element (10kg), which is cooled by heavy water. The reactor produces the most intense continuous neutron flux in the world, namely 1,5 x 10^{15} neutrons per second per cm^2. Its thermal power of 58 MW is not reused and is removed by a secondary cooling system supplied with water from the river Drac. The heavy water that contains the core is situated in a pool filled with demineralised water, which provides shielding form neutrons and gamma radiation produced by the core. The reactor is controlled by means of a neutron controlling rod, which is gradually withdrawn from the core as the uranium is burned up. In addition, there are other five safety rods, which are also neutron absorbing devices, and are used to shut down the reactor in the event of an emergency.

The neutrons produced in the reactor by fission are very high-energy neutrons with a speed of 20000 km/s. They are slowed down by the heavy water, triggering further fission events in order to sustain the chain reaction and supplying neutrons to the scientific instruments.

Three components, located in the immediate vicinity of the core, make it possible to produce hot neutrons as well as cold and ultra-cold neutrons, with speed of 10 km/s, 700 m/s and 10 m/s, respectively. These components are a hot source made of a graphite sphere maintained at a temperature of 2600˚C, and two cold sources, the largest of which is a sphere containing 20 litres

of deuterium maintained in a liquid state at -248˚C, in which neutrons are slowed down to the desired energy by a succession of collision with the deuterium atoms.
Neutrons are extracted from inside the reactor vessel by twenty beamtubes, some of which are directed at the hot source or one of the cold sources. These beamtubes, which extend outside the reactor pool in the form of neutron guides, then supply neutrons to around forty experimental areas equipped with leading-edge instruments, located up to 100 m from the reactor.

2.2.2. Neutron instrumentation

2.2.2.1. Single crystal diffractometer

All the neutron experiments were performed at the Institut Laue-Langevin (ILL) in Grenoble, France, on the diffractometer D19. D19 is a monochromatic thermal neutron single crystal diffractometer, a scheme of which is reported in Figure 2.15. It is usually employed for the structural determination of organometallic complexes, biological molecules and proteins; for the determination of the composition of a mineral; for studies on changes of the crystal structure with temperature; and for a deep comprehension of hydrogen bonded systems. It is also used for studies on hydrogen bonding and hydration in biopolymers and for magnetic studies on polycrystal samples.

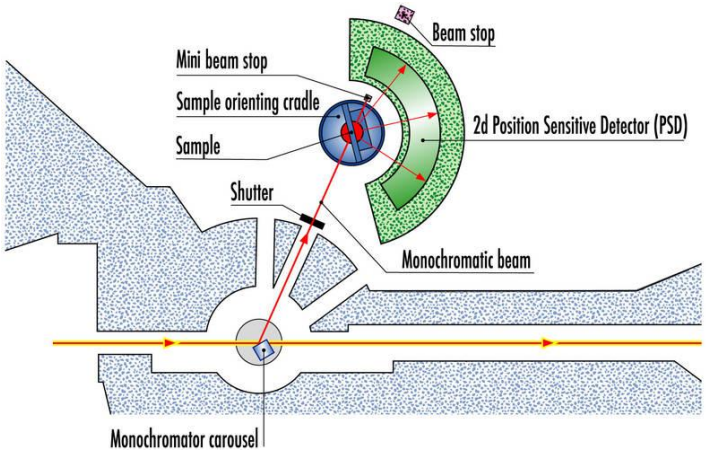

Figure 2.15. *Schematic representation of the D19 single crystal diffractometer at ILL*[66].

Within the ILL facility, D19 is placed close to the reactor, providing high flux for the experiments, and its shares the H11 thermal beam tube with the two powder diffractometers, D2B and D20. Its close proximity to the reactor core makes sure that D19 is the first to receive the neutrons from part of the H11 beam tube. Also the D19 monochromator is relatively close to the core, giving high flux and it has high resolution, due to a maximum monochromator take-off angle of 90˚. There is a total

of four monochromators, which can be rotated into diffracting position using an ILL box-shaped monochromator mounted so that the wavelength choice can be matched to the sample.

D19 has a range in wavelength between 0.8 and 2.4 Å and works very efficiently for crystals with large unit cell volumes. It is equipped with a very large (120° x 30°) "banana" position-sensitive detector (PSD), which works at high gas pressure: 5 atm of He + 1 atm of CF_4. This configuration provides the instrument with high efficiency coupled with high resolution. The detector, mounted horizontally, is set symmetrically about the equatorial plane, with the sample placed at the centre of the horizontal curvature. The "banana" PSD rotates on a γ-arm, where $\gamma = 2\theta$ in the equatorial plane, on air cushions, allowing the required positioning for the experiment. The sample is mounted on a C-shaped Eulerian cradle with offset phi axis; this allows for a larger range in ω than a conventional cradle and, also, for the installation of a 2-stage Displex, which can cool below 20K. A summary of the main features of D19 is reported in Table 2.5.

Monochromator	
Vertically focussed	Graphite (002)
	Germanium (11n), (335)
Flat	Copper (220), (331)
	Copper (111), (224)
Bragg angle $2\theta_m$	42.7°, 70° or 90°
Wavelength	0.8 Å < λ < 2.4 Å
Collimation	
Before monochromator	60' (natural)
Sample	
Maximum beam size	10 mm
Flux	$10^7 - 10^8$ n cm^{-2} s^{-1}
Angular range	-60° < γ < 140°
	-45° < ω < 210°
	+56° < χ < 205°
	-180° < φ < 180°
Position-sensitive detector	
Angular range	120° x 30°
Detector gas	^{3}He (5 atm) + CF_4 (1 atm)
Nominal resolution for fixed sample-detector distance of 76 cm	0.19° horizontally x 0.12° vertically

Table 2.5. *Main features of D19.*

In order to perform an experiment, a single crystal is mounted on the Eulerian cradle and centred in the beam. When the polychromatic beam comes out from the reactor, it arrives on the monochromator, where the desired wavelength is selected, and, then, goes on until it reaches the sample. The sample is rotated step by step around the vertical axis while the detector records the intensity profiles of the diffracted beam. The sample can be set to a specific orientation by rotating the three angles of the Eulerian cradle.

2.2.2.2. Powder diffractometer

D20 is a very high intensity 2-axis diffractometer equipped with a large micro-strip detector. Due to its extremely high neutron flux, it opens up new possibilities for real time experiments on very small samples. Its applications fall in various fields, such as thermo-diffractometry, magnetism, physisorption, studies of kinetics, analyses on texture, small samples and disordered systems. A scheme of the instrument configuration is reported in Figure 2.16.

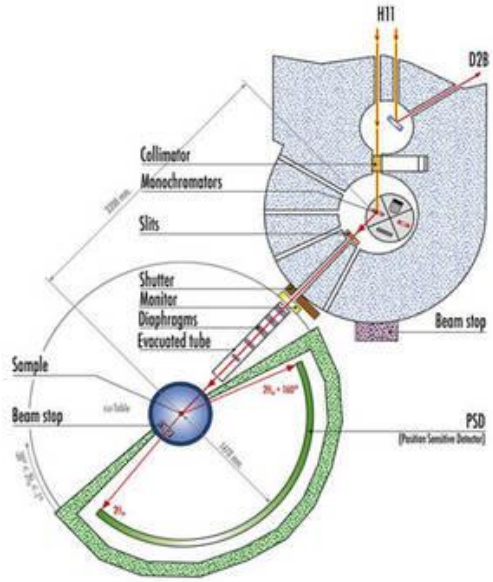

Figure 2.16. *Schematic representation of D20 high-flux powder diffractometer at ILL*[67].

The white neutron beam coming out of the reactor core can pass through four different monochromators, depending on which wavelength is needed for the diffraction experiment:

- a pyrolitic graphite HOPG (002) monochromator in reflection position with fixed vertical focussing offers a wavelength of 2.4 Å at a take-off angle of 42˚. A preceding pyrolitic graphite filter of 6 cm thickness in the incident beam suppresses second harmonics. The transmission at 2.4 Å is about 70%;
- a copper monochromator, Cu (200), in transmission geometry with fixed vertical focussing provides wavelengths 0.82, 0.88, 0.94 Å at take-off angles from 26˚ to 30˚;

- a second copper monochromator, Cu (200), with optimised fixed vertical focussing for a take-off angle of 42˚, gives a wavelength of 1.3 Å at 42˚. At this wavelength the monochromatic beam has its highest flux of about 9.8 x 10^7 n cm^{-2} s^{-1}. Soller collimators allow reduction of the natural divergence (27') of the incident polychromatic beam down to α_1 = 10' or 20';
- a variable vertical focussing Germanium monochromator (113) gives increased resolution at higher take-off angles and several out of plane reflections are also accessible. The resolution approaches $\Delta d/d = 10^{-3}$ with a flux of the order of 10^7 n s^{-1} cm^{-2} at the sample position, depending on the take-off angle.

The position-sensitive detector (PSD) housing aluminum provides a detection zone of about 4 m long x 0.15 m high. It is filled with 3.1 bar of ^{3}He and 0.8 bar of CF_4 and has a detection gap of 53 mm. For this large PSD, micro-strip gas chamber (MSGC) technology has been developed: chromium is sputtered onto the polished surface of electronically conducting glass plates. The chromium is etched to create conductive micro-strip electrodes, alternately 4 cathodes and 4 thin anodes per detection cell. The detection plates have each 32 cells of 2.568 mm (0.1˚), covering in total 3.2˚. The current PSD covers 153.6˚, with 48 plates mounted. Each cell of one plate has an independent output from the detector through a metal-ceramic plug. The strongest characteristics of the micro-strip detection system for D20 are the precise and perfectly stable geometry, resulting in a very homogeneous response and a very high stability, a high gaseous amplification with a relatively low voltage (750 V), and the possibility of very high counting rates because of the small distance between anode and cathode (170 µm) giving a fast evacuation of the positive ions. Each cell is connected to an amplifier, followed by an anti-coincidence logic (CLET). After the amplifier signal first passes the discriminator threshold for a particular cell, its neighbouring cells are prevented from counting the same event a second or third time for 1.5 µs. 2.5 µs after having passed the threshold a cell may count again an event. Therefore, the total dead time is about 5.5 µs in three different cells. It follows that the counting rate is only limited to about 50k s^{-1} per cell (dead time 27.5%). The amplifiers and discriminators are regrouped by 32 in one of the 48 boxes directly plugged on the rear of the detector. The data acquisition system (DAS) has a parallel input for up to 1600 cells. The dead time between two successive diagrams is 160 ms in conventional sequential data acquisition mode. This allows recording a series of short diagrams, typically a few seconds each, to observe irreversible kinetic phenomena. If the kinetic process is much faster and reversible, one can reproduce it many times in a cyclic way, and the DAS works in stroboscopic mode. Today, up to 256 complete diagrams or *slices* can be recorded, with a minimum active counting time *window* (open *gate*) of 1 µs inside each slice of at least 30 µs (so a maximum slice frequency of 33 kHz). The dead time between *slices* is negligible with only about 20 ns.

In a powder diffraction experiment, the powder sample is placed at the centre of the beam in a furnace or in a cryostat, depending on the kind of experiment. When the thermal neutron beam

comes out from the reactor, it first reaches one of the four monochromators. The monochromatic beam leaves the monochromatic shielding through one of its five take-off ports, each offering a different instrument resolution. Finally, it reaches the sample, which diffracts it in many directions. The diffracted beams are simultaneously counted by the large micro-strip multi-detector. The counts are accumulated during a certain time to give a powder diffraction pattern with suitable intensities.

2.2.3. Single crystal neutron diffraction data treatment

Due to various limitations such as the need for large sample volume and long data collection time, single crystal neutron diffraction (SND) is employed only when the structure of the crystal under study and its behaviour upon changes in temperature are already known, usually from single crystal X-ray diffraction experiments.

After selecting a large crystal, it is mounted on a vanadium pin and fixed to it by some glue, which can sustain low temperatures. Then, it is placed on top of the D19 diffractometer, in an Eulerian cradle, and, finally, it is orientated inside the neutron beam. Data collection is done by acquisition of several scans in ω at different values of γ, φ and χ, with a beam aperture of 6x6 mm and wavelength of 1.17000 Å, unless otherwise stated. A camera allows for the centring of the crystal inside the neutron beam, whose width can be varied using different sized slits, mounted just before the crystal. The choice of the slit defining the aperture of the neutron beam is crucial for a successful data collection: if the beam size is too wide, divergence of the signal onto the detector can occur; on the other hand, it is important that the whole crystal is inside the beam. This means that a compromise between crystal volume and beam size must be found. An ideal situation shows crystal dimensions of 3x3x3 mm and beam aperture of 5-6 mm.

Before starting a complete data collection, the quality of the crystal must be checked. A few acquisitions of 10-100 seconds at room temperature are collected to examine how well the crystal diffracts and to verify that it is single and free from defects. If the crystal is of sufficient quality, a one-hour long scan at room temperature is recorded in order to find a strong reflection in the middle of the detector to be used as reference for the integrity of the crystal during cooling to the desired temperature. Upon cooling the reference reflection should stay in the same box of the detector, while its intensity grows due to attenuation of the Debye-Waller factor. The scan collected at room temperature is also used to index the recorded intensities so that the unit cell parameters can be found to ensure that it is, in fact, the desired crystal.

To obtain a good structural refinement it is important to collect data at the lowest temperature the crystal can tolerate without breaking. All SND experiments carried out during the course of this work were performed at 20-30K.

Low temperatures are reached using a 2-stage Displex, with helium as refrigerant, formed by three components: a compressor, an expander/refrigerator and a vacuum pump. Three concentric vanadium cans are mounted on the Displex and fixed to it by screws. An indium strand is placed between the bottom of the Displex and the innermost can to ensure a tight vacuum. When the pressure inside the cans is $\sim 10^{-6}$, the compressor and the refrigerator are activated: the helium coming from the refrigerator passes through the compressor where it is compressed, cooled and finally returned to the expander by the dedicated supply line.

Once the desired temperature has been reached, a complete data collection begins: the crystal is oriented in different positions by varying the values for the two rotation angles χ and φ, while reflections are recorded during a scan in ω. In order to collect reflections at high angles, which are the ones responsible for a greater resolution in terms of d-spacing, it is possible to change the position of the detector varying the angle γ. The number of scans, also called NUMORs, with different combinations of χ and φ varies depending on the symmetry of the crystal: the higher the symmetry, the fewer are the scans needed to obtain a well refined structure. Data collection is stopped upon reaching a completeness of the data above 90%. In fact, even for the best quality crystal a completeness of 100% will be never achieved because of the presence of the cans.

Handling of the data coming from the diffractometer is carried out using the off-line program RETREAT, which reduces raw D19 area-detector data to Bragg intensities, introducing parameters such as orientation matrix and resolution function that control data reduction.

It is possible to start treating the data with RETREAT without waiting for the data collection to be complete. It is very useful to organise the workspace in sub-areas, one for each subroutine of RETREAT. Four sub-directories are created: PFIND, where the subroutine *pfind* will index all recorded reflections and calculate the orientation matrix; NEWRETREAT, where the subroutines *retreat, rafd19* and *compact* allows for the integration of the data and the creation of a *hkl*-file, listing all *hkl* reflections and their intensity; SHELXL, in which the refinement of the structure can take place by using the SHELXL-97 suite; and DVIEW, where the subroutine *dview* allows for the visual comparison between collected and calculated diffraction spots.

The first step in extracting information from peak intensities recorded on the D19 "banana" PSD is to search for strong reflections that are used to create a peak shape library, counting on the fact that the Bragg peaks on the detector have a shape similar to an ellipsoid. Depending on their intensity, reflections are classified in *strong*, *intermediate* and *weak*. The integration of strong peaks is based on the minimisation of the ratio $\sigma(I)/I$ between the standard deviation of the integrated intensity and the intensity I calculated over a series of points increasingly more distant from the peak of the reflection. The minimum value for $\sigma(I)/I$ sets the boundary for the integration of the peak.

Intermediate reflections are integrated in the same way as strong peaks, but they are not part of the library. When a reflection shows a low signal-to-noise ratio it is considered weak and its ellipsoid parameters and shape function are obtained by interpolation of nearby peaks. This means that high accuracy in data reduction can be achieved only when an accurate knowledge of the shape function, with a library as complete as possible, and the crystal orientation are available. The orientation of the crystal is calculated via the so-called orientation matrix, which allows indexing a reflection observed at a particular set of γ, ω, χ, φ angle values. When all angles are set to zero, the scattering vector h_ϕ in the laboratory axes is

$$h_\phi = UBh \qquad 2.51$$

in which *B* is a 3x3 matrix relating a triclinic reciprocal lattice to a set of Cartesian axes and *U* is a 3x3 rotation matrix that links these Cartesian axes to the laboratory frame; *U* is the orientation matrix, even though the product *UB* is commonly used.

When a good orientation matrix for the lowest temperature is available, it is copied into the *newretreat* area for the optimisation of all parameters controlling peak positions, shape and integration. This process is carried out by the subroutine *retreat*, which requires five mandatory files to operate: *filename.dat*, *codeword.use*, *codeword.num*, *codeword.dat*, and *rafd19.dat*, where *"codeword"* represents the name chosen to indicate the experiment, usually the abbreviation of the compound name followed by the temperature at which the data were collected. These files are opened by RETREAT in *read-mode* only. *Filename.dat* (Figure 2.17) is the first file to be read by the program, since it summarises all files needed and specifies their names.

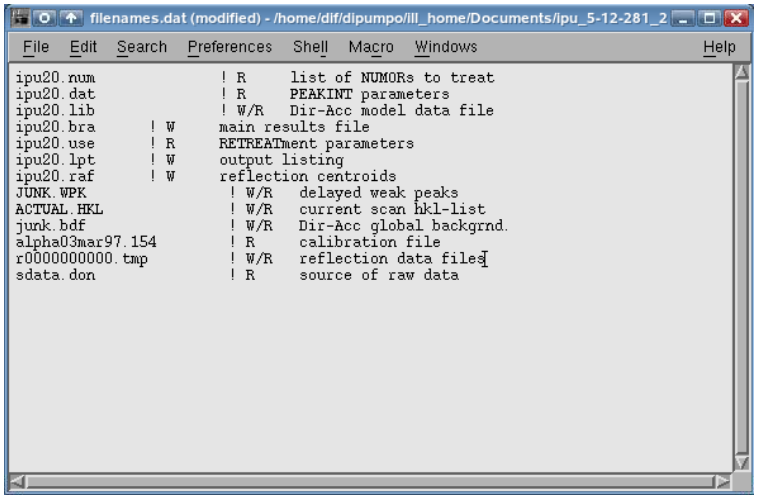

Figure 2.17. *Example of a filename.dat for the experiment performed on a crystal of the herbicide Isoproturon (IPU).*

The file *codeword.num* contains the number of NUMORs to be processed in a refinement cycle; *codeword.dat* includes all information needed for the integration of peaks, from the ellipsoidal integration volume to tests for the treatment of weak reflections; the file *codeword.use* presents the retreatment parameters.

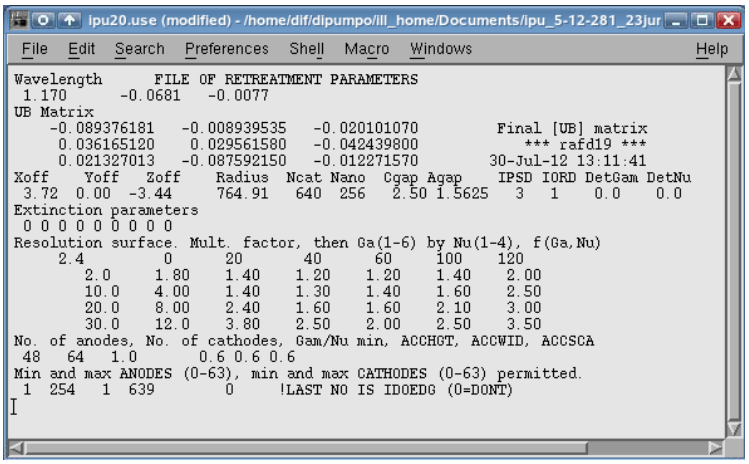

Figure 2.18. *Example of a codeword.use for the experiment performed on a crystal of the herbicide Isoproturon (IPU).*

As shown in Figure 2.18, the first parameter to be listed in *codeword.use* is the wavelength, whose value will override the one in the raw data files, followed by the values for the zero offsets in ω and χ and the six parameters for the orientation matrix. Below the *UB* matrix the zero offsets for the linear coordinates of the detector are reported with reversal of the signs. *IPSD* indicate the type of detector used, in this case 3 stands for the horizontally-curved area detector, and *DetGam* and *DetNu* are the nominal γ and ν angles for the perpendicular to the detector from the centre of the instrument, which can be chosen arbitrarily for curved detectors. *No. of anodes* and *No. of cathodes* indicate the dimensions of the reflection boxes along the anodes and cathodes in pixels. *ACCHGT*, *ACCWID* and *ACCSCA* define the central fraction of the reflection box that must be completely within the scan boundaries so that the reflection is not classified as *edge-affected*. Finally, the last number *IDOEDG* indicates whether or not the *edge-affected* reflections are to be recovered.

After one cycle of RETREAT is complete, the subroutine RAFD19 is launched for the optimization of the UB matrix, the offsets in ω, χ, x and z, and the unit cell parameters. The results are written in the file *ubfrom.raf* (Figure 2.19).

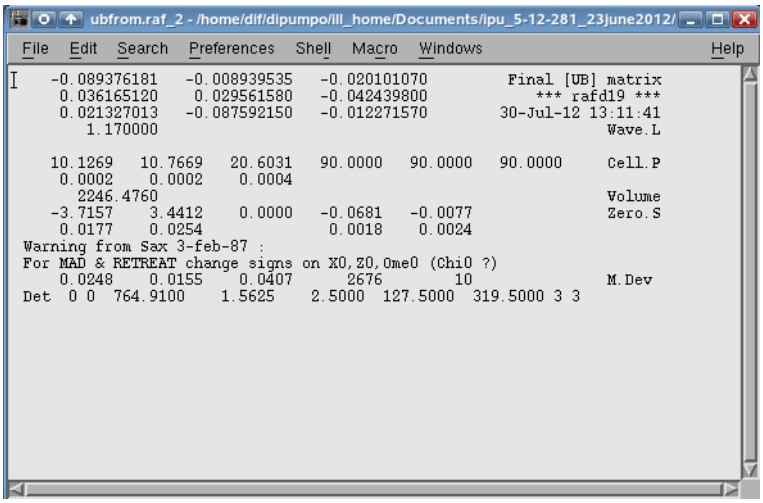

Figure 2.19. *Example of a ubfrom.raf file for the experiment performed on a crystal of the herbicide Isoproturon (IPU).*

The new *UB* matrix is copied into the *codeword.use* file and another RETREAT cycle can begin. These retreating cycles are terminated when all parameters have converged.

RETREAT creates two main output files: *codeword.lpt* and *codeword.bra*. The first file lists all recorded reflections, separating them in strong, intermediate and weak; for the first two groups, three stages are outlined. The first pass is a crude scan of the reflection: each NUMOR is divided in frames, listing the peak position on the detector, its intensity and the value of the background; the second pass finds the shape of the reflection, calculating the ellipsoid; and the third pass is the modelling of the reflection, in which both integration box and peak shape profile are shown.

If the reflection is classified as weak, the second and third passes will be skipped; a fourth pass will calculate the model ellipsoid based on the existing library.

The second output file is a reflection data file, *codeword.bra*. It displays all acquired and calculated information about all treated reflections. Each reflection is organised in 7 "COLL5 N-cards", where COLL5 is the name of the standard ILL reduction program for 1D single crystal diffraction data, and the N-cards refer to the key at the end of each record as they were physically when COLL5 was born. Other cards can be added to the file, as for the case of the program D19ABS, which is used for absorption correction based on the index of the crystal faces and it will add a C card.

The *codeword.bra* file is overwritten at the end of every RETREAT cycle and its final version is used by the subroutine COMPACT to create the *codeword.hkl* file needed for the refinement with SHELXL. The *codeword.ins* file, reporting information about the crystal symmetry and the atomic positions, is the one derived from single crystal X-ray diffraction experiments, but, in order to be used for structural refinement of neutron data, it must be modified so that the X-ray atomic scattering factors are replaced by neutron scattering lengths for the atoms present in the structure.

2.3. Differential Scanning Calorimetry

Differential scanning calorimetry (DSC) is a thermal technique used to investigate the response of a system when subjected to a temperature program. In a typical DSC analysis the difference in heat flow between a sample and a reference, as they are both subjected to a controlled temperature program, is measured. The main concept of DSC is based on the fact that changes in the structure of a material are accompanied by the consumption or the production of heat; by matching the temperatures of the sample and the reference, information on the type of thermal event, as melting, crystallization or phase transition, can be obtained. For this reason the temperatures of sample and reference are detected by temperature sensors. During a DSC analysis a temperature program is set and it compares the average value of the temperatures detected on the sample and on the reference to those selected by a temperature program. This difference gives a correction to the heating units.

There are two types of instrumentation for a DSC analysis: *power compensated DSC* and *heat flux DSC*. The first is constituted of two separate ovens, each with a temperature sensor. This DSC instrumentation is used to measure the amount of power that is necessary to compensate for the temperature differences between sample and reference. The power of the two ovens is controlled so that the temperature in the oven containing the sample is the same of that containing the reference.

In the case of a heat flux DSC, both sample and reference are placed on the same oven, but on different plates, which are heated by a thermo-electric platform. By using thermocouples positioned under the plates, the difference between the heat fluxes of sample and reference is measured. The outcoming information is a differential heat flux, which is proportional to the difference between the signals of the thermocouples.

DSC allows the analysis of various processes, such as fusion, evaporation and sublimation, which are endothermic events, but also crystallization, condensation and deposition, which are exothermic events. These processes are studied by measuring the latent heat, that is the heat which is released or absorbed when a material melts or freeze, boils or condense.

DSC can also be used for the investigation of glass transitions, for example in polymers, in which the specific heat C_p is defined. The specific heat indicates the quantity of heat that is necessary to increase by 1°C the temperature of 1g of material.

Finally, endothermic and exothermic chemical reactions can be studied by DSC, leading to the formulation of enthalpy values.

For the purpose of this thesis DSC analyses was used for the screening of temperature dependent behavior of new crystal structures of the materials under study, investigation of phase transitions and detection of melting points. All DSC analyses were performed on the TA Instruments DSC Q20, which works following variation of the heat flux, at the University of Bath. 2-3 mg of all the studied samples were placed on tin pans, which were hermetically closed with the appropriate lid to avoid spillage of the material. A N_2 flow guaranteed a non-reactive environment and, unless

otherwise stated, data were collected upon consecutive cycles of heating and cooling in a range in temperature between 20˚-200˚C, with a rate of 5˚C/min.

2.4. Computational studies

In collaboration with Christopher H. Hendon, computational calculations were undertaken on selected systems to assess the role played by the hydrogen bond in the crystal packing of these materials.

All electronic and structural calculations were performed within the DFT framework, using periodic boundary conditions to approximate the perfect solid. The Vienna *ab initio* simulation package (VASP)[68], a planewave code with PAW scalar relativistic pseudo potential[69], was employed for all geometric and electronic calculations. A constant single Gamma point k-grid was specified for all systems, as each cell was different sized, but relatively large. Starting with the experimentally determined unit cell, for each system the structures were geometrically relaxed (i.e. cell shape, volume and ionic position) using the semi-local Perdew–Burke–Ernzerhof exchange–correlation functional revised for solids (PBEsol)[70]. For these calculations, a 500 eV plane-wave cutoff basis set was found to be suitable for convergence of the systems, to within 0.01 eV per atom. In order to obtain quantitative electronic information, in particular for estimations of the band gaps, higher order hybrid- DFT calculations were performed using the HSE06 functional[71], with 25% of the short-range semi-local exchange functional replaced by the exact non-local Hartree–Fock exchange.

Chapter 3

3. Intramolecular H-bonded systems

3.1. Pendimethalin, *N-(1-ethylpropyl)-3,4-dimethyl-2,6-dinitrobenzamine*

3.1.1. Introduction

Pendimethalin (PDM) is a dinitroaniline herbicide, widely used across the world for the treatment of pre- and post-emergence of grasses and broadleaf weeds in a large variety of crops, such as cereals, corn, potatoes, legumes, fruits and vegetables. It achieves its function by inhibiting cell division and cell elongation in plants, as it interferes with the polymerization of the micro-filament protein tubulin.

In the solid state, pendimethalin can crystallize in two different crystal forms[72], which differ from one another in their colour. The triclinic modification of pendimethalin is the thermodynamically stable orange-coloured form, while the yellow monoclinic form is the metastable one.

The phenomenon of polymorphism in pendimethalin represents a problem in the manufacturing process for commercial use. Usually this kind of herbicide is formulated as liquid concentrates, emulsions or dispersible solids, which contain small crystals of the active molecule in an aqueous suspension stabilized by surfactants. Solid formulations can also be prepared by adsorption of the active molecule on a porous support, such as silica, alumina or clay, and then made wettable by addition of surfactants. These formulations are dispersed in water immediately before use and then applied on the crop field. The problem with this kind of solid formulations resides in the fact that solid-in-liquid dispersions are stable only within a narrow range of particle size. The polymorphic transformation of one form into the other results in a modification in the particle size distribution, which is, therefore, no longer homogeneous over time and stable. The behaviour leads to issues in the application of pendimethalin, because the conversion from one polymorph to the other causes particle aggregation, which can obstruct the nozzle of delivery equipment. In addition, the stability of the formulation of this material cannot be ensured, leading to issues regarding the application of pendimethalin at the correct concentration.

3.1.2. Experimental

3.1.2.1. Physical and chemical properties

The technical preparation of pendimethalin is a yellow-orange powder with melting point in a range of temperature from 53˚C to 58˚C[73], vapour pressure 3.0×10^{-5} mmHg[73] at 25˚C and water solubility of 0.275 ppm at 25˚C[74]. It is soluble in most organic solvents, such as acetone, xylene, benzene, toluene, chloroform, and dichloromethane.

From the literature[72] it is known that yellow pendimethalin can be produced upon melting of the orange form and cooling to room temperature. A re-conversion into the orange form can be achieved under thermodynamic control. However, this is a process that can take months or years to complete at a temperature of 25˚C.

3.1.2.2. Crystallisation from solution

For the purpose of this thesis, crystals of both forms of PDM were obtained from solution, using the commercial compound, re-crystallised from ethanol, as starting material to remove any impurities. A range of organic solvents, exhibiting different values of polarity, was taken into consideration to assess whether interactions between the molecules of PDM and the solvent could prove to be the driving force in the crystallisation of one form over the other. The experimental details regarding the preparation of each solution are reported in Table 3.1.

PDM quantity (g)	Solvent	Solvent quantity (ml)	Temperature (˚C)
0.10	Diethyl ether	10	-
0.10	Toluene	10	70
0.10	Ethyl acetate	10	-
0.16	Methanol	8	60
0.15	Ethanol	8	60
0.12	1-Propanol	8	60
0.12	Isopropanol	8	60
0.14	N,N'-dimethylformamide	8	60
0.12	Acetonitrile	8	70
0.12	Isopropyl alcohol/acetonitrile (IPA/ACN)	4+4	60

Table 3.1. *Solutions prepared.*

Due to the small available quantity of the starting material, saturation of the solution was achieved by adding the solvent to the solid in portions of 1 ml and waiting around 2 minutes between two

additions. All solutions were heated for 30 minutes at the temperature reported in Table 3.1, depending on the solvent used, and then left to cool and crystallise at room temperature. Crystallisation was obtained by the method of slow evaporation of the solvent, applying a few small holes on the parafilm cover of the crystallisation vials. Most of the solvents used for crystallization led to the formation of yellow pendimethalin. Crystals of orange PDM suitable for an X-ray diffraction experiment were obtained by evaporation of a solution of PDM : urea with 1 : 1 ratio in a 50 : 50 mixture of IPA : ACN , while a crystal of the yellow modification was obtained from a methanol solution.

No polymorphs were observed other than the already known orange and yellow forms.

3.1.2.3. Differential Scanning Calorimetry

In order to study the behaviour of the compound upon changes in temperature, three samples of PDM were analysed by DSC: a sample of the commercial material, one of the yellow-PDM, and one of the orange-PDM; the last two were re-crystallised from methanol and a mixture of IPA : ACN, respectively. To eliminate any traces of residual solvent, 3 mg of each sample were placed inside the instrument under a N_2 flow for 30 minutes. Calorimetric melting profiles were collected while heating from 20˚C to 60˚C at a heating rate of 1˚C/min and while cooling back to 20˚C at the same rate. The three profiles for yellow-PDM, orange-PDM, and the raw-PDM are reported in Figure 3.1, Figure 3.2, and Figure 3.3, respectively.

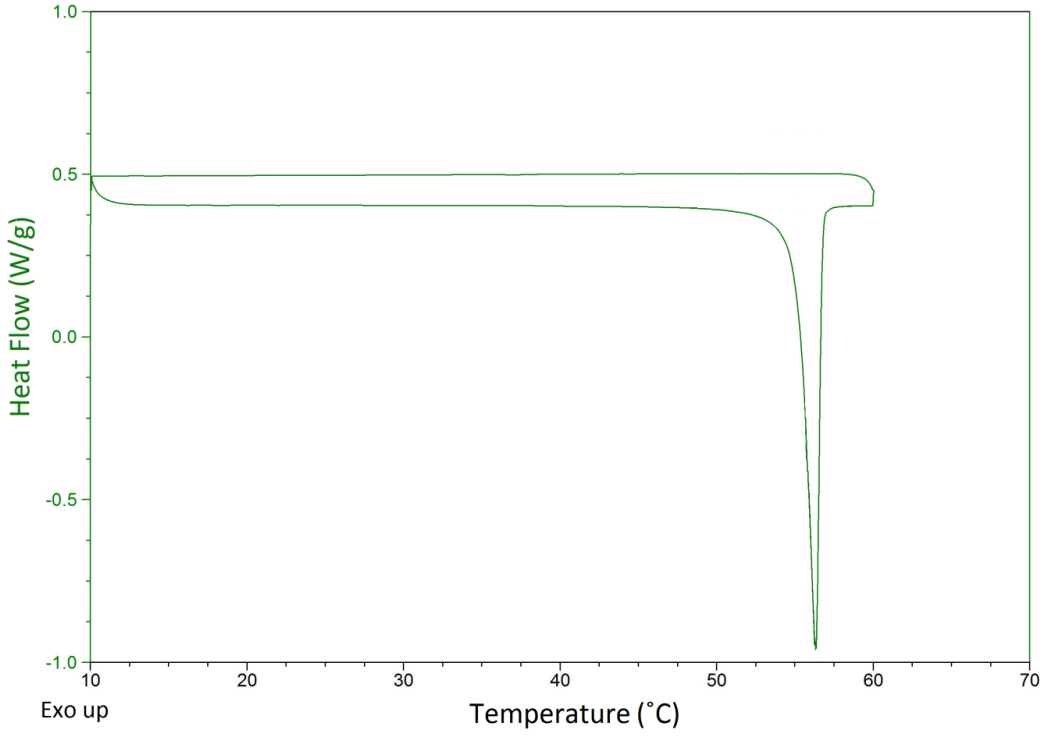

Figure 3.1. *DSC profile for a sample of yellow-PDM.*

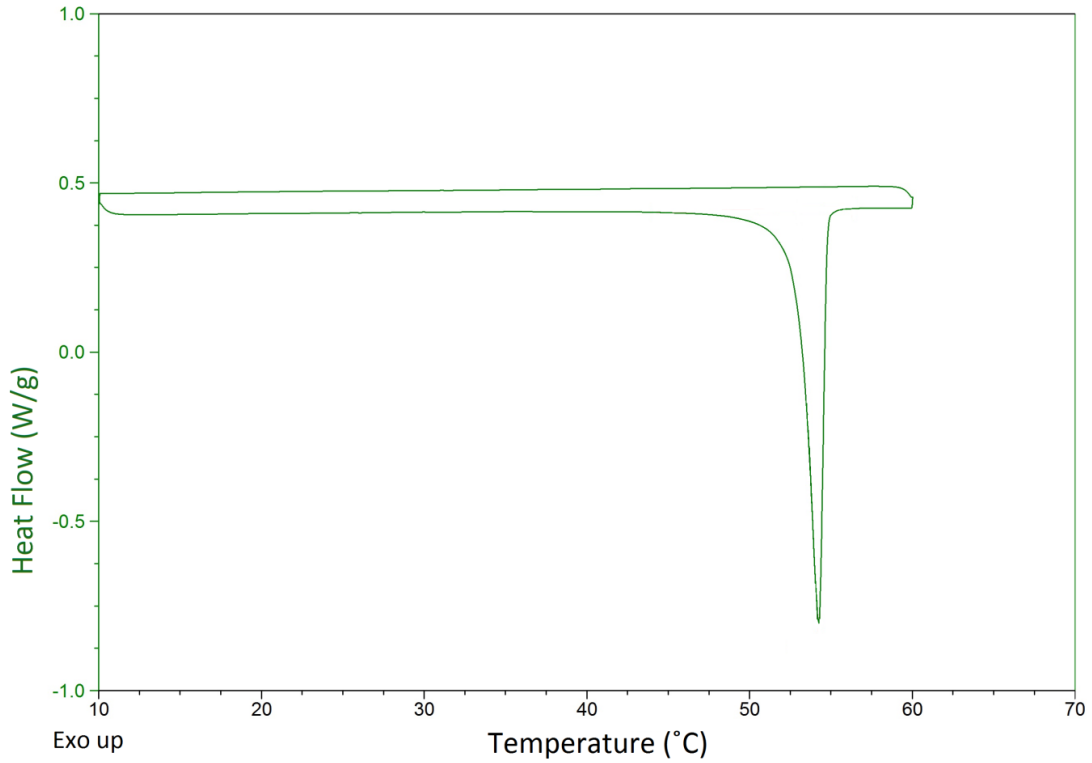

Figure 3.2. *DSC profile of a sample of orange-PDM.*

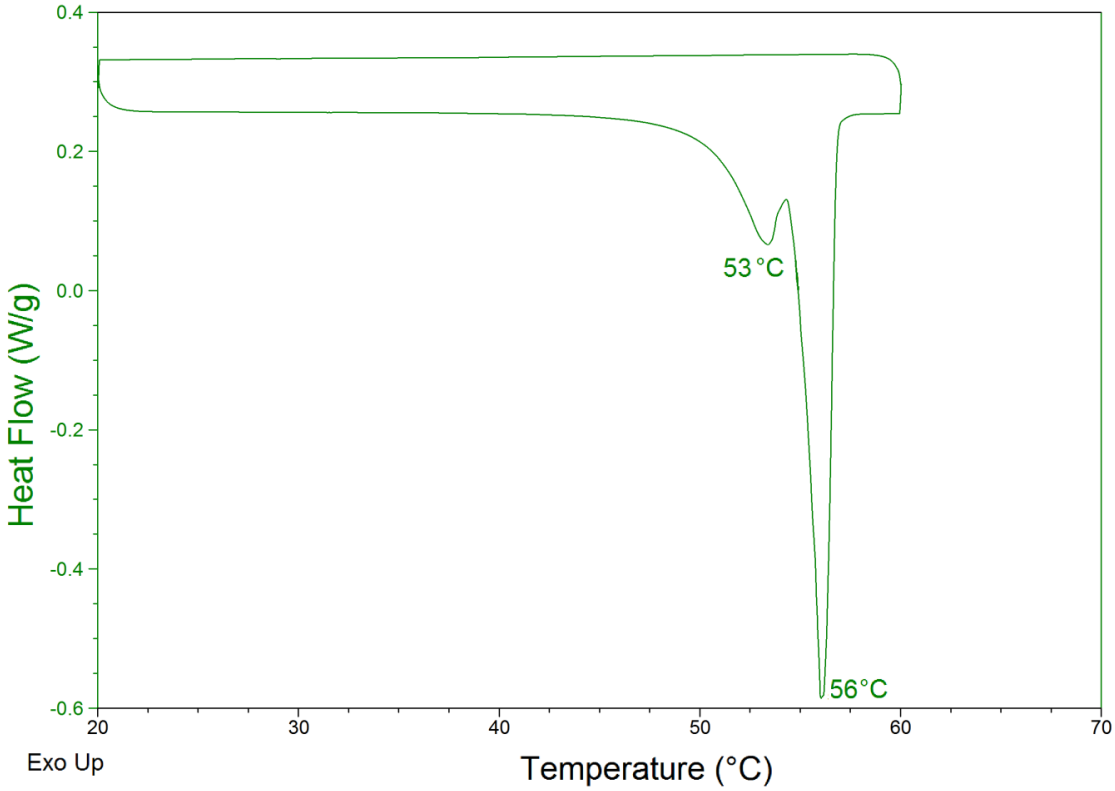

Figure 3.3. *DSC profile of a sample of raw PDM.*

Even though in the literature it is stated otherwise[72], the DSC profile of the yellow polymorph does not show any transition from the yellow meta-stable form to the orange stable one, but both profiles only display the endothermic events corresponding to their melting temperatures: ~54˚C for the orange modification and ~56˚C for the yellow polymorph. This behaviour indicates that the phase transition temperature might be higher than the melting point of both forms. A confirmation of this hypothesis can be found in the DSC profile for the commercial material: it is clearly visible that both forms are already present in the sample since the peak between the two valleys indicating the melting events does not reach the baseline. Finally, it is worth noting that there is an absence in all three DSC profiles of any exothermic events during the cooling process, which indicates that re-crystallisation of the samples does not immediately occur. This behaviour might be the result of a glass-like transition state between the liquid and the solid states: the glass-like state slows the crystallisation process, leading to the formation of the meta-stable yellow form.

3.1.2.4. Powder X-ray diffraction

Powder X-ray diffraction (PXD) was used to assess and verify the presence of polymorphs of the compound understudy. Powder patterns were collected for both yellow and orange PDM. The yellow modification was obtained by slow evaporation of a solution of PDM in methanol. Crystals of the orange form were obtained from a solution of IPA : ACN in a 50 : 50 ratio, with the addition of urea in a 1 : 1 stoichiometry. Urea did not form a co-crystal with PDM, but created the right conditions for large crystals of pure orange-PDM to crystallise. It was, however, not possible to separate the crystals of PDM from the urea crystals, since the latter grew on top of the former, so the crystals were ground together into a powder. In Figure 3.4, the powder patterns of yellow-PDM, orange-PDM+urea, and urea are reported.

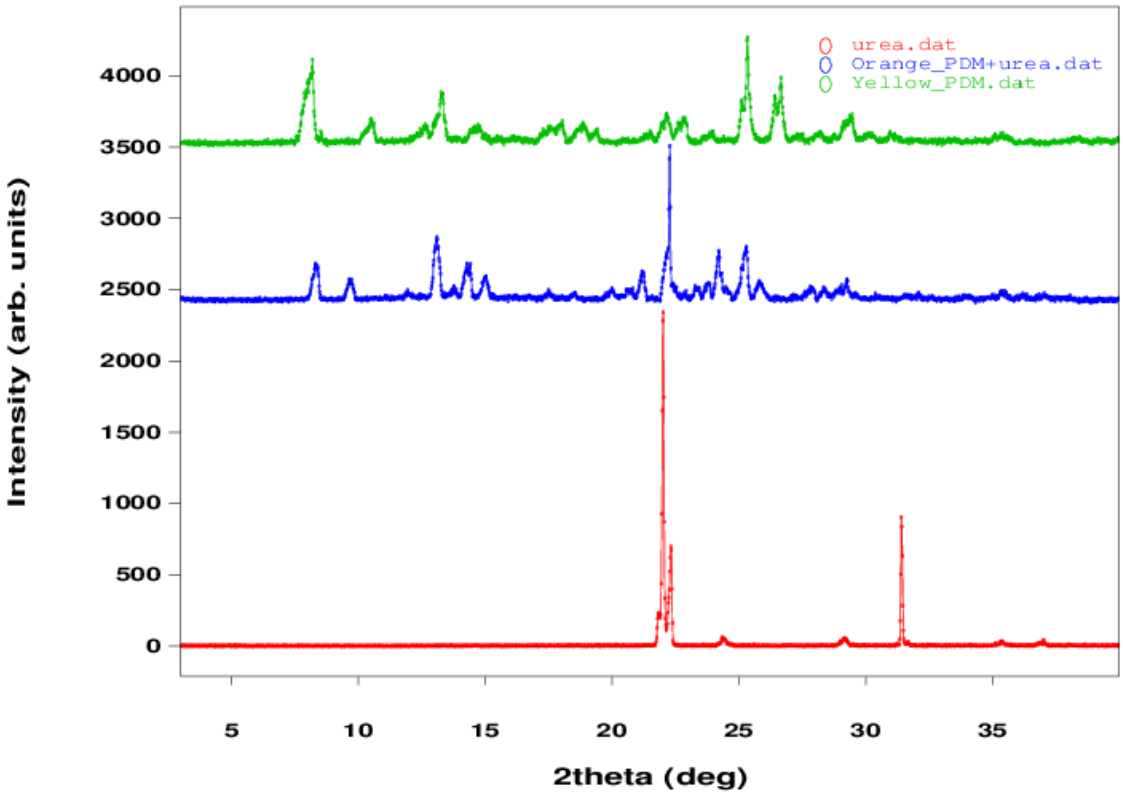

Figure 3.4. *Powder diffraction patterns for a sample of yellow-PDM (green), a sample of orange-PDM+urea (red), and a sample of urea (blue).*

Fortunately, solid urea shows a first high peak ~22° in *2θ*, which is easily recognisable in the pattern with the orange-PDM. Comparing the patterns for the two polymorphs of PDM, it is possible to see differences in the position of the Bragg peaks, especially in the range in *2θ* from 7° to 12°. Using powder X-ray diffraction, it is possible to confirm rapidly the presence or absence of two different pendimethalin crystal structures.

3.1.2.5. Single crystal X-ray diffraction

Crystals of both forms were analysed by single crystal X-ray diffraction on a Rigaku R-AXIS Spider diffractometer, which comprises a molybdenum sealed tube X-ray generator, an RAPID plate detector system with a quarter chi goniometer and a Oxford Cryosystems 600 Series CryoStream, providing a cold nitrogen flux and a temperature of collection of 120 K.
In Table 3.2 and Table 3.3, X-ray crystallographic data and refinement parameters for the orange form and the yellow form of PDM, respectively, are reported.

Name	Pendimethalin Orange form
Empirical formula	$C_{13}H_{19}N_3O_4$
Formula weight (g mol^{-1})	281.31
Temperature (K)	120
Wavelength (Å)	0.71073
Crystal system, space group	Triclinic, $P\bar{1}$
Unit cell dimensions	a = 7.5196(4) Å
	b =13.2348(8) Å
	c = 15.259(1) Å
	α = 97.891(7)°
	β = 100.882(7)°
	γ = 103.167(7)°
Volume ($Å^3$)	1426.0(2)
Z, calculated density (g cm^{-3})	4, 1.310
F(000)	600
Absorption coefficient (mm^{-1})	0.098
Theta range for data collection (˚)	3.05 to 27.46
Limiting indices	$-8 \leq h \leq 9$, $-16 \leq k \leq 17$, $-19 \leq l \leq 19$
Reflections collected / unique	17215 / 6221 [R_{int} = 0.0353]
Completeness to θ = 27.46	95.4 %
Refinement method	Full-matrix least-squares on F^2
Data / restrains / parameters	6221 / 0 / 514
Goodness-of-fit on F^2	1.011
Final R indices [I>2sigma(I)]	R_1 = 0.0459, wR_2 = 0.1393
R indices (all data)	R_1 = 0.0657, wR_2 = 0.1550
Extinction coefficient	0.002(2)
Largest diff. Peak and hole (e $Å^{-3}$)	0.29 and -0.22

Table 3.2. *X-ray crystallographic data and refinement parameters for a crystal of orange-PDM.*

Name	Pendimethalin Yellow form
Empirical formula	$C_{13}H_{19}N_3O_4$
Formula weight (g mol^{-1})	281.31
Temperature (K)	120
Wavelength (Å)	0.71073
Crystal system, space group	Monoclinic, $P2_1/c$
Unit cell dimensions	a = 6.9823(2) Å
	b = 21.9992(6) Å
	c = 9.3950(7) Å
	β = 100.195(7)°
Volume ($Å^3$)	1420.3(1)
Z, calculated density (g cm^{-3})	4, 1.316
F(000)	600
Absorption coefficient (mm^{-1})	0.099
Theta range for data collection (°)	3.11 to 27.47
Limiting indices	$-9 \leq h \leq 9$, $-26 \leq k \leq 28$, $-10 \leq l \leq 12$
Reflections collected / unique	7725 / 3222 [R_{int} = 0.0163]
Completeness to θ = 27.47	99.4 %
Refinement method	Full-matrix least-squares on F^2
Data / restrains / parameters	2861 / 0 / 258
Goodness-of-fit on F^2	1.083
Final R indices [I>2sigma(I)]	R_1 = 0.0393, wR_2 = 0.1175
R indices (all data)	R_1 = 0.0443, wR_2 = 0.1300
Extinction coefficient	0.002(2)
Largest diff. Peak and hole (e $Å^{-3}$)	0.29 and -0.27

Table 3.3. *X-ray crystallographic data and refinement parameters for a crystal of yellow-PDM.*

3.1.2.6. Single crystal neutron diffraction

Due to difficulties in growing large single crystals of either form of PDM (crystal volume > 10^3) sufficient for study using the D19 diffractometer at ILL, a different method of neutron diffraction was used to investigate the PDM crystals: the **Laue method**.

In a Laue-diffraction experiment in transmission mode a polychromatic (white) beam collides on a single crystal, which remains in a fixed position. A detector is placed behind the crystal, so to collect all the diffracted beams, as shown in Figure 3.5.

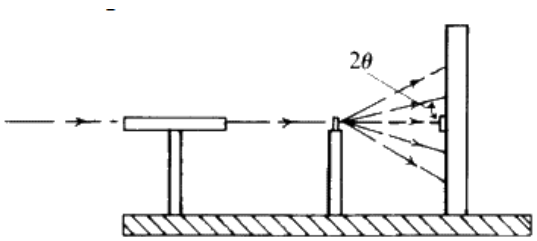

Figure 3.5. *Laue diffraction method in transmission mode*[75].

Since the incident beam is not monochromatic, but, on the contrary, contains a range of wavelengths $\lambda_{min} - \lambda_{max}$, the diffraction images collected with the Laue method are different from the ones recorded with a constant value of λ. In Figure 3.6 the transmission pattern of quartz is reported as an example.

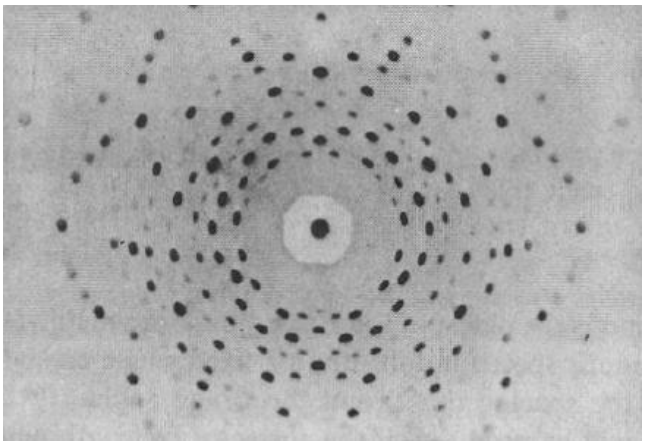

Figure 3.6. *Laue pattern of quartz, recorded in transmission mode. The incident beam is parallel to the hexagonal c-axis and the detector distance is 5.0 cm*[75].

A Laue diffraction image features a central and intense spot, which corresponds to the primary incident beam, and sets of spots all lying on ellipses. In order to understand the reason behind this arrangement of the diffracted intensities it is useful to introduce the concept of *zone*. A *zone*

represents a group of *hkl* faces all parallel to a specific direction *[uvw]* inside the unit cell. The definition of zone axis ***A*** allows writing Eq. 3.1:

$$\boldsymbol{A}(uvw) = ua_1 + va_2 + wa_3 \qquad \text{Eq. 3.1}$$

When an *hkl* face belongs to a *[uvw]* zone, the following equation (Eq. 3.2) is valid:

$$hu + kv + lw = 0 \qquad \text{Eq. 3.2}$$

which states that planar normals are perpendicular to the zone axis, $\boldsymbol{H}(hkl) \cdot \boldsymbol{A}(uvw) = 0$.

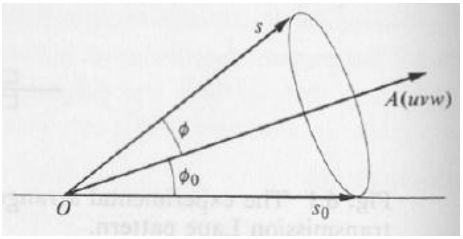

Figure 3.7 *Schematic representation of the [uvw] zone and its axis* ***A****(uvw)*[76].

With reference to Figure 3.7, by forming the scalar product of the Bragg law given in vector form (Eq. 3.3) and ***A****(uvw)*, it is possible to obtain Eq. 3.4:

$$s = s_0 + \lambda \boldsymbol{H}(hkl) \qquad \text{Eq. 3.3}$$

$$s \cdot \boldsymbol{A}(uvw) = s_0 \cdot \boldsymbol{A}(uvw) + \lambda \boldsymbol{H}(hkl) \cdot \boldsymbol{A}(uvw) \qquad \text{Eq. 3.4}$$

Since $\boldsymbol{H}(hkl) \cdot \boldsymbol{A}(uvw) = 0$, Eq. 3.4 clearly indicates that the two angles φ and φ_0, which are the angles formed by the ***A****(uvw)* axis with the beam reflected by any *hkl* plane belonging to the zone *[uvw]* and with the primary beam, respectively, are equal, defining a cone whose axis corresponds to the zone axis ***A****(uvw)*. When one of these cones is recorded on a detector normal to the primary beam, it gives rise to the sets of ellipses visible in a Laue pattern.

One of the advantages of the Laue method resides in the use of a polychromatic beam, which allows collection of a great number of reflections; that is, all the reflections satisfying the Bragg law in the chosen range of wavelengths $\lambda_{min} - \lambda_{max}$. Unfortunately, this characteristic constitutes also a problem: it is, in fact, possible that diffraction from two crystallographic planes, such as *hkl* and *2h2k2l*, occurs at the same value of 2θ at the same time, causing overlapping of the diffraction spots.

3.1.2.6.1. VIVALDI at ILL

Thanks to collaboration with Dr. Marie-Hélène Lemée-Cailleau, instrument scientist responsible of the single crystal diffractometer VIVALDI at ILL, diffraction data were collected on a single crystal of the yellow modification of PDM.

VIVALDI (**V**ery **I**ntense **V**ertical **A**xis **L**aue **DI**ffractometer) is a single crystal diffractometer receiving neutrons from the H22 neutron guide at ILL. It allows rapid surveying of large volumes of reciprocal space, thanks to a cylindrical image-plate detector, and it can be used when only small single crystals are available for the experiment. An image of the instrument is reported in Figure 3.8.

Figure 3.8. *Single crystal Laue diffractometer VIVALDI*[77].

The white neutron beam reaching VIVALDI has a range in wavelengths between 0.8 Å and 4.5 Å. For a primitive unit cell with edges up to 25 Å peak overlap is highly contained, allowing the use of the whole white beam. It is, anyway, possible to cut out part of the wavelengths with an optional filter placed upstream, so to deflect wavelengths longer than 3 Å. Air cushions provide easy movement of the entire instrument, allowing the selection of wavelengths: shorter than 3 Å, longer than 3 Å, or the full white beam. Two other instruments, the powder diffractometer D1B and the strain imager SALSA, receive neutrons from the same neutron guide as VIVALDI. These monochromatic instruments are placed upstream of the single crystal diffractometer, subtracting part of the wavelengths. As a result the beam hitting on VIVALDI is not truly a white beam, showing several sharp dips in the wavelength distribution. For this reason a time-of-flight spectrum analyser is located downstream, monitoring changes in the wavelength spectrum.

A real asset of VIVALDI is represented by its cylindrical image-plate detector. The neutron-sensitive plates are based on BaFBr doped with Eu^{2+} ions and addition of Gd_2O_3: the Gd^{3+} ions act

as neutron converter because of their high neutron capture cross section. A layout of VIVALDI is reported in Figure 3.9.

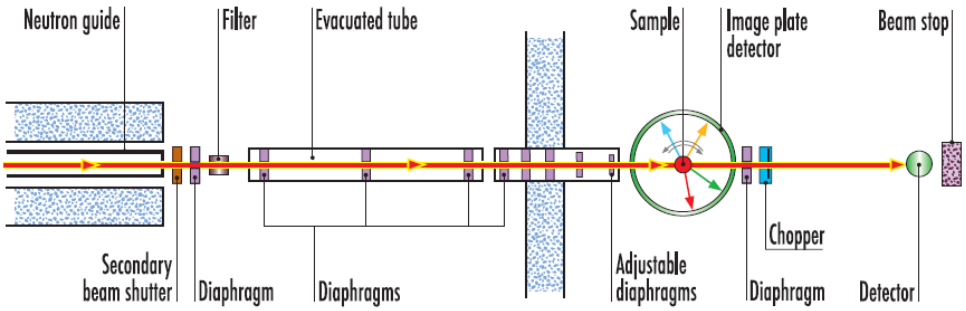

Figure 3.9. *VIVALDI layout*[77].

Different sample environments can be obtained using an "Orange" cryostat (Figure 3.7), which allows data collection temperatures from 1.5 K to 600 K and can also accept high-pressure cells up to 49 mm in diameter. A summary of the instrument characteristics is reported in Table 3.4.

Monochromators	
Laue	White thermal beam, $0.8 < \lambda < 4.5$ Å
Filtered, position 1	$0.8 < \lambda < 3$ Å
Filtered, position 2	$3 < \lambda < 4.5$ Å
Collimation	
Pinholes	0.5 to 10 mm in diameter
Sample	
Beam size	Up to 10 mm in diameter
Flux (unfiltered)	$1.2 \cdot 10^8$ $cm^{-2}s^{-1}$
Sample space	120 mm in diameter
Detector	
Neutron image-plate	Gd_2O_3 doped BaFBr : Eu^{2+}
Configuration	Vertical cylinder
Pixel size	100 x 100 μm^2; 200 x 200 μm^2; 400 x 400 μm^2
Readout time	~ 3.5 min
Time-of-flight spectrum analyser	
Chopper & ^{3}He detector	
Chopper frequency	6000 rpm
Path length	2.0 m
Resolution	$\Delta\lambda = 0.04$ Å

Table 3.4. *Summary of all characteristics of VIVALDI*[77].

Before starting an experiment on VIVALDI, a suitable single crystal is mounted on a vanadium pin and wrapped in aluminium foil so to avoid damage during the cooling process and loss of the sample inside the instrument in case a break of the crystal should occur. It is common practise to collect a short set of data at room temperature to ensure that the right crystal has been mounted and that its scattering power is of sufficient quality. The next step is the orientation of the sample and the erasing of the image-plate detector, so to delete signals from previous data collections. After the detector has been placed in the desired position, a complete data collection can begin: the beam shutter is opened and a series of four to ten Laue patterns are recorded rotating the crystal around the vertical axis of the detector of ~20 - 30°. After collection of each Laue pattern, the beam shutter is closed and a laser reads the image plates from the bottom to the top with a readout time of ~ 3 minutes. Once the pattern has been read, it is erased and a new data collection can start. The time of exposure to the neutron beam depends on several factors, such as sensitivity of the crystal to environmental conditions, its volume, and, obviously, on how well it diffracts neutron radiation. The symmetry of the crystal imposes the number of Laue pattern to be collected: the lower the symmetry, the greater the number of patterns. In the case of triclinic symmetry, diffraction data are collected after re-mounting of the crystal in different directions in order to ensure complete coverage of the unique volume of reciprocal space.

Once a Laue pattern has been recorded, it is possible to start the data reduction process, using the program LAUEGEN[78], a graphical user interface program created for processing Laue diffraction patterns. First, it is necessary to load the diffraction images and the unit cell information, usually derived from single crystal X-ray diffraction analysis, as was the case of the crystal of yellow PDM under study. It is, then, possible to proceed by finding the orientation matrix, which is of fundamental importance for indexing the pattern. In order to do this, a few low index nodal spots must be chosen: these are the spots placed at the intersection of many zones. LAUEGEN will, then, attempt to auto index the selected spots and it will produce a list of possible solutions. Since some of these solutions may be wrong, before making a choice it is highly recommended to display the calculated diffraction spots on the experimental Laue pattern: all real spots will be superimposed by the calculated predictions. When an approximate indexing of the pattern is available, it is necessary to refine the orientation: this is done by a series of refinement cycles until the best fit between observed and calculated data is reached. The last step before integrating the peak intensities is the refinement of the **soft limits**, which are the values of λ_{min} and d_{min}, very important to obtain the best results from integration. If these values are incorrect several problems may arise: missing reflections during data reduction, wrong indexing of reflections, and prediction of too many reflections, which can mislead the program to discard real spots. It is usually not necessary to change the value of λ_{min} on VIVALDI, but it is important to choose a value for d_{min} that allows coverage of all observed reflections in the calculated pattern.

Integration of peak intensities is carried out by the ARGONNE_BOXES[79] program. In order to work this program requires three files: an *.lmd* file, which contains the crystal parameters; a *.geasc* file, which contains parameters for each reflection; and a *fuji_borders* file, which contains information on the size and shape of the image-plates, and also any area that must not be integrated, such as the beam stop area and the plate joins and borders. The integration process uses information on strong peaks in order to integrate weaker peaks, optimising the ratio $\sigma(I)/I$. The first step of integration is the selection of strong peaks on the image and the determination of the spot size. Once the spot size has been found, it is important to check the results in the histograms and on the image. Integration of all reflections can now begin. It is possible to examine the results by looking at the profiles and check the shape and sizes of the spots, or to examine individual spots by picking a spot by index or from the image to check the integration. It is finally possible to get a summary of the integration statistics, where for each spot the $Mean\ I/sigI$ ratio is given.

The final step in the analysis of Laue diffraction data is the normalisation of the wavelength. This is done by the program LAUENORM[80], which works by comparing the equivalent reflections and refining a wavelength normalisation curve. This curve takes into account factors only dependent on wavelength, mainly the different flux and different wavelengths, and also the response of the image-plates to different wavelengths. The curve is empirical and is found by iteration. LAUENORM requires three files to work: *lnorm.com*, which is the command file that runs LAUENORM; lnorm.dat, which contains the parameters, such as cell dimension and symmetry of the crystal, to run LAUENORM; and the *.ge* file derived from the integration process. Once the normalisation process is complete, an *.hkl* file is produced and it is possible to refine the structure with SHELXL-97[57].

3.1.2.6.2. Experiment on VIVALDI

Due to the difficulties in growing large crystals of the orange-PDM, it was possible to collect neutron data only for the yellow modification: the selected crystal was grown by slow evaporation from a methanol solution. The Laue method allowed the analysis on a relative small crystal of yellow-PDM, with a crystal volume of ~1 mm^3: with such small size, the use of a monochromatic single crystal diffractometer was not possible.

The yellow crystal was mounted on a vanadium pin (0.5 mm in diameter) and wrapped in aluminium foil to avoid loss of the crystal inside the instrument in case it became detached.

Due to the small crystal volume, long acquisition times were set, leading to a data collection of 5 days at 120K. At the end of the experiment data were processed as described above (***cf. 3.1.2.6.1***).

In Table 3.5 neutron crystallographic data and refinement parameters for the yellow form of PDM are reported.

Name	Pendimethalin Yellow neutrons
Empirical formula	$C_{13}H_{19}N_3O_4$
Formula weight (g mol^{-1})	281.33
Temperature (K)	120
Wavelengths range (Å)	0.80 – 5.20
Crystal system, space group	Monoclinic, $P2_1/c$
Unit cell dimensions	a = 6.9823(2) Å
	b = 21.9992(6) Å
	c = 9.3950(7) Å
	β = 100.195(7)°
Volume ($Å^3$)	1420.3(1)
Z, calculated density (g cm^{-3})	4, 1.316
F(000)	267
Absorption coefficient (mm^{-1})	2.367
Theta range for data collection (°)	3.50 to 37.82
Limiting indices	$-6 \leq h \leq 6$, $-35 \leq k \leq 35$, $-16 \leq l \leq 11$
Reflections collected / unique	17236 / 2965 [R_{int} = 0.1486]
Completeness to θ = 37.82	38.8 %
Refinement method	Full-matrix least-squares on F^2
Data / restrains / parameters	2965 / 0 / 353
Goodness-of-fit on F^2	1.254
Final R indices [I>2sigma(I)]	R_1 = 0.0891, wR_2 = 0.2087
R indices (all data)	R_1 = 0.1308, wR_2 = 0.2271
Extinction coefficient	0.079(9)
Largest diff. Peak and hole (fm $Å^{-3}$)	1.04 and -1.12

Table 3.5. *Neutron crystallographic data and refinement parameters for a crystal of yellow-PDM.*

3.1.2.7. Computational studies

In collaboration with Christopher H. Hendon, computational calculations were made in order to rationalise the observable different colours of the two modification of Pendimethalin.
In the case of Pendimethalin the *electronic band structure* of the two polymorphs was investigated. In Table 3.6 the computational results are reported.

Colour	HOMO	LUMO	Computational Gap (eV)	Internal Energy (eV)
Yellow	-1,23	1,72	2,94	-1160,45
Orange	-1,26	1,38	2,64	-1159,98

Table 3.6 *Calculated HOMO (Highest Occupied Molecular Orbital) and LUMO (Lowest Unoccupied Molecular Orbital) for the yellow and orange modifications of PDM.*

As it is possible to see from Table 3.6, the energy gap between the HOMO and LUMO is slightly smaller in the orange modification, leading to the formation of a crystal with a different colour. The internal energy of the two polymorphs is very similar, which confirms the possibility of a polymorphic transition in the solid state from the meta-stable yellow form to the stable orange one.

3.1.3. Results and discussion

The crystal structures of the two polymorphs were solved, from X-ray data, and the cell parameters of both forms are reported in Table 3.7.

	Orange PDM	Yellow PDM
Space group	$P\bar{1}$	$P2_1/c$
a	7.5196(4) Å	6.9823(2) Å
b	13.2348(8) Å	21.9992(6) Å
c	15.259(1) Å	9.3950(7) Å
α	97.891(7)˚	90.00˚
β	100.882(7)˚	100.195(7)˚
γ	103.167(7)˚	90.00˚
V	1426.0(2) $Å^3$	1420.3(1) $Å^3$

Table 3.7. *Cell parameters for the two polymorphs of pendimethalin.*

Both structures show the presence of intra-molecular hydrogen bonds between the hydrogen atom of the aniline nitrogen and the oxygen atom of the adjacent nitro group.

3.1.3.1. Orange-PDM

The asymmetric unit of the orange modification is formed by two molecules of PDM, as shown in Figure 3.10 from the X-ray results.

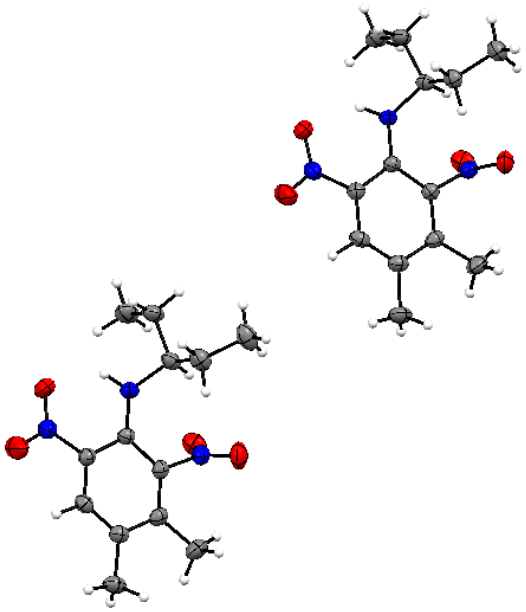

Figure 3.10. *ORTEP representation of the asymmetric unit in the orange modification of PDM. The probability level for all non-hydrogen ellipsoids is 50%, while the hydrogen atoms are drawn as fixed-size spheres of radius 0.15 Å.*

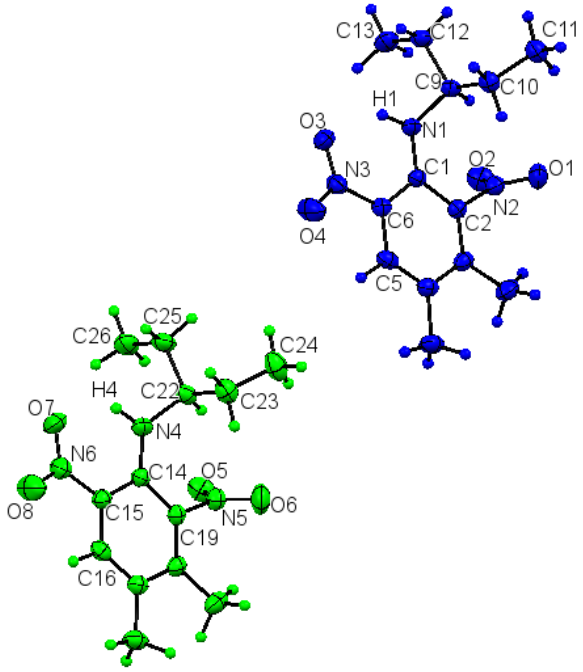

Figure 3.11. *The molecules are displayed in different colours, in order to easily discriminate between the two.*

Green molecule	
C15-C14-N4-H4	0.6(2.0)˚
C14-C15-N6-O7	9.1(3)˚
C14-C15-N6-O8	-171.6(2)˚
C14-C19-N5-O5	-69.4(3)˚
C14-C19-N5-O6	113.6(2)˚
C16-C15-C14-N4	-178.1(2)˚
C15-C14-N4-C22	156.4(2)˚
N4-C22-C23-C24	170.1(2)˚
N4-C22-C225-C26	-62.3(3)˚
Blue molecule	
C6-C1-N1-H1	1.3(2.0)˚
C1-C6-N3-O3	9.7(3)˚
C1-C6-N3-O4	170.8(2)˚
C1-C2-N2-O2	-77.2(3)˚
C1-C2-N2-O1	105.7(2)˚
C5-C6-C1-N1	179.6(2)˚
C6-C1-N1-C9	155.9(2)˚
N1-C9-C10-C11	168.3(2)˚
N1-C9-C12-C13	-64.2(2)˚

Table 3.8. *Torsion angles of interest. The colours refer to Figure 3.11.*

As expected from an aniline derivative, the amino group, N-H, is coplanar with the benzene ring, leading to torsion angles of 178.1(2)˚ and 179.6(2)˚ for the green and the blue molecules, which are shown in Figure 3.11, respectively. The two molecules, forming the asymmetric unit, differ slightly from one another in their conformation. Worthy of notice is the difference in the torsion angles involving the hydrogen and oxygen atoms implicated in the intra-molecular hydrogen bond. There is an increase in the blue molecule for both torsion angles C6-C1-N1-H1 and C1-C6-N3-O3. This change in the conformation leads to a slightly shortened distance of the hydrogen bond: 1.90(3) Å for the green molecule and 1.86(3) Å for the blue molecule.

Another interesting feature is represented by the fact that, while the nitro group involved in the hydrogen bond is almost perfectly coplanar with the benzene ring, so that the hydrogen bond can take place, the other nitro substituent is twisted almost perpendicularly in order to avoid the hindrance derived by the ethylpropyl chain on the nitrogen of the aniline ring.

The crystal packing is governed by the stack of the PDM molecules into piles, stabilized by π-π interactions, with distances between centroids of the offset parallel aromatic rings of 3.68(3) Å, and by the presence of an intra-molecular hydrogen bond between the hydrogen atom of the aniline and the nearest oxygen atom of the *ortho*-positioned nitro substituent on the benzene ring (Figure 3.12).

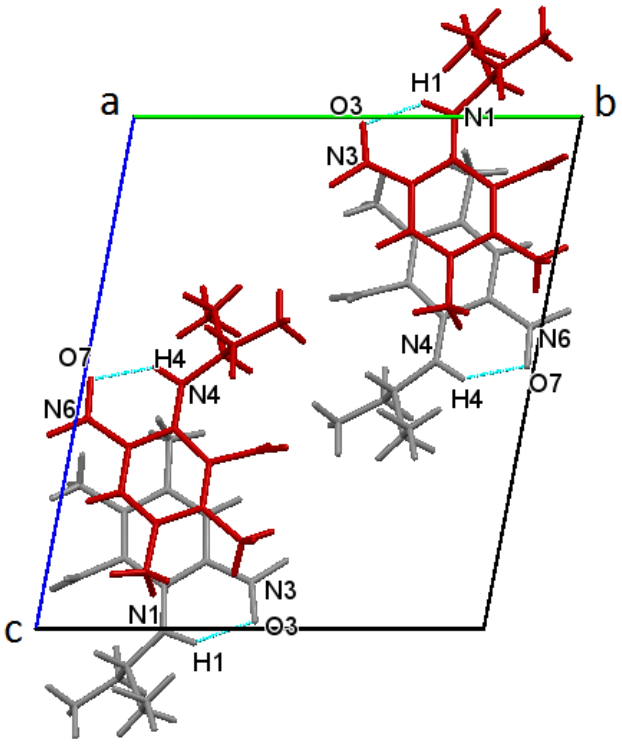

Figure 3.12. *Crystal packing of the orange modification of PDM, viewed along the* ***a****-axis.*

As can be seen from Figure 3.12, the molecules of pendimethalin arrange themselves into parallel planes (in Figure 3.12 different colours were assigned for different planes). The molecules that lie on the same plane are rotated of approximately 180˚ in respect of the molecules of the underlying plane. Each molecule is stabilized by an intra-molecular hydrogen bond, which main features are reported in Table 3.9.

Green molecule	
N4-H4	0.90(3) Å
N6-O7	1.238(3) Å
O7···H4	1.90(3) Å
O7···N4	2.63(3) Å
N4-H4···O7	136.7(2)˚
Blue molecule	
N1-H1	0.93(3) Å
N3-O3	1.246(2) Å
O3···H1	1.86(3) Å
O3···N1	2.642(2) Å
N1-H1···O3	139.3(2)˚

Table 3.9. *Hydrogen bond distances and angles for the orange PDM.*

3.1.3.2. Yellow-PDM

In the case of the yellow modification of Pendimethalin, just one molecule of PDM forms the asymmetric unit, as shown in Figure 3.13, from the X-ray results.

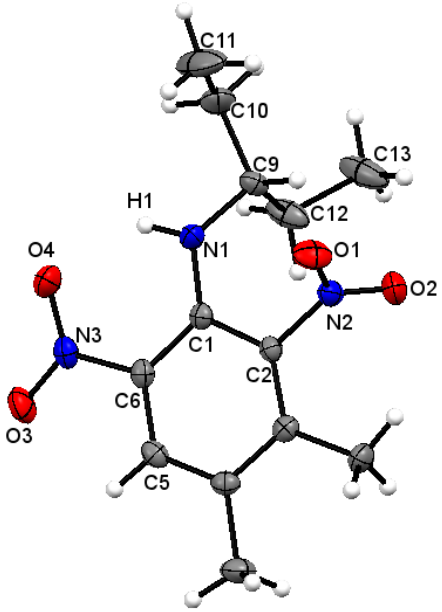

Figure 3.13. *ORTEP representation of the asymmetric unit in a crystal of yellow PDM. The probability level for all non-hydrogen ellipsoids is 50%, while the hydrogen atoms are drawn as fixed-size spheres of radius 0.15 Å.*

C6-C1-N1-H1	2.8(1.3)˚
C1-C6-N3-O4	-9.2(2)˚
C1-C6-N3-O3	170.9(1)˚
C1-C2-N2-O1	67.9(1)˚
C1-C2-N2-O2	-112.2(1)˚
C5-C6-C1-N1	179.0(1)˚
C6-C1-N1-C9	-140.3(1)˚
N1-C9-C12-C13	-165.8(1)˚
N1-C9-C10-C11	70.1(2)˚

Table 3.10. *Torsion angles of interest.*

Differences can be noticed in the torsion angle involving the hydrogen atom implicated in the hydrogen bond, C6-C1-N1-H1 = 2.8(1.3)˚. H8 is more twisted than in the case of the orange PDM, leading to a slightly longer distance of interaction. The main features already highlighted for the orange PDM are similar between the two polymorphs, but a difference can be found in the conformation of the ethylpropyl substituent. Since the carbon atoms of this substituent have a sp^3

hybridization and are all involved in single covalent bond with one another, the organic chain has got free rotation around N1-C9 bond. In the case of the orange modification, the carbon atoms linking the substituent to the aniline ring, C9 and C22, are both above the plane of the benzene ring, while in the yellow polymorph the atom C9 lies below the benzene plane, with a torsion angle C6-C1-N1-C9 of -140.3(1)˚.

Also for the yellow PDM the crystal packing is determined by the arrangement of the molecules into stacks and by the presence of an intra-molecular hydrogen bond, involving the same moieties as the orange form.

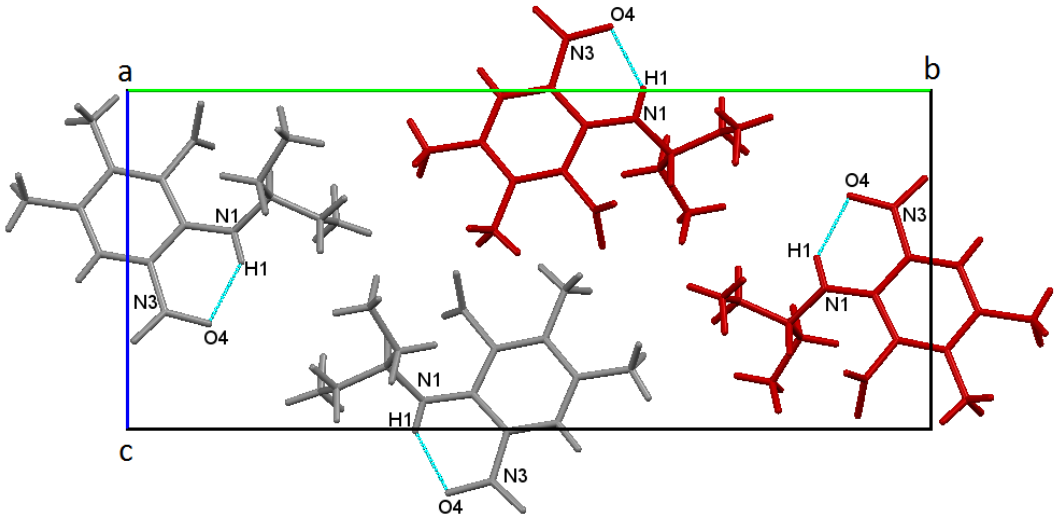

Figure 3.14. *Molecular arrangement in a crystal of yellow PDM, viewed along the* ***a****-axis.*

N1-H1	0.87(2) Å
N3-O4	1.24(2) Å
O4···H1	1.95(2) Å
O4···N1	2.65(2) Å
N1-H1···O4	136.7(3)˚

Table 3.11. *Hydrogen bond distances and angles for the yellow PDM.*

As shown in Figure 3.14, the PDM molecules organise themselves in parallel planes (in Figure 3.14 molecules belonging to the same plane are displayed in the same colour). Each molecule on one plane is rotated by 180˚ in respect to the molecule on an immediately underlying plane. Moreover, the planes are staggered so that a molecule on one plane corresponds to a void in the underlying plane, which is filled by the ethylpropyl chain of a molecule on the first plane.

Hydrogen bonds, the characteristics of which are reported in Table 3.11, between the hydrogen atom on the amino group and the oxygen atom of an adjacent nitro group in each PDM molecule are present in the structure. In this case the hydrogen bond is slightly longer than the one in the

orange modification, due to a different inclination of the hydrogen and oxygen atoms in respect to the aromatic ring.

In Table 3.12 a summary of the main characteristics of the intra-molecular hydrogen bond (intra-HB) for the orange and yellow modification is reported.

	Orange-PDM		Yellow-PDM
	Green molecule	Blue molecule	
intra-HB distance	1.90(3) Å	1.86(3) Å	1.95(2) Å
intra-HB angle	136.7(2)˚	139.3(2)˚	136.7(3)˚

Table 3.12. *Summary of the main characteristics of the intra-molecular hydrogen bond in the two modifications of PDM.*

Even though the Laue method allows smaller crystals to be analysed, there is an increase in the values for the R-factors when compared to data collected on a monochromatic single crystal diffractomer. This is due to the overlap of all the reflections that satisfy the Bragg's law for a range in wavelength from λ_{min} to λ_{max}. However, the higher statistics do not invalidate the accuracy of the derived model.

Neutrons allow achieving a ten-fold more precision in the definition of the hydrogen atom positions. In Table 3.13, a comparison of X-ray and neutron results for the intra-molecular hydrogen bond is reported.

	X-rays	Neutrons
N1 – H1	0.87(2) Å	1.009(6) Å
N1 ··· O4	2.652(2) Å	2.655(4) Å
H1 ··· O4	1.95(2) Å	1.843(7) Å
N1 – H1 ··· O4	136.7(3)˚	135.1(4)˚

Table 3.13. *Comparison of the main features of the intra-HB between X-ray and neutron results.*

Due to the ability of neutrons to directly interact with the nuclei of atoms, they can detect the position of hydrogen atoms more precisely than X-rays, providing additional information on the atomic displacement parameters (ADPs). The anisotropic refinement of the ADPs gives information on the probability density function of atomic displacement from mean atomic positions. This deviation from the mean position of any atom can be represented by a thermal, as displayed in Figure 3.15.

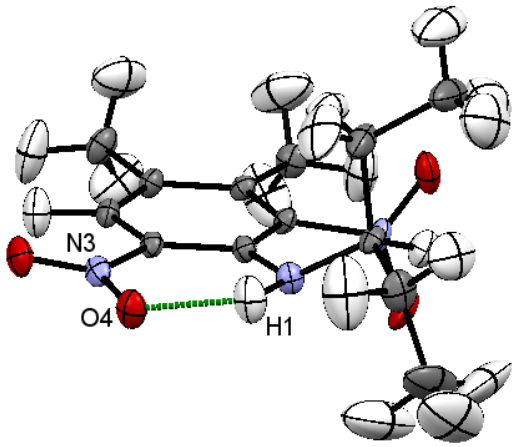

Figure 3.15. *ORTEP representation of a molecule of yellow-PDM derived from single crystal neutron Laue diffraction. The probability level for all ellipsoids is 50%.*

The deviation from the mean position of atom H1 takes place along an axis perpendicular to the hydrogen bond direction, confirming the presence of a medium-strength hydrogen bond as indicated by the hydrogen bond distance and geometry[81]. It is also interesting to notice the difference between the thermal ellipsoids of the hydrogen atoms on the aniline ring, of the two methyl groups and of the ethylpropyl chain opposed to the one of H1. Since H1 is involved in an intra-molecular interaction, its deviation from the mean position appears smaller than for the other hydrogen atoms.

In an X-ray diffraction study, various phenomena such as migration or atomic disorder can be characterised by investigating the electron density map of the entire crystallographic cell or just of a slant plane containing a particular interaction. Indeed, peaks of electron density usually indicate the presence of atoms in a particular area of the map. Unfortunately, X-rays are limited in the investigation of the electron density surrounding hydrogen atoms. By using single crystal neutron diffraction, it is possible to compute a "nucleon-density map", where nucleons are the protons and neutrons in atomic nuclei, showing the nuclear mass distribution of the atoms or molecules taken into consideration. The observation of this kind of map clearly shows any signs of migration or disorder. It is, however, important to remember that, when investigating a nucleon-density map, the presence of hydrogen atoms is indicated by holes in the mass distribution, due to the negative value for the hydrogen scattering length.

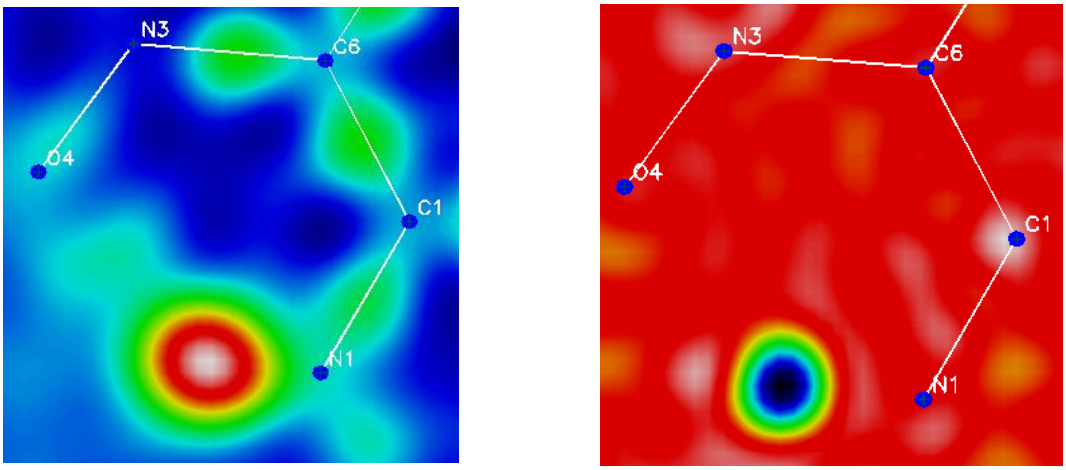

Figure 3.16. *Difference electron-density map (on the left) and "nucleon-density" map (on the right) for the intra-molecular hydrogen bond in a crystal of yellow-PDM.*

The absence of proton migration or disorder of the hydrogen atom involved in the intra-molecular hydrogen bond is confirmed by both X-rays and neutrons, as shown in Figure 3.16,

3.1.4. Conclusions

The issues that demanded for a deeper knowledge on the behaviour and characteristics of the herbicide Pendimethalin are for the major part related to its storage and its application on crop fields. Pendimethalin is usually prepared as aqueous suspensions stabilised by surfactants. The problem of this kind of formulation is that they are stable only in a narrow range of particle size. Any changes in the particle size distribution can cause formation of particle aggregates, which might obstruct the nozzles used for spraying the product on the field.

It is already known that in the solid state Pendimathalin can exists in two different crystal forms: the thermodynamically stable orange form and the meta-stable yellow modification. The orange form shows a lower melting temperature of ~54˚C, while the yellow polymorph has a higher melting point of ~56˚C. The DSC profiles of both forms show only the endothermic events corresponding to the melting of the substances, while no phase transition is visible before the melting temperature neither on heating nor on cooling. This behaviour may lead to think that the two polymorphs are monotropically related: there has to be complete melting of the stable form to allow the crystallisation of the meta-stable structure.

The meta-stable yellow modification is, in fact, usually obtained upon cooling of the liquid Pendimethalin, derived from the solid orange-PDM. Conversion back to the orange form can occur during a period of months, even years. However, this conversion is usually observed during transportation and storage of the finished product (orange-PDM). In these cases it is not uncommon

to have increase in temperature over the fusion temperature, which might trigger the phase transition.

Crystallisation from a variety of different organic solvents can also produce the yellow-PDM, as for the case of the orange polymorph if the right solvent is used[65]. During the course of this thesis the right conditions that led to production of orange crystals from solution were found only after addition of urea. The presence of a non-interactive co-former forced the PDM molecules to arrange themselves in the crystal packing of the thermodynamically stable modification.

Both polymorphs are characterised by the same intra-molecular hydrogen bond between the hydrogen atom on the aniline nitrogen and the neighbouring oxygen atom on the nitro group, and the crystal packing is mostly governed by π-π interactions, with a distance between aromatic rings of 3.68(3) Å. The different conformation of the PDM molecule in the two polymorhs, and the consequent different geometry of the intra-HB, is the cause for their different colour. Computational results demonstrate that the energy gap between the HOMO and the LUMO is higher for the yellow modification. However, the internal energies of the two forms are very similar, as shown by the close values of the melting temperatures.

3.2. Diflufenican, *N-(2,4-difluorophenyl)-2-[3-(trifluoromethyl)phenoxy]-3-pyridinecarboxamide*

3.2.1. Introduction

Diflufenican, DFF, is a carboxamide derivative herbicide used in both pre-emergence and post-emergence control of broad leaved grasses, like *Stellaria media* (chickweed), *Veronica Spp* (speedwell), *Geranium spp* (cranesbill) and *Laminum spp* (dead nettles). It acts by inhibiting the biosynthesis of carotenoid, thereby preventing photosynthesis and leading to plant death. In order to give a wider spectrum of control, diflufenican is also sold in premixed formulation with other herbicides, like isoproturon, pendimethalin and glyphosate.

3.2.2. Experimental

3.2.2.1. Physical and chemical properties

Diflufenican is usually commercialised as a white powder with a melting point of 161-162˚C and vapour pressure of 3.2×10^{-8} mmHg at 25˚C[82]. It is almost insoluble in water, but it is soluble in a variety of organic solvents, such as acetone, choloroform, xylene, methanol, ethanol, isopropanol, and acetonitrile, with greater solubility in less polar solvents.

3.2.2.2. Crystallisation from solution

All crystals of DFF analysed during the course of this thesis were grown from solution. Crystallisation from solution was attempted with different solvents, in order to find the best conditions for growing crystals suitable for X-ray and neutron single crystal diffraction. Table 3.14 reports all prepared solutions.

DFF quantity (g)	Solvent	Solvent quantity (ml)	Temperature (˚C)
0.20	Acetone	4	Room temperature (RT)
0.20	Xylene	12	60
0.19	Chloroform	2	Room temperature (RT)
0.30	Methanol	10	60
0.30	Ethanol	10	60
0.52	Isopropanol	20	60
0.30	Acetonitrile	8	60

Table 3.14. *Solvents used for the crystallisation of diflufenican.*

To help dissolution of DFF, the solution was heated for 30 minutes at the temperature reported in Table 3.14. Due to their high volatility and low boiling points, the solutions with acetone and chloroform were not heated. The chosen solvent was added 2 ml at a time to obtain saturation of the solution. After complete dissolution of DFF was reached, the solutions were transferred into crystallisation vials and covered with parafilm. Small holes were applied on the parafilm wrap so that the solvent could easily evaporate at room temperature. The best results were achieved using acetone as solvent: in fact, the crystals analysed with both X-ray and neutron diffraction were grown from an acetone solution. The attempts with different solvents were also tried in order to scan for the formation of possible polymorphs of DFF. Usually diflufenican crystallises in transparent flat plate-shaped crystals with a prismatic habit. Crystals grown from chloroform and acetonitrile solutions exhibited a different morphology: in fact their crystal habit was elongated and more similar to a needle than to a prism. Since all crystallisations led to the formation of well-shaped crystals, their crystal structure was analysed directly by single crystal X-ray diffraction rather than powder diffraction. For every crystal a short scan for the determination of the unit cell parameters was collected. All data led to the same results reported in Table 3.15.

a	12.2232
b	8.5335
c	15.8924
α	89.992
β	92.588
γ	89.978
Laue symmetry	$^2/_m$

Table 3.15. *General unit cell parameters for a crystal of DFF.*

Even the crystals with a different morphology showed the same crystal structure: the effect of different solvents caused only a change in the crystal habit.

3.2.2.3. Differential Scanning Calorimetry

The behaviour of diflufenican during changes in temperature was investigated by DSC. Two samples were analysed: DFF re-crystallised from an acetone solution so to eliminate any impurities that might be present in the raw material, and DFF crystallised from the melt, obtained at a temperature of 170˚C. The heating and cooling rate for the first sample was 3˚C/min, while for the second sample a heating and cooling rate of 5˚C/min was used. The two DSC profiles are reported in Figures 3.17 and 3.18

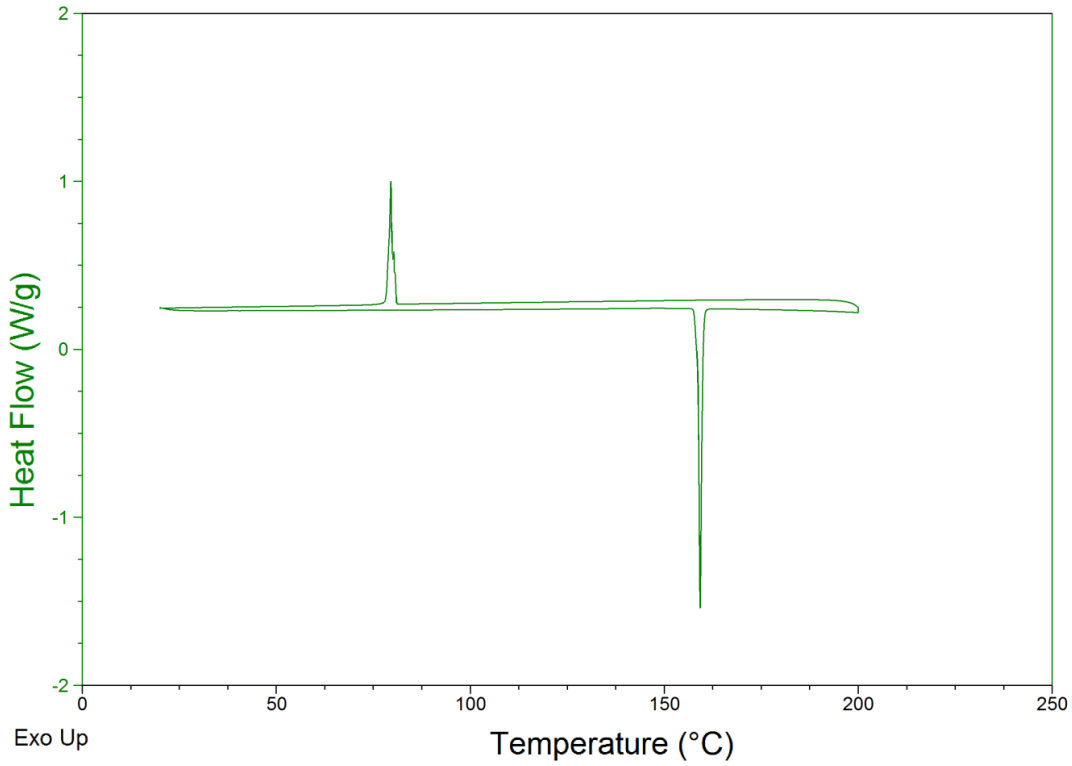

Figure 3.17. *DSC profile for a sample of DFF re-crystallised from an acetone solution.*

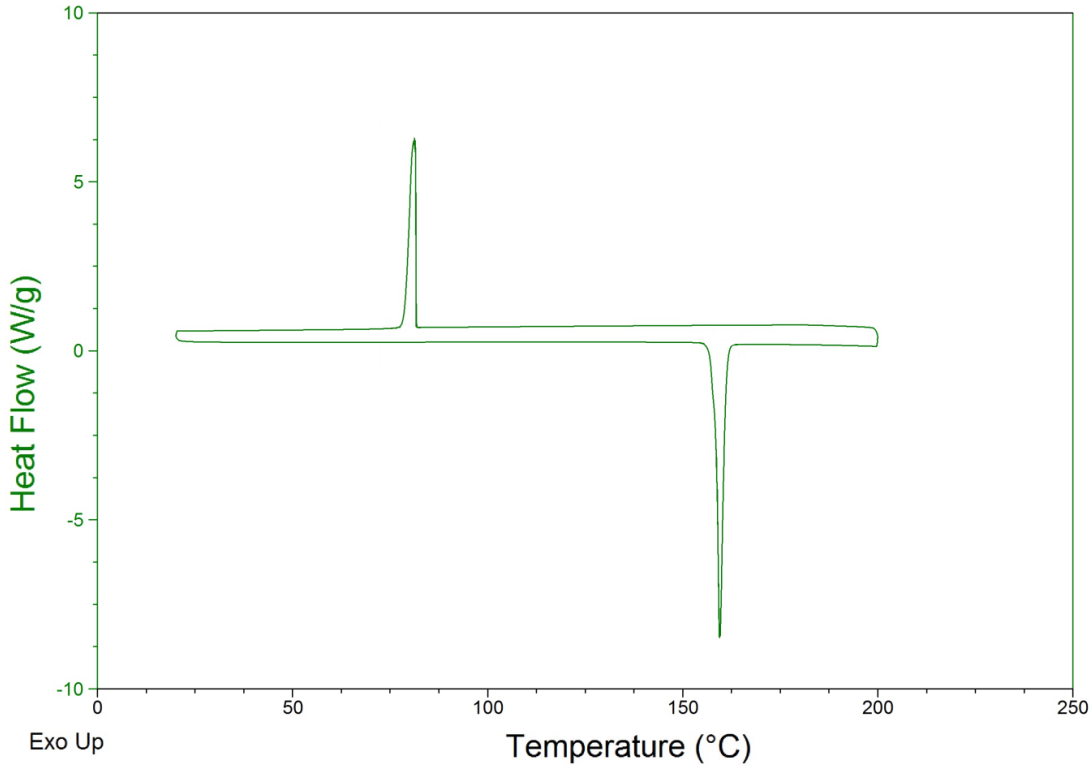

Figure 3.18. *DSC profile for a sample of DFF crystallised from the melt.*

Both DSC profiles show only an endothermic event, on heating, at ~159˚C, corresponding to the melting of the samples, and an exothermic event, during the cooling process, at ~79˚C for the DFF crystallised from solution, and at ~81˚C for the one crystallised from the melt. The large temperature difference between the fusion and the crystallisation events might be due to the fast rate of cooling that can prevent the prompt organisation of the DFF molecules in the solid state. No traces of any transitions are observed. Since the melting point of the two samples is the same, it is possible to conclude that no polymorph was formed after crystallisation from the melt. The slight difference in the crystallisation events may be due to the different cooling rate between the two samples.

3.2.2.4. Single crystal X-ray diffraction

A flat plate-shaped crystal of DFF grown from an acetone solution was selected for an SXD experiment and it was analysed on an Enraf-Nonius kappaCCD single crystal diffractometer at the University of Bath.

In Table 3.16, X-ray crystallographic data and refinement parameters for the Diflufenican crystal are reported.

Name	Diflufenican
Empirical formula	$C_{19}H_{11}N_2O_2F_5$
Formula weight (g mol^{-1})	394.30
Temperature (K)	150
Wavelength (Å)	0.71073
Crystal system, space group	Monoclinic, $P2_1/c$
Unit cell dimensions	a = 12.220(2) Å
	b = 8.530(2) Å
	c = 15.907(3) Å
	β = 92.61(3)˚
Volume ($Å^3$)	1656.4(6)
Z, calculated density (g cm^{-3})	4, 1.581
F(000)	800
Absorption coefficient (mm^{-1})	0.142
Theta range for data collection (˚)	1.67 to 27.49
Limiting indices	$-15 \leq h \leq 15$, $-11 \leq k \leq 11$, $-20 \leq l \leq 20$
Reflections collected / unique	12927 / 3782 [R_{int} = 0.0210]
Completeness to θ = 27.49	99.5 %
Refinement method	Full-matrix least-squares on F^2
Data / restrains / parameters	3782 / 0 / 298
Goodness-of-fit on F^2	1.120
Final R indices [I>2sigma(I)]	R_1 = 0.0438, wR_2 = 0.1351
R indices (all data)	R_1 = 0.0538, wR_2 = 0.1586
Extinction coefficient	0.025(6)
Largest diff. Peak and hole (e $Å^{-3}$)	0.46 and -0.26

Table 3.16. *X-ray crystallographic data and refinement parameters for a crystal of DFF.*

3.2.2.5. Single crystal neutron diffraction

A large crystal of DFF with prismatic habit, grown from an acetone solution, was selected for a SND experiment on the single crystal diffractometer D19 at ILL. The mounting of the crystal and the initial setup of the analysis were done by following the details reported in section **2.3.3**. For the crystal of DFF the collection temperature was initially set up to 20K. Unfortunately, the cooling process was started with a poor vacuum, which did not allow to reach a temperature lower than 120K. For this reason, data were collected at a temperature of 120K. After a day of data collection, the vacuum had improved, and it was decided to restart the cooling to 20K. Unfortunately, during data collection at 20K, the crystal broke: this was probably due to mechanical stresses induced by the glue. Since other two days of beamtime were available, a second set of neutron data was collected on another crystal. The second crystal was slightly smaller than the first and it had a flat, plate-shaped morphology. In order to avoid another break, this crystal was placed at the centre of a thin transparent glass tube, surrounded by glass wool to keep it from moving. Thanks to the tube it was possible to avoid stresses caused by the cooling of the glue. The data sets relative to both crystals were analysed and the results of the collection at 120K and 20K are reported in this thesis.
Data processing was done in the same way for the two crystals, following the steps described in Chapter 2, section **2.3.3**. When the neutron experiment was performed, the only structural information available was that present in literature[83]. The *.cif* file was downloaded from the CCDC database and it was used as a starting model for the structural refinement with RETREAT. Since it was encased inside the glass tube, it was not possible to apply the correction for absorption on the second crystal, because the crystal faces could not be indexed. Due to its simple morphology, the faces of the first crystal were guessed from the orientation of the crystal in respect to the D19 axes, after the break occurred. A schematic representation of the morphology of the first crystal is reported in Figure 3.19.

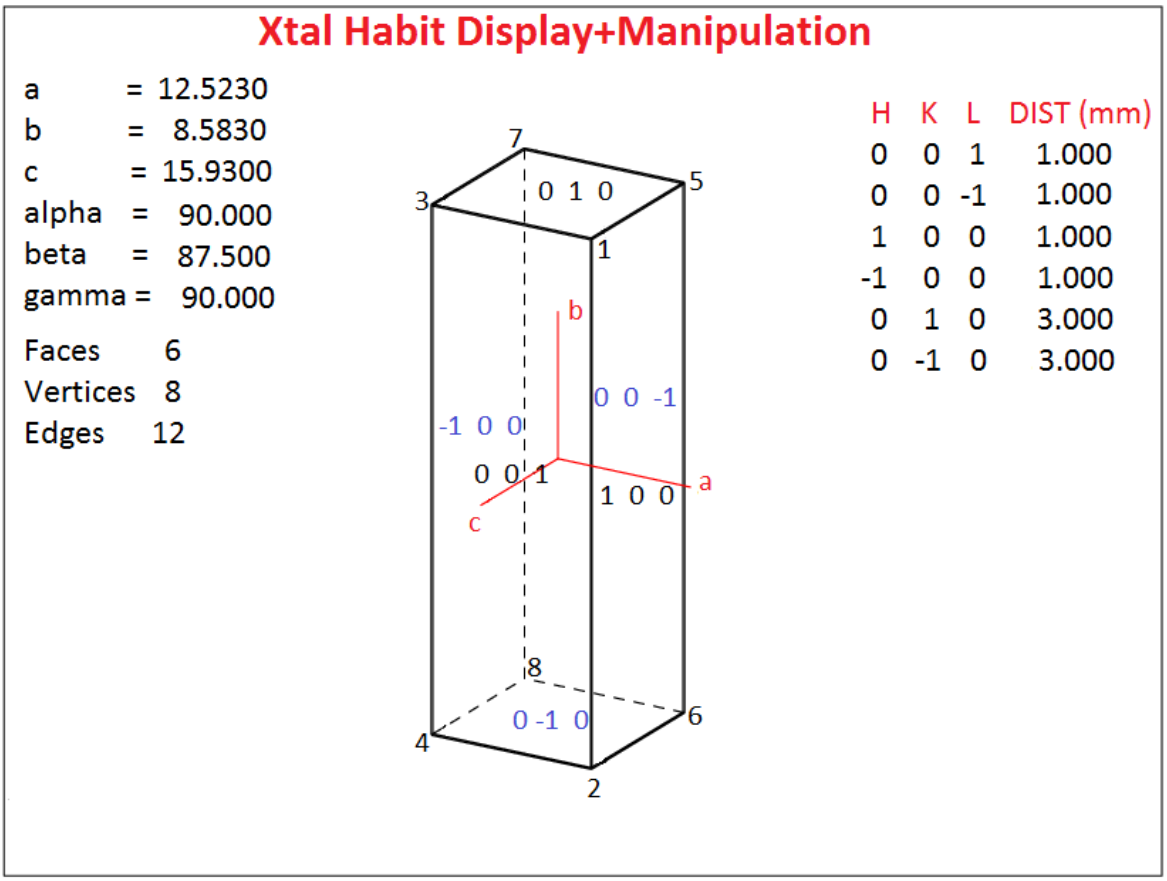

Figure 3.19. *Graphical representation of the DFF crystal morphology, obtained using the program platon.*

By comparing the values of the R1-factors for the structure without any correction, the one corrected only for the presence of the cans, and the one containing correction for absorption by the cans and by the crystal itself, 0.0988, 0.0471 and 0.0437, respectively, it is evident that the highest contribution to the attenuation of the diffracted radiation is represented by the three vanadium cans used to ensure a tight vacuum for the cooling process. For this reason, even though it was not possible to apply a correction for the absorption by the crystal, the structural refinement of the second crystal still produces a reliable model.

Neutron crystallographic data and refinement parameters for the crystals of Diflufenican at 120K (Table 3.17) and at 20K (Table 3.18) are reported.

Name	Diflufenican
Empirical formula	$C_{19}H_{11}N_2O_2F_5$
Formula weight (g mol^{-1})	394.30
Temperature (K)	120
Wavelength (Å)	1.1700
Crystal system, space group	Monoclinic, $P2_1/c$
Unit cell dimensions	a = 12.1567(4) Å
	b = 8.5268(3) Å
	c = 15.8883(5) Å
	β = 87.144(2)˚
Volume ($Å^3$)	1644.90(9)
Z, calculated density (g cm^{-3})	4, 1.473
F(000)	575
Absorption coefficient (mm^{-1})	0.114
Crystal size (mm)	2 x 2 x 6
Theta range for data collection (˚)	2.68 to 57.76
Limiting indices	$-17 \leq h \leq 17$, $-4 \leq k \leq 11$, $-22 \leq l \leq 22$
Reflections collected / unique	12870 / 4944 [R_{int} = 0.0493]
Completeness to θ = 57.76	91.4 %
Refinement method	Full-matrix least-squares on F^2
Data / restrains / parameters	4944 / 0 / 354
Goodness-of-fit on F^2	1.216
Final R indices [I>2sigma(I)]	R_1 = 0.0437, wR_2 = 0.0932
R indices (all data)	R_1 = 0.0506, wR_2 = 0.0984
Extinction coefficient	0.0056(2)
Largest diff. Peak and hole (fm $Å^{-3}$)	0.68 and -0.73

Table 3.17. *Neutron crystallographic data and refinement parameters for a crystal of DFF at 120K.*

Name	Diflufenican
Empirical formula	$C_{19}H_{11}N_2O_2F_5$
Formula weight (g mol^{-1})	394.30
Temperature (K)	20
Wavelength (Å)	1.1700
Crystal system, space group	Monoclinic, $P2_1/c$
Unit cell dimensions	a = 12.0522(2) Å
	b = 8.5067(2) Å
	c = 15.8018(3) Å
	β = 86.761(1)˚
Volume ($Å^3$)	1617.48(6)
Z, calculated density (g cm^{-3})	4, 1.473
F(000)	575
Absorption coefficient (mm^{-1})	0.114
Crystal size (mm)	1 x 2.6 x 4
Theta range for data collection (˚)	2.68 to 60.51
Limiting indices	$-17 \leq h \leq 17$, $-11 \leq k \leq 4$, $-22 \leq l \leq 22$
Reflections collected / unique	13588 / 4775 [R_{int} = 0.0628]
Completeness to θ = 60.51	80.9 %
Refinement method	Full-matrix least-squares on F^2
Data / restrains / parameters	4775 / 0 / 354
Goodness-of-fit on F^2	1.253
Final R indices [I>2sigma(I)]	R_1 = 0.0416, wR_2 = 0.1040
R indices (all data)	R_1 = 0.0432, wR_2 = 0.1051
Extinction coefficient	0.0106(3)
Largest diff. Peak and hole (fm $Å^{-3}$)	1.79 and -0.91

Table 3.18. *Neutron crystallographic data and refinement parameters for a crystal of DFF at 20K.*

3.2.3. Results and discussion

The asymmetric unit is constituted by a single molecule of diflufenican, as reported, from the X-results, in Figure 3.20. In Table 3.19 torsion angles of interest are reported.

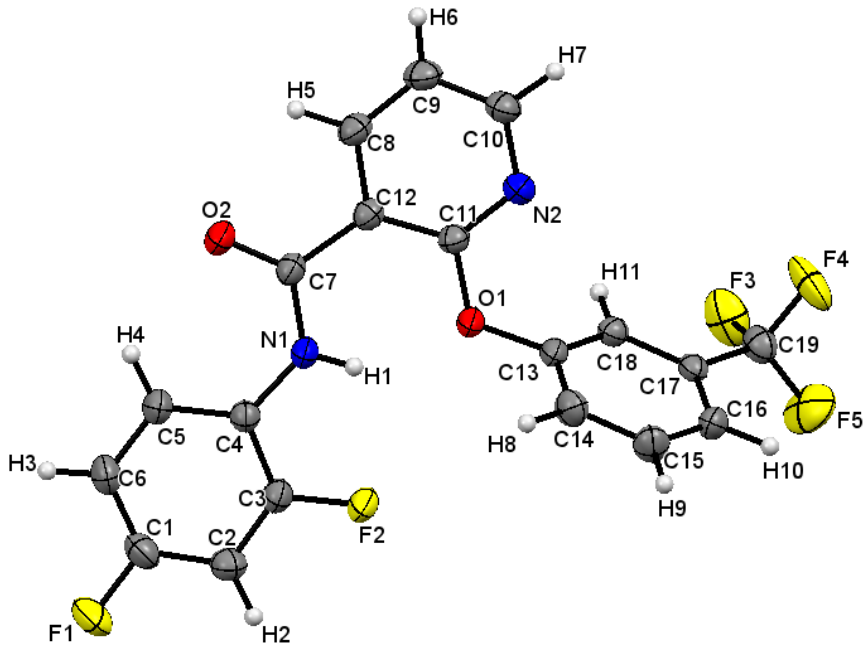

Figure 3.20. *ORTEP representation of a molecule of DFF modeled from single crystal X-ray diffraction. The probability level for all non-hydrogen ellipsoids is 50%, while the hydrogen atoms are drawn as fixed-size spheres of radius 0.15 Å.*

N1-C4-C5-C6	176.8(2)˚
N1-C4-C3-C2	-176.6(2)˚
C7-C12-C8-C9	177.0(2)˚
C7-C12-C11-N2	-177.0(2)˚
C11-O1-C13-C18	-75.8(2)˚
C11-O1-C13-C14	109.3(2)˚

Table 3.19. *Torsion angles of interest.*

Since Diflufenican is an amide derivative, the two aromatic rings at each part of the amide group lie on the same plane, whereas the trifluoromethylbenzyl substituent is twisted almost perpendicularly, with a torsion angle of 109.3(2)˚. The presence of the phenoxy substituent in position 2 of the pyridine ring allows the formation of an intra-molecular hydrogen bond between the hydrogen atom of the amide, H1, and the oxygen atom of the phenoxy ring, O1. The hydrogen bond length and angle are reported in Table 3.20.

N1-H1	0.81(2) Å
H1···O1	1.97(2) Å
N1-H1···O1	143(2)˚
N1···O1	2.668(2)Å

Table 3.20. *Length and angle of the intra-molecular hydrogen bond.*

Based on the values of distance and geometry of interaction[74], this hydrogen bond can be classified as moderate-weak. However, it is the presence of this hydrogen bond, in addition to π-π interactions, that stabilises the DFF molecules, allowing their arrangement in their crystal packing, as shown in Figure 3.21.

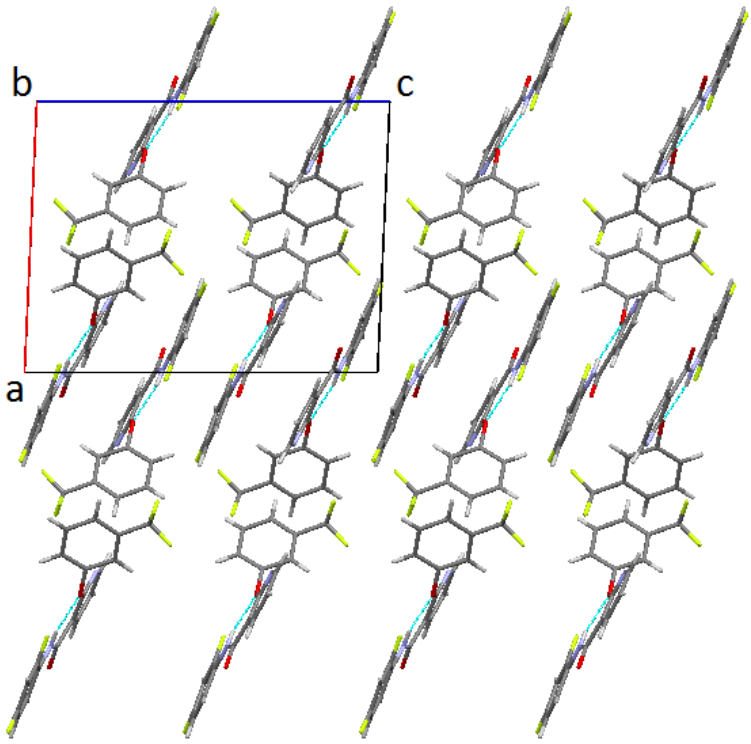

Figure 3.21. *Crystal packing of DFF viewed along the* ***b****-axis. The intra-molecular hydrogen bond is highlighted in light blue.*

The DFF molecules arrange themselves into lines, creating a fishbone-like network. As displayed in Figure 3.20, the amide is involved in the intra-molecular hydrogen bond, forcing all planar substituted amides into parallel strings. The trifluoromethyl-substituted phenoxy rings are rotated of an angle ~180˚ in respect to one another to avoid hindrance of the trifluoromethyl substituents.

The characterisation of the intra-molecular hydrogen bond is better defined by the model obtained from the neutron experiments. The "nucleon-density" map (Figure 3.22) shows that the hydrogen atom involved in the intra-molecular interaction, H1, is in a precise and defined position, without proton migration or disorder in the structure.

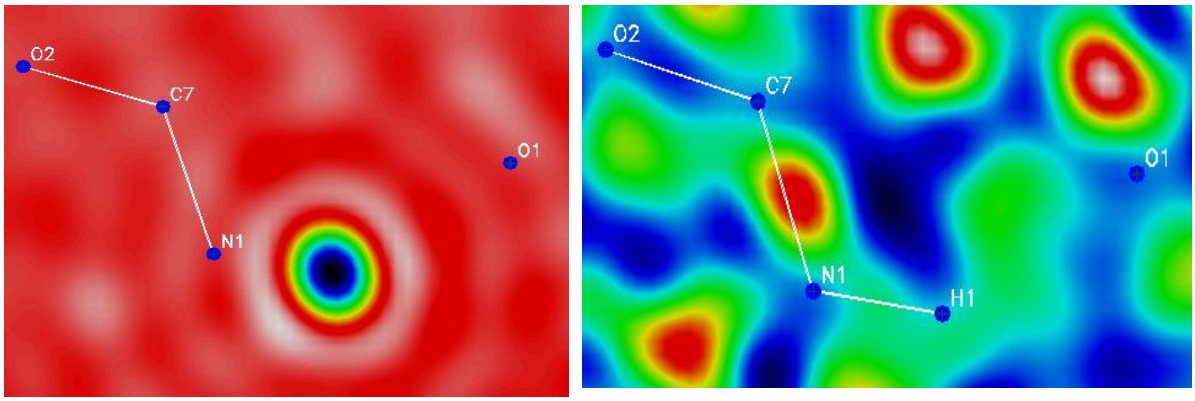

Figure 3.22. *"Nucleon-density" difference maps for the intra-molecular hydrogen bond. On the left, the atom H1 was removed from the refinement in order to find its exact position; on the right the atom H1 was re-introduced in the refinement.*

The two "nucleon-density" maps in Figure 3.22 confirm the absence of proton migration or disorder: once the atom H1 is re-introduced in the refinement, there is not any residual nuclear mass distribution, which in the case of hydrogen atoms detected by neutrons would be represented by a hole due to the negative value of the scattering length of hydrogen, relative to H1. A useful tool for the investigation of hydrogen atoms by neutron diffraction is represented by the possibility of displaying their anisotropic atomic displacement parameters (ADPs), as shown in Figure 3.23.

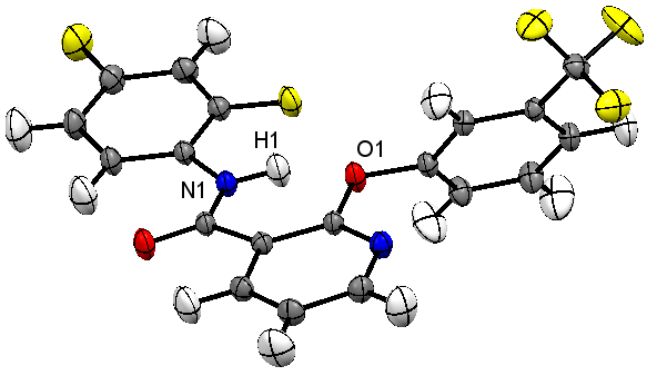

Figure 3.23. *ORTEP representation of a molecule of diflufenican, derived from neutron data. The probability level for all ellipsoids is 50%.*

Since the hydrogen atoms are the lightest atoms in the structure, their ADPs are bigger than those relative to carbon, nitrogen, oxygen and fluorine atoms. Worthy of notice is the ADP of H1: it is slightly smaller than the others due to the intra-molecular interaction that takes place. In Table 3.21 the hydrogen bond length and geometry, as derived from neutron data at 20 and 120K, are reported.

	20K	120K
N1-H1	1.017(2) Å	1.031(2) Å
H1···O1	1.790(2) Å	1.858(3) Å
N1-H1···O1	138.2(2)˚	139.3(2)˚
N1···O1	2.637(1)Å	2.723(3) Å

Table 3.21. *Hydrogen bond length and geometry for the intra-molecular hydrogen bond, derived from neutron diffraction.*

It is interesting to notice that the interatomic distance N1···O1 increases with the increasing temperature; the same trend is also exhibited by the covalent bond N1-H1. This behaviour might be due to the increase of the unit cell parameters, especially of the ***β*** angle, which allows an expansion and relaxation of the conformation of the molecule.

Other than the characterisation of the hydrogen bond, one of the reasons that merited a neutron study of Diflufenican is the investigation of the role played by the fluorine atoms in controlling the crystal structure of this compound. It is well known that fluorine-containing agrochemicals represent ~20% of currently active agrochemicals[84]. Extensive studies[85,86] have been made to investigate the characteristics of weak interactions, such as halogen···halogen contacts. It was demonstrated that the halogen atoms involved in these types of interaction exhibited an anisotropic distribution of the electron density surrounding the atom. This electronic distribution defines an elliptical area around the halogen atom, creating two different regions with opposite charge: a partially positive charge along the covalent bond C-X, where X is the halogen atom; and a partially negative charge placed perpendicularly to the covalent bond (Figure 3.24).

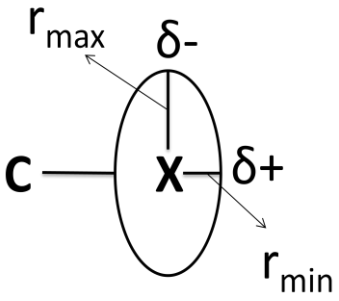

Figure 3.24. *Schematic representation of the electronic distribution around a halogen atom.*

This polarisation effect allows the formation of X···X contacts: their geometry will permit the formation of electrostatic interactions $\delta^- \cdots \delta^+$.

However, this kind of behaviour is not observed in all atoms belonging to the halogen group: fluorine-containing compounds do not exhibit F···F interactions. This is probably due to the smaller size and the higher value of electronegativity of the fluorine atom compared to the other halogens.

Since the electronic cloud surrounding the F atom is closer to the nucleus, it is more difficult to create an anisotropic distribution of the electron density, prohibiting the formation of a polarised electron density.

Even though the presence of F···F contacts in the structure of DFF is excluded, it is important to consider the effect that the fluorine atoms can have on weak interactions, such as C-H···F-C.

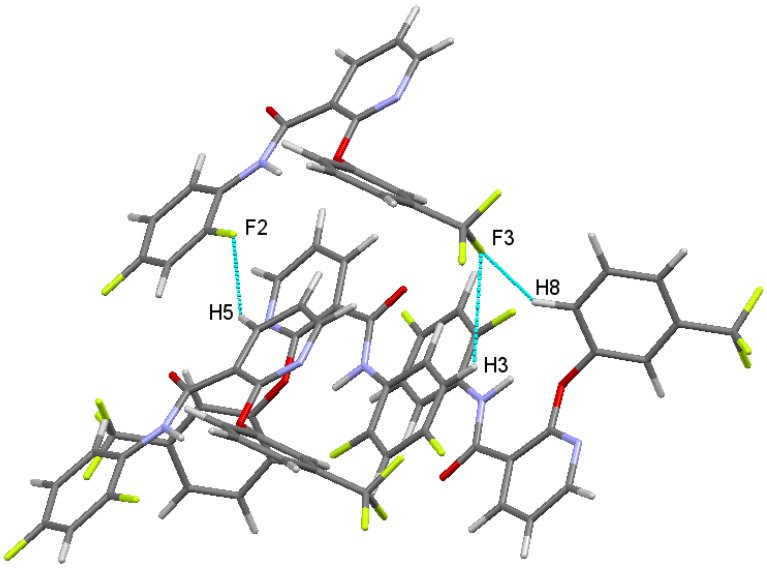

Figure 3.25. *Selected C-H···F-C contacts.*

As shown in Figure 3.25, three C-H···F-C contacts were selected because their lengths are smaller than the sum of their van der Waals radii. The characteristics of the three intermolecular interactions, derived from neutron data, are reported in Table 3.22.

		Length – vdW
F3···H8	2.360(3) Å	-0.408 Å
C14-H8···F3	130.0(2)˚	
F3···H4	2.462(3) Å	-0.200 Å
C5-H4···F3	140.2(2)˚	
F2···H5	2.352(3) Å	-0.314 Å
C8-H5···F2	124.7(2)˚	

Table 3.22. *Distances and angles of the three selected interatomic interaction.*

The results displayed in Table 3.22 show that, even though it is not possible to claim that the C-H···F-C interactions assume a key role in the arrangement of the DFF molecules, it is certain that they contribute to the formation of the most stable crystal packing, alongside the intra-molecular hydrogen bond and the π-π interactions.

Since Diflufenican had already been analysed by single crystal X-ray diffraction[83], the experimental results were compared to the crystal structure present in the CCDC database[87]. In Table 3.23 the unit cell parameters and the space group for the CCDC structure and the experimental results, for the X-ray determination, are reported.

	CCDC structure	**Experimental structure**
Space group	$P2_1/c$	$P2_1/c$
a	12.523(3) Å	12.220(2) Å
b	8.583(2) Å	8.530(2) Å
c	15.930(3) Å	15.907(3) Å
β	90.52(3)°	92.61(3)°
V	1712.1(6) $Å^3$	1656.1(6) $Å^3$
T	RT	RT

Table 3.23. *Unit cell parameters and space group for the CCDC and the experimental structures of DFF.*

During the refinement of a structure with SHELXL-97[57], it is important to remember that the program does not refine the unit cell dimensions in each refinement cycle, thus leaving the unit cell found at the end of data collection unchanged. Before starting a complete data collection on the crystal of DFF, short scans at room temperature were recorded in order to find the unit cell parameters, which were, then, used during the refinement. For this reason it is possible to compare the two structures. Table 10 clearly shows that, while the unit cell axes, ***a***, ***b*** and ***c***, are very similar, there is a significant variation in the value of the angle ***β***. However, the crystal packing of the two structures is the same. This might indicate that more than one primitive monoclinic unit cell can be chosen for the description of the crystal structure of DFF.

This problem presented itself again during the data processing of the neutron experiments. Table 3.24 reports a comparison of the unit cell parameters of DFF at three temperatures: 292K, 120K and 20K.

	292K	120K	20K
Space group	$P2_1/c$	$P2_1/c$	$P2_1/c$
a	12.513(3) Å	12.1567(4) Å	12.0522(2) Å
b	8.566(2) Å	8.5268(3) Å	8.5067(2) Å
c	15.961(4) Å	15.8883(5) Å	15.8018(3) Å
β	89.50(1)°	87.144(2)°	86.761(1)°
V	1710.8(6) $Å^3$	1644.90(9) $Å^3$	1617.48(6) $Å^3$

Table 3.24. *Unit cell parameters, derived from neutron diffraction, for the crystal of DFF at 292K, 120K, and 20K.*

During a neutron experiment, the orientation matrix is found by the subroutine *pfind*, which also indexes all reflections. Since it is not possible to see the crystal once the experiment has started, because it is enclosed inside three vanadium cans, it is common practise to index the recorded reflections at each temperature of collection: in this way, any variation of the intensity of a reflection is an indication of changes inside the crystal. Moreover, it also indicates that the unit cell parameters found by *pfind* at a particular temperature correspond to the unit cell at that temperature. Contrary to SHELXL, the refinement program RETREAT refines the unit cell parameters with every refinement cycle. From Table 3.24 it is possible to notice a reasonable expansion of the unit cell axes ***a***, ***b***, and ***c***, while increasing the temperature. It is, however, interesting to notice that, although the ***β***-angle reported in the CCDC is higher than 90˚, its value is closer to the SND results rather than the experimental structure refined from SXD measurements. This may confirm the hypothesis of the presence of multiple unit cell settings for crystals of DFF. The behaviour of the ***β*** angle is unusual: it exhibits a shrinking of ~3˚ while cooling from 292K to 20K. This variation in the ***β***-angle may explain the breaking of the first crystal. Unfortunately, the lack of data at temperatures below 100K did not allow the investigation of a possible phase transition in DFF. Powder neutron diffraction might represent a valuable technique in this case, but time restrictions and unavailability of a powder diffractometer at the ILL neutron facility did not allow a deeper investigation of the DFF system to be undertaken.

3.2.4. Conclusions

Diflufenican is a fluorine-containing herbicide, which crystallises in transparent flat, plate-like crystals from the most common organic solvents, such acetone and xylene. Even though the solvent does not affect the crystal structure of this compound, it plays a role in the definition of the morphology. The crystal habit of crystals grown from chloroform and acetonitrile solutions differ from the usual: these crystals are more elongated and more similar to a needle than to a plate.

Diflufenican does not show any evident transitions to a meta-stable form or changes in the crystal structure induced by a temperature variation in the range from 20K to 473K. However, neutron diffraction pointed out an unusual shrinking of the angle β by ~3˚ between the structure at 292K and the structure at 20K.

The crystal structure of Diflufenican was analysed by X-ray and neutron single crystal diffraction. Both highlighted the presence of a moderate-weak intra-molecular hydrogen bond between the hydrogen atom of the amide group and the oxygen atom of the phenoxy ring: H1···O1 = 1.790(2) Å. The crystal packing is held together by the intra-molecular hydrogen bond, π-π interactions, and possible, but not confirmed, C-H···F-C contacts. These interactions occur between fluorine atoms and hydrogen atoms that are made slightly more positively charged by the action of the ***–I*** effect typical of all halogens.

Chapter 4

4. Intermolecular H-bonded systems

4.1. Isoproturon, *N-(4-isopropylphenyl)-N',N'-dimethylurea*

4.1.1. Introduction

Isoproturon (IPU), is a urea derivative herbicide mostly used for pre- and post-emergence weed development in winter cereals. It is absorbed by roots and leaves and it acts by inhibiting the photosynthesis.

In recent years, concern about its use has grown significantly. It is known that Isoproturon has a highly toxic effect on aquatic fauna and flora[88], but studies report risks on contamination[89] and human health that cannot be overlooked. For these reasons a study of the solid state structure of this material has been undertaken. Understanding the detailed structural chemistry of the material should help identify the conditions under which this substance could exhibit polymorphism, leading to the formation of a different crystal form. A new polymorph might show, in its physical properties, less toxicity and it might be more available for a prompt absorption by the plant.

4.1.2. Experimental

4.1.2.1. Physical and chemical properties

Isoproturon is a white powder with a melting point of 155-156˚C, vapour pressure of 2.5×10^{-8} mmHg at 20˚C, and water solubility of 55 ppm at 20˚C[90]. It is soluble in a large variety of organic solvents, with higher solubility in increasingly more polar solvents.

4.1.2.2. Crystallisation from solution

Since Isoproturon has not yet been shown to exhibit polymorphism, various attempts to crystallise the herbicide from different organic solvents were made in order to assess whether the presence of a different solvent might induce changes in the crystal packing of the IPU molecules.

Due to its polar functional groups, a selection of polar organic solvents was used, as reported in Table 4.1.

IPU (g)	Solvent	Solvent quantity (ml)	Temperature (˚C)
0.19	Methanol	5	60
0.19	Ethanol	8	60
0.08	1-propanol	6	60
0.15	N,N'-dimethylformamide	14	70
0.17	Acetonitrile	14	70
0.14	Ethyl acetate	14	70
0.10	Pyridine	10	70
0.23	Cyclohexanone	16	70

Table 4.1. *Solvents used for crystallisation of isoproturon.*

The starting IPU for all sample preparations was of technical purity and it was used without further purification. Small amounts of IPU were solubilised in each solvent and every solution was heated for one hour at the chosen temperature reported in Table 4.1. Single crystals were obtained by the method of slow evaporation of the solvent: after heating, the solutions were transferred into small crystallisation vials, which were covered with parafilm wrap. Small holes on the parafilm cover allowed the solvent to evaporate and the crystals to form. By varying the number and the size of the holes on the parafilm cover, it is possible to control the rate of evaporation: a slow evaporation of the solvent allows the formation of large crystals. With the purpose of obtaining single crystals suitable for X-rays diffraction, large holes were made on the parafilm cover of each crystallization vial so to obtain crystal sizes of a fraction of a millimeter. Once the evaporation of the solvent was completed, a few well-shaped single crystals were isolated for further analysis. The remaining crystals were manually ground into a fine powder and analysed by X-ray powder diffraction (PXD), on a Siemens D5000 diffractometer. The powder diffraction patterns of all samples are reported in Figure 4.1.

All the crystals obtained were of the same modification: it could therefore be concluded that the solvent does not seem to play a key role in the arrangement of the molecules inside the crystal packing.

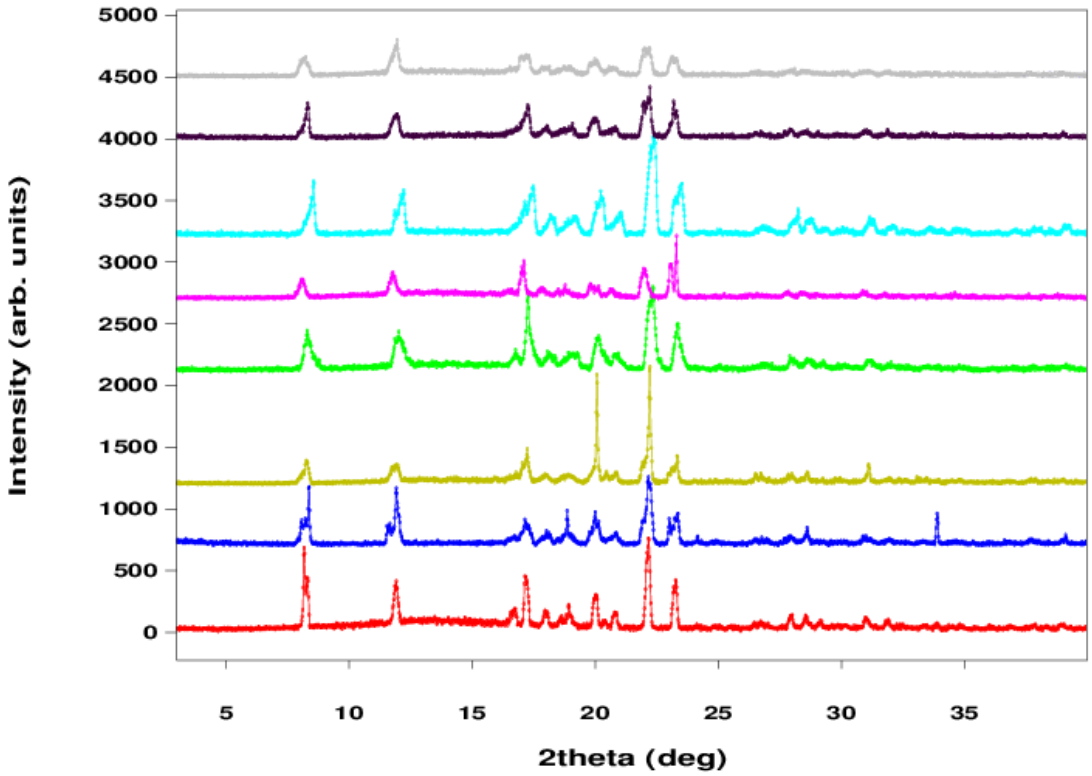

Figure 4.1. *Powder diffraction patterns of all the samples obtained. The colours refer to the different solvents used: in red, methanol; in blue, ethanol; in ochre, 1-propanol; in light green, ethyl acetate; in pink, acetonitrile; in light blue, N,N'-dimethylformamide; in black, cyclohexanone; and in gray, pyridine.*

4.1.2.3. Attempted crystallisation from the melt

Crystallisation from different solvents is not the only available option when screening for possible polymorphs of a compound. Temperature is also known for playing a significant role in the definition of the tri-dimensional order that defines a crystal structure. Re-crystallisation from the melt was attempted: for this purpose a DSC scan was recorded to verify the melting point of IPU present in the literature and to have a better understanding of the behaviour of the herbicide upon changes in temperature. The DSC profile for the sample of Isoproturon is reported in Figure 4.2.

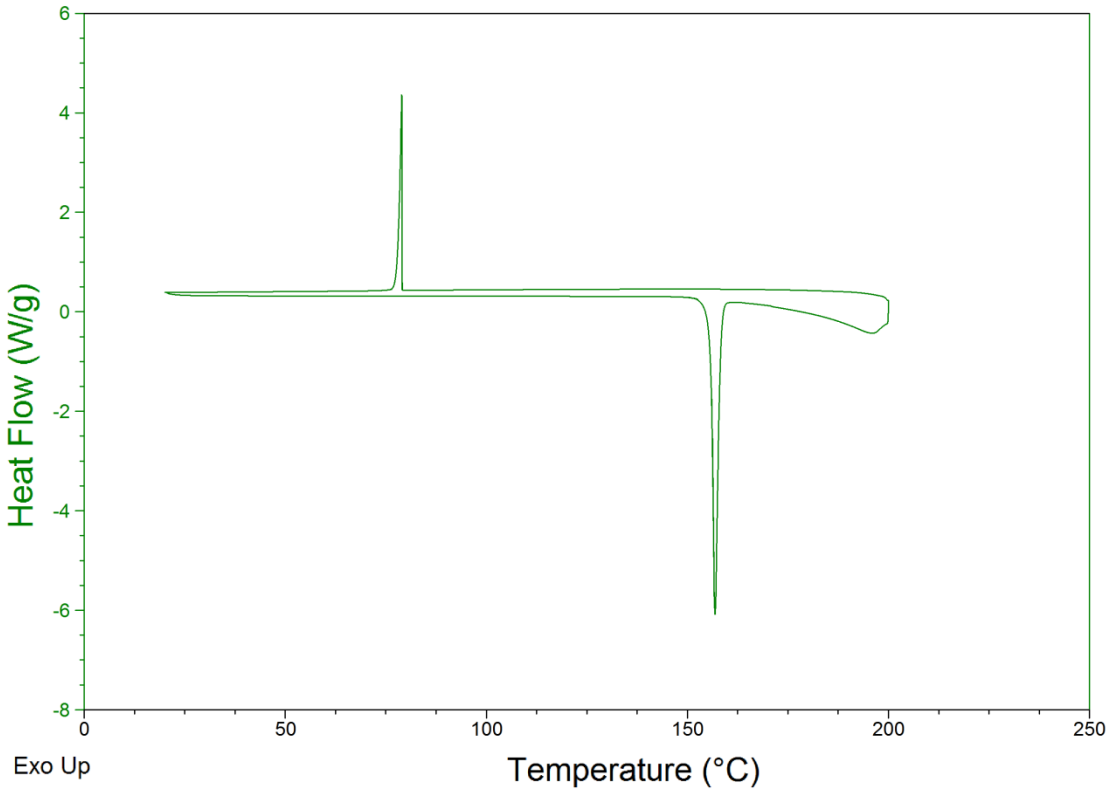

Figure 4.2. *DSC profile for a sample of IPU.*

Having verified the melting point of 156˚C and the absence of obvious changes in the structure due to the temperature, two samples of Isoproturon were transferred into an oven with the temperature already set at 160˚C: the first sample (1.7 g) was left to melt for four hours, while the second (1.6 g) for 24 hours. After the specified time, the melted IPU samples were removed from the oven and left to cool and crystallise at room temperature. The two solids obtained were manually ground into fine powders and X-ray powder diffraction patterns were collected on the Siemens D5000 diffractometer. Figure 4.3 displays the powder diffraction patterns of a sample of IPU crystallised from solution and the two patterns of the powders obtained from the melted IPU.

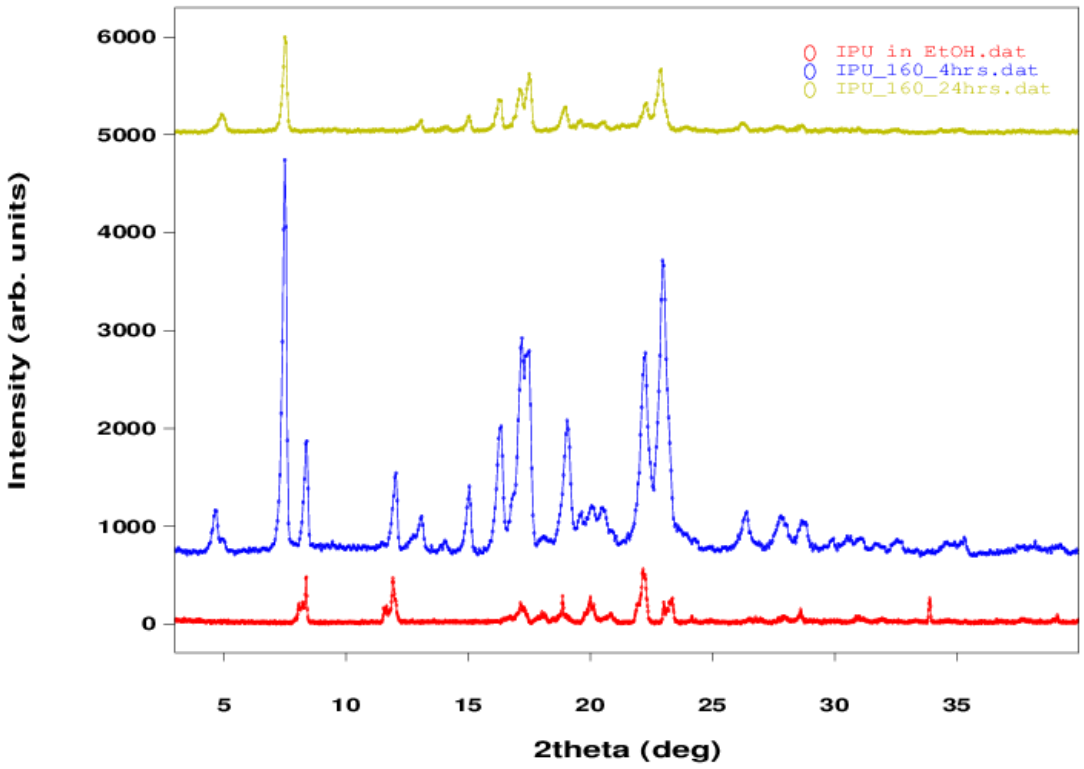

Figure 4.3. *Powder diffraction patterns: in blue, IPU crystallised from an ethanol solution; in red, IPU crystallized from the melt, left in the oven for 4 hours; in green, IPU crystallized from the melt, left in the oven for 24 hours.*

The powder diffraction patterns of the IPU crystallized from solution and the ones obtained from the melt clearly differ from one another, suggesting the formation of a different crystal structure. In addition, it is possible to notice the absence of the first two characteristic peaks of IPU at 8.23˚ and 11.89˚ in *2θ*, for the sample kept in the oven for 24 hours, suggesting, in the hypothesis of the formation of a polymorph, complete conversion between the two forms.

The powder obtained from the 24-hour-melt was dissolved in ethanol and crystallization of very thin needle shape-like crystals occurred. One crystal was isolated from the mother liquor and analysed by single crystal X-ray diffraction. The results are reported in Figure 4.4. Although the large thermal ellipsoids and the high values of the R-factors (R_1 = 0.1039; wR_2 = 0.2752; and GooF = 1.010) are indications of a poor refinement due to the very small dimensions and morphology of the crystal, the model obtained rejects the hypothesis that a polymorph of IPU might have formed.

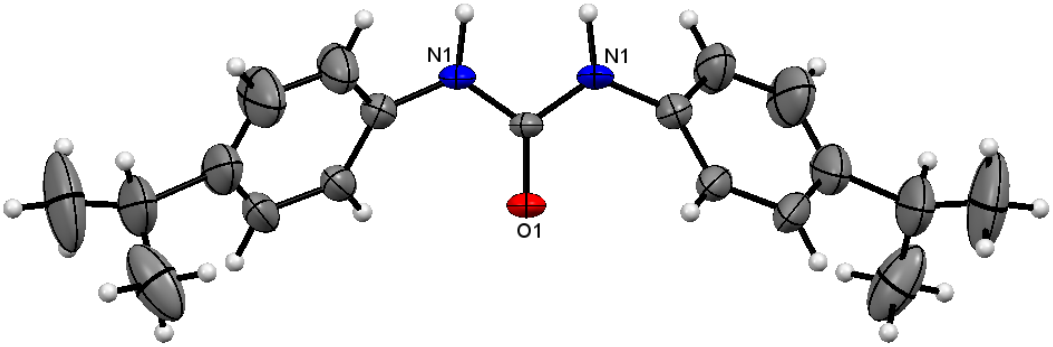

Figure 4.4. *ORTEP representation of the molecular structure of the crystal obtained from the melt. The probability level for all non-hydrogen ellipsoids is 50%, while the hydrogen atoms are drawn as fixed-size spheres of radius 0.15 Å.*

The temperature of 160˚C, while allowing the complete melting of the substance, also caused a chemical reaction, leading to the formation of the symmetrical urea, a known by-product of the synthesis of Isoproturon.

4.1.2.4. Single crystal X-ray diffraction of solution grown crystals

A well shaped crystal, collected from an ethanol solution, was analyzed on a Rigaku R-AXIS Spider diffractometer (***c.f. 3.1.2.5***) at 120K. Data treatment followed the details reported in chapter 2, paragraph ***2.1.4***.

In Table 4.2, X-ray crystallographic data and refinement parameters for the IPU crystal are reported.

Name	Isoproturon
Empirical formula	$C_{12}H_{18}N_2O$
Formula weight (g mol^{-1})	206.28
Temperature (K)	120
Wavelength (Å)	0.71073
Crystal system, space group	Orthorhombic, Pbca
Unit cell dimensions	a = 10.1466(4) Å
	b = 10.8493(6) Å
	c = 20.794(1) Å
Volume ($Å^3$)	2289.1(2)
Z, calculated density (g cm^{-3})	8, 1.197
F(000)	896
Absorption coefficient (mm^{-1})	0.077
Crystal size (mm)	0.4 x 0.3 x 0.5
Theta range for data collection (˚)	2.92 to 27.48
Limiting indices	$-12 \leq h \leq 13$, $-10 \leq k \leq 14$, $-27 \leq l \leq 20$
Reflections collected / unique	6548 / 2594 [R_{int} = 0.0344]
Completeness to θ = 27.48	98.8 %
Refinement method	Full-matrix least-squares on F^2
Data / restrains / parameters	2594 / 0 / 209
Goodness-of-fit on F^2	1.120
Final R indices [I>2sigma(I)]	R_1 = 0.0467, wR_2 = 0.1352
R indices (all data)	R_1 = 0.0571, wR_2 = 0.1684
Extinction coefficient	0.001(1)
Largest diff. Peak and hole (e $Å^{-3}$)	0.26 and -0.27

Table 4.2. *X-ray crystallographic data and refinement parameters for a crystal of IPU.*

4.1.2.5. Single crystal neutron diffraction

The IPU crystal selected for a single crystal neutron diffraction experiment was grown from an ethanol solution and it had the following dimensions: 0.46 x 1.15 x 2.7 mm.

The measurement was designed to collect the largest number of reflections in order to refine the structure, with particular attention to the hydrogen atom positions. Due to the cell dimensions, a wavelength of 1.17 Å was chosen and the beam width was of 5 mm. Data were collected at a temperature of 20K, with a cooling rate of 2 deg/min. Before starting a complete data collection, the subroutine *dview* was used on the scans recorded at room temperature to ascertain the presence of a single crystal; this subroutine allows for the visualisation of the diffraction spots on the detector. By superimposing the calculated diffraction images on the experimental data, it is possible to directly notice any discrepancy between the two that might suggest the presence of a second crystal. During the cooling process to 20K, both crystal and detector were positioned in order to record one strong reflection, $(2\bar{1}0)$, which was used to assess the integrity of the crystal upon decrease in temperature. Once the temperature of 20K was reached, the subroutine *pfind*, which gives the Miller indices *hkl* to each reflection present in one scan, in addition to their intensity and the temperature at which they were recorded, was run on all the cooling scans. The results were sorted by intensity and reported on a T vs. I plot so to highlight the correlation between the two. This plot is reported in Figure 4.5.

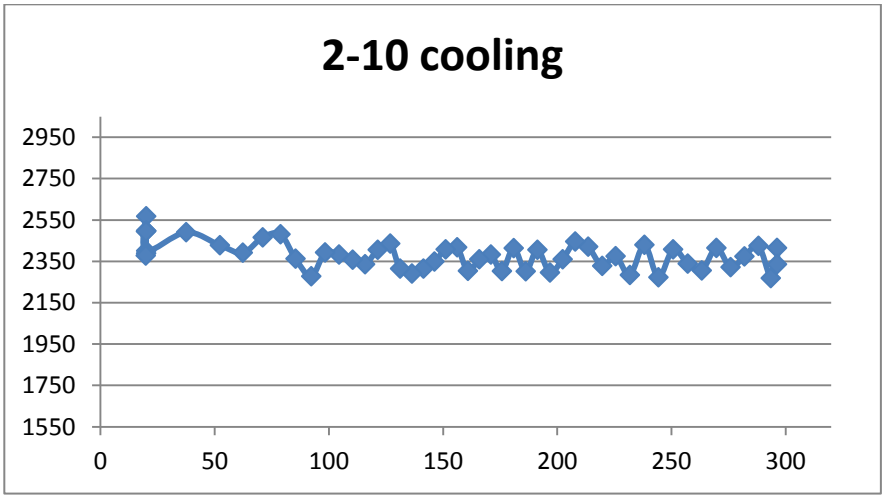

Figure 4.5. *Intensity profile for the strong reflection* $(\mathbf{2\bar{1}0})$ *upon decreasing of the temperature from room temperature to 20 K.*

A decrease in intensity of a reflection during the cooling process is usually an indication of a defects growing inside the crystal, for example from a phase transition. As it is possible to see in Figure 5, there is no significant variation in the intensity of the check reflection, indicating the complete absence of mechanical changes inside the crystal during the cooling to 20K.

In order to create a reliable model, the raw data were correct for the absorption due to the presence of the cans and to the crystal itself. These corrections were made with the D19 ABSCAN program; the one concerning the crystal requires the indexing of the crystal faces and the lengths of these faces from the centre of the crystal. The indexing was performed using a Huber optical goniometer, deducing the *hkl* indices by comparing the Huber-values for φ and χ with the D19 goniometer φ and χ. Six faces and two ends were found: a graphical representation of the crystal morphology is reported in Figure 4.6.

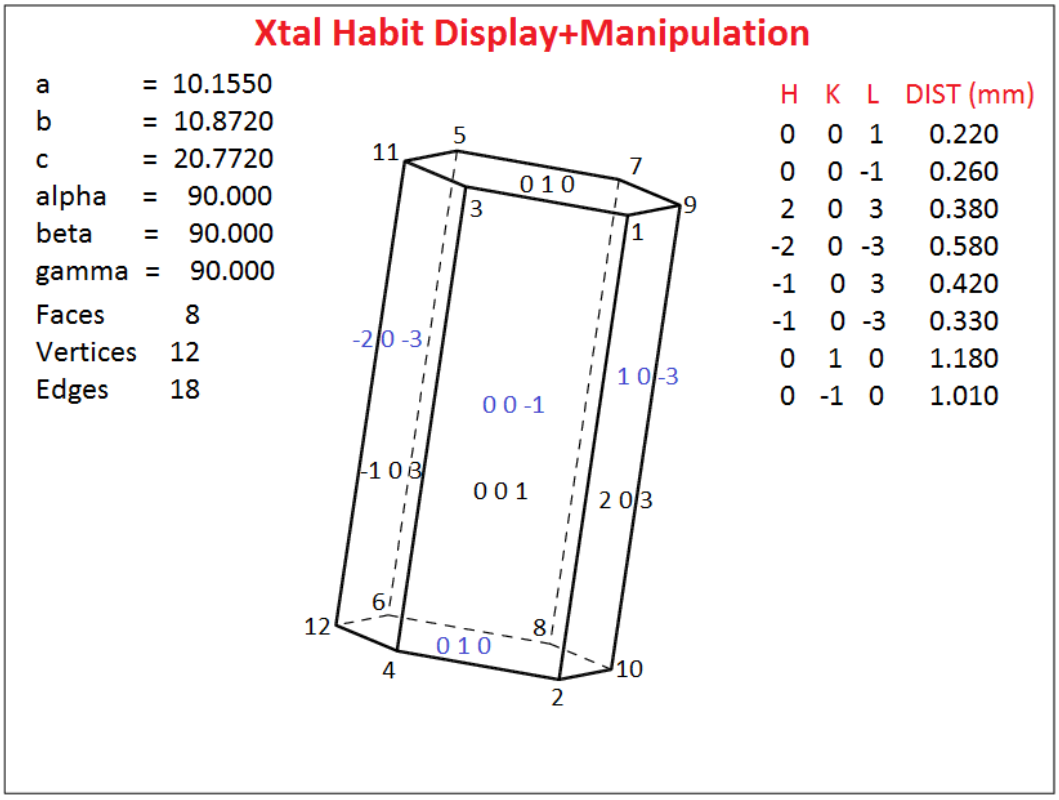

Figure 4.6. *Graphical representation of the IPU crystal morphology, obtained using the program platon.*

By comparing the R1-values for the structure without absorption corrections, the one with only the correction for the cans, and the structure corrected for both factors, 0.0391, 0.0364, and 0.0329, respectively, it is possible to notice a slight improvement, indicating a low absorption of the neutron radiation by the crystal.

In Table 4.3, neutron crystallographic data and refinement parameters for the IPU crystal are reported.

Name	Isoproturon
Empirical formula	$C_{12}H_{18}N_2O$
Formula weight (g mol^{-1})	206.29
Temperature (K)	20
Wavelength (Å)	1.17000
Crystal system, space group	Orthorhombic, Pbca
Unit cell dimensions	a = 10.1550(5) Å
	b = 10.8720(6) Å
	c = 20.772(2) Å
Volume ($Å^3$)	2293.3(2)
Z, calculated density (g cm^{-3})	8, 1.195
F(000)	296
Absorption coefficient (mm^{-1})	0.277
Crystal size (mm)	0.46 x 1.15 x 2.7
Theta range for data collection (˚)	4.62 to 60.79
Limiting indices	$-15 \leq h \leq 12$, $-15 \leq k \leq 3$, $-8 \leq l \leq 29$
Reflections collected / unique	8834 / 3512 [R_{int} = 0.0532]
Completeness to θ = 60.79	88.0 %
Refinement method	Full-matrix least-squares on F^2
Data / restrains / parameters	3512 / 0 / 299
Goodness-of-fit on F^2	1.098
Final R indices [I>2sigma(I)]	R_1 = 0.0329, wR_2 = 0.0569
R indices (all data)	R_1 = 0.0578, wR_2 = 0.0623
Extinction coefficient	0.0045(3)
Largest diff. Peak and hole (fm $Å^{-3}$)	0.71 and -0.67

Table 4.3. *Neutron crystallographic data and refinement parameters for a crystal of IPU.*

4.1.2.6. Computational studies

In collaboration with Christopher H. Hendon, computational calculations were made in order to assess the role played by the hydrogen bond in the crystal packing of IPU.

In the case of accessing the strength of the hydrogen bond, three variations to the calculations were made:

- the energy of the hydrogen bond and the dispersion forces were calculated using the experimental ionic positions;
- to isolate the energy of the H-bond, the calculation must include two monomers in a sufficiently large unit cell as to be non-interactive. Then, in the same size box, a truncated dimer from the experimental crystal structure was computed. The energy difference, E(diff) = E(monomers) - E(dimer). There will be an unavoidable minor contribution from dispersion forces;
- E(diff) is then scalar multiplied to the number of identical H bonds in the unit cell. The total energy of the unit cell, E(tot) can be crudely separated into the components E(vdW) = E(tot) - 4·E(diff).

4.1.3. Results and discussion

The cell parameters of IPU, derived from SXD measurements at 120K, are reported in Table 4.4.

Space group	Pbca
a	10.1466(4) Å
b	10.8493(6) Å
c	20.794(1) Å
V	2289.1(2) $Å^3$

Table 4.4. *Cell parameters for a crystal of IPU, derive from X-ray results.*

The asymmetric unit is formed by a single molecule of IPU (Figure 4.7).

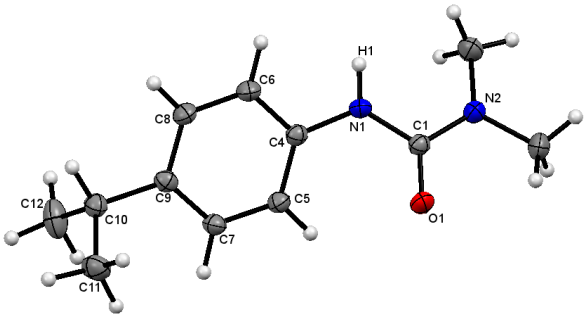

Figure 4.7. *Molecule of Isoproturon. The probability level for all non-hydrogen ellipsoids is 50%, while the hydrogen atoms are drawn as fixed-size spheres of radius 0.15 Å.*

C5-C4-N1-C1	-31.7(2)˚
C6-C4-N1-C1	150.9(1)˚
C6-C4-N1-H1	-20.1(1.4)˚
C5-C4-N1-H1	157.4(1.36)˚
C4-N1-C1-N2	174.7(1)˚
C12-C10-C9-C8	106.6(3)˚
C12-C10-C9-C7	-71.6(2)˚
C11-C10-C9-C7	53.1(2)˚
C11-C10-C9-C8	-128.7(1)˚

Table 4.5. *Torsion angles of interest.*

As a urea derivative, the urea skeleton is almost planar with a torsion angle C4-N1-C1-N2 of 174.7(1)˚. The benzene ring is twisted in respect to the urea part of 31.7(2)˚, due to the formation of a hydrogen bond between the hydrogen atom of the amino group of one molecule and the oxygen atom of the carbonyl group of a neighbouring molecule. The *para*-positioned isopropyl substituent is well centred on the benzene ring, with a torsion angle C5-C7-C9-C10 of 178.4(1)˚. In Figure 4.8, the crystal packing of IPU is reported.

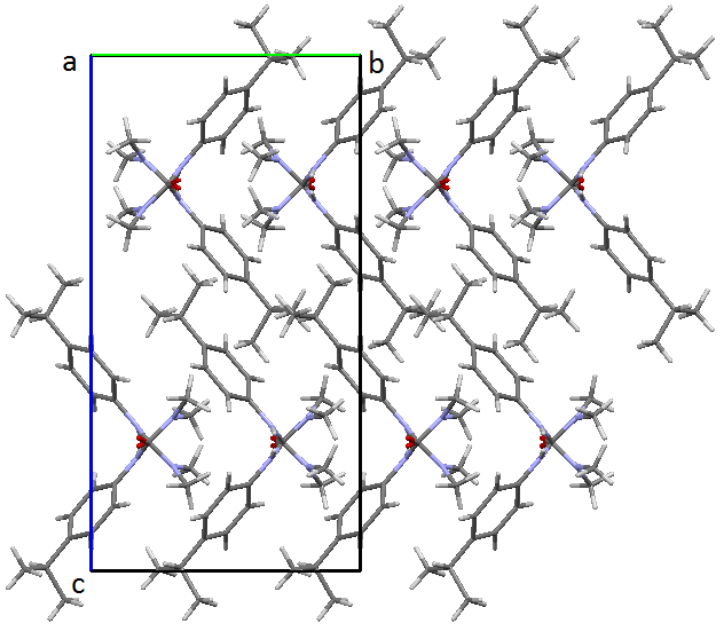

Figure 4.8. *Crystal packing of the molecules of IPU, viewed along the* ***a****-axis.*

The IPU molecules arrange themselves in order to create a network of linear hydrogen bonds between the hydrogen atom of the amino group and the oxygen atom of an adjacent carbonyl group. This disposition of the IPU molecules creates a layered structure inside the crystal: as shown in Figure 4.8, the polar groups, N-H and C=O, involved in the hydrogen bond, constitute one layer, while the organic residues cross one another, forming a hydrophobic layer. This feature can easily

explain the slight value of solubility of isoproturon in water: the hydrophilic groups are shielded by the presence of the organic residues.

Observation of the structure along the ***c*** axis (Figure 4.9) shows that the hydrogen bonding network forces the IPU molecules involved in the intermolecular interaction to lie almost perpendicular to one another, so that hindrance from the two methyl groups on the nitrogen atom of the urea part and the isopropyl substituent on the benzene ring may be avoided.

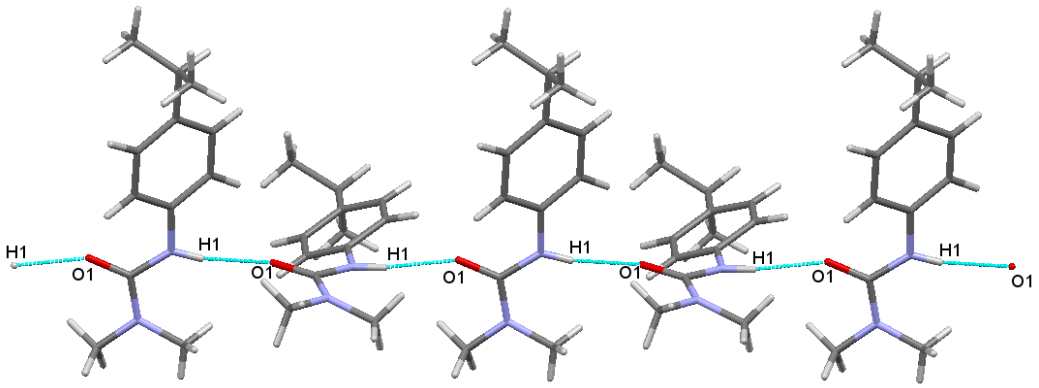

Figure 4.9. *Crystal packing of Isoproturon, viewed along the* ***c****-axis.*

N1-H12	0.873(19) Å
C11-O1	1.238(2) Å
H12···O1	2.09(2) Å
N1-H12···O1	166.9(2)˚

Table 4.6. *Bond lengths and distance and angle of interaction.*

As shown in Table 4.6, the hydrogen bond in a IPU crystal is of medium strength, based on its length of 2.09(2) Å and its almost linear geometry of interaction[81].

Computational calculations were made in order to assess the strength and nature of the hydrogen bond, and its role in the packing of the crystal.

The results of these calculations are reported in Table 4.7 and Table 4.8.

Formation energies for IPU	
Monomer	-233.7 kJ/mol
Dimer	-467.6 kJ/mol
Periodic structure	-1873.5 kJ/mol

Table 4.7. *Calculated formation energies for IPU.*

	eV	kJ/mol
Hydrogen bond energy per dimer	-0.3	-26.2
Hydrogen bond energy per unit cell	-1.1	-104.9
Dispersion interactions per unit cell	-1.9	-182.4
Crystal formation energy relative to monomer	-4.1	-392.2

Table 4.8. *Calculated energies for the hydrogen bond and other intermolecular interactions.*

From the observation of the results obtained it seems that the hydrogen bond is not the most important parameter in the definition of the arrangement of the IPU molecules in the crystal structure, but it plays an auxiliary role along side with weak π-π interactions with distances between centroids of two neighbouring benzene rings of 5.43(3) Å.

The model for the crystal structure of IPU derived from SND data is in accordance with the results derived from SXD analysis, but with much improved accuracy and precision in the definition of the hydrogen atoms positions, allowing the hydrogen bonding and the intermolecular interactions to be fully defined.
In Table 4.9 a comparison of the cell parameters between X-ray and neutron data is reported.

	X-rays (120K)	Neutrons (20K)
a	10.1466(4) Å	10.1550(5) Å
b	10.8493(6) Å	10.8720(6) Å
c	20.794(1) Å	20.772(2) Å
V	2289.1(2) $Å^3$	2293.3(2) $Å^3$

Table 4.9. *Cell parameters for the X-ray and neutron sets of data of IPU.*

The investigation of the anisotropic atomic displacement parameters (ADPs) allows achieving a better characterisation of the intermolecular interactions, as displayed in Figure 4.10 for two interacting molecules of IPU.

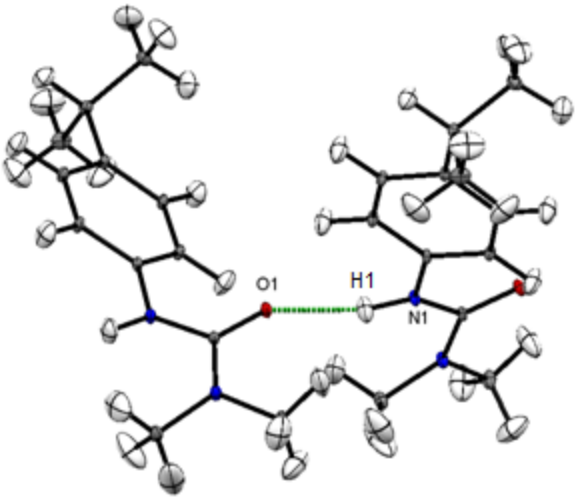

Figure 4.10. *ORTEP representation of two interacting molecules of IPU, derived from neutron results. The probability level for all ellipsoids is 50%.*

The thermal ellipsoid relative to H1, the hydrogen atom involved in the intermolecular interaction, shows a variation from the mean position perpendicular to the hydrogen bond, indicating the absence of possible proton migration to O1. This observation is consistent with the characterization of the interaction as a medium-strength hydrogen bond. The absence of proton migration or disorder in the structure was confirmed by both electron-density and nucleon-density maps, which are shown in Figure 4.11. The peak of electronic charge in the map on the left (electron-density map) and the hole in the one on the right (nucleon-density map) indicate that the hydrogen atom position is defined in a precise point and does not exhibit migration or disorder.

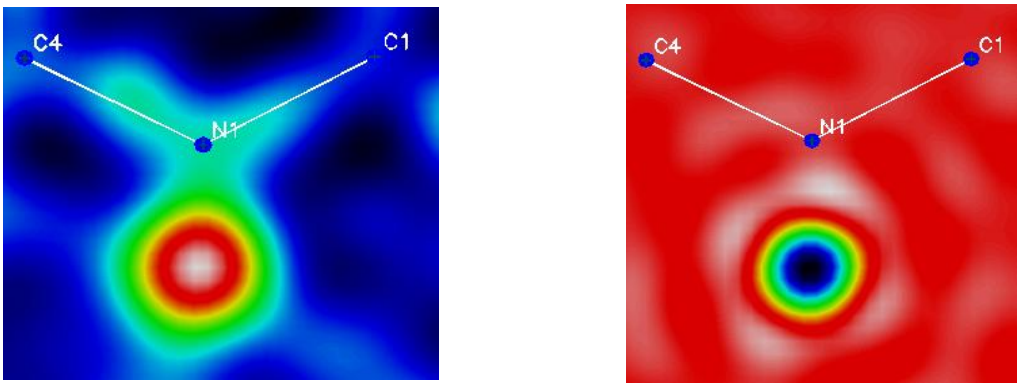

Figure 4.11. *On the left, the electron-density map of the amino group is displayed; whereas the picture on the right shows the nucleon-density map of the same group.*

In Table 4.10, a comparison of the main features of the IPU crystal structure between neutron and X-ray results is reported.

	Neutrons	X-rays
N1 – H1	1.022(2) Å	0.87(2) Å
C1 – O1	1.243(1) Å	1.238(2) Å
O1···H1	1.949(2) Å	2.09(2) Å
O1···N1	2.945(1) Å	2.946(2) Å
N1-H1···O1	163.9(2)°	167.0(2)°
C – H benzene ring	1.090(2) Å	0.97(2) Å
C – H methyl groups	1.095(2) Å	0.99(2) Å

Table 4.10. *Comparison between neutron and X-ray results.*

As expected, by using neutron diffraction we can observe a gain of a factor of ten in the accuracy and precision of the hydrogen atoms positions.

4.1.4. Conclusions

Due to its high toxicity on both the environment and human health, a structural study on the herbicide Isoproturon has been undertaken to find a solid form that might have reduced toxicity, for example from reduced solubility or volatility. In fact, there is a strict correlation between the physical properties shown by a material and its structure: the arrangement of atoms and molecules inside the packing of a crystal can affect properties such as colour, solubility and dissolution rate. The study on Isoproturon aimed to find the right experimental conditions that could allow observation of a different crystal structure.

Crystals of Isoproturon were obtained by two different methods: crystallisation by evaporation and crystallisation from the melt. The first technique is based on the increase of the concentration of the solution of IPU by slow evaporation of the solvent. Once the solution becomes oversaturated, spontaneous formation of crystals occurs. By varying the rate of evaporation is possible to have some control on the dimensions of the crystals; the slower the solvent evaporation, the larger the crystals.

When crystallisation from the melt is used, crystals are obtained by refrigeration of the melted substance. The rate of the refrigeration process determines the crystal size and might affect the crystal packing of the substance molecules, leading to the formation of a different crystal structure.

Neither of these techniques succeeded in finding a new crystal form for Isoproturon: the solvent does not play a role in the definition of the crystal packing of the IPU molecules, and extended heating at a temperature slightly higher than IPU melting point causes breaking of the amide part and production of the symmetrical urea.

The crystal structure of IPU was analysed by single crystal diffraction, using X-ray and neutron radiations. Even though the model obtained from SXD data is highly satisfying, neutrons allow achieving a greater precision in the definition of the hydrogen atom positions.

In their crystal packing the molecules of IPU interact in pairs, forming a hydrogen bond between the hydrogen atom on the amino group and the oxygen atom on the carbonyl group of a neighbouring molecule. The presence of the isopropyl chain on the benzene ring and the two methyl groups on the nitrogen atom of the urea part of IPU forces the molecules into a fishbone-like arrangement, while the hydrogen bonding network is set in linear long chains. From the refinement of neutron data, the hydrogen bond length, **O1···H1**, is 1.949(2) Å with an angle of interaction, **N1-H1···O1,** of 163.9(2)˚. The study of the hydrogen bond length and geometry indicates that the hydrogen bond is of medium strength, as confirmed by the computational results, which show that π-π interactions play an important role in the crystal arrangement.

Observation of the electron density and nuclear mass distribution for the hydrogen bond, N1-H1···O1, rules out the possibility of proton migration and disorder.

4.2. Glyphosate, *N-(phosphonomethyl)glycine*

4.2.1. Introduction

Glyphosate is a phosphonomethyl derivative of the amino acid glycine and a highly important herbicide. It is a non-selective, systematic weed killer used in post-emergence situation, especially on annual broadleaf weeds and grasses known to compete with commercial crops grown around the globe. It acts by inhibiting the enzyme involved in the synthesis of the amino acids tyrosine, tryptophan and phenylalanine. It is absorbed by leaves, and, then, moved into other positions of the plant. It is a strong chelator; it binds to nutrient compounds making them unavailable for the plant. It was firstly introduced as Roundup® herbicide by Monsanto Company in 1974 and it is currently used in over 160 countries[91]. Various concerns have been raised over the past years regarding the toxicity and carcinogenicity of glyphosate. In 2015 the European Commission started a dossier within the European Food Safety Authority on the potentially high risks on health caused by glyphosate. In accordance with Regulation (EC) No 1107/2009 the European Authority concluded that the risks posed by glyphosate on human health were contained and that a harmonized classification of glyphosate regarding its carcinogenic potential under Regulation (EC) No 1272/2008 was not necessary. Since the conclusions on the risks derived from the usage of glyphosate by the Agency for Research on Cancer and by the European Authority are divergent, under the Regulation (EU) No 2016/1056, the glyphosate dossier was submitted to the Committee for Risk Assessment of the European Chemicals Agency to decide whether a renewal of the approval for the use of glyphosate is appropriate. Until a decision is reached (December 2017), the usage of glyphosate as pesticide is permitted.

Currently, formulations of glyphosate are in form of water soluble solids, such as isopropylammonium, potassium, sodium and ammonium salts. Two samples were studied during the course of this thesis: glyphosate and its ammonium salt.

4.2.2. Experimental

4.2.2.1. Physical and chemical properties

In the solid state, glyphosate is a white and odourless crystalline powder, with a melting point of ~184˚C, and it decomposes at temperatures over 200˚C. It has three acid dissociation constants: pK_{a1} = 2.32, pK_{a2} = 5.86, and pK_{a3} = 10.86, for the carboxylate, phosphonate, and amino groups, respectively[92]. It has a vapour pressure of 9.8×10^{-8} mmHg and solubility in water of 10.5 g/L at pH of 1.9 and 20˚C[93]. It is insoluble in the most common organic solvents, such as acetone, ethanol, and xylene.

4.2.2.2. Single crystal X-ray diffraction

Small crystals of glyphosate suitable for X-ray single crystal diffraction were prepared from slow evaporation of an aqueous solution. The selected crystal was analysed at 150K on an Enraf-Nonius kappaCCD single crystal diffractometer (***c.f. 3.2.2.4***).
In Table 4.11, X-ray crystallographic data and refinement parameters for the glyphosate crystal are reported.

Name	Glyphosate
Empirical formula	$C_3H_8NO_5P$
Formula weight (g mol^{-1})	187.09
Temperature (K)	150
Wavelength (Å)	0.71073
Crystal system, space group	Monoclinic, $P2_1/c$
Unit cell dimensions	a = 8.682(2) Å
	b = 7.960(2) Å
	c = 9.828(2) Å
	β = 106.09(3)°
Volume ($Å^3$)	652.6(2)
Z, calculated density (g cm^{-3})	3, 1.428
F(000)	294
Absorption coefficient (mm^{-1})	0.306
Theta range for data collection (°)	2.44 to 27.50
Limiting indices	$-11 \leq h \leq 11$, $-10 \leq k \leq 10$, $-12 \leq l \leq 12$
Reflections collected / unique	2562 / 1488 [R_{int} = 0.0139]
Completeness to θ = 27.50	98.5 %
Refinement method	Full-matrix least-squares on F^2
Data / restrains / parameters	1488 / 0 / 123
Goodness-of-fit on F^2	1.047
Final R indices [I>2sigma(I)]	R_1 = 0.0281, wR_2 = 0.0953
R indices (all data)	R_1 = 0.0347, wR_2 = 0.1191
Extinction coefficient	none
Largest diff. Peak and hole (e $Å^{-3}$)	0.48 and -0.54

Table 4.11. *X-ray crystallographic data and refinement parameters for a crystal of glyphosate.*

4.2.2.3. Powder neutron diffraction

A deeper understanding of the characteristics of organic compounds, which contain functional groups capable of forming hydrogen bonding networks, is essential for the definition of the physical properties and the behaviour of such materials. Investigation of possible phase transitions and proton effects, for example proton migration or disorder that may occur in the crystal structure of glyphosate can be achieved using powder neutron diffraction (PND). The main advantage presented by a powder sample is the possibility of studying the behaviour of the structure of glyphosate over a wide range of temperature without the risk of damaging the sample, a risk that may occur in the case of a phase transition happening in a single crystal. The small dimension of the glyphosate molecule and the presence of hydrogen atoms, which seem to play an important role in the self-assembly of this compound, require the use of neutrons. A sample of finely ground glyphosate was analysed with neutron radiation on the high-flux powder diffractometer D20 at ILL. The sample was placed in a vanadium can at the centre of a cryofurnace and its height was adjusted in order to be in the middle of the neutron beam. The presence of the cryofurnace allowed data collection between 4K and 440K. In particular, powder patterns were collected at the following temperatures: 4K, 25K, 50K, 67.5K, 85K, 102.5K, 120K, 137.5K, 155K, 172.5K, 190K, 215K, 245K, 275K, 320K, 350K, 380K, 410K and 440K. Every acquisition lasted for 1 hour at each temperature and data were collected with a wavelength of $\lambda = 1.87$ Å.

In order to refine a structure from powder diffraction data, a good starting model derived from single crystal measurements must be available. For the purpose of the experiment, the SXD data were used. Structure refinement was carried out using the GSAS[59] package, with the EXPGUI user interface, following the details reported in section ***2.1.6***. Based on the experimental values for bond lengths, soft body constraints, reported in Table 4.12, were applied in order to prevent false minima in the profile and, consequently, to allow the determination of hydrogen atoms. The background was refined using a cosine Fourier series with 8 terms.

Atom 1	Atom 2	Constraint	Tolerance
C3	H2	1.080	0.004
C3	H4	1.080	0.004
C2	H7	1.080	0.004
C2	H8	1.080	0.004
N1	H6	1.040	0.004
N1	H5	1.040	0.004
N1	C3	1.480	0.002
N1	C2	1.480	0.002
P1	C3	1.800	0.002
P1	O3	1.570	0.002
P1	O4	1.480	0.002
P1	O5	1.495	0.002
O2	C1	1.210	0.002
O1	C1	1.310	0.002

Table 4.12. *Applied soft constraints for the refinement of glyphosate.*

The final fit of the data set collected at 4K, which was used as a starting point for the refinement of all successive data, is reported in Figure 4.12.

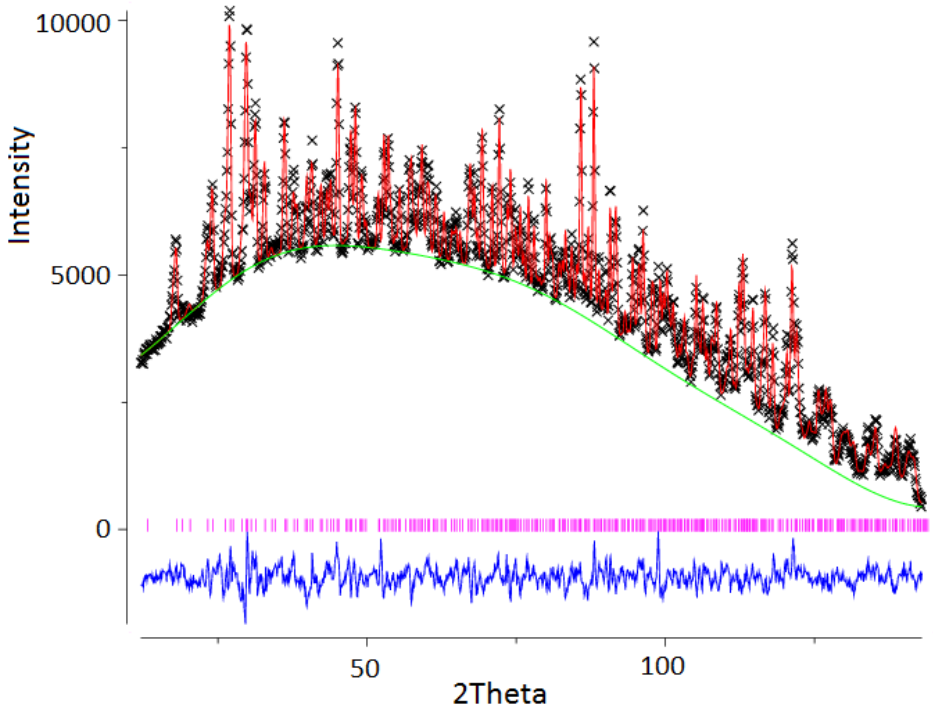

Figure 4.12. *Final fit for the structure of glyphosate at 4K: background (green); observed data (crosses); calculated data (red); difference between observed and calculated data (blue); Bragg peaks (magenta).*

4.2.3. Results and discussion

The glyphosate molecule has several dissociable hydrogen atoms: one on the phosphate group, one on the carboxylic acid and one on the amino group, with potential for formation of bidentate and tridentate coordination via a 5-membered chelate ring.

The molecular structure of glyphosate, derived from experimental single crystal X-ray diffraction, is reported in Figure 4.13.

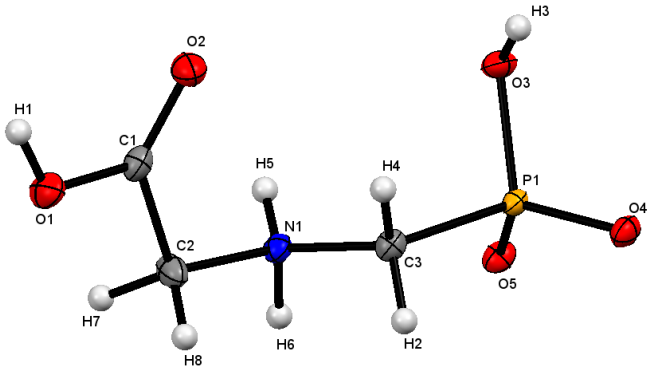

Figure 4.13. *ORTEP representation of a molecule of glyphosate, derived from experimental single crystal X-ray diffraction. The probability level for all non-hydrogen ellipsoids is 50%, while the hydrogen atoms are drawn as fixed-size spheres of radius 0.15 Å.*

In its crystalline state the molecule of glyphosate is in the form of a zwitterion, *i.d.* both positive and negative charges are present in the same molecule. In this case one oxygen atom on the phosphate group is deprotonated, forming a negative charge, while the amino group is protonated, leading to the formation of a positive charge.

The crystal packing is governed by an intricate network of hydrogen bonds, which force the glyphosate molecules to arrange themselves into lines, as shown in Figure 4.14.

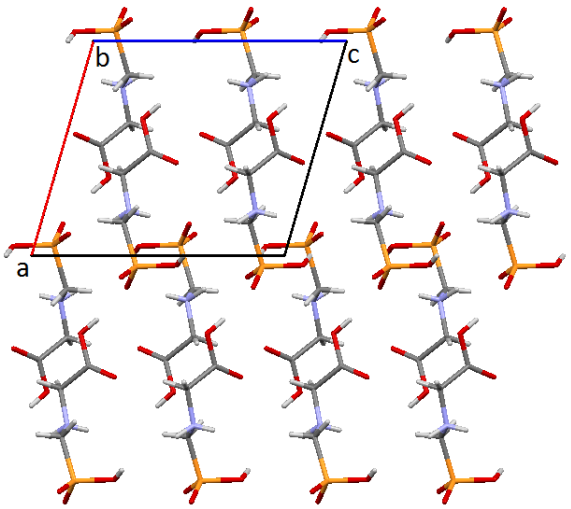

Figure 4.14. *Crystal packing of glyphosate, viewed along the* ***b****-axis.*

Each line of glyphosate molecules is slightly shifted in respect to the neighbouring one, so that the intermolecular interactions may take place. A single molecule of glyphosate is engaged in intermolecular hydrogen bonds with six different neighbouring molecules. Figure 4.15 displays a particular of the crystal packing, highlighting the hydrogen bonding network.

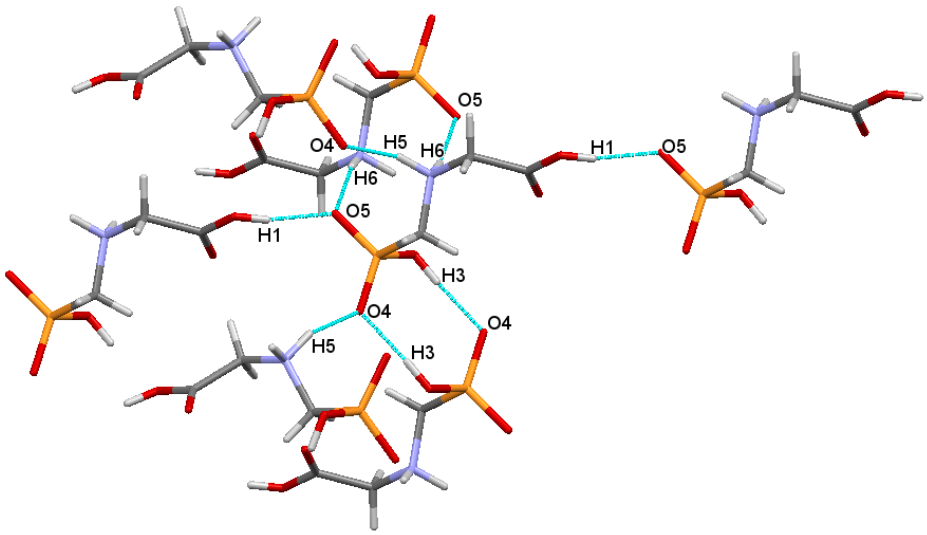

Figure 4.15. *Hydrogen bonding network in a crystal of glyphosate.*

There are two different types of hydrogen bond: a linear and a circular hydrogen bond. The linear hydrogen bonds are between the hydrogen atom of the carboxyl group and the oxygen atom of the phosphate group of a neighbouring molecule, and between the hydrogen atoms on the protonated amino group and the oxygen atoms belonging to two different phosphate groups. The chelate interaction is formed by two phosphate groups of two neighbouring molecules, leading to an 8-membered ring. Lengths and angles of the intermolecular interactions are reported in Table 4.13.

H1···O5	1.74(4) Å
O1-H1···O5	168(3)˚
H3···O4	1.74(4) Å
O3-H3···O4	174(3)˚
O5···H6	2.02(3) Å
N1-H6···O5	165(2)˚
H5···O4	1.82(3) Å
N1-H5···O4	153(3)˚

Table 4.13. *Distances and angles of the hydrogen bonds.*

With powder neutron diffraction data, it is possible to investigate the effect that temperature has on the crystal structure of glyphosate. Worthy of notice are the changes in the cell parameters and in

the hydrogen bonding network, due to changes in temperature. Figures 4.16, 4.17, and 4.18 display the variation of the unit cell axes, ***a***, ***b***, and ***c***, respectively, as a function of temperature, while in Figures 4.19 and 4.20 the profiles of the hydrogen bonds are shown.

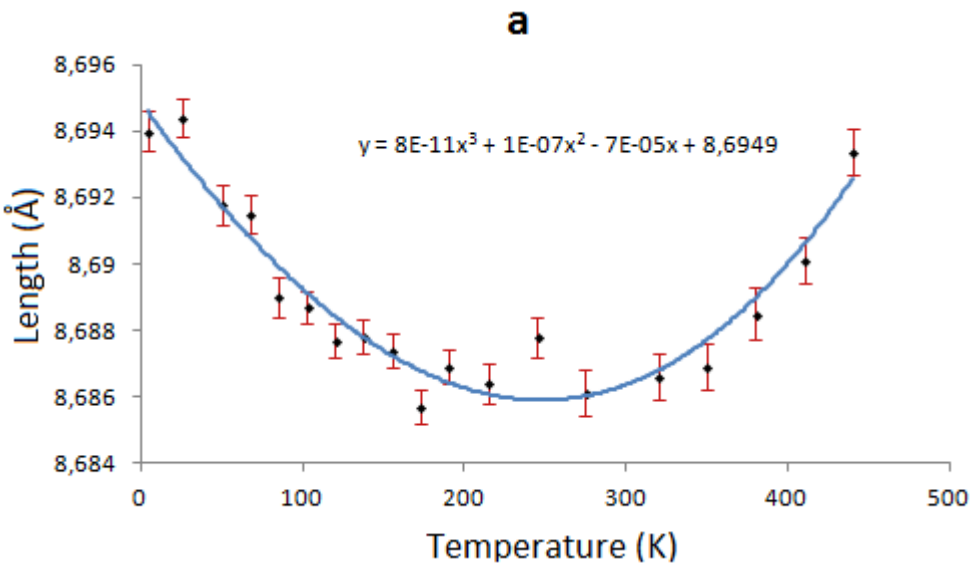

Figure 4.16. *Evolution of the cell parameter* ***a*** *as a function of temperature. The error bars are shown in red and the trendline equation is displayed on the chart.*

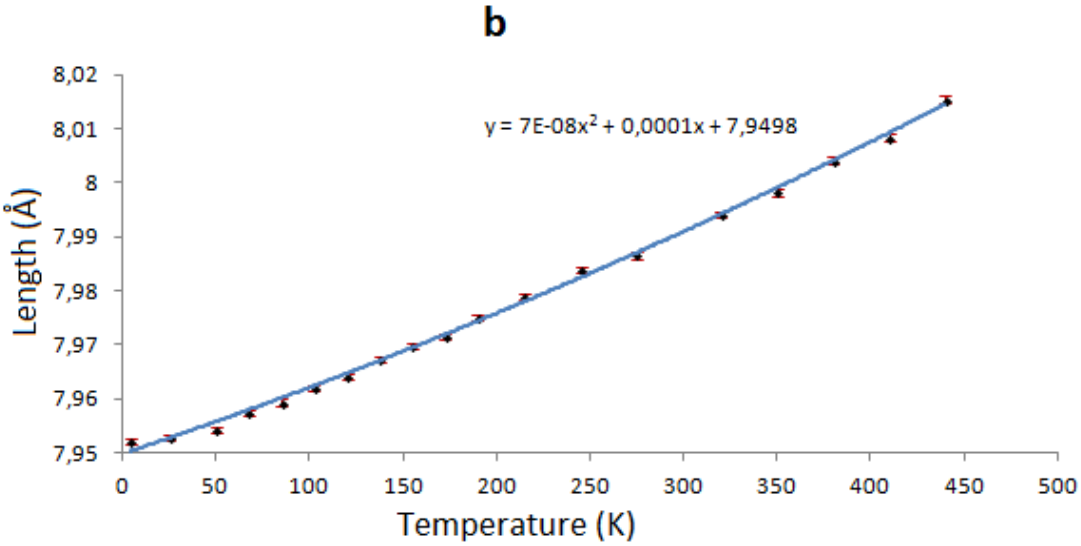

Figure 4.17. *Evolution of the cell parameter* ***b*** *as a function of temperature. The error bars are shown in red and the trendline equation is displayed on the chart.*

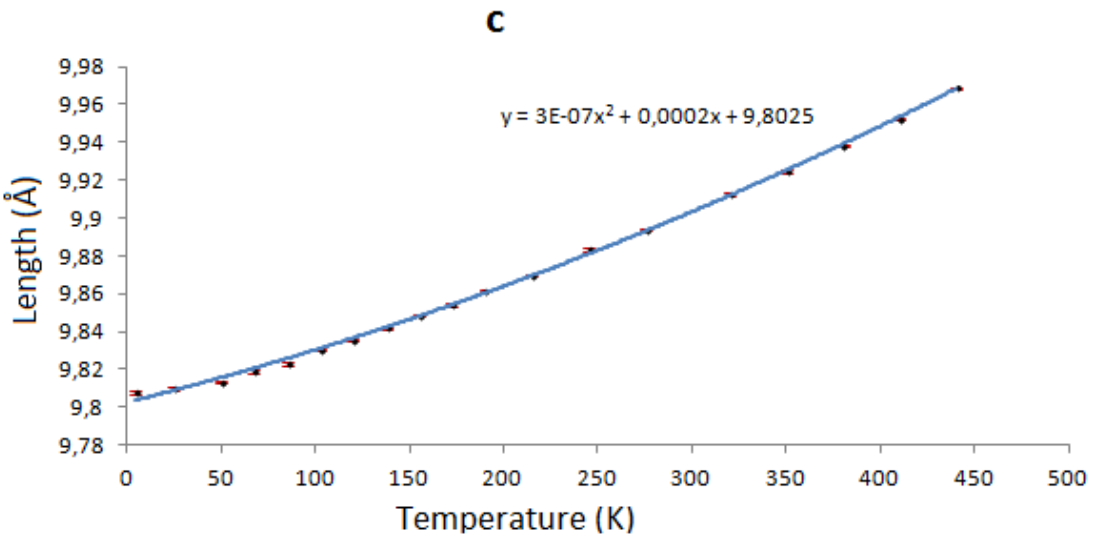

Figure 4.18. *Evolution of the cell parameter* ***c*** *as a function of temperature. The error bars are shown in red and the trendline equation is displayed on the chart.*

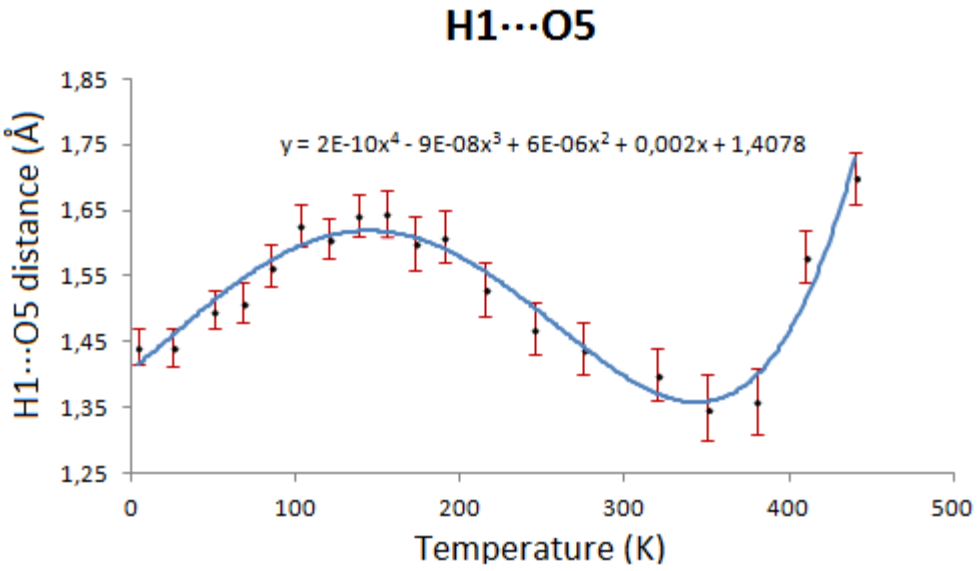

Figure 4.19. *Evolution of the linear hydrogen bond, H1···O5, as a function of temperature. The error bars are shown in red and the trendline equation is displayed on the chart.*

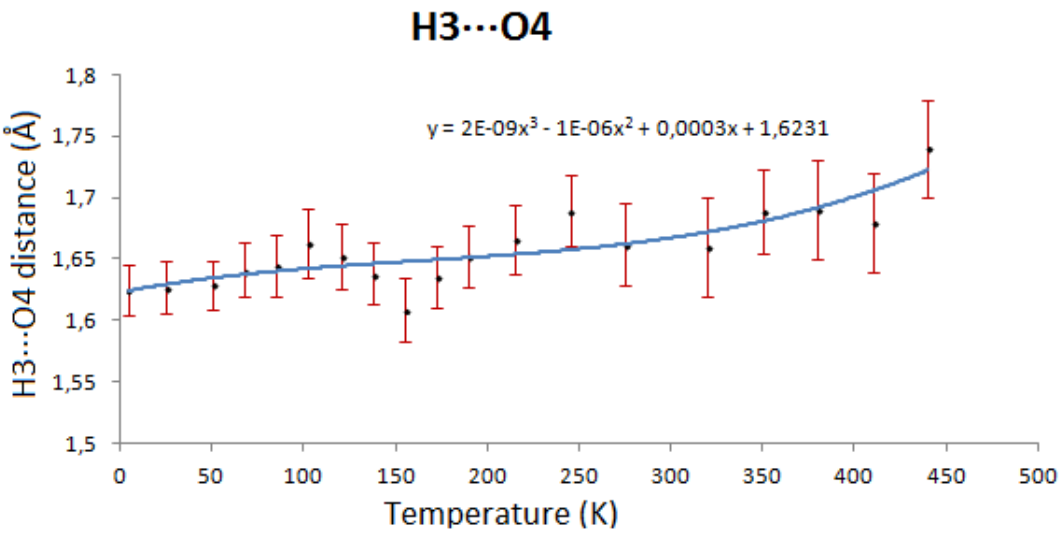

Figure 4.20. *Evolution of the circular hydrogen bond, H3···O4, as a function of temperature. The error bars are shown in red and the trendline equation is displayed on the chart.*

As expected, expansions of the cell parameters ***b*** and ***c*** occur with an increase in temperature. More unusual is the behaviour observed in the cell parameter ***a***, which, instead of increasing with an increase in temperature, initially decreases with a minimum between 200 and 300 K and an increase above 300K. This behaviour can be related to changes in the hydrogen bonding behaviour in the compound as a function of temperature. The linear hydrogen bond H1···O5 lies almost perfectly along the direction of the ***a***-axis as shown in Figure 4.21. This means that a change in the conformation of this hydrogen bond inevitably affects how the ***a*** parameter reacts in respect of the temperature increase.

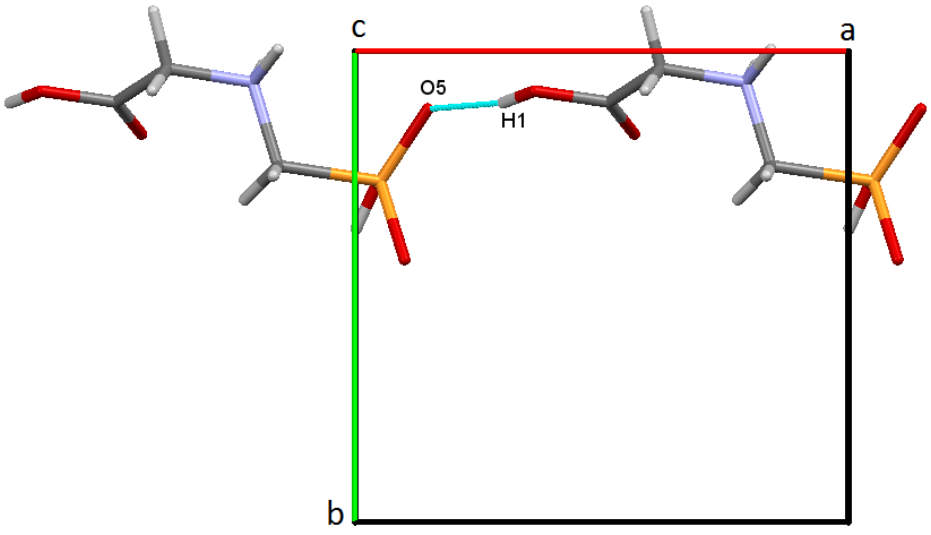

Figure 4.21. *Linear hydrogen bond H1···O5 aligned along the* ***a****-axis.*

The trends of the hydrogen bond H1···O5 and the cell parameter ***a*** show opposite behaviour, at least until 190K: the longer the distance of the hydrogen bond, the shorter the ***a*** parameter. It is, however, difficult to outline a clear behaviour of the variation of the hydrogen bond with the increasing temperature. While the changes of the hydrogen bonds responsible for the formation of a ring show an increasing trend during the heating to 440K, the length of the linear hydrogen bond is characterised by a high fluctuation, probably due to the increased mobility of the glyphosate molecules at higher temperatures.

4.3. Ammonium glyphosate

Amongst all the glyphosate salts present in commerce, ammonium-glyphosate is the most commercially important inorganic derivative, as it is less hygroscopic than other salts with advantages in formulation. As for the case of glyphosate, a more in depth understanding of the behaviour of the crystal structure of ammonium-glyphosate was reached by variable-temperature powder neutron diffraction experiments.

4.3.1. Experimental

4.3.1.1. Powder neutron diffraction

Due to difficulties in growing single crystals suitable for single crystal X-ray diffraction, a small quantity of ammonium glyphosate was analysed only by powder neutron diffraction (PND) on the instrument D20 at the neutron facility ILL.

The neutron experiment was similar to the one carried out on glyphosate. A sample of ammonium-glyphosate was placed inside the cryofurnace in a vanadium can and was adjusted to guarantee complete coverage of the sample by the neutron beam. Unfortunately, due to the limited number of days allocated for both experiments, a smaller number of acquisitions at different temperatures were collected for this salt. 2 hour-long acquisitions were collected at 40K, 120K, 200K, 280K, 360K and 400K with the same value of $\lambda = 1.87$ Å.

The starting model for the glyphosate ammonium salt was taken from the CCDC database[94]. Data processing followed the same refinement steps of glyphosate, and the background was refined with using a cosine Fourier series with 12 terms. Table 4.14 lists the soft constraints applied on the molecular structure of ammonium-glyphosate, while Figure 4.22 shows the final fit of the data set at 40K.

Atom 1	Atom 2	Constraint	Tolerance
C2	H6	1.080	0.002
C2	H5	1.080	0.002
C3	H9	1.080	0.002
C3	H10	1.080	0.002
N1	H7	1.020	0.002
N1	H8	1.020	0.002
N1	C2	1.490	0.003
N1	C3	1.490	0.003
N2	H1	1.020	0.002
N2	H3	1.020	0.002
N2	H4	1.020	0.002
P1	C3	1.800	0.002
P1	O3	1.500	0.004
P1	O4	1.570	0.004
P1	O5	1.500	0.004
O1	C1	1.240	0.004

Table 4.14. *Applied soft constraints for the refinement of ammonium-glyphosate.*

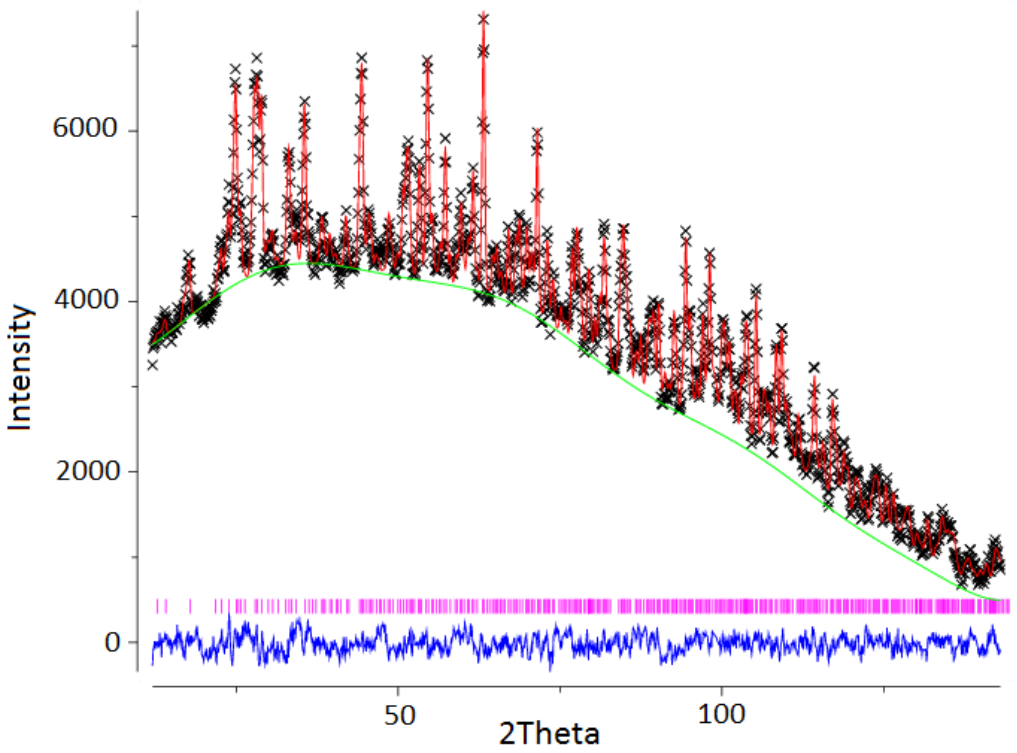

Figure 4.22. *Final fit for the structure of ammonium-glyphosate at 40K: background (green); observed data (crosses); calculated data (red); difference between observed and calculated data (blue); Bragg peaks (magenta).*

The refinement of the data set at 40K, used as a starting model for the refinement of the data at the other collection temperatures, shows a very good fit between observed and calculated data, as indicated by the absence of obvious peaks in the blue line in Figure 4.22.

4.3.2. Results and discussion

The asymmetric unit if formed by a molecule of deprotonated-glyphosate and the ammonium ion, as reported in Figure 4.23.

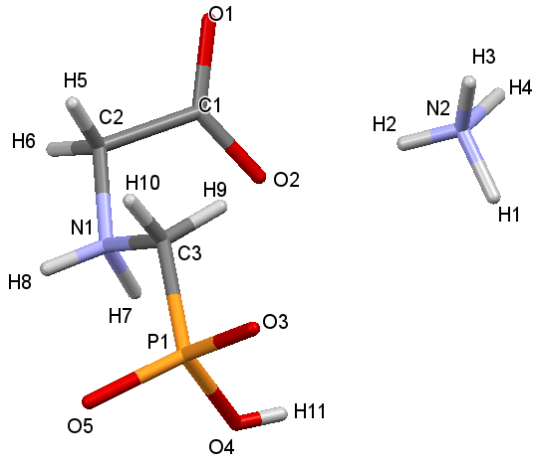

Figure 4.23. *Capped sticks representation for the asymmetric unit of a crystal of ammonium-glyphosate, derived from the structure present in the CCDC database*[94].

The salt is formed by the ionic interaction between the carboxylate group (negative charge 1-) of the glyphosate molecule and the ammonium cation, NH_4^+, positively charged.
In their crystalline state, the molecules of the anionic glyphosate(1-) arrange themselves in "herring-bone" lines (Figure 4.24) interlaced with the ammonium cations.

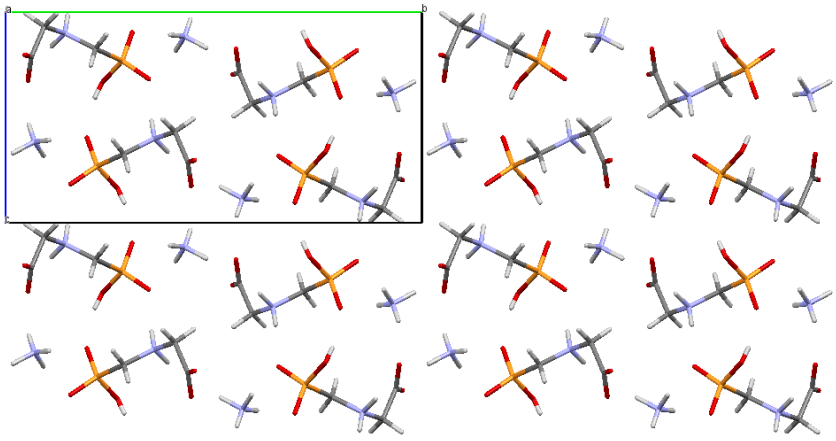

Figure 4.24. *Crystal packing of the salt ammonium-glyphosate, view along the* ***a****-axis.*

The crystal packing is held together by intermolecular hydrogen bonds. A molecule of glyphosate(1-) interacts with other four glyphosate(1-) molecules and three ammonium cations, as reported in Figure 4.25.

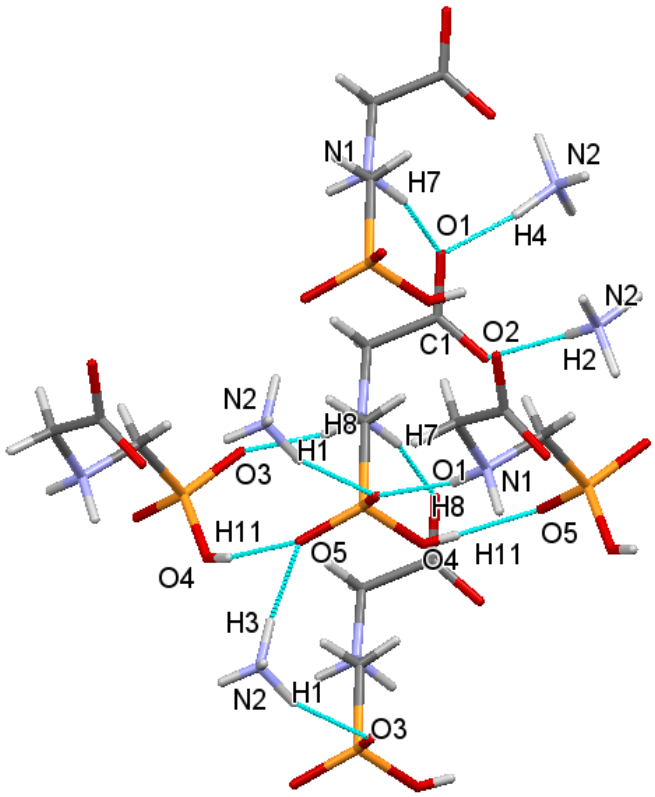

Figure 4.25. *Particulars of the hydrogen bonding network for a crystal of ammonium-glyphosate.*

Two hydrogen atoms of two ammonium cations, H2 and H4, form linear hydrogen bonds with the carboxylate group, while the remaining two, H1 and H3, form linear hydrogen bonds with oxygen atoms of two distinct phosphate groups, O3 and O5, respectively. There are hydrogen bonds involving the hydrogen atoms of the protonated amino group: one with a carboxylate oxygen, O1, and the other with O3, the oxygen atom on the phosphate group. Hydrogen bond lengths and angles are reported in Table 4.15.

O1···H4	1.72(2) Å	N2-H4···O1	164(1)°
O1···H7	1.87(3) Å	N1-H7···O1	158(1)°
O2···H2	2.02(2) Å	N2-H2···O2	164(1)°
O5···H3	1.99(2) Å	N2-H3···O5	166(1)°
O3···H1	1.89(2) Å	N2-H1···O3	159(1)°
O3···H8	1.87(3) Å	N1-H8···O3	168(1)°
O5···H11	1.81(3) Å	O4-H11···O5	165(1)°

Table 4.15. *Distances and angles of the hydrogen bonds.*

Investigation of the effect of temperature on the crystal structure of this salt was undertaken by studying the variations of the unit cell parameters ***a***, ***b***, and ***c*** (Figures 4.26, 4.27, and 4.28, respectively), and of the lengths of two hydrogen bonds, O5···H11 (Figure 4.29) and O2···H2 (Figure 4.30), as a function of temperature.

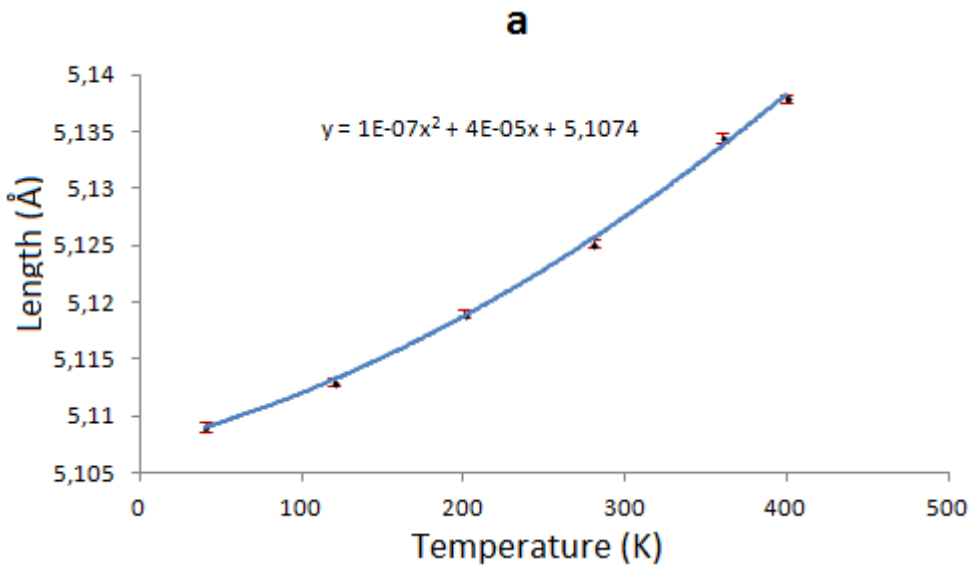

Figure 4.26. *Evolution of the cell parameter* ***a*** *as a function of temperature. The error bars are shown in red and the trendline equation is displayed on the chart.*

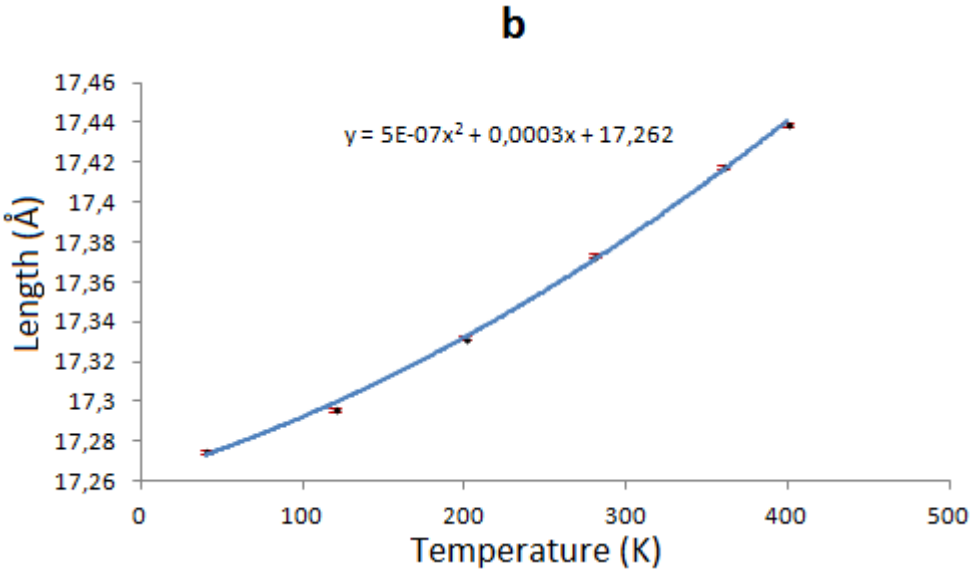

Figure 4.27. *Evolution of the cell parameter* ***b*** *as a function of temperature. The error bars are shown in red and the trendline equation is displayed on the chart.*

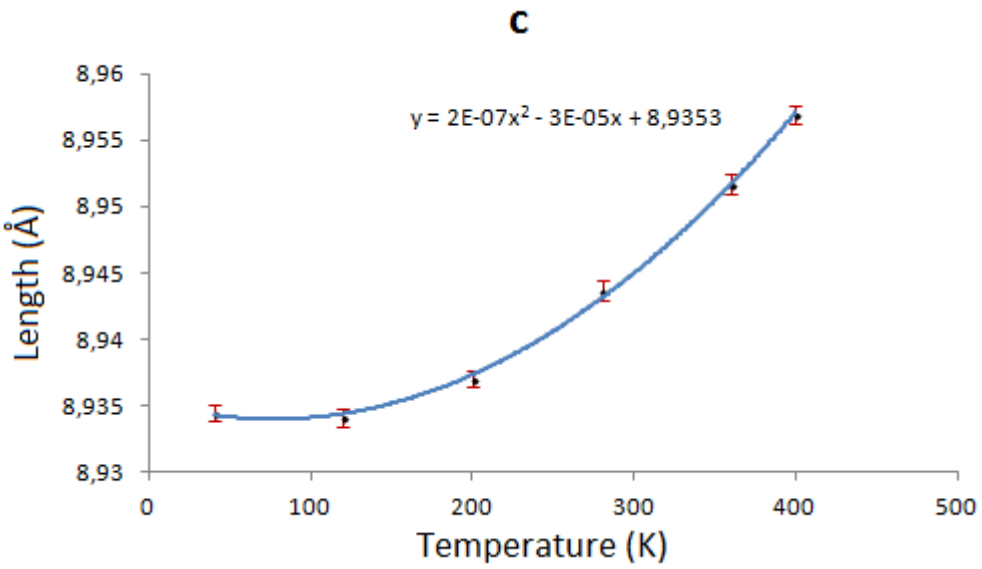

Figure 4.28. *Evolution of the cell parameter* ***c*** *as a function of temperature. The error bars are shown in red and the trendline equation is displayed on the chart.*

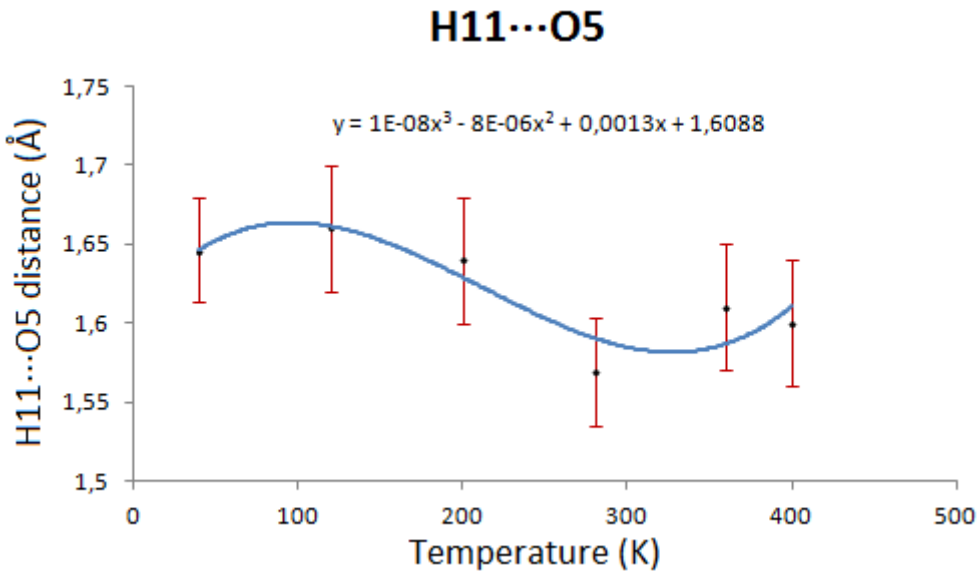

Figure 4.29. *Evolution of the hydrogen bond, H11···O5, as a function of temperature. The error bars are shown in red and the trendline equation is displayed on the chart.*

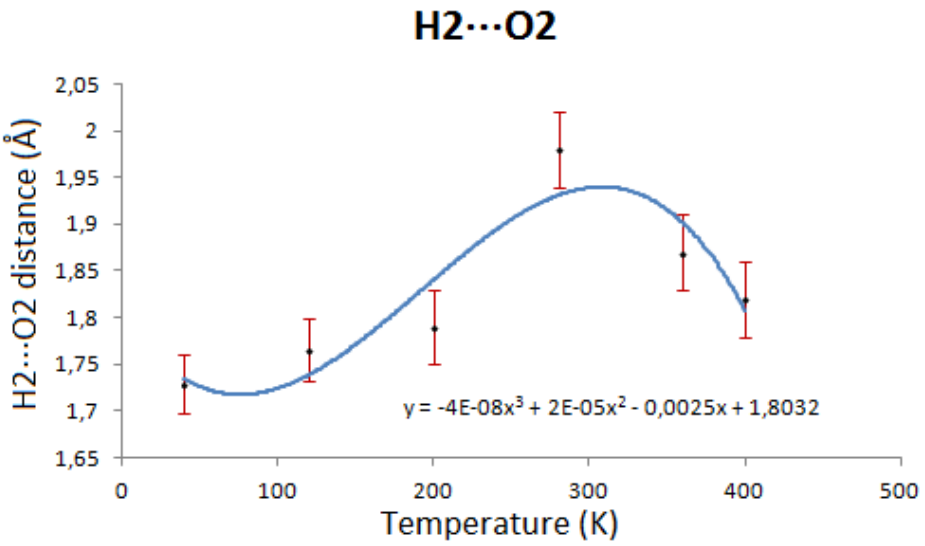

Figure 4.30. *Evolution of the hydrogen bond, H2···O2, as a function of temperature. The error bars are shown in red and the trendline equation is displayed on the chart.*

All cell parameters for the ammonium salt increase with the increasing temperature. With regard to the behaviour of the hydrogen bonds, a slight shortening of the hydrogen bond between two phosphate groups of two neighbouring molecules of glyphosate occurs, while the hydrogen bond between the glyphosate molecule and the ammonium ion is getting slightly longer with the increase of temperature.

4.3.3. Conclusions

During the course of this thesis the evolution of the crystal structure of glyphosate and its ammonium salt as a function of temperature was studied. Changes in the structures were monitored by powder neutron diffraction starting from 4K until a temperature of 440K was reached.

Since the crystal structures of both samples feature intricate hydrogen bonding networks, the behaviour of these hydrogen bonds and of the unit cell parameters was investigated by PND by increasing the temperature. It is usual to observe an expansion of the unit cell as the temperature increases. This is the case of the ammonium-glyphosate, where all three ***a***, ***b***, and ***c*** axes show an almost linear profile. An exception is represented by the unit cell parameter ***a*** of the sample of glyphosate. In fact, the length of the ***a***-axis appears to shorten with an increase in temperature, only to expand again above 250K. This peculiar behaviour is a result of the changes in the conformation of the hydrogen bond H1···O5, which lies almost perfectly along the ***a***-axis, as shown in Figure 4.21. A possible explaination for the peculiar behaviour of the cell parameter ***a*** can be found comparing the evolution of the hydrogen bond length, H1···O5, to that of the related angle, O1-H1···O5, which is displayed in Figure 4.31.

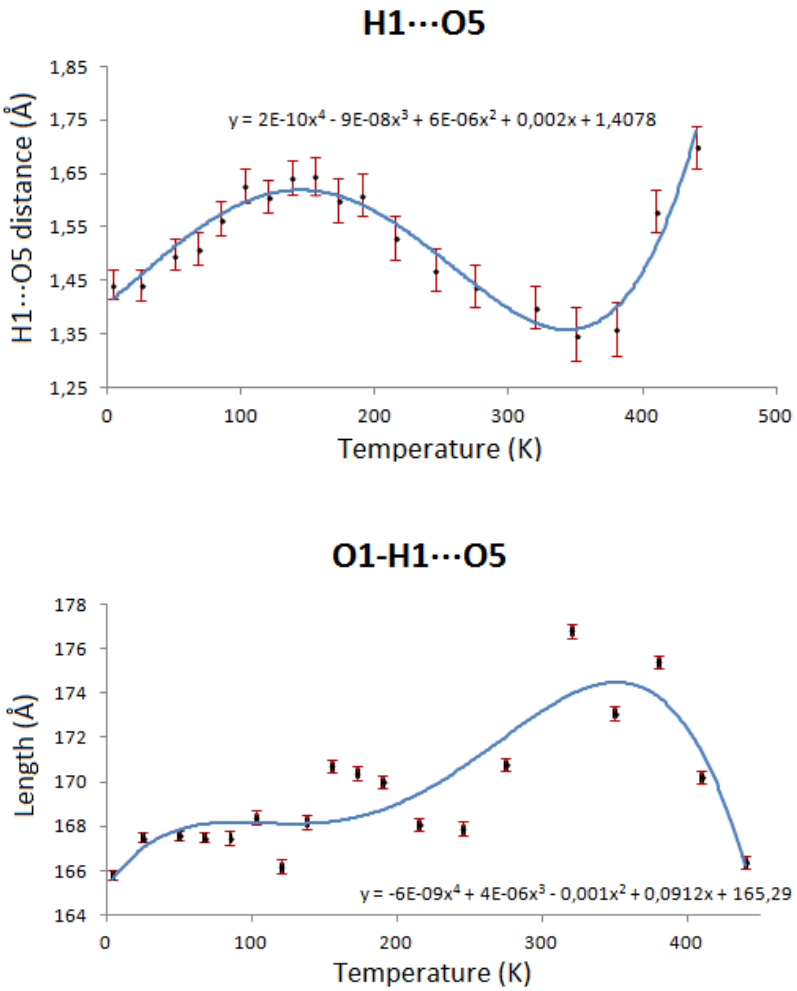

Figure 4.31. *Evolution as a function of temperature of the length (on top) and the angle (on bottom) of the hydrogen bond O1-H1···O5 in crystals of glyphosate. The error bars are shown in red and the trendline equation is displayed on the chart.*

From the observation of Figure 4.31 it is possible to notice a slight increase in both hydrogen bond length and angle until around 200K, corresponding to a decrease of the ***a***-axis. The opening of the angle towards a value of 180˚ accompanied by a stretching of the hydrogen bond length might force the interacting glyphosate molecules to vary their relative position slightly, gliding one on top of the other and causing the compression of the cell parameter ***a***. At temperatures above 200K, a shortening of the hydrogen bond length corresponds to a more accentuated increase of the O1-H1···O5 angle and the glyphosate molecules inside the crystal packing relax, leading to the observed gradual increase of the ***a***-axis from 250K to 440K. The variable-temperature powder neutron diffraction experiments performed on glyphosate and its ammonium salt show that the hydrogen bonding networks in these crystalline materials is not rigid, but a certain degree of freedom between the interacting molecules prevents major disruption in the crystal structure, explaining the absence of temperature-dependent polymorphs for these substances.

Chapter 5

5. The fungicide cyprodinil

5.1. Cyprodinil, 4-cyclopropyl-6-methyl-N-phenylpyrimidin-2-amine

5.1.1. Introduction

Cyprodinil (CYP) is an anilinopyrimidine derivative fungicide that can control a wide range of pathogens by inhibiting the secretion of fungal hydrolytic enzymes. Since its first introduction in France in 1993[95], Cyprodinil has been used as a foliar fungicide in cereal grains, grapes, pome fruit, stone fruit, and ornamentals. It is usually formulated as water dispersible molecules, WG, or as emulsifiable concentrates, EC. It can be used in combination with other agrochemicals, such as triazoles, fludioxonil, fenpropidin, and acibenzolar-*S*-methyl.

Cyprodinil exists in two different polymorphs, characterized by different melting points: form A exhibits a melting point around 70°-72°C, while form B has a melting point between 74°-76°C. From the literature[96] it is known that the thermodynamic stability of the two polymorphs is enantiotropically related and shows a phase transition temperature between 15°-40°C, although variation of the transition temperature can occur due to environmental conditions. Below this phase transition temperature the stable form is form A, while form B is stable above the phase transition temperature. The exhibition of polymorphism by this fungicide represents a problem from a practical and commercial point. The spontaneous conversion of the metastable form B into the thermodynamically stable one causes the formation of larger aggregates that can obstruct the nozzle of delivery equipments on the crop field. The process of re-crystallisation of one form into the other affects the storing of this material, making it very difficult to maintain a homogeneous formulation of the product and limiting the formulation of cyprodinil only to those formats in which it can be solubilised, such as emulsion concentrates. Consequently, additional issues, due to difficulties in ensuring the correct concentration, may arise during the transfer to dilution tanks.

The work undertaken during this thesis aims to a better understanding of the stability relations between the two polymorphs of cyprodinil and to the discovery of possible co-crystals, which may represent a step forward towards the production and formulation of the fungicide that are stable over time and in wide range of temperatures upon storage.

5.1.2. Experimental

5.1.2.1. Physical and chemical properties

Form A of Cyprodinil is a white powder, whereas form B has a light beige colour. In the literature[88] it is stated that commercial Cyprodinil has a melting point of 75.9˚C, which refers to form B, as proved during the course of this thesis. Crystal modification A of Cyprodinil has a vapour pressure at 25˚C of $5.1 \cdot 10^{-4}$ Pa, while modification B has a vapour pressure at the same temperature of $4.7 \cdot 10^{-4}$ Pa. Cyprodinil is soluble in most organic solvents, with a slight decrease in solubility in more polar solvents. It is slightly soluble in water at 25˚C, displaying different values of solubility depending on the pH of the aqueous solution: 20 mg/l at pH 5.0; 13 mg/l at pH 7.0; and 15 mg/l at pH 9.0. Also the partition coefficient log P_{OW} (*n*-octanol/water)[97] varies with pH: 3.9 at pH 5.0; 4.0 at pH 7.0 and pH 9.0.

5.1.2.2. Crystallisation from solution

Since it is the thermodynamically stable form, modification A of cyprodinil crystallises mainly from solution in long, thin, transparent, needle-shaped crystals, but it can also be obtained by slow conversion in the solid state from the metastable form B. On the other hand, modification B can be obtained by melting form A and letting it cool down to room temperature. Unfortunately, this method leads to the formation of crystals not always suitable for an X-ray diffraction analysis. For this reason, various attempts for obtaining modification B from solution were made, using a large variety of different organic solvents in order to investigate whether interactions between the molecules of cyprodinil and those of the solvent might act as the driving force for the crystallisation of form B.

The choice of the solvents to be used was made considering the solubility of cyprodinil in different organic solvents. It was noted that the less polar the solvent, the higher was the solubility of the substance. Solubility plays a role in crystal growth: it is usually observed that a high value of solubility of a substance in a solvent leads to the formation of smaller crystals, while larger crystal sizes can be obtained using a solvent in which the compound is less soluble. For this reason, for the X-ray experiment, crystals grown from a toluene solution were used, while ethanol was the solvent chosen for growing crystals suitable for a neutron analysis. The solvents used for the crystallization of cyprodinil are reported in Table 5.1. All solvents used were of analytical standard, except for toluene, which was used in anhydrous formulation.

Cyprodinil (g)	Solvent	Solvent quantity (ml)	Temperature (˚C)
0.98	Acetone	8	-
0.09	Diethyl ether	3	-
0.12	Toluene	5	70
0.55	Xylene	16	70
0.11	Cyclohexane	5	70
0.55	Methylcyclohexane	16	70
0.06	Chloroform	3	-
0.12	Methanol	4	70
0.12	Ethanol	6	70
0.43	1-propanol	12	70
0.50	2-propanol	10	70
0.10	Acetonitrile	4	70

Table 5.1. *All prepared solutions.*

Once the cyprodinil was fully dissolved, the solutions were heated at the temperature reported in Table 5.1; due to their high volatility and low boiling points, the solutions with acetone, diethyl ether and chloroform were not heated. All solutions were kept at the chosen temperature, while continuously stirring, for ~ 1 hour and, then, they were transferred in small crystallisation vials, covered with parafilm and left to cool and crystallise at room temperature. To allow slow evaporation of the solvent, a maximum of four small holes were applied on the parafilm wrap.

The crystals obtained were ground into a fine powder and analysed with powder diffraction on the D5000 diffractometer, in order to verify which form had crystallised. The experimental powder patterns are reported in Figure 5.1, while Figure 5.2 displays the powder patterns of forms A and B of cyprodinil, calculated from the single crystal X-ray diffraction results.

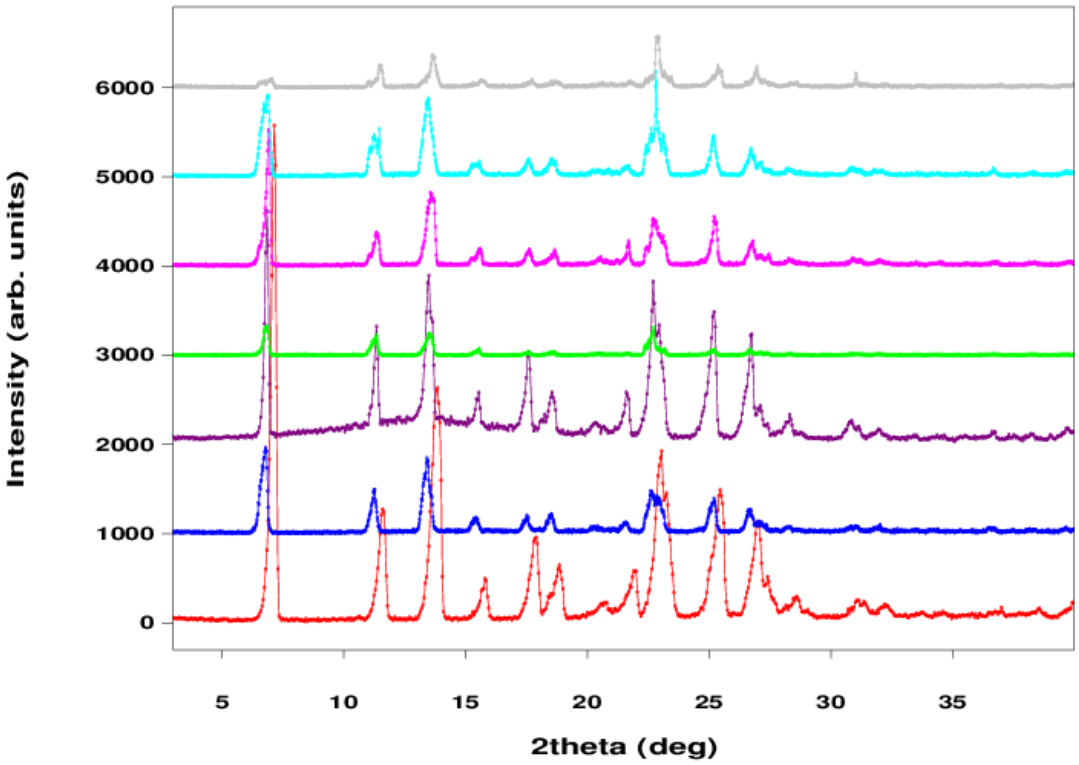

Figure 5.1. *Powder patterns of the crystals grown from the following solvents: red, ethanol; blue, 1-propanol; purple, 2-propanol; light green, cyclohexane; pink, methylcyclohexane; light blue, toluene; gray, xylene.*

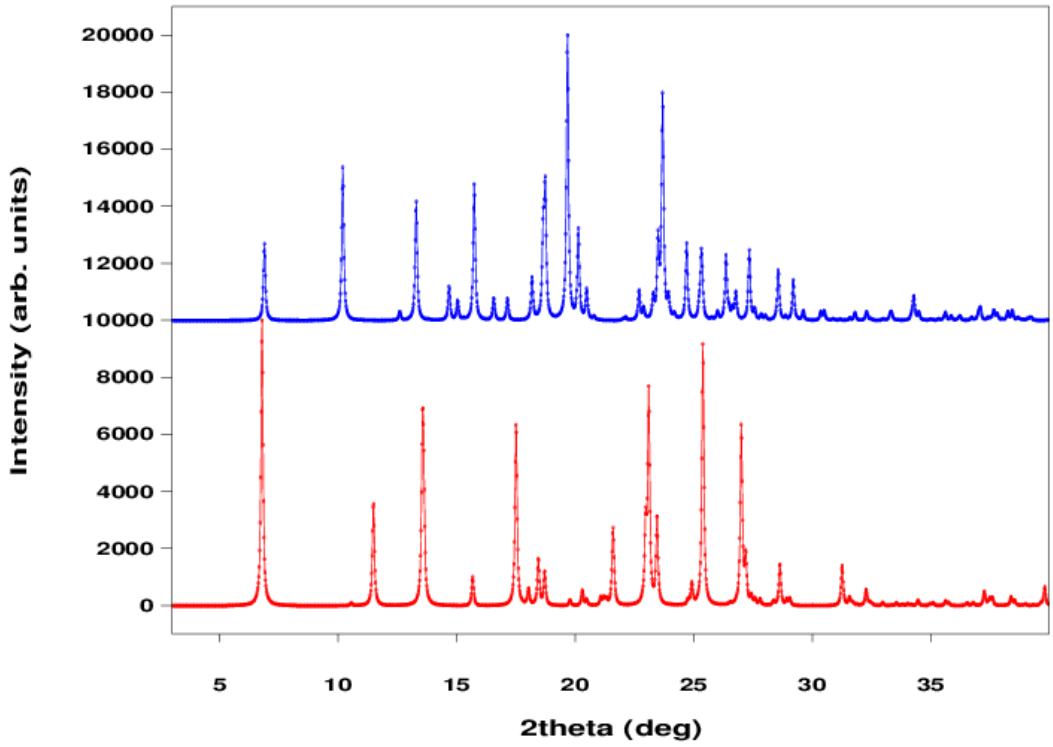

Figure 5.2. *Powder patterns of form A (in red) and form B (in blue) of cyprodinil, calculated from the single crystal X-ray diffraction experiments.*

By comparing the positions of the Bragg peaks in the calculated pattern (Figure 5.2) to the experimental values (Figure 5.1), it is possible to recognise only the growth of crystals of form A from the selected organic solvents. Crystals grown from acetone, diethyl ether, chloroform, methanol, and acetonitrile were of size and shape suitable for single crystal X-ray diffraction: a few scans were collected on these crystals, but the unit cell parameters were those of form A.

5.1.2.3. Crystallisation from the melt

To verify the presence of a conversion into a metastable polymorph, ~ 2 g of commercial Cyprodinil were kept in the oven at 78˚C for eight hours. The molten substance was, then, left to cool and crystallise at room temperature. The molten Cyprodinil was not liquid, but rather viscous, with a consistency that resembled glue. This characteristic of the melted state caused a very slow crystallisation process, which took almost 24 hours to reach completeness. The solid was ground into a fine powder in an agate mortar and analysed on the powder diffractometer D5000. Figure 5.3 reports a comparison between a sample of cyprodinil crystallised from solution and the sample solidified from the molten substance.

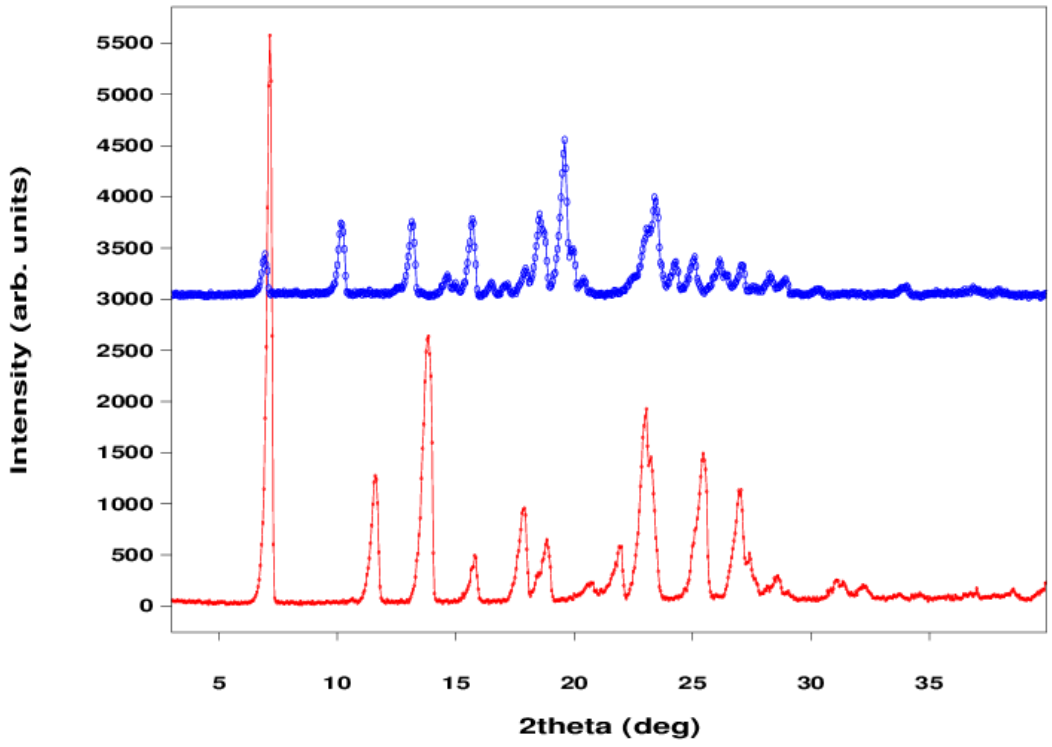

Figure 5.3. *Powder patterns of modification A (blue) and B (red) of cyprodinil.*

The diffraction profiles confirm the presence of two polymorphs of cyprodinil. The differences in the position of the Bragg's reflections are clearly visible in the first three peaks of both patterns: at 7.1˚, 11.5˚, and 13.8˚ for form A, opposed to 6.8˚, 10.1˚, and 13.1˚ for form B (Figure 5.2).

Having verified the formation of polymorph B from the melt, a small amount of this form was solubilised in ethanol as a last attempt to obtain single crystals of form B from solution. This time no heat was applied to the solution and crystallisation occurred by slow evaporation of the solvent at room temperature. Usually, crystallisation from solution produces crystals of the thermodynamically stable form. However, in this case even though the starting material was the metastable form, crystals of form B were obtained from the ethanol solution. An explanation can be found in the so-called ***crystalline memory*** effect[98]: if the starting material is kept at temperatures below its fusion temperature, it may happen that at the temperature of crystallisation some clusters preserve their crystal structure, acting as seeds for the crystallisation process.

5.1.2.4. Differential Scanning Calorimetry

Investigations of the phenomenon of polymorphism in the fungicide cyprodinil were carried out by DSC analyses. Data were collected on a sample of form A, re-crystallised from toluene, and on one of form B, obtained from the melt, during both heating from 10˚C to 80˚C and cooling back to 10˚C with a rate of 1˚C/min. Figures 5.4 and 5.5 report the thermal profiles for polymorph A and B, respectively.

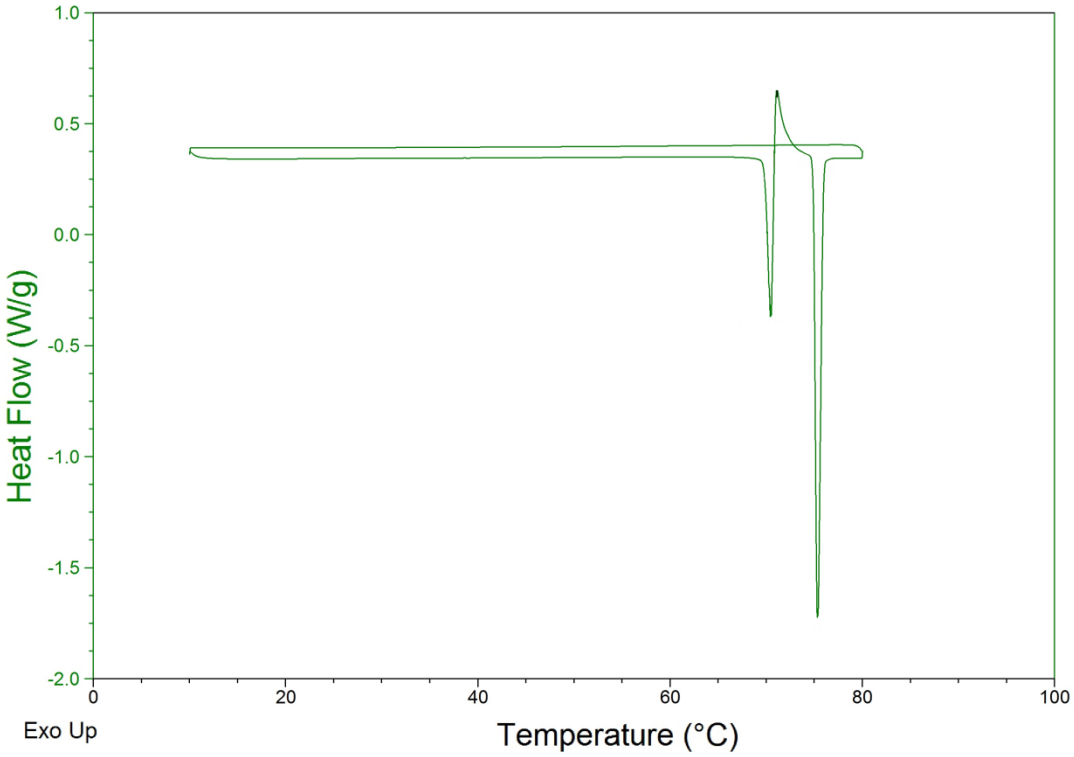

Figure 5.4. *DSC profile for a sample of modification A of cyprodinil.*

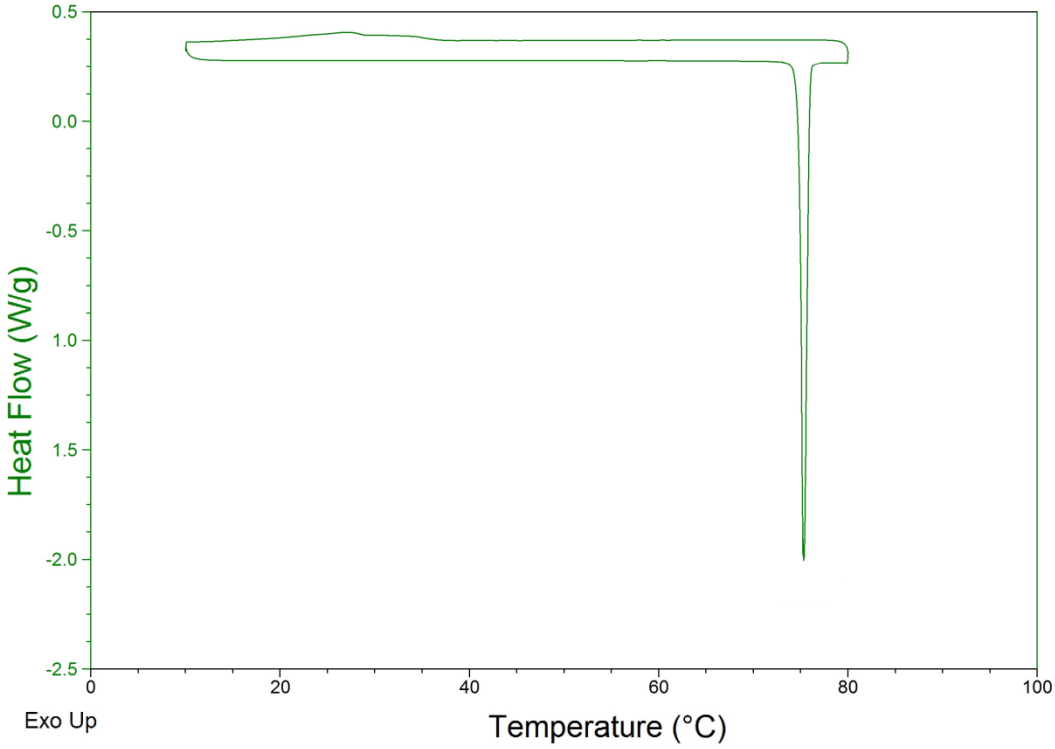

Figure 5.5. *DSC profile of a sample of modification B of cyprodinil.*

The DSC profile of form A shows a first endothermic event at ~70˚C, corresponding to the melting of form A, followed soon after by the conversion and crystallisation of the metastable form B at ~71˚C, and, finally, the melting of form B at ~75˚C. This behaviour of modification A of Cyprodinil confirms the enantiotropic correlation between the two polymorphs. Worthy of notice is the complete absence of any crystallisation event during cooling from 80˚C to 10˚C.

On the contrary, in the thermal profile of form B only the melting event of this form, at ~75˚C, is present during heating, while a probable conversion to the thermodynamically stable form A is visible upon cooling ~28˚C, as highlighted in Figure 5.6. This value of the transition temperature is in accordance with the literature[96], which states that the phase transition from form B to form A lies in a range in temperature between 15˚ - 40˚C.

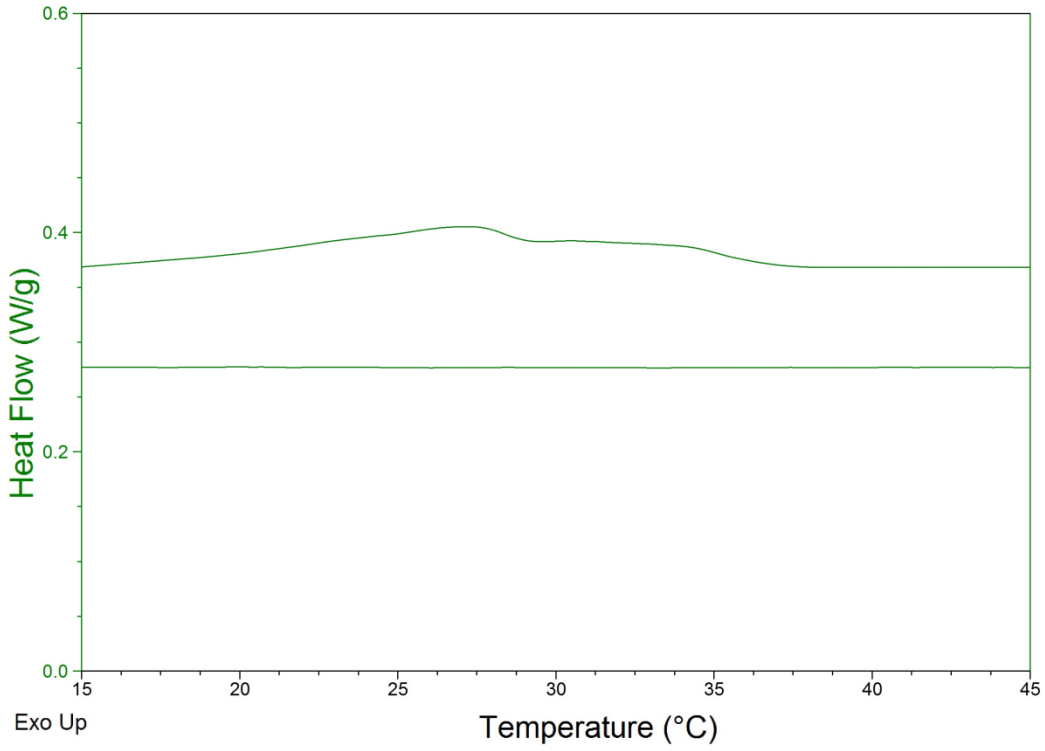

Figure 5.6. *Conversion of form B into form A.*

5.1.2.5. Single crystal X-ray diffraction

The crystal structures of both polymorphs of cyprodinil were analysed by single crystal X-ray diffraction on an Agilent Technologies Gemini A Ultra CCD diffractometer at the University of Bath. An Oxford Cryojet apparatus allowed reaching collection temperature of 150K.

The selected crystal of form A was grown from a toluene solution, while the crystal of form B was obtained by sublimation: ~ 1 g of commercial cyprodinil was put in a round-bottom flask along with a glass slide, which was positioned vertically; the flask was attached to a Schlenk line in order to create a vacuum environment. An oil bath guaranteed a constant temperature of 78˚C. Twenty minutes after the cyprodinil had melted, crystals formed on top of the glass slide. In Figure 5.7 schematic representations of the crystal habits of the two forms are reported.

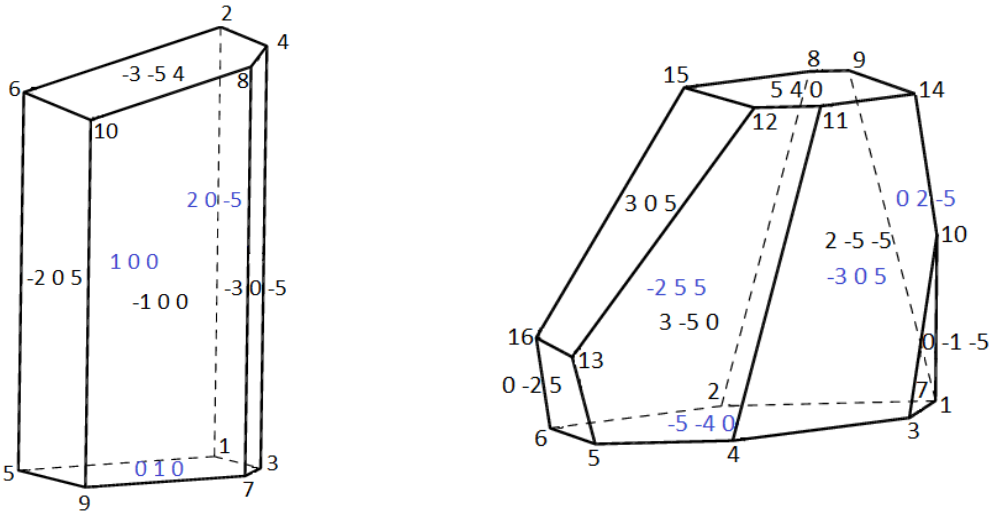

Figure 5. 7. *Schematic representations of the crystal morphology of form A (on the left) and of form B (on the right).*

In Tables 5.2 and 5.3, X-ray crystallographic data and refinement parameters for form A and form B of Cyprodinil, respectively, are reported.

Name	Cyprodinil – Form A
Empirical formula	$C_{14}H_{15}N_3$
Formula weight (g mol^{-1})	225.29
Temperature (K)	150
Wavelength (Å)	0.71073
Crystal system, space group	Monoclinic, $P2_1/c$
Unit cell dimensions	a = 13.2114(6) Å
	b =5.3100(2) Å
	c = 17.0174(7) Å
	β = 100.334(4)°
Volume ($Å^3$)	1174.4(8)
Z, calculated density (g cm^{-3})	4, 1.274
F(000)	480
Absorption coefficient (mm^{-1})	0.078
Crystal size (mm)	0.15 x 0.36 x 0.65
Theta range for data collection (°)	3.12 to 26.36
Limiting indices	$-16 \leq h \leq 12$, $-6 \leq k \leq 6$, $-17 \leq l \leq 21$
Reflections collected / unique	5225 / 2401 [R_{int} = 0.0189]
Completeness to θ = 26.36	99.9 %
Refinement method	Full-matrix least-squares on F^2
Data / restrains / parameters	2401 / 0 / 215
Goodness-of-fit on F^2	1.040
Final R indices [I>2sigma(I)]	R_1 = 0.0365, wR_2 = 0.0918
R indices (all data)	R_1 = 0.0437, wR_2 = 0.0985
Extinction coefficient	0.006(2)
Largest diff. Peak and hole (e $Å^{-3}$)	0.21 and -0.16

Table 5.2. *X-ray crystallographic data and refinement parameters for a crystal of modification A of cyprodinil.*

Name	Cyprodinil – Form B
Empirical formula	$C_{14}H_{15}N_3$
Formula weight (g mol^{-1})	225.29
Temperature (K)	150
Wavelength (Å)	0.71073
Crystal system, space group	Monoclinic, $P2_1$
Unit cell dimensions	a = 8.0820(3) Å
	b =11.7675(6) Å
	c = 12.8281(5) Å
	β = 93.424(4)°
Volume ($Å^3$)	1217.8(9)
Z, calculated density (g cm^{-3})	4, 1.229
F(000)	480
Absorption coefficient (mm^{-1})	0.075
Crystal size (mm)	0.13 x 0.22 x 0.31
Theta range for data collection (°)	2.90 to 26.37
Limiting indices	$-10 \leq h \leq 10$, $-10 \leq k \leq 14$, $-16 \leq l \leq 16$
Reflections collected / unique	9926 / 4056 [R_{int} = 0.0264]
Completeness to θ = 26.37	99.9 %
Refinement method	Full-matrix least-squares on F^2
Data / restrains / parameters	4056 / 1 / 428
Goodness-of-fit on F^2	1.011
Final R indices [I>2sigma(I)]	R_1 = 0.0326, wR_2 = 0.0752
R indices (all data)	R_1 = 0.0388, wR_2 = 0.0789
Extinction coefficient	0.013(2)
Largest diff. Peak and hole (e $Å^{-3}$)	0.19 and -0.13

Table 5.3. *X-ray crystallographic data and refinement parameters for a crystal of modification B of cyprodinil.*

5.1.2.6. Single crystal neutron diffraction

Both modifications of Cyprodinil were analysed by SND on the single crystal diffractometer D19 at ILL. Crystals of forms A and B were grown from ethanol solutions by slow evaporation of the solvent at room temperature.

For both crystals data were collected with a wavelength of λ = 1.17000 Å; the D1/D2 windows, which define the aperture of the neutron beam as it comes from the reactor core, were 12 x 12 mm^2 and the diameter of the beam hitting on the samples was 6 mm. For the crystal of form A data were collected at 20K with a cooling rate of 3K/min; whereas for the crystal of modification B data collection temperature was 30K with a cooling rate of 2K/min. Before cooling to the desired temperature, a two-hour long scan at room temperature was collected on both crystals, in order to assess the quality and to verify the presence of a single crystal. The integrity of the crystals during cooling was monitored following strong reflections, (2 0 $\bar{2}$) for form A and (2 1 1) for form B, whose I vs. T plots are reported in Figures 5.8 and 5.9.

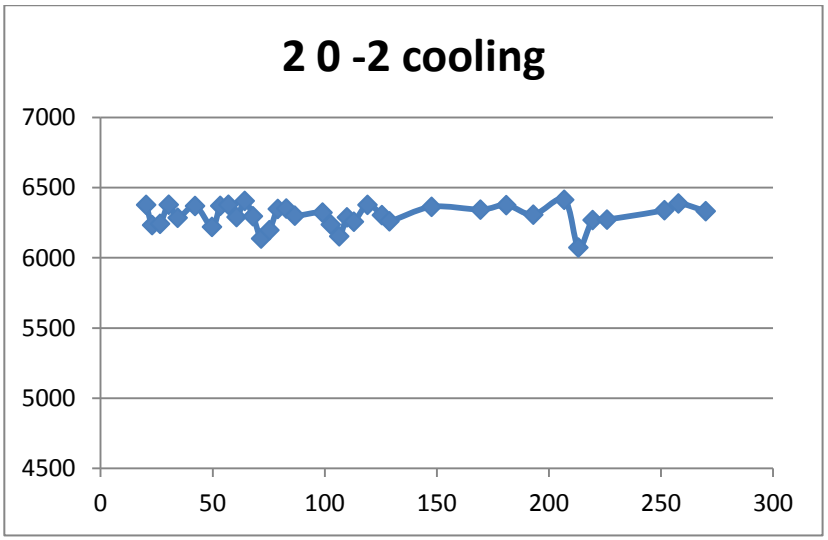

Figure 5.8. *Intensity profile for the strong reflection* (**2 0 $\bar{2}$**) *upon cooling of the crystal of form A of cyprodinil from room temperature to 20K.*

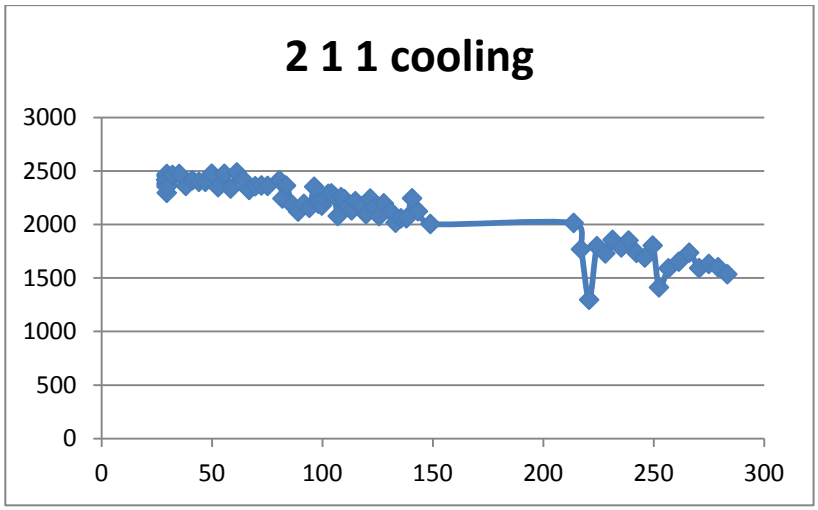

Figure 5.9. *Intensity profile for the strong reflection* (**2 1 1**) *upon cooling of the crystal of form B of cyprodinil from room temperature to 30K.*

For both crystals it is possible to observe the absence of any significant variation in the intensity values for the selected reflections, indicating that no changes in the crystal structures occurred with the temperature decreasing. For the crystal of form A the intensity of the reference reflection is constant throughout cooling, whereas for the crystal of form B it is possible to observe an increase of the reflection intensity with the decrease in temperature due to attenuation of the Debye-Waller factor.

The models of both structures were corrected for the attenuation of the intensities due to absorption by the cans and the crystal itself. This correction was done by the D19ABSCAN program: it is an analytical correction based on the indexing of the crystal faces and the crystal dimensions. In Figures 5.10 and 5.11 the schematic representations of the crystals of form A and form B, respectively, are reported.

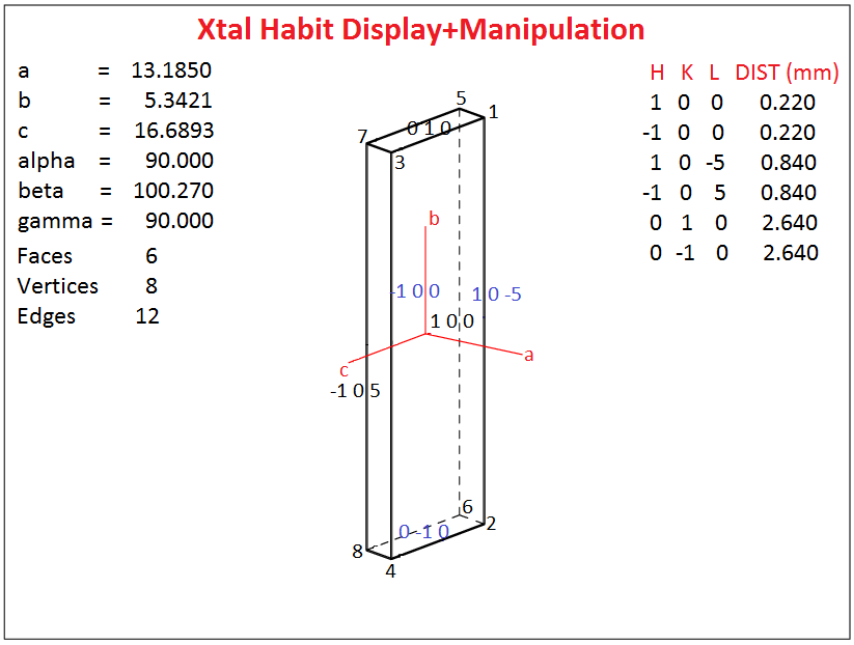

Figure 5.10. *Graphic representation of the morphology of a crystal of modification A of cyprodinil.*

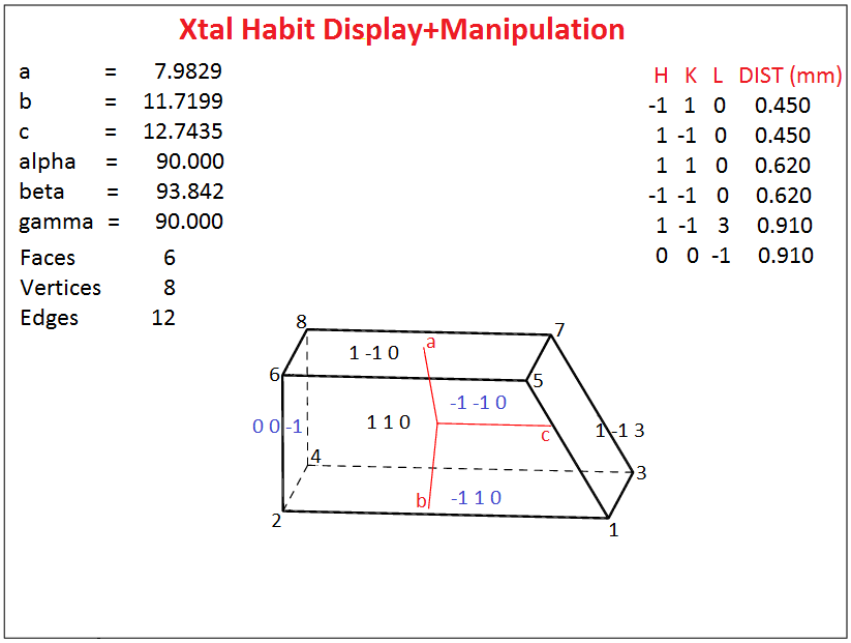

Figure 5.11. *Graphic representation of the morphology of a crystal of modification B of cyprodinil.*

By comparing the R1-values for the structures without absorption corrections, the ones with only the correction for the cans, and the structures corrected for both factors, summarised in Table 5.4 for the two polymorphs, it is possible to notice a slight improvement, indicating a low absorption of the neutron radiation by the crystal. The correction for the cans is the major contribution to the absorption correction.

	Form A	Form B
No correction	0.0608	0.0378
Correction cans	0.0513	0.0314
Correction cans+crystal	0.0471	0.0298

Table 5.4. *R1-values for both forms with different absorption corrections.*

Before applying the absorption correction using D19ABSCAN, the contribution of the crystal to the attenuation of reflection intensities was assessed collecting a series of so-called REN-scans. The principle [9] on which this method is based suggests that radiation absorption by the crystal varies when the crystal is rotated around the direction normal to a Bragg's reflection. Experimentally, the chosen reflection must have a value for the χ-angle as close as possible to 90°. Once the reflection has been chosen, a scan in φ is collected. The result is a I vs. φ plot in which the evolution profile of the Bragg's intensity displays a double wave curve. This method was initially created to correct data derived from biological samples, e.g. proteins, due to the difficulties of indexing the crystal faces of such specimens.

For a crystal of form A, three reflections were selected: the strong (0 3 1) reflection; the intermediate (0 4 0) reflection; and the weak (0 3 2) reflection. The three I vs. φ plots are reported in Figures 5.12, 5.13, and 5.14.

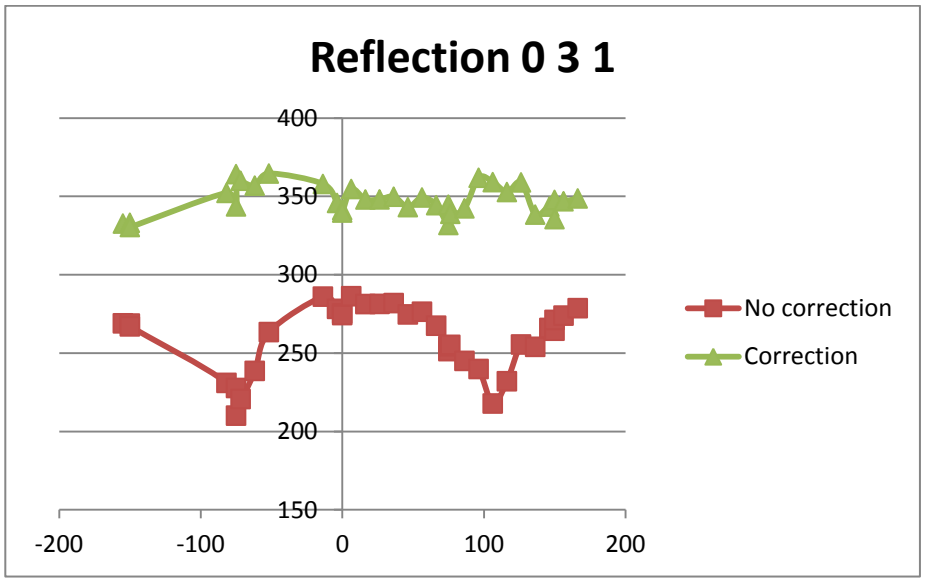

Figure 5.12. *Evolution of the strong Bragg's reflection* (**0 3 1**) *as a function of the angle φ: profile without absorption correction (red); profile with absorption correction (green).*

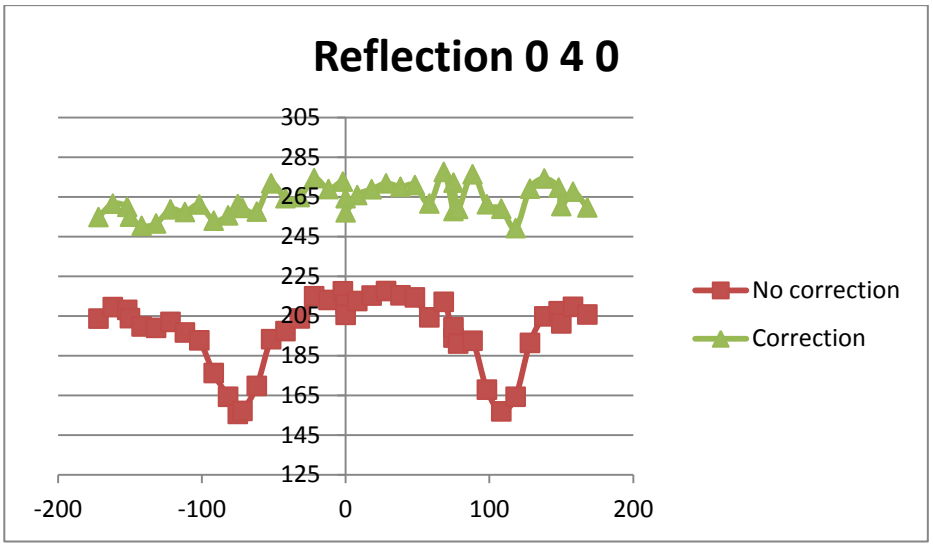

Figure 5.13. *Evolution of the intermidiate Bragg's reflection* (**0 4 0**) *as a function of the angle φ: profile without absorption correction (red); profile with absorption correction (green).*

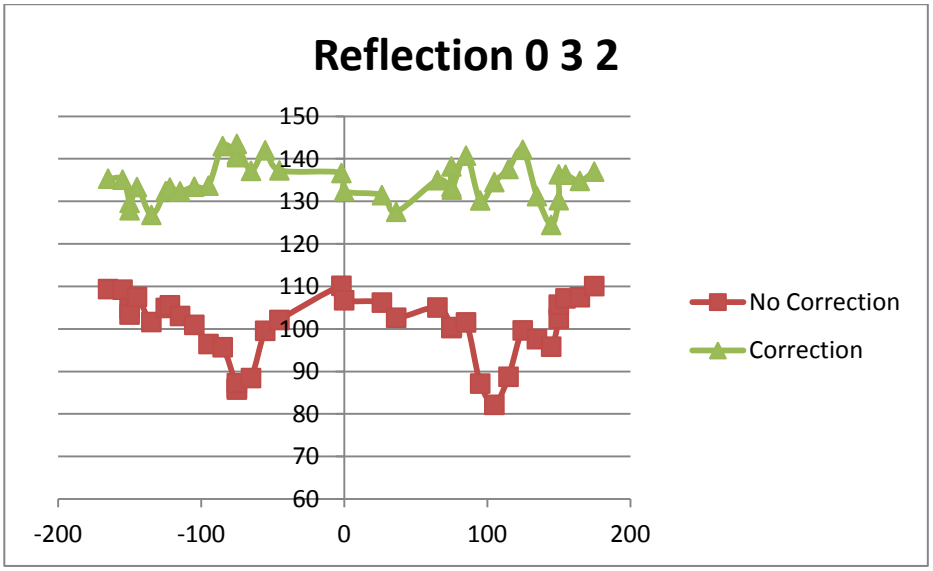

Figure 5.14. *Evolution of the weak Bragg's reflection* (**0 3 2**) *as a function of the angle φ: profile without absorption correction (red); profile with absorption correction (green).*

The profiles for the three reflections show the characteristic double wave curve when no absorption correction is applied to the set of data. On the contrary, by applying the absorption correction using D19ABSCAN, the intensity of the selected reflections exhibits a constant trend. The double wave profile is noticeable especially for those crystals which have a thin elongated morphology, because the contribution to absorption depends also on the path length inside the crystal. This is the case for the crystal of form A understudy: as shown in Figure 9, the crystal has a length of ~1.7 mm and width of ~0.5 mm.

The same data collection technique was used on a crystal of form B. This time, due to time restriction, only one reflection, (1 0 11), was selected. The I vs. φ plot for this reflection is reported in Figure 5.15.

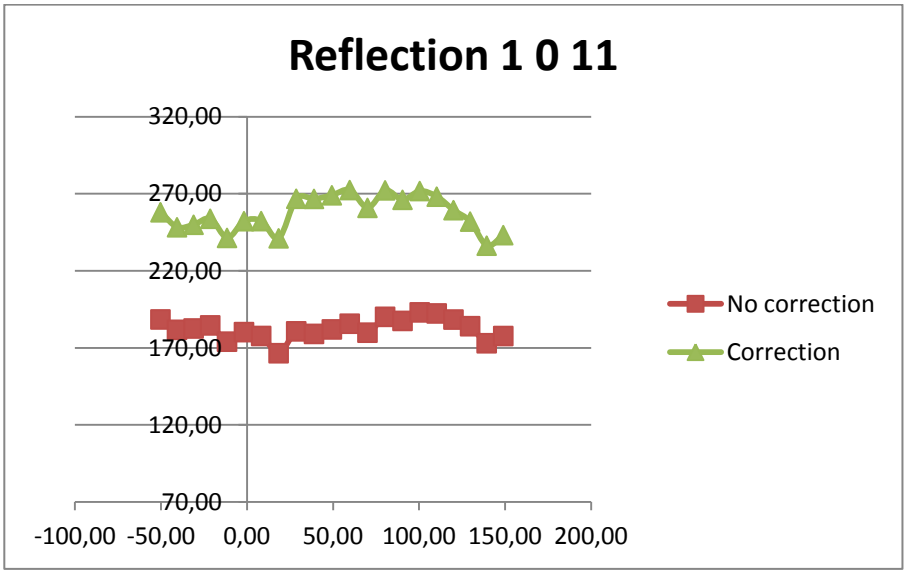

Figure 5.15. *Evolution of Bragg's reflection as a function of the angle φ: profile without absorption correction (red); profile with absorption correction (green).*

Since the crystal of form B has a prismatic morphology (Figure 5.10), the difference between the path lengths along two normal directions is minimal: in fact, the crystal length is ~1.2 mm, while its width is ~0.9 mm. For this reason the profile of the REN-scan is not a double wave curve.

In Tables 5.5 and 5.6, neutron crystallographic data and refinement parameters for form A and form B, respectively, are reported.

Name	Cyprodinil - Form A
Empirical formula	$C_{14}H_{15}N_3$
Formula weight (g mol^{-1})	225.29
Temperature (K)	30
Wavelength (Å)	1.17000
Crystal system, space group	Monoclinic, $P2_1/c$
Unit cell dimensions	a = 13.1850(2) Å
	b = 5.3421(1) Å
	c = 16.6893(3) Å
	β = 100.270(1)˚
Volume ($Å^3$)	1156.69(3)
Z, calculated density (g cm^{-3})	4, 1.294
F(000)	260
Absorption coefficient (mm^{-1})	0.230
Crystal size (mm)	0.5 x 1.7 x 5.3
Theta range for data collection (˚)	2.58 to 57.21
Limiting indices	$-18 \leq h \leq 18$, $-1 \leq k \leq 7$, $-23 \leq l \leq 23$
Reflections collected / unique	13337 / 3406 [R_{int} = 0.0506]
Completeness to θ = 57.21	94.7 %
Refinement method	Full-matrix least-squares on F^2
Data / restrains / parameters	3406 / 0 / 290
Goodness-of-fit on F^2	1.049
Final R indices [I>4sigma(I)]	R_1 = 0.0471, wR_2 = 0.1414
R indices (all data)	R_1 = 0.0507, wR_2 = 0.1440
Extinction coefficient	0.0013(3)
Largest diff. Peak and hole (fm·$Å^{-3}$)	1.39 and -1.13

Table 5.5. *Neutron crystallographic data and refinement parameters for a crystal of modification A of cyprodinil.*

Name	Cyprodinil - Form B
Empirical formula	$C_{14}H_{15}N_3$
Formula weight (g mol^{-1})	225.29
Temperature (K)	30
Wavelength (Å)	1.17000
Crystal system, space group	Monoclinic, $P2_1$
Unit cell dimensions	a = 7.9829(1) Å
	b = 11.7199(2) Å
	c = 12.7435(2) Å
	β = 93.842(1)˚
Volume ($Å^3$)	1189.6(3)
Z, calculated density (g cm^{-3})	4, 1.258
F(000)	260
Absorption coefficient (mm^{-1})	0.223
Crystal size (mm)	0.9 x 1.2 x 1.8
Theta range for data collection (˚)	5.09 to 61.78
Limiting indices	$-12 \leq h \leq 11$, $-17 \leq k \leq 17$, $-3 \leq l \leq 17$
Reflections collected / unique	13754 / 7238 [R_{int} = 0.0342]
Completeness to θ = 61.78	92.5 %
Refinement method	Full-matrix least-squares on F^2
Data / restrains / parameters	7238 / 1 / 578
Goodness-of-fit on F^2	1.082
Final R indices [I>4sigma(I)]	R_1 = 0.0298, wR_2 = 0.0656
R indices (all data)	R_1 = 0.0310, wR_2 = 0.0661
Extinction coefficient	0.0009(1)
Largest diff. Peak and hole (fm·$Å^{-3}$)	0.90 and -1.08

Table 5.6. *Neutron crystallographic data and refinement parameters for a crystal of modification B of cyprodinil.*

5.1.2.7. Powder neutron diffraction

Powder neutron diffraction data were collected on different samples of finely ground Cyprodinil on the high-flux powder diffractometer D20 at ILL.

Three different experiments were done on the sample of Cyprodinil:

i. Crystallisation *in situ* of Cyprodinil from a solution of deutereted ethanol (d6-ethanol). The aim was to monitor the crystallisation process of polymorph A. The deutereted solvent was chosen to eliminate the scattering from the hydrogen atoms, so that the hydrogen atoms present in the sample were easily refined. A sample of Cyprodinil was dissolved in d6-ethanol and the solution was put in a vanadium can. The can was secured on D20 and its height inside the neutron beam was adjusted. Evaporation of the solvent was achieved by positioning a heat gun nearby the vanadium can. Data were collected with a wavelength of $\lambda = 1.89$ Å.

ii. Investigation of the crystal structure of polymorph A. A sample of form A, re-crystallised from ethanol, was put into a vanadium can and, then, transferred into a cryofurnace, which allowed data collection from 130K to 360K. A three-hour long data collection at 130K was recorded, in order to have a good and reliable model at the lowest temperature that was reached. Before the long scan at 130K, data were collected continuously upon cooling. An additional data collection was recorded during heating until melting of Cyprodinil and on cooling back to room temperature. This cycle allowed observation of the phase transition from form A to form B.

iii. Investigation of the crystal structure of polymorph B. A sample of form B was put into a vanadium can and, then, transferred into a cryofurnace. The sample was cooled down to 130K and a one-hour long scan was collected at this temperature. After, data were collected continuously upon heating until melting of Cyprodinil was reached, and on cooling back to room temperature. The aim was to identify the phase transition temperature for the conversion of form B into the stable one.

All data were treated following the steps described in Chapter 2, section ***2.1.7***. Structural refinement was done using the Rietveld method and the initial atomic information was taken from the results of the SND experiments on polymorphs A and B. Unfortunately, when the atomic positions were included in the refinement, this became very unstable, producing a wrong model. This issue is related to the incoherent scattering derived from the large number of hydrogen atoms present in the structures. In fact, the refinement continued to be unstable even if soft body constraints, such as the same U_{iso} for the atoms of the same element, were applied.

5.1.2.8. Computational studies

In collaboration with Christopher H. Hendon, computational calculations were made in order to assess the stability of the two polymorphs of Cyprodinil.
The results of these calculations are reported in Table 5.7. Even if by just a small amount, form A is confirmed to be the thermodynamically stable form.

	HOMO	LUMO	Computational Gap (eV)	Internal Energy (eV)
Form A	-0.51	3.82	4.34	-1001.46
Form B	-0.82	3.08	3.90	-995.31

Table 5.7. *Calculated HOMO (Highest Occupied Molecular Orbital), LUMO (Lowest Unoccupied Molecular Orbital) and internal energy for the two modification of cyprodinil.*

5.1.3. Results and discussion

The crystal structures of the two polymorphs of cyprodinil were solved and the cell parameters are reported in Table 5.8.

	Form A	Form B
Space Group	P $2_1/c$	P 2_1
a	13.2114(6) Å	8.0820(3) Å
b	5.3100(2) Å	11.7675(6) Å
c	17.0174(7) Å	12.8281(5) Å
β	100.334(4)°	93.424(4)°
V	1175.45(8) $Å^3$	1217.84(9) $Å^3$

Table 5.8. *Unit cell parameters and space groups for both modification of cyprodinil, derived from X-ray diffraction.*

Both structures are stabilized by the presence of hydrogen bonds, involving the amino group of the molecule and the nitrogen atom of the pyrimidine ring. The existence of the two forms lies in the different hydrogen bonding network.

5.1.3.1. Polymorph A

In form A, the asymmetric unit is formed by one molecule of cyprodinil, as shown in Figure 5.16 from the X-ray results. The benzene and the pyrimidine rings are not co-planar: the benzene is

8.5(2)˚ off the plane containing the pyrimidine ring. This is probably due to the presence of the cyclopropyl substituent, which points in the direction of the benzene ring, causing hindrance.

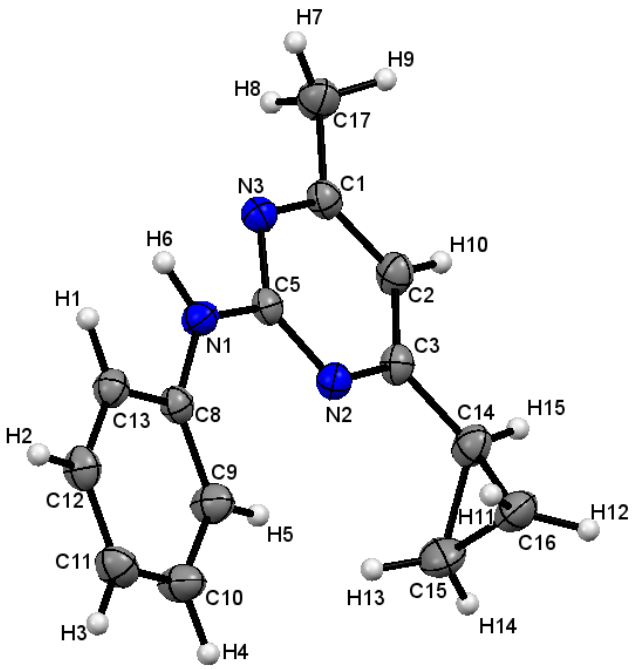

Figure 5.16. *ORTEP representation of a molecule in a crystal of form A of cyprodinil, derived from single crystal X-ray diffraction. The probability level for all non-hydrogen ellipsoids is 50%, while the hydrogen atoms are drawn as fixed-size spheres of radius 0.15 Å.*

C5-N1-C8-C9	-8.5(2)˚
N2-C3-C14-C15	36.2(2)˚
N2-C3-C14-C16	-32.7(2)˚
C5-N2-C3-C14	179.9(1)˚
N3-C5-N1-H6	-6(1)˚

Table 5.9. *Torsion angles of interest.*

As can be seen in Table 5.9, the cyclopropyl is centred in respect to the pyrimidine ring, forming torsion angles up and down the ring of, respectively, 36.2(2)˚ and -32.7(2)˚.

Also the hydrogen atom, H6, which forms an intermolecular hydrogen bond with a neighbouring molecule of Cyprodinil, is twisted in respect to the pyrimidine ring of 6(1)˚. This value of the torsion angle N3-C5-N1-H6 allows the formation of an intermolecular hydrogen bond: each molecule of cyprodinil forms two hydrogen bonds with two different neighbouring molecules, as shown in Figure 5.17.

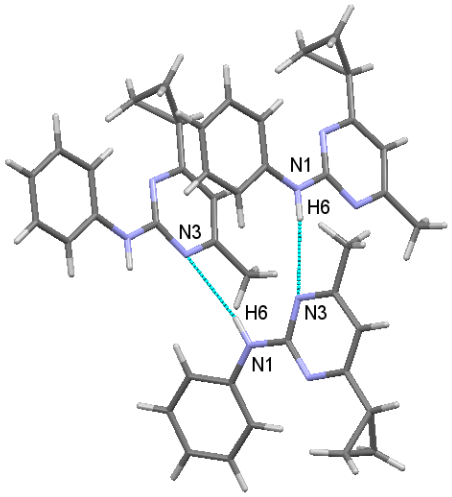

Figure 5.17. *Hydrogen bonding network in a crystal of form A of cyprodinil.*

The crystal packing is governed by intermolecular hydrogen bonds and by the stacking of cyprodinil molecules in piles displaying an off-set arrangement so that the pyrimidine part of a cyprodinil molecule can interact with the benzene ring of a neighbouring molecule, leading to the formation of π-π interactions with a distance between centroids of 3.87(2) Å. The hydrogen bonding network is formed by linear hydrogen bonds between the hydrogen atom of the amino group and the nitrogen atom on the pyrimidine ring of a neighbouring molecule. Each cyprodinil molecule engages in two intermolecular hydrogen bonds with two different molecules, acting both as donor and as acceptor of the hydrogen bond. In Table 5.10 hydrogen bond length and geometry are reported.

N1-H6	0.89(1) Å
H6···N3	2.68(1) Å
N1···N3	3.534(1) Å
N1-H6···N3	163(1)˚

Table 5.10. *Hydrogen bond length and geometry for a crystal of form A of cyprodinil, studied by X-ray radiation.*

The SND experiment allowed the production of a model in accordance with the SXD results, but it was able to gain a ten-fold improvement in the accuracy of the hydrogen atom positions. Since the hydrogen bond plays an important role in the definition of the crystal structure of both polymorphs of cyprodinil, single crystal neutron diffraction represents the best technique for their investigation. In Table 5.11 the unit cell parameters for the crystal of form A at 292K and 20K are reported.

	Form A	
Temperature	292K	20K
a	13.3233(7) Å	13.1850(2) Å
b	5.2996(3) Å	5.3421(1) Å
c	17.414(1) Å	16.6893(3) Å
β	100.76(3)˚	100.270(1)˚
Space Group	P 2_1/c	P 2_1/c

Table 5.11. *Unit cell parameters for the crystal structure of polymorph A at 292K and 20K, derived from SND experiment.*

As expected, from the values displayed in Table 5.11, it is possible to observe a slight reduction of the unit cell dimensions upon cooling to 20K.

Thanks to neutron radiation, the atomic displacement parameters (ADPs) for all hydrogen atoms were refined anisotropically, providing a more realistic model of the hydrogen bonding network. Figure 5.18 reports a particular of the crystal packing of form A, highlighting the ADPs for the hydrogen atoms.

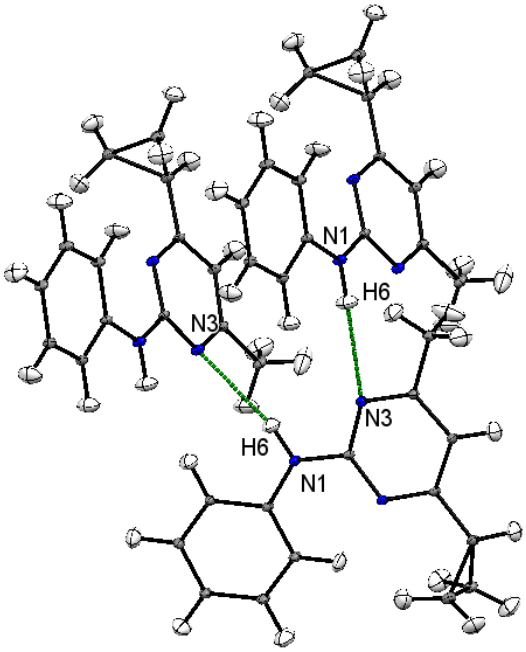

Figure 5.18. *ORTEP representation of the hydrogen bonding network in modification A of cyprodinil, derived from neutron results. The probability level for all ellipsoids is 50%.*

The atomic deviation of H6 from the mean position occurs along an axis normal to the direction of the hydrogen bond, indicating the absence of proton migration. Worth of notice is the difference in the ADPs between the hydrogen atom H6 and the hydrogen atoms on the methyl groups and the cyclopropyl-substituent: the latter are larger and more elongated, due to the fact that they are not

involved in intermolecular interactions. The absence of proton migration or disorder in this structure is confirmed by both electron-density and nucleon-density maps (Figure 5.19). In both maps the hydrogen atom H6 is fixed in a precise position.

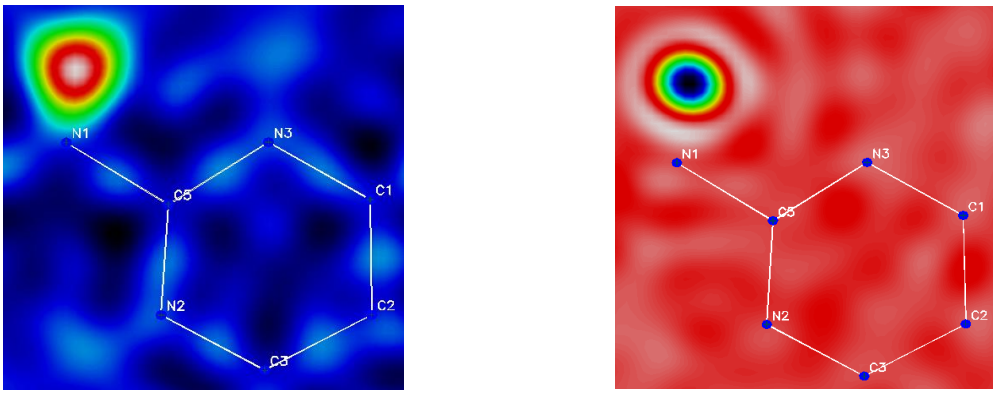

Figure 5.19. *Electron-density difference map (on the left) and nucleon-density difference map (on the right) for the atom H6.*

A summary of the main characteristic of the hydrogen bond, N1-H6···N3, is reported in Table 5.12.

N1-H6	1.012(3) Å
H6···N3	2.526(3) Å
N1···N3	3.502(1) Å
N1-H6···N3	162.0(3)˚

Table 5.12. *Hydrogen bond and geometry for modification A of cyprodinil, derived from neutron diffraction.*

5.1.3.1.1. Crystallisation *in situ*

The first experiment done on D20 focused on the investigation of crystallisation of form A from a solution of deutereted ethanol (d6-ethanol). Because of the high incoherent scattering of the hydrogen atoms, the choice of the right solvent fell on a deutereted one: in this way, the only visible hydrogen atoms were those of the sample of cyprodinil.

The heating for the evaporation of the solution was provided by a heat gun, which was carefully positioned next to the diffractometer head so to not be inside the neutron beam. A series of scans were collected on pure d6-ethanol in order to calibrate the temperature of the heat gun: the evaporation of the solvent was followed monitoring the intensity of the amorphous signal recorded in the powder pattern. In Figure 5.20 three patterns, collected every five minutes, are reported. The heat gun temperature was set to 160˚C, which corresponded to a sample temperature of ~55˚C.

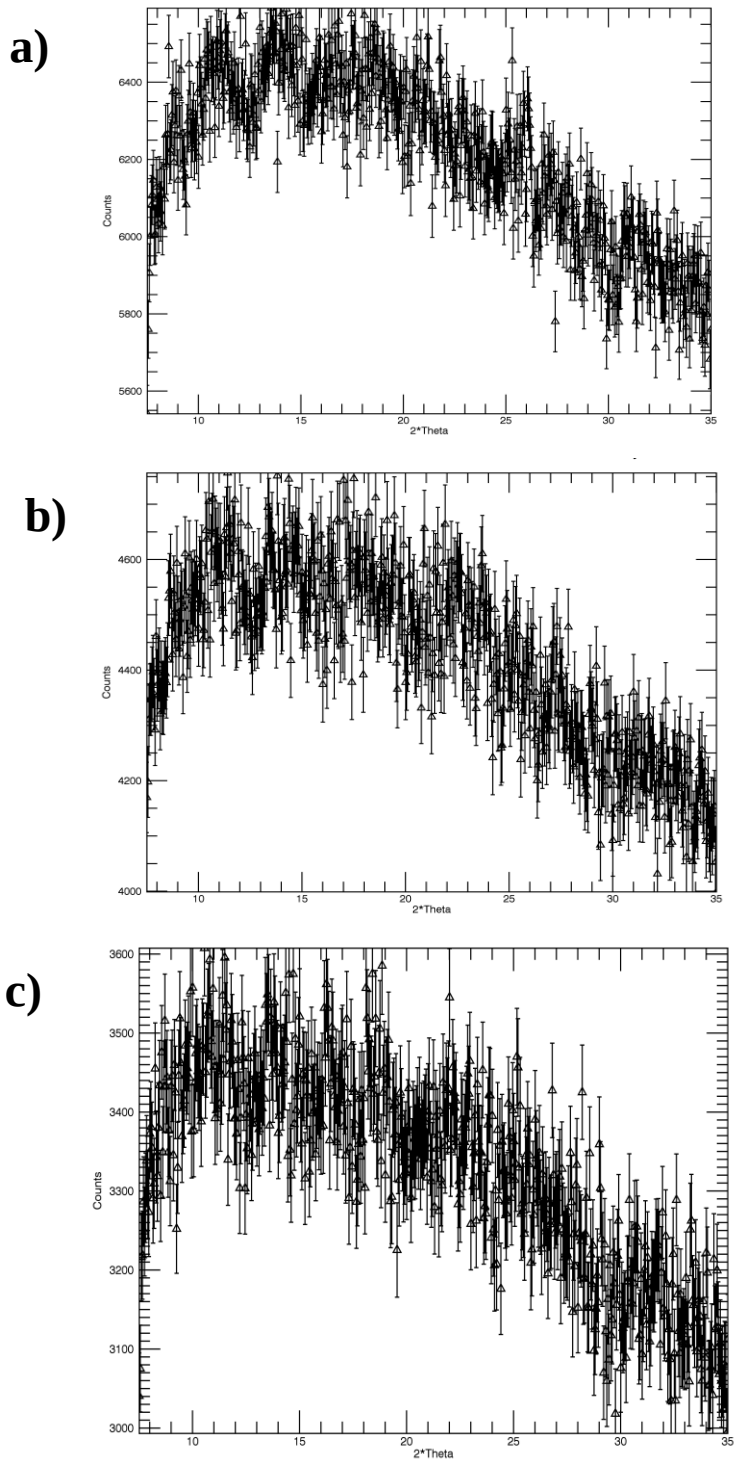

Figure 5.20. *Amorphous profile for d6-ethanol : a) profile collected at the start of the evaporation process – 6400 counts; b) profile collected five minutes after evaporation began – 4600 counts; c) profile collected ten minutes after evaporation – 3400 counts.*

The decrease of the intensity, in counts, of the ethanol signal indicates that the d6-ethanol was in fact evaporating. In order to discriminate between the two polymorphs, powder patterns for both forms were calculated, with $\lambda = 1.89$ Å, from SND results. The calculated patterns are reported in Figure 5.21.

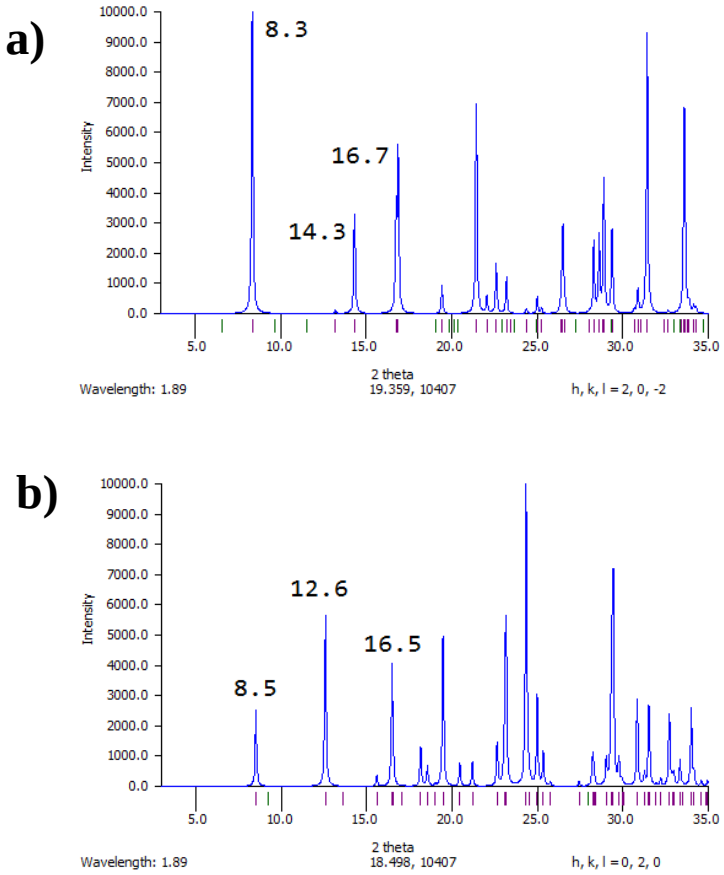

Figure 5.21. *Calculated powder pattern with λ = 1.89 Å of form A (a) and form B (b).*

The first three characteristic peaks of form A are positioned at ~8.3˚, ~14.3˚, and ~16.7˚.

The same procedure done for the sample of pure d6-ethanol was followed for a few millilitres of solution (cyprodinil in d6-ethanol). Unfortunately, no crystallisation of form A was observed, even during evaporation of the solvent. Another attempt was made by preparing a d6-ethanol solution saturated in cyprodinil at 50˚C. This solution was transferred on D20 and data collection was started. The results are reported in Figure 5.22.

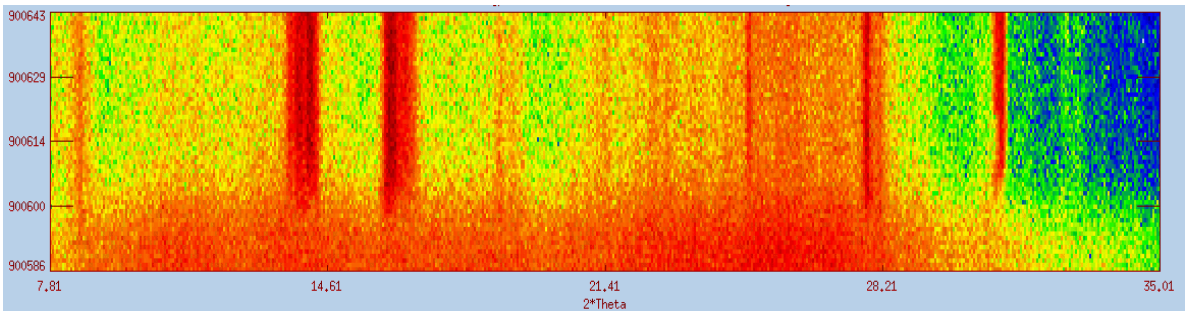

Figure 5.22. *Powder pattern of form A crystallised* ***in situ*** *from solution.*

By comparing the positions of the first three Bragg's peaks, at ~8.5˚, ~14.2˚, and ~16.5˚, with the calculated values, it is possible to identify the sample as form A of cyprodinil. The crystallisation

of form A occurred without any application of external heating. Other than confirming the crystallisation of the stable form from solution, this experiment proved that powder neutron diffraction can be applied for *in situ* studies.

5.1.3.1.2. Variable temperature studies

In order to assess any variations in the crystal structure and in the hydrogen bonding network as a function of temperature, a variable temperature (VT) experiment was done on a sample of modification A of Cyprodinil. A vanadium can (7 mm in diameter) was filled with the sample and placed inside a cryofurnace on D20. Data were collected continuously in ten-minute blocks during cooling from 298K to 130K with a rate of 0.3K/min. When the temperature of 130K was reached, a three-hour long scan was recorded in order to have a reliable model suitable for the refinement.
Thanks to the program LAMP it is possible to observe all collected data sets into one plot so that any change in the powder patterns is immediately visible. In Figure 5.23 data collected upon cooling are reported.

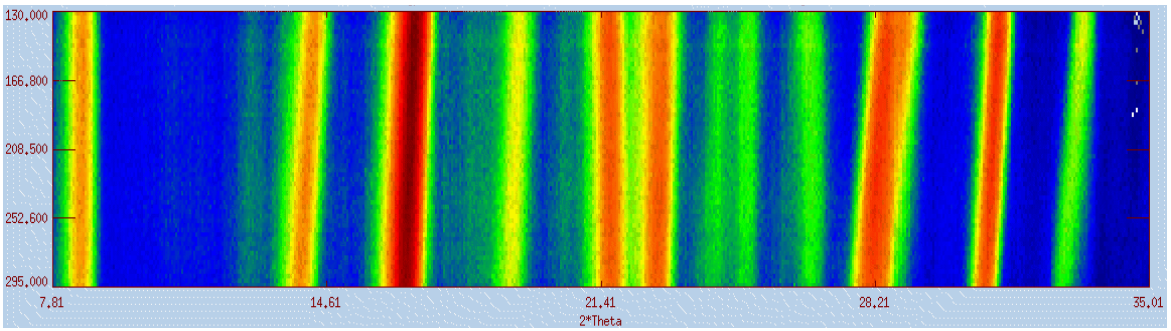

Figure 5.23. *Powder patterns of form A collected on D20 upon cooling from 298K to 130K.*

The same crystal structure is retained during the cooling process; the shift of some peaks toward higher 2θ angles indicates the reduction of the unit cell as a result of the decreased temperature.
The structural refinement was done using SEQGSAS available in the GSAS package. SEQGSAS allows automatic Rietveld refinement on a series of sequential powder data sets, provided that there are no major changes in the structure, such as phase transition or change of symmetry. Obviously, the first refinement must be done manually, but then the routine can replicate the refinement for all sets of data, using the last refinement as a starting model for the next. The long scan collected at 130K was manually refined and used as starting point for the sequential refinement. In Figure 5.24 the final fit for the structure at 130K between observed and calculated data is reported.

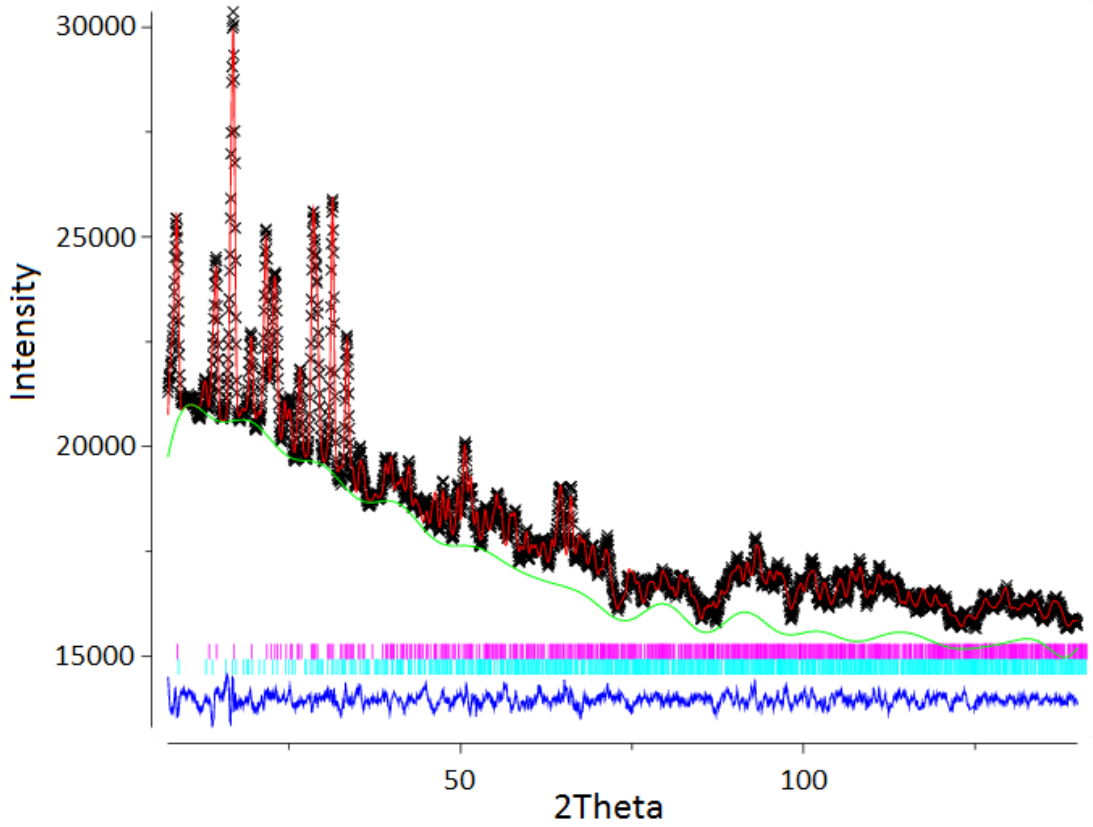

Figure 5.24. *Fit of the powder pattern at 130K: background (green); observed data (crosses); calculated data (red); difference between observed and calculated data (blue); Bragg's peaks for form A (magenta); Bragg's peaks for form B (light blue).*

The refinement pointed out that the sample was not pure form A, but traces of form B were also present. The profiles for the two forms were refined with different scaling factors.

Since data were collected upon cooling and the first refinement referred to the structure at 130K, the data sets were refined in reverse order. In Figures 5.25, 5.26, 5.27, and 5.28 the VT plost for the unit cell parameters are reported.

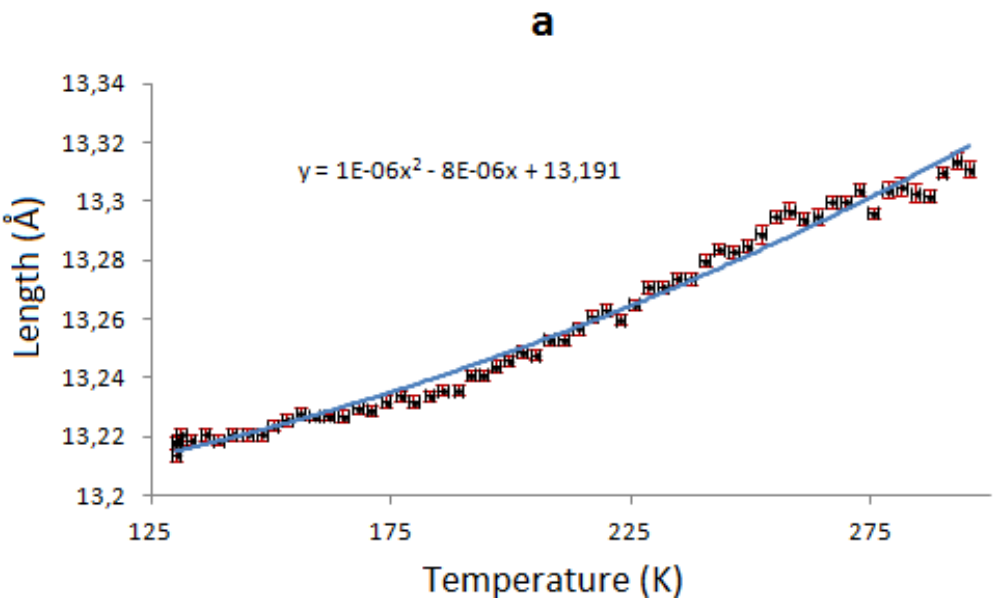

Figure 5.25. *Evolution of the unit cell parameter* ***a*** *of form A as a function of temperature. The error bars are shown in red and the trendline equation is displayed on the chart.*

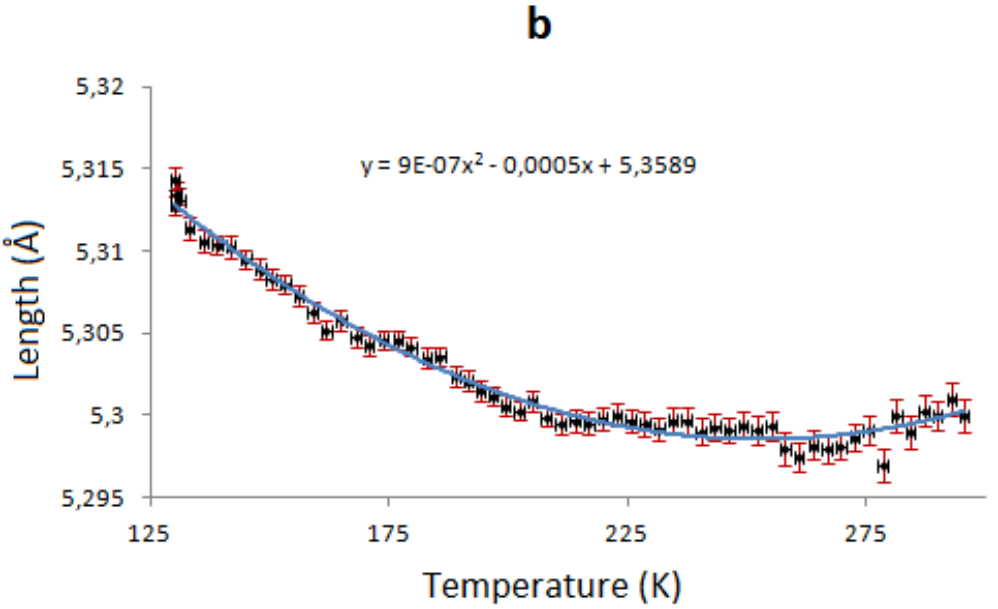

Figure 5.26. *Evolution of the unit cell parameter* ***b*** *of form A as a function of temperature. The error bars are shown in red and the trendline equation is displayed on the chart.*

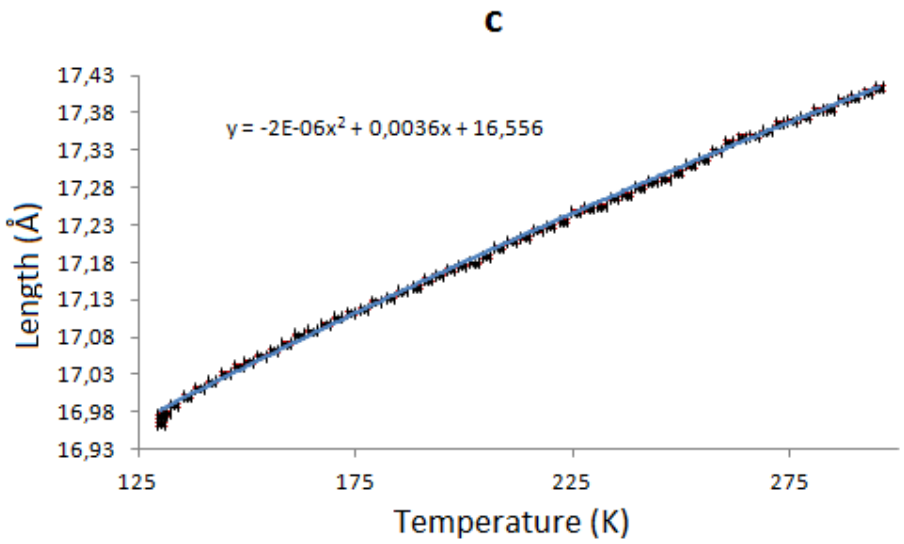

Figure 5.27. *Evolution of the unit cell parameter* ***c*** *of form A as a function of temperature. The error bars are shown in red and the trendline equation is displayed on the chart.*

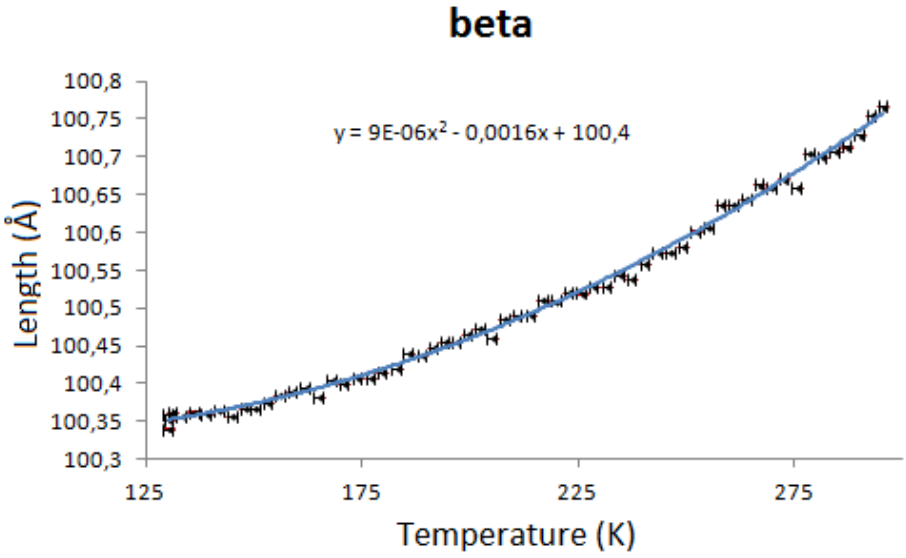

Figure 5.28. *Evolution of the unit cell parameter* ***β*** *of form A as a function of temperature. The error bars are shown in red and the trendline equation is displayed on the chart.*

The cooling process shows the usual shrinking of all unit cell parameters except the ***b***-axis, which slightly increased its length during cooling.

This VT experiment allowed also the investigation of the hydrogen bonding structure as a function of temperature. However, it is important to remember that it was not possible to refine the atomic positions of the hydrogen atoms, because the refinement was very unstable. However, an evaluation of the behaviour of the hydrogen bond can be made considering variations in the donor-acceptor distance, N1···N3, as a function of temperature, as shown in Figures 5.29

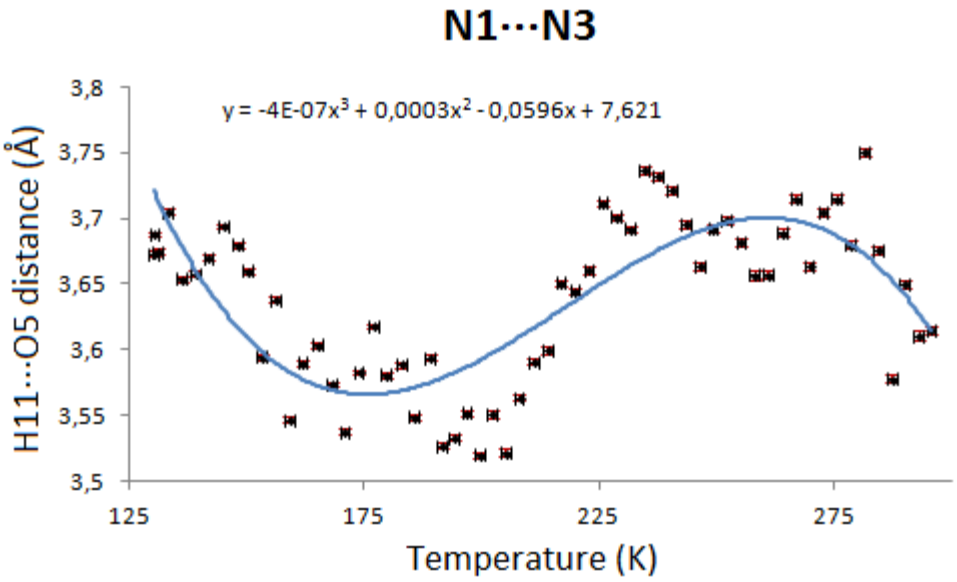

Figure 5.29. *Evolution of the interatomic distance N1···N3 as a function of temperature. The error bars are shown in red and the trendline equation is displayed on the chart.*

The evolution of the donor-acceptor interatomic distance does not follow the smooth increase with temperature showed by the unit cell parameters a, c, and β, but it varies continuously: an initial decrease until 175K is followed by an increase of the relative position of the two interacting molecules of cyprodinil.

Another PND experiment was done on a sample of modification A of cyprodinil to monitor the phase transition to the metastable form B. Data were collected in 2-minute blocks heating from room temperature to 360K and during cooling back to 330K, with a rate of 0.5K/min. The results are reported in Figure 5.30.

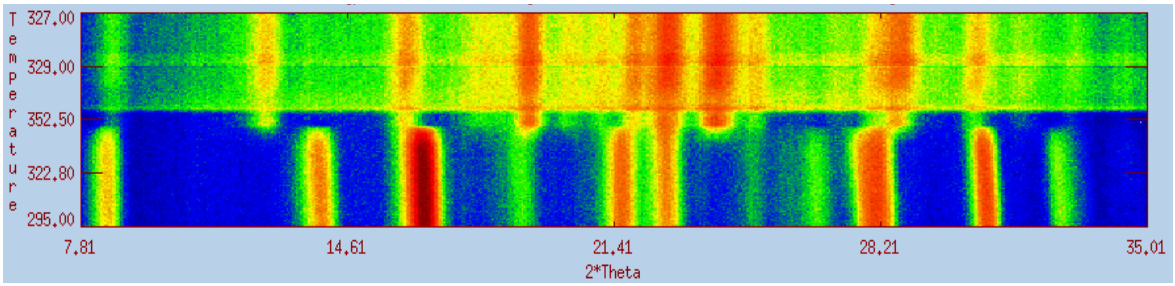

Figure 5.30. *Powder patterns collected on a sample of form A heating from 295K to 360K and cooling back to 330K.*

PND confirms what was found by the DSC (Figure 5.4): the phase transition occurs soon after reaching the temperature of fusion of form A and form B crystallises. However, it is interesting to notice that the powder patterns do not shown an amorphous signal at the melting point of form A, indicating that the conversion happens in the solid state.

5.1.3.2. Polymorph B

The asymmetric unit in the modification B is formed by two molecules of cyprodinil, as showed in Figures 5.31 and 5.32 from the X-ray results.

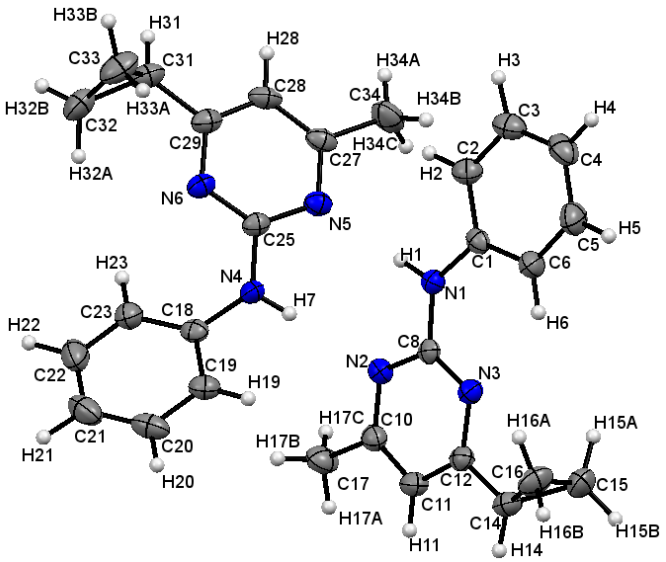

Figure 5.31. *ORTEP representation of the asymmetric unit in modification B of cyprodinil, derived from single crystal X-ray diffraction. The probability level for all non-hydrogen ellipsoids is 50%, while the hydrogen atoms are drawn as fixed-size spheres of radius 0.15 Å.*

.

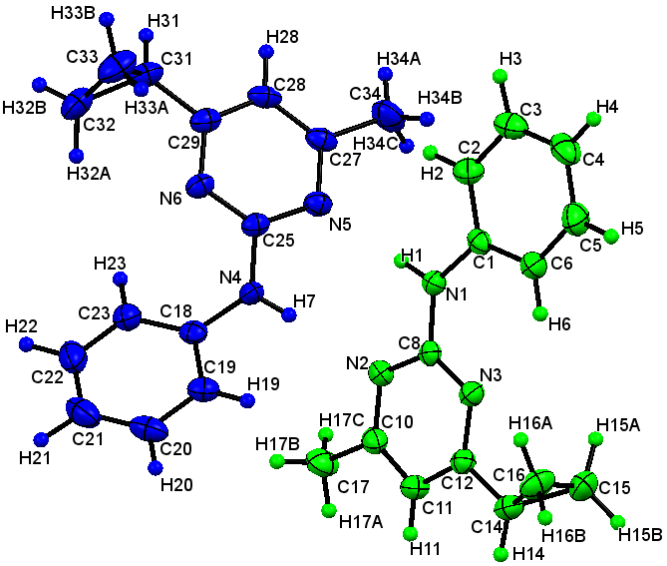

Figure 5.32. *Asymmetric unit in modification B of cyprodinil: the molecules are displayed in different colours, in order to easily discriminate between the two.*

Green molecule	
C8-N1-C1-C6	2.1(3)˚
N3-C12-C14-C15	-39.9(2)˚
N3-C12-C14-C16	28.4(2)˚
C8-N1-C10-C15	-179.6(2)˚
N2-C8-N1-H1	-2(1)˚
Blue molecule	
C25-N4-C18-C23	30.5(3)˚
N6-C29-C31-C32	-13.5(3)˚
N6-C29-C31-C33	55.5(2)˚
C25-N6-C29-C31	-178.3(1)˚
N5-C25-N4-H7	-1(1)˚

Table 5.13. *Torsion angles of interest. The colours refer to Figure 5.32.*

The two molecules of cyprodinil lie almost perpendicular to one another, forming a fishbone motif in the crystal packing.

It is possible to notice several differences between the two molecules. As can be seen in Table 5.13, there is a significant difference in the orientation of the benzene ring in respect to the plane formed by the aminopyrimidine part: in the green molecule (Figure 5.32), the benzene and the pyrimidine rings are almost co-planar, with a torsion angle C8-N1-C1-C6 of 2.1(3)˚, while the comparative torsion angle in the blue molecule, C25-N4-C18-C23, has a value of 30.5(3)˚. Also the cyclopropyl substituent is placed differently in the molecules: almost centred in respect to the pyrimidine ring in the green molecule, while in the blue one it is placed under the plane of the pyrimidine ring, due to the presence of the methyl group of a non-interacting neighbouring molecule of cyprodinil.

As for modification A, the molecules of cyprodinil in form B arrange themselves in off-set parallel lines, allowing the formation of π-π interactions, with distance between centroids of the pyrimidine and the benzene rings of 4.28(3) Å, and hydrogen bonds. In this case, the geometry of the hydrogen bonding network highly differs from the one in form A (Figure 5.33).

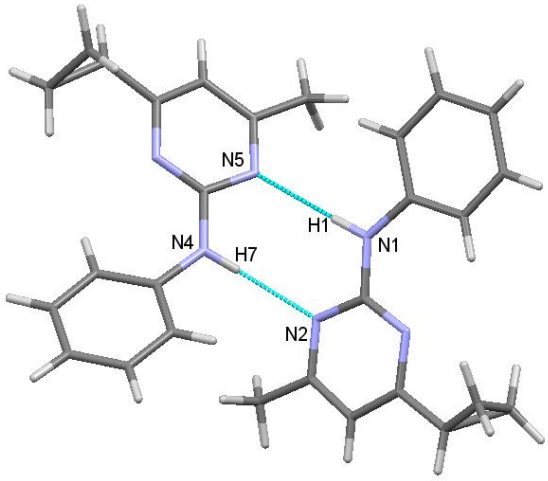

Figure 5.33. *Hydrogen bonding network in modification B of cyprodinil.*

The hydrogen bonding network is constituted by the formation of two hydrogen bonds between two molecules, involving the hydrogen atom of the amino group of one molecule and the nitrogen atom of the pyrimidine ring of an adjacent molecule. This geometry of interaction leads to an 8-membered ring, stronger than a simple linear hydrogen bond, which can justify the higher melting point of form B compared to form A. In Table 5.14, hydrogen bond distances and angles of interaction are reported. The hydrogen bonds are shorter and more linear than those present in the modification A.

N1-H1	0.92(2) Å
H1···N5	2.21(2) Å
N1···N5	3.124(2) Å
N1-H1···N5	174(1)˚
N4-H7	0.86(2) Å
H7···N2	2.12(2) Å
N4···N2	2.976(2) Å
N4-H7···N2	172(1)˚

Table 5.14. *Hydrogen bond lengths and geometry for a crystal of modification B of cyprodinil, studied X-ray radiation.*

Since a good starting model was need for the powder neutron diffraction experiment, data collection on the crystal of form B lasted for four days at 30K, leading to excellent results. In Table 5.15 the unit cell parameters of form B at 295K and 30K are reported. It is possible to notice a slight reduction of the unit cell dimensions and a small increase in the value of the angle β.

	Form B	
Temperature	295K	30K
a	8.250(3) Å	7.9829(1) Å
b	11.900(4) Å	11.7199(2) Å
c	12.891(5) Å	12.7435(2) Å
β	92.66(2)˚	93.842(1)˚
Space Group	P 2_1	P 2_1

Table 5.15. *Unit cell parameters for the crystal structure of form B, derived from neutron diffraction.*

As for the case of form A, investigation of the nature and characteristics of the hydrogen bonding network can be achieved thanks to the intrinsic properties of neutrons. Figure 5.34 shows the molecules of cyprodinil, displaying the anisotropic ADPs for all atoms, while in Figure 5.35 both electron-density and nucleon-density maps are reported.

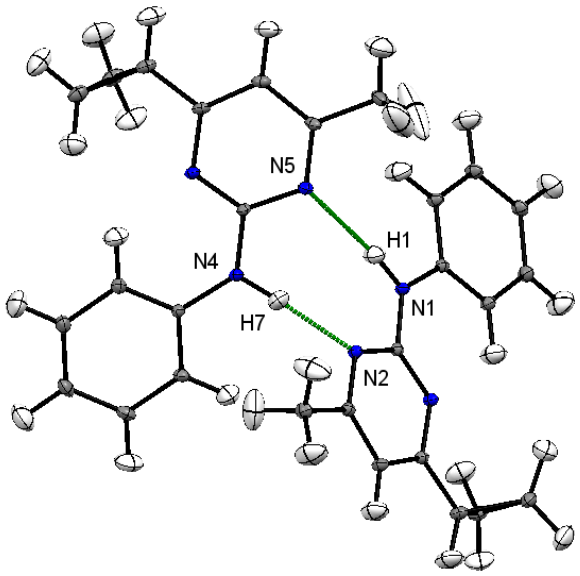

Figure 5.34. *ORTEP representation of the molecules of xyprodinil in the form B.*

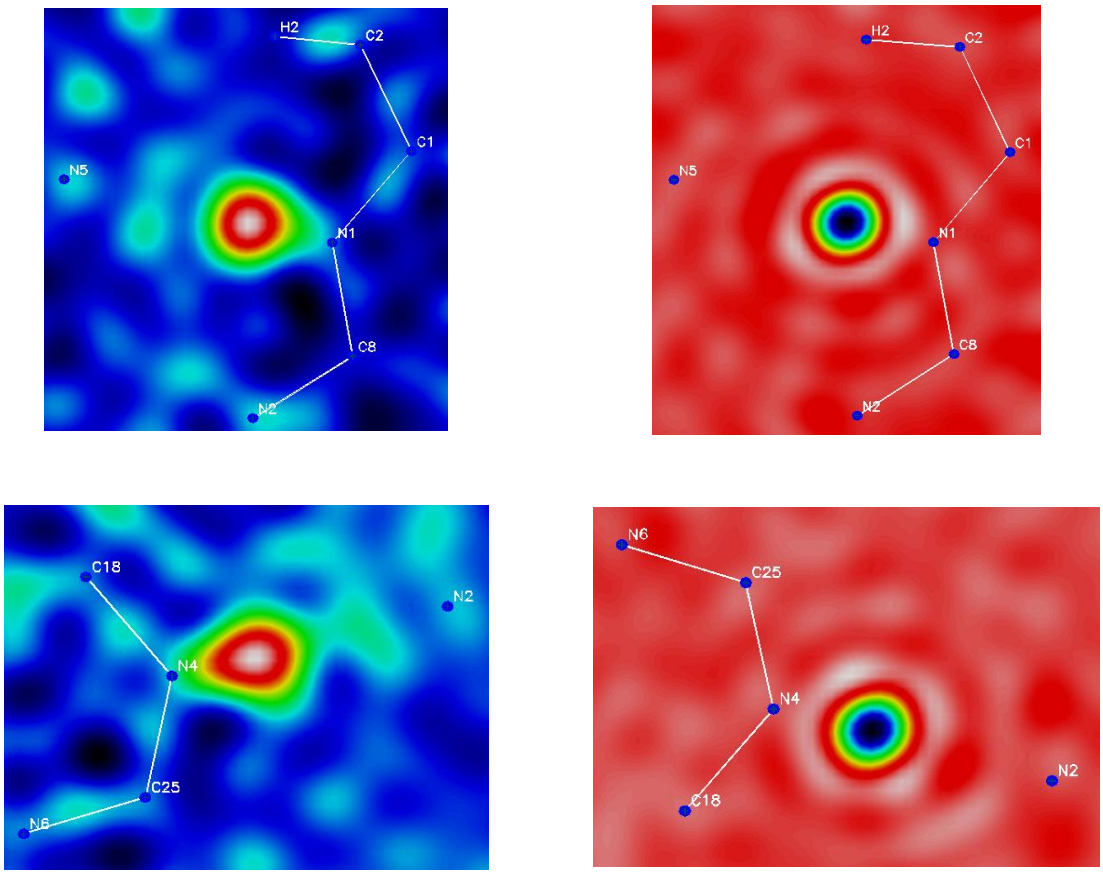

Figure 5.35. *Electron-density maps (on the left) and nucleon-density maps (on the right) for the the circular hydrogen bond, N1-H1···N5 and N4-H7···N2.*

The crystal structure of modification B of cyprodinil does not show proton migration or disorder. The thermal ellipsoids of the hydrogen atoms involved in the hydrogen bonds are elongated along the direction normal to the intermolecular interactions. In this case, the difference in the sizes of the ADPs between the hydrogen atoms of the methyl groups and H1 and H7 is more pronounced than in form A. In Table 5.16 a comparison of the hydrogen bond lengths and geometries between the two polymorphs of cyprodinil are reported.

Form A		Form B			
N1-H6	1.012(3) Å	N1-H1	1.024(3) Å	N4-H7	1.026(3) Å
H6···N3	2.526(3) Å	H1···N5	2.089(3) Å	H7···N2	1.929(3) Å
N1···N3	3.502(1) Å	N1···N5	3.101(1) Å	N4···N2	2.953(1) Å
N1-H6···N3	162.0(3)˚	N1-H1···N5	169.6(2)˚	N4-H7···N2	176.4(2)˚

Table 5.16. *Hydrogen bond lengths and geometry for both forms of cyprodinil, derived from neutron diffraction.*

By the summary reported in Table 5.16, it may be speculated that form B is the more stable form both for hydrogen bond lengths, whose values are smaller than in form A, and for the angles of interaction, which are more linear in form B. Moreover, it is well known that a hydrogen bond formed by an 8-membered ring is more stable than a simple linear one. However, the literature and the calculations made by C. Hendon both state that form A is the stable form and form B the metastable one. An explanation can be found in the geometry of interaction between two molecules of cyprodinil in form B: the interacting molecules do not display the planar conformation that is usually observed in dimers, but they are highly twisted, as shown in Figure 5.36, forming an angle of ~59°, which may contribute to destabilise the structure. Additionally, this twisted arrangement causes a weakening of the π-π interactions, whose distances pass from 3.87(2) Å in form A to 4.28(3) Å in form B.

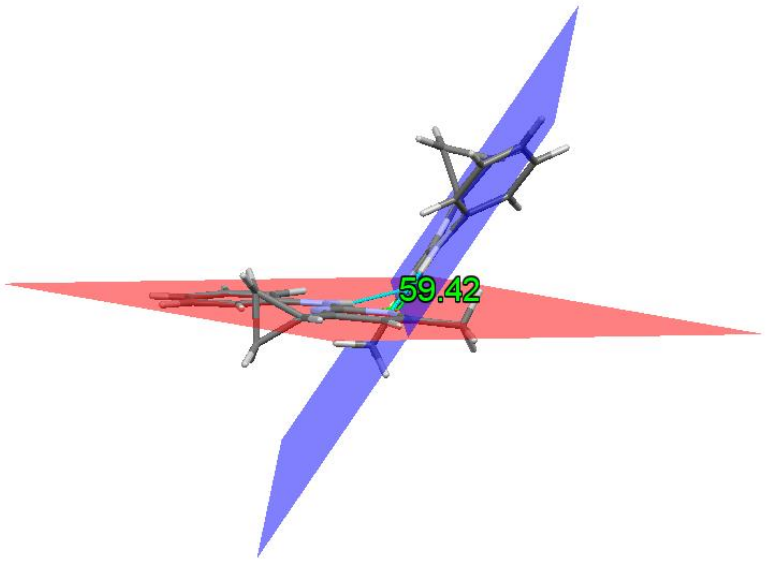

Figure 5.36. *Geometry of interaction between two molecules of cyprodinil in form B. Each molecule lies on a different coloured plane.*

5.1.3.2.1. Variable temperature studies

VT experiments were done also on modification B of cyprodinil. A vanadium can (9 mm in diameter) was filled with the sample and placed in a cryofurnace on D20. Before starting the experiment the temperature was set to 130K. After recording a one-hour long scan at 130K, data were collected in 15-minute blocks while slowly heating from 130K to 330K at a rate of 0.5K/min. The results of this data collection are reported in Figure 5.37.

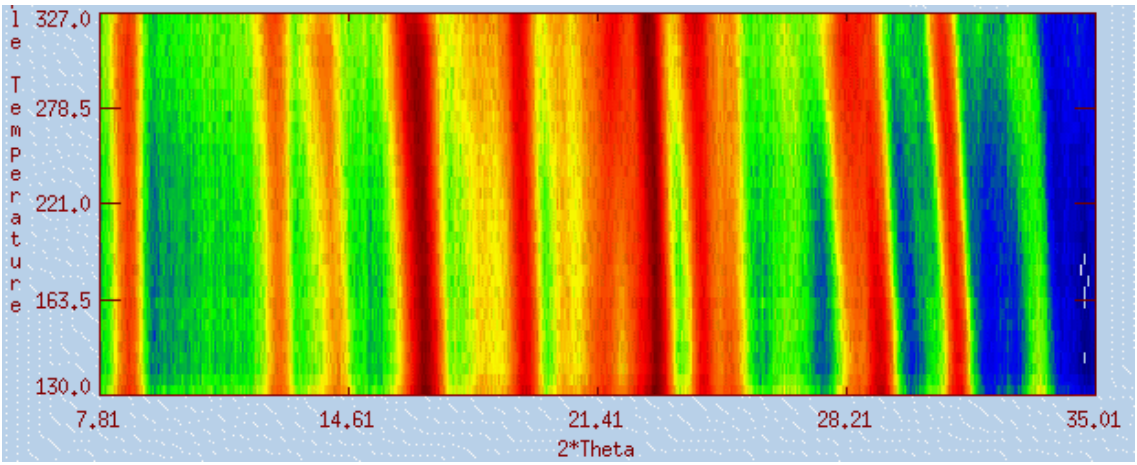

Figure 5.37. *Powder patterns of form B collected on D20 while heating from 130K to 330K.*

As for form A, no significant changes happened to the crystal structure with the increase in temperature. It is, anyway, possible to notice an expansion of the unit cell, as indicated by the shift of the Bragg's reflections towards lower values of 2θ.

The structural refinement of all data sets was done using SEQGSAS, starting with the manually refined structure at 130K. In Figure 5.38 the final fitted profile of the powder pattern at 130K of form B is reported.

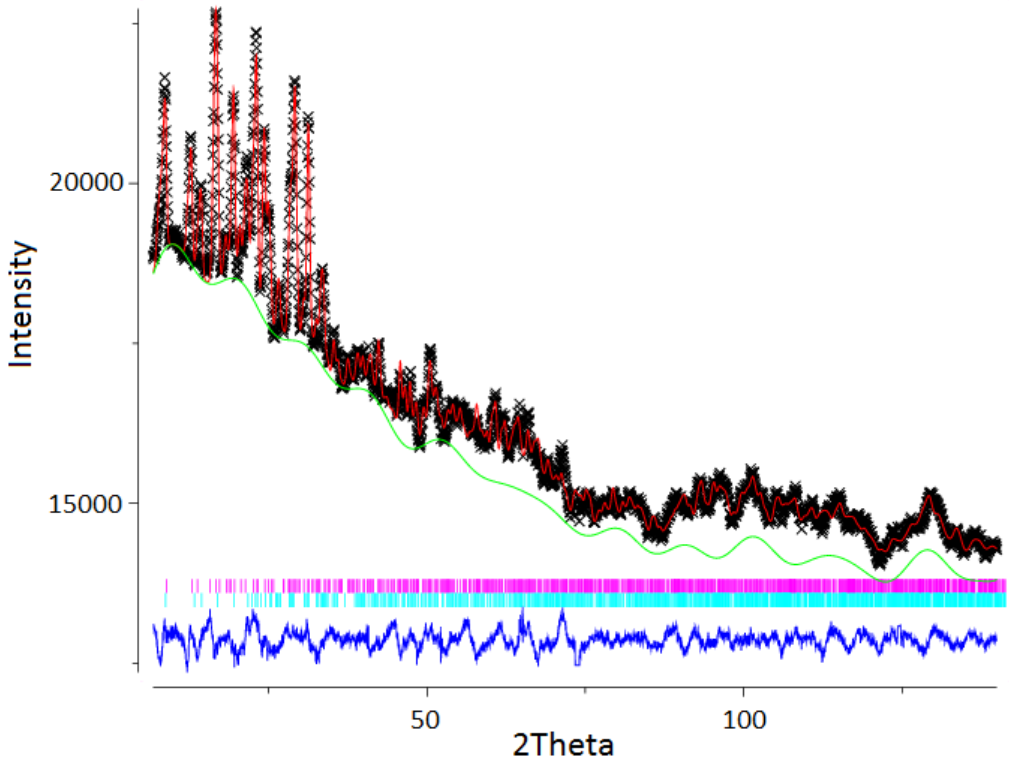

Figure 5.38. *Fitted profile for the powder pattern of modification B at 130K : background (green); observed data (crosses); calculated data (red); difference between observed and calculated data (blue); Bragg's peaks of form B (magenta); Bragg's peaks of form A (light blue).*

The sample of form B was not pure: the peak at ~14.3° belongs clearly to form A. It is, however, unclear whether the contamination was already present in the sample or if a phase transition to the stable form occurred. During data treatment, the two phases were refined with different scaling factors. In Figures 5.39, 5.40, 5.41, and 5.42 the changes of the unit cell parameters during heating are reported.

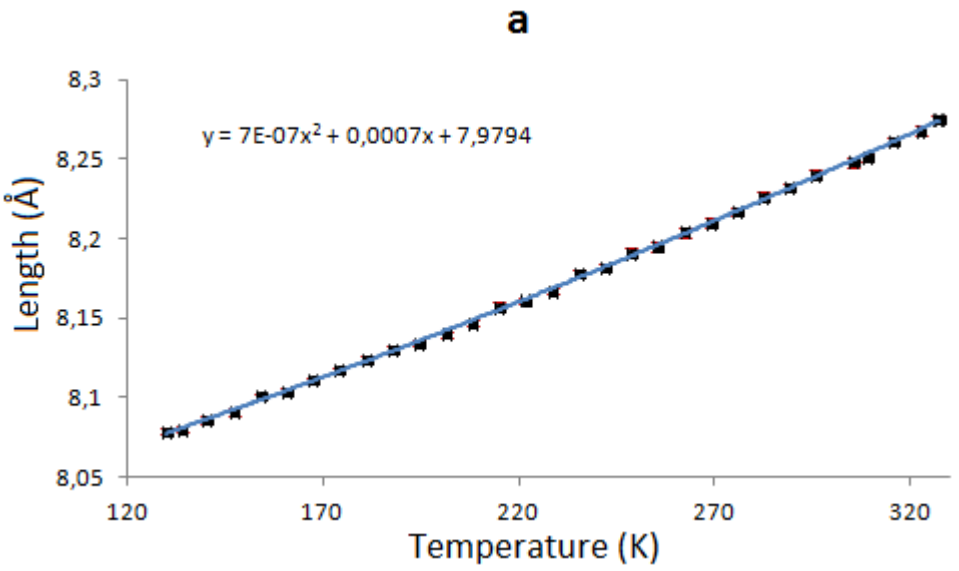

Figure 5.39. *Evolution of the unit cell parameter* ***a*** *of form B as a function of temperature. The error bars are shown in red and the trendline equation is displayed on the chart.*

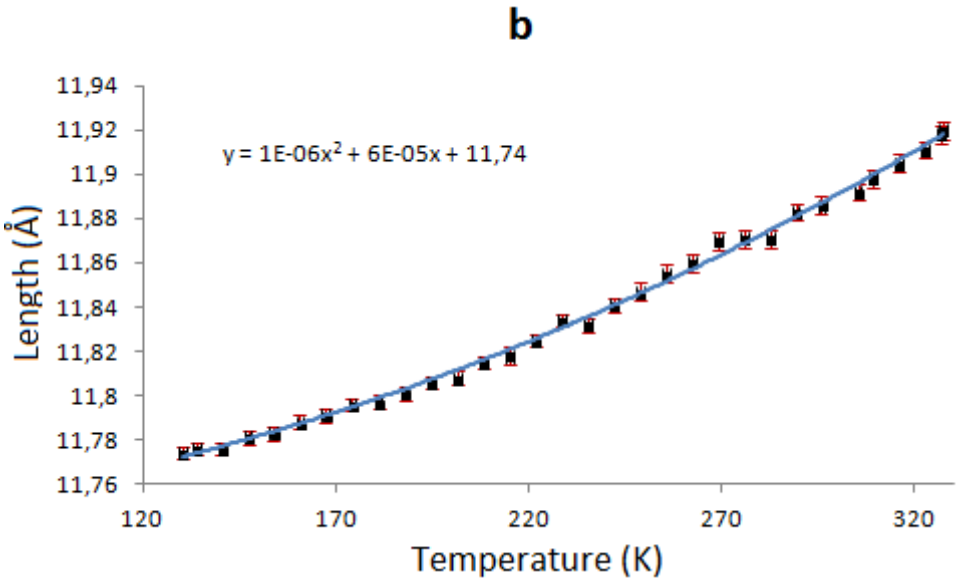

Figure 5.40. *Evolution of the unit cell parameter* ***b*** *of form B as a function of temperature. The error bars are shown in red and the trendline equation is displayed on the chart.*

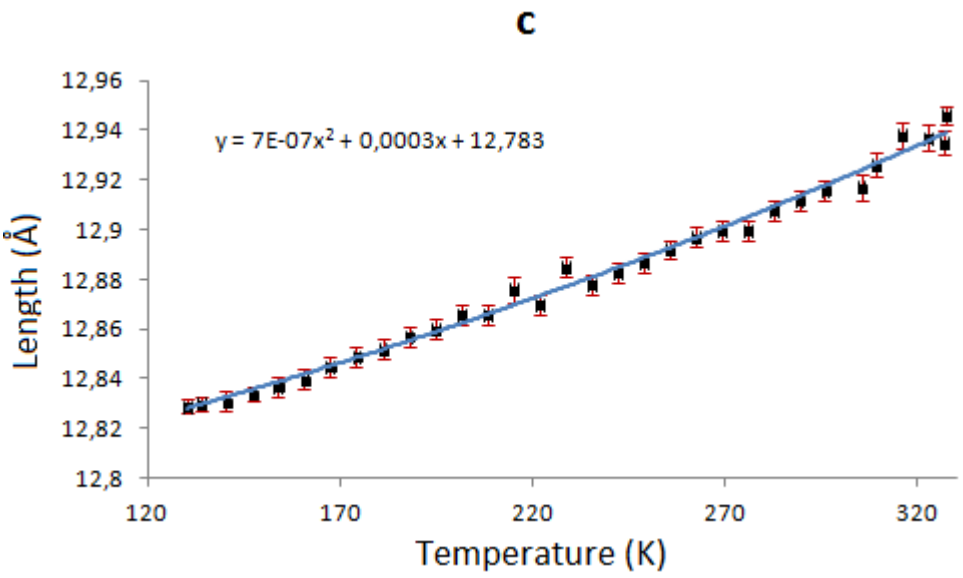

Figure 5.41. *Evolution of the unit cell parameter* ***c*** *of form B as a function of temperature. The error bars are shown in red and the trendline equation is displayed on the chart.*

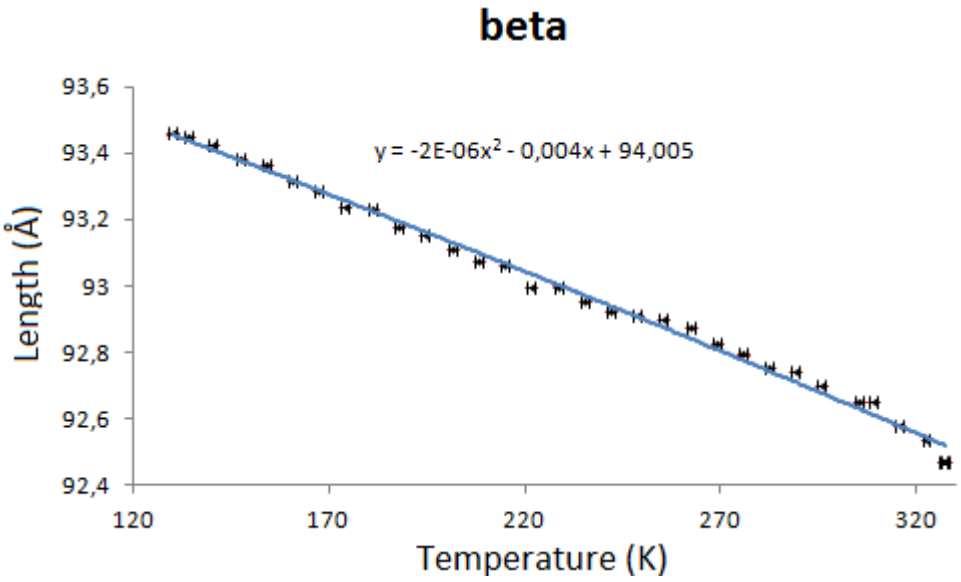

Figure 5.42. *Evolution of the unit cell parameter* ***β*** *of form B as a function of temperature. The error bars are shown in red and the trendline equation is displayed on the chart.*

The three unit cell axes, ***a***, ***b*** and ***c***, show a smooth expansion with increasing temperature, while the value of the angle ***β*** decreases of almost 1°. This behaviour is in accordance with the SND results: ~92.6° at room temperature opposed to ~93.8° at 30K.

As for the case of modification A, it was not possible to refine the coordinates of the hydrogen atoms, due to high instability of the refinement cycles. However, changes in the donor-acceptor distances for the two hydrogen bonds, N1···N5 and N4···N2, reported in Figures 5.43 and 5.44,

respectively, are an indication of the behaviour of the hydrogen bond in the crystal structure of form B.

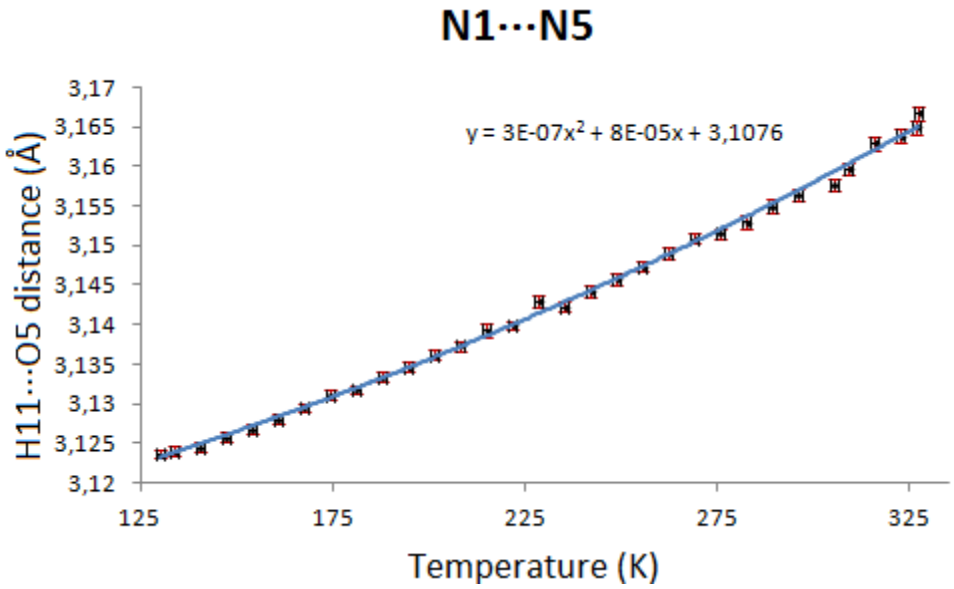

Figure 5.43. *Evolution of the donor-acceptor distance, N1···N5, as a function of temperature. The error bars are shown in red and the trendline equation is displayed on the chart.*

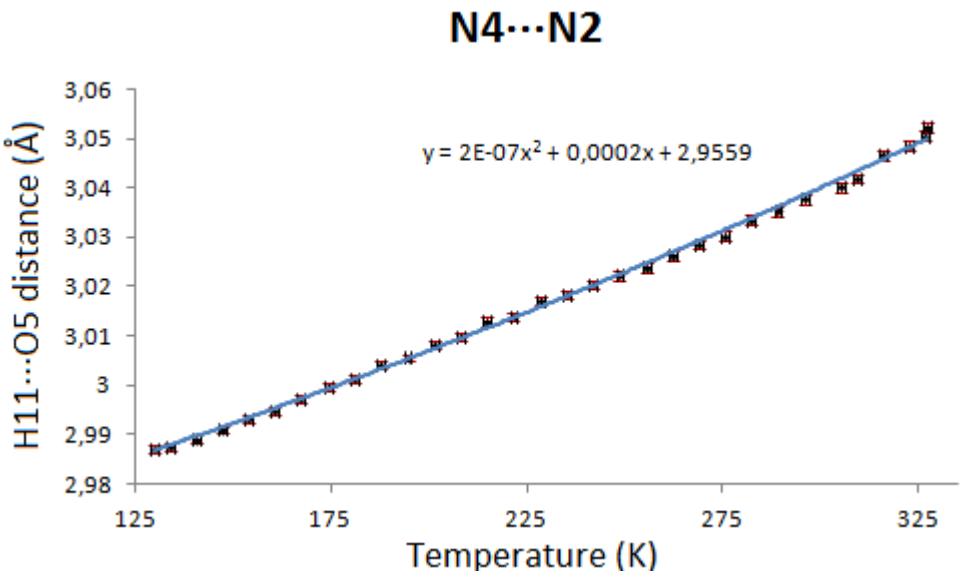

Figure 5.44. *Evolution of the donor-acceptor distance, N4···N2, as a function of temperature. The error bars are shown in red and the trendline equation is displayed on the chart.*

As shown in the figures above, the distance between two interacting molecules increases smoothly with increasing temperature, suggesting that each cyprodinil molecule slightly moves away from its neighbour. However, it is important to underline that the exact positions of the hydrogen atoms inside these hydrogen bonds cannot be known due to the lack of refined proton coordinates.

PND was also used on a sample of form B to corroborate the hypothesis of a phase transition temperature around 28˚C, as found by the DSC analysis (Figure 5.5). Data were collected on a sample of form B in 2-minute blocks from 330K to 358K and during cooling to 283K with a rate of 0.5 K/min. As shown in Figure 5.45, it is not possible to notice any phase transition.

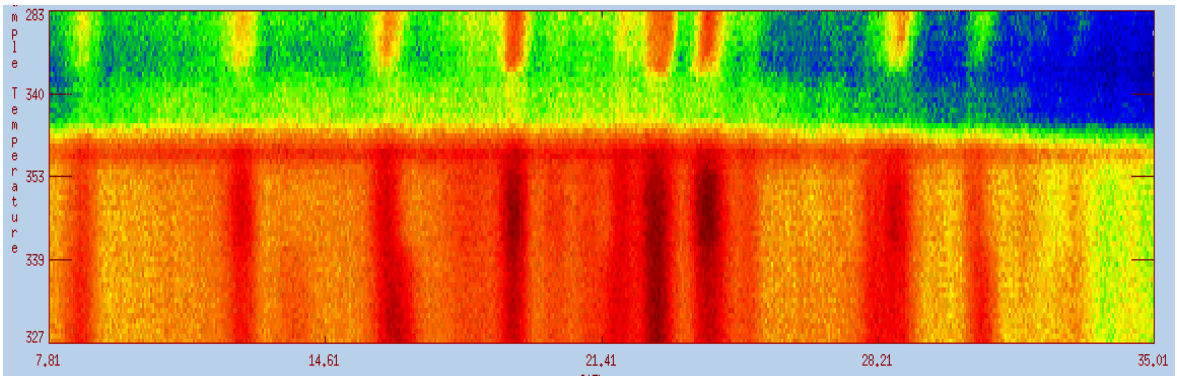

Figure 5.45. *Powder pattern of form B collected in a temperature cycle: from 330K to 358K to 283K.*

Form B reaches the fusion temperature, but on cooling the form that crystallises is still form B. This result nullifies the hypothesis of a transition temperature of ~28˚C: most likely, the thermal event recorded by the DSC upon cooling corresponds to the re-crystallisation of form B and the difference between the two re-crystallisation temperatures, ~40˚C observed from the PND data opposed to ~28˚C detected by the DSC analysis, is probably due to the different rate of cooling used in the two measurements.

5.1.4. Conclusions

The fungicide cyprodinil can crystallise in two different crystal structures: form A and form B. Form A is the thermodynamically stable form, while form B is the metastable one. The two polymorphs are enantiotropically related, which indicates that the conversion between the two forms occurs without leaving the solid state. The phenomenon of polymorphism in cypronidil represents a problem from a practical point of view: the spontaneous conversion between forms can cause the formation of particle aggregates, which in turn can obstruct the nozzle of spraying equipments used for the application of the product on the crop field.

Crystals of form A can be easily grown from solution, using a large variety of organic solvent from acetone to toluene to alcohols. Their crystal habit is similar to a long, thin, transparent needle. On the contrary, form B can be obtained from solidification of the molten form A and it is possible to grow crystals by sublimation. It is, however, interesting to notice that form B can crystallise from

solution thanks to the crystalline memory effect: some clusters will retain the crystal structure, acting as seed for the nucleation of modification B, provided that no heat is applied.

The crystal structures of the two polymorphs were analysed by both X-ray and neutron single crystal diffraction. They differ from one another because of a different hydrogen bonding network: a linear hydrogen bond, N1-H6···N3 = 2.526(3) Å, for form A, while form B exhibit a chelate hydrogen bond between two molecules of cyprodinil, leading to the formation of a 8-membered ring, with N1-H1···N3 = 2.089(3) Å and N4-H7···N2 = 1.929(3) Å.

Variable temperature studies on both polymorphs of cyprodinil show that the same crystal structure is retained during cooling to low temperature and upon heating near the fusion temperature of each form. Unfortunately, the high hydrogen content of the cyprodinil samples did not allow to refine the coordinates of the hydrogen atoms, preventing to reach a more in depth investigation of the hydrogen bond in this material and of the differences between the two polymorphs. The difficulties in the refinement of the hydrogen atom positions are due to the incoherent scattering of hydrogen, which highly contributes to increasing the background, destabilising the structural refinement. However, hypothesis on the changes of the crystal packing of the two forms can be made considering the variations that the carbon structure of cyprodinil undergoes during the heating from 130K to the melting point of the two polymorphs. The behaviour of the unit cell parameters ***b*** in form A and ***β*** in form B can be linked to variation of the hydrogen bonding network in each form. In form A it is possible to notice that the decrease of the ***b***-axis is accompanied by an initial decrease of the donor-acceptor distance, N1···N3, which suggests that the molecules involved in the linear hydrogen bonds move slightly toward one another while the temperature increases. Since the two linear hydrogen bonds that each cyprodinil molecule maintains with other two neighbouring molecules are aligned perpendicular to the ***b***-axis, the shortening of the interatomic distances between molecules causes a compression of the unit cell and a decrease of the value of the cell parameter ***b***. A reverse situation can be observed in the crystal structure of form B. The circular hydrogen bond, which is constituted by two intermolecular interactions, N1-H1···N5 and N4-H7···N2, between two molecules of cyprodinil lies on the plane formed by the ***a*** and the ***c*** axes; the angle between these axes is the angle ***β*** of the unit cell. Due to the hindrance of the cyprodinil molecule, and especially of the cyclopropyl bonded to the pyrimidine ring, a decrease of the value of the ***β***-angle forces the two cyprodinil molecules of the dimer to move away from each other, causing a lengthnening of the donor-acceptor distances, N1···N5 and N4···N2.

The PND experiments also proved that the phase transition from the stable form A to the metastable form B occurs in the solid state, without passing through the melting of form A. However, the heating and cooling cycle done on a sample of form B did not show a transition back to the stable form A, but only re-crystallisation of form B, confirming the possibility of clusters of form B in the melt, acting as seeds for the crystallisation process of the metastable form.

Chapter 6

6. Co-crystals of cyprodinil – Part I

A solution to the practical problem of the spontaneous conversion of cyprodinil from one polymorph to the other during storage can be found in the rational design of molecular complexes, where the presence of a co-former that interact with the active molecule can change the properties and affect the stability of the substance understudy. This field of study is called *crystal engineering*, whose ultimate aim is the design of supramolecular structures, which exhibit specific and desired physical properties, using intermolecular interactions as building blocks, for example intermolecular hydrogen bonds. For this reason, during the course of this thesis, co-crystals of the fungicide cyprodinil were obtained selecting as co-formers those molecules capable of establishing intermolecular hydrogen bonds. In particular, because cyprodinil had already shown the ability to form an intermolecular 8-membered ring interaction in modification B, the choice fell on those compounds with functional groups exhibiting a bidentate coordination.

6.1. Cyprodinil / 2-aminopyrimidine co-crystal

6.1.1. Introduction

Since the molecule of cyprodinil is an aminopyrimidine derivative, the first co-former to be chosen for the process of co-crystallisation was the molecule of 2-aminopyrimidine. The attempt to design this co-crystal had already been made[99]. However, the only available information on this complex was an X-ray powder diffraction pattern without further details on the crystal structure. In order to have a deeper understanding of the characteristics and nature of the intermolecular interactions in cyprodinil and their effect on the stability of the compound, the adduct cyprodinil/2-aminopyrimidine was synthesised and the crystal structure was solved by single crystal X-ray diffraction.

2-aminopyrimidine crystallises in the orthorhombic system, space group ***Pbca***, and it displays a single molecule in the asymmetric unit. The crystal packing of this material, which is shown in Figure 6.1, is governed by the formation of dimers, held together by circular hydrogen bonds between the hydrogen atom on the amino group of one molecule and the nitrogen atom on the pyrimidine ring of a neighbouring molecule. The dimers organise into alternate lines, forming a herring-bone motif.

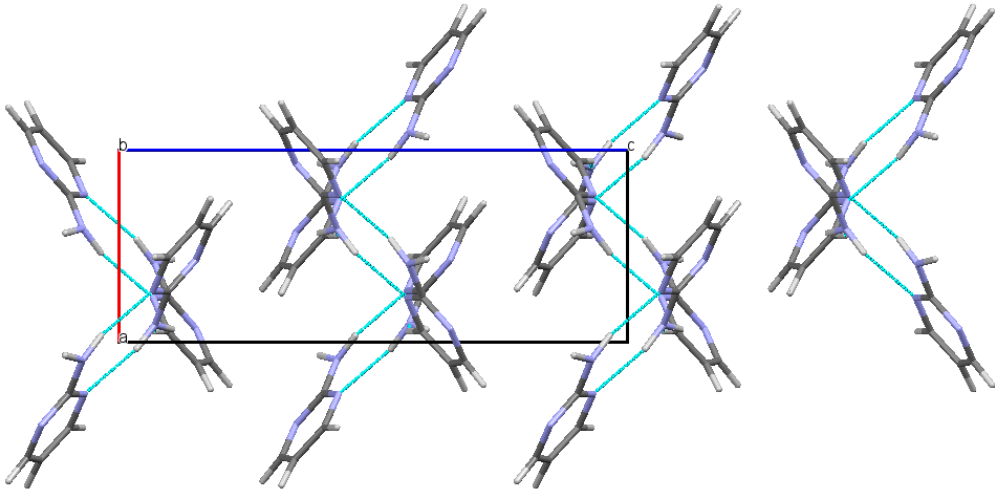

Figure 6.1. *Crystal packing of the 2-aminopyimidine molecules, viewed along the* ***b****-axis.*

6.1.2. Experimental

6.1.2.1. Synthesis from solution

In order to obtain high-quality crystals suitable for single crystal X-ray diffraction, the synthesis of the co-crystal was done from solution. The first solvent to be chosen was ethanol, due to the good solubility of the two materials in it. In Table 6.1 the quantities of each substance used to prepare the solution are reported.

Substance	Quantity
Cyprodinil	2.00 g
2-Aminopyrimidine	0.85 g
Ethanol	16 ml

Table 6.1. *Reagents used to synthesise the adduct cyprodinil/2-aminopyrimidine.*

An equimolar ratio, 1:1, of the two compounds was dissolved in ethanol. The solution was heated to 50˚C and kept at that temperature for one hour, while continuously stirring. It was, then, transferred into a small crystallisation vial, which was covered with parafilm. Several small holes were applied to the film cover to allow evaporation of the solvent and crystallisation at room temperature. Once the crystallisation was complete, all crystals were collected and ground into a fine powder with an agate mortar. An X-ray powder diffraction pattern was recorded on the D5000 powder diffractometer. The results are reported in Figure 6.2.

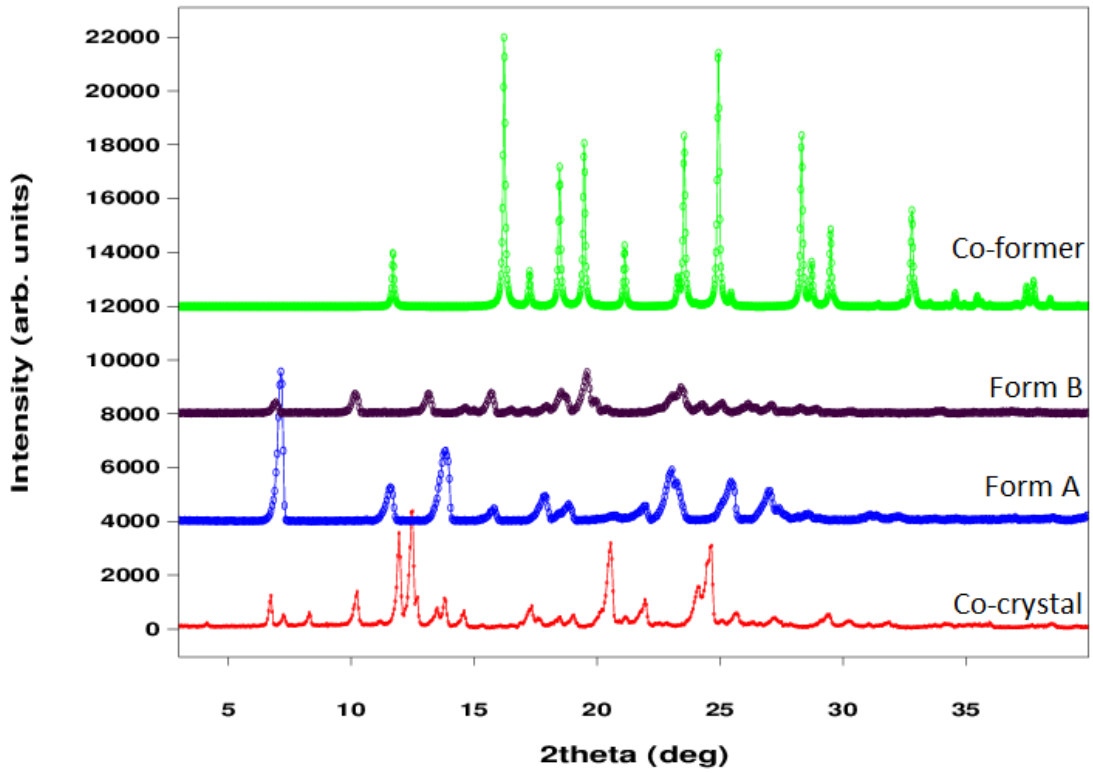

Figure 6.2. *X-ray powder diffraction patterns for the co-crystal cyprodinil/2-aminopyrimidine (in red), 2-aminopyrimidine (in green), polymorph A (in blue), and polymorph B (in black) of cyprodinil.*

The comparison between the powder pattern of the co-crystal and those of the two polymorphs of cyprodinil and the 2-aminopyrimidine indicates that a different crystal structure had formed. It is also interesting to notice that a small amount of modification A of cyprodinil is still present in the sample. In fact, the comparison of the experimental powder pattern of the co-crystal with that of form A and the one calculated from the experimental SXD data collected on a crystal of the adduct, which are reported in Figure 6.3, indicates that the two small peaks at ~ 7˚ and ~ 11˚ in 2θ in the powder pattern of the co-crystal are both ascribable to form A.

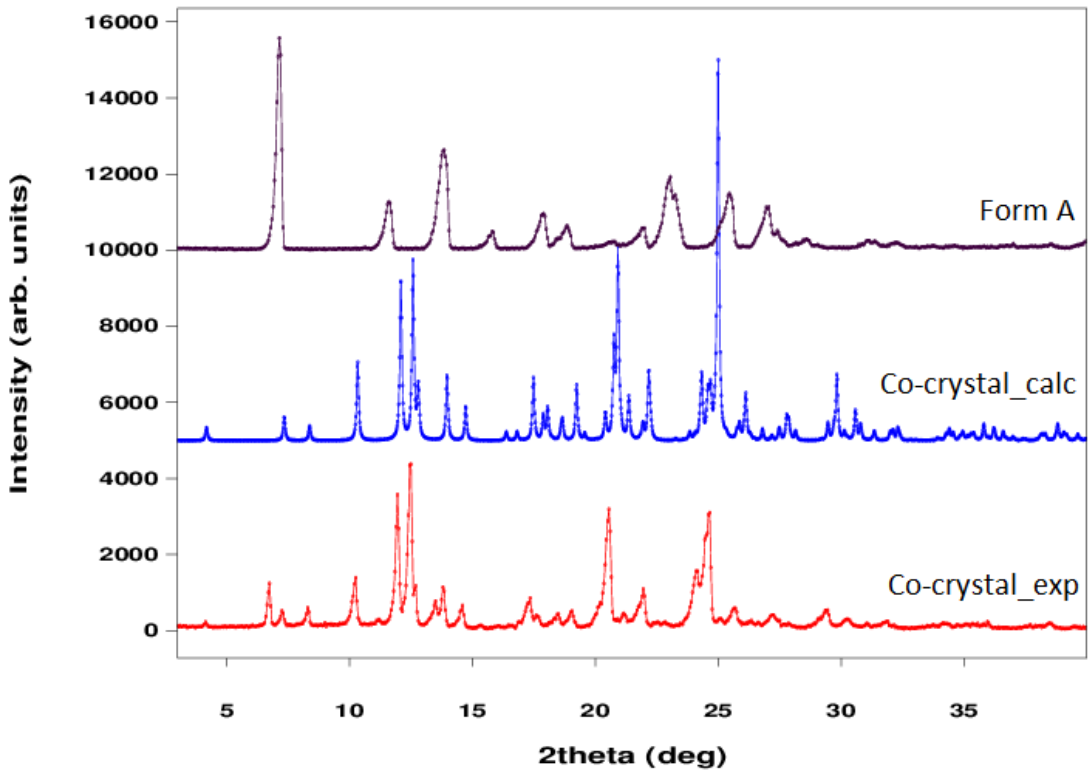

Figure 6.3. *In red, experimental PXD pattern of the co-crystal grown from an ethanol solution; in blue, PXD of the co-crystal that was calculated from the experimental SXD data; in black, experimental PXD pattern of form A of cyprodinil.*

However, the crystallisation from an ethanol solution did not produce crystals of sufficient quality for a single crystal diffraction analysis. For this reason a second solution with the same molar ratio as the previous one was prepared, using methanol as solvent, as shown in Table 6.2.

Substance	Quantity
Cyprodinil	1.0281 g
2-Aminopyrimidine	0.4246 g
Methanol	10 ml

Table 6.2. *Reagents used to synthesise the adduct cyprodinil/2-aminopyriminide.*

The two components were solubilised in methanol at room temperature, until dissolution was complete. The solution was heated at 50˚C and it was kept at the same temperature for an hour, while continuously stirring. It was, finally, transferred into a crystallisation vial covered with parafilm wrap. To allow crystallisation of high-quality crystals, the parafilm cover was left untouched so to slow down the evaporation of the solvent as much as possible. This time fewer crystals crystallised from solution; they were of sufficient quality for a single crystal X-ray diffraction experiment. Due to the low number of crystals produced, it was not possible to collect a

powder diffraction pattern to verify that the same crystal structure had been produced from both ethanol and methanol solutions. For this reason a powder pattern calculated from the single crystal results of the structure formed using methanol as solvent was obtained with the program Mercury[100]. In Figure 6.4 the calculated and experimental powder patterns for the co-crystal are reported.

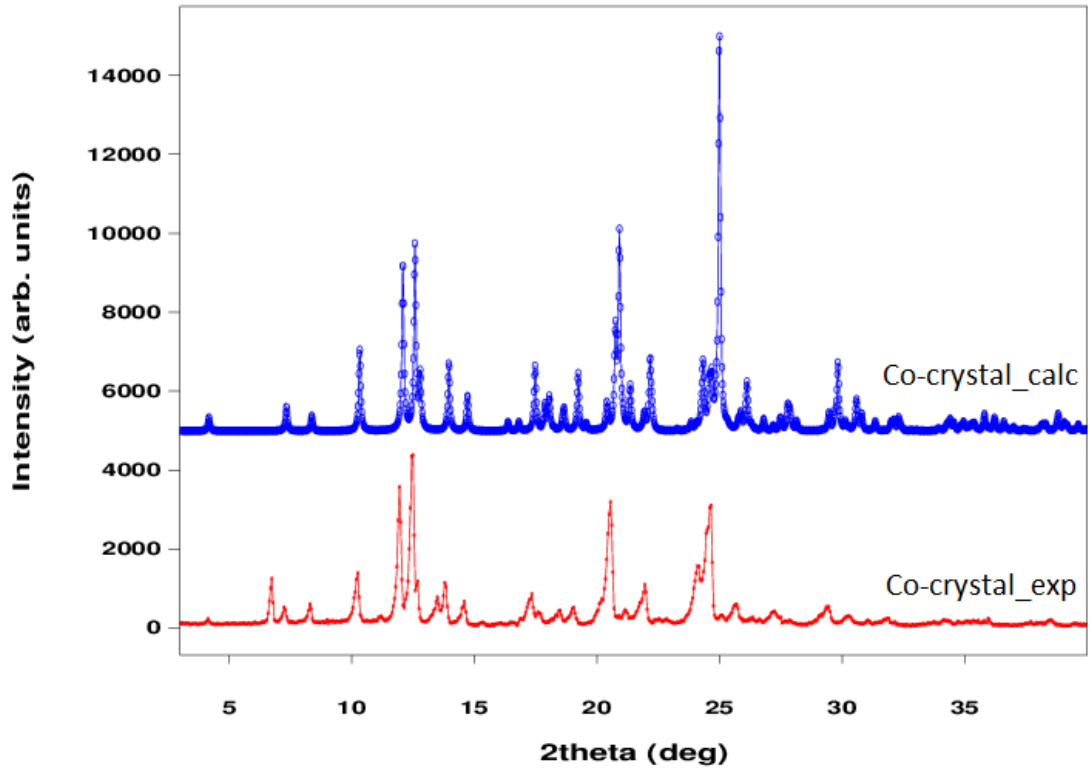

Figure 6.4. *In red, experimental PXD pattern of the co-crystal grown from methanol; in blue, PXD pattern of the co-crystal that was calculated from the experimental single crystal X-ray diffraction results.*

The calculated powder pattern refers to the crystals grown from the methanol solution, while the experimental pattern belongs to the crystals obtained using ethanol as solvent. The positions of the Bragg peaks of the two powder patterns confirm the crystallisation of the co-crystal from both ethanol and methanol solutions.

6.1.2.2. Synthesis in the solid state

There are several routes for the synthesis of a co-crystal. The most common, and the one that yields more results, requires the preparation of a solution. Changes to the experimental conditions, such as temperature and pH of the solution, can be made according to the system understudy. It is,

however, possible to obtain the formation of an adduct without leaving the solid state by applying mechanical stresses to the sample, for example by grinding the two components together. If simple grinding should prove insufficient for the co-crystallisation process, a variation to the technique can be applied by using the so-called *kneading* method (also known as *solvent-drop grinding*, SDG), which consists in the addition of a catalytic amount of solvent during grinding.

During the course of this thesis, co-crystallisation in the solid state was attempted to assess the tendency of cyprodinil to form molecular complexes. The materials used are listed in Table 6.3.

Substance	Quantity
Cyprodinil	1.0155 g
2-Aminopyrimidine	0.4452 g

Table 6.3. *Materials used for the co-crystallisation in the solid state.*

The two components, in a 1:1 molar ratio, were manually ground together in an agate mortar for 30 minutes, without any additional solvent. The powder was transferred on a Perspex sample holder and a powder X-ray diffraction pattern was recorded with the D5000 powder diffractometer. In Figure 6.5 the powder patterns for the co-crystal obtained from solution and in the solid state are reported.

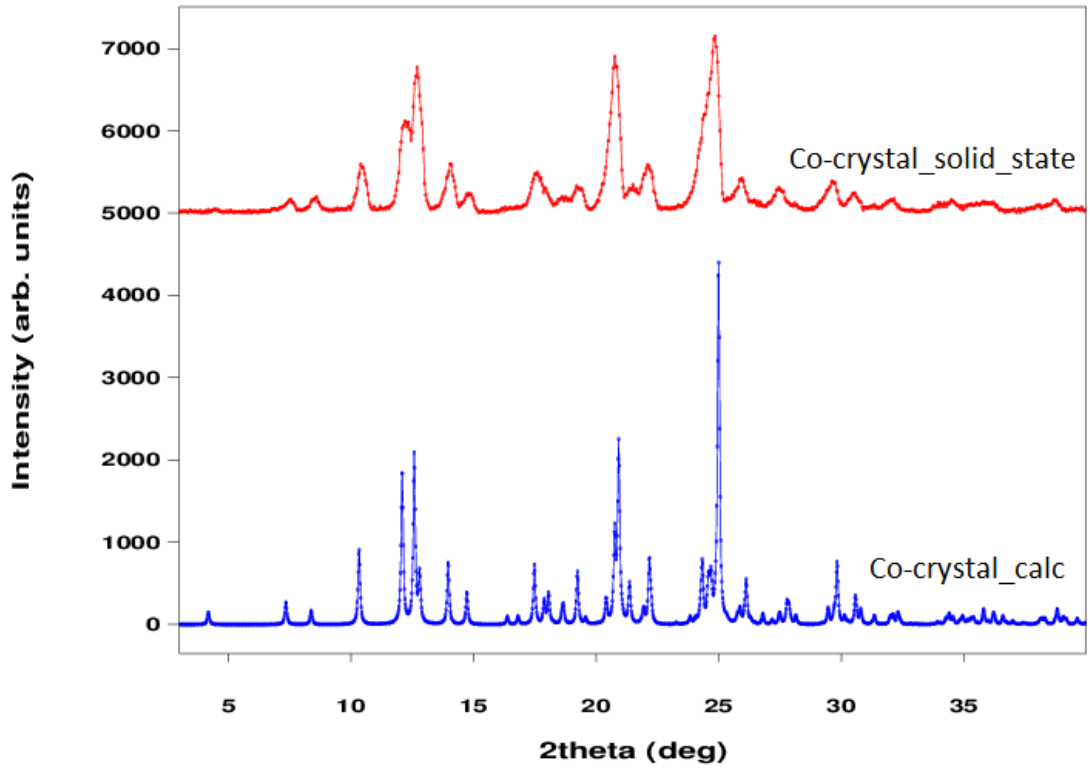

Figure 6.5. *Powder diffraction patterns for the co-crystal calculated from the experimental SXD (in blue) and the one synthesised in the solid state (in red).*

The two patterns exhibit the same Bragg peak positions, indicating that the same crystal structure can be obtained in the solid state by grinding the two materials together.

6.1.2.3. Single crystal X-ray diffraction

The crystal structure of the co-crystal cyprodinil/2-aminopyrimidine was solved using single crystal X-ray diffraction (SXD). The crystal that was selected for the diffraction analysis was grown from a methanol solution by slow evaporation of the solvent. Two sets of data were collected to assess whether significant changes to the structure occurred at different temperatures: one set was collected at 150K and the second was collected at room temperature (RT). For the collection at 150K, the crystal was mounted on an Enraf-Nonius kappaCCD single crystal diffractometer. Since the second data set was collected at RT, the more powerful Xcalibur diffractometer was chosen in order to deal with the decrease of peak intensity due to higher experimental temperatures. However, during the structural refinement at RT, it was not possible to refine all the hydrogen atoms: the ones involved in intermolecular interactions were refined manually, while the positions of the remaining hydrogen atoms were calculated.
In Table 6.4, X-ray crystallographic data and refinement parameters for the co-crystal at 150K are reported.

Name	CYP / 2-aminopyrimidine
Empirical formula	$C_{14}H_{15}N_3$ $C_4H_5N_3$
Formula weight (g mol^{-1})	320.40
Temperature (K)	150
Wavelength (Å)	0.71073
Crystal system, space group	Monoclinic, $P2_1$
Unit cell dimensions	a = 5.409(1) Å
	b = 14.629(3) Å
	c = 21.092(4) Å
	β = 91.33(3)°
Volume ($Å^3$)	1668.5(6)
Z, calculated density (g cm^{-3})	4, 1.275
F(000)	680
Absorption coefficient (mm^{-1})	0.081
Theta range for data collection (°)	1.69 to 26.37
Limiting indices	$-6 \leq h \leq 5$, $-18 \leq k \leq 18$, $-26 \leq l \leq 26$
Reflections collected / unique	10209 / 6643 [R_{int} = 0.0271]
Completeness to θ = 26.37	99.7 %
Refinement method	Full-matrix least-squares on F^2
Data / restrains / parameters	6643 / 1 / 594
Goodness-of-fit on F^2	1.173
Final R indices [I>2sigma(I)]	R_1 = 0.0491, wR_2 = 0.1149
R indices (all data)	R_1 = 0.0577, wR_2 = 0.1345
Extinction coefficient	0.19(1)
Largest diff. Peak and hole (e $Å^{-3}$)	0.47 and -0.57

Table 6.4. *X-ray crystallographic data and refinement parameters for the co-crystal, collected at 150K.*

6.1.3. Results and discussion

The asymmetric unit of the co-crystal is formed by two molecules of cyprodinil and two molecules of 2-aminopyrimidine, as shown in Figure 6.6.

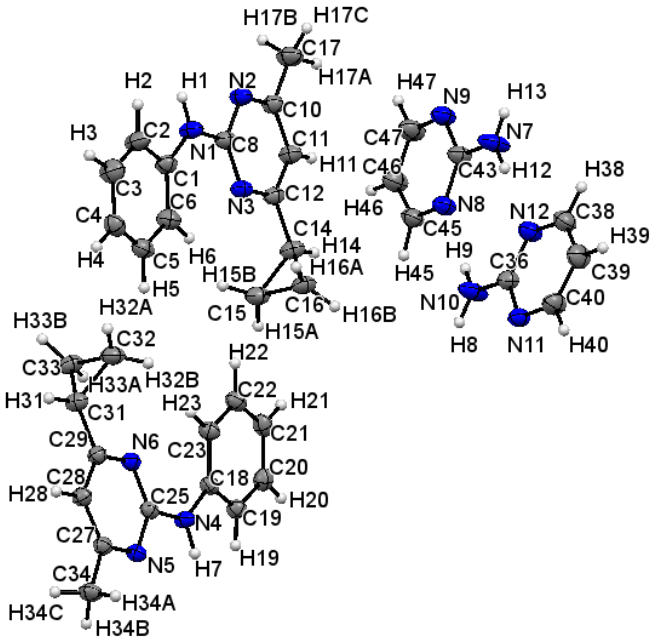

Figure 6.6. *ORTEP representation of the asymmetric unit of the co-crystal cvyprodinil/2-aminopyrimidine, derived from SXD. The probability level for all non-hydrogen ellipsoids is 50%, while the hydrogen atoms are drawn as fixed-size spheres of radius 0.15 Å.*

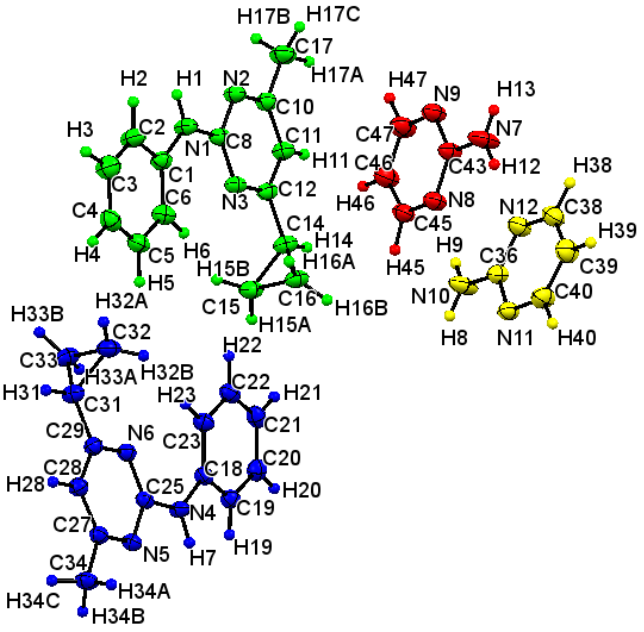

Figure 6.7. *Asymmetric unit of the co-crystal: the molecules are displayed in different colours to allow prompt identification.*

Green molecule			Blue molecule		
	150K	RT		150K	RT
C8-N1-C1-C6	-6.1(3)˚	-6.0(6)˚	C25-N4-C18-C23	12.8(3)˚	13.3(5)˚
N3-C12-C14-C15	31.6(3)˚	31.7(5)˚	N6-C29-C31-C32	-38.3(3)˚	-39.1(5)˚
N3-C12-C14-C16	-36.6(3)˚	-36.2(5)˚	N6-C29-C31-C33	30.2(3)˚	29.1(5)˚
C8-N3-C12-C14	179.2(2)	179.8(3)˚	C25-N6-C29-C31	179.4(2)˚	-179.9(3)˚
N2-C8-N1-H1	1(2)˚	-6(2)˚	N5-C25-N4-H7	1(1)˚	-8(3)˚
Red molecule			Yellow molecule		
	150K	RT		150K	RT
N7-C43-N9-C47	176.1(2)˚	176.3(4)˚	N10-C36-N11-C40	-179.5(2)˚	-178.8(3)˚
N7-C43-N8-C45	-175.9(2)˚	-175.6(4)˚	N10-C36-N12-C38	179.7(2)˚	178.7(4)˚

Table 6.5. *Torsion angles of interest. The colours refer to Figure 6.7.*

The two molecules of cyprodinil display a similar conformation. Both cyclopropyl are almost centred in respect to the pyrimidine ring, with torsion angles of 31.6(3)˚ and -36.6(3)˚ for the green molecule, and of 30.2(3)˚ and -38.3(3)˚ for the blue molecule, at 150K. The benzene and the pyrimidine rings are not co-planar in either molecule, but they are slightly twisted due to the presence of the cyclopropyl group. The conformation of the two cyprodinil molecules is very similar to the one in form B, as the two structures display a similar network of the intermolecular interactions. The 2-aminopyrimidine molecules show an almost perfectly planar conformation, as reported in Table 6.5. All carbon structures are preserved at RT without any significant changes.

The crystal packing of the co-crystal is governed by intermolecular hydrogen bonds and π-π interactions, which contribute to the formation of parallel strings of cyprodinil molecules rotated along the 2-fold screw axis, as shown in Figure 6.8. π-π interactions of 3.58(3) Å are formed between the pyrimidine moiety of cyprodinil and the benzene ring of a neighbouring molecule, while the distance between two 2-aminopyrimidine parallel molecules is 3.96(3) Å.

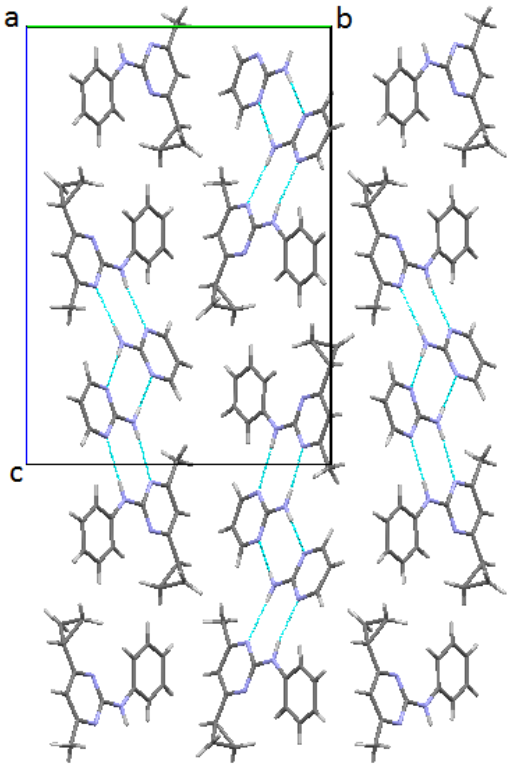

Figure 6.8. *Crystal packing of the co-crystal, viewed along the* ***a****-axis.*

The two cyprodinil molecules do not directly interact with one another, but each molecule is engaged in two intermolecular hydrogen bonds with one 2-aminopyrimidine molecule, leading to the formation of an 8-membered ring: both molecules act as donor and acceptor of the hydrogen bonds through the amino group and the cyclic N. An additional 8-membered interaction takes placed between the two molecules of co-former, as clearly visible from Figure 6.9. In Table 6.6, hydrogen bond lengths and geometry are reported.

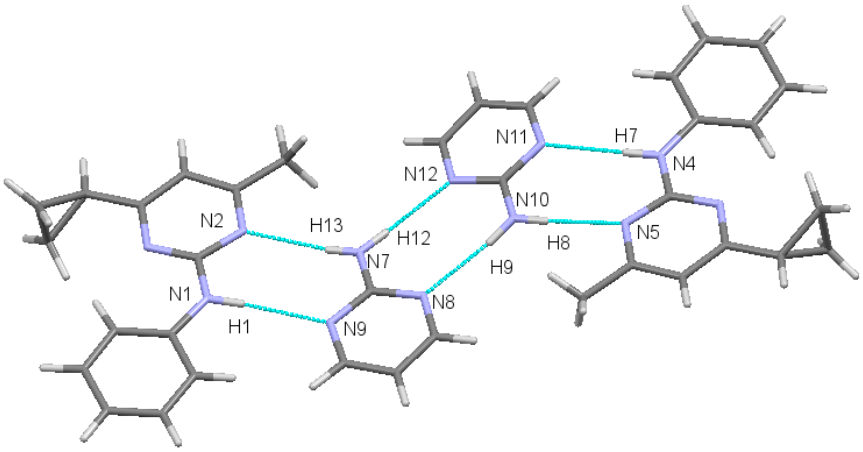

Figure 6.9. *Particular of the crystal packing viewed along the* ***b****-axis.*

	150K	RT		150K	RT
N1-H1	0.88(3) Å	1.05(5) Å	N10-H9	0.87(3) Å	0.79(4) Å
H1···N9	2.34(3) Å	2.16(5) Å	H9···N8	2.18(3) Å	2.28(4) Å
N1···N9	3.216(2) Å	3.201(4) Å	N10···N8	3.042(3) Å	3.073(5) Å
N1-H1···N9	176(2)˚	171(4)˚	N10-H9···N8	174(3)˚	176(4)˚
N7-H13	0.81(3) Å	0.85(4) Å	N10-H8	0.86(3) Å	0.87(5) Å
H13···N2	2.24(3) Å	2.21(4) Å	H8···N5	2.17(3) Å	2.21(5) Å
N7···N2	3.046(3) Å	3.057(5) Å	N10···N5	3.035(3) Å	3.084(5) Å
N7-H13···N2	172(3)˚	175(3)˚	N10-H8···N5	177(2)˚	175(5)˚
N7-H12	0.85(3) Å	0.95(4) Å	N4-H7	0.90(2) Å	0.91(4) Å
H12···N12	2.20(3) Å	2.09(4) Å	H7···N11	2.30(2) Å	2.32(4) Å
N7···N12	3.056(3) Å	3.038(5) Å	N4···N11	3.192(2) Å	3.230(5) Å
N7-H12···N12	178(3)˚	177(4)˚	N4-H7···N11	171(2)˚	174(3)˚

Table 6.6. *Hydrogen bond lengths and geometry in the co-crystal cyprodinil/2-aminopyrimidine.*

Considering the structure at 150K, the hydrogen bond lengths vary between 2.17(3) – 2.34(3) Å, indicating the presence of medium-strength hydrogen bonds[81]. Contrary to the case of modification B of cyprodinil, the planes containing the interacting molecules are almost planar, with a difference of ~3˚ for the interaction between the green and the red molecules, and of ~12˚ for the other two. This structure proves to be more stable than form B of cyprodinil as indicated by the higher value of the melting point: ~96˚C opposed to ~75˚C of form B. No significant changes are present in the structure at RT. It is, anyway, possible to observe a slight increase of the covalent bond lengths due to a higher thermal vibration.

Since the hydrogen atoms involved in intermolecular interactions were refined manually, it is possible to study the electron-density maps for those atoms to investigate the presence of proton migration or disorder in the structure. Figures 6.10, 6.11, 6.12, 6.13, 6.14, and 6.15 display the difference electron-density maps for the atoms H1, H7, H8, H9, H12, and H13, respectively.

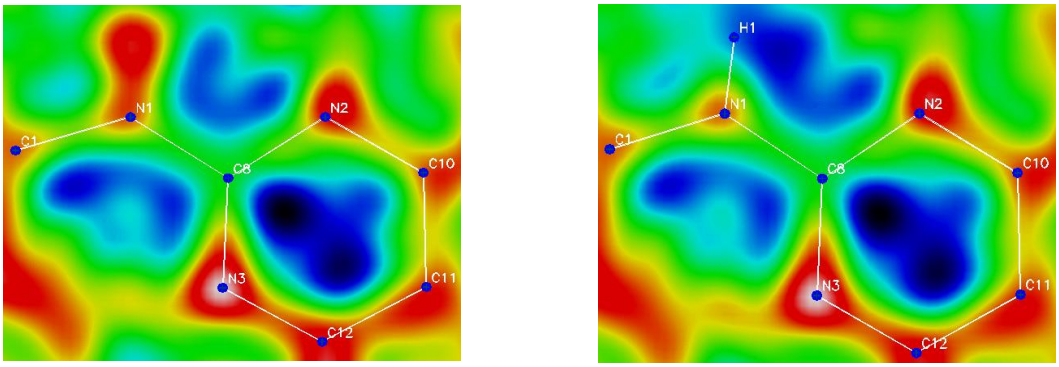

Figure 6.10. *Difference electron-density maps where the hydrogen atom H1 was excluded from (on the left) and included in (on the right) the refinement.*

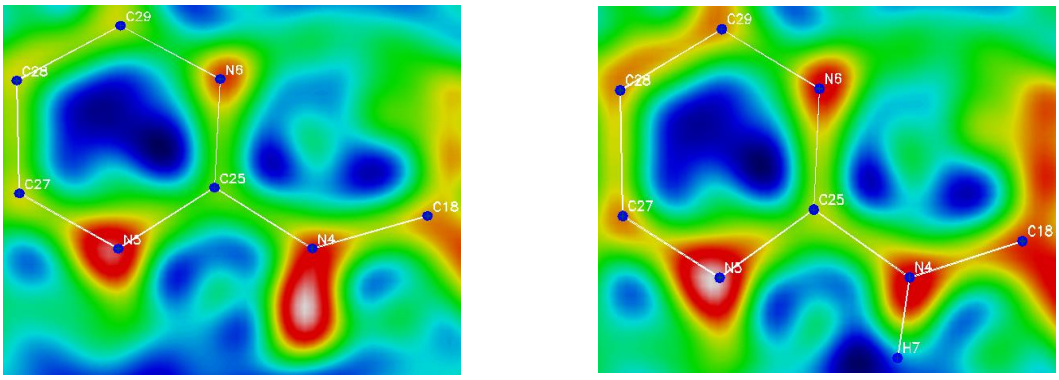

Figure 6.11. *Difference electron-density maps where the hydrogen atom H7 was excluded from (on the left) and included in (on the right) the refinement.*

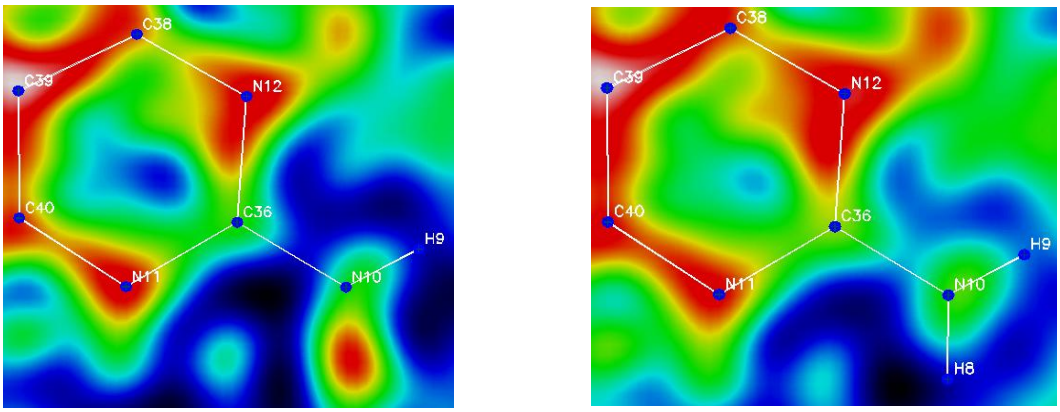

Figure 6.12. *Difference electron-density maps where the hydrogen atom H8 was excluded from (on the left) and included in (on the right) the refinement.*

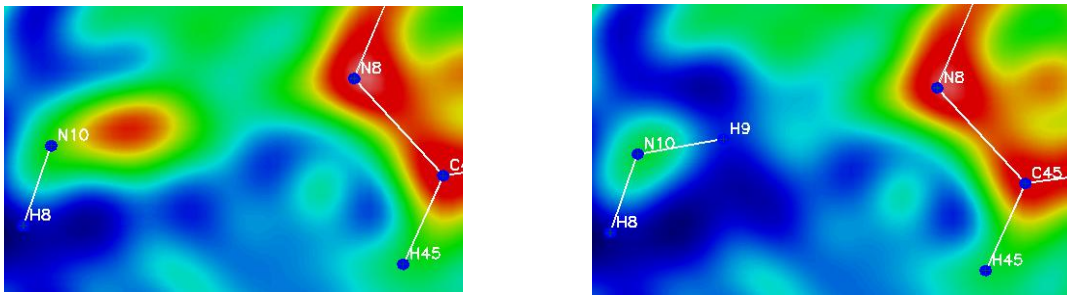

Figure 6.13. *Difference electron-density maps where the hydrogen atom H9 was excluded from (on the left) and included in (on the right) the refinement.*

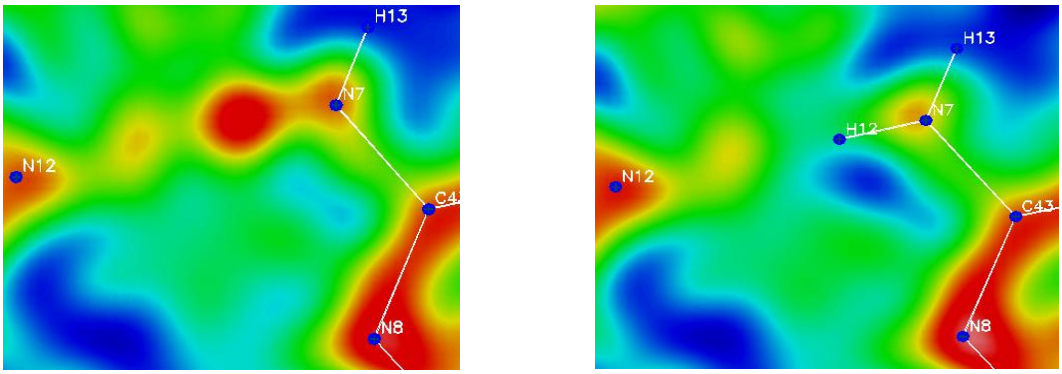

Figure 6.14. *Difference electron-density maps where the hydrogen atom H12 was excluded from (on the left) and included in (on the right) the refinement.*

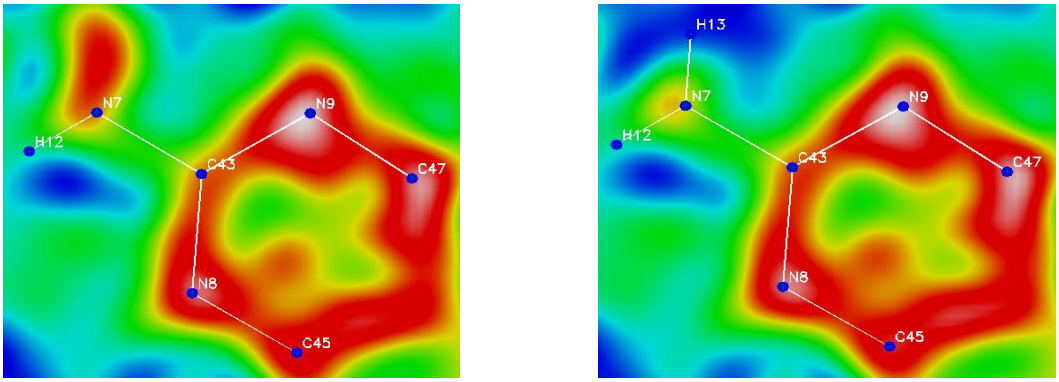

Figure 6.15. *Difference electron-density maps where the hydrogen atom H13 was excluded from (on the left) and included in (on the right) the refinement.*

The electron-density maps show the absence of disorder or proton migration. In fact, when the electron density displayed in the difference Fourier maps is refined as a hydrogen atom, no residual density around the refined hydrogen atom is detected.

6.1.4. Conclusions

The design of crystal structures through specific intermolecular interactions can lead to the formation of co-crystals with modified physical properties, such as colour, temperature of fusion, solubility and stability to storage. The spontaneous conversion between polymorphs of cyprodinil that takes place during storage can, thus, be avoided by using a co-former with the aim of inhibiting the phase transition. Given that cyprodinil is a pyrimidine derivative, the molecule of 2-aminopyrimidine was the first choice in the synthesis of the co-crystal. The adduct can be synthesised both from solution and in the solid state. A variety of organic solvents can be used, but the work carried out in this thesis proved that the best results can be obtained when methanol is used as solvent. A key role in the crystallisation of the co-crystal is played by the velocity of the

evaporation of the solvent: this must be slow in order to obtain crystal suitable for SXD for both size and quality. Synthesis in the solid state can be achieved by simple grinding of the two components in an agate mortar.

The crystal structure of the co-crystal is characterised by the presence of medium-strength hydrogen bonds between a molecule of cyprodinil and a molecule of the co-former. The resulting interaction is an 8-membered ring, which lends additional stability to the structure, increasing the melting point of cyprodinil from ~75˚C in form B to ~96˚C in the co-crystal.

6.2. Cyprodinil / maleimide co-crystal

6.2.1. Introduction

The co-crystallisation process was carried out with co-formers exhibiting different functionality and functional groups. Having proved the ability of cyprodinil to form a molecular complex with 2-aminopyrimidine, the study moved towards heterogeneous interactions, involving oxygen atoms as acceptor of the hydrogen bond. The molecule of maleimide (Figure 6.16) was selected: it is a cyclic imide, where two carbonyl groups are covalently bound to a nitrogen atom.

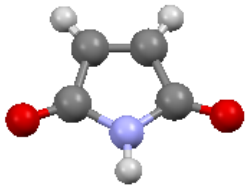

Figure 6.16. *Molecule of maleimide: C atoms (gray); H atoms (light gray); O atoms (red); N atom (blue).*

The configuration of maleimide can lead to a bidentate coordination, where the N-H group acts as donor of the hydrogen bond and the oxygen atom is the acceptor.

Maleimide crystallises in the triclinic system, space group $\boldsymbol{P\bar{1}}$, and it displays four molecules in the asymmetric unit. The long-range order of the three-dimensional structure is characterised by the organisation of the maleimide molecules into centrosymmetric dimers, arranged into parallel planes, leading to the formation of hydrogen bonds, constituted by 8-membered rings, between two neighbouring amide groups, as shown in Figure 6.17.

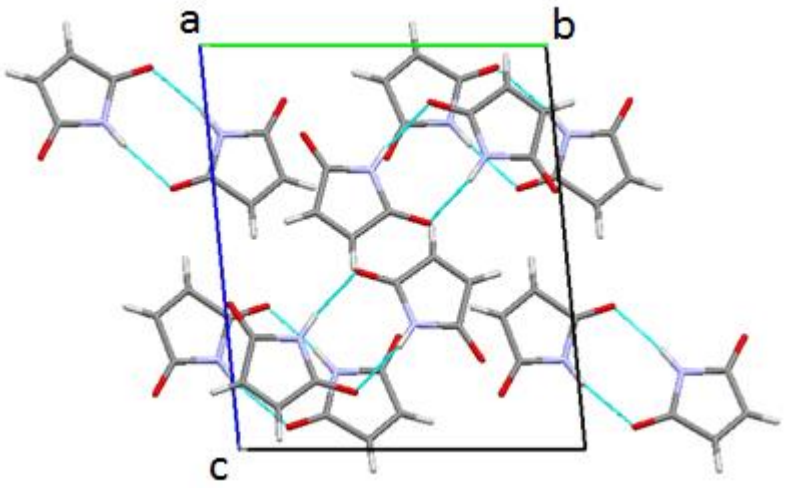

Figure 6.17. *Crystal packing of maleimide, viewed along the* ***a****-axis.*

6.2.2. Experimental

6.2.2.1. Physical and chemical properties of maleimide

Maleimide is a light beige crystalline powder with a temperature of fusion of ~93˚C and vapour pressure of 8 hPa a 115˚C[101]. It is soluble in water and in a large variety of organic solvents, such as alcohols, acetone, and acetonitrile.

6.2.2.2. Synthesis from solution

The synthesis of the co-crystal cyprodinil/maleimide was carried out in solution with the aim of growing crystals suitable for SXD measurements. Since cyprodinil has low solubility in water, various different solvents that were proven to give the best results for the crystallization of the pure fungicide were investigated. Table 6.7 summarises the details for each solution studied.

Solvent	Quantity of solvent (ml)	Cyprodinil (g)	Maleimide (g)
Ethanol	30 ml	2.01	0.86
Methanol	10 ml	1.02	0.43
Isopropanol	20 ml	1.01	0.43
Acetonitrile (ACN)	10 ml	1.02	0.43
Isopropanol (IPA) / Acetonitrile (ACN)	2 + 2 ml	1.02	0.43

Table 6.7. *Solution compositions investigated for the cyprodinil/maleimide system.*

The solutions were prepared at room temperature by dissolving a stoichiometric 1 : 1 amount of the two components in the selected solvent. Subsequently, they were kept at ~50˚C for one hour to achieve complete dissolution of the solutes, while stirring continuously. The crystallisation process was carried out at room temperature in crystallisation vials that were covered with perforated parafilm in order to slow down the evaporation of the solvent and to obtain good quality crystals. The formation of the co-crystal was immediately visible: once the solvent was poured on the two compounds, both light beige in colour, the solution turned bright yellow. The phenomenon was also observed when the cyprodinil and the co-former were placed in contact with each other in a flask containing acetone vapour.

Not all solutions produced crystals of sufficient quality for a diffraction experiment. The dimensions of the crystals grown from the methanol and the 2-propanol solutions were too small and the shape was that of very thin and long needles; whereas from the ethanol and ACN solutions it was possible to obtain only a fine powder. The best results were achieved with the mixture of solvents (IPA/ACN in 50 : 50 ratio): the morphology was still needle-like, the colour bright yellow, but the crystals were larger and thicker.

6.2.2.3. Differential Scanning Calorimetry

The behaviour of the co-crystal upon variations of temperature was monitored by DSC. In Figure 6.18 the thermal profile for the co-crystal cyprodinil/maleimide is reported.

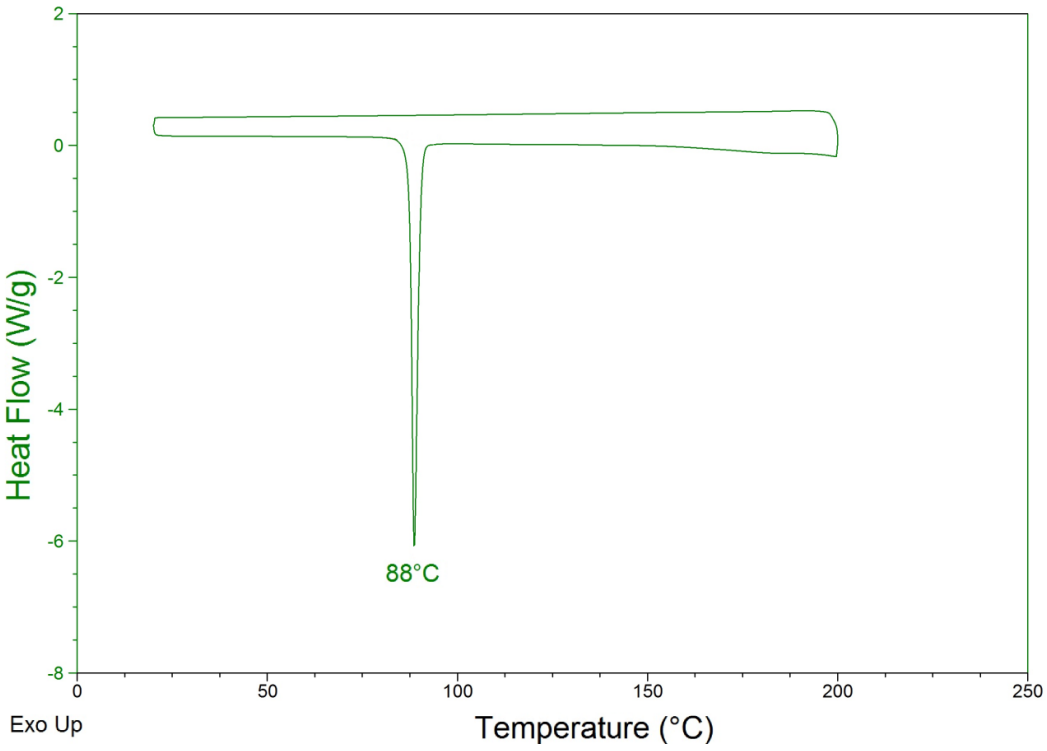

Figure 6.18. *DSC profile for the co-crystal cyprodinil/maleimide.*

The DSC analysis shows one endothermic event corresponding to the melting of the co-crystal at ~ 88˚C, but there is no evidence of re-crystallisation during cooling to 20˚C. The co-crystal displays a higher temperature of fusion compared to the two polymorphs of cyprodinil.

6.2.2.4. Powder X-ray diffraction

The formation of a new crystal structure was verified by powder X-ray diffraction, because this technique provides immediate discrimination among crystalline materials thanks to the different positions of the Bragg peaks, which are characteristic for each compound. The crystals grown from the IPA/ACN solution were manually ground into a fine powder in an agate mortar and transferred on the D5000 powder diffractometer. The results of the analysis are reported in Figure 6.19.

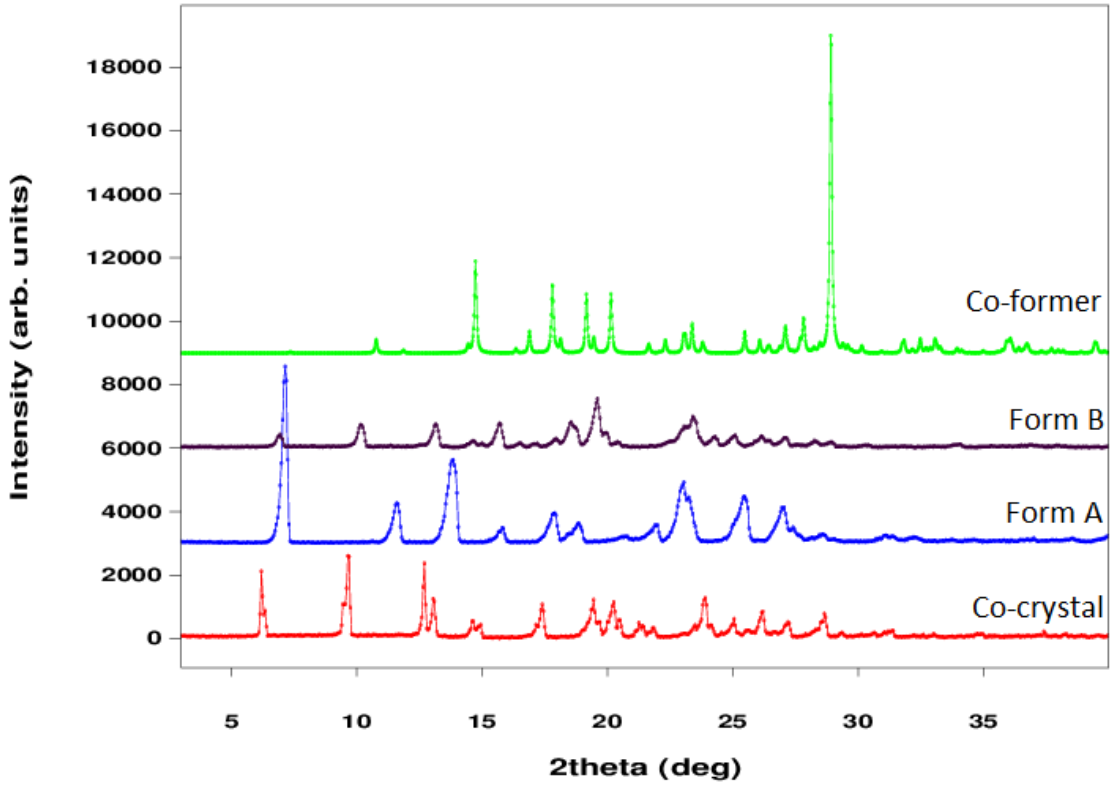

Figure 6.19. *Powder diffraction patterns for the co-crystal (red), modification A (blue) and B (black) of cyprodinil, and maleimide (green).*

The comparison between the powder patterns of the co-crystal and of the two components clearly shows the formation of a new different crystal structure. The synthesis route was also shown to give a pure single phase as no traces of the two reagents could be found in the powder pattern of the co-crystallisation product.

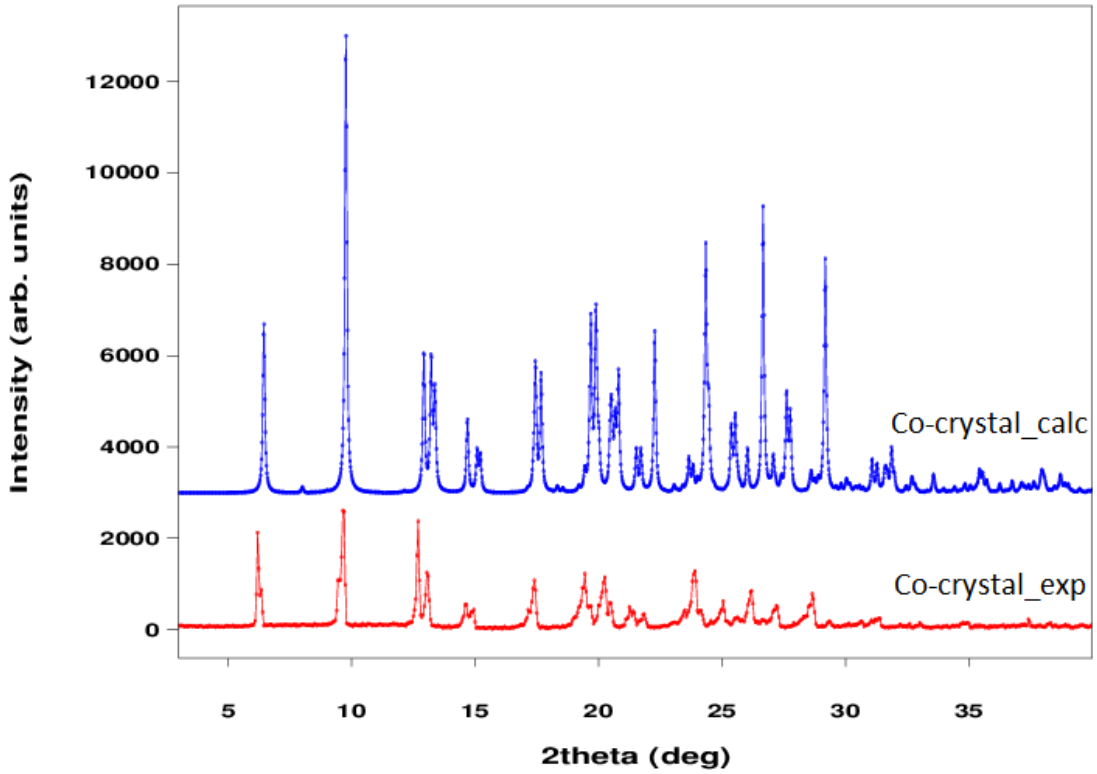

Figure 6.20. *In red, experimental PXD of the co-crystal grown from the IPA/ACN solution; in blue, PXD pattern of the co-crystal that was calculated from experimental SXD results.*

This new crystal structure can be identified as that of the co-crystal, as shown in Figure 6.20, where the powder pattern obtained from the ground crystals is compared to the one that was calculated from the single crystal X-ray diffraction analysis undertaken on the co-crystal cyprodinil/maleimide.

6.2.2.5. Single crystal X-ray diffraction

The formation of the co-crystal cyprodinil/maleimide was proved by SXD analysis, which also allows determination of the atomic positions. The crystal selected for the analysis (crystal volume ~ 0.02 mm^3) was grown from an IPA/ACN 50 : 50 solution by the method of slow evaporation of the solvent. Data were collected on an Enraf-Nonius kappaCCD single crystal diffractometer at the temperature of 150K. Data reduction presented difficulties, starting from the choice of the crystal system. The initial analysis of the crystal, done by XPREP[55], suggested an orthorhombic cell, with R_{sym} = 0.061 (usually R_{sym} should be lower than 0.1) and the cell parameters (*a*, *b*, *c*, α, β, and γ): 9.830, 12.044, 27.328, 90.00, 90.00, and 90.00. However, by choosing the orthorhombic crystal system, no acceptable space groups were found to fit the data set.

The choice of a space group is usually determined considering three factors: *(i)* the normalised structure factors, E-values, statistics, which indicates whether there is a higher probability of

having a centrosymmetric space group; *(ii)* the systematic absences, which are generated by translational elements of symmetry, such as screw axes and glide planes; and *(iii)* the frequency of the space group inside the Cambridge Structural Database (CSD). The CFOM (Combined Figure Of Merit) value takes into account all three factors; it should be as close to one as possible and should not be greater than 5. In the case of the co-crystal cyprodinil/maleimide, XPREP[55] suggests the presence of three $\boldsymbol{2_1}$ screw axes normal to the three directions ***a***, ***b***, and ***c***, and a ***c***-glide plane perpendicular to ***b***. The presence of a screw axis $\boldsymbol{2_1}$ and a ***c***-glide plane perpendicular to it suggests the space group $\boldsymbol{P2_1/c}$ as the most likely. The crystal system was manually changed to monoclinic and it was possible to assign the right space group to the crystal structure: $\boldsymbol{P2_1/c}$.

The space group $\boldsymbol{P2_1/c}$ is, indeed, centrosymmetric, as indicated by the calculated $|E^2 - 1|$ value of 0.918, which is close to the expected value (0.968) for centrosymmetric structures. In this case the systematic absences allow the assignment of the space group without any doubts. The new expected systematic absences for the monoclinic space group agree with the experimental data. For the two-fold screw axis $\boldsymbol{2_1}$ and the ***c***-glide plane none of the systematic absences are present, confirming the existence of these symmetry elements inside the crystal structure of the co-crystal. It is, finally, important to notice that the value of R_{sym} decreased from 0.061 of the orthorhombic system to 0.047 of the monoclinic cell, proving the accuracy of the analysis. The final parameters for the monoclinic unit cell are 9.816(2), 27.366(5), 12.049(2), 90, 90.85(3), and 90. The ambiguity in the crystal system is probably due to the value of the angle β, which is close to 90°.

Unfortunately, the diffracting quality of the crystal was not sufficient to allow a complete characterisation of all atoms present in the structure: the position of the hydrogen atoms were calculated, except those of the ones involved in hydrogen bonds, H1, H7, H8, and H9, which were found in the Fourier difference maps. Even though the R values, $\boldsymbol{R_1 = 0.1129}$ and $\boldsymbol{wR_2 = 0.3191}$, are high, a ***GooF*** of 1.088 indicates a good fit between calculated and experimental data, confirming the synthesis of the co-crystal. The statistically poor quality of the data is correlated to the not ideal morphology of the crystal: a thin, long needle.

In Table 6.8, X-ray crystallographic data and refinement parameters for the co-crystal at 150K are reported.

Name	Cyprodinil / Maleimide
Empirical formula	$C_{14}H_{15}N_3$ / $C_4H_3NO_2$
Formula weight (g mol^{-1})	322.36
Temperature (K)	150
Wavelength (Å)	0.71073
Crystal system, space group	Monoclinic, $P2_1/c$
Unit cell dimensions	a = 9.816(2) Å
	b = 27.366(6) Å
	c = 12.049(2) Å
	β = 90.86(3)°
Volume ($Å^3$)	3236.3(1)
Z, calculated density (g cm^{-3})	8, 1.323
F(000)	1360
Absorption coefficient (mm^{-1})	0.089
Theta range for data collection (˚)	1.49 to 27.59
Limiting indices	$-12 \leq h \leq 12$, $-35 \leq k \leq 34$, $-15 \leq l \leq 15$
Reflections collected / unique	22045 / 7346 [R_{int} = 0.0663]
Completeness to θ = 27.59	98.0 %
Refinement method	Full-matrix least-squares on F^2
Data / restrains / parameters	7346 / 0 / 450
Goodness-of-fit on F^2	1.088
Final R indices [I>2sigma(I)]	R_1 = 0.1129, wR_2 = 0.2962
R indices (all data)	R_1 = 0.1396, wR_2 = 0.3191
Extinction coefficient	0.045(5)
Largest diff. Peak and hole (e $Å^{-3}$)	0.87 and -0.56

Table 6.8. *X-ray crystallographic data and refinement parameters for the cyprodinil/maleimide co-crystal at 150K.*

6.2.3. Results and discussion

The asymmetric unit of the co-crystal is formed by two molecules of cyprodinil and two molecules of the co-former, as displayed in Figure 6.21.

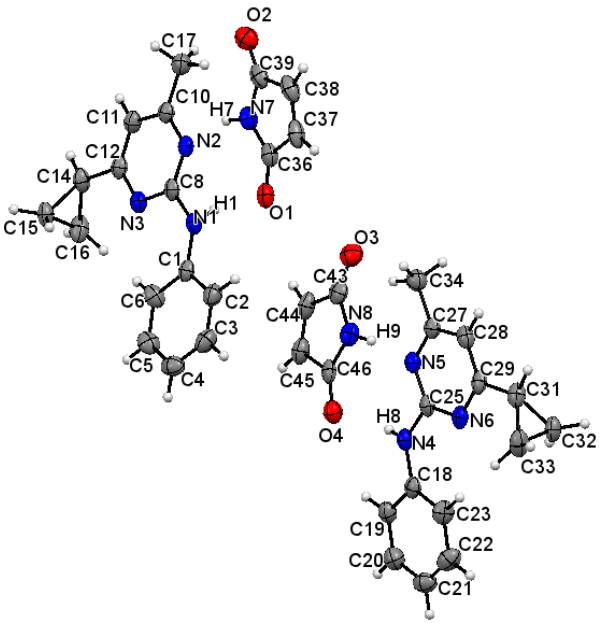

Figure 6.21. *ORTEP representation of the asymmetric unit of the co-crystal cvyprodinil/maleimide, derived from SXD. The probability level for all non-hydrogen ellipsoids is 50%, while the hydrogen atoms are drawn as fixed-size spheres of radius 0.15 Å.*

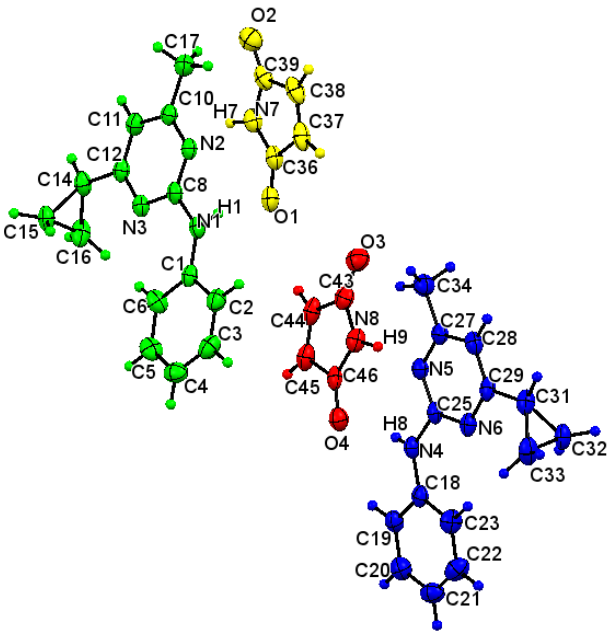

Figure 6.22. *Asymmetric unit of the co-crystal, viewed along the* ***a****-axis: the molecules are displayed in different colours.*

Green molecule		Blue molecule	
C8-N1-C1-C6	6.2(7)˚	C25-N4-C18-C23	9.2(7)˚
N3-C12-C14-C15	42.7(5)˚	N6-C29-C31-C32	44.1(5)˚
N3-C12-C14-C16	-25.5(5)˚	N6-C29-C31-C33	-24.8(5)˚
C8-N3-C12-C14	-177.6(3)˚	C25-N6-C29-C31	-178.1(3)˚
N2-C8-N1-H1	5(3)˚	N5-C25-N4-H8	5(5)˚
Yellow molecule		Red molecule	
C36-O1	1.212(5) Å	C43-O3	1.190(5) Å
C39-O2	1.203(5) Å	C46-O4	1.209(5) Å
C36-C37-C38-C39	-0.7(5)˚	C43-C44-C45-C46	0.7(5)˚

Table 6.9. *Torsion angles and bond lengths of interest. The colours refer to Figure 6.22.*

The conformation of the two molecules of cyprodinil is similar to the case of the co-crystal with 2-aminopyrimidine. The cyclopropyl-substituent is slightly decentred in respect to the pyrimidine ring, with torsion angles of 42.7(5)˚ and -25.5(5)˚ for the green molecule, and of 44.1(5)˚ and -24.8(5)˚ for the blue cyprodinil. The pyrimidine and the benzene rings are not co-planar, due partly to the presence of the cyclopropyl-substituent and partly to the sp^3 hybridisation of the atoms N1 and N4. Three sp^3 orbitals are involved in the three covalent bonds, while the fourth contains the lone pair of electrons of the nitrogen atom.

Because of the sp^2 hybridisation of all carbon atoms of maleimide, the two molecules of co-former appear almost perfectly planar. The covalent bond C=O length is slightly longer when the oxygen atom is the acceptor of an intermolecular hydrogen bond.

The crystal packing of the co-crystal is characterised by the stacking of the cyprodinil and maleimide molecules into parallel lines forming a fishbone-like motif, held together by π-π interactions between a molecule of cyprodinil and one of maleimide with distances in the range 3.70(5) – 3.72(5) Å, as shown in Figure 6.23.

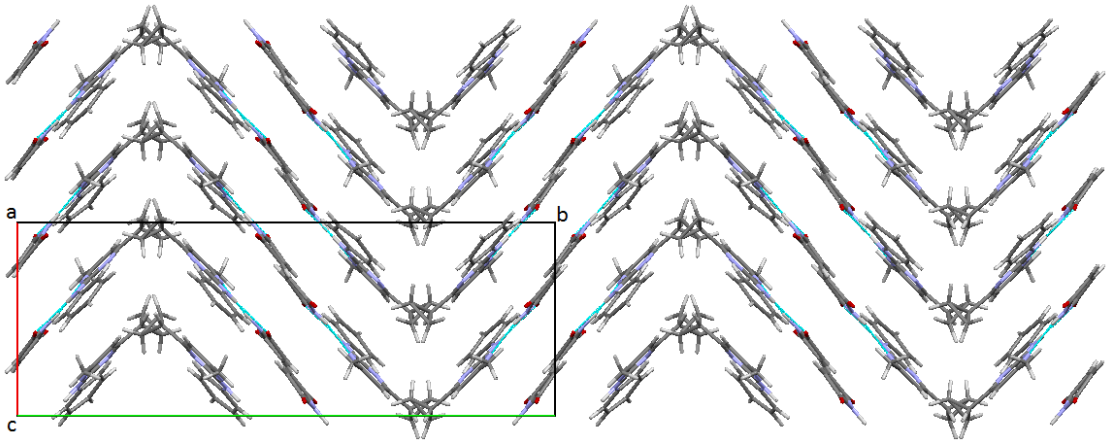

Figure 6.23. *Crystal packing of the co-crystal, viewed along the* ***c****-axis.*

The main feature of this crystal structure is represented by a cyclic hydrogen bond between a molecule of cyprodinil and a molecule of maleimide. In particular two hydrogen bonds, one between the amino group on cyprodinil and the oxygen atom of maleimide, and the other involving the N-H moiety on maleimide as donor and the pyrimidine N atom on cyprodinil as acceptor, lead to the formation of an 8-membered ring, as reported in Figure 6.24.

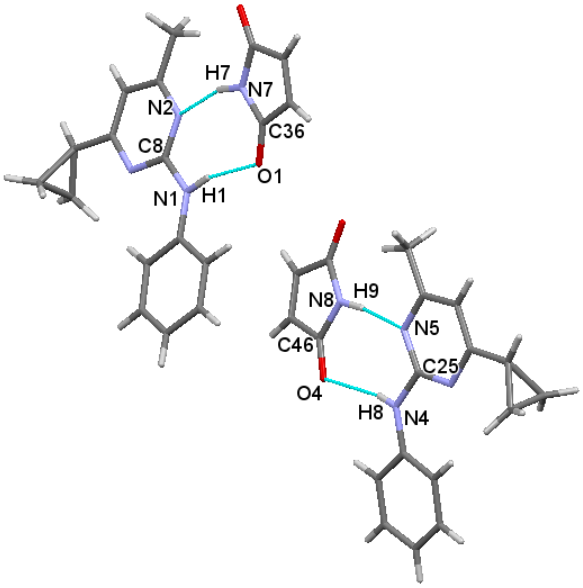

Figure 6.24. *Particular of the crystal packing, showing the hydrogen bonding network that takes place in the co-crystal. The view is along the* ***a****-axis.*

N1-H1	0.95(4) Å	N4-H8	0.74(6) Å
H1···O1	2.11(4) Å	H8···O4	2.33(6) Å
N1···O1	3.047(4) Å	N4···O4	3.066(4) Å
N1-H1···O1	166(4)˚	N4-H8···O4	169(6)˚
N7-H7	1.01(5) Å	N8-H9	0.88(6) Å
H7···N2	1.98(5) Å	H9···N5	2.10(6) Å
N7···N2	2.953(5) Å	N8···N5	2.970(5) Å
N7-H7···N2	161(5)˚	N8-H9···N5	169(6)˚

Table 6.10. *Hydrogen bond lengths and geometry in the co-crystal cyprodinil/maleimide.*

Table 6.10 reports the main characteristics for the two 8-membered intermolecular hydrogen bonds. The distances between the two interacting molecules are similar in both cases, N1···O1 ≈ N4···O4 and N7···N2 ≈ N8···N5, indicating that any differences between the four hydrogen bonds, N1-H1···O1, N7-H7···N2, N4-H8···O4, and N8-H9···N5, are intrinsic to each interaction. Having different chelating moieties interacting with each other, N2-C8-N1-H1 and N5-C25-N4-H8 for cyprodinil and O1-C36-N7-H7 and O4-C46-N8-H9 for maleimide, affects the geometry of the

hydrogen bond, especially for N1-H1···O1 and N7-H7···N2: the angles of these interactions are farther from the ideal value of 180° than in the case of the co-crystal cyprodinil/2-aminopyrimidine. Considering the bond lengths and the geometry of interaction, it is possible to qualify all hydrogen bonds present in the structure as medium-strength hydrogen bonds[81].

The investigation of the electron-density maps allows assessing the presence of proton migration or disorder in the structure. In Figures 6.25, 6.26, 6.27, 6.28 the difference electron-density maps for the atoms involved in intermolecular interactions, H1, H7, H8, and H9, respectively are reported.

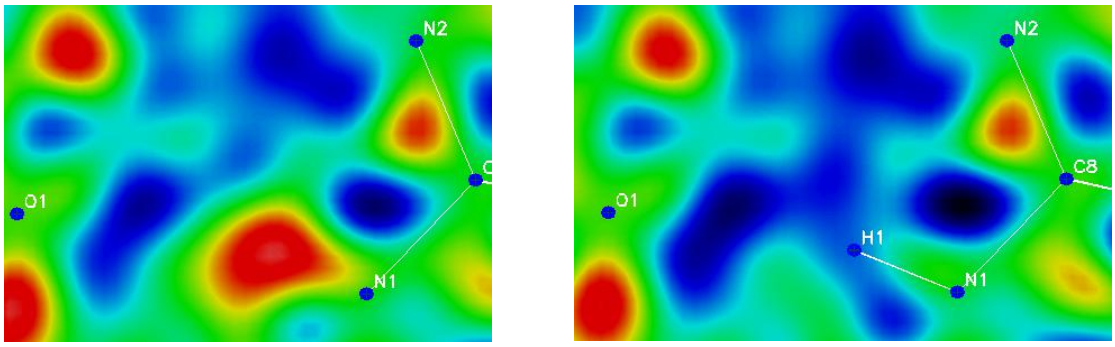

Figure 6.25. *Difference electron-density maps where the hydrogen atom H1 was excluded from (on the left) and included in (on the right) the refinement.*

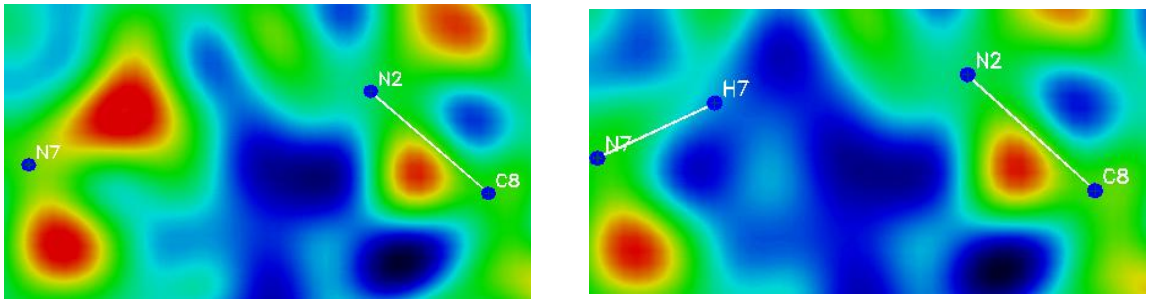

Figure 6.26. *Difference electron-density maps where the hydrogen atom H7 was excluded from (on the left) and included in (on the right) the refinement.*

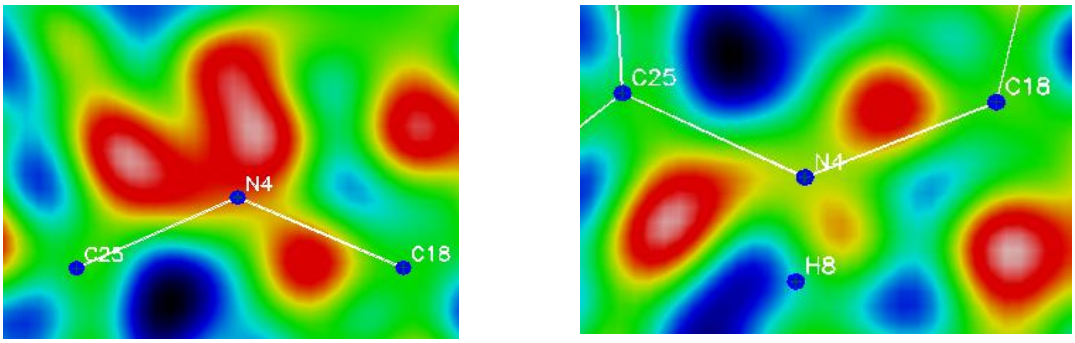

Figure 6.27. *Difference electron-density maps where the hydrogen atom H8 was excluded from (on the left) and included in (on the right) the refinement.*

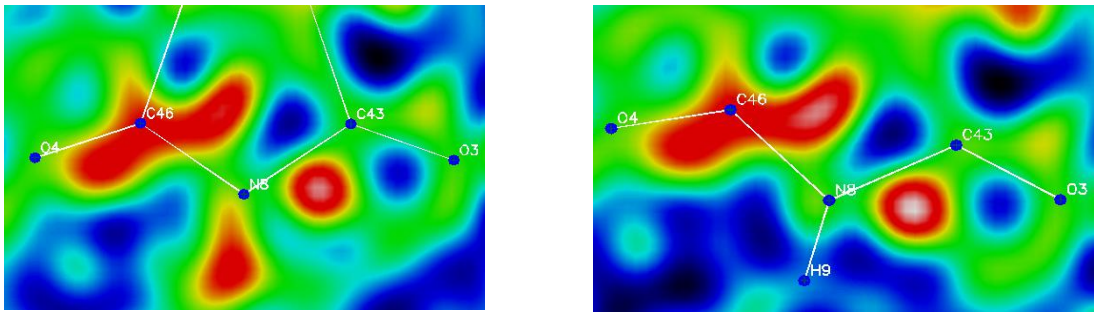

Figure 6.28. *Difference electron-density maps where the hydrogen atom H9 was excluded from (on the left) and included in (on the right) the refinement.*

From the difference Fourier maps displayed in figures above it is possible to notice that, when the hydrogen atoms are included in the refinement, no residual electron density is present, indicating that the crystal structure is not disordered and that the hydrogen atoms involved in the intermolecular interactions are in single positions.

However, it is important to remember that even though the model fits the data, the statistics, expressed through the R_1 and wR_2 values, indicate that discrepancies between calculated data and real structure might be present, especially in the definition of the hydrogen atom positions. Single crystal neutron diffraction represents a valid option for the complete characterisation of the hydrogen bonding network of this co-crystal. Unfortunately, it was impossible to grow large crystals of sufficient quality for an SND experiment.

6.2.4. Conclusions

The work carried out in this thesis proved that cyprodinil is not only capable of forming molecular complexes with co-former exhibiting the same functional group as the fungicide (***cf. 6.1.***), but it can engage in intermolecular hydrogen bonds also with materials showing a different moiety of interaction, in this case the molecule of maleimide.

The co-crystal cyprodinil/maleimide was synthesised from solution, using a mixture of two solvents, isopropanol (IPA) and acetonitrile (ACN), in an equal volumetric amount. The formation of the co-crystal was immediately visible, because the solution changed colour, turning from transparent to bright yellow. This colour change is probably due to the formation of the intermolecular hydrogen bonds that varied the electronic properties of the material. Crystallisation of the complex was achieved by the method of slow evaporation of the solvent at room temperature, in order to obtain crystals of sufficient quality for a single crystal X-ray diffraction experiment.

PXD initially indicated the presence of a crystal structure that was different from both cyprodinil and maleimide, and this was confirmed by SXD. SXD analysis generated a model defining all atomic positions and the symmetry relations that create the long-range order of the crystal. The

identification of the unit cell was difficult due to the close value of the angle $\boldsymbol{\beta}$ to 90˚, which caused some ambiguity in the selection of the crystal system. An accurate analysis of the data set allowed the correct assignment of the space group, $\boldsymbol{P2_1/c}$, leading to the following unit cell parameters ($\boldsymbol{a}$, $\boldsymbol{b}$, $\boldsymbol{c}$, $\boldsymbol{\alpha}$, $\boldsymbol{\beta}$, $\boldsymbol{\gamma}$): 9.816(2) Å, 27.366(5) Å, 12.049(2) Å, 90˚, 90.85(3)˚, 90˚. The crystal packing is governed by π-π interactions and intermolecular hydrogen bonds between a molecule of cyprodinil and a molecule of maleimide: the amino group and the pyrimidine N atom of cyprodinil act as donor and acceptor, respectively, of the hydrogen bond, while on the molecule of maleimide the acceptor is the oxygen atom of the carbonyl group. The resulting interaction is an 8-membered ring, where the length of the two hydrogen bonds varies between 1.98(5) – 2.10(6) Å, when the acceptor is the N atom, and between 2.11(4) – 2.33(6) Å, when the O atom is the acceptor. Investigation of the electron-density maps showed that the structure is not disordered and that there is not a migration of the hydrogen atom along the hydrogen bond.

DSC analysis proved that the crystal structure is stable until ~ 88˚C, temperature at which the melting of the complex occurs. The higher value of the temperature of fusion of the co-crystal compared to both polymorphs of cyprodinil indicates that the heterogeneous intermolecular hydrogen bonds are stronger in the case of the molecular complex.

6.3. Cyprodinil / benzoic acid co-crystal

6.3.1. Introduction

The carboxylic functionality is often used as a *synthon* for the design of different crystal structures. Displaying both donor and acceptor moieties in the hydroxyl and carbonyl group, respectively, it has the ability of forming circular hydrogen bonding networks through a bidentate coordination.

Numerous studies[102] have been carried out on heterogeneous intermolecular interactions, such as N-H···O and O-H···N, that can take place between carboxylic acids and pyridine or pyrimidine molecules. One in particular[103] considers the competitiveness among pyridine and pyrimidine derivatives in the formation of hydrogen bonds with aromatic carboxylic acids. This work demonstrates that even though the pyridine molecule is more basic than unsubstituted pyrimidine, the addition of an amino group in position 2 of the pyrimidine ring increases the basic property of this molecule making it the preferred co-former in co-crystals with carboxylic acids. Supramolecular reactants, displaying both pyridine and aminopyrimidine sites, form co-crystals with several different carboxylic acids: in all cases the interacting moieties are the carboxylic functionality and the aminopyrimidine. One example of such a structure is reported in Figure 6.29.

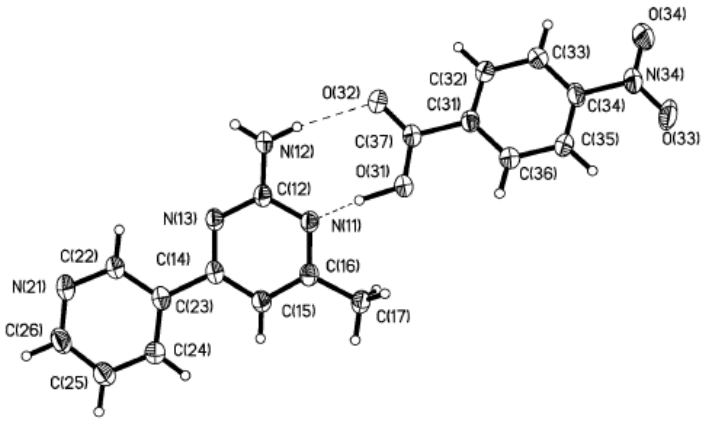

Figure 6.29. *1 : 1 binary co-crystal of 3-(2-amino-4-methylpyrimidin-6-yl)pyridine/4-nitrobenzoic acid*[103].

The interaction of the carboxylic and aminopyrimidine moieties consists always of two hydrogen bonds, one between the H atom on the hydroxyl and the pyrimidine N atom and a second between the H atom on the amino group and the carboxylic O atom, leading to the formation of an almost planar 8-membered ring. Recent studies confirm the occurrence of such interactions between the molecules of 2-amino-4,6-dimethylpyrimidine and benzoic acid[104] and between 2-aminopyrimidine and two different carboxylic acids, 1,4-cyclohexanedicarcoxylic acid and butane-1,2,3,4-tetracarboxylic acid[105]. The acid and the base interact in the same manner, as displayed in Figure 6.30. Worthy of notice is the formation of a salt in the case of 2-aminopyrimide/butane-1,2,3,4-tetracarboxylic acid: by comparing the molecular structure of the sole 2-aminopyrimidine in the salt to the one of the pure molecule, it is possible to observe a shortening of the $C_{ring} - N_{amino}$ bond length (1.325(4) Å in the salt and 1.342(2) Å in the pure crystal) and a decrease of around 2° of the $N_{ring} - C_{ring} - N_{ring}$ angle (123.1(3)° opposed to 125.2(1)°), due to an increase of the ***p*** character of the pyrimidine ring orbitals[106]. In fact, since the ***p*** electrons are less attacted by the positive charge of the nucleus, they cause an increase of the ***p*** character of the hybrid orbitals that are directly involved in the covalent bond with an electronegative substitutent, which, in the case of 2-aminopyrimidine, is the nitrogen atom of the amino group. It follows that a larger contribution of the ***p*** electrons in the ***σ***-bonding $C_{ring} - N_{amino}$ induces a shift of the electron density towards the amino group, decreasing the bond length and the endocyclic angle $N_{ring} - C_{ring} - N_{ring}$.

a)

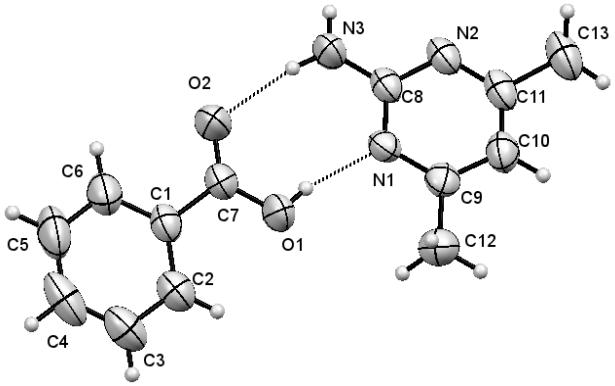

b)

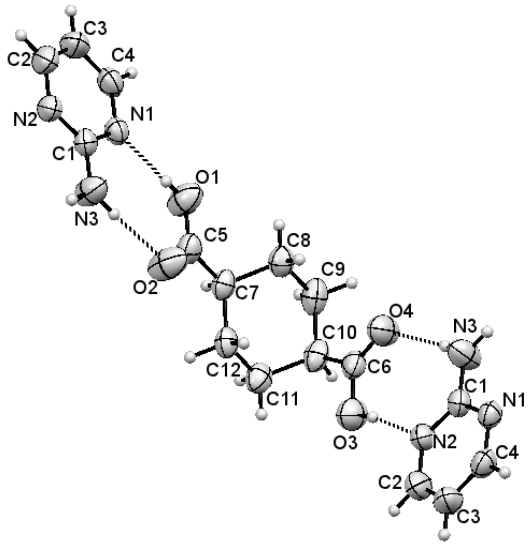

c)

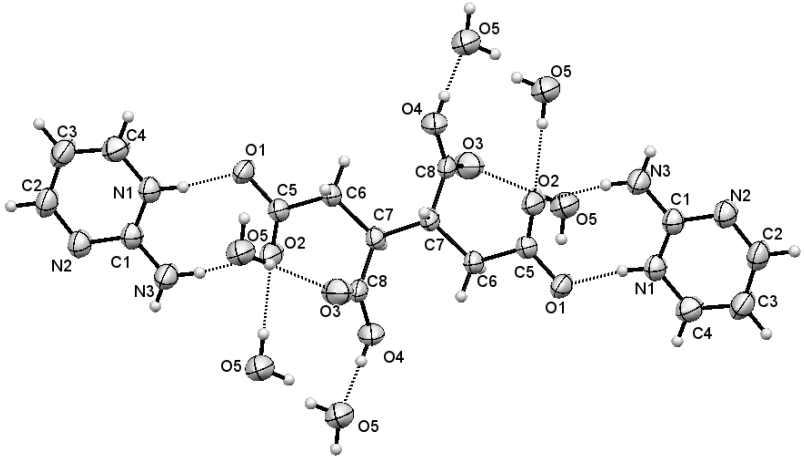

Figure 6.30. *Crystal structure of: a) co-crystal 2-amino-4,6-dimethylpyrimidine/benzoic acid[107]; b) co-crystal 2-aminopyrimidine/1,4-cyclohexanedicarboxylic acid[108]; and salt 2-aminopyrimidine/butane-1,2,3,4-tetracarboxylic acid[109].*

Since cyprodinil is an aminopyrimidine derivative, in this thesis work the synthesis of the 1 : 1 binary co-crystal of cyprodinil with benzoic acid was attempted and the resulting crystal structure was analysed by SXD.

6.3.1.1.Benzoic acid

A deeper understanding of the characteristics and nature of the intermolecular interactions that take place in the molecular complex cyprodinil/benzoic acid will be obtained later in this section by comparing the crystal structure of the co-crystal to those of the individual components, where available. A search in the literature showed that extensive work had already been done on the crystal structure of benzoic acid. Due to the focus of the present work on the hydrogen bond, the structure chosen for the characterisation of the crystal packing of benzoic acid was derived by single crystal neutron diffraction, on the single crystal diffractometer SXD at ISIS spallation neutron source[110]. In this study the structure of a crystal of benzoic acid was refined at five temperatures 20, 50, 100, 125, and 175K. The molecules of benzoic acid interact in dimers forming circular hydrogen bonds. However, worth of noting is the presence in all structures of disorder of the hydrogen atom on the carboxylic group, the one that is involved in the intermolecular interaction, leading to two configurations of the acid molecule, as shown in Figure 6.31.

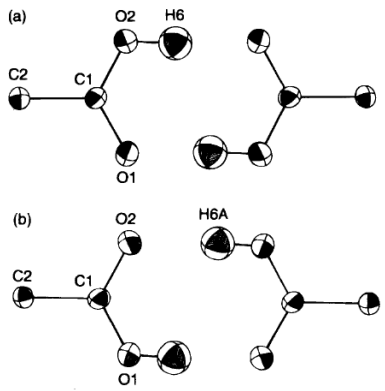

Figure 6.31. *ORTEP plots depicting the A configuration (a) and the B configuration (b) of the refined benzoic acid dimer motif at 175K*[110].

The study proved that the degree of disorder increases with temperature as shown by the increase of the dimensions of the anisotropic thermal ellipsoids of the hydrogen atom H6 (Figure 6.32).

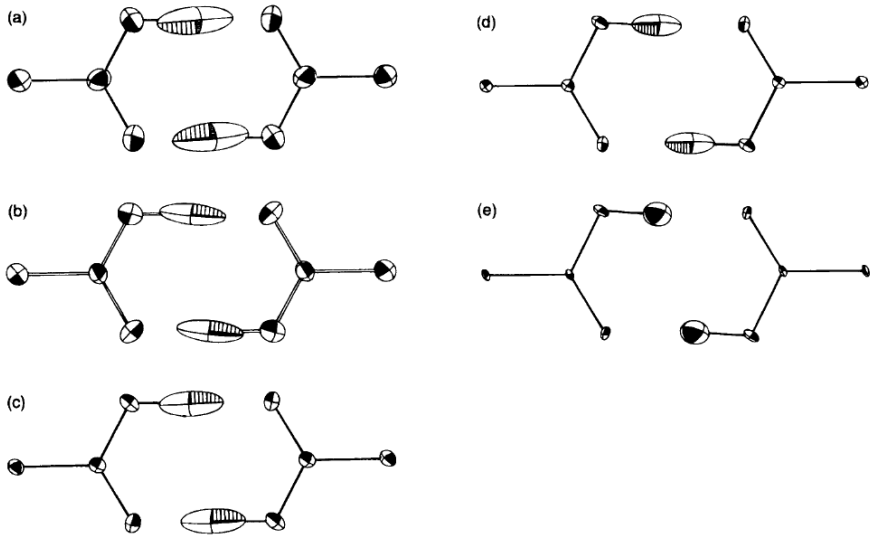

Figure 6.32. *ORTEP plots of the dimer motif in benzoic acid. The highly anisotropic thermal vibration ellipsoid of atom H6 indicates the presence of disorder at the site, which is observed to decrease with temperature. The structure is shown at (a) 175K, (b) 125K, (c) 100K, (d) 50K, and (e) 20K*[110].

6.3.2. Experimental

6.3.2.1. Physical and chemical properties of benzoic acid

The solid form of benzoic acid is a white crystalline powder with melting point in the range 121˚-125˚C and boiling point of 249˚C. It has vapour pressure of 13 hPa at 132˚C and a pH of 2.5-3.5 at 20˚C, with water solubility of 2.9 g/l at 25˚C[111]. It is soluble in a large variety of organic solvents, such as acetone, benzene, chloroform, alcohols, and ethyl ether.

6.3.2.2. Synthesis from solution

Crystals of the adduct cyprodinil/benzoic acid of size and quality suitable for SXD were prepared from solution. Taking into account the solubility of both compounds, the selection of the solvent fell on ethanol. Table 6.11 reports the quantities used for the solution.

Substance	Quantity
Cyprodinil	0.52 g
Benzoic acid	0.30 g
Ethanol	10 ml

Table 6.11. *Quantities used for the preparation of the solution.*

The two components were dissolved in ethanol at room temperature in a 1 : 1 ratio. Complete dissolution was achieved by heating the solution to around 60˚C. This temperature was kept for two hours, during which the solution was continuously stirred. After that time, it was transferred into a crystallisation vial that was covered with parafilm in the double intent of preventing impurities to get in contact with the solution and to slow down the evaporation process. Crystallisation occurred at room temperature and yield plate-like, transparent co-crystals.

6.3.2.3. Differential Scanning Calorimetry

Possible variations in the structure of the co-crystal as a function of temperature were monitored by DSC analysis. The results of the DSC analysis are reported in Figure 6.33. The DSC profile of the co-crystal shows only an endothermic event around ~ 97˚C, which corresponds to its temperature of fusion. No other significant thermal signals are recorded and no re-crystallisation is noticeable during the cooling to 20˚C. The increase of the melting point of the co-crystal compared to the sole cyprodinil (~70˚C for form A and ~75˚C for form B) indicates that the formation of intermolecular interactions between the two components leads to a more stable structure.

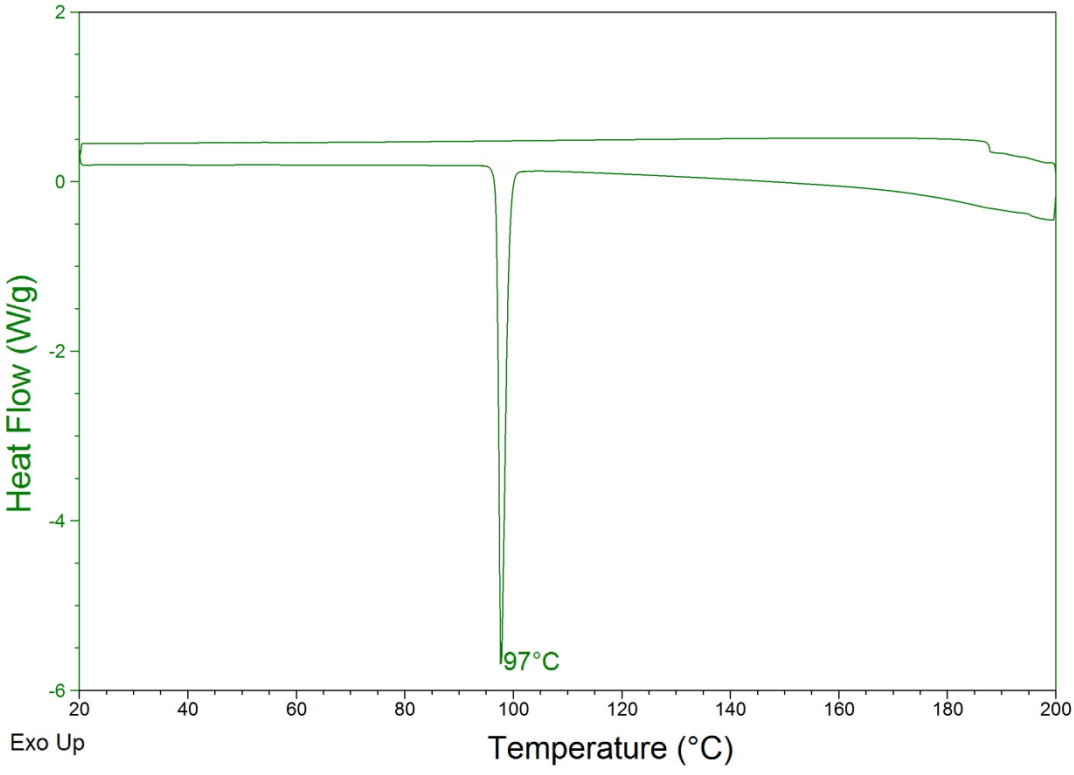

Figure 6.33. *DSC profile of the co-crystal.*

6.3.2.4. Powder X-ray diffraction

At first, the positive outcome of the synthesis of the co-crystal was assessed by PXD. The crystals obtained from the ethanol solution were manually ground into a fine powder in an agate mortar and a small quantity of powder was placed on a Perspex sample holder. Data were collected on the powder diffractometer D5000. In Figure 6.34 the I vs. 2θ plot is reported.

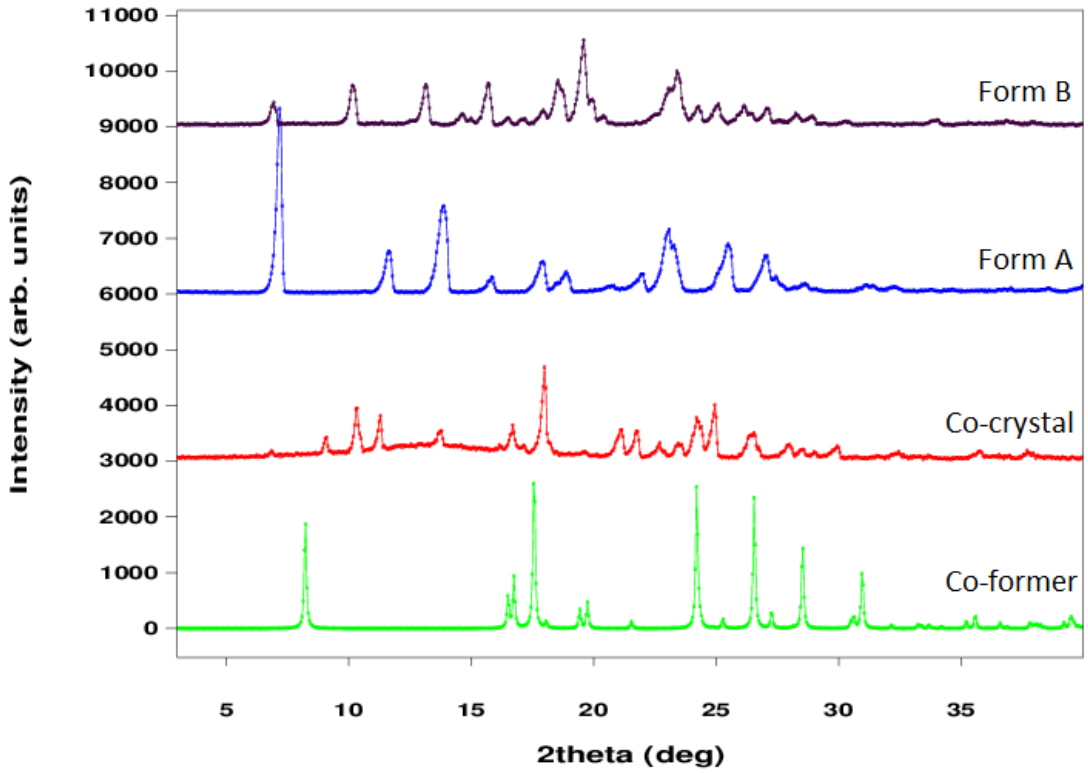

Figure 6.34. *PXD patterns for the co-crystal (red), forms A (blue) and B (black) of cyprodinil, and benzoic acid (green).*

The different positions of the Bragg peaks of the co-crystal compared to the two separate components indicate the occurrence of a different crystal structure. To verify the formation of the co-crystal, single crystal X-ray diffraction was the technique of choice. It is possible to calculate a PXD pattern of the co-crystal from the SXD results and, by comparing it to the experimental powder pattern, to assess the success of the co-crystallisation, as shown in Figure 6.35. The same positions of the Bragg peaks in the two patterns confirm the formation of the co-crystal cyprodinil/benzoic acid.

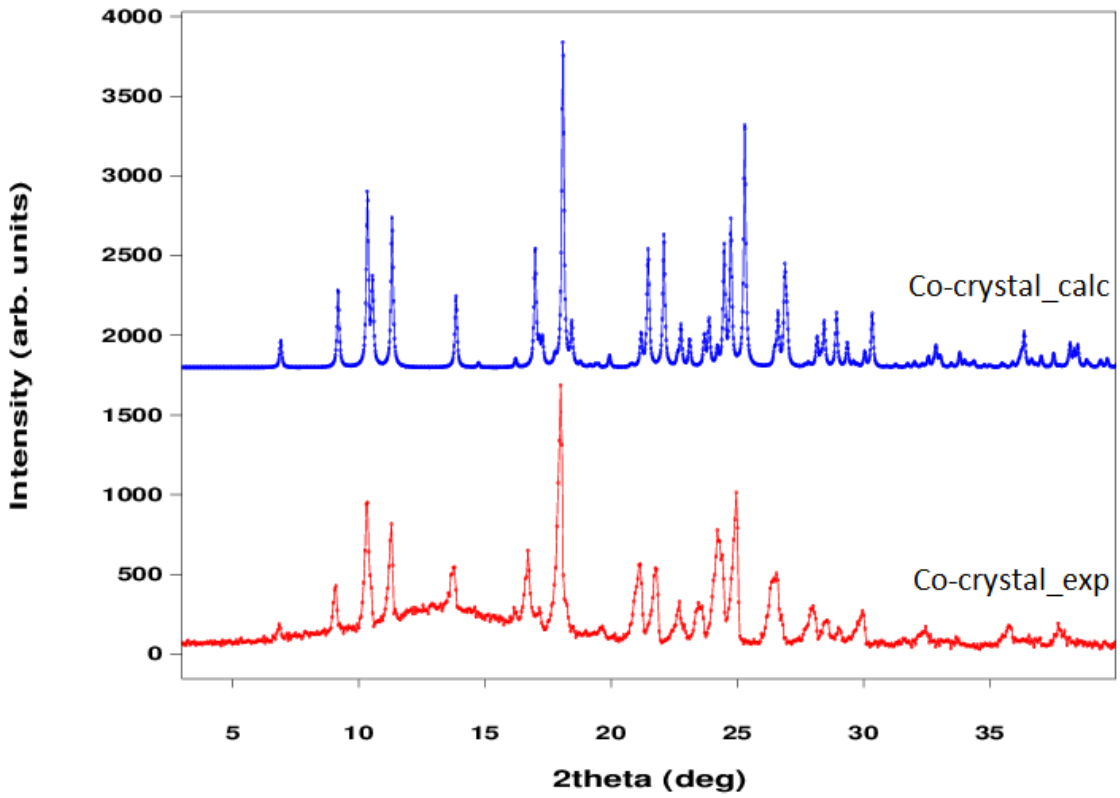

Figure 6.35. *In red, experimental PXD of the co-crystal grown from the ethanol solution; in blue, PXD pattern of the co-crystal that was calculated from experimental SXD results.*

6.3.2.5. Single crystal X-ray diffraction

The morphology of the co-crystal resembled a thin, colourless plate. The crystal selected for the SXD measurement (crystal volume ~0.03 mm^3) was grown from an ethanol solution by the method of slow evaporation of the solvent at room temperature. Data were collected on the Xcalibur single crystal diffractometer at a temperature of 150K. The structure displays disorder in the position of the hydrogen atom H7 that is the one involved in an intermolecular interaction between the hydroxyl and the pyrimidine N atom of cyprodinil. The two hydrogen positions, H7A and H7B, were refined with fixed isotropic thermal factors (U_{iso} = 0.05 $Å^2$). In addition, fixed bond lengths were assigned to O2-H7A (0.90(2) Å) and N2-H7B (0.92(2) Å).

In Table 6.12, X-ray crystallographic data and refinement parameters for the co-crystal at 150K are reported.

Name	Cyprodinil / benzoic acid
Empirical formula	$C_{14}H_{15}N_3$ / $C_7H_6O_2$
Formula weight (g mol^{-1})	347.41
Temperature (K)	150
Wavelength (Å)	0.71073
Crystal system, space group	Orthorhombic, $P2_12_12_1$
Unit cell dimensions	a = 5.4169(3) Å
	b = 17.0864(9) Å
	c = 19.233(1) Å
Volume ($Å^3$)	1780.1(2)
Z, calculated density (g cm^{-3})	4, 1.296
F(000)	736
Absorption coefficient (mm^{-1})	0.085
Theta range for data collection (˚)	3.39 to 26.37 deg
Limiting indices	$-6 \leq h \leq 6$, $-21 \leq k \leq 17$, $-22 \leq l \leq 24$
Reflections collected / unique	13199 / 3632 [R_{int} = 0.0274]
Completeness to θ = 26.37	99.7 %
Refinement method	Full-matrix least-squares on F^2
Data / restrains / parameters	3632 / 2 / 323
Goodness-of-fit on F^2	1.043
Final R indices [I>2sigma(I)]	R_1 = 0.0306, wR_2 = 0.0720
R indices (all data)	R_1 = 0.0350, wR_2 = 0.0750
Extinction coefficient	0.006(1)
Largest diff. Peak and hole (e $Å^{-3}$)	0.15 and -0.15

Table 6.12. *X-ray crystallographic data and refinement parameters for the co-crystal cyprodinil/benzoic acid at 150K.*

6.3.3. Results and discussion

The asymmetric unit of the co-crystal is formed by a molecule of cyprodinil and one of benzoic acid, as displayed in Figure 6.36.

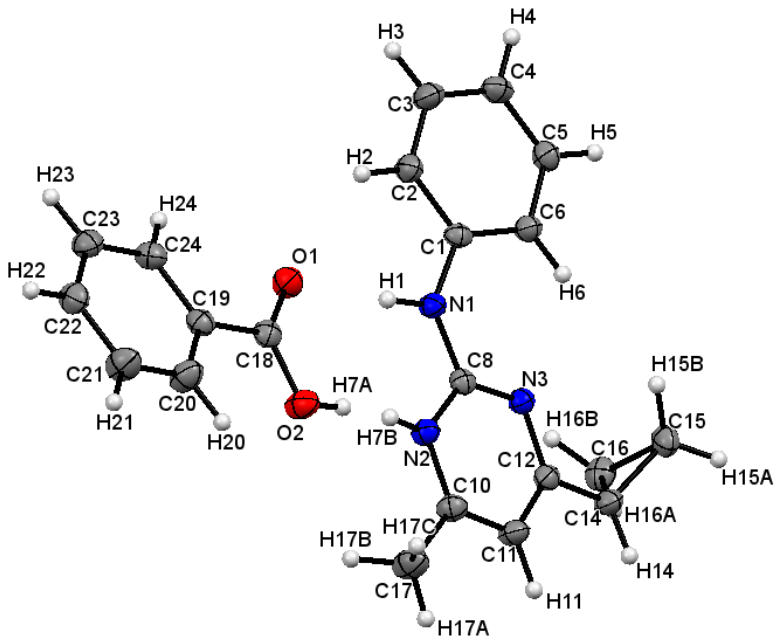

Figure 6.36. *ORTEP representation of the asymmetric unit of the co-crystal, viewed along the* ***c****-axis, derived from SXD. The probability level for all non-hydrogen ellipsoids is 50%, while the hydrogen atoms are drawn as fixed-size spheres of radius 0.15 Å.*

C8-N1-C1-C6	-5.8(2)˚
N3-C12-C14-C15	25.3(2)˚
N3-C12-C14-C16	-42.8(2)˚
C8-N3-C12-C14	176.5(1)˚
N2-C8-N1-H1	-7(1)˚
O2-C18-C19-C20	10.4(2)˚
C18-C19-C20-C21	-179.8(1)˚
C18-C19-C24-C23	179.4(1)˚

Table 6.13. *Torsion angles of interest.*

From the observation of Table 6.13, which lists the values of selected torsion angles, it is possible to notice that the conformation of the cyprodinil molecule is very similar to the one displayed in the previous two co-crystals of the fungicide with 2-aminopyrimidine and maleimide. The pyrimidine and benzene rings are not co-planar, but they are twisted by an angle of ~5.8(2)˚, and the cyclopropyl substituent is not centred in respect to the pyrimidine moiety. The benzoic acid

displays the planar conformation typical of aromatic compounds, but the carboxylic functionality is twisted by an angle of ~10.4(2)˚ in respect to benzene ring. The two interacting molecules do not lie on the same plane, but they form an angle of ~19.2(2)˚.

The crystal packing is held together by the formation of heterogeneous dimers created by the interaction between one molecule of cyprodinil and one of benzoic acid. The resulting interaction is a circular hydrogen bond, leading to an 8-membered ring, as reported in Figure 6.37. The dimers stack themselves into piles forming a fishbone motif, as shown in Figure 6.38.

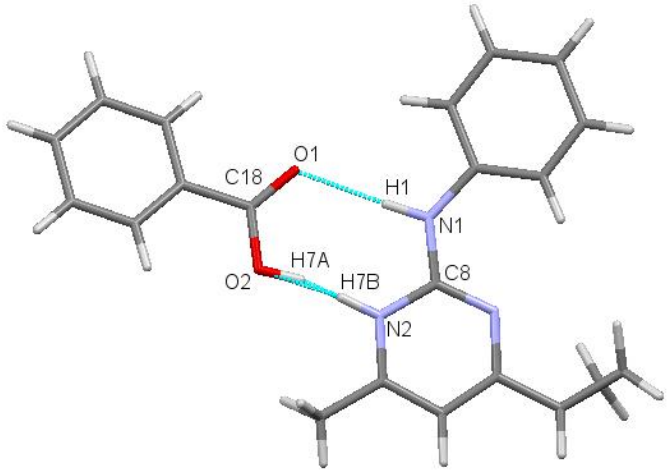

Figure 6.37. *Heterogeneous dimer formed by the two components of the co-crystal.*

N1-H1	0.92(2) Å
H1···O1	2.00(2) Å
N1···O1	2.925(2) Å
N1-H1···O1	177(1)˚
O2-H7A	0.90(2) Å
H7A···N2	1.79(2) Å
N2-H7B	0.89(8) Å
H7B···O2	1.80(8) Å
O2-H7A···N2	168(2)˚
N2-H7B···O2	164(8)˚
O2···N2	2.675(2) Å

Table 6.14. *Hydrogen bond lengths and geometry of interaction.*

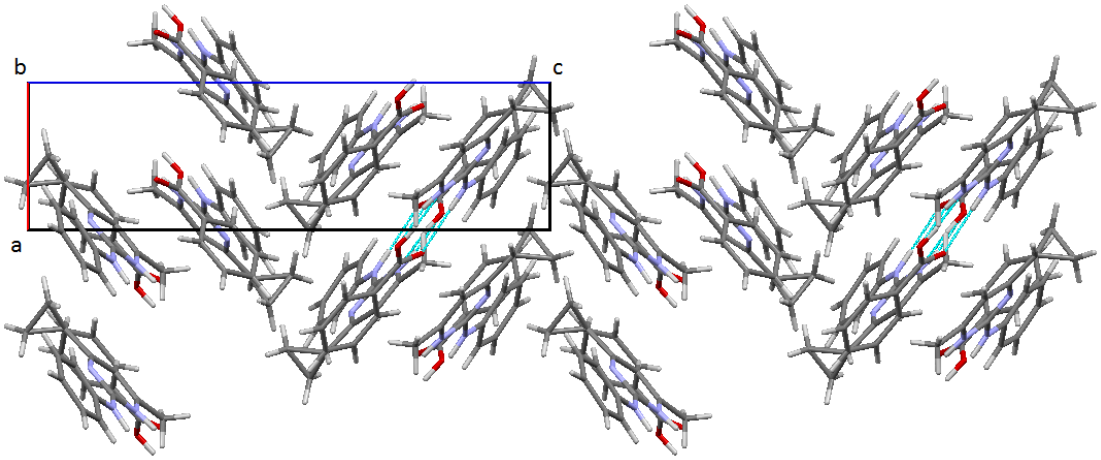

Figure 6.38. *Crystal packing of the co-crystal, viewed along the* ***b****-axis.*

As clearly displayed in Figure 6.36, the hydrogen atom that belongs to the hydroxy group is disordered between two positions. Table 6.15 reports the value for the site occupancy factors (***sof***) of atoms H7A and H7B, when they are allowed to refine following a free variable.

Atom	***sof***
H7A	0.825(30)
H7B	0.174(30)

Table 6.15. *Site occupancy factors for atoms H7A and H7B.*

Usually for an atom in a general position the value of the ***sof*** is fixed to 1, indicating that this particular atom is present in only that specific position inside the unit cell. In the case of an atom in a special position, that is when the atom coordinates coincide with an element of symmetry, the occupancy factor is adjusted depending on the type of symmetry: for example, when an atom is positioned on a two-fold axis, a mirror plane or an inversion centre, the site occupancy is reduced to 0.5. When the site occupancy factor of an atom is allowed to refine freely, the ***sof*** will be as close as possible to the expected value, 1 for the general position and 0.5 for the two-fold axis or mirror plane. It follows that if the refined value of the occupancy factor for an atom in a general position is not close to unity, then most probably that atom is disordered over two positions. The two values reported in Table 5 indicate that the hydrogen atom is positioned in conformation H7A for around 80% of the time; the remaining 20% will be in conformation H7B.

Additional proof of the presence of disorder can be found in the difference Fourier maps, shown in Figure 6.39.

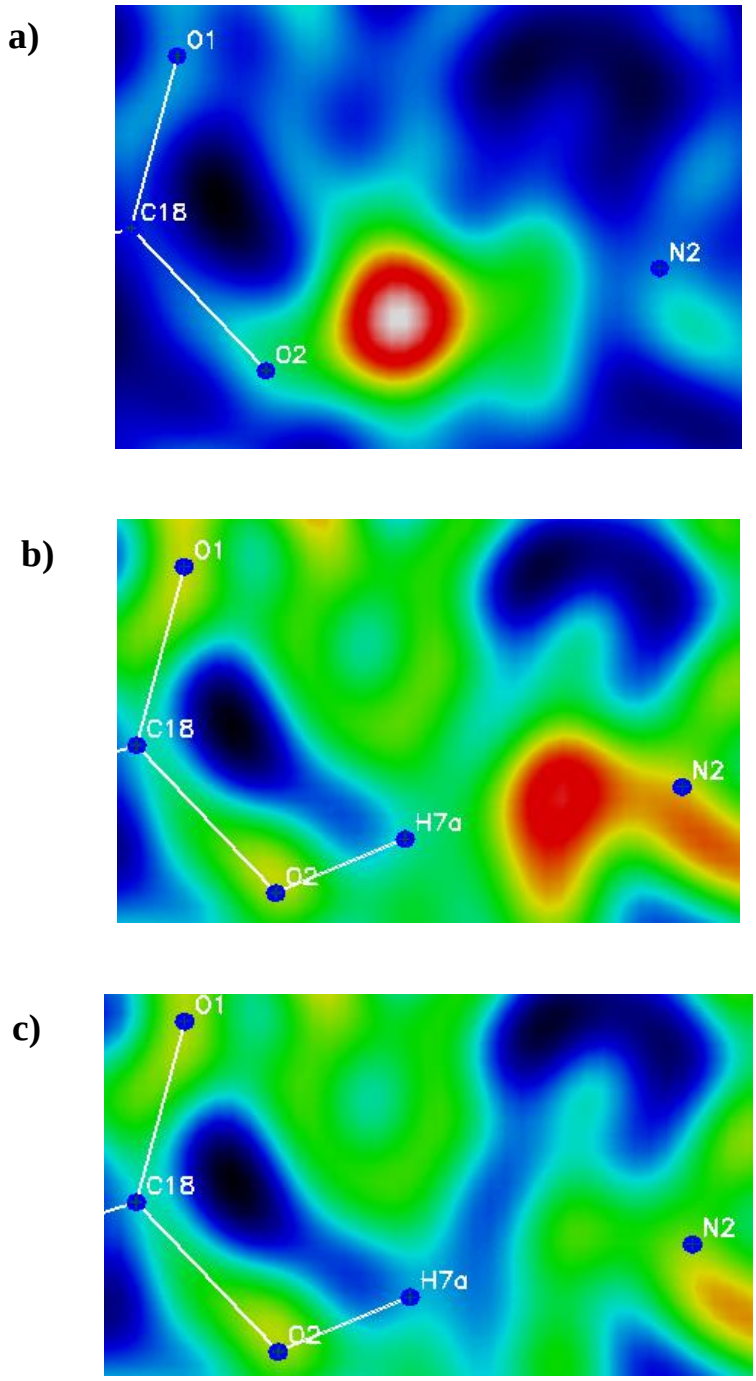

Figure 6.39. *Electron-density maps for the hydrogen bond O2-H7···N2: a) the atom H7 was taken out of the refinement; b) the atom H7 was refined in position H7A; c) addition in the refinement of position H7B.*

As displayed in Figure 6.39a, by observing the difference Fourier map indicating the presence of the hydrogen atom, it is possible to notice a slight elongation of the electron density towards the nitrogen atom of a cyprodinil molecule, a first indication of disorder. When the electron density is refined as an hydrogen atom covalently bonded to atom O2, an excess of electron density appears near nitrogen N2, in line with the interaction O2-H7A···N2, and at a reasonable distance to justify

the H7B-N2 bond (Figure 6.39b). After identification of position H7B and refinement of the disorder introducing a free variable, which defines the partition between the two hydrogen positions, no additional electron density can be found in the difference Fourier map (Figure 6.39c), confirming the hypothesis of disorder.

In contrast to the case of the crystal structure of benzoic acid, in the co-crystal the disorder affects only one of the two hydrogen bonds responsible for the intermolecular interaction. A reason for this behaviour can be found in the interatomic distances O1···N1 and O2···N2, which are reported in Table 6.16.

O1···N1	2.925(2) Å
O2···N2	2.675(2) Å

Table 6.16. *Intermolecular distances between interacting molecules at 150K.*

The interatomic distance O2···N2 is significantly shorter than O1···N1, leading to a hydrogen bond which is borderline between those classed as moderate and strong[81]. Since neutrons and X-rays determine atom heavier than hydrogen, such as oxygen and nitrogen atoms, to a similar degree of accuracy, it possible to compare the interatomic distance O2···N2 of the co-crystal, 2.675(5) Å, to the equivalent interaction, O2···O1', in benzoic acid, 2.629(7) Å[110]. It is, however, important to remember that the degree of disorder present in the co-crystal is low with an 80 : 20 ratio.

6.3.4. Conclusions

Synthesis of the 1 : 1 binary co-crystal cyprodinil/benzoic acid was achieved from an ethanol solution by slow evaporation of the solvent at room temperature and it produced colourless, plate-like crystals.

As shown by the DSC variations in the temperature do not induce any changes in the crystal structure of the adduct, but the presence of intermolecular interactions with the co-former contribute to stabilise the cyprodinil molecules, increasing the temperature of fusion from 70-75˚C of the fungicide to 97˚C of the molecular complex.

The molecules of cyprodinil and co-former interact with one another by forming a circular ring composed by two hydrogen bonds (HBs): a moderate HB of 2.00(2) Å and a stronger one of 1.79(2) Å, which exhibits disorder of the hydrogen atom position. The degree of disorder is, however, low and the hydrogen atom is bonded to the oxygen of the hydroxyl on benzoic acid for more than 80% of the time; the remaining 20% displays the hydrogen bound to the nitrogen atom on cyprodinil. However, it is important to remember that the hypothesis of a disordered structure can only be corroborated by SND. Unfortunately, time restriction in the schedule of D19 at ILL did not allow collection of SND data on this co-crystal.

Chapter 7

7. Co-crystals of cyprodinil – Part II

In order to gain a deeper understanding of the nature and characteristics of the hydrogen bond inside co-crystals of cyprodinil, a series of differently substituted benzoic acids were used as co-formers. The aim of this study was to assess whether the presence of a substituent on the benzene ring, its position and its properties, had a role in the formation of the intermolecular hydrogen bonds between cyprodinil and the carboxylic moiety. The species that were chosen as substituents on benzoic acid display different values of the ***inductive effect***. This is an electrostatic effect, indicated by the symbol ***I***, and it refers to the tendency of an atom or a group of atoms to attract (effect ***–I***) or repel (effect ***+I***) electron density. Since it is based on movement of electrons along a chain, usually made of carbon atoms, the inductive effect is strictly dependent on the electronegativity of the atoms involved: the higher the electron-withdrawing power of a group, the higher the value of the effect ***–I***. On the contrary, electron-releasing species display effect ***+I***. The study carried out in this thesis involved as substituents four electron-withdrawing groups, here listed with decreasing value of the effect ***–I***, NO_2 > F > Cl > NH_2, and one electron-releasing group, -CH_3.

7.1. Cyprodinil / monoaminobenzoic acids

7.1.1. Introduction

The first co-formers to be selected for the co-crystallisation with cyprodinil were the three isomers of monoaminibenzoic acid: 2-aminobenzoic acid, 3-aminobenzoic acid, and 4-aminobenzoic acid. Searches in literature showed that the crystal structures of all isomers had been already described.
Three polymorphs of 2-aminobenzoic acid are known: they were firstly identified by McCrone[112], who named them modification I, II, and III. Form I crystallises in the orthorhombic system, space group ***$P2_1cn$***, and it is stable until 81˚C. Above that temperature the stable polymorph is modification II, which also belongs to the orthorhombic system with space group ***Pbca***. The third polymorph is the higher-melting form, with a temperature of fusion of 145˚C, and it crystallises in the monoclinic system, space group ***$P2_1/c$***. As reported by McCrone, crystals of modification III can be obtained upon cooling the molten substance or from a solvent, such as acetic acid, ethyl acetate and water. Also form II grows from solution, but when the rate of cooling of the solution is very slow, crystals of form I appear. Even though polymorph I is the form stable at room

temperature, commercial 2-aminobenzoic acid is constituted for the major part of crystals of form III.

The crystal structure of form I displays two molecules in the asymmetric unit[113]: one molecule is neutral, while the other one is a zwitterion, as reported in Figure 7.1a.

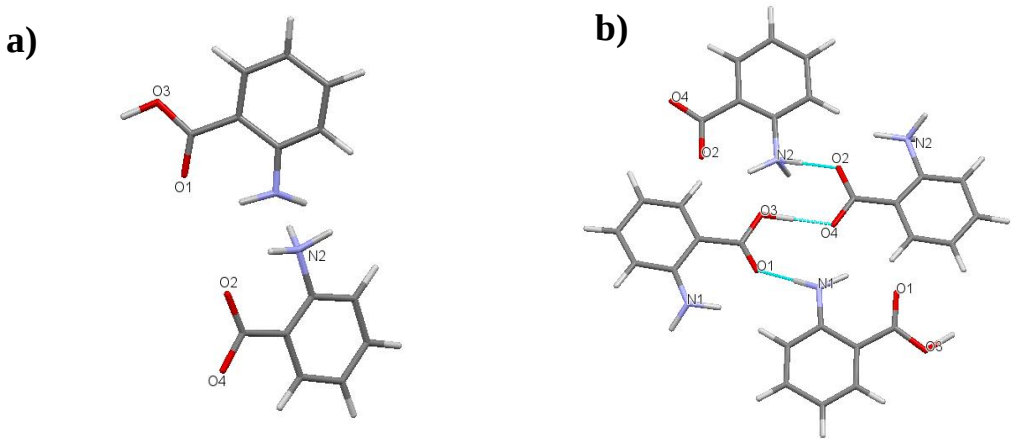

Figure 7.1. *a) Asymmetric unit of form I of 2-aminobenzoic acid; b) intermolecular interactions inside the crystal packing*[114].

The presence of the zwitterion does not allow the formation of dimers. Instead, each molecule interacts with two different neighbouring molecules, as shown in Figure 7.1b, by linear hydrogen bonds, whose lengths are 1.46 Å, for the one involving the hydroxyl group, and 1.78 Å when the amino group is the hydrogen bond donor.

The crystal structures of forms II[115] and III[116] are highly different from form I. In these cases the interacting molecules arrange themselves in dimers, leading to the formation of circular hydrogen bonds between the two carboxylic groups. Differences in the two forms can be found in the molecular conformation of the 2-aminobenzoic acid molecule: in form II the carboxylic group is twisted in respect to the benzene ring of an angle of 0.25˚, opposed to an angle of 3.08˚ in form III. This causes a shortening of the hydrogen bond lengths: 1.95 Å in form II and 1.73 Å in form III. Figure 7.2 reports the crystal packing of form II and III.

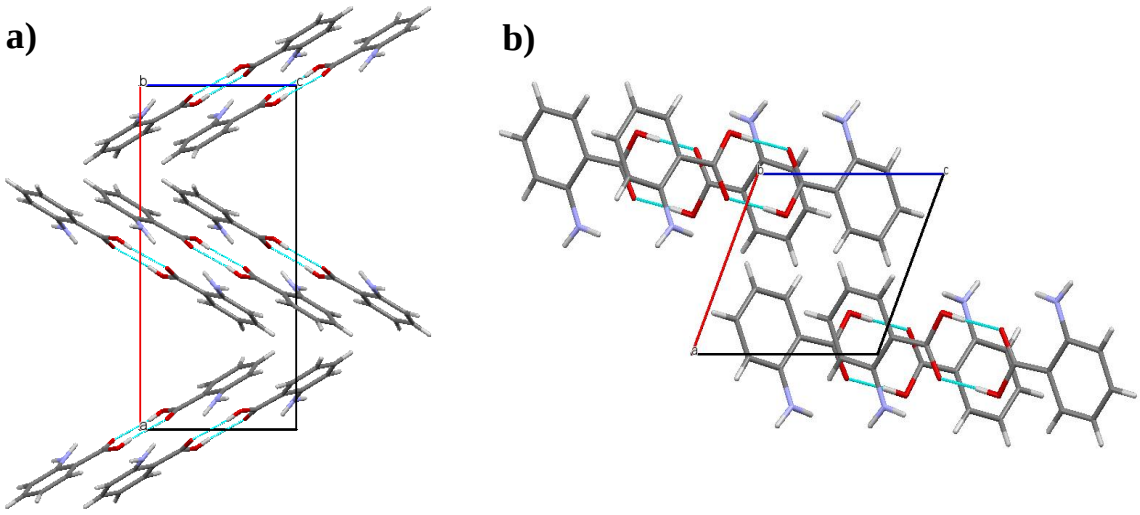

Figure 7.2. *Crystal packing of a) form II[117] and b) form III[118], both viewed along the* ***b****-axis.*

The crystal structures of 3-aminobenzoic acid[119] and 4-aminobenzoic acid[120] are similar to form II of o-aminobenzoic acid. Both structures are monoclinic: the former crystallizes in the space $\boldsymbol{P2_1/c}$ and the latter in $\boldsymbol{P2_1/n}$. In both cases the asymmetric unit is formed by two molecules of the acid, *A* and *B*, as reported in Figure 7.3. The molecules arrange themselves in dimers, held together by circular hydrogen bonds, but, while in the case of 3-aminobenzoic acid the dimers are of the type *A*-*B*, in 4-aminobenzoic acid the dimers are *A*-*A* and *B*-*B* (Figure 7.4). Hydrogen bond lengths range between 1.60 Å and 1.74 Å in 3-aminobenzoic acid, and between 1.81 Å and 1.84 Å in 4-aminobenzoic acid.

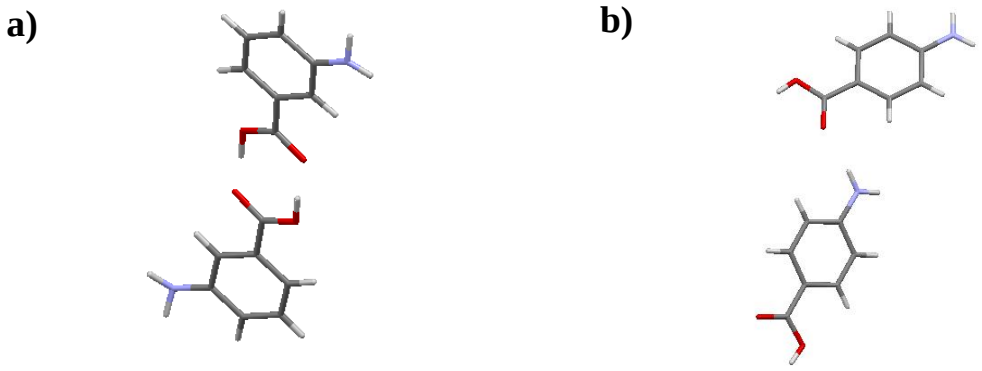

Figure 7.3. *Asymmetric unit of a) 3-aminobenzoic acid[121] and b) 4-aminobenzoic acid[122], both viewed along the* ***b****-axis.*

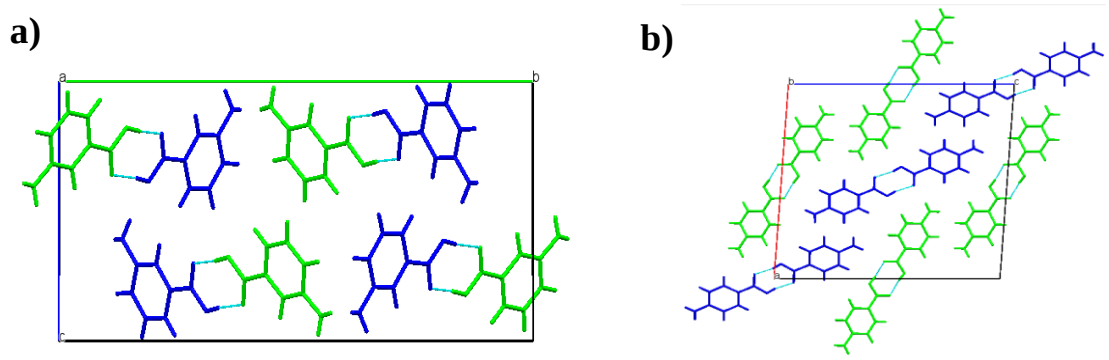

Figure 7.4. *Hydrogen bonding network in a) 3-aminobenzoic acid (viewed along the* ***a****-axis) and b) 4-aminobenzoic acid (viewed along the* ***b****-axis). The molecules are coloured by symmetry equivalence to discriminate between A and B.*

It is, finally, interesting to point out that before the characterisation of the monoclinic structure of 4-aminobenzoic acid, Killean, Tollin, Watson, and Young[123] found three distinct crystallographic forms of the compound, all twins, belonging to the symmetry class *mmm*. The refinement of the structures, in particular the observation of the electron-density maps, showed that also in these cases the acid molecules are organised in dimers.

7.1.2. Experimental

7.1.2.1. Physical and chemical properties of co-formers

2-Aminobenzoic acid[124], also known as anthralinic acid, is a white crystalline powder with a melting temperature of 144˚-148˚C. It has a water solubility of 5.7 g/L at 25˚C and it is also soluble in a large variety of organic solvents from chloroform to pyridine, to alcohols and ethyl ether.

In the solid state 3-aminobenzoic acid[125] is a light brown crystalline powder with temperature of fusion in the range 178˚-180˚C and relative density of 1.506 g/cm^3 at 20˚C. It is slightly soluble in water, with a solubility of 5.9 g/L at 15˚C. Its solubility increases in organic solvents, such as acetone, alcohols, chloroform and ether.

4-aminobenzoic acid[126] is a beige crystalline powder with melting point of 187˚-189˚C and boiling point of 340˚C. Its relative density is 1.374 g/cm^3 and it has a pH of 3.5 at 20˚C. As the other isomers, it is slightly soluble in water, with a solubility of 1 g/170 ml at 25˚C, which increases to 1 g/90 ml at 90˚C. However, it is soluble in the most common organic solvents, such as acetone, ethyl ether, methanol, ethanol, and chloroform.

7.1.2.2. Synthesis from solution

Crystals of the molecular complexes of cyprodinil with the three isomers of monoaminobenzoic acid were obtained from solution. The materials were of analytical standard and were used without further purification. In Table 7.1 a summary of the prepared solutions is reported.

Substance	Quantity
Cyprodinil	0.52 g
2-Aminobenzoic acid	0.31 g
Ethanol	10 ml
Cyprodinil	0.50 g
3-Aminobenzoic acid	0.30 g
Ethanol	10 ml
Cyprodinil	0.51 g
4-aminobenzoic acid	0.31 g
Ethanol	10 ml

Table 7.1. *Prepared solutions.*

The solutions were prepared by gradual addition of ethanol to a 1 : 1 stoichiometric amount of the reactants in order to obtain a saturated solution. Heat was applied until the temperature of 60˚C was reached; this temperature was kept stable for two hours, during which the solutions were stirred continuously. They were, then, transferred into crystallisation vials, which were covered with a film to prevent contamination from the environment. Small holes were applied on the cover to allow slow evaporation of the solvent at room temperature. The morphology of the co-crystals with 2-aminobenzoic acid (C2ABA) and 4-aminobenzoic acid (C4ABA) was similar: the two molecular complexes crystallise into thick, colourless, elongated needles. The crystal habit of the co-crystal cyprodinil/3-aminobenzoic acid (C3ABA) was that of small, very thin needles, which prevented the measurement with SXD.

7.1.2.3. Powder X-ray diffraction

PXD was used to assess whether different crystal structures had formed from the three ethanol solutions. Validation of the successful synthesis of the adducts could only be obtained by SXD. Nonetheless PXD represents an essential tool in the identification and discrimination amongst known structures. For this reason, powder patterns of two co-crystals, C2ABA and C3ABA, were collected on the D5000 diffractometer. Figures 7.5 and 7.7 diplay a comparison between the powder patterns of both polymorphs of cyprodinil and those of the co-crystals, while in Figure 7.6

the experimental powder pattern of C2ABA and the one that was calculated from the SXD data collected on a single crystal of C2ABA are reported in order to prove that the new structure obtained from solution is indeed the co-crystal.

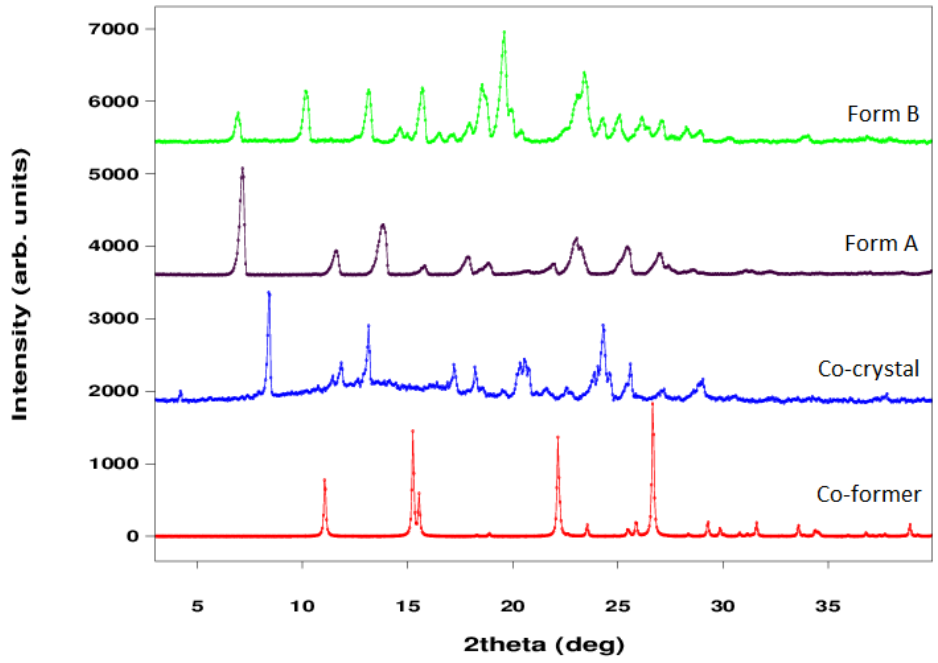

Figure 7.5. *Powder patterns of modification A (black) and B (green) of cyprodinil, 2-aminobenzoic acid (red), and 1 : 1 binary co-crystal (blue).*

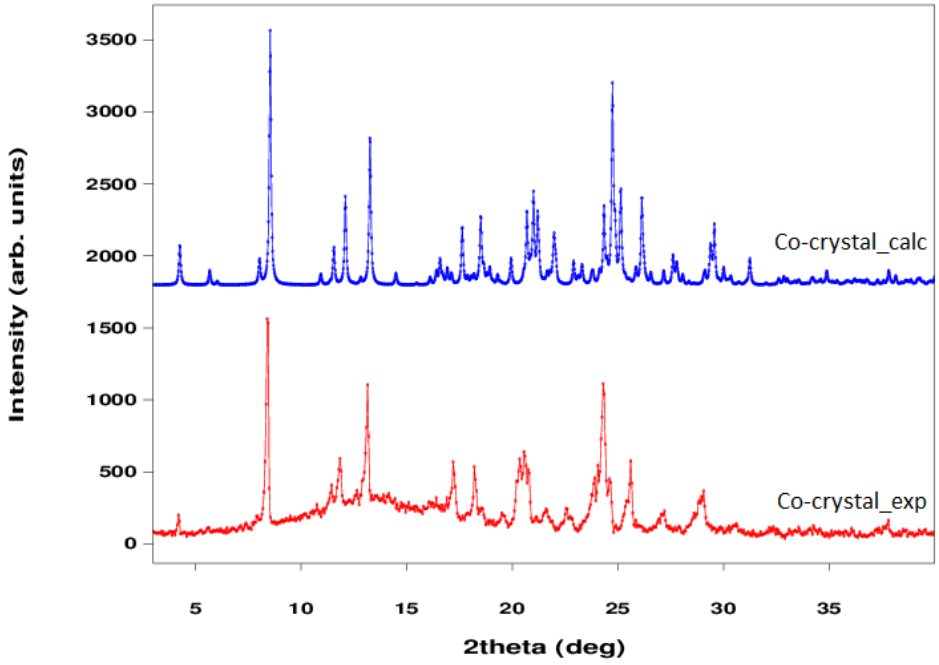

Figure 7.6. *In red, experimental PXD pattern of C2ABA; in blue, PXD pattern of C2ABA that was calculated from the experimental SXD results.*

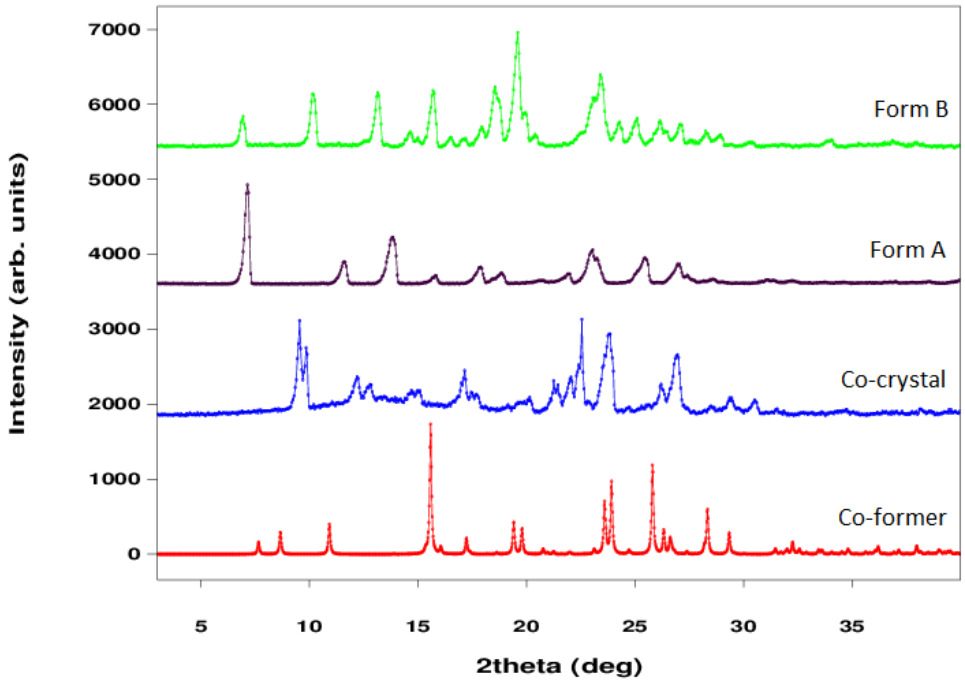

Figure 7.7. *Powder patterns of modification A (black) and B (green) of cyprodinil, 3-aminobenzoic acid (red), and of the 1 : 1 binary co-crystal (blue).*

The powder patterns of both co-crystals are different from the constituting components, as clearly visible in the positions of the Bragg peaks, indicating the formation of a different crystal structure. Complete characterisation of the self-assembly of the co-crystals with 2-aminobenzoic acid and 4-aminobenzoic acid was obtained by SXD. Unfortunately, crystals of C3ABA were too small and too thin to allow the production of a reliable model from SXD measurements. For this reason, contrary to the case of C2ABA, it was not possible to identify without doubt the formation of the co-crystal C3ABA by comparing the experimental PXD pattern to the calculated one, due to the lack of SXD data on C3ABA.

7.1.2.4. Differential Scanning Calorimetry

DSC was used to investigate possible changes in the structure of the adducts during variation of temperature. Unfortunately, due to scarce availability of the samples and to time restrictions, it was possible to obtain a DSC profile only on the co-crystal with 2-aminobenzoic acid as a co-former. The results are reported in Figure 7.8.

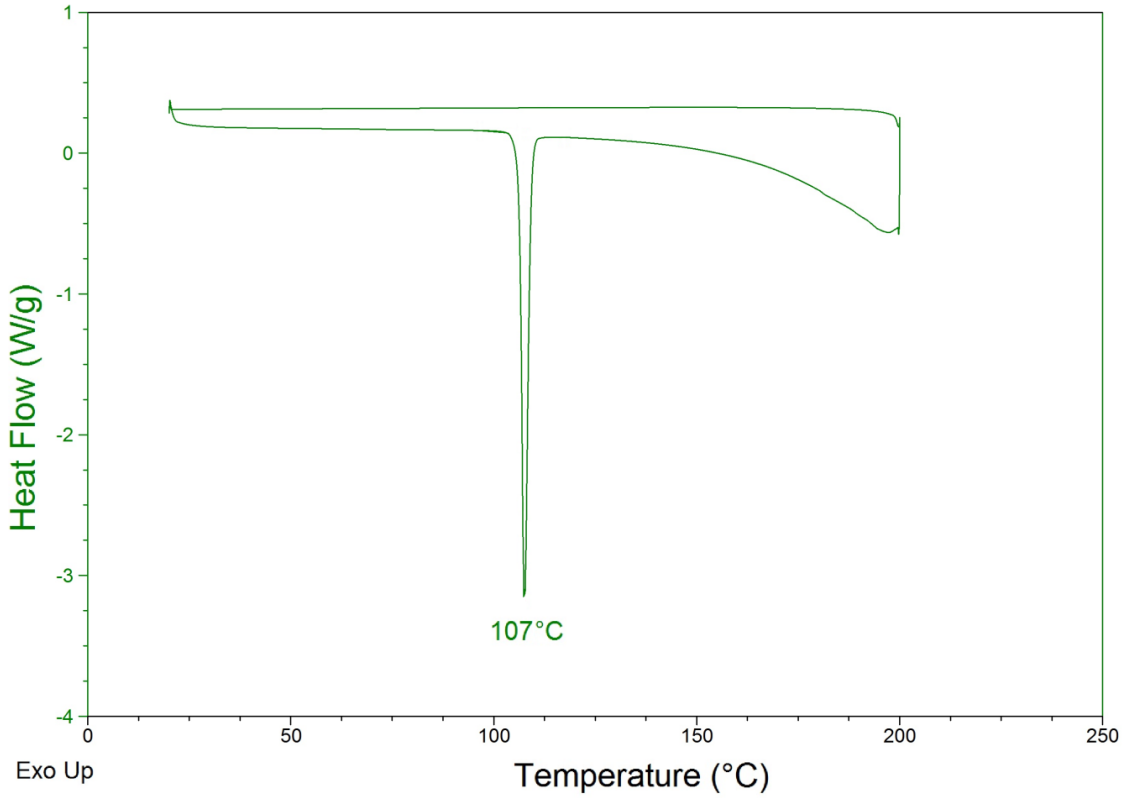

Figure 7.8. *DSC profile of the co-crystal cyprodinil/2-aminobenzoic acid.*

From the observation of the DSC profile no significant changes of the crystal structure of the adduct occur during the temperature cycle between 20˚-200˚C. One endothermic event is present during heating at around 107˚C, indicating the melting of the co-crystal. No signal was recorded in the cooling process. The interaction with a co-former increased the stability of the fungicide. It is interesting to notice that this co-crystal exhibit a temperature of fusion around 10˚ higher than the one with benzoic acid: 107˚C opposed to 97˚C.

7.1.2.5. Single crystal X-ray diffraction

Validation and characterisation of the crystal structures of the co-crystals cyprodinil/2-aminobenzoic acid (C2ABA) and cyprodinil/4-aminobenzoic acid (C4ABA) was done by SXD measurements. The two single crystals were grown separately from ethanol solutions by the method of slow evaporation of the solvent. For both adducts the crystallisation led to the formation of thick, colourless, needle-like crystals. All SXD measurements were done on the Agilent Xcalibur single crystal diffractometer with collection temperature of 150K.

In Tables 7.2 and 7.3, X-ray crystallographic data and refinement parameters for crystals of C2ABA and C4ABA, respectively, are reported.

Name	CYP / 2-aminobenzoic acid (C2ABA)
Empirical formula	$C_{14}H_{15}N_3$ $C_7H_7NO_2$
Formula weight (g mol^{-1})	362.43
Temperature (K)	150
Wavelength (Å)	0.71073
Crystal system, space group	Triclinic, $P\bar{1}$
Unit cell dimensions	a = 5.4678(2) Å
	b = 16.4003(7) Å
	c = 21.626(1) Å
	α = 73.026(4)°
	β = 87.462(4)°
	γ = 81.786(4)°
Volume ($Å^3$)	1835.8(1)
Z, calculated density (g cm^{-3})	4, 1.311
F(000)	768
Absorption coefficient (mm^{-1})	0.087
Theta range for data collection (˚)	3.56 to 26.37
Limiting indices	$-6 \leq h \leq 6$, $-20 \leq k \leq 20$, $-27 \leq l \leq 26$
Reflections collected / unique	14457 / 7492 [R_{int} = 0.0139]
Completeness to θ = 26.37	99.8 %
Refinement method	Full-matrix least-squares on F^2
Data / restrains / parameters	7492 / 0 / 664
Goodness-of-fit on F^2	1.019
Final R indices [I>2sigma(I)]	R_1 = 0.0360, wR_2 = 0.0882
R indices (all data)	R_1 = 0.0433, wR_2 = 0.0935
Extinction coefficient	0.0036(6)
Largest diff. Peak and hole (e $Å^{-3}$)	0.27 and -0.19

Table 7.2. *X-ray crystallographic data and refinement parameters for a crystal of C2ABA at 150K.*

Name	CYP / 4-aminobenzoic acid (C4ABA)
Empirical formula	$C_{14}H_{15}N_3$ $C_7H_7NO_2$
Formula weight (g mol^{-1})	362.43
Temperature (K)	150
Wavelength (Å)	0.71073
Crystal system, space group	Orthorhombic, $Pca2_1$
Unit cell dimensions	a = 17.0047(8) Å
	b = 5.7672(3) Å
	c = 18.7717(8) Å
Volume ($Å^3$)	1840.9(2)
Z, calculated density (g cm^{-3})	4, 1.308
F(000)	768
Absorption coefficient (mm^{-1})	0.087
Theta range for data collection (˚)	3.53 to 26.37
Limiting indices	$-14 \leq h \leq 21$, $-7 \leq k \leq 7$, $-9 \leq l \leq 23$
Reflections collected / unique	5299 / 2652 [R_{int} = 0.0185]
Completeness to θ = 26.37	99.8 %
Refinement method	Full-matrix least-squares on F^2
Data / restrains / parameters	2652 / 1 / 338
Goodness-of-fit on F^2	1.062
Final R indices [I>2sigma(I)]	R_1 = 0.0292, wR_2 = 0.0620
R indices (all data)	R_1 = 0.0332, wR_2 = 0.0639
Extinction coefficient	0.0099(8)
Largest diff. Peak and hole (e $Å^{-3}$)	0.16 and -0.16

Table 7.3. *X-ray crystallographic data and refinement parameters for a crystal of C4ABA at 150K.*

7.1.3. Results and discussion

7.1.3.1. Cyprodinil / 2-aminobenzoic acid (C2ABA)

The co-crystal C2ABA crystallizes in the triclinic system, space group $\boldsymbol{P\bar{1}}$, and it displays four molecules in the asymmetric unit: two molecules of cyprodinil and two of 2-aminobenzoic acid, as reported in Figure 7.9 for the structure studied with X-ray radiation.

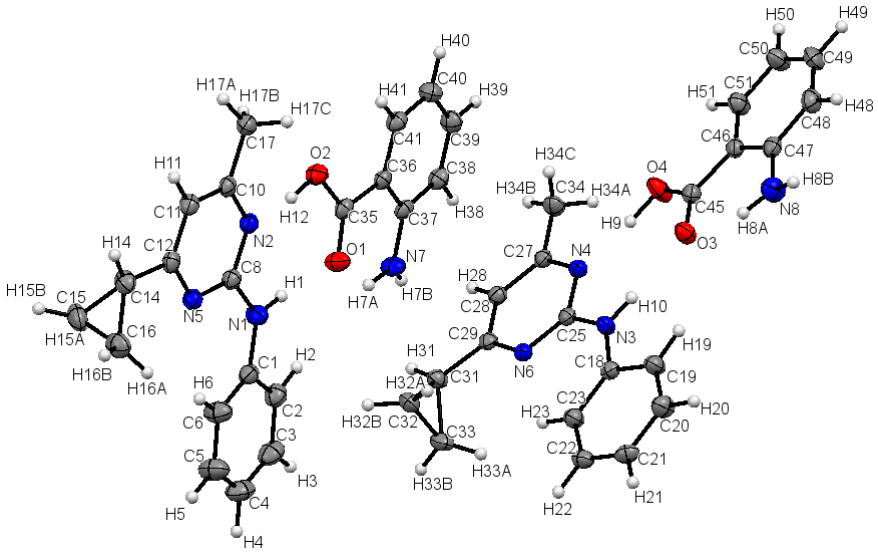

Figure 7.9. *ORTEP representation of the asymmetric unit of C2ABA, viewed along the* ***a****-axis, derived from SXD. The probability level for all non-hydrogen ellipsoids is 50%, while the hydrogen atoms are drawn as fixed-size spheres of radius 0.15 Å.*

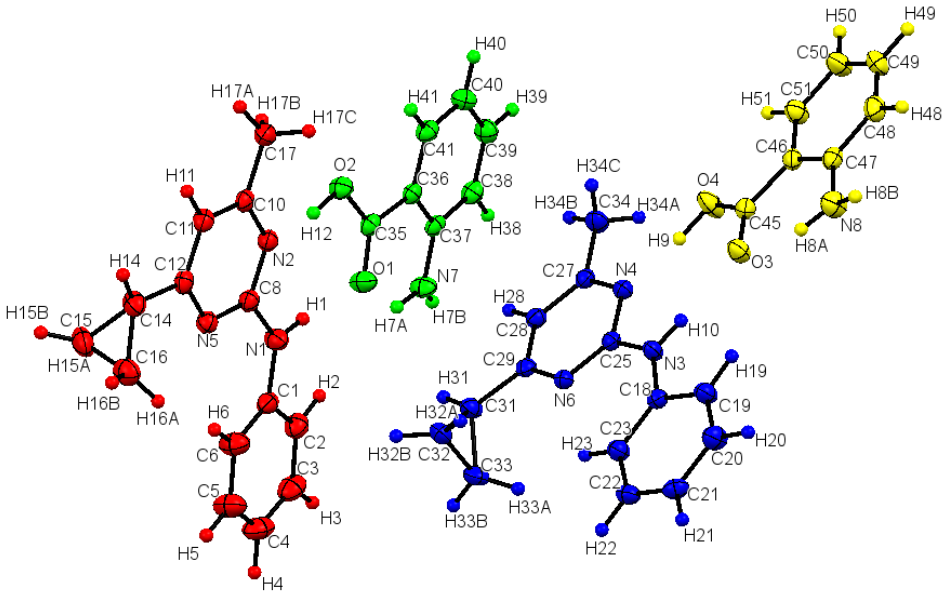

Figure 7.10. *Asymmetric unit of the co-crystal: the molecules are displayed in different colours to allow prompt identification.*

Red molecule		Blue molecule	
C8-N1-C1-C6	-11.4(2)˚	C25-N3-C18-C23	1.4(2)˚
N5-C12-C14-C15	-44.7(2)˚	N6-C29-C31-C32	33.0(2)˚
N5-C12-C14-C16	23.4(2)˚	N6-C29-C31-C33	-34.7(2)˚
C8-N5-C12-C14	175.6(1)˚	C25-N6-C29-C31	-176.8(1)˚
N2-C8-N1-H1	-2(1)˚	N4-C25-N3-H10	4(1)˚
Green molecule		Yellow molecule	
O2-C35-C36-C41	12.3(2)˚	O4-C45-C46-C51	1.2(2)˚
C35-C36-C41-C40	-177.3(1)˚	C45-C46-C51-C50	178.5(1)˚
C35-C36-C37-C38	177.3(1)˚	C45-C46-C47-C48	-179.9(1)˚

Table 7.4. *Torsion angles of interest. The colours refer to Figure 7.10.*

As shown in Table 7.4, the conformation of cyprodinil changes considerably from the red molecule to the blue one. In both cases the pyrimidine ring and the benzene group are not co-planar, but the red molecule shows a larger deviation from planarity, having a torsion angle of around -11.4(2)˚ opposed to 1.4(2)˚ of the blue molecule. Also the position of the cyclopropyl substituent is different: it is almost centred on the pyrimidine moiety in the blue molecule, while in the red is placed below the plane containing the remaining part of the molecular structure. The hydrogen atoms bonded to the amino groups, H1 and H10, are slightly twisted in respect to the pyrimidine ring, due to the hybridisation sp^3 of the nitrogen atoms N1 and N3. The two molecules of 2-aminobenzoic acid retain the planarity that is characteristic of aromatic materials, but the carboxylic group is twisted of around 12.3(2)˚ in the green molecule and of 1.2(2)˚ in the yellow one.

The crystal packing is governed by intermolecular hydrogen bonds. The hydrogen bonding network is the same to that present in the co-crystal with benzoic acid: the molecules of cyprodinil and 2-aminobenzoic acid form heterogeneous dimers, leading to circular hydrogen bonds, as shown in Figure 7.11. The two types of dimers are the ones present in the asymmetric unit, where the red molecule interacts with the green one and the blue with the yellow, and they arrange into alternate lines, as reported in Figure 7.12. The parallel lines of cyprodinil molecules are highly off-set in respect to each other so to prevent the formation of significant π-π interactions between pyrimidine and benzene rings in neighbouring molecules.

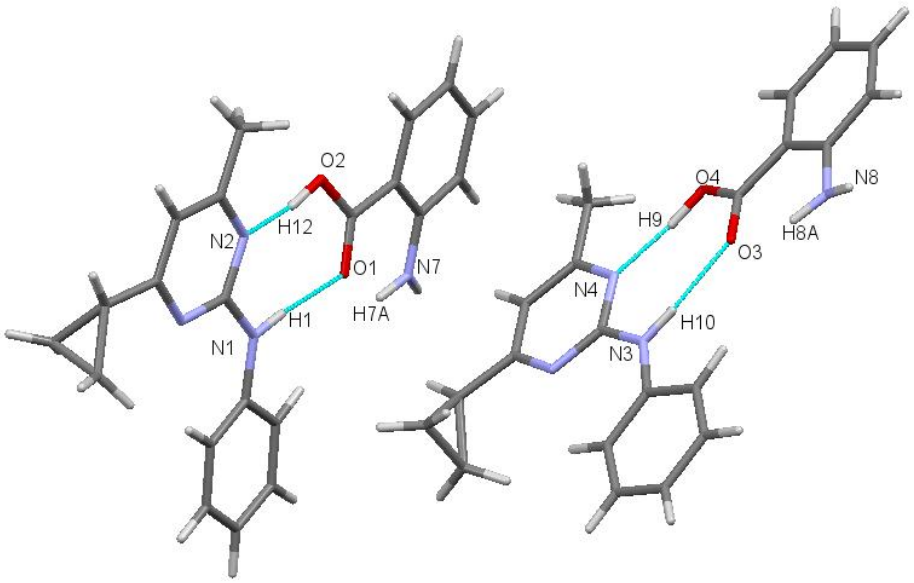

Figure 7.11. *Hydrogen bonding network in C2ABA, viewed along the* ***a****-axis.*

Intermolecular hydrogen bonds			
N1-H1	0.91(2) Å	N3-H10	0.89(1) Å
H1···O1	1.94(2) Å	H10···O3	1.98(1) Å
N1-H1···O1	175(2)˚	N3-H10···O3	174(1)˚
N1···O1	2.852(1) Å	N3···O3	2.866(1) Å
O2-H12	1.04(2) Å	O4-H9	1.00(2) Å
H12···N2	1.59(2) Å	H9···N4	1.65(2) Å
O2-H12···N2	171(2)˚	O4-H9···N4	170(2)˚
O2···N2	2.627(1) Å	O4···N4	2.649(1) Å
Intramolecular hydrogen bonds			
N7-H7A	0.91(2) Å	N8-H8A	0.88(2) Å
H7A···O1	1.99(2) Å	H8A···O3	2.02(2) Å
N7-H7A···O1	131(1)˚	N8-H8A···O3	129(2)˚
N7···O1	2.677(2) Å	N8···O3	2.671(1) Å

Table 7.5. *Hydrogen bond lengths and geometry of interaction.*

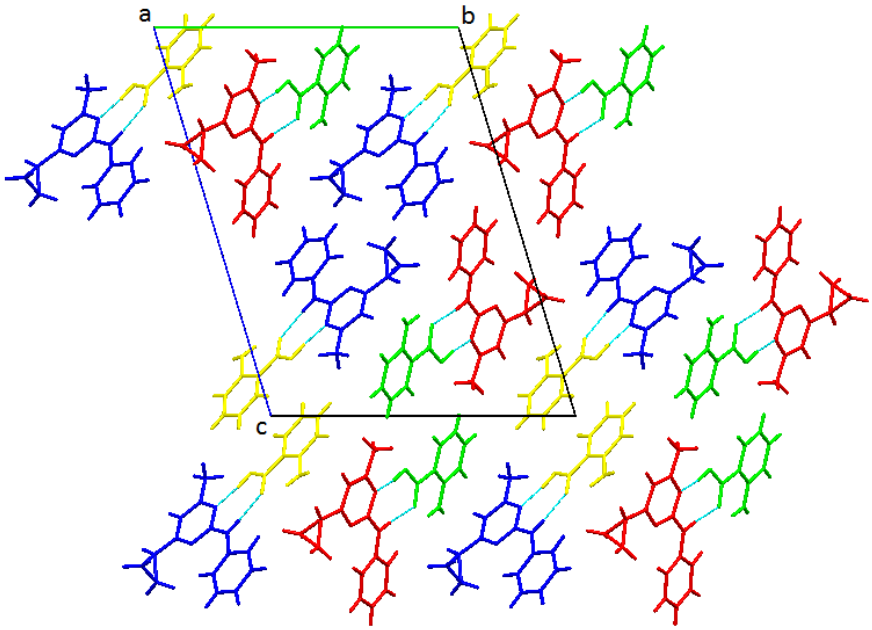

Figure 7.12. *Crystal packing of C2ABA, viewed along the* ***a****-axis. The molecules are coloured following the same scheme reported in Figure 7.10.*

Based on bond lengths, donor-acceptor distances and angle of interaction[81], it is possible to identify two moderate hydrogen bonds, N1-H1···O1 and N3-H10···O3, between the amino group on cyprodinil and the oxygen atom on the carboxyl, and two moderate-strong hydrogen bonds, O2-H12···N2 and O4-H9···N4, involving the hydroxyl group of the acid and the nitrogen atom on the pyrimidine ring of cyprodinil. In addition, each molecule of 2-aminobenzoic acid presents an intramolecular hydrogen bond between one hydrogen atom of the amino group in position 2 and the oxygen atom on the carbonyl.

Investigation of disorder or proton migration in the structure was carried out studying the electron-density maps for the hydrogen bonds, H1···O1, H10···O3, H12···N2, and H9···N4. Those maps are reported in Figures 7.13, 7.14, 7.15, and 7.16, respectively.

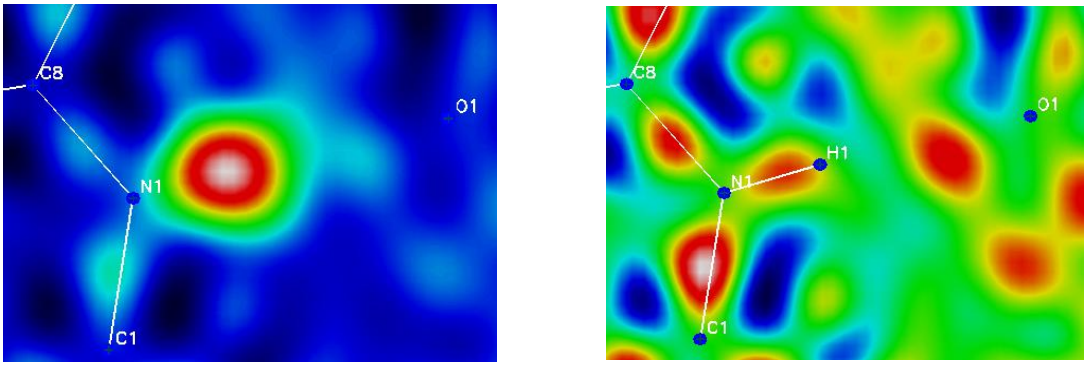

Figure 7.13. *Difference electron-density maps for the hydrogen bonds N1-H1···O1, where atom H1 was excluded (left) and included (right) in the refinement.*

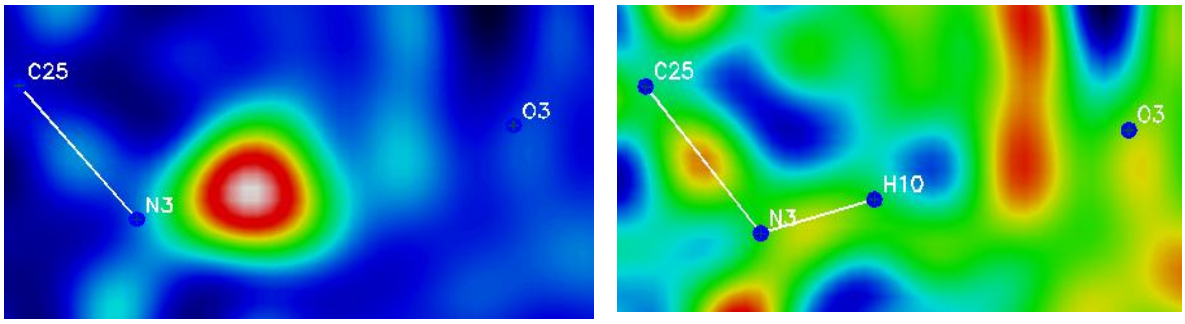

Figure 7.14. *Difference electron-density maps for the hydrogen bonds N3-H10···O3, where atom H10 was excluded (left) and included (right) in the refinement.*

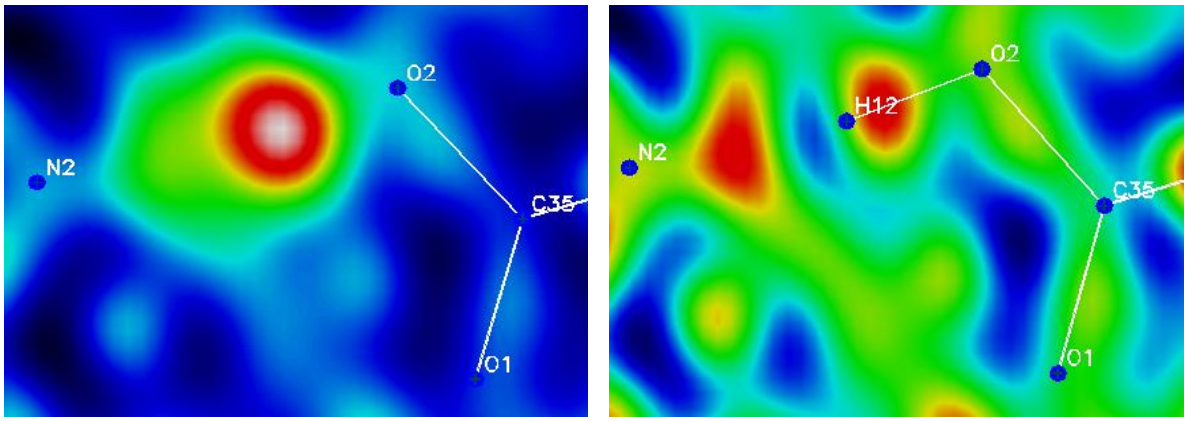

Figure 7.15. *Difference electron-density maps for the hydrogen bonds O2-H12···N2, where atom H12 was excluded (left) and included (right) in the refinement.*

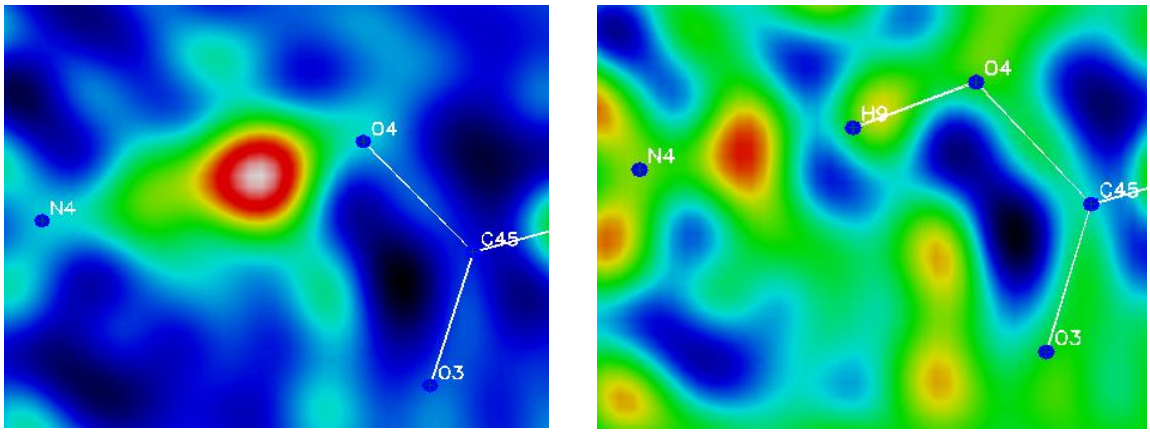

Figure 7.16. *Difference electron-density maps for the hydrogen bonds O4-H9···N4, where atom H9 was excluded (left) and included (right) in the refinement.*

The electron densities of atoms H1 and H10 show no sign of disorder, while those of atoms H12 and H9 are elongated along the direction of interaction. In addition, the shape of those electron densities is slightly bilobed, suggesting the presence of a second site. However, due to the limits that X-rays have in treating hydrogen atoms, it is difficult to recognise without any doubt the

presence of disorder in the structure. Several factors can indicate disorder. The first sign is the value of the thermal parameters, U_{iso} for hydrogen atoms: a large value of U_{iso} can point towards a disordered structure. In C2ABA the U_{iso} values for H12 and H9 are 0.072 and 0.074, respectively, opposed to 0.045 for H1 and 0.029 for H10.

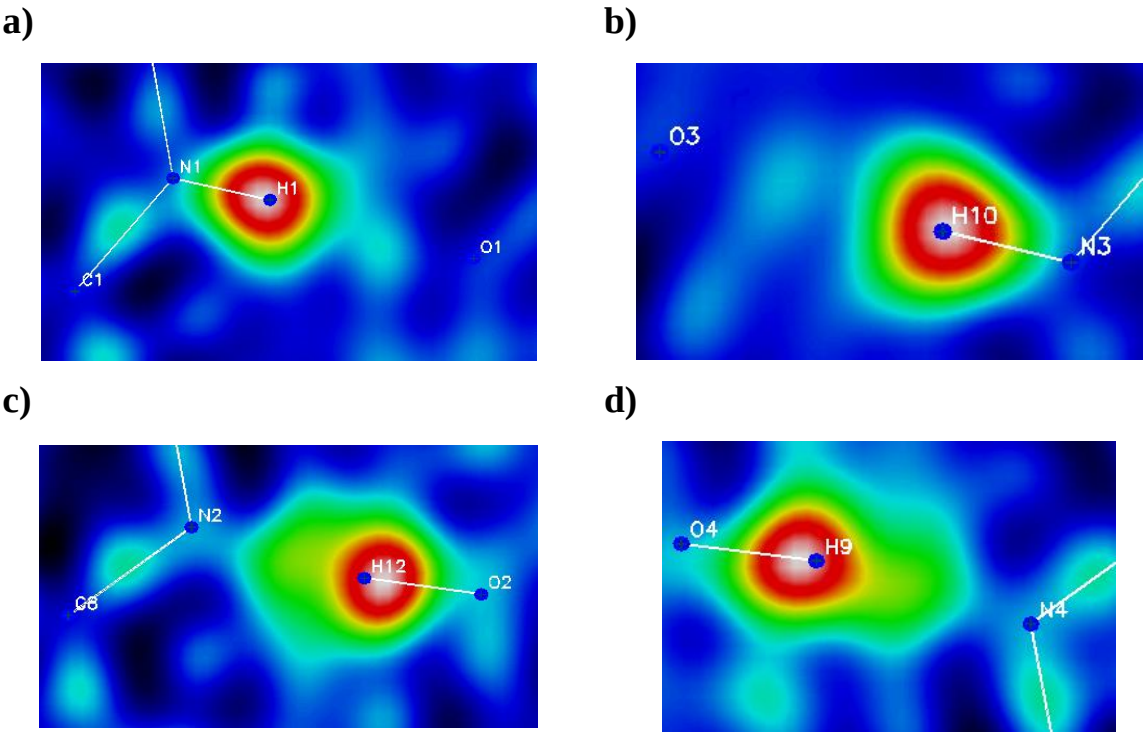

Figure 7.17. *Difference electron-density maps where the hydrogen atoms were excluded from the refinement, but their atomic coordinates were superimposed on the electron density.*

From Figure 7.17 it is possible to notice that, while the coordinates of H1 and H10 coincide with the maximum of electron density, H12 and H9 are not refined on the maximum, but SHELXL averages their position in respect of the total electron density. A careful examination of the Fourier difference maps showed the presence of weak electron densities, indicated as Q peaks, alongside the intermolecular hydrogen bonds O2-H12···N2 and O4-H9···N4. For the refinement of disorder, bond lengths O2-H12A, N2-H12B, O4-H9A, and N4-H9B were fixed at 0.90(1) Å and their U_{iso} were fixed at 0.05 $Å^2$. Table 7.6 reports the values of the ***s.o.f.*** after introduction of disorder, while in Table 7.7 main distances and angles of interaction are listed.

Atom	s.o.f.
H12A	0.72(2)
H12B	0.28(2)
H9A	0.74(2)
H9B	0.26(2)

Table 7.6. *Site occupancy factors for atoms H12A, H12B, H9A, and H9B.*

O2-H12A	0.89(2) Å	O4-H9A	0.89(1) Å
H12A···N2	1.75(2) Å	H9A···N4	1.76(1) Å
O2-H12A···N2	170(2)˚	O4-H9A···N4	171(1)˚
O2···N2	2.629(1) Å	O4···N4	2.651(1) Å
N2-H12B	0.91(4) Å	N4-H9B	0.92(2) Å
H12B···O2	1.72(4) Å	H9B···O4	1.77(3) Å
N2-H12B···O2	170(4)˚	N4-H9B···O4	159(3)˚
H12···H12B	0.84(4) Å	H9A···H9B	0.88(3) Å

Table 7.7. *Distances and angles of interaction for the disordered hydrogen bonds.*

The degree of disorder is similar in the two hydrogen bonds: for more than 70% of the time both dimers exhibit the neutral conformation of the constituting molecules, while the remaining 30% shows protonation of the pyrimidine nitrogen atom of cyprodinil. However, the introduction of disorder in the structure does not contribute much to the improvement of the refinement between not-disordered and disordered structures in terms of R-factors: in fact, R1 varies from 0.0360 to 0.0357, wR2 from 0.0935 to 0.0926, and the GooF from 1.019 to 1.010. Moreover, it is interesting to notice that the covalent bond lengths of the carboxylic group, C-O and C=O, are in line with the case of a neutral acid: 1.23(1) Å for C35-O1 and C35-O3, and 1.31(1) Å for C45=O2 and C45-O4. Finally, the electron-density maps of the disordered hydrogen bonds still show residual electron density in correspondence to the H atoms, as reported in Figure 7.18.

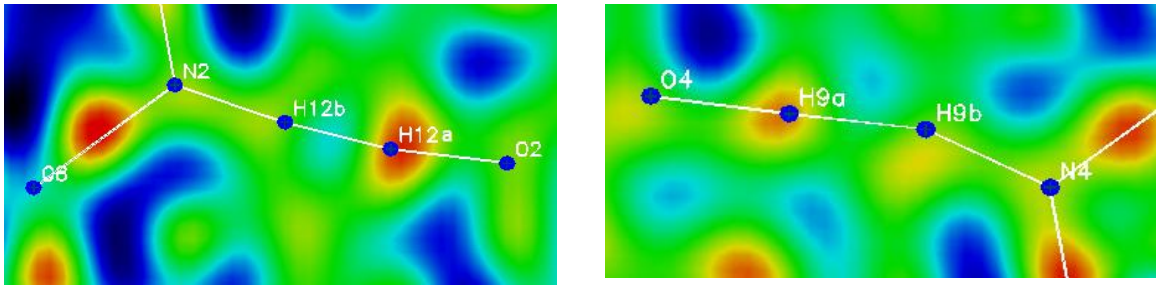

Figure 7.18. *Electron-density maps after introduction of disorder for the hydrogen bonds O2-H12···N2 (left) and O4-H9···N4 (right).*

From these considerations follows that it is not possible to state beyond doubt the presence of disorder and that it is very difficult to investigate the nature and characteristics of the hydrogen bond with X-rays alone.

7.1.3.2. Cyprodinil / 4-aminobenzoic acid (C4ABA)

Crystals of C4ABA grow in the orthorhombic system, space group ***Pca2$_1$***. The asymmetric unit displays one molecule of cyprodinil and one of acid, forming a dimer, as shown in Figure 7.19 for the strcutre studied with SXD.

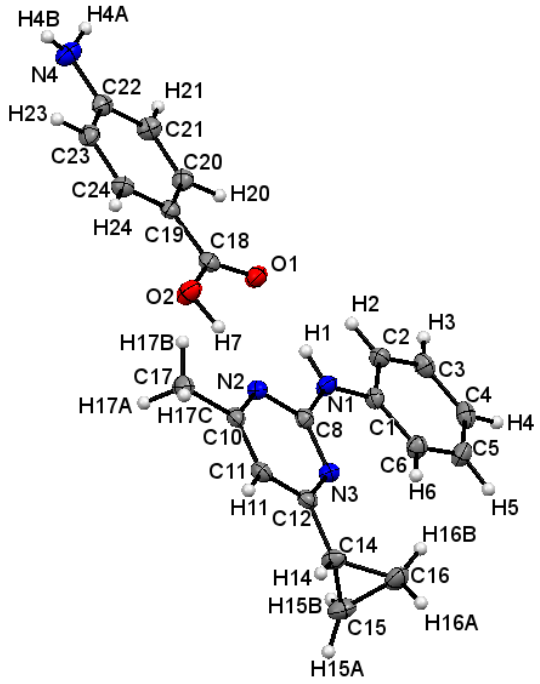

Figure 7.19. *ORTEP representation of the asymmetric unit of C4ABA, viewed along the* ***b****-axis, derived from SXD. The probability level for all non-hydrogen ellipsoids is 50%, while the hydrogen atoms are drawn as fixed-size spheres of radius 0.15 Å.*

C8-N1-C1-C6	-7.5(3)˚
N3-C12-C14-C15	-45.4(2)˚
N3-C12-C14-C16	23.6(3)˚
C8-N3-C12-C14	-180.0(2)˚
N2-C8-N1-H1	-5(1)˚
O2-C18-C19-C24	10.6(3)˚
C18-C19-C24-C23	176.9(2)˚
C18-C19-C20-C21	-177.1(2)˚

Table 7.8. *Torsion angles of interest.*

The conformation adopted by cyprodinil is similar to the one exhibited in the co-crystal with benzoic acid: the benzene ring is off from the pyrimidine plane of -7.5(3)˚ and the cyclopropyl substituent is positioned below the same plane. The dimer is not perfectly planar, but the two

molecules are twisted by an angle of around 9(2)˚. Also the carboxylic group is not co-planar with the rest of the aromatic ring, but it is distorted by 10.6(3)˚.

The molecules organise in heterogeneous dimers, forming cyclic interactions, which are constituted by two intermolecular hydrogen bonds: one between the hydroxyl group and the pyrimidine N atom of cyprodinil and a second between the amino group of cyprodinil and the carbonyl of 4-aminobenzoic acid. A representation of this type of interaction is reported in Figure 7.20, while Table 7.9 lists hydrogen bond lengths and angles.

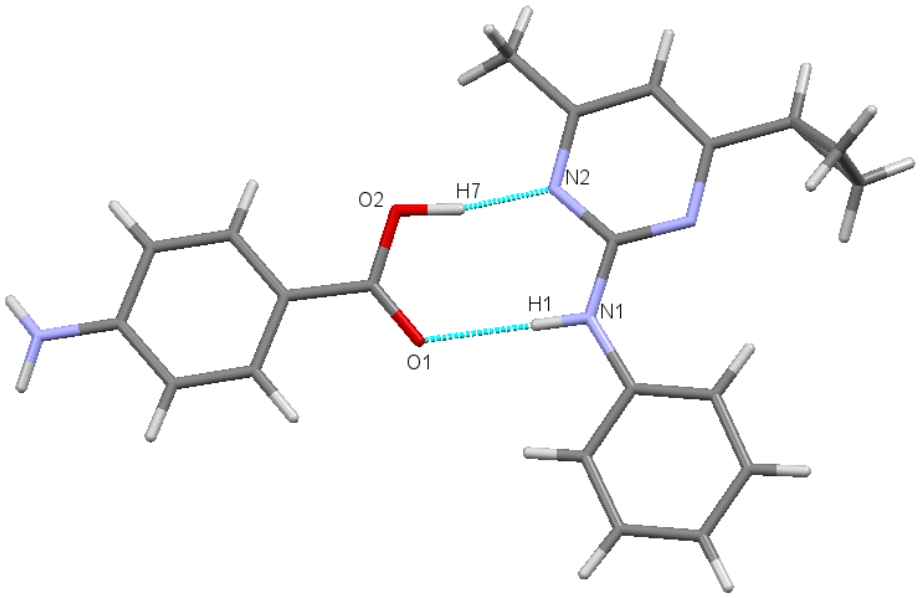

Figure 7.20. *Cyclic hydrigen bond in crystals of C4ABA.*

N1-H1	0.90(2) Å
H1···O1	1.98(2) Å
N1-H1···O1	177(2)˚
N1···O1	2.889(2) Å
O2-H7	1.07(3) Å
H7···N2	1.61(4) Å
O2-H7···N2	169(3)˚
O2···N2	2.677(2) Å

Table 7.9. *Hydrogen bond lengths and geometry of interaction.*

Considering the covalent bond lengths, the donor-acceptor distances and the angles of interaction[81], it is possible to identify a moderate hydrogen bond, N1-H1···O1, and a moderate-strong one, O2-H7···N2. The amino group in position 4 of the acid is not involved in intra- or intermolecular interactions.

In the crystal packing the dimers are organized into largely off-set parallel lines, forming a fishbone motif, as displayed in Figure 7.21.

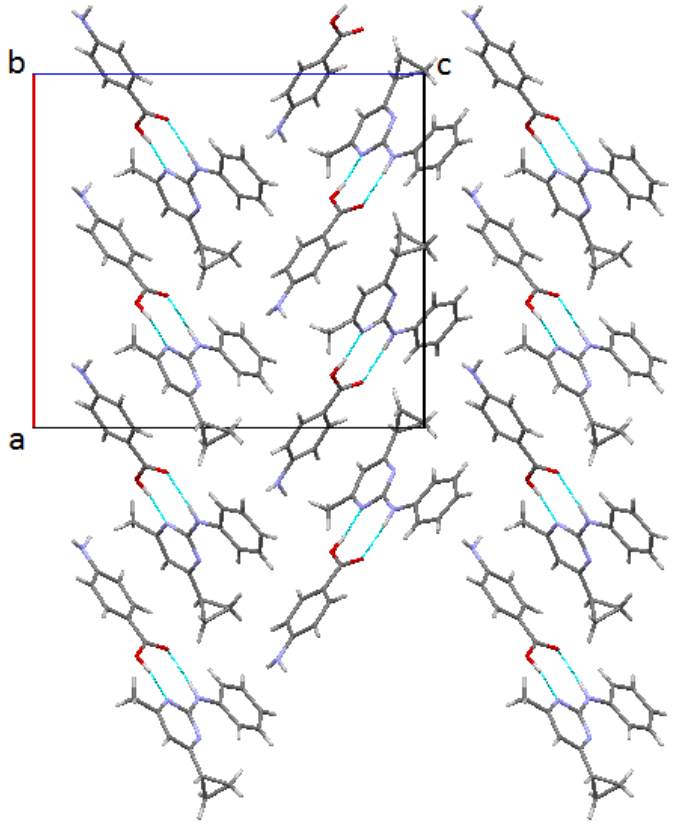

Figure 7.21. *Crystal packing of C4ABA, viewed along the* ***b****-axis.*

As for the case of C2ABA, investigation of disorder and proton migration was done through the observation of the difference electron-density maps for the two hydrogen bonds, N1-H1···O1 and O2-H7···N2, which are reported in Figures 7.22 and 7.23, respectively.

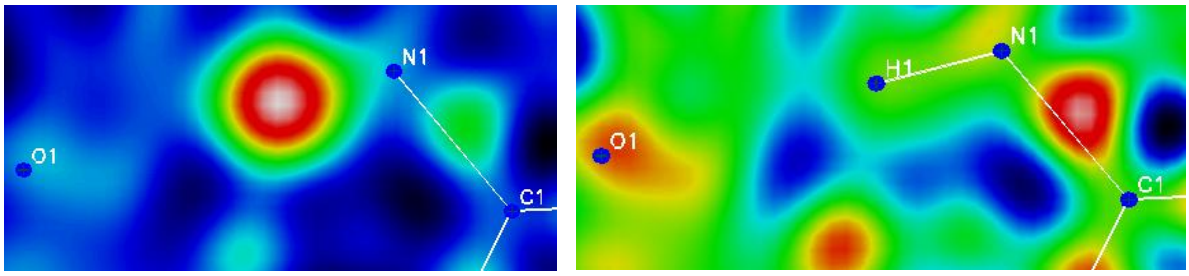

Figure 7.22. *Difference electron-density maps of the hydrogen bond N1-H1···O1, where the atom H1 was excluded (left) and included (right) in the refinement.*

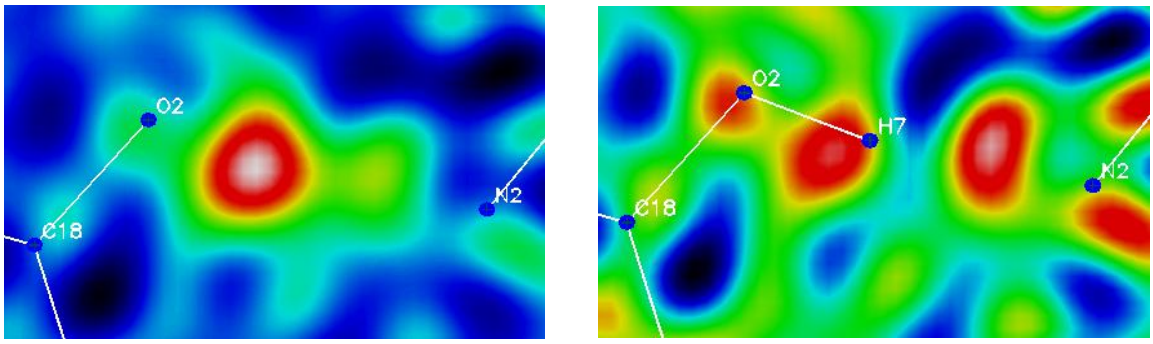

Figure 7.23. *Difference electron-density maps of the hydrogen bond O2-H7···N2, where the atom H7 was excluded (left) and included (right) in the refinement.*

The situation is similar to the previous case: while the electron density of atom H1 is centred on a specific position close to N1, that of atom H7 is elongated along the direction of the intermolecular interaction towards the non-bonding N2. Again, the shape of the electron density shows a second lobe of weaker intensity, which suggests the presence of an additional site for atom H7. This hypothesis is supported by the higher value of U_{iso} for H7 compared to H1: 0.066(9) opposed to 0.028(6). In addition, a Q peak, whose intensity could be referred to a hydrogen atom, was found in the Fourier difference map, positioned in the direction of interaction. The disorder was refined using fixed bond lengths for O2-H7A and H7B-N2, 0.90(1) Å and 0.92(1) Å respectively, and fixed U_{iso} of 0.03 for the two hydrogen atoms, H7A and H7B. The results of the refinement of disorder are reported in Tables 7.10 and 7.11 and in Figure 7.24.

Atom	***s.o.f***
H7A	0.70(3)
H7B	0.30(3)

Table 7.10. *Site occupancy factors for atom H7A and H7B.*

O2-H7A	0.89(2) Å
H7A···N2	1.80(2) Å
O2-H7A···N2	167(2)˚
O2···N2	2.678(2) Å
N2-H7B	0.92(4) Å
H7B···O2	1.77(4) Å
N2-H7B···O2	170(4)˚

Table 7.11. *Distances and angles of interaction for the disordered hydrogen bond O2-H7A···H7B-N2.*

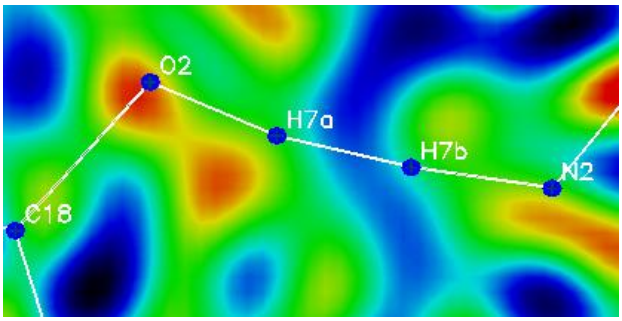

Figure 7.24. *Difference electron-density map for the hydrogen bond O2-H7A···H7B-N2, in which both hydrogen sites were refined.*

No residual electron density is detected near the atomic sites and SHELXL refines a disorder of 70 : 30, indicating that for the major part the carboxylic acid is in its neutral conformation, while for 30% of the time the hydrogen of the hydroxyl group is transferred to the pyrimidine N of cyprodinil.

However, as for the case of C2ABA, the limits of X-ray diffraction in the definition of hydrogen atoms decrease, to some extent, the reliability of the disordered hydrogen bond. The refinement improves only slightly after the introduction of the disorder: a comparison of the R-factors and GooF without and with disorder is reported in Table 7.12.

	Structure without disorder	**Structure with disorder**
R_1	0.0292	0.0289
wR_2	0.0639	0.0631
GooF	1.062	1.049

Table 7.12. *R-factors without and with disorder.*

7.1.4. Conclusions

Synthesis of the co-crystals of cyprodinil with the three isomers of monoaminobenzoic acid was achieved for all cases in ethanol solution, and single crystals of each molecular complex were obtained by the method of slow evaporation of the solvent. The formation of a crystal structure that differed from the constituting components was assessed firstly by powder X-ray diffraction (PXD) and finally validated by single crystal X-ray diffraction (SXD). Unfortunately, size and shape of crystals of C3ABA did not allow investigation by SXD. However, since the co-crystals with the other two isomers had formed and PXD results show Bragg peaks at different positions than in the parenting components, it is highly probable that the new crystal structure was that of C3ABA.

The hydrogen bonding network and the crystal packing are very similar to those exhibited in the co-crystal with benzoic acid: heterogeneous dimers interacting through cyclic hydrogen bonds, stacked in off-set parallel lines. The hydrogen bonds are of moderate strength and they appear to be slightly shorter in the case of C2ABA: 1.94(2) Å for H1···O1 in C2ABA and 1.98(2) Å for H1···O1 in C4ABA. Indeed, the interacting molecules are closer in C2ABA than in C4ABA: the donor-acceptor distances, N1···O1 and O2···N2, are 2.852(1) Å and 2.627(1) Å for C2ABA, and 2.889(2) Å and 2.677(2) Å in C4ABA. This variation is probably due to the effect ***–I*** of the amino group: the electron-withdrawing power of $–NH_2$ subtracts electron density from the carboxylic group, making the hydrogen atom more acidic, and its effect decreases from the *ortho* to the *para* position.
It is not completely clear whether disorder of the hydrogen atom on the hydroxyl group is present in both structures, but undoubted characterisation of the hydrogen bond can only be achieved through single crystal neutron diffraction.

7.2. Cyprodinil / toluic acids

7.2.1. Introduction

The three isomers of toluic acid were selected for the co-crystallisation process with the fungicide cyprodinil in order to assess the effect of the methyl group on the crystal packing of the molecular complexes involving substituted benzoic acid.
The crystal structures of *o*-toluic acid, *m*-toluic acid and *p*-toluic acid have already been studied and described[127,128,129]. *Ortho* and *meta* substituted toluic acids crystallise in the monoclinic system, space group $\boldsymbol{P2_1/n}$ for the former and $\boldsymbol{P2_1/c}$ for the latter, while *p*-toluic acid belongs to the triclinic system, space group $\boldsymbol{P\bar{1}}$**.** In all three structures the molecules organise in dimers around an inversion centre for the case of *o*- and *p*-toluic acid, while the molecules of *m*-toluic acid are symmetrically independent, but still exhibit a similar hydrogen bonded ring. The dimers of *o*-toluic acid, *m*-toluic acid and *p*-toluic acid are reported in Figures 7.25, 7.26 and 7.27, respectively

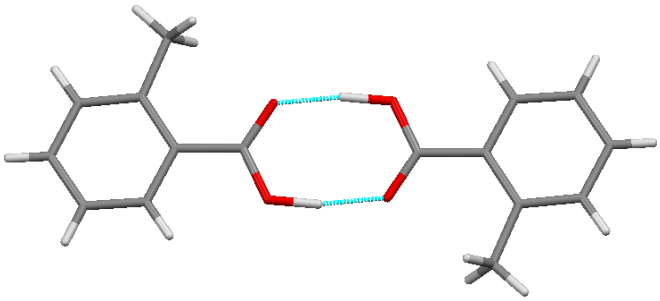

Figure 7.25. *Centrosymmetric dimer in o-toluic acid*[130].

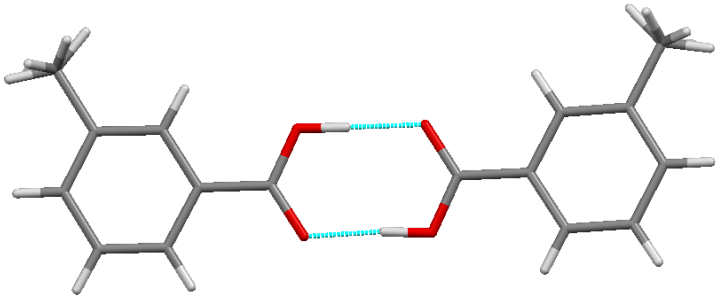

Figure 7.26. *Interacting dimer in m-toluic acid*[131].

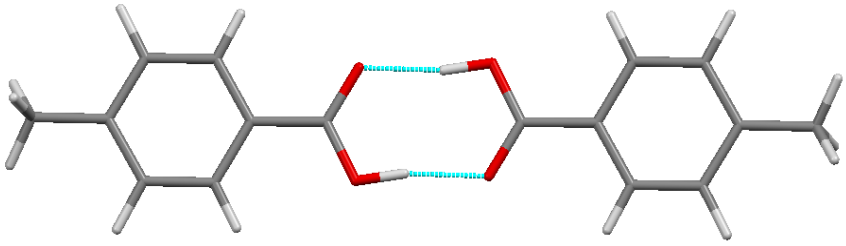

Figure 7.27. *Centrosymmeric dimer in p-toluic acid*[132].

The presence of the methyl group as substituent on the benzene ring makes toluic acid more acidic than benzoic acid: the value of the acidity, which indicates the tendency of an acid to release a proton, decreases in the series *o*-toluic acid > *m*-toluic acid > *p*-toluic acid. This is reflected on the characteristics of the hydrogen bonds in the three structures (Table 7.13): the higher the acidity of the acid, the longer is the covalent bond in the hydroxyl group. It is, however, important to note that the hydrogen atom of the carboxyl group in *p*-toluic acid was not refined.

	o-Toluic acid	*m*-Toluic acid	*p*-Toluic acid
O-H	1.12 Å	0.98(2)-1.00(2) Å	0.97 Å
O···H	1.53 Å	1.62(2)-1.64(2) Å	1.67 Å

Table 7.13. *Hydrogen bond lengths and distances.*

The aim of this study was to investigate whether the different acidities of the isomers of toluic acid affected the crystal packing of their co-crystals with cyprodinil.

7.2.2. Experimental

7.2.2.1. Physical and chemical properties of co-formers

o-Toluic acid[133] is commercially available as a beige crystalline powder. It has melting point in the range 102˚-104˚C, boiling point around 258˚C, and its relative density is 1.062 g/cm^3 at 25˚C. It is slightly soluble in water, with solubility < 1 g/L at 20˚C, but it is soluble in the most common organic solvents, such as alcohols.

The solid state of *m*-toluic acid[134] is a light yellow crystalline powder with a temperature of fusion between 107˚-113˚C and boiling point of ~263˚C. It has a relative density of 1.054 g/cm^3 and vapour pressure of 1mmHg at 97˚C. As for the *ortho* isomer, it is slightly soluble in water, but soluble in alcohols.

p-Toluic acid[135] is a beige, crystalline solid with a relative density of 1.06 g/cm^3; it starts melting around 177˚C and boiling around 274˚C. It is only slightly soluble in water, but soluble in alcohols.

7.2.2.2. Synthesis from solution

Synthesis of the co-crystals cyprodinil/*o*-toluic acid (CoTA) and cyprodinil/*p*-toluic acid (CpTA) was achieved in ethanol solutions; co-crystallisation with *m*-toluic acid was unsuccessful. Table 7.14 lists the materials used for the preparation of the two solutions from which successful co-crystallisation was achieved. All materials were of analytical standard and were used without further purification.

Substance	Quantity
Cyprodinil	0.51 g
o-Toluic acid	0.31 g
Ethanol	8 ml
Cyprodinil	0.50 g
p-Toluic acid	0.31 g
Ethanol	8 ml

Table 7.14. *Prepared solutions.*

The solutions were prepared in a 1 : 1 ratio of the two components, by addition of 2 ml of ethanol at a time so to create a saturated solution. Low heat, with temperature set around 60˚C, was applied for two hours, during which the solutions were continuously stirred. Crystallisation was achieved at room temperature, using the method of slow evaporation of the solvent allowed by the presence of

small holes on the film cover of the crystallisation vials. CoTA grows in thick, colourless, parallelepiped crystals, while those of CpTA are thin, colourless plates.

7.2.2.3. Differential Scanning Calorimetry

Changes in the crystal structure of CoTA as a function of temperature were monitored by DSC. Data were collected on ~ 4 mg of co-crystal on the DSC Q20. The heat flow vs. temperature profile is reported in Figure 7.28.

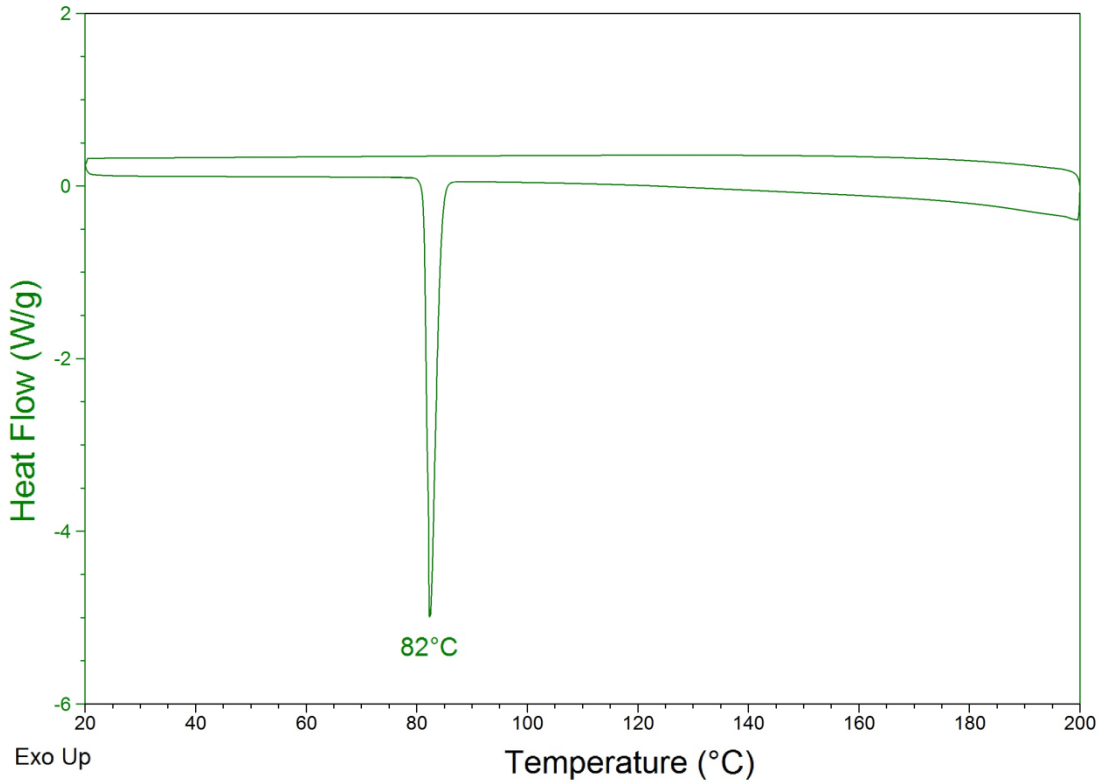

Figure 7.28. *DSC profile for a sample of CoTA.*

The DSC profile of CoTA shows only one endothermic event, which corresponds to the fusion of the co-crystal, occurring around 82˚C. No re-crystallisation is observed during cooling, probably because cyprodinil goes through a dense slurry state before solidification occurs. The presence of the co-former causes the co-crystal to have a higher melting point than pure cyprodinil: 82˚C for the former compared to 72˚-75˚C for the latter.

7.2.2.4. Single crystal X-ray diffraction

The crystal structures of CoTA and CpTA were analysed by SXD for the definition of the atomic positions. A crystal of CoTA was mounted on the Enraf-Nonius kappaCCD single crystal

diffractometer and data were recorded at 150K. For the crystal of CpTA, data were collected on the Gemini A Ultra CCD diffractometer at 150K.

In Tables 7.15 and 7.16, X-ray crystallographic data and refinement parameters for the crystals of CoTA and CpTA, respectively, are reported.

Name	CYP / *o*-toluic acid (CoTA)
Empirical formula	$C_{14}H_{15}N_3$ $C_8H_8O_2$
Formula weight (g mol^{-1})	361.43
Temperature (K)	150
Wavelength (Å)	0.71073
Crystal system, space group	Monoclinic, $P2_1/n$
Unit cell dimensions	a = 11.505(2) Å
	b = 7.967(2) Å
	c = 21.202(4) Å
	β = 102.48(3)˚
Volume ($Å^3$)	1897.4(7)
Z, calculated density (g cm^{-3})	4, 1.265
F(000)	768
Absorption coefficient (mm^{-1})	0.082
Theta range for data collection (˚)	1.87 to 26.37
Limiting indices	$-14 \leq h \leq 14$, $-9 \leq k \leq 9$, $-26 \leq l \leq 26$
Reflections collected / unique	7022 / 3860 [R_{int} = 0.0146]
Completeness to θ = 26.37	99.5 %
Refinement method	Full-matrix least-squares on F^2
Data / restrains / parameters	3860 / 0 / 337
Goodness-of-fit on F^2	1.132
Final R indices [I>2sigma(I)]	R_1 = 0.0487, wR_2 = 0.1257
R indices (all data)	R_1 = 0.0585, wR_2 = 0.1470
Extinction coefficient	0.21(1)
Largest diff. Peak and hole (e $Å^{-3}$)	0.43 and -0.46

Table 7.15. *X-ray crystallographic data and refinement parameters for a crystal of CoTA at 150K.*

Name	CYP / *p*-toluic acid (CpTA)
Empirical formula	$C_{14}H_{15}N_3$ $C_8H_8O_2$
Formula weight (g mol^{-1})	361.43
Temperature (K)	150
Wavelength (Å)	0.71073
Crystal system, space group	Orthorhombic, $P2_12_12_1$
Unit cell dimensions	a = 5.0406(2)Å
	b = 14.1865(6) Å
	c = 26.016(1) Å
Volume ($Å^3$)	1860.4(1)
Z, calculated density (g cm^{-3})	4, 1.290
F(000)	768
Absorption coefficient (mm^{-1})	0.084
Crystal size (mm)	0.11 x 0.22 x 0.38
Theta range for data collection (°)	2.87 to 26.37
Limiting indices	$-6 \leq h \leq 4$, $-17 \leq k \leq 14$, $-24 \leq l \leq 32$
Reflections collected / unique	5683 / 3668 [R_{int} = 0.0263]
Completeness to θ = 26.37	99.8 %
Refinement method	Full-matrix least-squares on F^2
Data / restrains / parameters	3668 / 0 / 337
Goodness-of-fit on F^2	1.038
Final R indices [I>2sigma(I)]	R_1 = 0.0396, wR_2 = 0.0832
R indices (all data)	R_1 = 0.0505, wR_2 = 0.0890
Extinction coefficient	0.007(1)
Largest diff. Peak and hole (e $Å^{-3}$)	0.16 and -0.16

Table 7.16. *X-ray crystallographic data and refinement parameters for a crystal of CpTA at 150K.*

7.2.2.5. Single crystal neutron diffraction

For a better characterisation of the hydrogen bonds present in the structure, a large crystal of CoTA (crystal dimensions, 1.4 x 1.7 x 4.2 mm; volume ~10 mm^3) was selected from a batch grown in ethanol solution. Data were collected on the single crystal diffractometer D19 at ILL. After preliminary checks at room temperature to assess the diffracting power and the quality of the crystal, three sets of data were collected at three temperatures: 30, 200, and 300K. The quality and integrity of the crystal during the cooling process to 30K was monitored following the intensity of a strong reflection, $(\bar{1}\ 0\ \bar{3})$, as reported in Figure 7.29. No significant variation of the reflection intensity are present, indicating that the crystal did not suffer mechanical stresses caused by the hardening of the glue or changes to the structure upon cooling. It is, however, possible to notice a gradual increase of the intensity of the reflection due to the attenuation of the thermal motion at low temperatures.

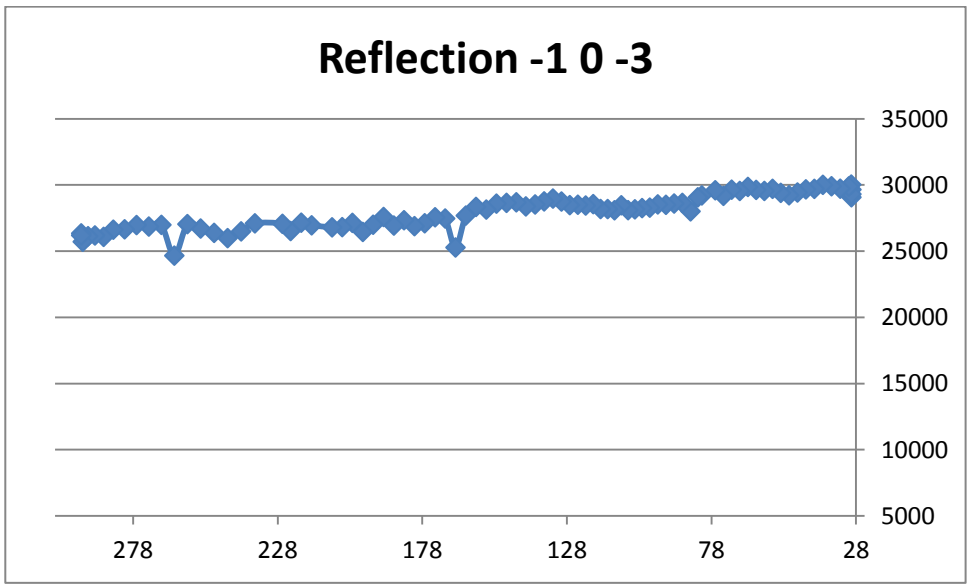

Figure 7.29. *Intensity profile of the strong reflection* $(\bar{\mathbf{1}}\ \mathbf{0}\ \bar{\mathbf{3}})$ *during cooling to 30K.*

All three sets of data were corrected for two types of absorption: one caused by the presence of the vanadium cans around the sample and one due to the crystal itself. The latter is an analytical correction, performed by the program ABSCAN and it is done by indexing the crystal faces and measuring the distance of each face from an arbitrary centre. A schematic representation of the crystal morphology and a list of all crystal faces are reported in Figure 7.30.

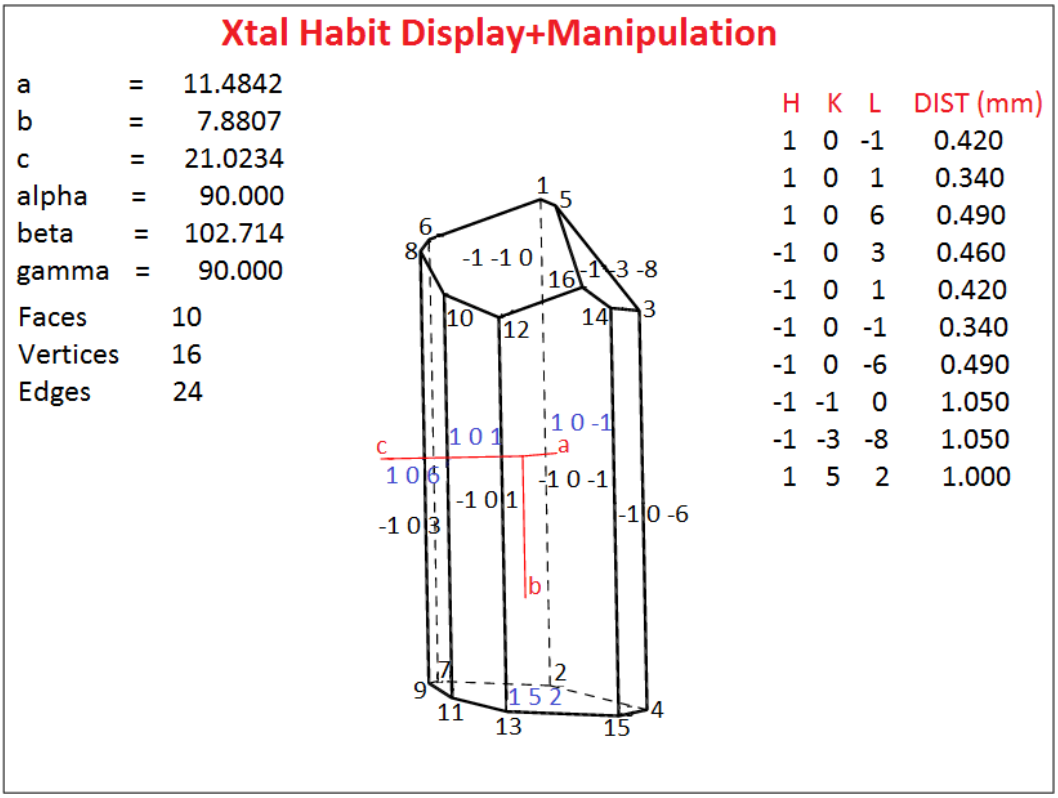

Figure 7.30. *Schematic representation of the crystal habit of CoTA, obtained with the program PLATON.*

Before applying the correction for the absorption by the crystal, a REN-scan (***c.f. 5.1.2.6***) was collected on the reflection $(0\ \bar{4}\ \bar{2})$. Figure 7.31 shows the ***I*** vs. ***φ*** plot.

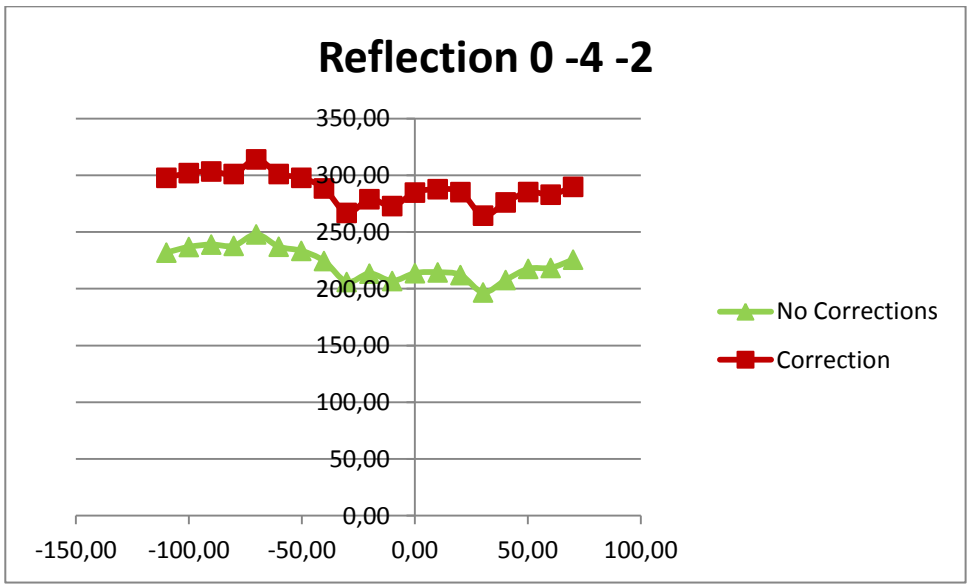

Figure 7.31. *Evolution of the Bragg's reflection as a function of the angle φ: profile without absorption correction (red) and with absorption correction (green).*

The profile of the reflection exhibits a similar trend before and after the application of the corrections, indicating that the absorption by the crystal is minimal. This is confirmed by the results produced with the program ABSCAN.

	No corrections	**Correction for cans**	**Correction cans+crystal**
$\mathbf{R_1}$	0.0435	0.0344	0.0321
$\mathbf{wR_2}$	0.1137	0.0890	0.0808

Table 7.17. *Variation of R-factors after correction for the two types of absorption.*

As shown in Table 7.17, the major contribution to the improvement of the refinement is done by the correction for the presence of the three vanadium cans, while the correction for the absorption by the crystal has a minor effect.

In Table 7.18, neutron crystallographic data and refinement parameters for the crystal of CoTA at 30, 200, and 300K are reported.

Name		CYP / o-toluic acid (CoTA)		
Empirical formula		$C_{14}H_{15}N_3$ $C_8H_8O_2$		
Formula weight (g mol^{-1})		361.43		
Temperature (K)		30	200	300
Wavelength (Å)		1.17000		
Crystal system, space group		Monoclinic, $P2_1/n$		
Unit cell dimensions	a (Å) =	11.4842(2)	11.4827(4)	11.495(1)
	b (Å) =	7.8807(1)	7.9963(4)	8.0850(9)
	c (Å) =	21.0234(3)	21.2215(7)	21.390(2)
	β (˚) =	102.714(1)	102.443(2)	102.249(5)
Volume ($Å^3$)		1856.03	1902.8	1942.6
Z, calculated density (g cm^{-3})		4, 1.265		
F(000)		400		
Absorption coefficient (mm^{-1})		0.214		
Crystal size (mm)		1.4 x 1.7 x 4.2		
Theta range for data collection (˚)		5.13 to 61.53		
Limiting indices		$-17 \leq h \leq 17$, $-11 \leq k \leq 3$, $-29 \leq l \leq 31$		
Reflections collected / unique		15214 / 6024	14591 / 6162	16548 / 6317
		[R_{int} = 0.0405]	[R_{int} = 0.0564]	[R_{int} = 0.0703]
Completeness to θ = 61.53		89.5 %	90.6 %	89.9 %
Refinement method		Full-matrix least-squares on F^2		
Data / restrains / parameters		6024 / 0 / 452	6162 / 0 / 452	6317 / 0 / 453
Goodness-of-fit on F^2		1.158	1.045	1.015
Final R indices [I>2sigma(I)]		R_1 = 0.0321,	R_1 = 0.0542,	R_1 = 0.0607,
		wR_2 = 0.0785	wR_2 = 0.1302	wR_2 = 0.1314
R indices (all data)		R_1 = 0.0373,	R_1 = 0.0811,	R_1 = 0.1211,
		wR_2 = 0.0808	wR_2 = 0.1514	wR_2 = 0.1615
Extinction coefficient		0.0024(1)	0.0020(3)	0.0030(3)
Largest diff. Peak and hole (fm $Å^{-3}$)		0.73 and -0.93	0.78 and -1.10	0.58 and -0.73

Table 7.18. *Neutron crystallographic data and refinement parameters for a crystal of CoTA at 30K, 200K and 300K.*

7.2.3. Results and discussion

7.2.3.1. Cyprodinil / o-toluic acid (CoTA)

Crystals of CoTA belong to the monoclinic system, space group ***P2$_1$/n***. The asymmetric unit of CoTA is formed by two molecules: one of cyprodinil and the other of *o*-toluic acid, as reported in Figure 7.32 for the structure studied by X-rays. The results from SND are in accordance with those derived from SXD measurements, as displayed in Tables 7.19 and 7.20.

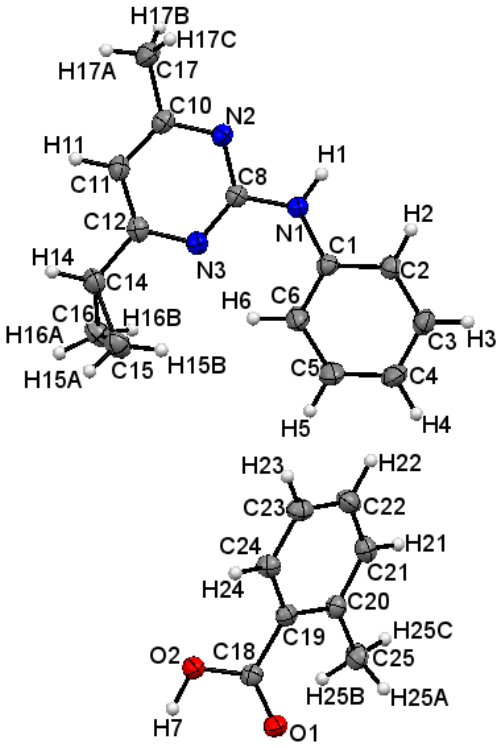

Figure 7.32. *ORTEP representation of the asymmetric unit of CoTA, viewed along the* ***b****-axis, derived from SXD. The probability level for all non-hydrogen ellipsoids is 50%, while the hydrogen atoms are drawn as fixed-size spheres of radius 0.15 Å.*

	X-rays	**Neutrons**		
	150K	**30K**	**200K**	**300K**
C8-N1-C1-C6	28.5(2)˚	28.4(1)˚	28.4(2)˚	29.2(3)˚
N3-C12-C14-C15	27.9(2)˚	26.7(1)˚	28.4(2)˚	29.4(3)˚
N3-C12-C14-C16	-40.2(2)˚	-41.0(1)˚	-39.7(2)˚	-38.5(3)˚
C8-N3-C12-C14	179.3(1)˚	179.6(1)˚	179.3(1)˚	179.0(2)˚
N2-C8-N1-H1	1(1)˚	2.1(1)˚	2.1(2)˚	1.8(3)˚

Table 7.19. *Torsion angles and bond lengths of interest in the cyprodinil molecule.*

	X-rays	Neutrons		
	150K	**30K**	**200K**	**300K**
O2-C18-C19-C24	29.9(2)˚	30.1(1)˚	30.0(2)˚	29.2(2)˚
C18-C19-C24-C23	178.4(1)˚	178.6(1)˚	178.7(1)˚	178.7(2)˚
C18-C19-C20-C21	-179.8(1)˚	-179.9(1)˚	-179.7(1)˚	-179.7(2)˚
C18-C19-C20-C25	2.3(2)˚	2.2(1)˚	2.5(2)˚	2.1(3)˚
C18-O1	1.22(2) Å	1.237(1) Å	1.220(2) Å	1.212(3) Å
C18-O2	1.31(1) Å	1.322(1) Å	1.308(2) Å	1.293(3) Å

Table 7.20. *Torsion angles and bond lengths of interest in the acid molecule.*

From Tables 7.19 and 7.20, it is possible to notice that the conformation of the cyprodinil molecule is very different from that adopted in the previous co-crystals. In this case the benzene and the pyrimidine rings are twisted by an angle C8-N1-C1-C6 of 28.5(2)˚, due to the hindrance of the methyl group in the *ortho* position of the acid. The cyclopropyl substituent is not centred in respect to the plane of the pyrimidine moiety, while the hydrogen atom involved in an intermolecular interaction, H1, is only slightly off the same plane.

The planarity, which is typical of aromatic compounds, is retained in the conformation of *o*-toluic acid, but the carboxylic group is twisted by an angle of 29.9(2)˚ in respect to the benzene ring to avoid hindrance of the methyl group. The bond lengths in the carboxylic moiety, C18 – O1 and C18 – O2, are, respectively, 1.22(2) Å and 1.31(2) Å, which are reasonable values for the neutral conformation of the acid.

As a recurring motif in all co-crystals with substituted benzoic acid, the crystal packing is held together by cyclic hydrogen bonds between a molecule of cyprodinil and one of *o*-toluic acid, leading to the formation of heterogeneous dimers (Figure 7.33), which stack themselves into lines creating a zig-zag array (Figure 7.34).

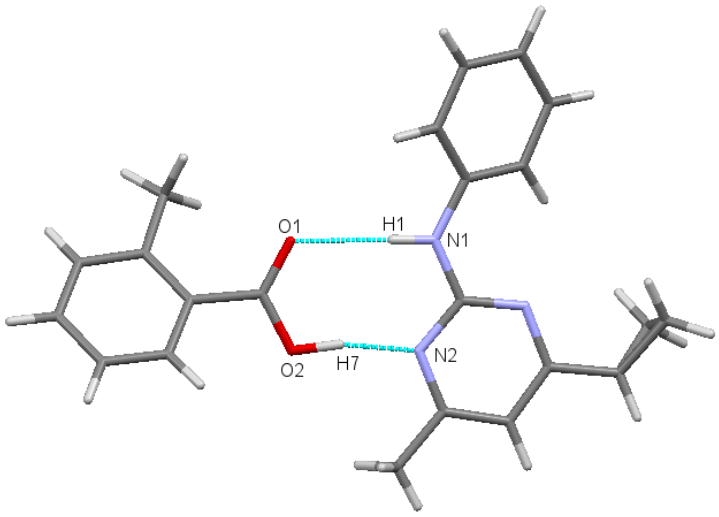

Figure 7.33. *Heterogeneous dimers in CoTA.*

	X-rays	Neutrons		
	150K	**30K**	**200K**	**300K**
N1-H1	0.88(2) Å	1.022(2) Å	1.016(4) Å	1.006(5) Å
H1···O1	2.10(2) Å	1.963(2) Å	1.966(4) Å	1.965(5) Å
N1-H1···O1	173(2)˚	169.6(2)˚	169.5(3)˚	169.7(4)˚
N1···O1	2.975(2) Å	2.974(1) Å	2.971(2) Å	2.961(3) Å
O2-H7	1.00(2) Å	1.051(2) Å	1.048(4) Å	1.039(5) Å
H7···N2	1.65(3) Å	1.592(2) Å	1.600(4) Å	1.610(4) Å
O2-H7···N2	168(2)˚	170.4(2)˚	170.2(3)˚	170.2(4)˚
O2···N2	2.635(2) Å	2.634(1) Å	2.638(2) Å	2.640(3) Å

Table 7.21. *Bond lengths and angles for the hydrogen bonds N1-H1···O1 and O2-H7···N2.*

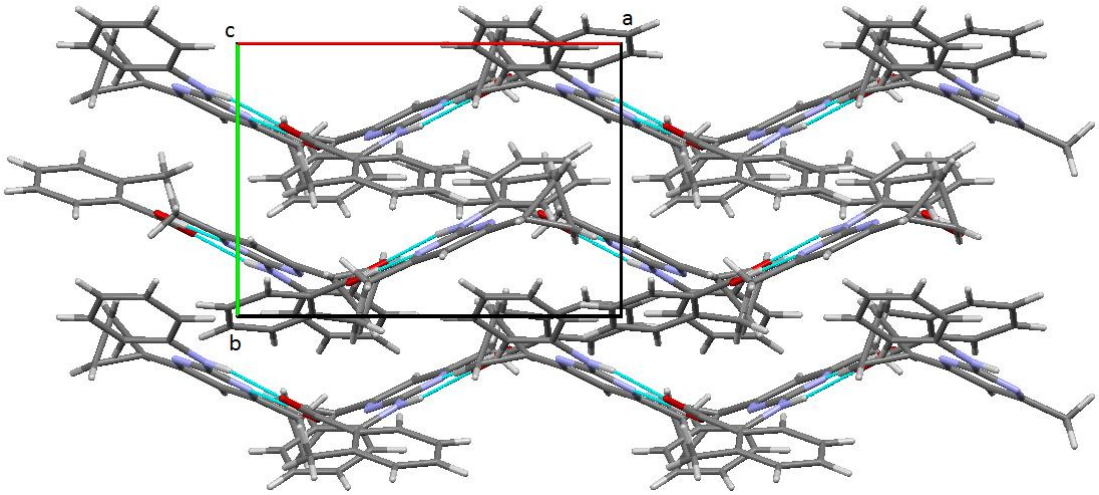

Figure 7.34. *Crystal packing of CoTA, viewed along the* ***c****-axis.*

As shown in Table 7.21, neutron radiation allowed gaining a ten-fold improvement in the definition and precision of the hydrogen atom positions and also provided an accurate nuclear position for the hydrogen atom.

Based on bond lengths, interatomic distances and geometry of interaction[81], it is possible to identify the two hydrogen bonds as moderate-strength HBs, although O2-H7···N2 is stronger than N1-H1···O1.

Investigation of disorder or proton migration was undertaken by observation of the nucleon-density maps, which are the neutron counterparts of the electron-density maps. Figures 7.35, 7.36, and 7.37 display the nucleon-density maps for the two hydrogen bonds, N1-H1···O1 and O2-H7···N2, at

30K, 200K and 300K, respectively, while in Figure 7.38 the electron density maps at 150K for the same hydrogen bonds are reported.

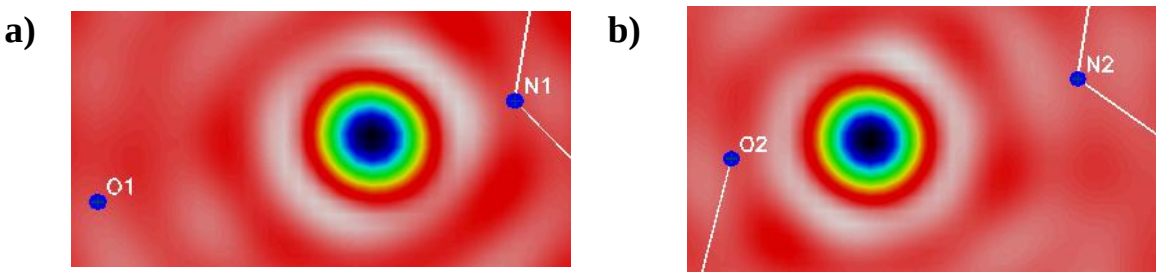

Figure 7.35. *Difference nucleon-density maps for N1-H1···O1 (a) and O2-H7···N2 (b) at 30K.*

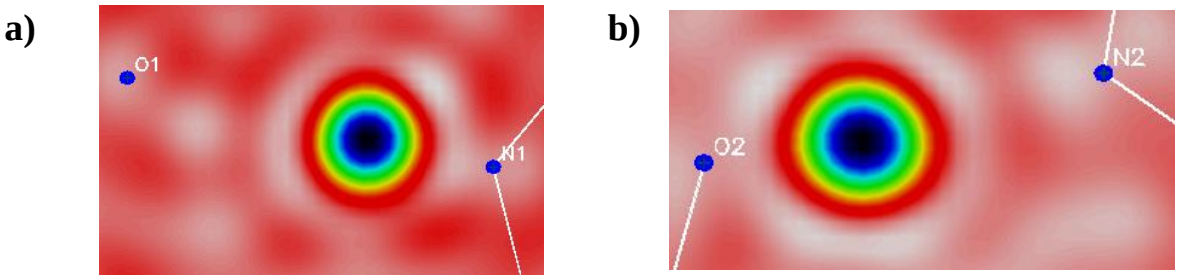

Figure 7.36. *Difference nucleon-density maps for N1-H1···O1 (a) and O2-H7···N2 (b) at 200K.*

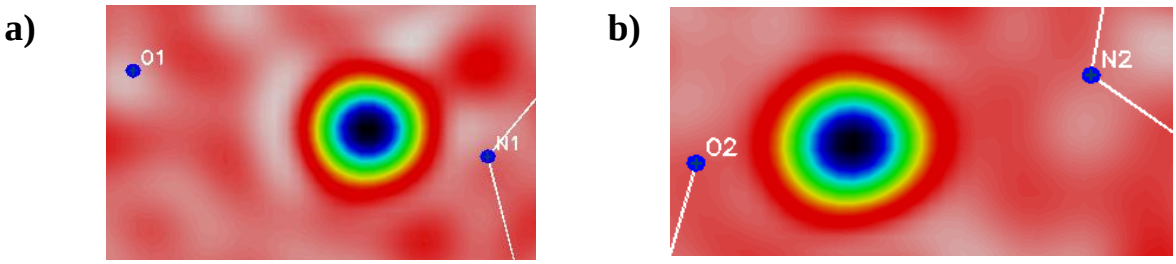

Figure 7.37. *Difference nucleon-density maps for N1-H1···O1 (a) and O2-H7···N2 (b) at 300K.*

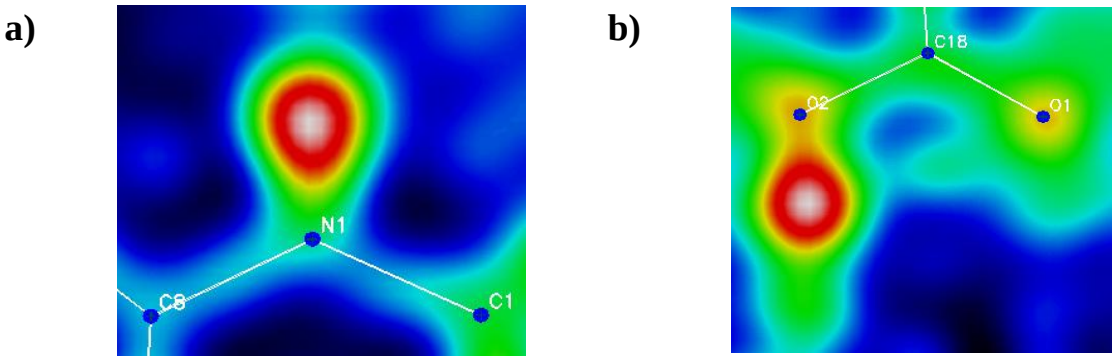

Figure 7.38. *Difference electron-density maps for N1-H1···O1 (a) and O2-H7···N2 (b) at 150K.*

Both X-rays and neutrons show the absence of disorder or proton migration in the structure, even though the electron-density map of O2-H7···N2 displays an elongation of the electron density of H7 in the direction of the intermolecular interaction. This is also confirmed by the shape and size of H1 and H7 ADPs, which could also be refined anisotropically using neutron radiation, as shown in Figures 7.39, 7.40, and 7.41 for the structures at 30K, 200K, and 300K, respectively. At all temperatures, the ADPs of atoms H1 and H7 are elongated in the direction normal to the hydrogen bond, confirming that they are found in only one specific position.

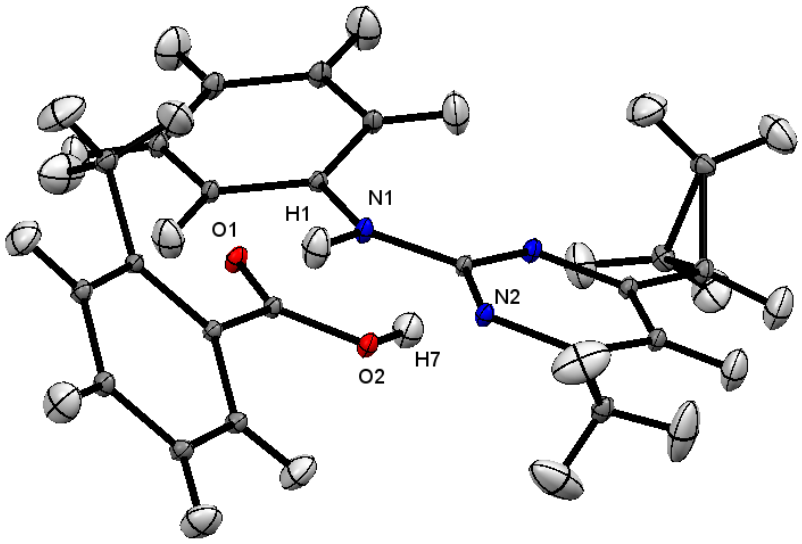

Figure 7.39. *ORTEP representation of the heterogeneous dimer from SND results at 30K. The probability level for all ellipsoids is 50%.*

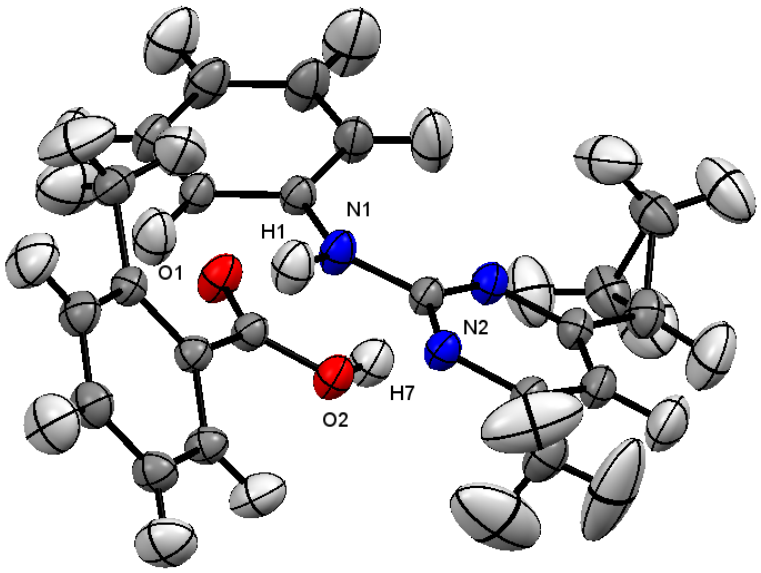

Figure 7.40. *ORTEP representation of the heterogeneous dimer from SND results at 200K. The probability level for all ellipsoids is 50%.*

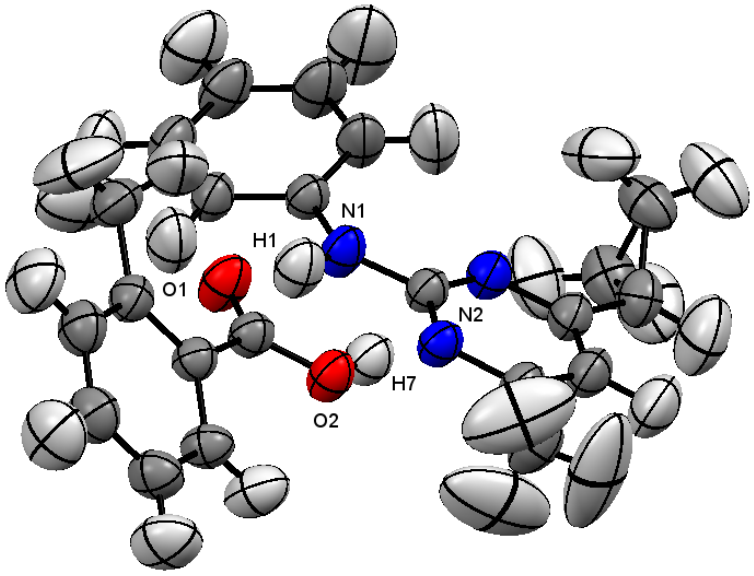

Figure 7.41. *ORTEP representation of the heterogeneous dimer from SND results at 300K. The probability level for all ellipsoids is 50%.*

It is interesting to notice the variation in the size of all thermal ellipsoids with the change of temperature, especially visible for the hydrogen atoms. This is due to the increased thermal motion of the atoms at higher temperatures.

7.2.3.2. Cyprodinil / p-toluic acid (CpTA)

CpTA crystallises in the orthorhombic system, space group ***P2$_1$2$_1$2$_1$***. As for the *ortho* isomer, the asymmetric unit of CpTA displays one molecule of cyprodinil, forming a dimer with one molecule of *p*-toluic acid, as shown in Figure 7.42 for the structure derived from SXD analysis.

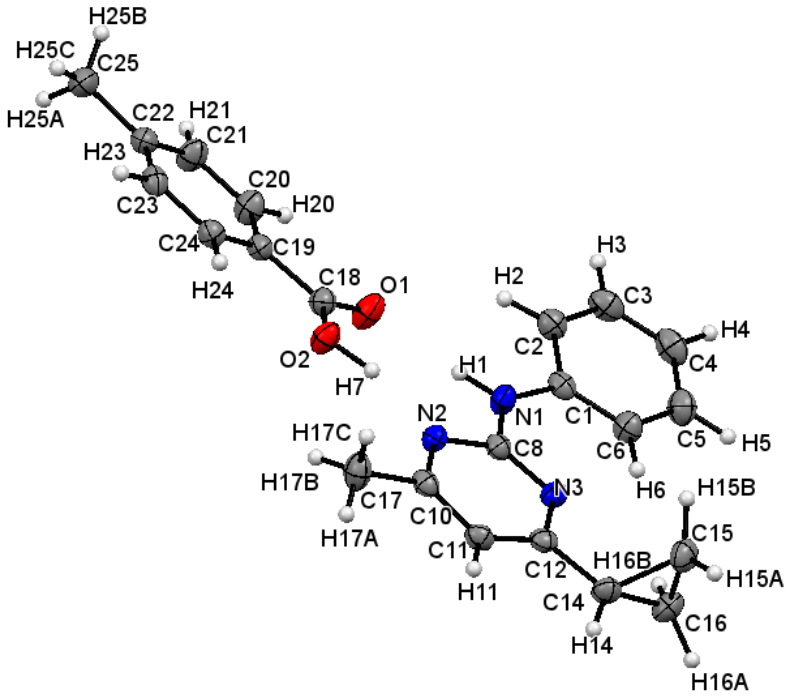

Figure 7.42. *ORTEP representation of the asymmetric unit of CpTA, viewed along the* ***b****-axis, derived from SXD. The probability level for all non-hydrogen ellipsoids is 50%, while the hydrogen atoms are drawn as fixed-size spheres of radius 0.15 Å.*

C8-N1-C1-C6	10.9(3)˚
N3-C12-C14-C15	50.6(2)˚
N3-C12-C14-C16	-17.4(3)˚
C8-N3-C12-C14	-177.1(2)˚
N2-C8-N1-H1	-7(1)˚
O2-C18-C19-C24	3.2(2)˚
C18-C19-C24-C23	178.2(2)˚
C18-C19-C20-C21	-178.7(2)˚

Table 7.22. *Torsion angles of interest.*

The conformation that the molecule of cyprodinil exhibits in CpTA is very different from that of CoTA: the benzene is less twisted in respect to the pyrimidine ring than in CoTA, with an angle

C8-N1-C1-C6 of 10.9(3)˚, and the cyclopropyl substituent is strongly decentred above the plane containing the rest of the molecule.

Contrary to the case of *o*-toluic acid, the carboxylic group of *p*-toluic acid in CpTA is almost co-planar with the benzene, showing a torsion angle O2-C18-C19-C24 of 3.2(2)˚ The bond lengths C18=O1 and C18-O2 are in accordance with the neutral conformation of the acid, being 1.22(2) Å and 1.31(2) Å, respectively.

The hydrogen bonding network is similar to CoTA: molecules of cyprodinil and of *p*-toluic acid join together in heterogeneous, forming cyclic hydrogen bonds (Figure 7.43). The crystal packing of CpTA is characterised by the stacking of the dimers in parallel lines, which are highly off-set in respect to one another, forming a fishbone motif, as shown in Figure 7.44.

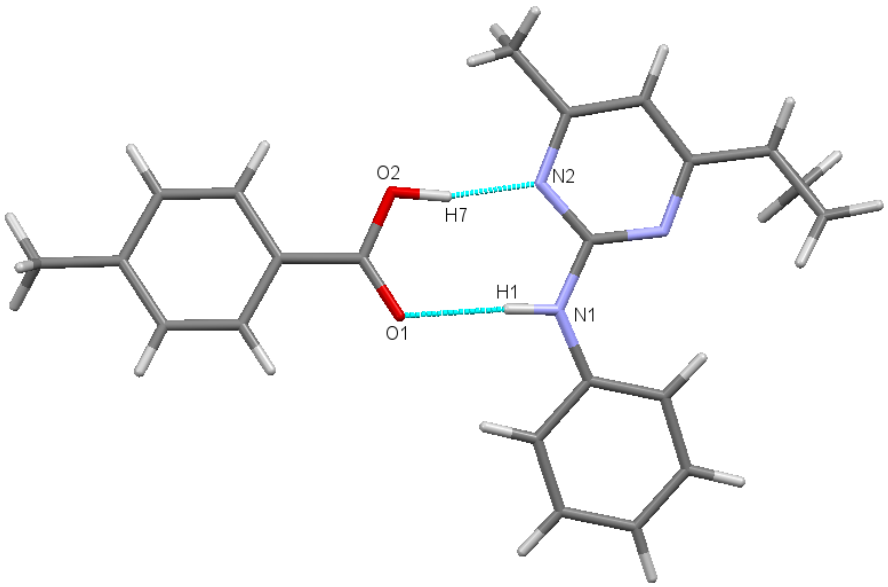

Figure 7.43. *Heterogeneous dimer in CpTA, forming a circular hydrogen bond.*

N1-H1	0.93(2) Å
H1···O1	2.00(2) Å
N1-H1···O1	176(2)˚
N1···O1	2.929(2) Å
O2-H7	1.01(2) Å
H7···N2	1.67(2) Å
O2-H7···N2	166(2)˚
O2···N2	2.663(2) Å

Table 7.23. *Hydrogen bond lengths and geometry of interaction.*

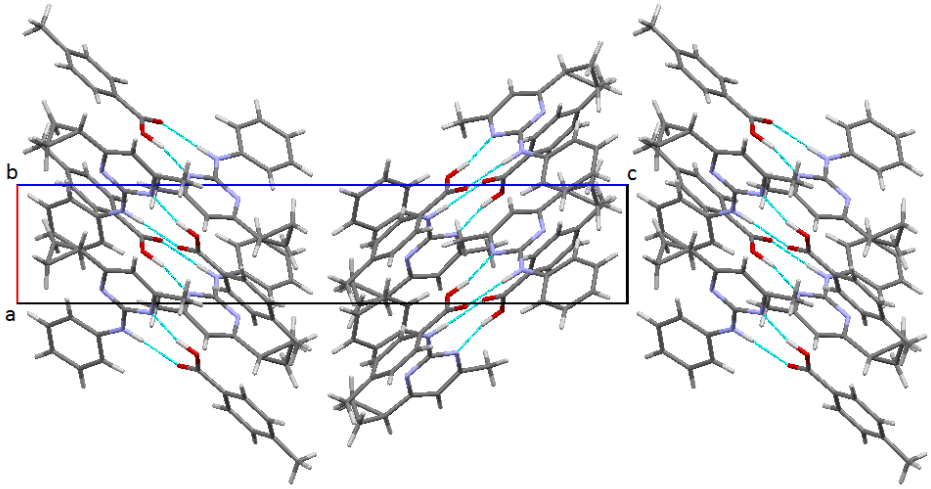

Figure 7.44. *Crystal packing of CpTA, viewed along the* ***b****-axis.*

The two hydrogen bonds, N1-H1···O1 and O2-H7···N2, are of moderate strength[81], although the latter is slightly stronger than the former. By comparing the dimer conformation in CoTA and CpTA with that of the co-crystal cyprodinil/benzoic acid, a summary of which is reported in Table 7.24, it is possible to notice the effect that the methyl substituent has on the two hydrogen bonds, N1-H1···O1 and O2-H7···N2. Even though alkyl substituents have an electron-releasing power, which would tend to destabilise the conjugate base of the acid, the presence of the methyl group in the *ortho* position makes *o*-toluic acid more acidic than benzoic acid. This is due to the hindrance caused by the presence of the methyl substituent that, in the case of *o*-toluic acid, forces the carboxylic moiety to rotate in respect of the plane containing the benzene ring, allowing a more stable state. This effect decreases from the *ortho* to the *para* position, causing *p*-toluic acid to be less acidic than *o*-toluic acid. The higher value of the k_a of *o*-toluic acid allows the hydroxyl group to be closer to the cyprodinil molecule: in fact, the interatomic distance O2···N2 is shorter in CoTA, 2.635(2) Å, than in the co-crystal with benzoic acid, 2.675(2) Å.

	CoTA	CpTA	Cyprodinil / benzoic acid
N1-H1	0.88(2) Å	0.93(2) Å	
H1···O1	2.10(2) Å	2.00(2) Å	
N1-H1···O1	173(2)°	176(2)°	
N1···O1	**2.975(2) Å**	**2.929(2) Å**	**2.925(2) Å**
O2-H7	1.00(2) Å	1.01(2) Å	
H7···N2	1.65(3) Å	1.67(2) Å	
O2-H7···N2	168(2)°	166(2)°	
O2···N2	**2.635(2) Å**	**2.663(2) Å**	**2.675(2) Å**

Table 7.24. *Comparison of the hydrogen bond characteristics in the two co-crystals.*

Investigation of the electron-density maps of the hydrogen bonds (Figure 7.45) shows the absence of disorder or proton migration. The electron density of atoms H1 and H7 is localised in a specific position and SHELXL refines their positions on the maxima of electron density.

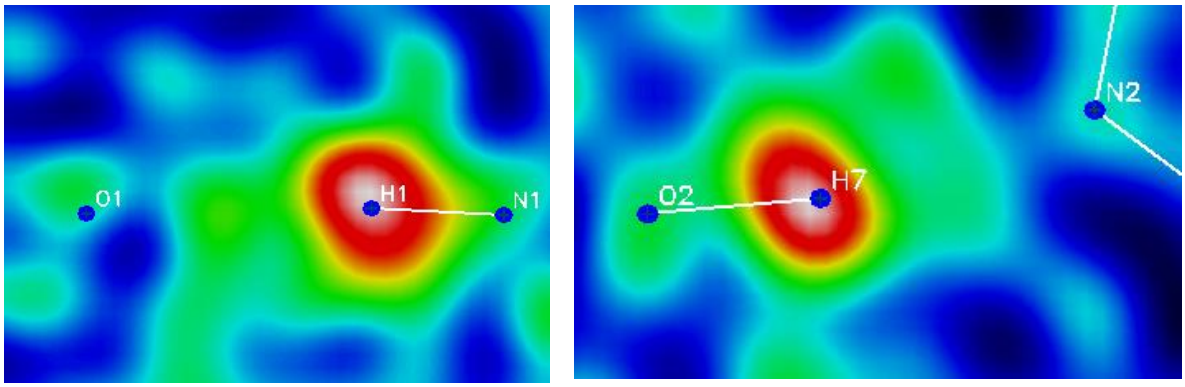

Figure 7.45. *Electron-density maps for N1-H1···O1 (left) and O2-H7···N2 (right). The atoms H1 and H7 were taken out of the refinement, but their coordinates were superimposed to the images.*

7.2.4. Conclusions

Synthesis of the molecular complexes CoTA and CpTA was obtained in ethanol solution by applying low heat for two hours. CoTA grows in thick, colourless parallelepiped crystals, belonging to the monoclinic system, while CpTA crystallises in the orthorhombic system as thin, colourless plates.

The crystal structures of the two co-crystals were analysed by single crystal X-ray diffraction at 150K in order to gain an exact knowledge of all atomic positions, at least concerning non-hydrogen atoms. In addition, single crystal neutron diffraction measurements were performed on CoTA at 30, 200 and 300K so to have a better characterisation of the hydrogen bond, having gained a ten-fold improvement in the precision and also the accuracy of the hydrogen atom positions.

The crystal packing of both co-crystals is characterised by the organisation of the molecules into heterogeneous dimers, leading to the formation of an 8-membered ring, and stacked into lines, creating a fishbone motif. The circular interaction is constituted by two linear hydrogen bonds: one between the hydrogen atom of the amino group on cyprodinil and the oxygen atom on the carbonyl of the acid, and a second displaying the hydroxyl group as the donor and the nitrogen atom on the pyrimidine ring as the acceptor. They are of moderate strength and slightly shorter than in the co-crystal with benzoic acid, demonstrating that the presence of the methyl group as a substituent on the benzene does play a role in the crystal packing of these materials.

7.3. Cyprodinil / nitrobenzoic acids

7.3.1. Introduction

Investigation of the effect that electron-withdrawing substituent on benzoic acids have on the hydrogen bonding network of co-crystals of cyprodinil was carried out using the three isomers of mononitrobenzoic acid as co-formers.

2-Nitrobenzoic acid[136] crystallises in the triclinic space group $\boldsymbol{P\bar{1}}$ and displays only one molecule in the asymmetric unit. As for the case of other substituted benzoic acid, the crystal packing is characterised by the presence of dimers, held together by centrosymmetric circular hydrogen bonds. Due to presence of the large substituent in the *ortho* position, the molecule is not planar, but both carboxyl and nitro group are twisted in respect to the benzene ring of 24.0(2)˚ and 54.9(2)˚, respectively.

3-Nitrobenzoic acid exists in two different structures: form I[137] crystallises in space group $\boldsymbol{P2_1/c}$ and form II[138] in $\boldsymbol{P2_1/n}$. The asymmetric unit of form I displays two independent molecules, A and B, which present different conformations: in molecule A the carboxyl and nitro groups form with the aromatic ring angles of ~4.5˚ and ~21.7˚ respectively, opposed to values of ~1.6˚ and ~5.3˚ in molecule B. Also the environment of the two molecules is different; specifically, the nitro group on molecule A engages in many intermolecular interactions, which are shorter than those of molecule B, resulting in smaller ***r.m.s.*** amplitudes of vibration for the nitro group in molecule A than in molecule B, indicating that the atomic vibrations in molecule A are more restricted. The two molecules organise in dimers, with the nitro groups positioned in the *trans*- configuration, as shown in Figure 7.46a.

Form II of 3-nitrobenzoic acid retains the same dimeric structure of modification I, but in this case the two independent molecules, A and B, are in the *cis*- configuration, as shown in Figure 7.46b. The crystal packing is less compact than in form I, which explains the lower value of the density of this specimen compared to form I: 1.498 g/cm^3 in form II, opposed to 1.519 g/cm^3 in form I. The hydrogen bonds are stronger and shorter than in modification I, with O···O intermolecular distances of 2.559(7) Å and 2.642(7) Å in form II, and of 2.630(7) Å and 2.666(7) Å in form I. Finally, the similar values of the C-O bonds of the carboxyl group in form II, 1.274(8) Å and 1.278(8) Å, suggest the present of disorder in the structure of the dimers.

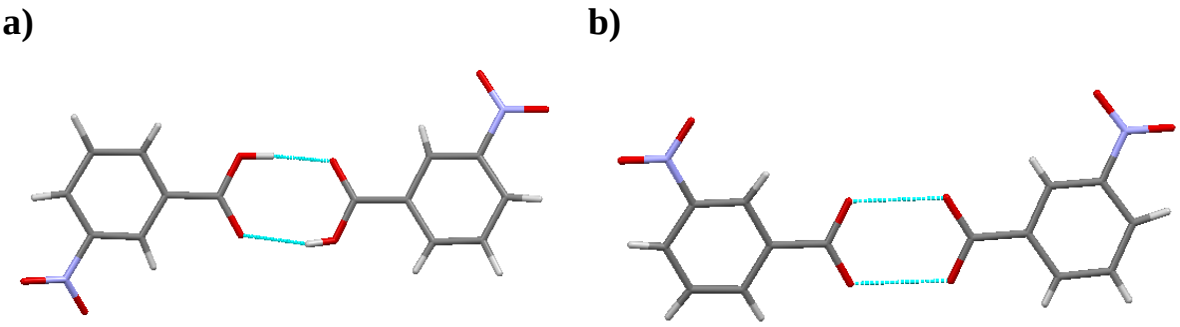

Figure 7.46. *Dimeric unit in form I[139] and form II[140] of 3-nitrobenzoic acid.*

The crystal structure of 4-nitrobenzoic acid[141] is similar to those of the *ortho* and *meta* isomers: the only molecule present in the asymmetric unit is reproduced into the three-dimensional lattice forming dimers, which are related by a centre of symmetry. The hydrogen bonds are of moderate strength, exhibiting O···O intermolecular distance of 2.660(2) Å, O-H bond length of 1.04(2) Å and hydrogen bond length H···O of 1.62(2) Å with an angle of interaction of 177(2)˚. Similarly to the previous two isomers, the carboxyl and nitro groups are not co-planar with the aromatic ring, but are twisted by ~1.8˚ and ~13.7˚, respectively.

7.3.2. Experimental

7.3.2.1. Physical and chemical properties of co-formers

2-Nitrobenzoic acid[142] is a white crystalline powder with temperature of fusion of 146˚-148˚C and relative density of 1.57 g/cm^3. It is soluble in water, with solubility of 7.8 g/L at 25˚C, and in the most organic solvents, such as acetone and alcohols.

The solid state of 3-nitrobenzoic acid[143] is a light yellow powder with melting point in the range 139˚-141˚C. It has a relative density of 1.49 g/cm^3 at 20˚C. Its water solubility is of 3 g/L at 25˚C and it is soluble in organic solvents.

4-Nitrobenzoic acid[144] is commercially available as a light yellow powder with melting temperature between 237˚C and 240˚C. Its relative density is 1.58 g/cm^3. It exhibits water solubility around 1 g/L.

7.3.2.2. Synthesis from solution

Synthesis of the three co-crystals cyprodinil/2-nitrobenzoic acid (C2NBA), cyprodinil/3-nitrobenzoic acid (C3NBA), and cyprodinil/4-nitrobenzoic acid (C4NBA) was achieved from solution. A summary of the conditions used in the preparation of the materials is reported in Table 7.25. All materials were of analytical standard and were used without further purification.

Substance	Quantity	Colour of materials	Colour of solution	Colour of crystals
Cyprodinil	0.51 g	White	Colourless	Colourless
2-Nitrobenzoic acid	0.37 g	White		
Ethanol	14 ml	Colourless		
Cyprodinil	0.51 g	White	Bright yellow	Bright yellow
3-Nitrobenzoic acid	0.37 g	Light yellow		
Ethanol	14 ml	Colourless		
Acetonitrile	10 ml	Colourless		
Cyprodinil	0.50 g	White	Bright yellow	Light yellow
4-Nitrobenzoic acid	0.37 g	Light yellow		
2-Propanol	5 ml	Colourless		
Acetonitrile	5 ml	Colourless		

Table 7.25. *Solutions that were prepared for the synthesis of the three co-crystals.*

The solutions were prepared with a 1 : 1 ratio of the two components by adding 2 ml of the solvent at a time in order to create a saturated solution. For the case of C3NBA and C4NBA a mixture of solvents was used to facilitate dissolution of the solid materials. The solutions were heated at a constant temperature of around 60˚C for two hours, during which time they were stirred continuously. Crystallisation by the method of slow evaporation of the solvent occurred at room temperature, in crystallisation vials that were covered with a film in order to prevent contamination and to slow the evaporation process. Crystals with two different crystal habits were found in the same batch of C2NBA: some had a colourless, thick, prismatic shape, while others grew as colourless, thin needles. C3NBA crystallises in very thin, large, colourless plates, whereas crystals of C4NBA grew as very thin, small needles.

7.3.2.3. Differential Scanning Calorimetry

Possible changes in the crystal structure of C3NBA upon variations in temperature were analysed by DSC. The results are reported in Figure 7.47.

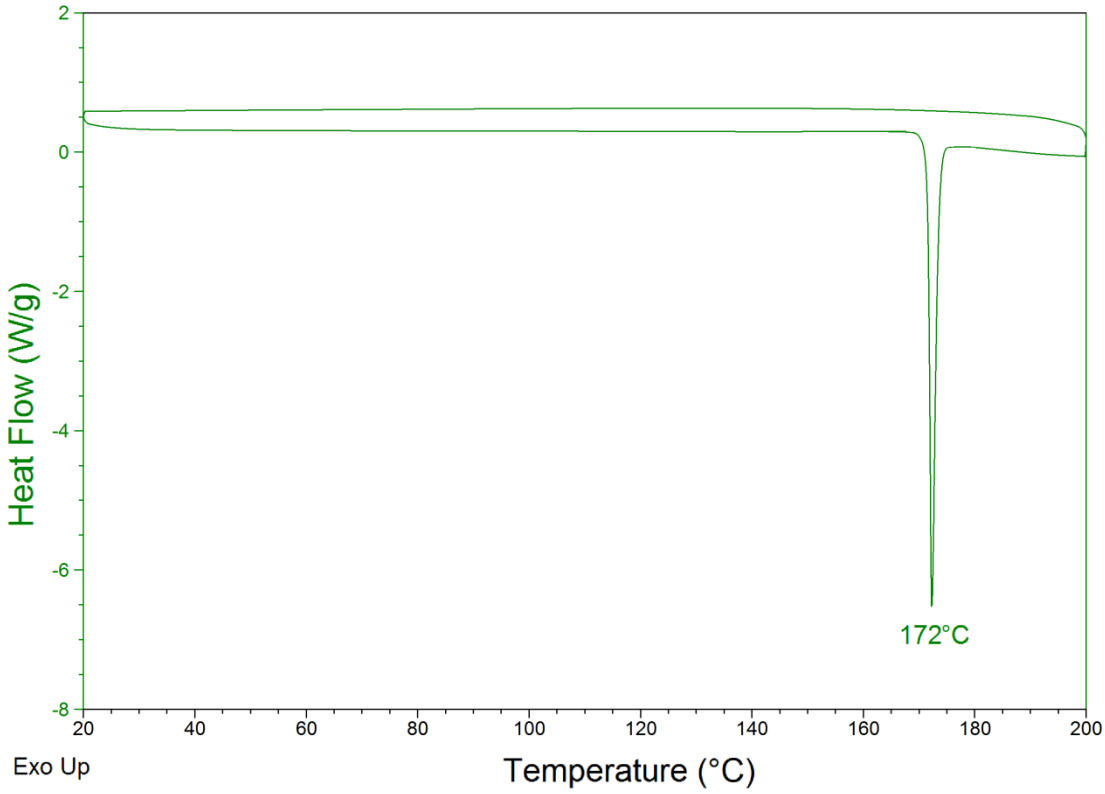

Figure 7.47. *DSC profile for a sample of C3NBA.*

The DSC profile of C3NBA shows one endothermic event around 172˚C, corresponding to the fusion of the co-crystal. Similarly to the cases of the other co-crystals of cyprodinil, no re-crystallisation was observed during the cooling process back to 20˚C.

7.3.2.4. Powder X-ray diffraction

Since the only available crystals of C4NBA were very thin, small needles, which did not sufficiently diffract X-ray radiation, it was not possible to investigate the crystal structure by SXD. However, the crystals present in the batch were ground into a fine powder and PXD pattern was collected on the D5000 diffractometer. Figure 7.48 diplays a comparison between the powder patterns of the co-crystal and of its components.

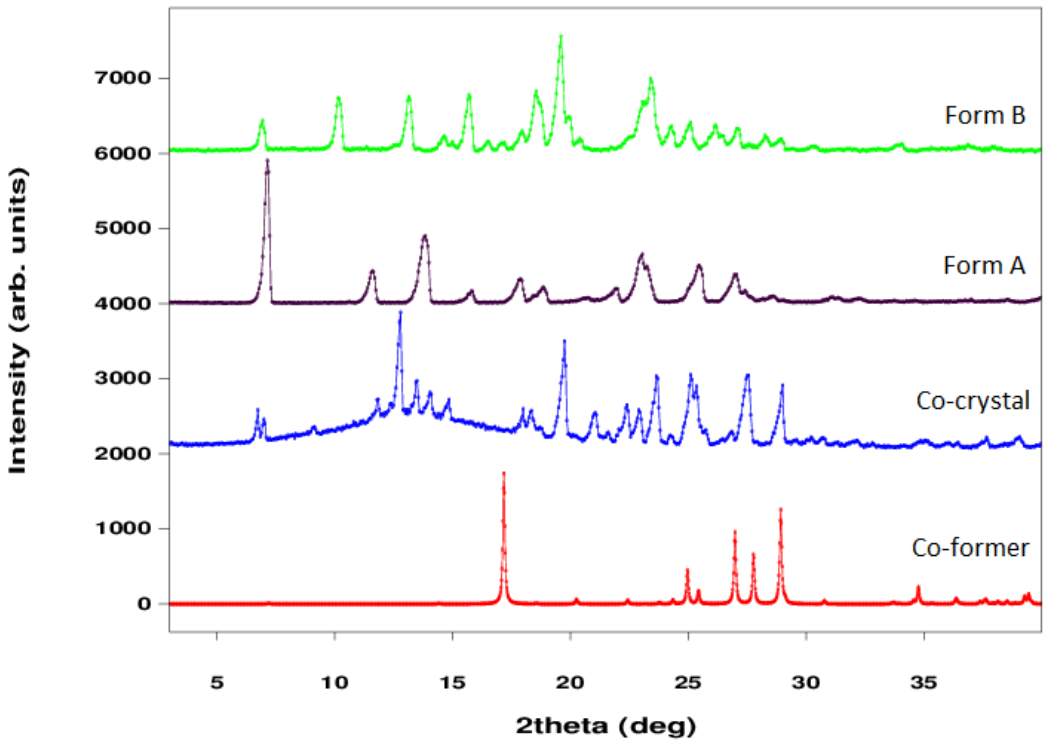

Figure 7.48. *Powder patterns of modification A (blue) and B (black) of cyprodinil, 4-nitrobenzoic acid (green), and C4NBA (red).*

From the comparison of the powder pattern of C4NBA with those of the components it is possible to observe a different pattern of the Bragg peak positions, indicating the presence of a new crystal structure. Unfortunately, structure solution from powder diffraction data is only possible, but still difficult, when very high quality data are recorded, e. g. at synchrothron facilities. As such data was not available for this investigation, no further analysis of the structure of C4NBA was undertaken.

7.3.2.5. Single crystal X-ray diffraction

The crystal structures of C2NBA and C3NBA were analysed by single crystal X-ray diffraction. Two different forms of C2NBA were found in the same batch: crystals of form I have a thick, prismatic habit, while form II crystallises as thin, long needles. SXD data were collected on an Enraf-Nonius kappaCCD single crystal diffractometer. Two sets of data were recorded on both polymorphs, one at 150K and one at room temperature to assess whether changes in the structures occurred upon variation of temperature.

C3NBA crystallises in thin, large plates and the crystal selected for the SXD measurement was grown from an ethanol : acetonitrile solution. Two sets of data were collected on the Agilent Xcalibur single crystal diffractometer at 150K and at room temperature.

For all co-crystals analysed by SXD it is possible to notice an increase of the R-factors from the data sets collected at 150K and those recorded at 293K. This slight worsening of the statistics is

due to the increase of the thermal vibration of all atoms at higher temperatures, affecting the peak intensities.

X-ray crystallographic data and refinement parameters are reported in Table 7.26 for form I of C2NBA at 150K and 293K; in Table 7.27 for form II of C2NBA at 150K and 293K; in Tables 7.28 for C3NBA at 150K and 293K.

Name		C2NBA form I	
Empirical formula		$C_{14}H_{15}N_3$ $C_7H_5NO_4$	
Formula weight (g mol^{-1})		392.41	
Temperature (K)		150	293
Wavelength (Å)		0.71073	
Crystal system, space group		Monoclinic, $P2_1/c$	
Unit cell dimensions	a (Å) =	8.324(2)	8.396(2)
	b (Å) =	21.917(4)	22.370(5)
	c (Å) =	11.110(2)	11.117(2)
	β (˚) =	104.80(3)	105.39(3)
Volume ($Å^3$)		1959.6(7)	2013.1(7)
Z, calculated density (g cm^{-3})		4, 1.330	4, 1.295
F(000)		824	
Absorption coefficient (mm^{-1})		0.094	
Theta range for data collection (˚)		1.86 to 26.37	
Limiting indices		$-10 \leq h \leq 10$, $-27 \leq k \leq 27$, $-13 \leq l \leq 13$	
Reflections collected / unique		7847 / 3998 [R_{int} = 0.0147]	14634 / 4101 [R_{int} = 0.0258]
Completeness		99.8 %	99.7 %
Refinement method		Full-matrix least-squares on F^2	
Data / restrains / parameters		3998 / 0 / 343	4101 / 0 / 343
Goodness-of-fit on F^2		1.243	1.190
Final R indices [I>2sigma(I)]		R_1 = 0.0644, wR_2 = 0.1561	R_1 = 0.0678, wR_2 = 0.1650
R indices (all data)		R_1 = 0.0830, wR_2 = 0.1871	R_1 = 0.0909, wR_2 = 0.1937
Extinction coefficient		0.25(2)	0.22(2)
Largest diff. Peak and hole (e $Å^{-3}$)		0.69 and -0.75	0.50 and -0.47

Table 7.26. *X-ray crystallographic data and refinement parameters for form I of C2NBA at 150K and 293K.*

Name		C2NBA form II	
Empirical formula		$C_{14}H_{15}N_3$ $C_7H_5NO_4$	
Formula weight (g mol^{-1})		392.41	
Temperature (K)		150	293
Wavelength (Å)		0.71073	
Crystal system, space group		Monoclinic, $P2_1/n$	
Unit cell dimensions	a (Å) =	a = 14.587(3)	14.633(3)
	b (Å) =	b = 7.610(2)	7.756(2)
	c (Å) =	c = 17.176(3)	17.292(4)
	β (˚)	β = 102.01(3)	102.10(3)
Volume ($Å^3$)		1864.9(6)	1918.9(7)
Z, calculated density (g cm^{-3})		4, 1.398	
F(000)		824	
Absorption coefficient (mm^{-1})		0.099	
Theta range for data collection (˚)		1.67 to 26.37	
Limiting indices		-18≤ h ≤18, -8≤ k ≤9, -21≤ l ≤21	-15≤ h ≤15, -8≤ k ≤8, -18≤ l ≤18
Reflections collected / unique		6247 / 3784 [R_{int} = 0.0395]	4525 / 2434 [R_{int} = 0.0271]
Completeness		99.1 %	98.7 %
Refinement method		Full-matrix least-squares on F^2	
Data / restrains / parameters		3784 / 0 / 343	2434 / 0 / 343
Goodness-of-fit on F^2		1.109	1.219
Final R indices [I>2sigma(I)]		R_1 = 0.0625, wR_2 = 0.1387	R_1 = 0.0776, wR_2 = 0.1533
R indices (all data)		R_1 = 0.1099, wR_2 = 0.1754	R_1 = 0.1123, wR_2 = 0.1925
Extinction coefficient		0.047(4)	0.100(9)
Largest diff. Peak and hole (e $Å^{-3}$)		0.64 and -0.66	0.66 and -0.66

Table 7.27. *X-ray crystallographic data and refinement parameters for form II of C2NBA at 150K and 293K.*

Name		C3NBA	
Empirical formula		$C_{14}H_{15}N_3$ $C_7H_5NO_4$	
Formula weight (g mol^{-1})		392.41	
Temperature (K)		150	293K
Wavelength (Å)		0.71073	
Crystal system, space group		Monoclinic, $P2_1/c$	
Unit cell dimensions	a (Å) =	11.8454(4)	11.8557(4)
	b (Å) =	7.7074(2)	7.8766(3)
	c (Å) =	21.4100(6)	21.5102(7)
	β (°) =	103.963(3)	104.102(4)
Volume ($Å^3$)		1896.9(1)	1948.1(1)
Z, calculated density (g cm^{-3})		4, 1.374	
F(000)		824	
Absorption coefficient (mm^{-1})		0.098	
Crystal size (mm)		0.04 x 0.23 x 0.34	0.05 x 0.21 x 0.35
Theta range for data collection (°)		3.45 to 26.37	
Limiting indices		-14≤ h ≤14, -9≤ k ≤9, -26≤ l ≤26	-13≤ h ≤14, -9≤ k ≤9, -25≤ l ≤26
Reflections collected / unique		14859 / 3878 [R_{int} = 0.0379]	15874 / 3972 [R_{int} = 0.0394]
Completeness		99.8 %	99.8 %
Refinement method		Full-matrix least-squares on F^2	
Data / restrains / parameters		3878 / 2 / 346	3972 / 2 / 346
Goodness-of-fit on F^2		1.014	1.024
Final R indices [I>2sigma(I)]		R_1 = 0.0426, wR_2 = 0.0892	R_1 = 0.0527, wR_2 = 0.0995
R indices (all data)		R_1 = 0.0712, wR_2 = 0.1016	R_1 = 0.1061, wR_2 = 0.1196
Extinction coefficient		0.0028(7)	0.0041(9)
Largest diff. Peak and hole (e $Å^{-3}$)		0.22 and -0.19	0.15 and -0.16

Table 7.28. *X-ray crystallographic data and refinement parameters for C3NBA at 150K and 293K.*

7.3.3. Results and discussion

7.3.3.1. C2NBA form I

Modification I of C2NBA crystallises in the monoclinic system, space group ***P2$_1$/c***. There are two molecules in the asymmetric unit, one of protonated cyprodinil and one of 2-nitrobenzoate, indicating the formation of a salt, as shown in Figure 7.49 for the structure studied with X-ray radiation. Table 7.29 lists the derived torsion angles and bond lengths.

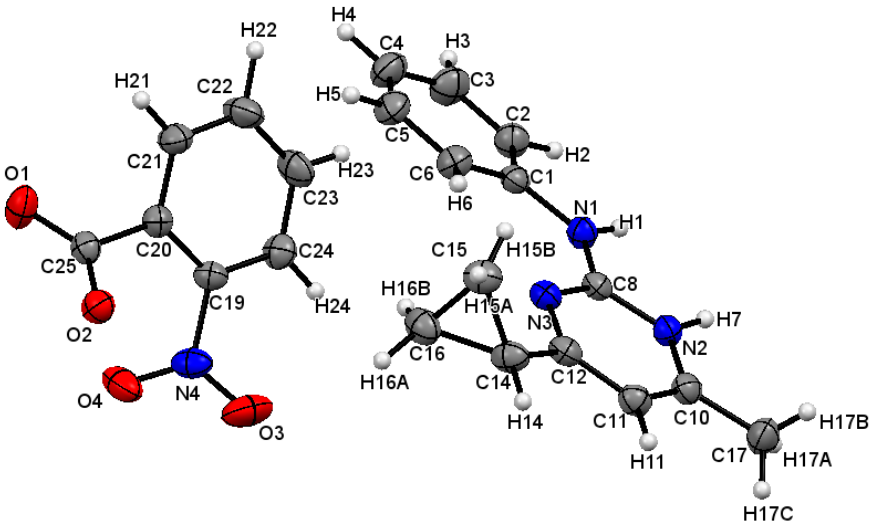

Figure 7.49. *ORTEP representation of the asymmetric unit of form I of C2NBA, viewed along the* ***b****-axis, derived from SXD at 150K. The probability level for all non-hydrogen ellipsoids is 50%, while the hydrogen atoms are drawn as fixed-size spheres of radius 0.15 Å.*

	150K	293K
C8-N1-C1-C6	9.7(3)˚	10.9(3)˚
N3-C12-C14-C15	-45.4(2)˚	-45.0(3)˚
N3-C12-C14-C16	21.8(2)˚	22.6(3)˚
C8-N3-C12-C14	176.7(1)˚	176.9(2)˚
N2-C8-N1-H1	-7(2)˚	1(2)˚
N1-C8-N2-H7	8(2)˚	4(2)˚
O1-C25-C20-C21	42.5(2)˚	43.9(3)˚
C25-C20-C21-C22	175.7(2)˚	175.9(2)˚
C25-C20-C19-C24	-174.7(2)˚	-175.2(2)˚
O3-N4-C19-C24	48.4(2)˚	46.7(3)˚
O3-N4-C19-C20	-135.1(2)˚	-129.8(2)˚
C25-O1	1.247(2) Å	1.239(2)
C25-O2	1.259(2) Å	1.252(2)

Table 7.29. *Torsion angles and bond lengths of interest.*

The benzene and the pyrimidine rings of cyprodinil are not co-planar, but they are twisted by an angle of 9.7(3)˚. The cyclopropyl substituent is positioned below the plane containing the pyrimidine moiety and the two hydrogen atoms bonded to N1 and N2 are slightly twisted from the cyprodinil molecule in opposite direction in order to interact with the oxygen atoms of the benzoate.

Due to the high hindrance of the nitro substituent in the *ortho* position, both carboxyl and nitro groups are twisted in respect to the benzene ring of 42.5(2)˚ and 48.4(2)˚, respectively. The benzene retains the planarity typical of aromatic compounds and the lengths of C25-O1 and C25-O2 confirm the presence of the carboxylate ion, being intermediate values between a single and a double bond, allowing delocalization of the electron density. The conformation of the two molecules is retained in the structure at 293K, indicating that the proton transfer is not temperature dependent.

The supramolecular structure is characterized by the formation of heterogeneous dimers, leading to circular hydrogen bonds between the protonated aminopyrimidine of cyprodinil and the carboxylate, as shown in Figure 7.50. The geometry of the intermolecular hydrogen bond is almost planar, but the benzene ring of the acid is twisted of ~50(2)˚ in respect to the cyprodinil molecule. The dimers stack themselves into lines, which are shifted in order to accommodate the acid molecules, creating a zig-zag motif, as displayed in Figure 7.51.

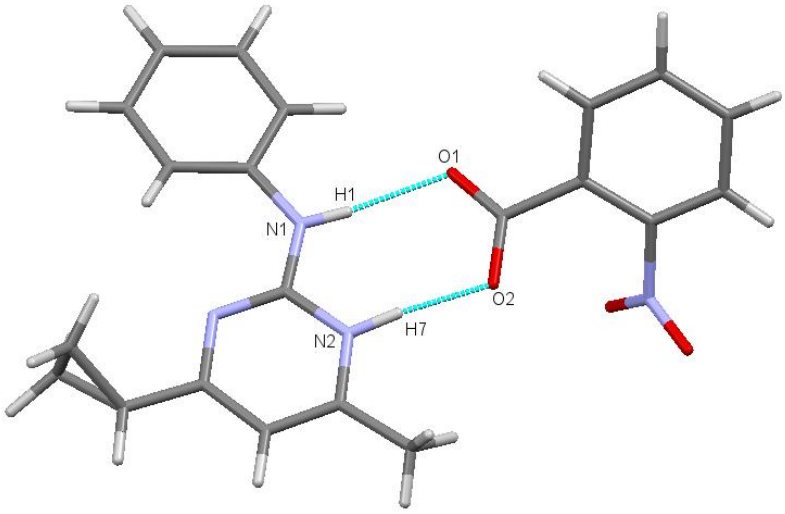

Figure 7.50. *Heterogeneous dimer in form I of C2NBA.*

	150K	293K
N1-H1	0.82(3) Å	0.88(2) Å
H1···O1	1.93(3) Å	1.88(3) Å
N1-H1···O1	174(2)˚	168(2)˚
N1···O1	2.752(2) Å	2.753(2) Å
N2-H7	0.92(3) Å	0.91(3) Å
H7···O2	1.73(3) Å	1.73(3) Å
N2-H7···O2	174(2)˚	173(2)˚
N2···O2	2.642(2) Å	2.642(2) Å

Table 7.30. *Hydrogen bond lengths and geometry of interaction.*

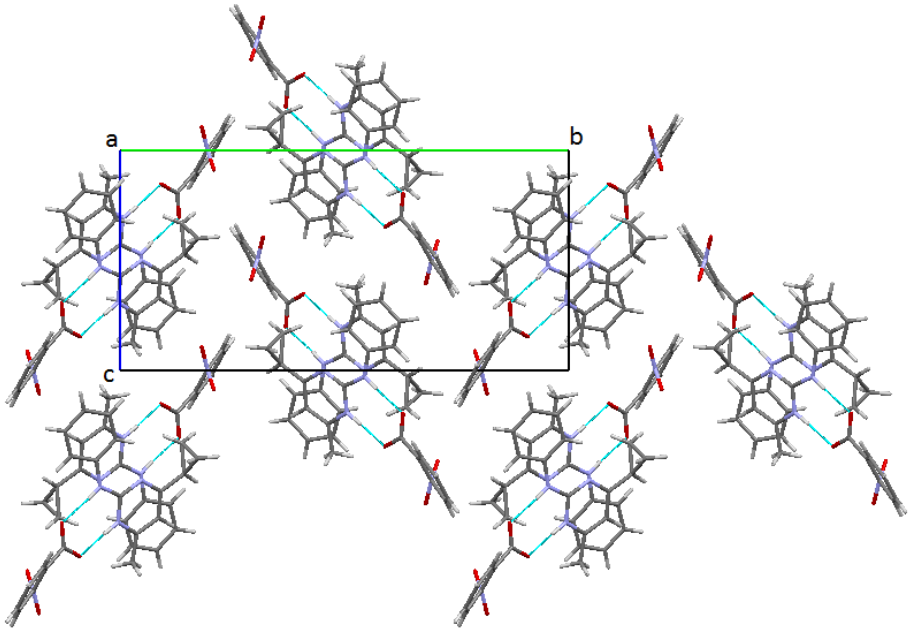

Figure 7.51. *Crystal packing of form I of C2NBA, viewed along the* ***a****-axis.*

Based on the bond lengths, donor-acceptor distances and geometry of interaction, which are listed in Table 7.30, it is possible to identify N1-H1···O1 and N2-H7···O2 as moderate hydrogen bonds[81]. The hydrogen bonding network is retained in the structure at 293K with no significant differences in bond lengths or angles.

The formation of a salt instead of a neutral molecular complex can be explained considering the acidity of 2-nitrobenzoic acid, which has a $\boldsymbol{pK_a}$ value of 2.17[145]: in fact, the presence of the nitro group as substituent on the benzene ring makes 2-nitrobenzoic acid more acidic than benzoic acid. The nitro group exhibits inductive effect ***–I*** due to the higher electronegativity of the constituting atoms. This effect contributes to destabilise the acid, removing electron density from the carboxylic group. As a consequence, the hydrogen atom of the hydroxyl group, H7, will be less attracted by

the oxygen atom, facilitating proton extraction by a base. The electron-density maps of the two hydrogen bonds, reported in Figure 7.52, at both temperatures exclude the migration of the proton back to the acid.

150K **293K**

a)

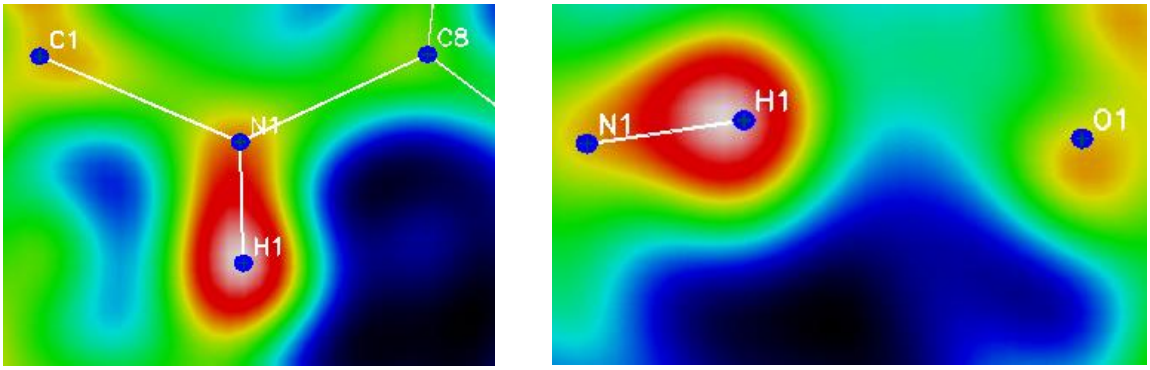

b)

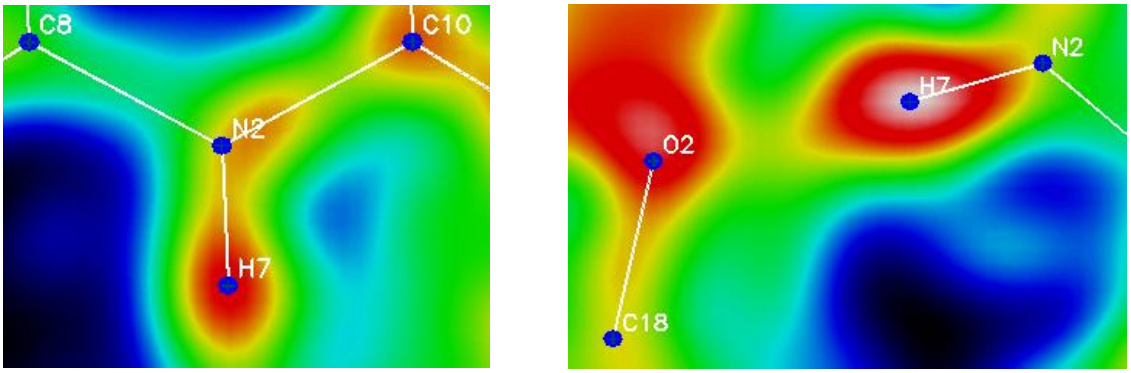

Figure 7.52. *Difference electron-density maps for a) N1-H1···O1 and b) N2-H7···O2 . The atoms H1 and H7 were excluded from the refinement, but their coordinates were superimposed on the images.*

7.3.3.2. C2NBA form II

Form II of C2NBA crystallises in long, colourless needles, belonging to the monoclinic system, space group ***$P2_1/n$***. The asymmetric unit displays one molecule of cyprodinil and one of 2-nitrobenzoic acid, already organised in a dimer, as reported in Figure 7.53 for the structure derived from SXD results. Table 7.31 reports a list of torsion angles and bond lengths.

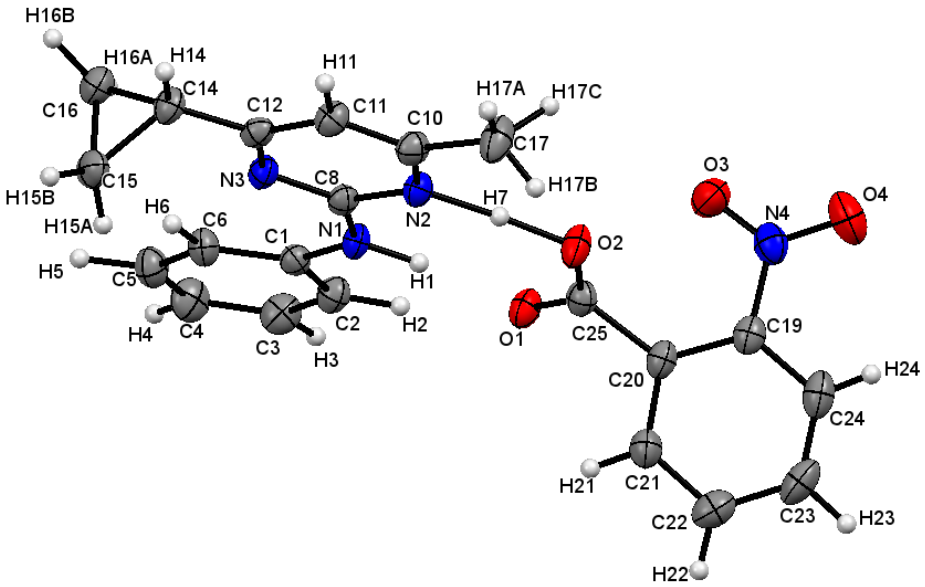

Figure 7.53. *ORTEP representation of the asymmetric unit of form II of C2NBA, viewed along the* ***c****-axis, derived from SXD at 150K. The probability level for all non-hydrogen ellipsoids is 50%, while the hydrogen atoms are drawn as fixed-size spheres of radius 0.15 Å.*

	150K	293K
C8-N1-C1-C6	-7.9(4)˚	-7.6(6)˚
N3-C12-C14-C15	41.8(3)˚	41.7(5)˚
N3-C12-C14-C16	-26.3(4)˚	-27.0(5)˚
C8-N3-C12-C14	-177.1(2)˚	-176.7(3)˚
N2-C8-N1-H1	2(2)˚	-1(2)˚
N1-C8-N2-H7	1(2)˚	-4(2)˚
O2-C25-C20-C19	-68.3(3)˚	-69.7(5)˚
C25-C20-C19-C24	173.6(3)˚	174.7(4)˚
C25-C20-C21-C22	-174.9(3)˚	-175.4(4)˚
O3-N4-C19-C20	-15.4(4)˚	-13.8(6)˚
O3-N4-C19-C24	162.3(3)˚	163.3(4)˚
C25-O1	1.237(4) Å	1.234(5)
C25-O2	1.264(3) Å	1.265(5)
N2-H7	1.35(4) Å	1.27(5) Å
H7-O2	1.26(4) Å	1.34(5) Å

Table 7.31. *Torsion angles and bond distances of interest.*

The conformation adopted by cyprodinil is similar to modification I of C2NBA: the benzene ring position is out of the plane of the aminopyrimidine by an angle of -7.9(4)˚, and the cyclopropyl substituent is positioned below the aromatic pyrimidine moiety. There are no significant variations in the cyprodinil conformation between the structure at 150K and that at 293K.

The main differences between the two polymorphs of C2NBA can be found in the different conformation exhibited by 2-nitrobenzoic acid: in form II the carboxylic group is even more twisted in respect to the benzene ring than in form I, with a torsion angle O2-C25-C20-C19 of -68.3(3)˚, while the nitro group is positioned more in plane with the benzene, with a torsion angle O3-N4-C19-C20 that from 48.4(2)˚ in form I becomes of -15.4(4)˚ in form II. Also the relative position of the two interacting molecules is different in the two polymorphs, as reported in Figure 7.54.

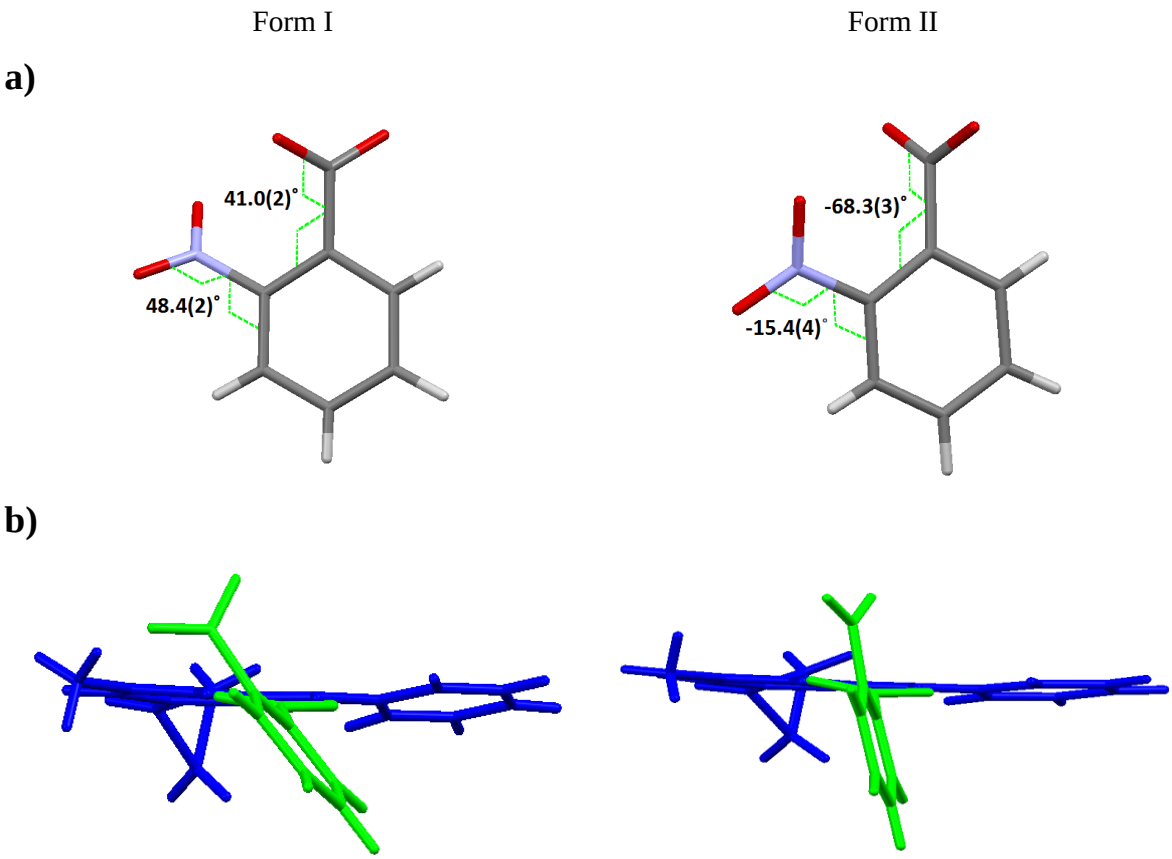

Figure 7.54. *a) Conformation of 2-nitrobenzoic acid and b) relative position of the interacting molecules in the two forms of C2NBA.*

The different conformation of the carboxylic group in form II makes the delocalisation of the electron density from the carboxyl to the benzene ring less pronounced, avoiding the transfer of the proton. Instead, the hydrogen atom H7 is refined almost in the middle of the interatomic distance O2···N2. Comparing the structure of form II at 150K to the one measured at 293K, it is possible to observe the migration of atom H7 from the acid towards the nitrogen atom of cyprodinil with the increased temperature. The shape of the electron density of atoms H1 and H7 at the two temperatures excludes the presence of disorder, as reported in Figure 7.55.

150K **293K**

a)

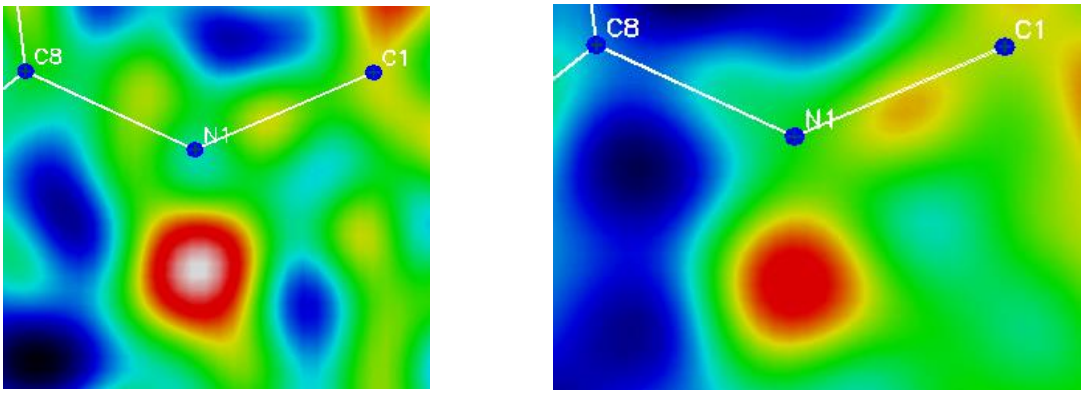

b)

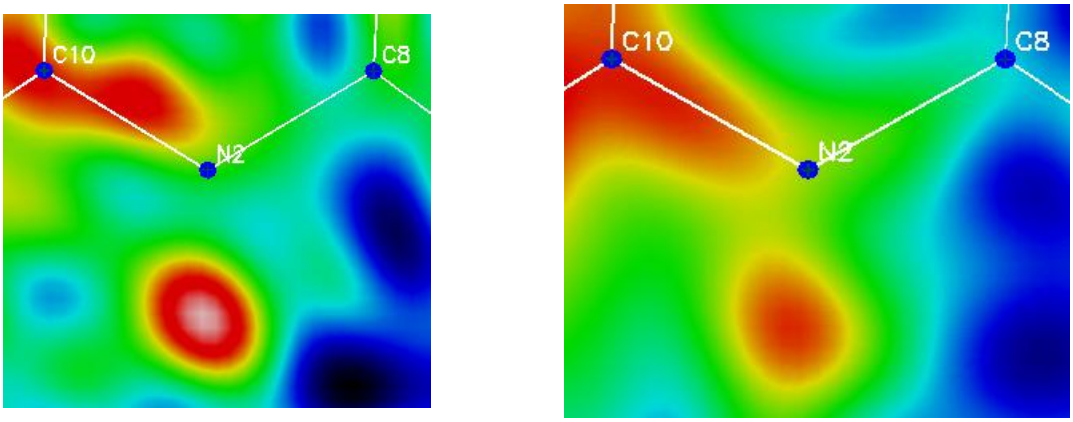

Figure 7.55. *Difference electron-density maps for a) N1-H1···O1 and b) O2···H7···N2 in form II of C2NBA.*

The crystal packing is characterised by heterogeneous dimers formed by the interaction of a molecule of cyprodinil with the carboxyl group of 2-nitrobenzoic acid. The interaction is a circular hydrogen bond, leading to the formation of an 8-membered ring, as shown in Figure 7.56. Based on bond lengths, donor-acceptor distances and geometry of interaction[81], it is possible to identify a moderate hydrogen bond, N1-H1···O1, and a strong one, O2···H7···N2, in which the hydrogen atom is shared between the two electronegative atoms. In Table 7.32 a list of the hydrogen bond length and geometry is reported.

The crystal packing is governed by the staking of the dimers into off-set parallel piles, allowing the formation of π-π interactions between two neighbouring cyprodinil molecules with distances of 3.74(3) Å. The various layers display a different orientation of the dimer, which is rotated by 180° in respect to the dimer positioned on the layer above, as shown in Figure 7.57.

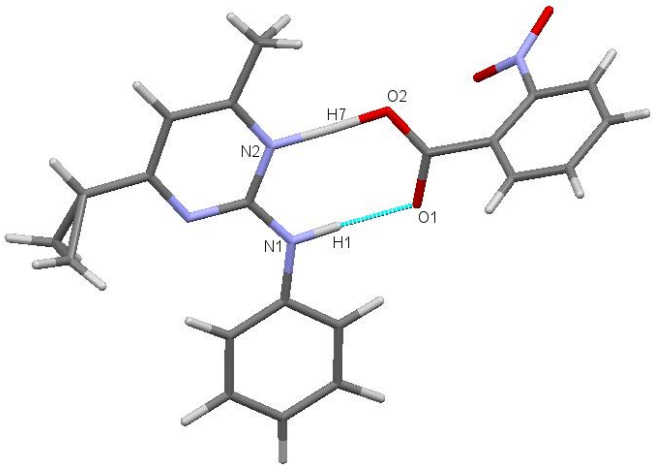

Figure 7.56. *Heterogeneous dimer in form II of C2NBA.*

	150K	**293K**
N1-H1	1.02(3) Å	0.93(4) Å
H1···O1	1.78(3) Å	1.85(4) Å
N1-H1···O1	176(3)˚	170(4)˚
N1···O1	2.799(3) Å	2.812(4) Å
N2-H7	**1.35(4) Å**	**1.27(5) Å**
H7-O2	**1.26(4) Å**	**1.34(5) Å**
N2···O2	2.603(3) Å	2.609(4) Å

Table 7.32. *Hydrogen bond lengths and geometry of interaction in form II of C2NBA.*

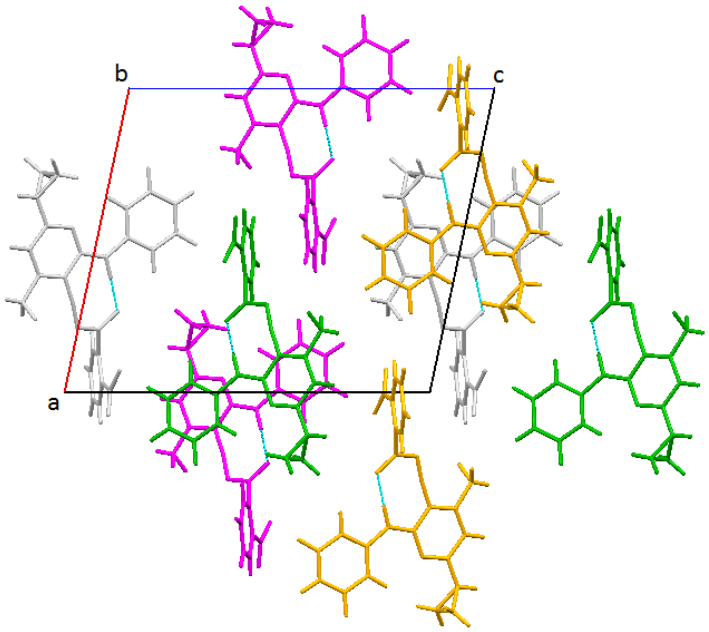

Figure 7.57. *Crystal packing of form II of C2NBA, viewed along the* ***b****-axis. The colours refer to the dimers lying on different layers.*

Computational work, undertaken by C. Hendon at the University of Bath, was carried out on the two polymorphs of C2NBA, in order to investigate the nature of the proton transfer. The results are reported in Table 7.32. The ***HOMO*** (*Highest Occupied Molecular Orbital*) is based on the amine, while the ***LUMO*** (*Lowest Unoccupied Molecular Orbital*) is based on the nitrobenzene.

	Internal energy (eV)	N1-H1 (Å)	N2-H7 (Å)	O2-H7 (Å)	O1-H1 (Å)
Form I	-1582,59	1,08	1,05	1,54	1,69
Form II	-1581,55	1,11	1,06	1,49	1,73

Table 7.33. *Computational results of modifications I and II of C2NBA.*

By observing Table 7.33, it is possible to notice that the two polymorphs have similar values for their internal energy, which might explained the crystallization of both modifications in the same batch under the same experimental conditions. However, the calculations formalise a proton transfer also in the crystal structure of form II, which is not confirmed by the experimental observations.

7.3.3.3. C3NBA

C3NBA crystallises in large, thin, bright yellow plates, belonging to the monoclinic system, space group ***P2$_1$/c***. The asymmetric unit represents one molecule of cyprodinil and one of 3-nitrobenzoic acid, both in their neutral state, as shown in Figure 7.58 for the structure derived from SXD results. Tables 7.34 and 7.34 report a list of selected torsion angles and bond lengths, obtained from the SXD results.

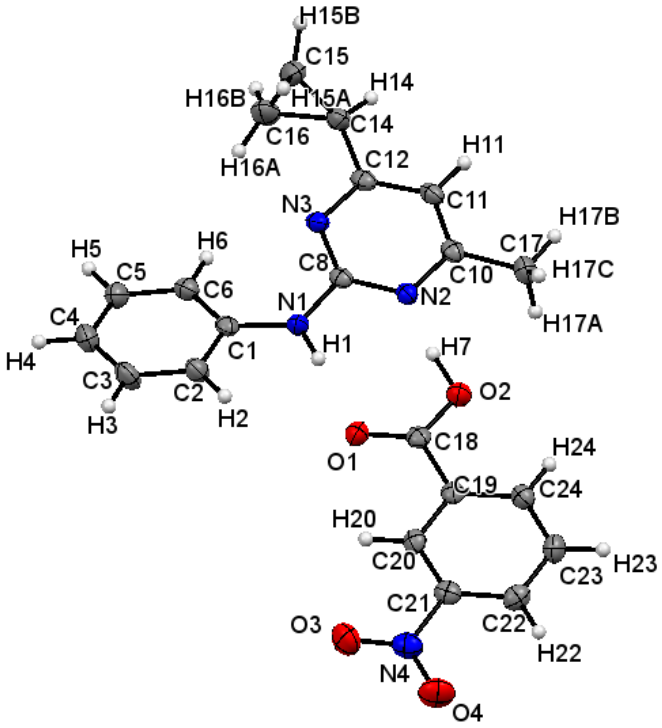

Figure 7.58. *ORTEP representation of the asymmetric unit of C3NBA, viewed along the* ***b****-axis, derived from SXD at 150K. The probability level for all non-hydrogen ellipsoids is 50%, while the hydrogen atoms are drawn as fixed-size spheres of radius 0.15 Å.*

	150K	**293K**
C8-N1-C1-C6	-20.1(3)˚	-19.2(3)˚
N3-C12-C14-C15	54.5(2)˚	53.2(3)˚
N3-C12-C14-C16	-13.9(2)˚	-15.1(3)˚
C8-N3-C12-C14	178.8(1)˚	179.6(2)˚
N2-C8-N1-H1	12(1)˚	6(1)˚

Table 7.34. *Torsion angles and bond lengths of interest in the cyprodinil molecule, as derived from SXD data.*

	150K	293K
O2-C18-C19-C24	0.0(2)˚	0.2(3)˚
C18-C19-C24-C23	-180.0(2)˚	-180.0(2)˚
C18-C19-C20-C21	179.3(1)˚	179.4(2)˚
O3-N4-C21-C20	-4.3(2)˚	-4.9(3)˚
O3-N4-C21-C22	176.7(2)˚	176.0(2)˚
C18-O1	1.226(2) Å	1.221(3) Å
C18-O2	1.299(2) Å	1.296(3) Å

Table 7.35. *Torsion angles and bond lengths of interest in the acid molecule, as derived from SXD data.*

No significant changes in the conformation of the cyprodinil molecule occur during heating from 150K to room temperature: the benzene and the cyclopropyl substituents are placed, respectively, below and above the pyrimidine ring to avoid hindrance due to the large dimensions of the cyclopropyl.

Also the conformation of 3-nitrobenzoic acid is retained at the two different temperatures. The aromatic ring is planar and, contrary to the case of the polymorphs of C2NBA, the carboxyl group is on the same plane of the benzene, while the nitro group in the *meta* position is only slightly rotated by -4.3(2)˚. This conformation allows a higher delocalisation of the electron density of the carboxyl and nitro groups on the entire molecule, contributing to the destabilisation of the neutral acid. However, although 3-nitrobenzoic acid ($\boldsymbol{pK_a}$ = 3.46)[137] is more acidic than benzoic acid ($\boldsymbol{pK_a}$ = 4.20)[137], the inductive effect ***–I*** is less pronounced in the *meta* position than in the *ortho*, explaining the absence of the proton transfer in C3NBA.

The supramolecular assembly in C3NBA is characterised by the presence of heterogeneous dimers, formed by the interaction of the aminopyrimidine functionality of cyprodinil with the carboxyl group of the acid. The result is a circular hydrogen bond of medium strength[81]. A representation of the dimer is reported in Figure 7.59, while in Table 7.36 hydrogen bond lengths and geometry of interaction for the structure at 150K are listed. The dimers organise into layers, forming a motif similar to a herring-bone, held together by π-π interactions of 3.48(2) Å between the pyrimidine moiety of cyprodinil and the aromatic ring of the acid. Each dimer is rotated by 180˚ in respect to the one lying on the layer below, as shown in Figures 7.60 and 7.61.

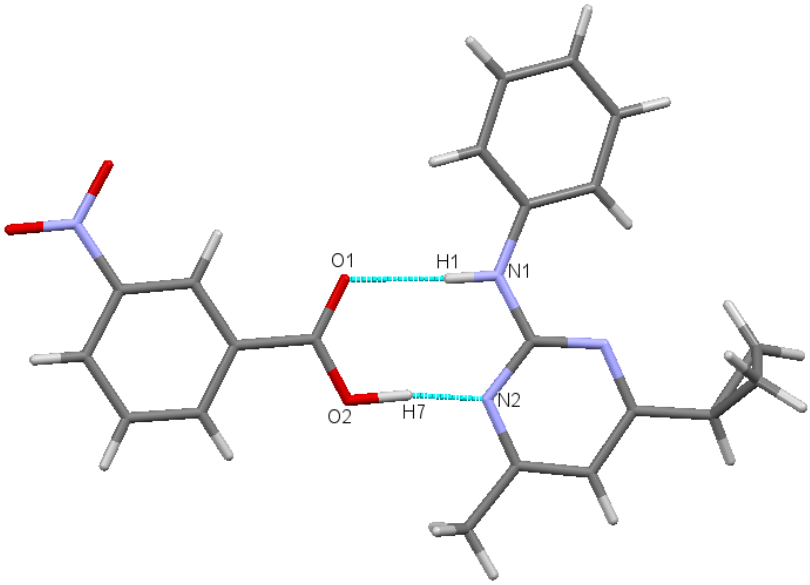

Figure 7.59. *Heterogeneous dimer in C3NBA at 150K.*

	150K	**293K**
N1-H1	0.91(2) Å	0.89(2) Å
H1···O1	1.94(2) Å	1.97(2) Å
N1-H1···O1	177(2)˚	178(2)˚
N1···O1	2.850(2) Å	2.866(2) Å
O2-H7	1.12(2) Å	1.15(3) Å
H7···N2	1.47(2) Å	1.45(3) Å
O2-H7···N2	172(2)˚	170(3)˚
O2···N2	2.579(2) Å	2.597(2) Å

Table 7.36. *Hydrogen bond lengths and geometry of interaction for C3NBA at 150K and 293K.*

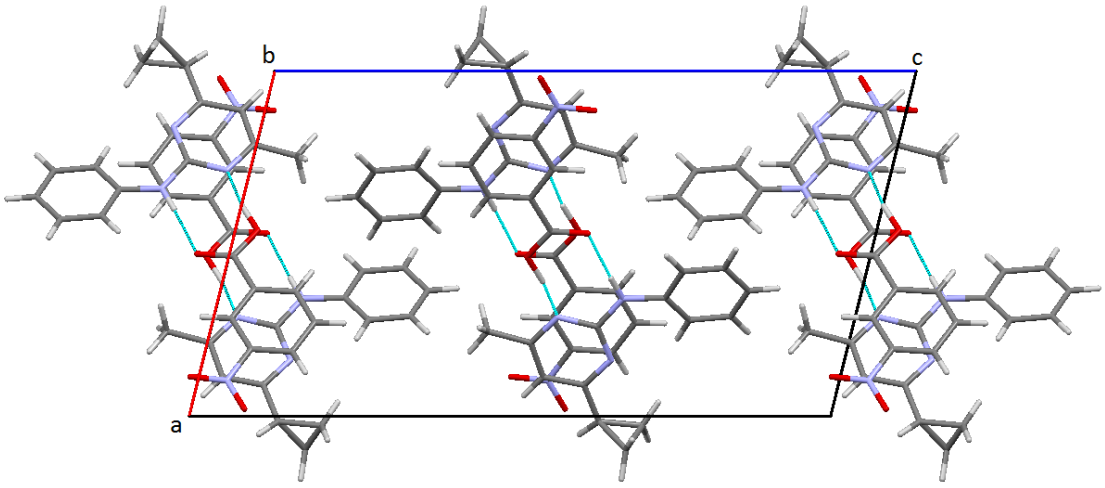

Figure 7.60. *Crystal packing of C3NBA, viewed along the* ***b****-axis.*

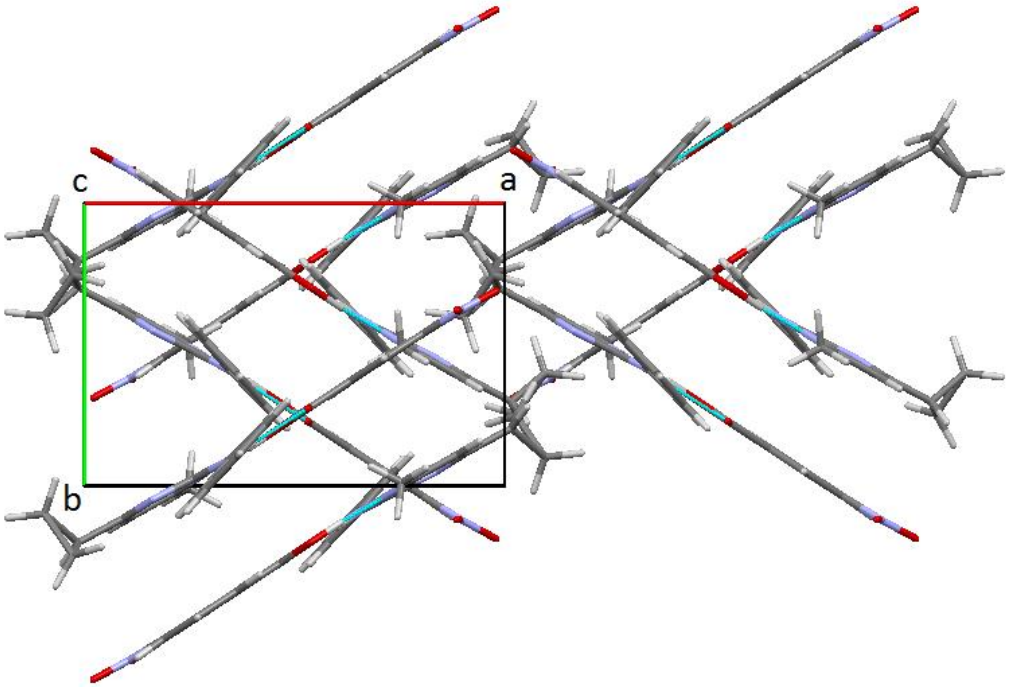

Figure 7.61. *Crystal packing of C3NBA, viewed along the* ***c****-axis.*

From the observation of Table 7.36, it is possible to notice that the bond length of O2-H7 is longer than usual: 1.12(2) Å and 150K and 1.15(3) Å at 293K. An explanation can be found investigating the electron density of atom H7 (Figure 7.62). Usually, in a good refinement done by SHELXL, the atomic coordinates are refined on the maximum of electron density, as shown in Figure 7.62 for the structure at 150K. However, at 293K the bilobated shape of the electron density of atom H7 forces SHELXL to refine the coordinates of H7 not on the density peak maximum, but to average its position over the all electron density, causing a stretching of the covalent bond O2-H7.

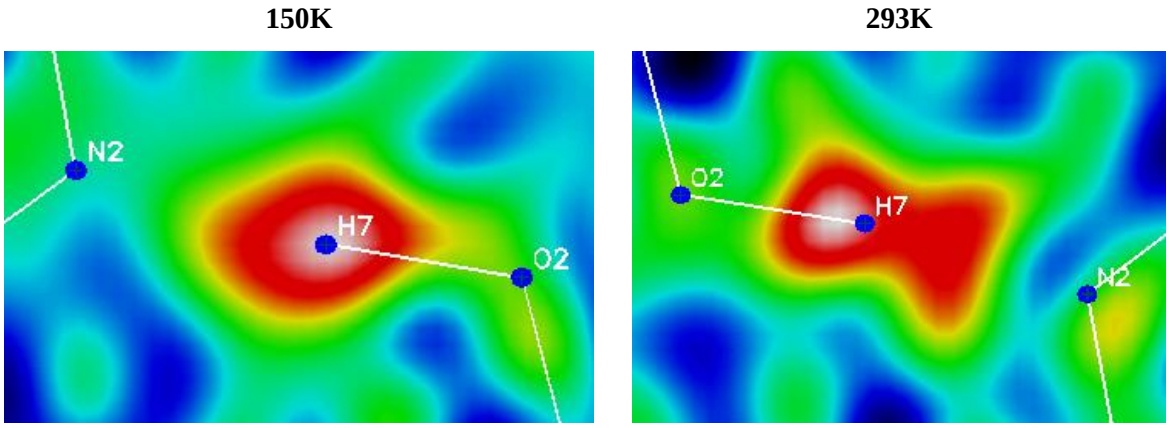

Figure 7.62. *Difference electron-density maps for the hydrogen bond O2-H7···N2. The atom H7 was excluded from the refinement, but the coordinates were superimposed to the images.*

The shape of the electron density of H7 at 293K and the averaged values of its coordinates indicate the presence of disorder at room temperature. On the contrary, at 150K the electron density of H7 is only slightly elongated towards the nitrogen atom of cyprodinil and its position is refined on the maximum of ρ. The refinement of positional disorder for atom H7 at 293K was carried out using fixed values for O2-H7A and N2-H7B, 0.90(1) Å and 0.92(1) Å respectively, and fixed U_{iso} of 0.05 $Å^2$. The results are reported in Figure 7.63 and in Table 7.37.

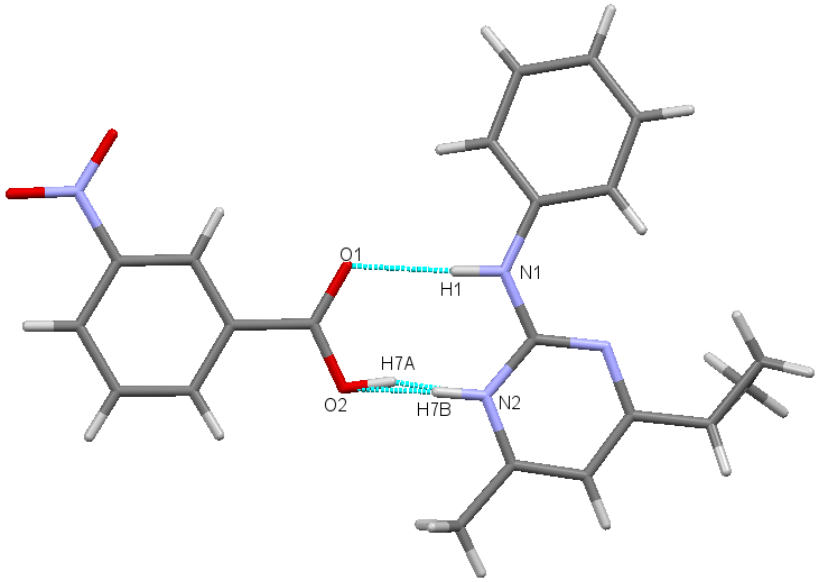

Figure 7.63. *Positional disorder of H7 in C3NBA at 293K.*

Atom	s.o.f.
H7A	0.57(3)
H7B	0.43(3)

Table 7.37. *Site occupancy factors for positions H7A and H7B at 293K.*

The refinement of the structure of C3NBA at 293K shows a 57 : 43 disorder of the position of H7, indicating that the molecule of co-former displays the acid conformation for roughly as much time as the carboxylate form. However, it is important to remember that these results derive from SXD measurement and are, thus, affected by the limitations of the X-ray radiation concerning the treating and refinement of hydrogen atoms.

7.3.4. Conclusions

Syntheses of the co-crystals of cyprodinil with the *ortho* (C2NBA) and *meta* (C3NBA) isomers of mononitrobenzoic acid were achieved from solution and crystallization occurred by the method of

slow evaporation of the solvent at room temperature. Crystals were also obtained in the solution containing cyprodinil and 4-nitrobenzoic acid; unfortunately, they were not suitable for SXD measurement and the formation of the co-crystal could not be validated. However, powder X-ray diffraction data showed encouraging results in that a new phase was obtained.

C2NBA exists in two polymorphs, both monoclinic: form I crystallises as thick prisms in the space group $\boldsymbol{P2_1/c}$, while crystals of form II are needles, belonging to the space group $\boldsymbol{P2_1/n}$. Modification I of C2NBA is a salt, displaying a molecule of protonated cyprodinil and one of 2-nitrobenzoate, whereas the molecules in modification II are in their neutral state. The reason for this difference can be found in the different conformation of 2-nitrobenzoic acid: the carboxyl group is twisted in respect to the benzene ring by an angle of ~40˚ in form I, which is smaller than in form II, where its value is ~68˚. The smaller rotation from the benzene allows higher delocalisation of the electron density, which is attracted by the inductive effect $\boldsymbol{-I}$ of the nitro group. As a consequence, the hydrogen atom of the hydroxyl group is less affected by the electron density of the carboxyl and it can be extracted by a base. Since the effect $\boldsymbol{-I}$ of the nitro group decreases from the *ortho* to the *para* position, the crystal structure of C3NBA does not show proton transfer from the acid to the base. However, the electron density of atom H7 at 293K indicates the presence of disorder inside the hydrogen bond O2-H7···N2. Validation of this hypothesis can only be obtained by single crystal neutron diffraction, which allows complete characterisation of light atoms due to their interaction with the nuclei of atoms rather than electron density.

7.4. Cyprodinil / fluorobenzoic acids

7.4.1. Introduction

The study of the nature and characteristics of the hydrogen bonding network in co-crystals of cyprodinil with differently substituted benzoic acids focused of monofluorobenzoic acids as co-formers, with the purpose of investigating the role played by the fluorine atom in the definition of the crystal packing of these materials.

The three isomers of fluorobenzoic acid, *o*-fluoro[146], *m*-fluoro[147], and *p*-fluorobenzoic acid[148], crystallise in the monoclinic system, space group $\boldsymbol{P2_1/c}$ for the former and $\boldsymbol{P2_1/n}$ for the last two. Similarly to other carboxylic acids, the crystal packing of these materials is characterised by the arrangement of the acid molecules into centrosymmetric dimers, held together by the formation of two hydrogen bonds, as shown in Figure 7.64.

o-Fluorobenzoic acid (o-FBA)

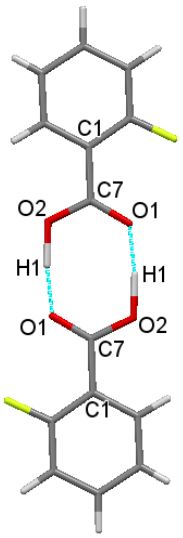

m-Fluorobenzoic acid (m-FBA)

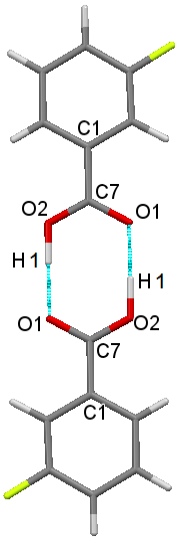

p-Fluorobenzoic acid (p-FBA)

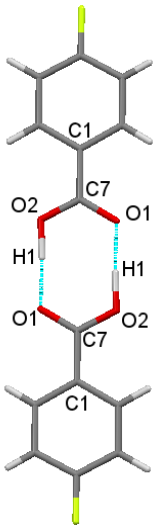

Figure 7.64. *Centrosymmetric dimers in the crystal structures of o-FBA[149], m-FBA[150], and p-FBA[151].*

The main difference in the crystal structures of the three isomers lies on a different conformation of the acid molecule, caused by the presence of the fluorine as substituent on the aromatic ring. In fact, the carboxylic group is not co-planar with the benzene, but it is rotated along the single bond C1-C7 (Figure 1) by 10.4(3)˚ in *o*-FBA, by 5.0(3)˚ in *m*-FBA and by 4.7(3)˚ in *p*-FBA. The presence of the fluorine atom affects also the covalent and hydrogen bond lengths in the carboxyl group, a list of which is reported in Table 7.38. There is a significant stretching of the covalent bond O2-H1 from the usual X-ray diffraction determined value of 0.85 Å, indicating the transfer of the hydrogen atom along the direction of the intermolecular interaction. The value of 1.21(5) Å for the hydroxyl group in crystals of *o*-FBA can be explained considering the nature of the fluorine atom. Fluorine is a strongly electronegative species, exhibiting inductive effect ***–I***. Its electron-withdrawing power makes the proton on the hydroxyl group to be less attracted by the carboxylic moiety and to be affected by the lone pair on the oxygen atom of a neighbouring molecule.

	***o*-FBA**	***m*-FBA**	***p*-FBA**
O2-H1	1.21(5) Å	1.06(3) Å	1.11(4) Å
H1···O1	1.44(5) Å	1.57(3) Å	1.51(4) Å
O2-H1···O1	172(4)˚	176(3)˚	176(3)˚
O2···O1	2.638(2) Å	2.631(2) Å	2.618(2) Å

Table 7.38. *Hydrogen bond lengths and geometry of interaction in the three isomers. The values are taken from the .cif files deposited in the CCDC.*

The effect ***–I*** decreases in intensity from the *ortho* to *para* position, justifying the shorter values for O2-H7 in *m*-FBA and *p*-FBA compared to *o*-FBA.

7.4.2. Experimental

7.4.2.1. Physical and chemical properties of co-formers

2-Fluorobenzoic acid[152] is a beige powder with temperature of fusion in the range 122˚-125˚C, boiling point of around 245˚C, and it has a relative density of 1.46 g/cm^3 at 20˚C. It is very soluble in water, exhibiting a value of solubility of 7.2 g/L at 25˚C, and it has a $\boldsymbol{pK_a}$ of 3.27 at 25˚C[145]. It is soluble in a large variety of organic solvents, such as acetone and alcohols.

Commercially available as an off-white powder, 3-fluorobenzoic acid[153] has a melting point between 122˚-124˚C, boiling point around 251˚C and relative density of 1.47 g/cm^3. Its solubility in water is about 1.5 g/L at 25˚C and it has a $\boldsymbol{pK_a}$ of 3.86 at 25˚C[145]. It is soluble in the most common organic solvents.

4-Fluorobenzoic acid[154] is a white crystalline solid with melting point between 182˚-184˚C, it starts boiling around 254˚C and it has a relative density of 1.49 g/cm^3. It shows a $\boldsymbol{pK_a}$ of 4.15 at 25˚C[145] and water solubility of 1.2 g/L at the same temperature. As the other two isomers of monofluorobenzoic acid, it is soluble in a variety of organic solvents, including acetone and alcohols.

7.4.2.2. Synthesis from solution

Syntheses and crystallizations of the three co-crystals cyprodinil/2-fluorobenzoic acid (C2FBA), cyprodinil/3-fluorobenzoic acid (C3FBA), and cyprodinil/4-fluorobenzoic acid (C4FBA) were obtained from solution. The choice of the solvent was undertaken by considering the solubility of each component. Apolar solvents and water were excluded: the former because of the carboxylic acids and the latter due to the very low solubility of cyprodinil in water. A compromise was found in ethanol: all components were soluble in it and it led to successful results in the syntheses of the other co-crystals of cyprodinil with the differently substituted carboxylic acids. A summary of the quantities used for the preparation of each solution is reported in Table 7.39. All material were of analytical standard and were used without further purification.

Substance	Quantity	Colour of solution	Colour of crystals
Cyprodinil	0.50 g		
2-Fluorobenzoic acid	0.31 g	Colourless	Colourless
Ethanol	8 ml		
Cyprodinil	0.50 g		
3-Fluorobenzoic acid	0.31 g	Colourless	Colourless
Ethanol	10 ml		
Cyprodinil	0.50 g		
4-Fluorobenzoic acid	0.31 g	Colourless	Colourless
Ethanol	10 ml		

Table 7.39. *Prepared solutions.*

The solutions were prepared with a molar 1 : 1 ratio of the two components by adding the solvent 2 ml at a time in order to create a saturated solution. Low, constant heat, with temperature around 60˚C, was applied for two hours, during which time the solutions were continuously stirred. Crystallisation by the method of slow evaporation of the solvent occurred at room temperature in crystallisation vials that were covered with a film, having the double purpose of preventing contamination from the environment and of slowing the evaporation of ethanol. Crystals of C2FBA have a prismatic habit and are colourless; however, they tend to turn cloudy and white within a week of storage at room temperature. C3FBA grows as long, colourless rods, while crystals of C4FBA are large, thin, colourless plates.

7.4.2.3. Differential Scanning Calorimetry

Investigation of the behaviour of C2FBA crystals was carried out using DSC to assess whether changes in the structure can be responsible for the variation of colour upon storage. Data were collected on ~ 2 mg of C2FBA on the DSC Q20. The results are reported in Figure 7.65.

The DSC profile of C2FBA shows a weak endothermic event at around 78˚C, which may indicate a phase transition. Indeed, two endothermic events, corresponding to the fusion of the specimen at similar temperatures, one at ~92˚C and a second at ~94˚C, would indicate that two different phases are present at this point, possibly suggesting the transition at ~78°C is incomplete at the rapid heating rate used in the DSC instrument.

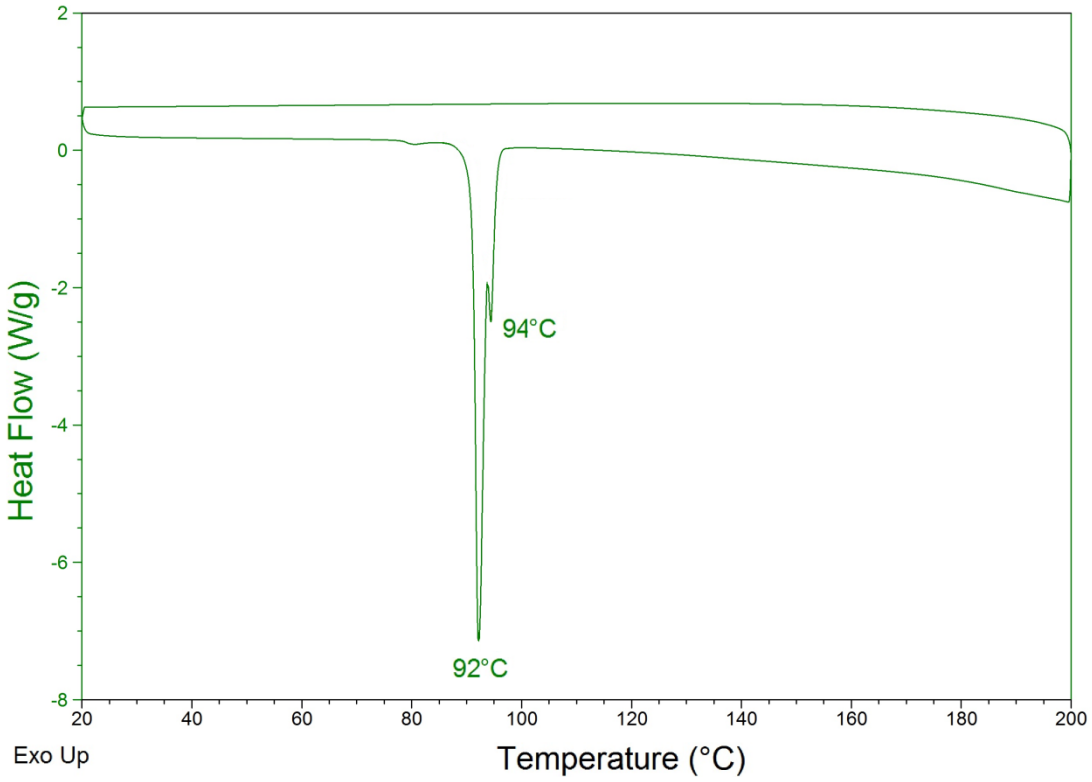

Figure 7.65. *DSC profile for a sample of C2FBA.*

It is possible that, if there is a phase transition in C2FBA, it could occur slowly at room temperature and be responsible for the observed increasing opacity of crystals on long term storage. No re-crystallisation events are observed during the cooling from 200˚C to 20˚C, probably because of the dense consistency of the fungicide.

7.4.2.4. Single crystal X-ray diffraction

Investigation of the crystal structure of the three co-crystals was undertaken using single crystal X-ray diffraction (SXD), which allows identification of the unit cell parameters and space group of a crystal, providing, in addition, a complete list of atomic positions and thermal vibrations.

Crystals of C2FBA and C3FBA were analysed on the Gemini A Ultra CCD diffractometer using Mo radiation at 150K, while C4FBA data were collected on the Agilent Technologies SuperNova Dualwavelength diffractometer, with Cu radiation, due to the smaller size of the crystal, at 150K.

A variable temperature (VT) study was performed on a crystal of C2FBA (dimensions 0.44 x 0.50 x 0.61 mm) in order to investigate the change of colour when the crystal is separated from the mother liquor. Five sets of data were collected at 100, 150, 200, 250, and 298K.

In Tables 7.40, 7.41, and 7.42, X-ray crystallographic data and refinement parameters of C2FBA, C3FBA, and C4FBA, respectively, are reported.

Name – Formula weight (g mol^{-1})		CYP / 2-fluorobenzoic acid (C2FBA) - $C_{14}H_{15}N_3$ $C_7H_5O_2F$ - 365.40				
Temperature (K)		100	150	200	250	298
Wavelength (Å)		0.71073				
Crystal system, space group		Monoclinic, $P2_1/n$				
Unit cell dimensions	a (Å) =	11.0969(4)	11.1307(3)	11.1398(6)	11.1590(3)	11.1793(3)
	b (Å) =	8.1618(3)	8.1926(2)	8.2446(5)	8.2559(3)	8.3079(3)
	c (Å) =	20.6207(7)	20.6780(6)	20.689(1)	20.7712(7)	20.8555(7)
	β (˚) =	102.863(3)	102.974(3)	102.946(6)	103.012(3)	103.010(3)
Volume ($Å^3$)		1820.8(1)	1837.5(1)	1851.9(2)	1864.5(1)	1887.3(1)
Z, calculated density (g cm^{-3})		4, 1.333				
F(000)		768				
Absorption coefficient (mm^{-1})		0.094				
Theta range for data collection (˚)		3.13 to 26.37				
Limiting indices		$-13 \leq h \leq 13$, $-8 \leq k \leq 10$, $-25 \leq l \leq 22$				
Reflections collected / unique		8948 / 3721	8889 / 3744	8754 / 3785	9138 / 3800	9253 / 3841
R_{int}		0.0129	0.0144	0.0300	0.0157	0.0160
Data / restrains / parameters		3721 / 0 / 325	3744 / 0 / 325	3785 / 0 / 325	3800 / 0 / 25	3841 / 0 / 325
Goodness-of-fit on F^2		1.023	1.025	1.028	1.041	1.043
Final R indices [I>2sigma(I)]		R_1 = 0.0329, wR_2 =0.0858	R_1 =0.0351, wR_2=0.0908	R_1 = 0.0394, wR_2=0.1019	R_1 = 0.0379, wR_2=0.0991	R_1 = 0.0426, wR_2 =0.1144
R indices (all data)		R_1 = 0.0353, wR_2 =0.0879	R_1 =0.0384, wR_2=0.0937	R_1 = 0.0451, wR_2 = 0.1074	R_1 = 0.0449, wR_2 = 0.0.1048	R_1 = 0.0524, wR_2 = 0.1227
Extinction coefficient		0.009(1)	0.011(1)	0.017(2)	0.015(2)	0.015(2)
Largest diff. Peak and hole (e $Å^{-3}$)		0.26 and -0.20	0.23 and -0.18	0.20 and -0.17	0.17 and -0.17	0.21 and -0.18

Table 7.40. *X-ray crystallographic data and refinement parameters for C2FBA.*

Name	CYP / 3-fluorobenzoic acid (C3FBA)
Empirical formula	$C_{14}H_{15}N_3$ $C_7H_5O_2F$
Formula weight (g mol^{-1})	365.40
Temperature (K)	150
Wavelength (Å)	0.71073
Crystal system, space group	Orthorhombic, $P2_12_12_1$
Unit cell dimensions	a = 5.4252(2) Å
	b = 17.3734(7) Å
	c = 18.917(1) Å
Volume ($Å^3$)	1783.0(1)
Z, calculated density (g cm^{-3})	4, 1.361
F(000)	768
Absorption coefficient (mm^{-1})	0.096
Crystal size (mm)	0.07 x 0.11 x 0.66
Theta range for data collection (˚)	3.18 to 26.37
Limiting indices	$-6 \leq h \leq 5$, $-21 \leq k \leq 19$, $-14 \leq l \leq 23$
Reflections collected / unique	5473 / 3463 [R_{int} = 0.0318]
Completeness to θ = 26.37	99.7 %
Refinement method	Full-matrix least-squares on F^2
Data / restrains / parameters	3463 / 0 / 325
Goodness-of-fit on F^2	1.015
Final R indices [I>2sigma(I)]	R_1 = 0.0448, wR_2 = 0.0803
R indices (all data)	R_1 = 0.0675, wR_2 = 0.0899
Extinction coefficient	0.007(1)
Largest diff. Peak and hole (e $Å^{-3}$)	0.19 and -0.17

Table 7.41. *X-ray crystallographic data and refinement parameters for C3FBA at 150K.*

Name	CYP / 4-fluorobenzoic acid (C4FBA)
Empirical formula	$C_{14}H_{15}N_3$ $C_7H_5O_2F$
Formula weight (g mol^{-1})	365.40
Temperature (K)	150
Wavelength (Å)	1.54178
Crystal system, space group	Monoclinic, $P2_1/n$
Unit cell dimensions	a = 9.2434(2) Å
	b = 10.0472(2) Å
	c = 19.3950(5) Å
	β = 91.491(2)˚
Volume ($Å^3$)	1800.61(7)
Z, calculated density (g cm^{-3})	4, 1.348
F(000)	768
Absorption coefficient (mm^{-1})	0.783
Crystal size (mm)	0.09 x 0.27 x 0.38
Theta range for data collection (˚)	4.56 to 72.07
Limiting indices	$-11 \leq h \leq 11$ $-12 \leq k \leq 12$, $-23 \leq l \leq 18$
Reflections collected / unique	20156 / 3525 [R_{int} = 0.0447]
Completeness to θ = 72.07	99.4 %
Refinement method	Full-matrix least-squares on F^2
Data / restrains / parameters	3525 / 0 / 325
Goodness-of-fit on F^2	1.030
Final R indices [I>2sigma(I)]	R_1 = 0.0466, wR_2 = 0.1282
R indices (all data)	R_1 = 0.0501, wR_2 = 0.1326
Extinction coefficient	0.0000(2)
Largest diff. Peak and hole (e $Å^{-3}$)	0.23 and -0.24

Table 7.42. *X-ray crystallographic data and refinement parameters for C4FBA at 150K.*

7.4.2.5. Single crystal neutron diffraction

A variable temperature (VT) single crystal neutron diffraction experiment was carried out on a large crystal of C2FBA (crystal dimensions 1.0 x 1.8 x 2.2 mm; volume ~4 mm^3) to better characterise the role played by the hydrogen bonding in the crystal packing. The crystal that was selected for the SND measurement was grown from an ethanol solution by the method of slow evaporation of the solvent and and data were collected on the single crystal diffractometer D19 at ILL at four temperatures, 30, 100, 200, and 298K, in order to compare the structure with the SXD results.

Preliminary checks on the quality of the crystal were done at room temperature to ensure the presence of a single crystal and assess its scattering power. Identification of the unit cell parameters and creation of an initial orientation matrix were achieved collecting a two-hour long scan at room temperature.

The temperature of 30K was reached by cooling slowly, with a rate of 2K/min, in order to avoid damages to the crystal. The integrity of the crystal during the cooling process was assessed recording the check reflection $(1\ 2\ \bar{4})$: a variation of intensity might indicate the appearance of defects inside the structure. An ***I vs. T*** plot for the check reflection is reported in Figure 7.66.

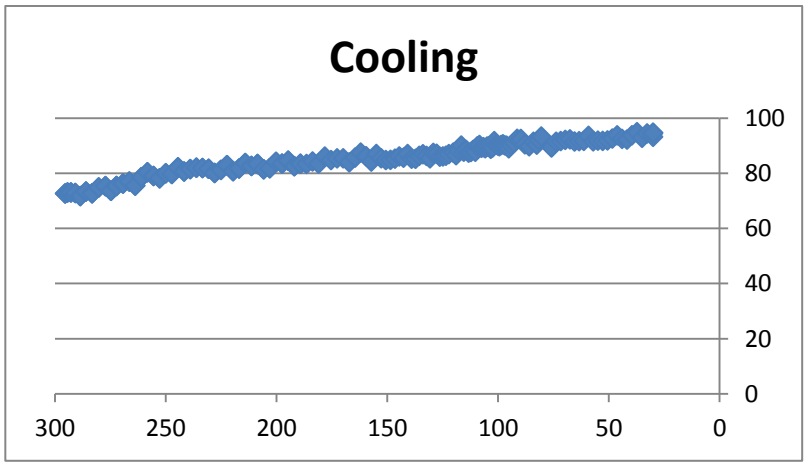

Figure 7.66. *I vs. T plot for the check reflection* (**1 2 $\bar{4}$**) *during cooling from 295K to 30K.*

As shown in Figure 7.66, no significant changes in the intensity of the check reflection occurred during the cooling process, but it is possible to observe an increase in intensity, due to the attenuation of the Debye-Waller factor at lower temperatures.

For all sets of data, Bragg's intensities were corrected for the attenuation caused by the presence of the three vanadium cans and for the attenuation due to absorption by the crystal. As for the case of CoTA (***c. f. 7.2.2.5***), the second type of correction was done by the program D19ABSCAN, which performs an analytical valuation of the extent of the absorption based on the crystal dimensions and

the indexing of the crystal faces. A schematic representation of the crystal morphology is shown in Figure 7.67, while Table 7.43 lists the values of the R-factors before and after the attenuation corrections.

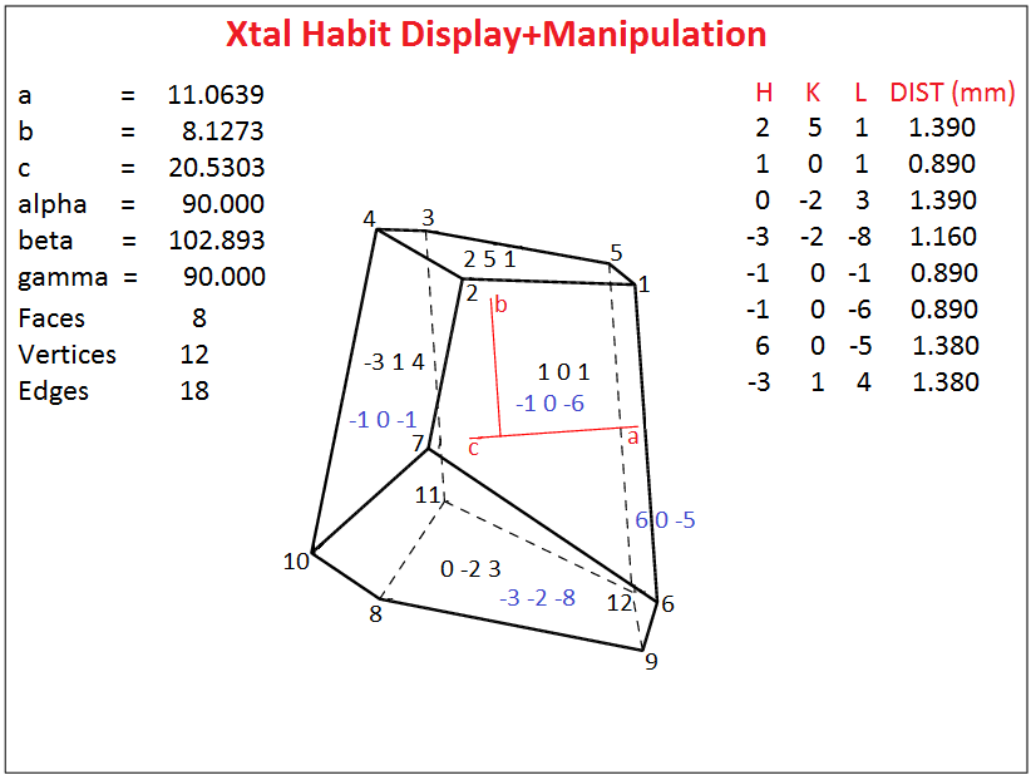

Figure 7.67. *Schematic representation of C2FBA crystal morphology.*

	No Corrections	Correction for cans	Correction cans+crystal
		30K	
$\mathbf{R_1}$	0.0354	0.0305	0.0305
$\mathbf{wR_2}$	0.0933	0.0713	0.0678
		100K	
$\mathbf{R_1}$	0.0396	0.0336	0.0339
$\mathbf{wR_2}$	0.0947	0.0808	0.0767
		200K	
$\mathbf{R_1}$	0.0458	0.0449	0.0446
$\mathbf{wR_2}$	0.1105	0.1039	0.0956

Table 7.43. *Variations of the R-factor after the correction for the two types of intensity attenuation.*

Both types of absorption corrections contribute only slightly to the improvement of the refined structure, indicating that in this case the intensity attenuation is contained, especially the one due to the chemical composition of the crystal. This is confirmed by the collection of a REN-scan (***c. f. 5.1.2.6***) on the strong reflection ($4\ \bar{1}\ \bar{9}$), as shown in Figure 7.68. Since the morphology of the crystal is not a plate, where there is a difference in path length between two normal directions, the profile of the intensity as a function of the angle $\boldsymbol{\varphi}$ is not a perfect double-wave curve, but it is possible to notice a variation of intensity as the crystal is rotated along $\boldsymbol{\varphi}$.

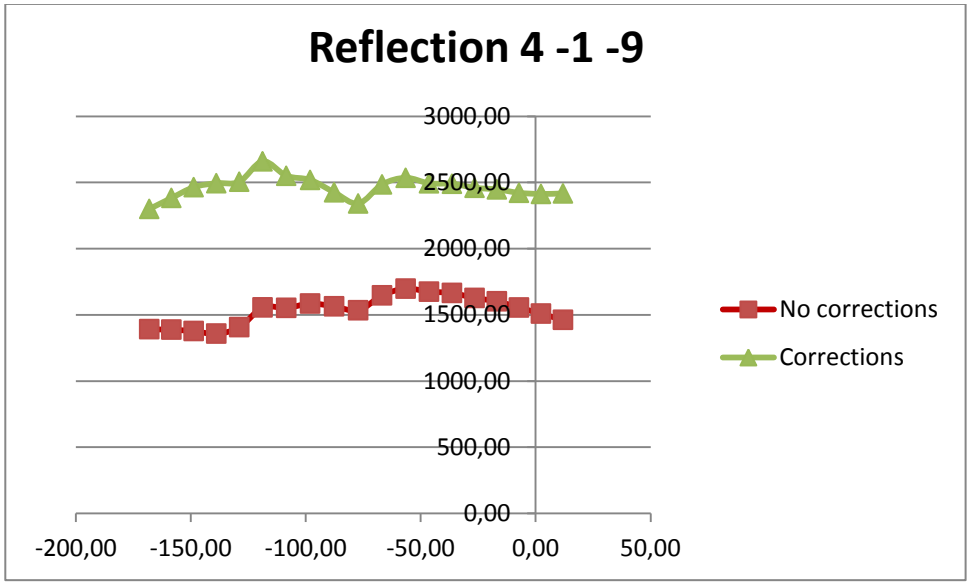

Figure 7.68. *Evolution of the Bragg's reflection* (**4 $\bar{1}$ $\bar{9}$**) *as a function of the angle φ at 30K: profile without absorption correction (red) and with absorption correction (green).*

The two profiles, without and with absorption corrections, show a similar trend, indicating that the contribution to the attenuation of the reflection intensities by the crystal is minimal.

It was not possible to treat the set of data collected at 298K. The very high values for the R-factors, $\boldsymbol{R_1}$ = 0.1621, $\boldsymbol{wR_2}$ = 0.3716 and ***GooF*** = 1.474, indicated that some problems occurred during data collection, affecting the structural refinement of C2FBA. Since in a SND experiment on D19 it is not possible to see the crystal because it is enclosed in three vanadium cans, it is good practice to introduce into the data collection strategy a "check" reflection, which is periodically recorded, to ascertain the integrity of the crystal throughout the whole experiment: any variations in the intensity of the "check" reflection can indicate damages to the sample. Table 7.44 lists the intensity of the reflection for every *numor* in which it was recorded, while in Figure 7.69 the intensity of the reflection ($1\ 2\ \bar{4}$) plotted against time (expressed as increasing number of *numors*) is reported.

Numor	H	K	L	Intensity
19965	1	2	-4	718.36
19969	1	2	-4	730.54
19973	1	2	-4	718.19
19977	1	2	-4	721.20
19981	1	2	-4	709.33
19982	1	2	-4	742.61
19985	1	2	-4	724.42
19986	**1**	**2**	**-4**	**742.90**
19992	**1**	**2**	**-4**	**396.47**
19995	1	2	-4	295.87
19999	1	2	-4	242.26
20003	1	2	-4	204.51
20006	1	2	-4	193.87
20009	1	2	-4	188.51

Table 7.44. *Intensity of the "check" reflection* (**1 2 $\bar{4}$**) *in every numor it was recorded at 298K.*

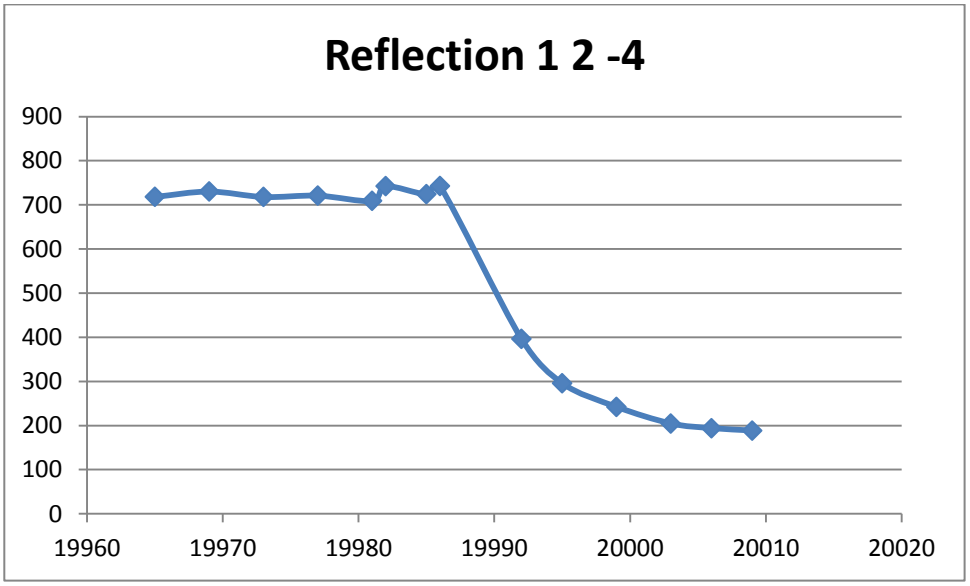

Figure 7.69. *Evolution in time of the intensity of the check reflection of C2FBA at 298K.*

Figure 7.69 shows a sudden drop of intensity of the "check" reflection around 17 hours after the beginning of data collection at 298K. When the crystal was taken off the diffractometer head, it had turned white, as had happened to other C2FBA crystals stored at room temperature.

In order to investigate whether the damage to the crystal was due to changes in the structure or to mechanical stresses caused by the glue, the data collected at 298K were divided in two sets: the first included all data recorded up to the *numor* 19986, before the change of intensity occurred (cut_1); the second included data from the *numor* 19992 (cut_2). For both groups a search for the

hydrogen bonds between the molecules of cyprodinil and 2-fluorobenzoic acid was done using the program *PLATON*. The results are reported in Table 7.45.

	Cut_1	Cut_2
O2-H7	1.01(2) Å	1.12(2) Å
H7···N2	1.56(2) Å	1.50(2) Å
O2···N2	2.561(9) Å	2.61(1) Å

Table 7.45. *Hydrogen bond lengths in the two groups of data at 298K.*

As shown in Table 7.44, the length of the covalent bond of the hydroxyl group increases of 0.11 Å, suggesting a migration of the proton towards the cyprodinil molecule: the change in the position of atom H7 may cause a disruption in the long-range order of the crystal structure. This behaviour might be the reason behind the change of colour of crystals of C2FBA at room temperature. However, the refinement of the structure derived from SXD measurements at 298K did not exhibit the same problem, suggesting that the variation in the hydrogen atom position might also be time dependent.

In Table 7.46, neutron crystallographic data and refinement parameters for a crystal of C2FBA at 30, 100, and 200K are reported.

Name – Formula weight (g mol^{-1})		CYP / 2-fluorobenzoic acid (C2FBA) - $C_{14}H_{15}N_3$ $C_7H_5O_2F$ - 365.40		
Temperature (K)		30	100	200
Wavelength (Å)		1.17000		
Crystal system, space group		Monoclinic, $P2_1/n$		
Unit cell dimensions	a (Å) =	a = 11.0639(1)	11.0911(1)	11.1332(2)
	b (Å) =	b = 8.1273(1)	8.1566(1)	8.2283(1)
	c (Å) =	c = 20.5303(2)	20.5791(2)	20.6867(3)
	β (˚) =	β = 102.8928(6)	102.9568(8)	103.007(1)
Volume ($Å^3$)		1799.5	1814.3	1846.4
Z, calculated density (g cm^{-3})		4, 1.333		
F(000)		441		
Absorption coefficient (mm^{-1})		0.194		
Theta range for data collection (˚)		5.15 to 61.32		
Limiting indices		$-12 \leq h \leq 16$, $-12 \leq k \leq 11$, $-30 \leq l \leq 25$	$-10 \leq h \leq 16$, $-12 \leq k \leq 11$, $-30 \leq l \leq 25$	$-10 \leq h \leq 16$, $-12 \leq k \leq 11$, $-30 \leq l \leq 25$
Reflections collected / unique		19125 / 6091 [R_{int} = 0.0408]	16910 / 6082 [R_{int} = 0.0406]	17043 / 6190 [R_{int} = 0.0502]
Data / restrains / parameters		6091 / 0 / 425	6082 / 0 / 425	6190 / 0 / 426
Goodness-of-fit on F^2		1.214	1.116	1.043
Final R indices [I>2sigma(I)]		R_1 = 0.0305, wR_2 = 0.0672	R_1 = 0.0339, wR_2 = 0.0743	R_1 = 0.0446, wR_2 = 0.0853
R indices (all data)		R_1 = 0.0320, wR_2 = 0.0678	R_1 = 0.0395, wR_2 = 0.0767	R_1 = 0.0752, wR_2 = 0.0956
Extinction coefficient		0.00479(13)	0.00491(16)	0.0059(2)
Largest diff. Peak and hole (fm $Å^{-3}$)		0.53 and -0.72	0.88 and -1.50	0.87 and -1.36

Table 7.46. *Neutron crystallographic data and refinement parameters for a crystal of C2FBA at 30, 100, and 200K.*

7.4.3. Results and discussion

7.4.3.1. Cyprodinil / 2-fluorobenzoic acid (C2FBA)

C2FBA crystallises in the monoclinic system, space group ***P2$_1$/n*** and it displays two molecules in the asymmetric unit: one of cyprodinil and one of 2-fluorobenzoic acid, as shown in Figure 7.70 for the structure studied by X-ray radiation.

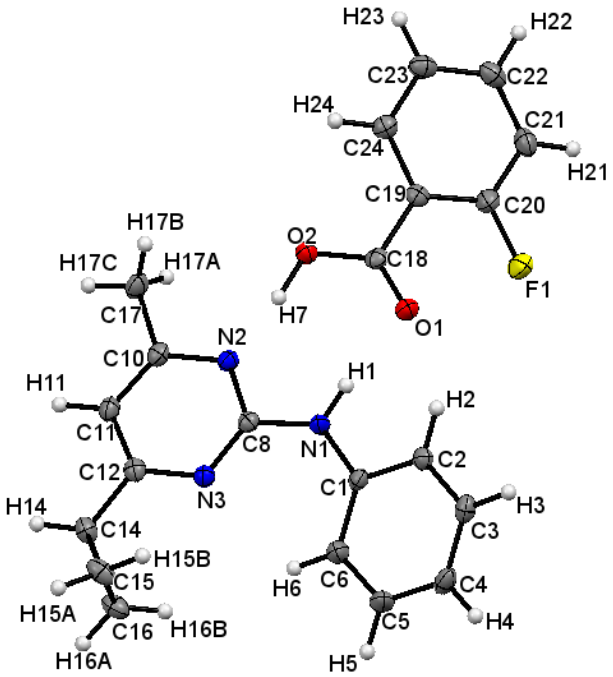

Figure 7.70. *ORTEP representation of the asymmetric unit of C2FBA, viewed along the* ***b****-axis, derived from SXD at 100K. The probability level for all non-hydrogen ellipsoids is 50%, while the hydrogen atoms are drawn as fixed-size spheres of radius 0.15 Å.*

	100K	150K	200K	250K	298K
C8-N1-C1-C6	23.9(2)˚	24.1(2)˚	24.2(2)˚	25.0(2)˚	25.3(2)˚
N3-C12-C14-C15	33.2(1)˚	32.1 (2)˚	32.4(2)˚	32.7(2)˚	32.9(2)˚
N3-C12-C14-C16	-35.6(1)˚	-35.8(2)˚	-35.8(2)˚	-35.5(2)˚	-35.3(2)˚
C8-N3-C12-C14	-179.8(1)˚	-179.7(1)˚	-179.8(1)˚	-179.8(1)˚	-179.(1)˚
N2-C8-N1-H1	-1(1)˚	-1(1)˚	-1(1)˚	-1(1)˚	-1(1)˚
O2-C18-C19-C24	29.0(1)˚	28.6(2)˚	28.4(2)˚	28.2(2)˚	27.6(2)˚
C18-C19-C24-C23	176.9(1)˚	177.3(1)˚	177.7(1)˚	177.9(1)˚	178.2(2)˚
C18-C19-C20-C21	-179.2(1)˚	-179.6(1)˚	-179.9(1)˚	-180.0(1)˚	-179.7(2)˚
C18-O1	1.227(1) Å	1.225(1) Å	1.223(1) Å	1.218(1) Å	1.217(2) Å
C18-O2	1.305(1) Å	1.306(1) Å	1.302(1) Å	1.301(1) Å	1.297(2) Å
C-C$_{\text{aromatic ring}}$	1.388(2) Å	1.387(2) Å	1.383(2) Å	1.380(2) Å	1.377(3) Å

Table 7.47. *Torsion angles and bond lengths of interest, derived from SXD measurements.*

The benzene and the pyrimidine rings of the cyprodinil molecule are not co-planar, but the former is twisted off the plane by 23.9(2)˚ to avoid hindrance of the cyclopropyl substituent, which is centred in respect to the pyrimidine moiety. The hydrogen atom of the amino group, H1, is twisted slightly below the nitrogen atom, as required by the sp^3 hybridisation of N1.

The presence of a substituent in the *ortho* position of the benzoic acid forces the carboxylic group to rotate around the single bond C18-C19 of 29.0(1)˚. The planarity of the benzene ring is retained in the conformation of the 2-fluorobenzoic acid molecule and the fluorine substituent does not cause any significant distortions of the C-C lengths in the aromatic ring. The lengths of the two covalent bonds of the carboxylic group, C18-O1 and C18-O2, confirm the neutral conformation of the acid, being a double bond of 1.227(1) Å and a single bond of 1.305(1) Å, respectively.

The conformations of both molecules do not vary significantly with temperature, but it is possible to notice a slight shortening of the covalent bonds due to the larger thermal vibration of all atoms at higher temperatures.

In the long-range order of the three-dimensional structure the molecules of cyprodinil and 2-fluorobenzoic acid organise in heterogeneous dimers, interacting *via* circular hydrogen bonds, which are formed by two distinct interactions, N1-H1···O1 and O2-H7···N2, as shown in Figure 7.71. Based on bond lengths, donor-acceptor distances and geometry of interaction[81], which are listed in Tables 7.48 and 7.49 from SXD and SND measurements, respectively, it is possible to identify the two hydrogen bonds as of moderate strength. The crystal packing is governed by the stacking of the dimers into parallel lines, which are shifted in order to accomadate the cyclopropyl, as displayed in Figure 7.72.

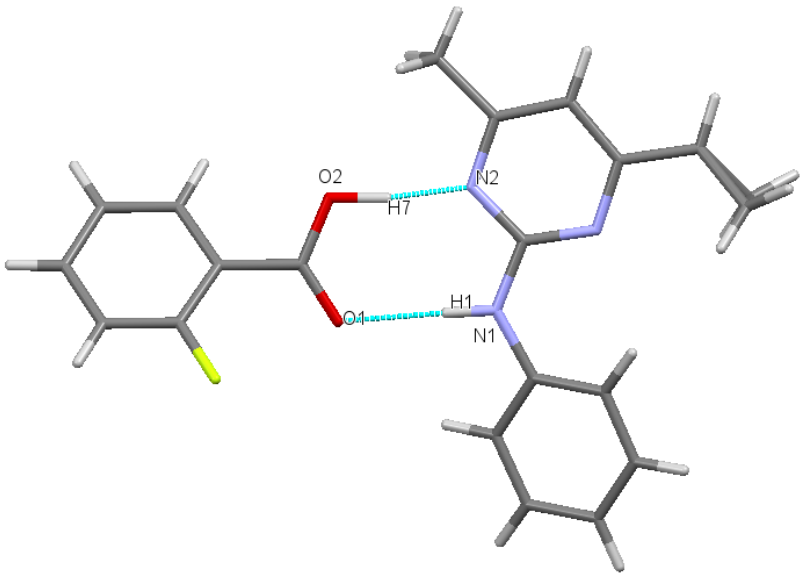

Figure 7.71. *Heterogeneous dimer in crystals of C2FBA.*

	100K	150K	200K	250K	298K
N1-H1	0.90(2) Å	0.91(2) Å	0.89(2) Å	0.90(2) Å	0.88(2) Å
H1···O1	1.99(2) Å	1.98(2) Å	2.01(2) Å	2.01(2) Å	2.02(2) Å
N1-H1···O1	169(1)˚	169(1)˚	170(1)˚	168(1)˚	169(2)˚
N1···O1	2.879(1) Å	2.885(1) Å	2.888(2) Å	2.891(2) Å	2.895(2) Å
O2-H7	1.04(2) Å	1.04(2) Å	1.10(3) Å	1.10(3) Å	1.04(3) Å
H7···N2	1.55(2) Å	1.56(3) Å	1.50(3) Å	1.51(3) Å	1.58(3) Å
O2-H7···N2	172(2)˚	171(2)˚	173(2)˚	171(2)˚	174(2)˚
O2···N2	2.589(1) Å	2.596(1) Å	2.597(1) Å	2.603(2) Å	2.610(2) Å

Table 7.48. *Hydrogen bond lengths and geometry of interaction in crystals of C2FBA. The results derive from SXD experiments.*

	30K	100K	200K
N1-H1	1.029(2) Å	1.023(2) Å	1.015(3) Å
H1···O1	1.866(2) Å	1.869(2) Å	1.869(3) Å
N1-H1···O1	169.5(1)˚	169.0(2)˚	168.9(2)˚
N1···O1	2.885(1) Å	2.880(1) Å	2.870(2) Å
O2-H7	1.098(2) Å	1.096(2) Å	1.095(3) Å
H7···N2	1.505(2) Å	1.501(2) Å	1.497(3) Å
O2-H7···N2	171.1(1)˚	171.2(2)˚	171.2(2)˚
O2···N2	2.595(1) Å	2.589(1) Å	2.584(2) Å

Table 7.49. *Hydrogen bond lengths and geometry of interaction in crystals of C2FBA. The results derive from SND experiments.*

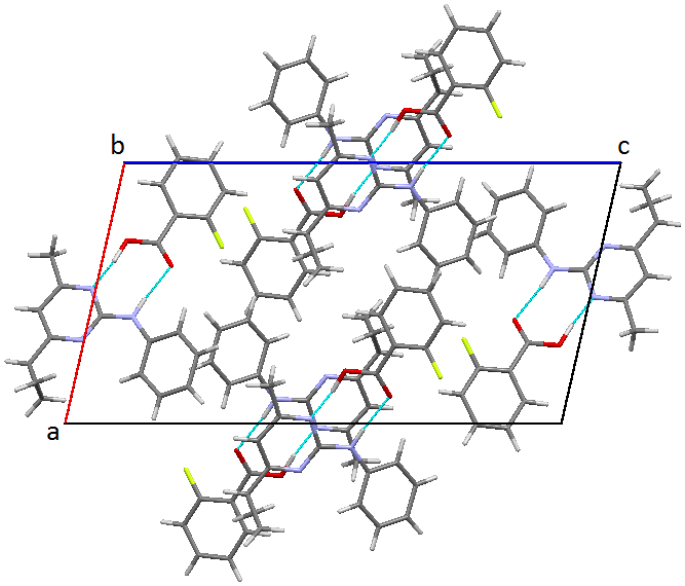

Figure 7.72. *Crystal packing of C2FBA, viewed along the* ***b****-axis.*

By comparing the results on the hydrogen bonds obtained by SXD to those derived from SND, it is possible to notice significant differences in the definition of the hydrogen bonds done by the two techniques, especially in the case of O2-H7···N2. The high value of 1.04(2) Å at 100K, which becomes longer at higher temperatures, for O2-H7 detected by X-rays suggests the possible presence of proton migration or disorder in the crystal structure. Worthy of notice is the value of O2-H7 at 298K, which does not follow the increasing trend exhibited from 100K to 250K, but it is similar to the structure at 100K. Investigation of proton migration or disorder was undertaken by studying the electron-density and nucleon-density maps for O2-H7···N2, which are reported in Figures 7.73 and 7.74.

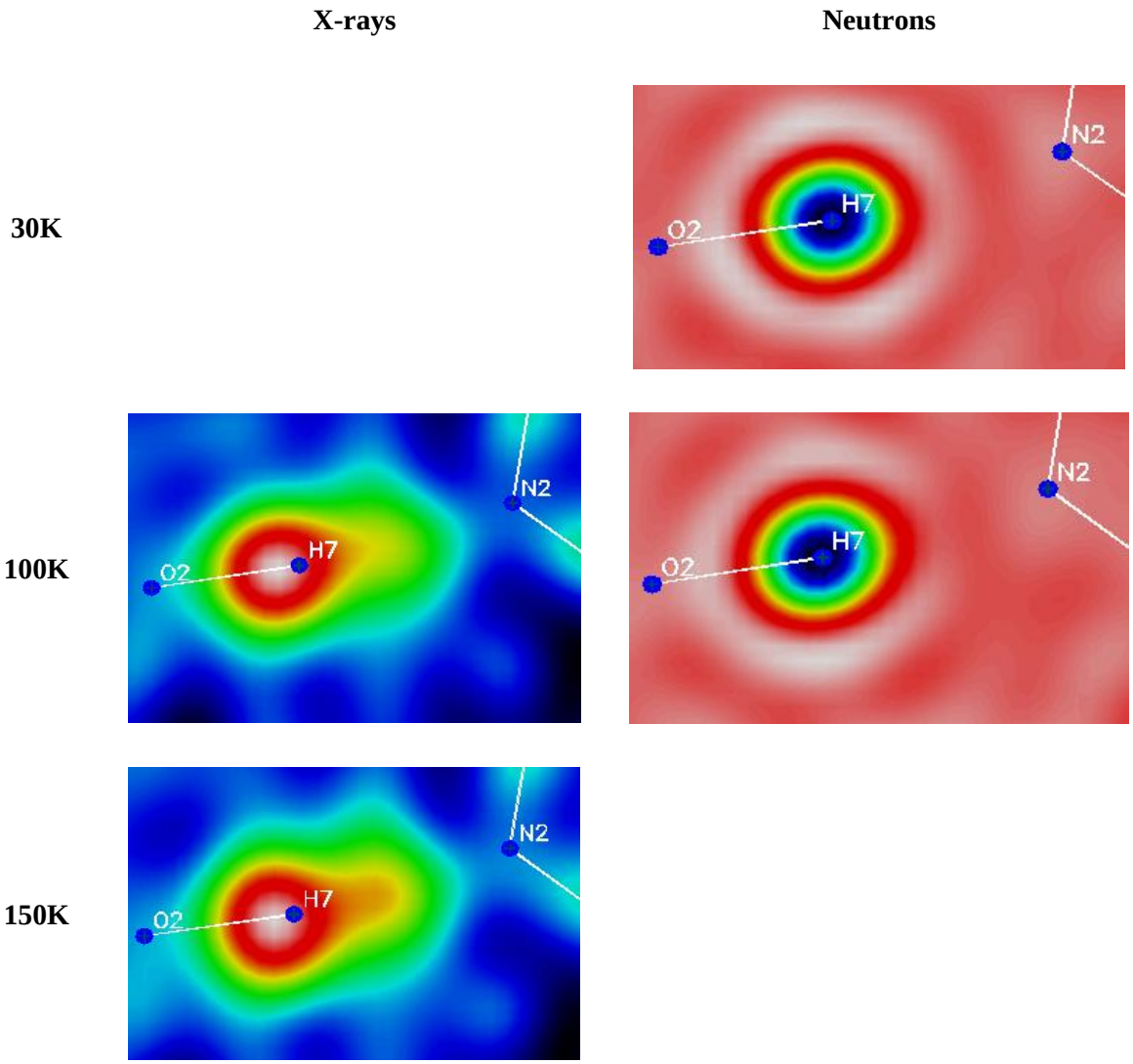

Figure 7.73. *Difference electron-density (left) and nucleon-density (right) maps for the hydrogen bond O2-H7···N2 at 30K, 100K and 150K. Atom H7 was taken out of the refinement but its coordinates were superimposed on the images.*

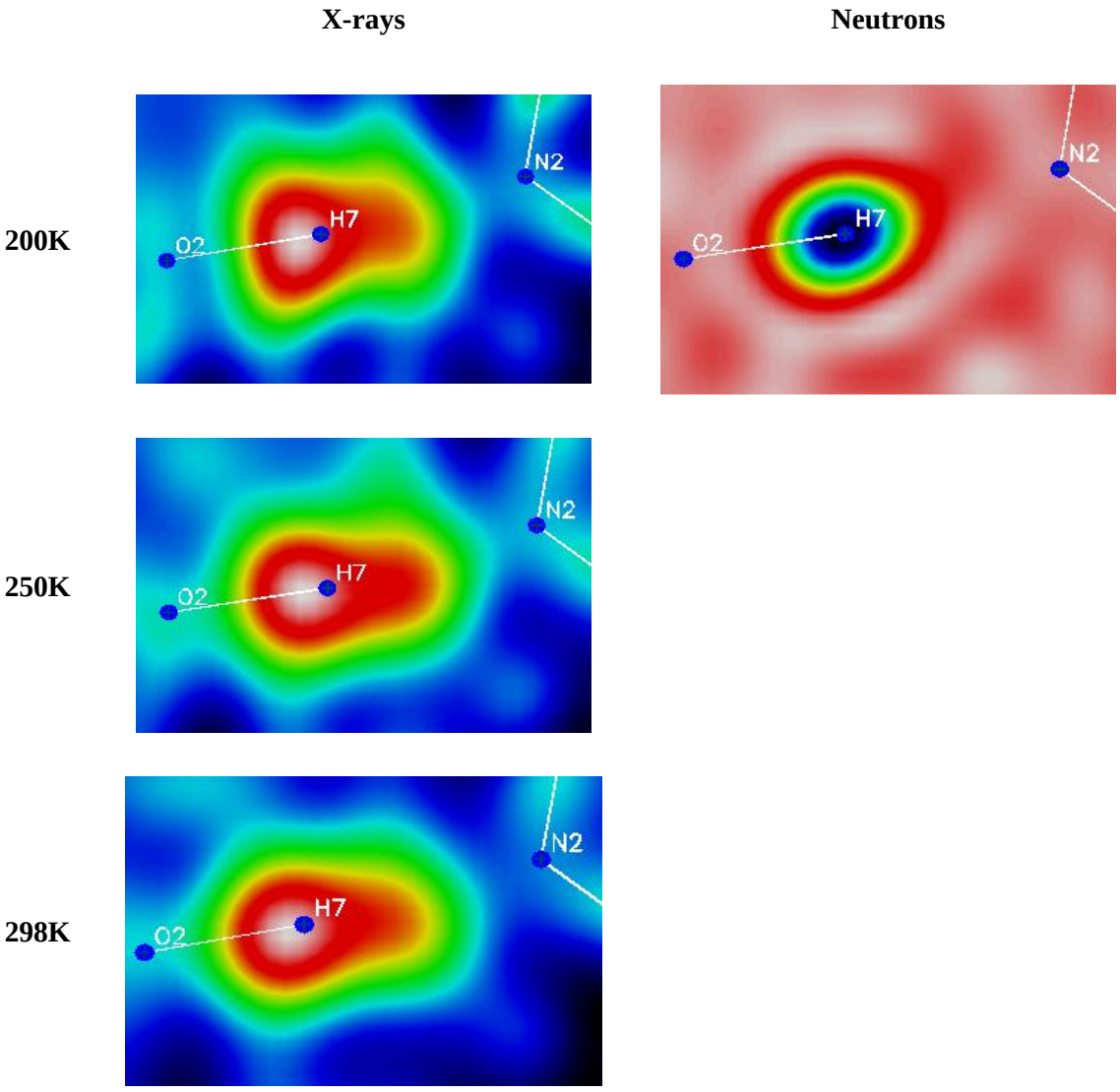

Figure 7.74. *Difference electron-density (right) and nucleon-density (left) maps for the hydrogen bond O2-H7···N2 at 200K, 250K and 298K. Atom H7 was taken out of the refinement but its coordinates were superimposed on the images.*

The shape of the electron density of H7 is, indeed, elongated and a second site closer to N2 appears, especially for the structures at 200, 250, and 298K. However, the hypothesis of positional disorder of the hydrogen atom is discredited by the SND results, which show that the nucleus of H7 is present in only one site. This is reflected in the length of the hydrogen bond, H7···N2, and of the covalent bond, O2-H7, which are observed to beome shorter by 0.008 Å and 0.003 Å, respectively, at 200K, because of the effect of larger thermal vibrations of the atoms at higher temperatures. This phenomenon is better described through the visualisation of the thermal ellipsoids of the hydrogen atoms, as displayed in Figure 7.75.

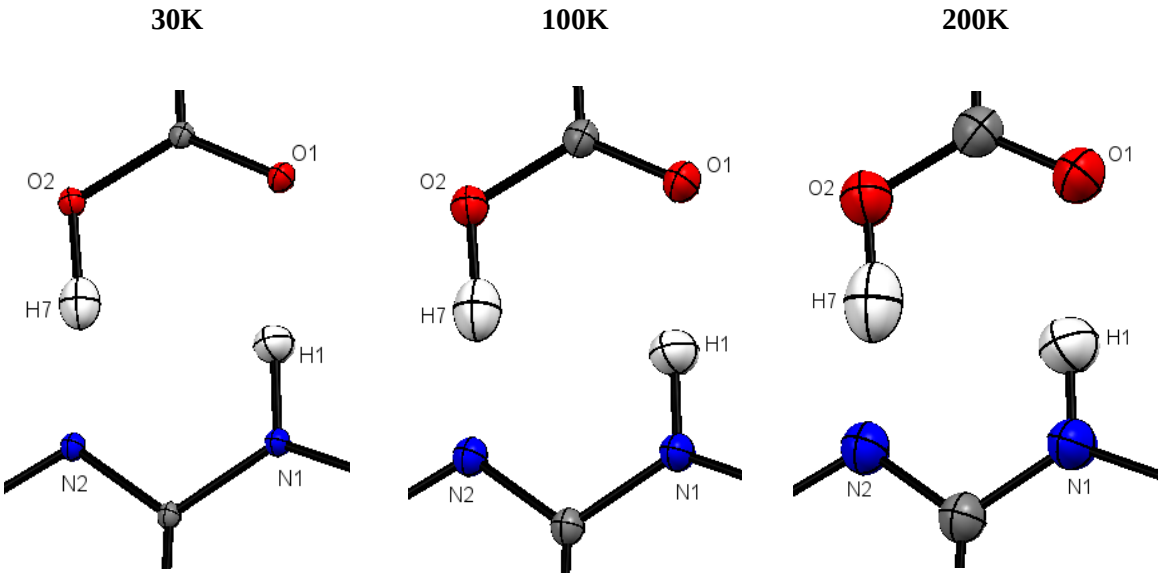

Figure 7.75. *ORTEP representation of the circular hydrogen bond in crystals of C2FBA, derived from SND measurements.*

The shape of the ADP for atom H7, which represents the atomic displacement from the mean position, is elongated along the direction of the intermolecular interaction, indicating that the hydrogen atom, which is partially positively-charged, is attracted by the lone pair on N2 of the cyprodinil molecule. The difference between the ADPs of H1 and H7 can be due to the longer donor-acceptor distance of N1···O1 compared to O2···N2, 2.885(1) Å opposed to 2.595(1) Å, suggesting that O2-H7···N2 is a stronger hydrogen bond than N1-H1···O1.

7.4.3.2. Cyprodinil / 3-fluorobenzoic acid (C3FBA)

Crystals of C3FBA grow in the orthorhombic system, space group ***P2$_1$2$_1$2$_1$***. The asymmetric unit displays a heterogeneous dimer, formed by the interaction of a molecule of cyprodinil and one of 3-fluorobenzoic acid, as reported in Figure 7.76 for the structure derived from SXD analysis.

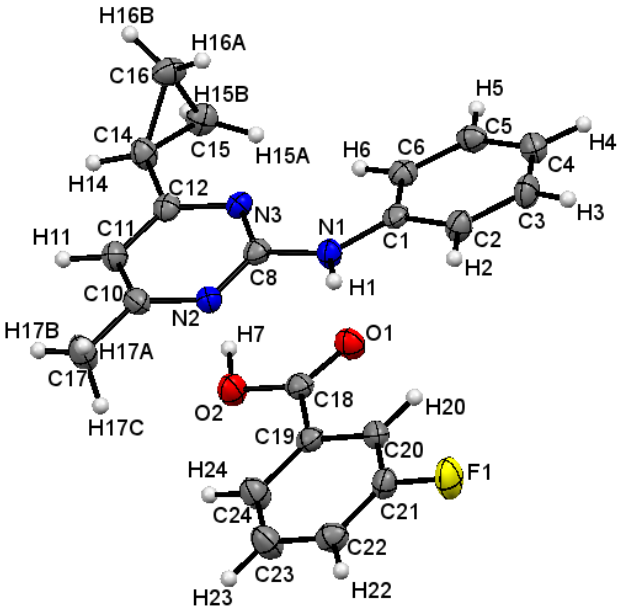

Figure 7.76. *ORTEP representation of the asymmetric unit of C3FBA, viewed along the* ***a****-axis, derived from SXD. The probability level for all non-hydrogen ellipsoids is 50%, while the hydrogen atoms are drawn as fixed-size spheres of radius 0.15 Å.*

C8-N1-C1-C6	-6.7(4)˚
N3-C12-C14-C15	23.6(3)˚
N3-C12-C14-C16	-44.8(3)˚
C8-N3-C12-C14	176.4(2)˚
N2-C8-N1-H1	-10(2)˚
O2-C18-C19-C24	7.1(3)˚
C18-C19-C24-C23	179.6(2)˚
C18-C19-C20-C21	179.5(2)˚
C18-O1	1.216(3) Å
C18-O2	1.314(3) Å
C-C$_{\text{aromatic ring}}$	1.380(3) Å

Table 7.50. *Torsion angles and bond lengths of interest.*

The conformation of the cyprodinil molecule is similar to that exhibited in C2FBA, although in this case the benzene ring is less twisted in respect to the pyrimidine moiety, with a torsion angle of

6.7(4)˚ opposed to 23.9(2)˚ in C2FBA, causing the cyclopropyl substituent to be placed above the pyrimidine ring to avoid hindrance.

The aromatic ring of the acid displays an almost perfect planarity and the fluorine atom does not introduce any significant distortions in the value of the C-C bonds. The carboxylic group is slightly rotated in respect to the benzene ring of 7.1(3)˚, a smaller value than in C2FBA due to the different position of the substituent. The bond lengths of C18-O1 and C18-O2 are reasonable values for a double and single bond, respectively, indicating that the acid is present in its neutral conformation.

The supramolecular self-assembly is characterised by heterogeneous dimers, formed by the interaction of the aminopyrimidine functionality on cyprodinil and the carboxylic acid (Figure 7.77), leading to circular hydrogen bonds, whose main features are reported in Table 7.51. The dimers organise into parallel lines, which are shifted in respect to each other, forming a fishbone motif, as shown in Figure 7.78.

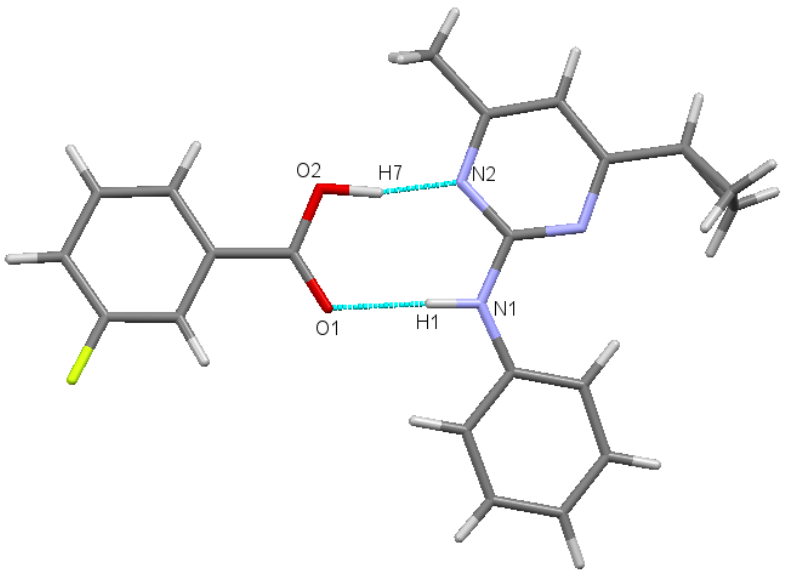

Figure 7.77. *Heterogeneous dimer in crystals of C3FBA.*

N1-H1	0.96(3) Å
H1···O1	1.94(3) Å
N1-H1···O1	174(2)˚
N1···O1	2.899(3) Å
O2-H7	1.09(3) Å
H7···N2	1.57(3) Å
O2-H7···N2	168(3)˚
O2···N2	2.641(3) Å

Table 7.51. *Bond lengths and geometry of interaction of the circular hydrogen bonds in crystals of C3FBA.*

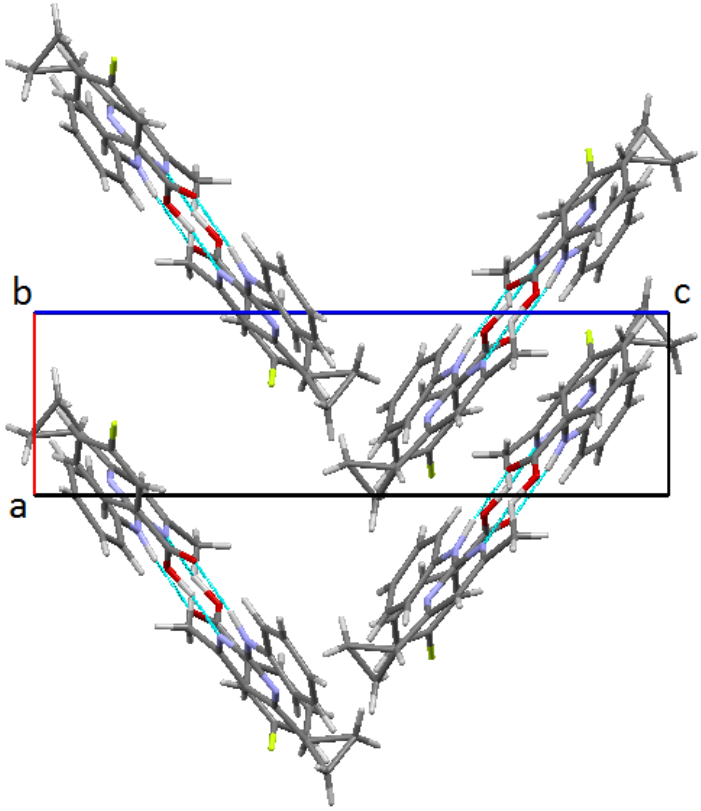

Figure 7.78. *Crystal packing of C3FBA, viewed along the* ***b****-axis.*

As shown in Table 7.51, there are two linear hydrogen bonds forming the circular interaction in the dimers, N1-H1···O1 and O2-H7···N2. The characteristics of the former classify it as a hydrogen bond of moderate strength[81], while the latter seems to be stronger, having an O2-H7 covalent bond unusually long for a hydroxyl group. A better characterisation of the two hydrogen bonds was undertaken by studying the electron-density maps of the hydrogen atoms H1 and H7, as shown in Figure 7.79.

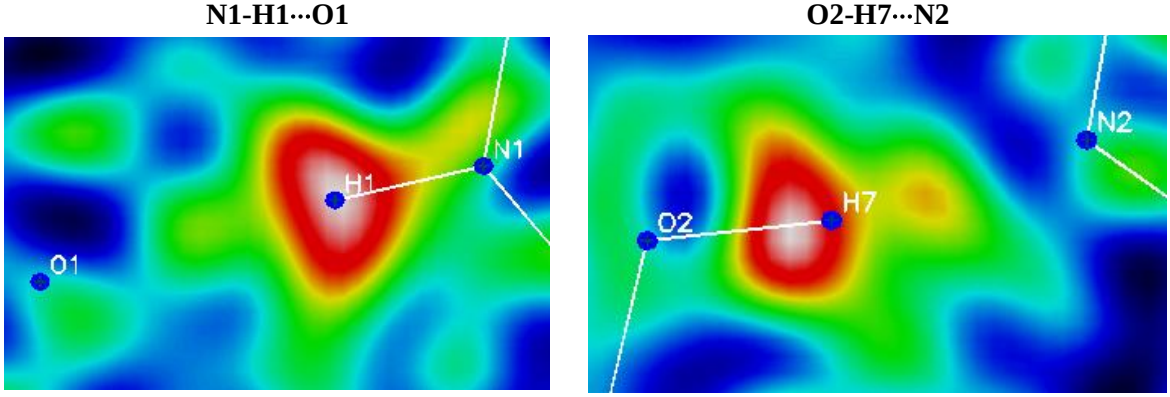

Figure 7.79. *Difference electron-density maps for the two hydrogen bonds in C3FBA at 150K.*

The poor refinement of atom H7 and the presence of a second peak of electron density alongside the direction of the intermolecular interaction suggest that atom H7 is disordered between two sites, leading to two configurations of the dimer: one displaying both molecules in their neutral state and one picturing the protonated N2 on cyprodinil and the carboxylate anion. The disorder was introduced in the structure and it was refined fixing the values of the covalent bonds O2-H7A and N2-H7B to 0.90(1) Å and 0.91(2) Å, respectively, and U_{iso} to 0.5 $Å^2$. The results of the final refinement show a degree of disorder of 72 : 28, indicating that for 72% of the time the dimer is in the neutral configuration. However, the improvement of the refinement gained after the introduction of disorder is minimal, with $\boldsymbol{R_1}$ passing from 0.0448 to 0.0446 and $\boldsymbol{wR_2}$ from 0.0899 to 0.0897, and it is possible to notice some residual electron density around H7A and H7B, as shown in Figure 7.80. Moreover, the length of the covalent bond C18-O2 of 1.314(3) Å typical of a neutral carboxylic group is not in agreement with a disordered hydrogen bond.

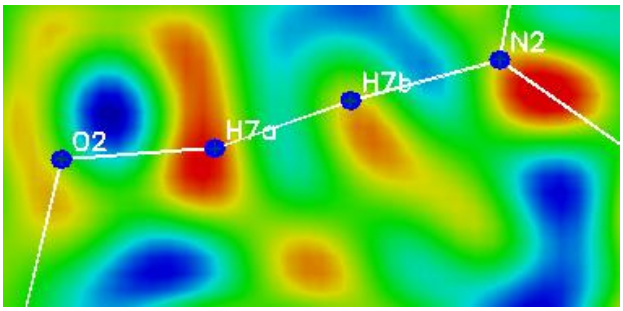

Figure 7.80. *Difference electron-density map of the disordered hydrogen bond O2-H7···N2. Both H7A and H7B were included in the refinement.*

All factors explained above seem to discredit the hypothesis of positional disorder of the hydrogen atom H7 in the structure. Similarly to the case of C2FBA, only a single crystal neutron diffraction experiment can clarify the nature of the hydrogen bond O2-H7···N2. Unfortunately, the time allocated on D19 at ILL was limited and it was not possible to undertake further investigation of this co-crystal.

7.4.3.3. Cyprodinil / 4-fluorobenzoic acid (C4FBA)

C4FBA crystallises in the monoclinic system, space group $\boldsymbol{P2_1/n}$. The asymmetric unit is constituted by a heterogeneous dimer, formed through the interaction of the aminopyrimidine functionality of cyprodinil and the carboxylic group of 4-fluorobenzoic acid, as shown in Figure 7.81 for the structure studied with X-ray radiation. In Table 7.52 torsion angles and bonds lengths of interest are listed.

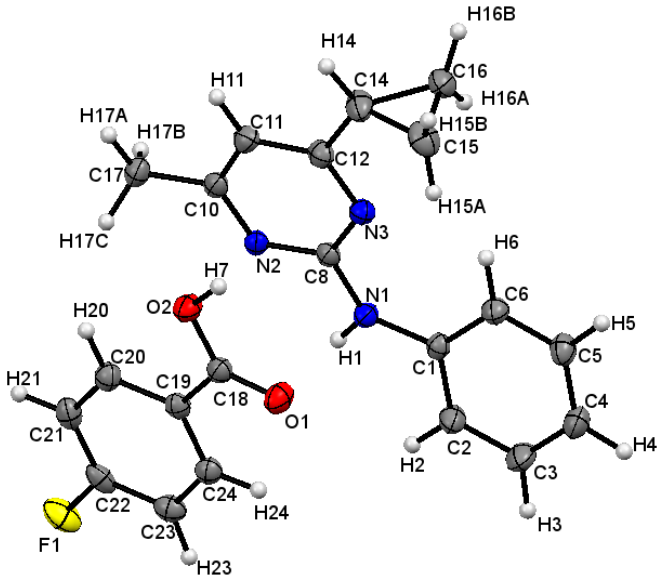

Figure 7.81. *ORTEP representation of the asymmetric unit of C4FBA, viewed along the* ***b****-axis, derived from SXD. The probability level for all non-hydrogen ellipsoids is 50%, while the hydrogen atoms are drawn as fixed-size spheres of radius 0.15 Å.*

C8-N1-C1-C6	-15.0(2)˚
N3-C12-C14-C15	-26.0(2)˚
N3-C12-C14-C16	41.9(2)˚
C8-N3-C12-C14	-178.4(2)˚
N2-C8-N1-H1	-1(1)˚
O2-C18-C19-C20	-3.6(2)˚
C18-C19-C24-C23	176.7(1)˚
C18-C19-C20-C21	-177.2(1)˚
C18-O1	1.225(2) Å
C18-O2	1.313(2) Å
C-$C_{\text{aromatic ring}}$	1.386(2) Å

Table 7.52. *Torsion angles and bond lengths of interest.*

Similarly to the cases of C2FBA and C3FBA, the conformation of the cyprodinil molecule is not planar, but the benzene ring is rotated from the plane containing the pyrimidine moiety by -15.0(2)˚, forcing the cyclopropyl substituent to be positioned slightly above the same plane, with a torsion angle N3-C12-C14-C16 of 41.9(2)˚, to avoid hindrance.

The benzene ring of 4-fluorobenzoic acid is almost perfectly planar, but the carboxylic group is rotated only slightly along the single bond C18-C19 of -3.6(2)˚, due to the fluorine substitution in the *para* position, which allows the carboxylic functionality to be closer to planarity with the benzene ring.

As displayed in the asymmetric unit, the molecules of the components of C4FBA organise themselves into heterogeneous dimers *via* circular hydrogen bonds, formed by two intermolecular interactions: one between the hydrogen atom of the amino group of cyprodinil and the oxygen atom of the carbonyl group of the acid, and a second featuring the hydroxyl moiety as the hydrogen bond donor and the nitrogen atom of the pyrimidine ring of cyprodinil as the acceptor, as reported in Figure 7.82. In the three-dimensional arrangement of the crystal packing, shown in Figure 7.83, the dimers organise into off-set parallel lines, allowing the formation of π-π interactions with distances of 3.70(2) Å between the pyrimidine moiety of cyprodinil and the aromatic ring of the acid, forming a zig-zag motif. Along every line each dimer is rotated by 180° in respect to the one above in order to accommodate the cyclopropyl substituent of cyprodinil.

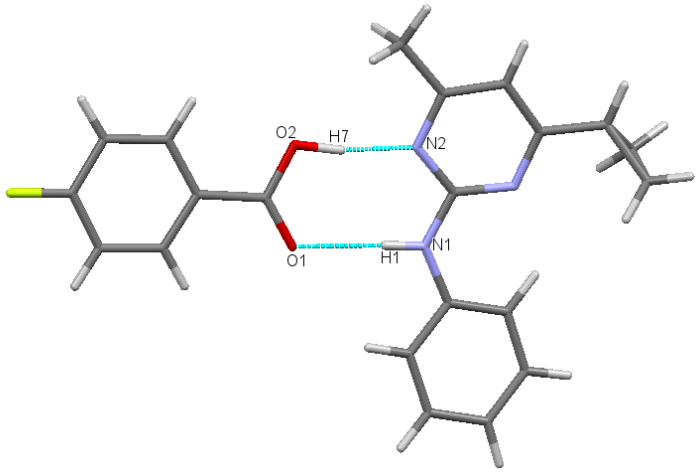

Figure 7.82. *Heterogeneous dimer in C4FBA.*

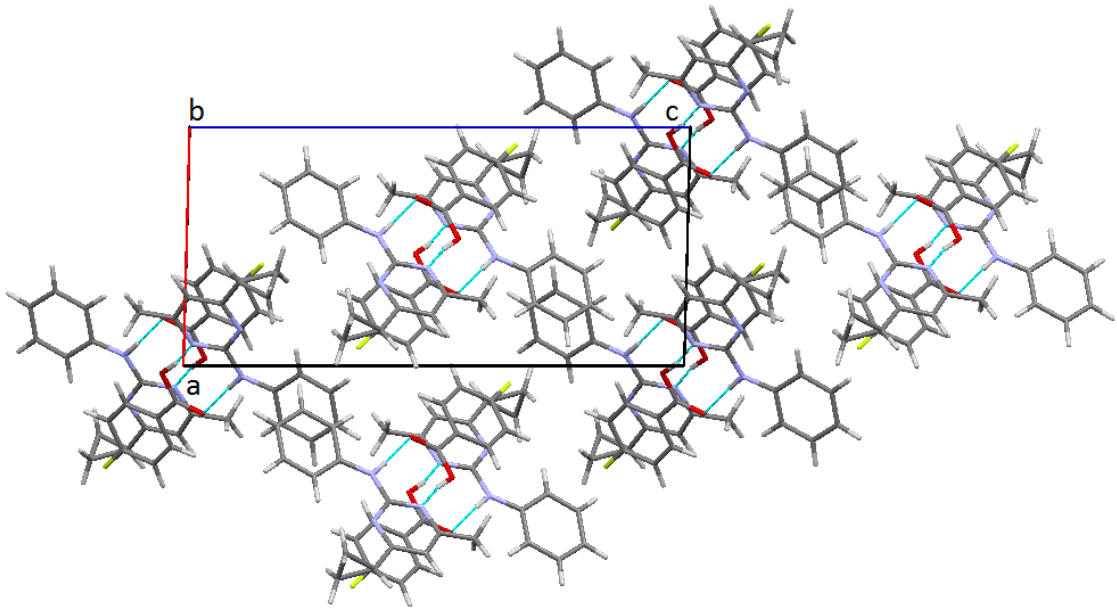

Figure 7.83. *Crystal packing of C4FBA, viewed along the* ***b****-axis.*

N1-H1	0.88(2) Å
H1···O1	2.04(2) Å
N1-H1···O1	177(2)˚
N1···O1	2.921(2) Å
O2-H7	1.01(2) Å
H7···N2	1.65(2) Å
O2-H7···N2	170(2)˚
O2···N2	2.650(2) Å

Table 7.53. *Hydrogen bond lengths and geometry of interaction in a crystal of C4FBA at 150K, collected by SXD.*

Considering the hydrogen bond lengths, the donor-acceptor distances and the geometry of interaction[81], which are listed in Table 7.53, the two hydrogen bonds N1-H1···O1 and O2-H7···N2 can be classified as of moderate strength, although the latter appears to be stronger than the former. The length of the covalent bond O2-H7 is longer than usual, indicating that the atom H7 is, indeed, involved in an intermolecular hydrogen bond with a molecule of cyprodinil. A better characterisation of the hydrogen bonds can be gained by the investigation of the electron-density maps regarding the two hydrogen atoms H1 and H7, as displayed in Figure 7.84. The shape and size of the electron densities of H1 and H7 exclude the presence of proton migration or disorder in the structure.

N1-H1···O1 **O2-H7···N2**

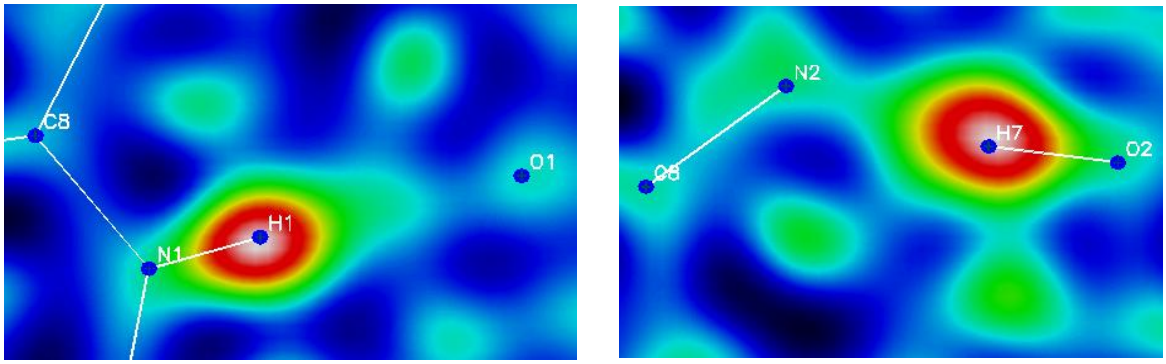

Figure 7.84. *Difference electron-density maps for the two hydrogen bonds, N1-H1···O and O2-H7···N2. Atoms H1 and H7 were excluded from the refinement, but their coordinates were superimposed on the images.*

Since SXD data at 150K are available for all three co-crystals of cyprodinil, C2FBA, C3FBA, and C4FBA, it is possible to compare the crystal structures to investigate the role played by the fluorine atom as a substituent on the benzene ring of the carboxylic acid. A summary of the hydrogen bond characteristics in the three co-crystals is reported in Table 7.54.

	C2FBA	C3FBA	C4FBA
N1-H1	0.90(2) Å	0.96(3) Å	0.88(2) Å
H1···O1	1.99(2) Å	1.94(3) Å	2.04(2) Å
N1-H1···O1	169(1)˚	174(2)˚	177(2)˚
N1···O1	2.879(1) Å	2.899(3) Å	2.921(2) Å
O2-H7	1.04(2) Å	1.09(3) Å	1.01(2) Å
H7···N2	1.55(2) Å	1.57(3) Å	1.65(2) Å
O2-H7···N2	172(2)˚	168(3)˚	170(2)˚
O2···N2	2.589(1) Å	2.641(3) Å	2.650(2) Å

Table 7.54 *Comparison of the hydrogen bond characteristics in the three co-crystals at 150K.*

The presence of the fluorine atom as substituent on the carboxylic acid makes the three isomers more acidic than benzoic acid: in fact, the value of the pK_a decreases from 4.20 of benzoic acid, to 4.15 of 4-fluorobenzoic acid, to 3.86 of 3-fluorobenzoic acid, to 3.27[137] of 2-fluorobenzoic acid. This trend is caused by the inductive effect ***–I*** of the fluorine, which by being an electron-withdrawing group stabilises the conjugate base that is the carboxylate anion, facilitating the release of a proton; this effect decreases from the *ortho* to the *para* position. The hydrogen atom of the hydroxyl group is, then, less attracted by the electronic cloud of the carboxyl and it can be affected by the presence of a more electronegative atom belonging to a different molecule and be extracted more easily by a base. The effect that the different position of the substituent has on the definition of the crystal packing of these co-crystals can be noticed, firstly, in the relative position of the molecules of cyprodinil and co-former: the intermolecular distances N1···O1 and O2···N2 increase passing from the *ortho*, through the *meta*, to the *para* position. This is reflected in a lengthening of the hydrogen bond in C4FBA compared to C2FBA, indicating a weaker intermolecular interaction for the former case. Peculiar is the case of C3FBA, which shows a bond length O2-H7 0.05Å longer than C2FBA, suggesting that the inductive effect is stronger in the *meta* position rather than in the *ortho*. However, it is important to remember the limitations of X-ray techniques in the definition of the hydrogen atoms: in fact, the shape and extended size of the electron density of H7 in C3FBA forces SHELXL to refine the position of the hydrogen atom in the middle of ρ, making the bond length of the hydroxyl group unusually long.

7.4.4. Conclusions

Syntheses of the co-crystals of cyprodinil with the three isomers of monofluorobenzoic acid were achieved in ethanol solutions at the temperature of 60˚C. Crystallisation of C2FBA, C3FBA, and C4FBA occurred at room temperature and was obtained by the method of slow evaporation of the solvent. C2FBA and C4FBA are monoclinic, both belonging to the space group $P2_1/n$, but while

crystals of C2FBA have a colourless, prismatic habit, C4FBA grows as thin, colourless plates. Orthorhombic C3FBA crystallises as thin, long, colourless rods.

The crystal structures of the co-crystals were analysed by single crystal X-ray diffraction at 150K to gain an exact knowledge on the atomic positions and thermal vibrations of all non-hydrogen atoms for the production of reliable models. A variable temperature SXD experiment was performed on a crystal of C2FBA with the aim to investigate the change of colour that occurred during storage at room temperature. The study on the crystal structure of C2FBA was deepened by a variable temperature SND measurement in order to ascertain the role played by the hydrogen atoms in the definition of the crystal packing of this material. The SND results exclude the presence of proton disorder in the hydrogen bond O2-H7···N2 hinted by the SXD analysis. However, they suggest a possible proton migration from the hydroxyl group of the acid to the pyrimidine nitrogen of cyprodinil. This variation of the hydrogen atom position with time is probably the cause of the change of colour that C2FBA crystals show upon storage at room temperature.

The three-dimensional structure is similar in all co-crystals: it shows the interaction between the molecules of the two components through the formation of two hydrogen bonds of moderate strength, one between the amino group of cyprodinil and the carbonyl of the acid and a second involving the hydroxyl group of the acid and the nitrogen atom of the pyrimidine ring of cyprodinil, leading to 8-membered rings. Comparing the results on C2FBA and C4FBA it is possible to notice the effect that the different position of the fluorine atom has on the crystal structure of the two co-crystals: the hydrogen bonds are shorter in C2FBA because of the more acidic nature of 2-fluorobenzoic acid, as indicated by the longer values of the covalent bonds N1-H1 and O2-H7, suggesting that intermolecular hydrogen bonds are taking place.

This study underlines the importance of neutron diffraction in the characterisation of the hydrogen atoms: indeed, what was identified by X-rays as disorder in C2FBA was defined by neutrons as an elongation of the ADP along the direction of the intermolecular interaction.

7.5. Cyprodinil / chlorobenzoic acids

7.5.1. Introduction

The study on the effect that different substituents on benzoic acid have on the crystal packing of their co-crystals with the fungicide cyprodinil was concluded using monochlorobenzoic acids as co-formers. As the other halogens, chlorine exhibits inductive effect ***–I***, due to the higher electronegativity when compared to lighter elements, such as carbon atoms. Although the electronegativity decreases going down a group because of the increased atomic radius, differently substituted chlorobenzoic acids are slightly more acidic than the corresponding fluorobenzoic

acids. This can be explained considering the atypical nature of the fluorine atom in compounds: in fact, its electronegativity value, the highest amongst all the elements of the period table, combined with its small atomic dimensions, exercises a stronger attraction on the electron cloud surrounding the nucleus, preventing it, in the case of substituted benzoic acids, to be delocalised on the benzene ring. On the contrary, the larger dimensions of chlorine allow a donation of the electron density back to the benzene.

The crystal structures of 2-chlorobenzoic acid (2-CBA)[155], 3-chlorobenzoic acid (3-CBA)[156] and 4-chlorobenzoic acid (4-CBA)[157] are known. 2-CBA and 3-CBA crystallise in the monoclinic system, space group ***C2/c*** for the former and ***P2$_1$/c*** the latter, while crystals of 4-CBA are triclinic, space group ***P$\bar{1}$***. They are all characterised by the formation of centrosymmetric dimers, held together by intermolecular hydrogen bonds between two carboxylic groups, as shown in Figure 7.85.

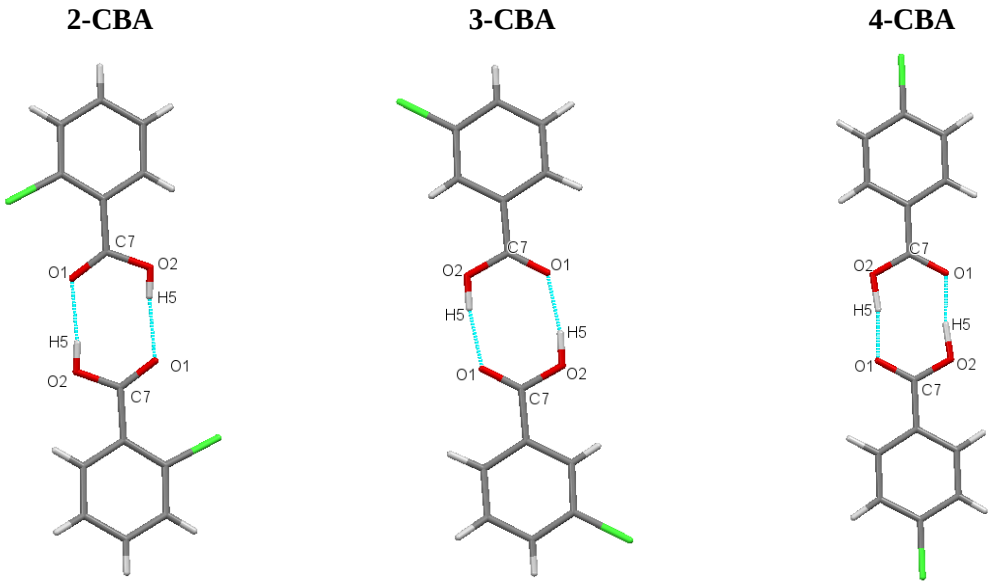

Figure 7.85. *Centrosymmetric dimmers in crystals of 2-CBA[158], 3-CBA[159] and 4-CBA[160]. The graphics were produced using the program Mercury[100].*

Due to the hindrance caused by the chlorine atom in the *ortho* position, the carboxylic group of 2-CBA is forced to rotate of around 14.4˚ in respect to the benzene ring, while in the conformation of the 3-CBA and 4-CBA molecules the carboxylic group is twisted only slightly, by ~2.1˚ and ~5.6˚, respectively. Since all structures were analysed by single crystal X-ray diffraction, the accuracy and precision in the definition of the hydrogen atom positions are affected by the limitations of X-ray techniques, derived from the fact that X-rays interact with the electrons, thus being less effective in the study of hydrogen atoms. It is, however, possible to estimate the strength of a hydrogen bond considering the donor-acceptor distance O1···O2, which is 2.633(2) Å in 2-CBA, 2.663(4) Å in 3-CBA and 2.618(2) Å in 4-CBA, all reasonable values for hydrogen bonds of moderate strength.

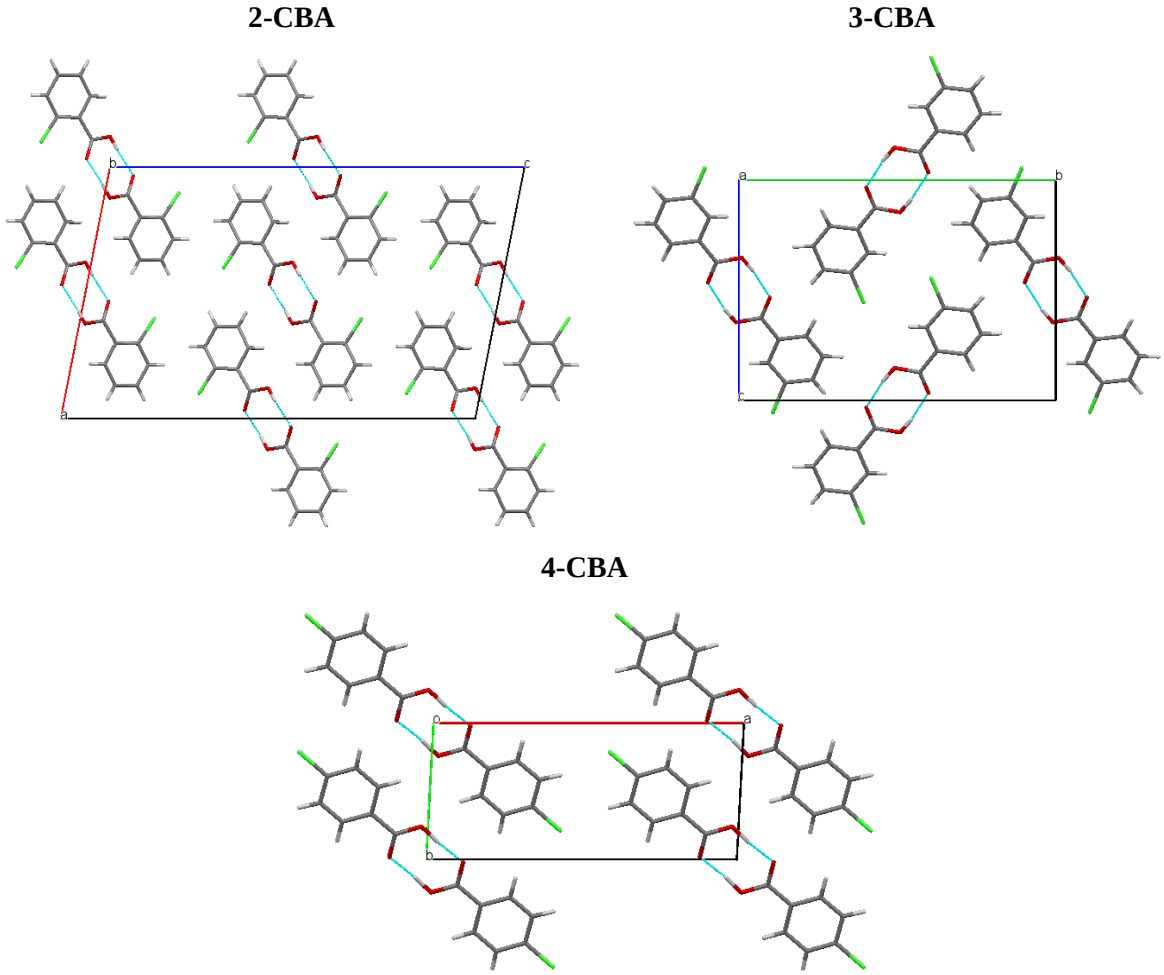

Figure 7.86. *Crystal packing of 2-CBA, 3-CBA and 4-CBA.*

As shown in Figure 7.86, the crystal packing of 2-CBA and 4-CBA are similar: both display the organisation of the dimers into parallel lines, which are slightly shifted in respect to one another. On the contrary, the dimers of 3-CBA stack themselves in lines of alternate orientation, forming a "herring-bone" motif.

7.5.2. Experimental

7.5.2.1. Physical and chemical properties of co-formers

2-Chlorobenzoic acid[161] is a white crystalline powder with temperature of fusion of 138-140˚C and boiling point around 285˚C. It has a relative density of 1.544 g/cm^3 at 20˚C and a pK_a of 2.90[145] at 25˚C. It is soluble in water, with a solubility of 21 g/L, and in the most common organic solvents.

3-Chlorobenzoic acid[162] is commercially available as a white powder with a melting point of 153-157˚C, relative density at 20˚C of 1.496 g/cm^3 and a pK_a of 3.84[145] at 25˚C. It is soluble in water and in a variety of organic solvents, such as acetone and alcohols.

The solid state of 4-chlorobenzoic acid[163] is a fine, white powder with melting temperature in the range 238-241˚C and boiling point around 275˚C. It has a relative density at 20˚C of 1.54 g/cm^3 and a pK_a of 4.00[145] at 25˚C. It is slightly soluble in water, but soluble in the most common organic solvents, such as acetone and alcohols.

7.5.2.2. Synthesis from solution

The three co-crystals cyprodinil/2-chlorobenzoic acid (C2CBA), cyprodinil/3-chlorobenzoic acid (C3CBA), and cyprodinil/4-chlorobenzoic acid (C4CBA) were synthesised in ethanol solution. The solvent was chosen considering the nature and characteristics of the components: water was not a suitable solvent due to the very low solubility of cyprodinil in it, but less polar solvents, such as toluene and xylene, were not good candidates for the dissolution of the monosubstituted chlorobenzoic acids. Alcohols represented a valid option, since all the materials used in this study displayed good solubility in them; in addition, ethanol had already given successful results in the synthesis of other co-crystals of cyprodinil with differently substituted benzoic acids (***c.f. 7.1-7.4***). In Table 7.55 a summary of the quantities and the materials used for the preparation of the co-crystals C2CBA, C3CBA, and C4CBA is reported. All materials were of analytical standard and were used without further purification.

Substance	Quantity	Colour solution	Colour crystals
Cyprodinil	0.50 g		
2-Chlorobenzoic acid	0.35 g	Bright yellow	Colourless
Ethanol	10 ml		
Cyprodinil	0.50 g		
3-Chlorobenzoic acid	0.35 g	Colourless	Colourless
Ethanol	10 ml		
Cyprodinil	0.50 g		
4-Chlorobenzoic acid	0.35 g	Colourless	Colourless
Ethanol	20 ml		

Table 7.55. *Solutions that were prepared for the synthesis of the three co-crystals C2CBA, C3CBA, and C4CBA.*

The solutions were prepared with a 1 : 1 molar ratio of the two components, adding the solvent 1 ml at a time to reach saturation. The solutions were kept at a temperature of around 60˚C for two

hours, during which time they were continuously stirred to facilitate dissolution of the solid materials. Crystallisation was achieved at room temperature by the method of slow evaporation of the solvent applying small holes on the film used as cover of the crystallisation vials.

Crystals of C2CBA and C4CBA grow as thin, colourless rods, while the solution for the synthesis of C3CBA reported in Table 1 led to the formation of monoclinic crystals with a colourless, parallelepiped habit (C3CBA-II). However, when a second solution for the production of C3CBA was prepared using half the quantities displayed in Table 1 but the same experimental conditions, crystallisation of triclinic crystals of C3CBA (C3CBA-I) with a colourless, prismatic morphology occurred. As for the case of C2FBA, crystals of triclinic C3CBA-I become opaque upon storage at room temperature.

7.5.2.3. Differential Scanning Calorimetry

Differential scanning calorimetry (DSC) was used to assess and investigate structural changes in C2CBA and C3CBA upon variation of temperature. Time restrictions and scarce availability of the sample did not allow performing a DSC analysis on C4CBA.

DSC data on a sample of C2CBA were collected on the DSC Q20. The results are reported in Figure 7.87.

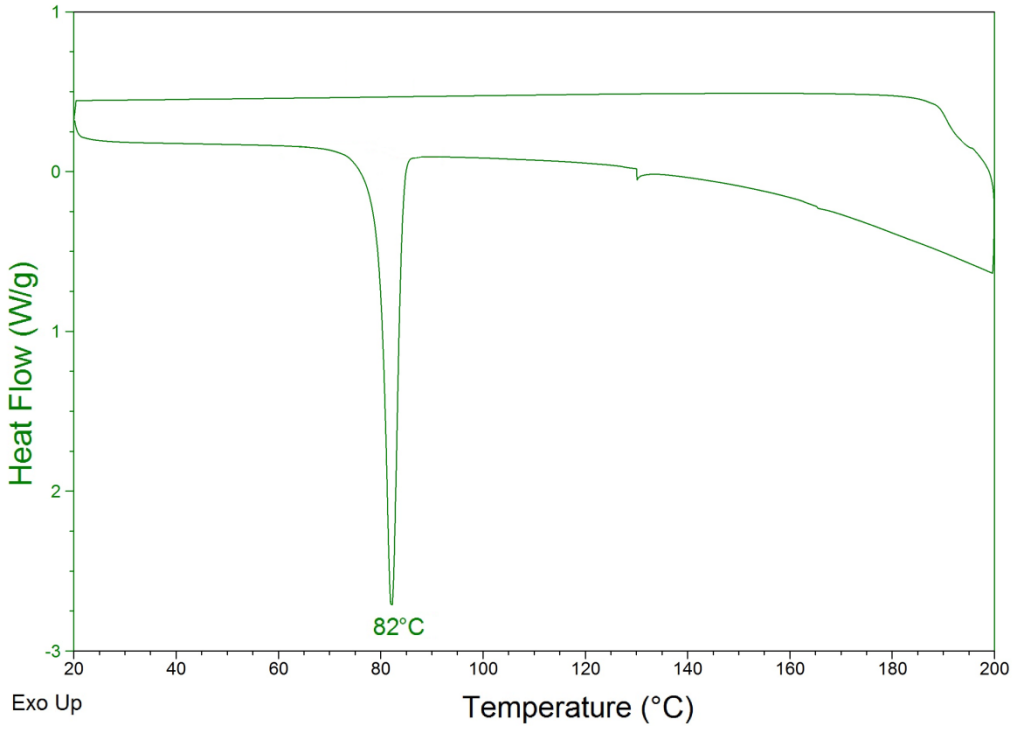

Figure 7.87. *DSC profile of a sample of C2CBA.*

The DSC profile of C2CBA presents an endothermic event at around 82˚C, corresponding to the melting of the co-crystal. The progressive decrease of the heat flow from 130˚C to 200˚C might indicate a possible degradation of the materials present in the sample. In fact, no re-crystallisation event is visible during the cooling process, supporting the likelihood of sample degradation.

The DSC analysis on a sample of triclinic C3CBA-I was performed at the Institut Laue-Langevin (ILL) on a Setaram DSC-131 instrument, which allows data collection down to -120˚C thanks to the LN2 accessory that is mounted on top of the furnace and that can contain liquid nitrogen.
Two DSC profiles were recorded: in the first, displayed in Figure 7.88, data were collected in a cycle of heating and cooling between 25˚C and 80˚C at a rate of 1˚C/min. Only one endothermic event is present during heating, around 71˚C, which corresponds to the melting of the co-crystal. No re-crystallisation occurs in the cooling to room temperature, probably because of the high viscosity of molten cyprodinil and very slow crystallisation rate in the presence of the chlorobenzene.

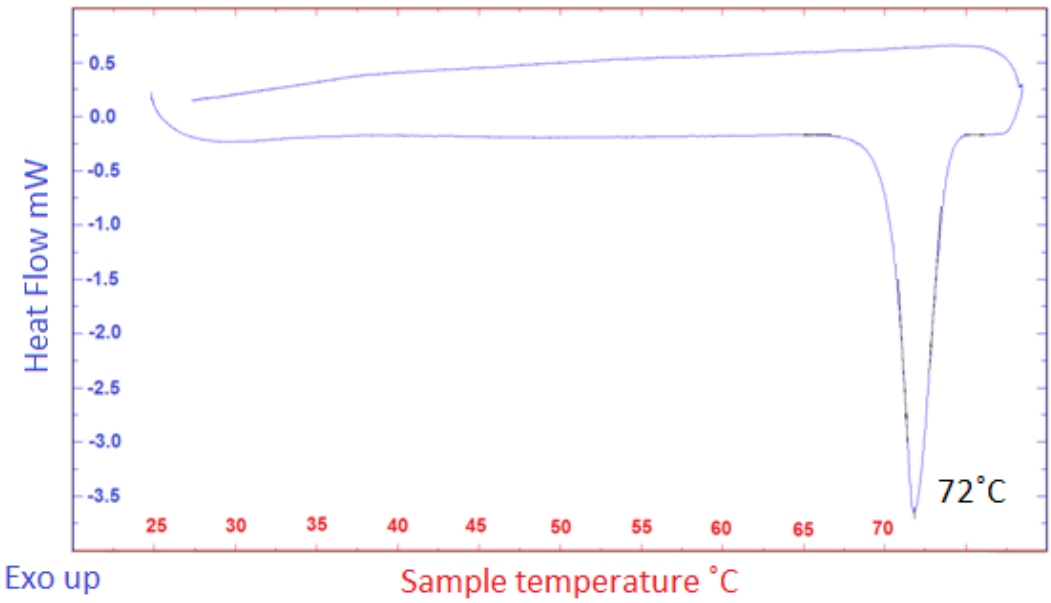

Figure 7.88. *DSC profile of a sample of C3CBA-I, collected between 25-80˚C.*

A second DSC analysis, displayed in Figure 7.89, was carried out on a sample of triclinic C3CBA-I, recording data from -80˚C to 15˚C at a heating rate of 1˚C/min, in order to investigate whether changes to the structure occurred below room temperature. Although the signal of the heat flow (in blue) is not stable, due to the difficulties in keeping the Dewar for the liquid nitrogen always filled to ensure the right temperature, it is possible to notice a small endothermic event at around -24˚C, which indicates change in the crystal structure.

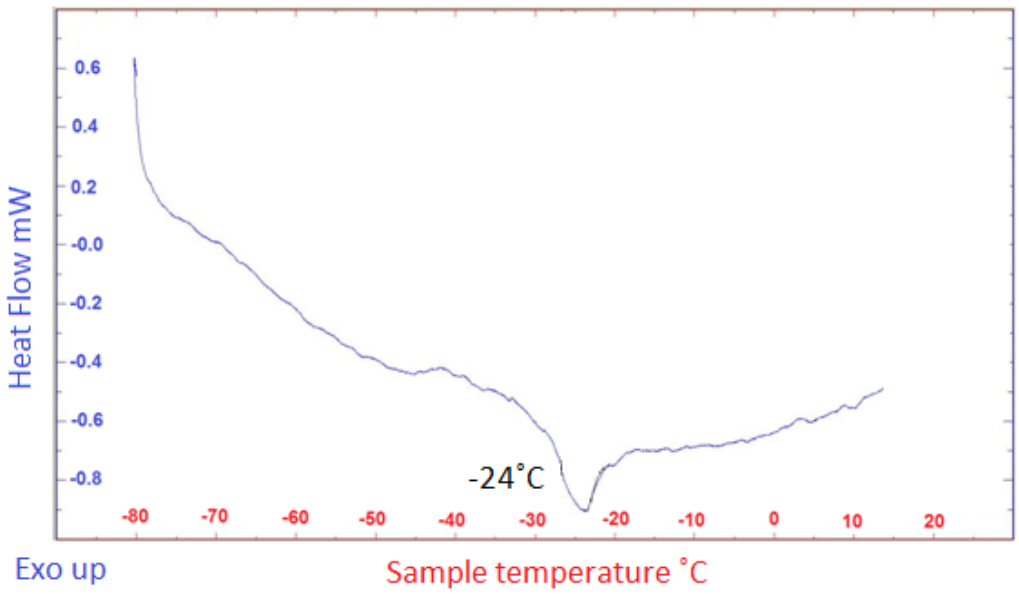

Figure 7.89. *DSC profile of a sample of C3CBA-I, collected between -80˚C and 15˚C.*

7.5.2.4. Single crystal X-ray diffraction

The crystal structures of the co-crystals C2CBA, C3CBA and C4CBA were characterised by single crystal X-ray diffraction (SXD), which allows the definition of the atomic positions along with their atomic displacement parameters (ADPs). All crystals analysed with SXD were grown from ethanol solutions by the method of slow evaporation of the solvent. Due to crystal dimensions and availability of the instruments, three different single crystal diffractometers were used for data collection: the Gemini A Ultra CCD diffractometer for a crystal of C2CBA; the Agilent Technologies Xcalibur single crystal diffractometer for the analysis on the monoclinic form of C3CBA-II and for C4CBA; and the Agilent Technologies SuperNova dualwavelength diffractometer for the triclinic form of C3CBA-I. All data were collected using Mo radiation, λ = 0.71073 Å, at a temperature of 150K. Variable temperature studies were performed on both forms of C3CBA, the triclinic and the monoclinic one, to better characterise the differences in the two crystal structures and to investigate the reasons behind the change of colour in crystals of triclinic C3CBA-I after several week of storage at room temperature. Data on monoclinic C3CBA-II were collected at 150, 220, and 300K, while five data sets were recorded on the triclinic C3CBA-I (dimensions 0.25 x 0.25 x 0.39 mm) at 150, 180, 220, 260, and 300K.

In Tables 7.56, 7.57, 7.58, and 7.59, X-ray crystallographic data and refinement parameters for C2CBA, triclinic C3CBA-I, monoclinic C3CBA-II and C4CBA, respectively, are reported.

Name	CYP / 2-chlorobenzoic acid (C2CBA)
Empirical formula	$C_{14}H_{15}N_3$ $C_7H_5O_2Cl$
Formula weight (g mol^{-1})	381.85
Temperature (K)	150
Wavelength (Å)	0.71073
Crystal system, space group	Monoclinic, $P2_1/n$
Unit cell dimensions	a = 7.5354(5) Å
	b = 25.6978(16) Å
	c = 10.3397(8) Å
	β = 110.357(8)˚
Volume ($Å^3$)	1877.2(2)
Z, calculated density (g cm^{-3})	4, 1.351
F(000)	800
Absorption coefficient (mm^{-1})	0.225
Crystal dimensions (mm)	0.07 x 0.10 x 0.32
Theta range for data collection (˚)	2.92 to 26.37
Limiting indices	$-9 \leq h \leq 9$, $-32 \leq k \leq 32$, $-12 \leq l \leq 12$
Reflections collected / unique	20126 / 3840 [R_{int} = 0.0635]
Completeness to θ = 26.37	99.9 %
Refinement method	Full-matrix least-squares on F^2
Data / restrains / parameters	3840 / 0 / 324
Goodness-of-fit on F^2	1.176
Final R indices [I>2sigma(I)]	R_1 = 0.0805, wR_2 = 0.2446
R indices (all data)	R_1 = 0.1044, wR_2 = 0.2577
Largest diff. Peak and hole (e $Å^{-3}$)	0.68 and -0.40

Table 7.56 *X-ray crystallographic data and refinement parameters for a crystal of C2CBA at 150K.*

Name - Formula weight (g mol^{-1})		CYP / 3-chlorobenzoic acid (C3CBA-I) - $C_{14}H_{15}N_3$ $C_7H_5O_2Cl$ - 381.85				
Temperature (K)		150	180	220	260	300
Wavelength (Å)		0.71073				
Crystal system, space group		Triclinic, $P\bar{1}$				
Unit cell dimensions	a (Å) =	7.7903(4)	7.8118(3)	7.8457(5)	7.8757(3)	7.9443(4)
	b (Å) =	16.104(1)	16.1252(5)	16.1657(7)	16.1775(5)	16.1999(6)
	c (Å) =	16.4103(7)	16.4173(6)	16.3994(9)	16.4156(6)	16.4266(8)
	α (˚) =	64.117(5)	64.280(3)	64.676(5)	64.793(3)	64.824(4)
	β (˚) =	86.385(4)	86.872(3)	88.012(5)	88.595(3)	88.899(4)
	γ (˚) =	82.967(5)	83.546(3)	84.878(5)	85.497(4)	85.727(4)
Volume ($Å^3$)		1838.1(2)	1851.3(1)	1872.6(2)	1886.4(1)	1907.7(1)
Z, calculated density (g cm^{-3})		4, 1.380				
F(000)		800				
Absorption coefficient (mm^{-1})		0.230				
Theta range for data collection (˚)		2.86 to 26.37				
Limiting indices		$-9\leq h \leq 9$, $-16\leq k \leq 20$, $-20\leq l \leq 20$				
Reflections collected / unique		16423 / 7522 [R_{int} = 0.0278]	15240 / 7563 [R_{int} = 0.174]	15290 / 7637 [R_{int} = 0.0189]	15459 / 7694 [R_{int} = 0.0186]	15648 / 7775 [R_{int} = 0.0223]
Data / restrains / parameters		7522 / 0 / 647	7563 / 0 / 647	7637 / 0 / 647	7694 / 0 / 647	7775 / 0 / 647
Goodness-of-fit on F^2		1.043	1.077	1.043	1.055	1.040
Final R indices [I>2sigma(I)]		R_1 = 0.0455, wR_2 = 0.1098	R_1 =0.0373, wR_2 = 0.0996	R_1 = 0.0415, wR_2 = 0.1115	R_1 = 0.0471, wR_2 = 0.1230	R_1 = 0.0536, wR_2 = 0.1431
R indices (all data)		R_1 = 0.0657, wR_2 = 0.1243	R_1 = 0.0425, wR_2 = 0.1036	R_1 = 0.0494, wR_2 = 0.1185	R_1 = 0.0582, wR_2 = 0.1318	R_1 = 0.0700, wR_2 = 0.1578
Largest diff. Peak and hole (e $Å^{-3}$)		0.50 and -0.35	0.29 and -0.45	0.29 and -0.46	0.36 and -0.43	0.29 and -0.45

Table 7.57. *X-ray crystallographic data and refinement parameters for a crystal of triclinic C3CBA-I at 150, 180, 220, 260, and 300K.*

Name		CYP / 3-chlorobenzoic acid (C3CBA-II)		
Empirical formula		$C_{14}H_{15}N_3$ $C_7H_5O_2Cl$		
Formula weight (g mol^{-1})		381.85		
Temperature (K)		150	220	300
Wavelength (Å)		0.71073		
Crystal system, space group		Monoclinic, $P2_1/c$		
Unit cell dimensions	a (Å) =	11.3639(7)	11.4201(4)	11.4485(3)
	b (Å) =	11.6919(5)	11.8092(3)	11.9402(3)
	c (Å) =	14.8423(9)	14.9326(5)	14.9961(4)
	β (˚) =	110.294(7)	110.284(4)	110.559(3)
Volume ($Å^3$)		1849.6(2)	1889.0(1)	1919.37(9)
Z, calculated density (g cm^{-3})		4, 1.371		
F(000)		800		
Absorption coefficient (mm^{-1})		0.228		
Crystal dimensions (mm)		0.20 x 0.39 x 0.49		
Theta range for data collection (˚)		3.37 to 26.37		
Limiting indices		$-14 \leq h \leq 9$, $-14 \leq k \leq 14$, $-18 \leq l \leq 18$	$-14 \leq h \leq 14$, $-9 \leq k \leq 14$, $-17 \leq l \leq 18$	$-14 \leq h \leq 13$, $-14 \leq k \leq 14$, $-18 \leq l \leq 18$
Reflections collected / unique		8547 / 3775 [R_{int} = 0.0149]	15282 / 3853 [R_{int} = 0.0206]	15706 / 3916 [R_{int} = 0.0158]
Completeness to θ = 26.37		99.8 %	99.8 %	99.8 %
Refinement method		Full-matrix least-squares on F^2		
Data / restrains / parameters		3775 / 0 / 320	3853 / 0 / 320	3916 / 0 / 320
Goodness-of-fit on F^2		1.037	1.028	1.046
Final R indices [I>2sigma(I)]		R_1 = 0.0522, wR_2 = 0.11389	R_1 = 0.0539, wR_2 = 0.1536	R_1 = 0.0545, wR_2 = 0.1653
R indices (all data)		R_1 = 0.0606, wR_2 = 0.1472	R_1 = 0.0593, wR_2 = 0.1592	R_1 = 0.0686, wR_2 = 0.1806
Largest diff. Peak and hole (e $Å^{-3}$)		2.02 and -0.46	1.54 and -0.44	1.13 and -0.33

Table 7.58. *X-ray crystallographic data and refinement parameters for a crystal of monoclinic C3CBA-II at 150, 220, and 300K.*

Name	CYP / 4-chlorobenzoic acid (C4CBA)
Empirical formula	$C_{14}H_{15}N_3$ $C_7H_5O_2Cl$
Formula weight (g mol^{-1})	381.85
Temperature (K)	150
Wavelength (Å)	0.71073
Crystal system, space group	Orthorhombic, $P2_12_12_1$
Unit cell dimensions	a = 5.0014(2) Å
	b = 13.9904(7) Å
	c = 26.2515(14) Å
Volume ($Å^3$)	1836.9(1)
Z, calculated density (g cm^{-3})	4, 1.381
F(000)	800
Absorption coefficient (mm^{-1})	0.230
Theta range for data collection (˚)	3.43 to 26.37 deg
Limiting indices	$-5\leq h \leq 6$, $-17\leq k \leq 17$, $-32\leq l \leq 31$
Reflections collected / unique	5889 / 3323 [R_{int} = 0.0144]
Completeness to θ = 26.37	99.6 %
Refinement method	Full-matrix least-squares on F^2
Data / restrains / parameters	3323 / 0 / 324
Goodness-of-fit on F^2	1.048
Final R indices [I>2sigma(I)]	R_1 = 0.0282, wR_2 = 0.0681
R indices (all data)	R_1 = 0.0320, wR_2 = 0.0704
Largest diff. Peak and hole (e $Å^{-3}$)	0.20 and -0.18

Table 7.59. *X-ray crystallographic data and refinement parameters for a crystal of C4CBA at 150K.*

7.5.2.5. Single crystal neutron diffraction

The triclinic structure of C3CBA-I was analysed by single crystal neutron diffraction (SND) on the single crystal diffractometer D19 at ILL to better characterise the hydrogen bonding network in this co-crystal. The selected crystal (dimensions 1.65 x 2.60 x 3.00 mm) was grown from an ethanol solution by the method of slow evaporation of the solvent: the slow evaporation process was achieved by placing the crystallisation vial in a polystyrene box, so to avoid a fast decrease of the temperature of the solution, and by covering it with a film, in which a few small holes had been made. These crystallisation conditions allowed the formation of large single crystals suitable for the SND experiment. The crystal was secured to a vanadium pin (diameter 0.5 mm) with a thick glue, which is resistant to low temperatures, and it was mounted on the D19 diffractometer head. Three concentric vanadium cans were fixed around the crystal to ensure a tight vacuum, which is essential for the cooling process. The quality and scattering power of the sample were checked acquiring a few 100-seconds long scans, followed by a two-hour long scan at room temperature to produce a preliminary orientation matrix for the indexing of the Bragg's reflections. Three sets of data were collected: the first at 30K, the second at 220K and the third at 300K. The cooling process to 30K was monitored following the intensity of a so-called "check" reflection, in this case the strong reflection ($\bar{1}\ \bar{5}\ 1$). Figure 7.90 reports the ***I vs. T*** plot for the "check" reflection during the cooling to 30K. Any sudden variation of the intensity of the "check" reflection may indicate damage to the crystal.

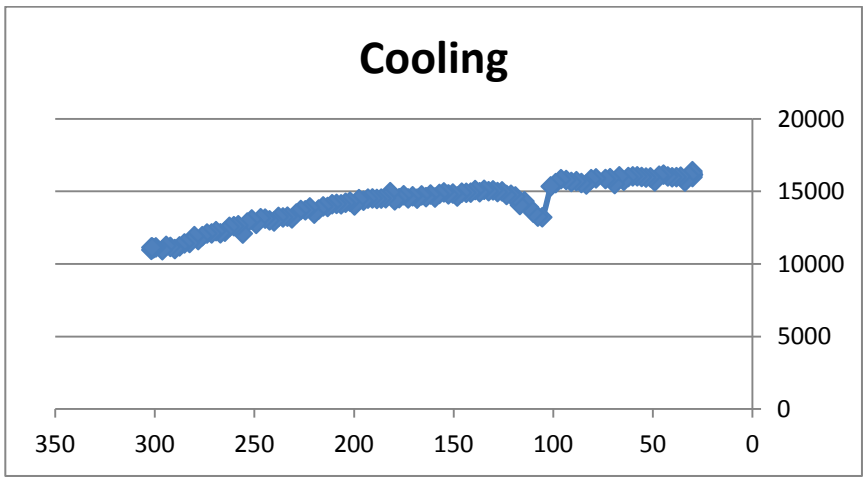

Figure 7.90. I vs. T *plot for the "check" reflection* ($\bar{\mathbf{1}}\ \bar{\mathbf{5}}\ \mathbf{1}$) *during the cooling to 30K.*

No drastic variations of the "check" reflection intensity occurred during cooling, apart from the increase of the intensity value due to the attenuation of the thermal motion of all atoms at lower temperatures. It is, however, possible to notice a slight loss of signal between 125K and 100K, regained soon after passing 100K. This effect might be either due to a small variation in the

position of the detector, which made it no longer centred on the "check" reflection, or to the significant variation of the β and γ angles of the unit cell, which were found to decrease by around 2° during cooling from 180K to 30K.

Three additional days of beamtime were granted on D19 after one month from the previous experiment on triclinic C3CBA-I, which allowed collection of two more datasets on the same material, one at 180K and one at 260K, giving the possibility to compare the structure with the SXD results.

Since the crystal of the first SND analysis had become opaque inside, a second one, with dimensions 1.40 x 1.50 x 6.00 mm, was mounted on D19 and it was enclosed in the three concentric vanadium cans. As for the previous experiment, all preliminary checks were done at room temperature and the collection of a two-hour long scan at the same temperature allowed the production of an orientation matrix and the indexing of the Bragg's peaks. The integrity of the crystal during cooling to 180K was monitored following the intensity of the "check" reflection ($\bar{3}\,\bar{1}\bar{1}\,1$), whose profile as a function of temperature is reported in Figure 7.91. The intensity of the "check" reflection gradually increases with the decrease of temperature, due to the attenuation of the Debye-Waller factor, and no sudden loss of the signal is registered, indicating that the crystal was not damage in the cooling to 180K.

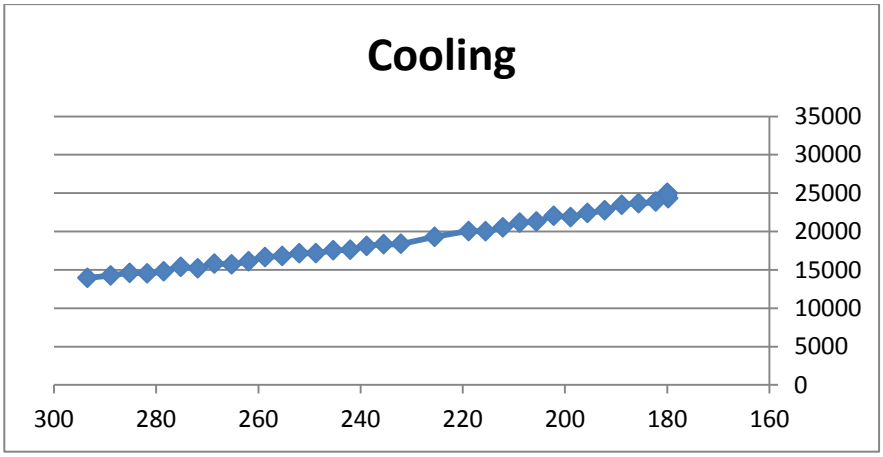

***Figure 7.91. I vs. T** plot for the "check" reflection* ($\bar{\mathbf{3}}\,\bar{\mathbf{11}}\,\mathbf{1}$) *during the cooling process to 180K.*

Corrections due to the presence of the cans and to radiation absorption by the crystal were applied to all data sets collected at the five temperatures. The two types of corrections were applied using the program D19ABSCAN, which estimates the entity of the radiation attenuation caused by the chemical composition of the sample based on the indexing of all crystal faces and their distance from an arbitrary centre inside the crystal itself. In Figure 7.92, schematic representations of the morphology of the two crystals analysed in the two experiments are shown, while Table 7.60 reports the values for the R-factors before and after the application of the correction for the structures at the five temperatures.

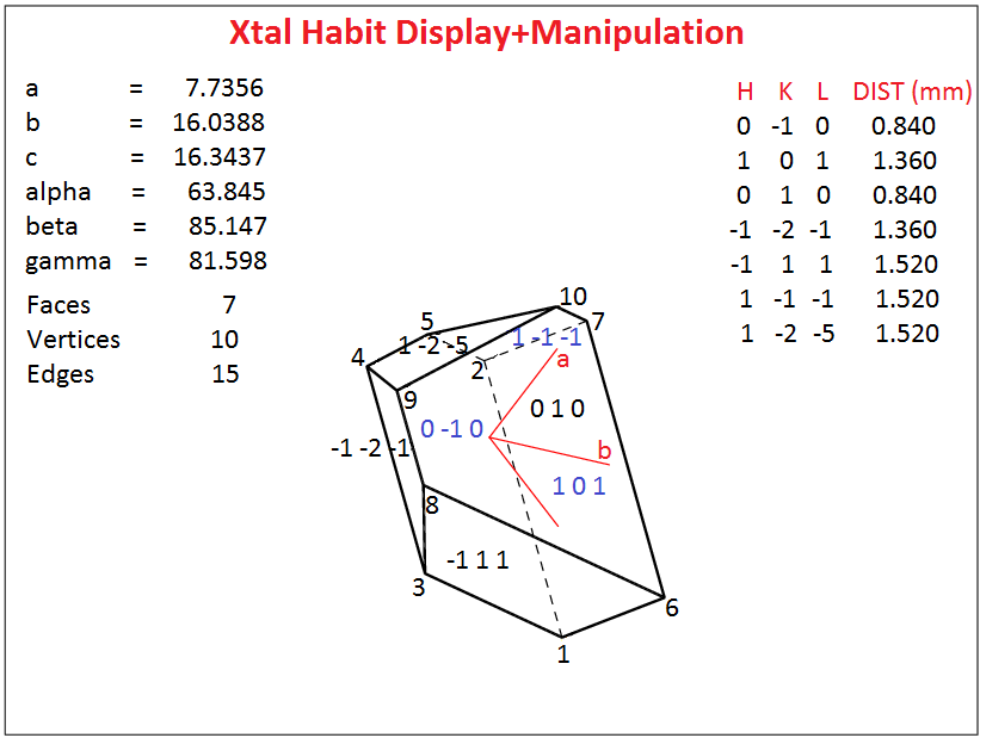

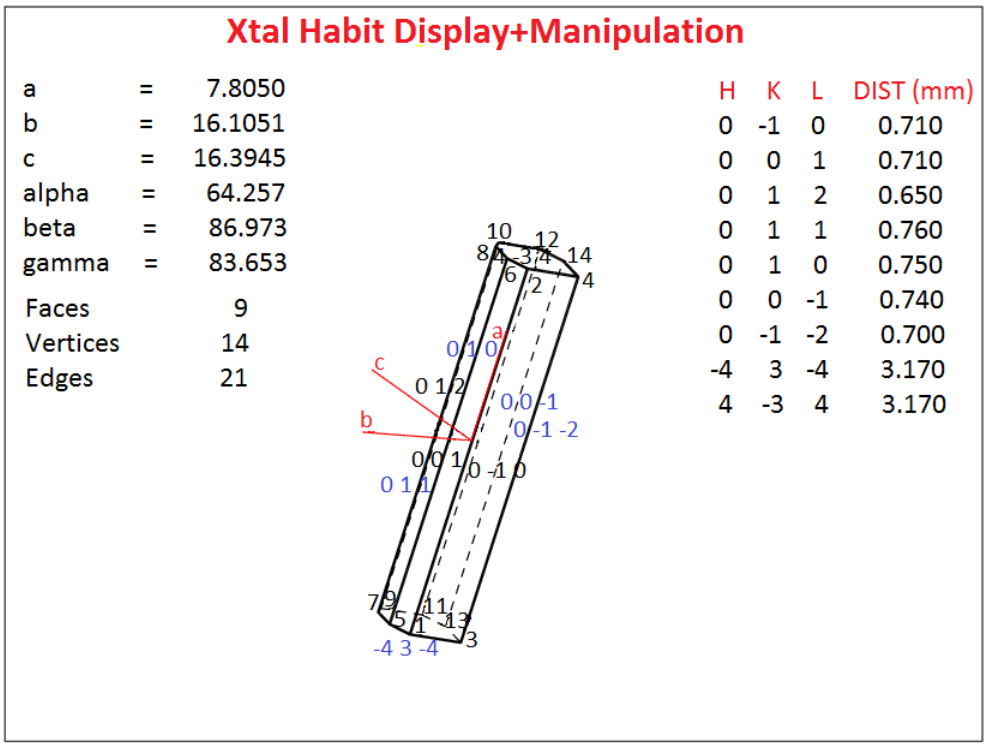

Figure 7.92. *Schematic representation of the crystal used in the first SND experiment at 30K (top) and the one used in the second SND experiment at 180K (bottom). The graphics were made using the program PLATON.*

		No corrections	Corrections cans+crystal
30K	R_1	0.0600	0.0506
	wR_2	0.1789	0.1196
180K	R_1	0.0998	0.0925
	wR_2	0.3359	0.3035
220K	R_1	0.1362	0.0868
	wR_2	0.4233	0.2687
260K	R_1	0.1163	0.1102
	wR_2	0.3980	0.3610
300K	R_1	0.1329	0.1076
	wR_2	0.4271	0.3457

Table 7.60 *Evolution of the R-factors before and after application of absorption corrections at the five data collection temperatures.*

The corrections for the attenuation of the neutron radiation slightly improve the statistics of the final refinements of the five crystal structures, as shown in Table 7.60. Worthy of notice is the comparison of the two data sets collected at 180K and 260K before and after the absorption corrections: in fact, in this case the improvement is minimal due to the rod-like morphology of the crystal understudy. This is particularly evident from the results of the REN-scans (***c. f. 5.1.2.6***) on the reflection ($\bar{2}$ 4 12) for the data recorded at 30, 220, and 300K, and on the reflection ($\bar{6}$ 1 1) for the data set at 260K. Due to time restrictions it was not possible to collect a REN-scan at 180K. In Figures 7.93, 7.94, 7.95, and 7.96, the evolutions of the reflection intensity ***I*** as a function of the angle φ at 30K, 220K, 260, and 300K, respectively, are reported.

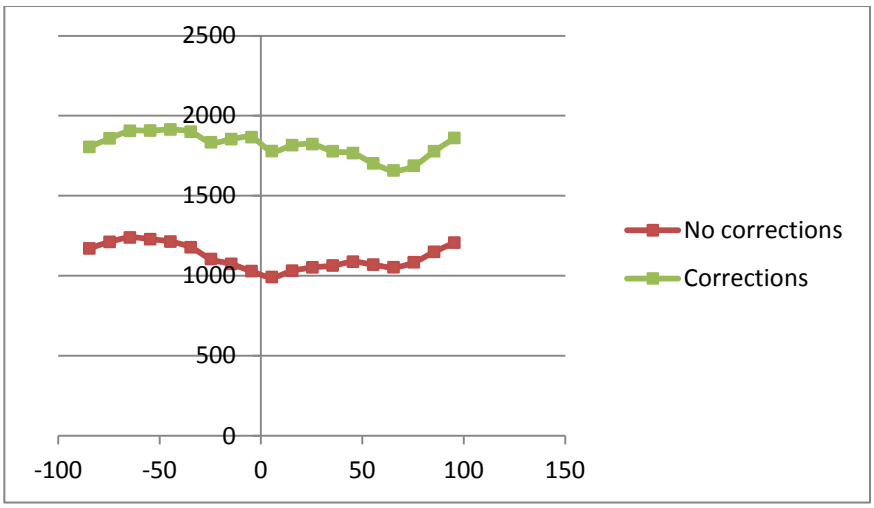

Figure 7.93. *Evolution of the intensity of reflection* ($\bar{\mathbf{2}}$ **4 12**) *used for the REN-scans at 30K.*

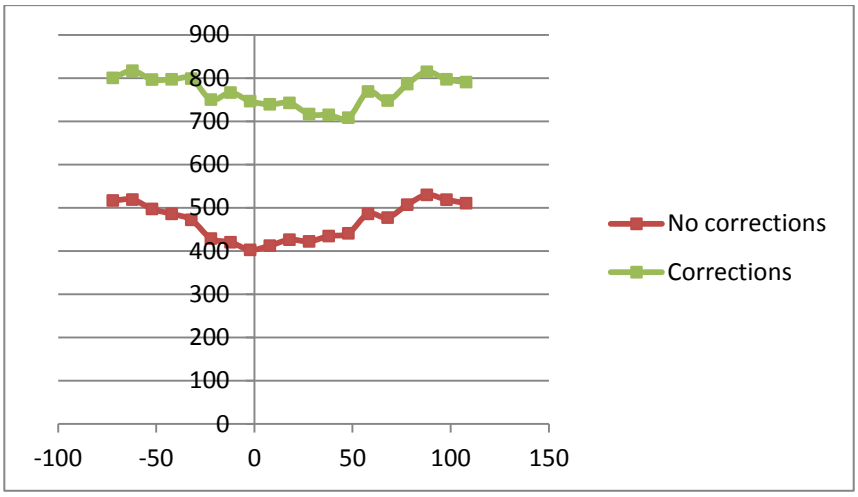

Figure 7.94. *Evolution of the intensity of reflection* ($\bar{\mathbf{2}}$ **4 12**) *used for the REN-scans at 220K.*

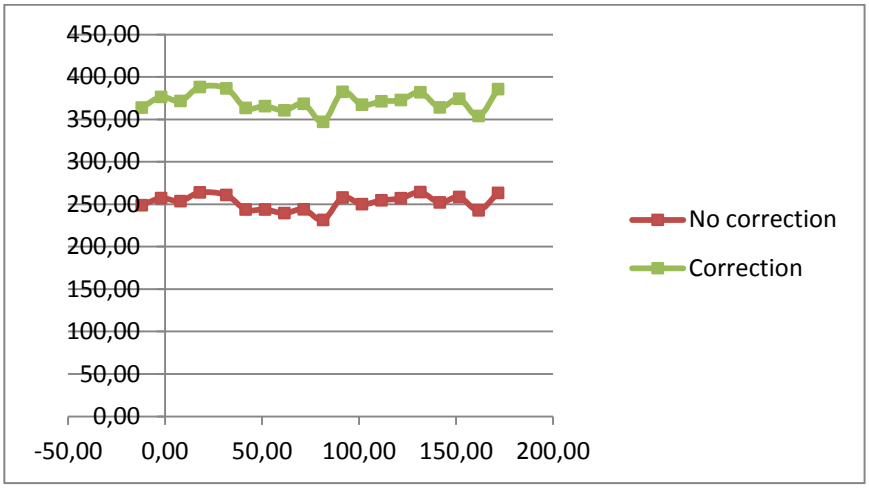

Figure 7.95. *Evolution of the intensity of reflection* ($\bar{\mathbf{6}}$ **1 1**) *used for the REN-scans at 260K.*

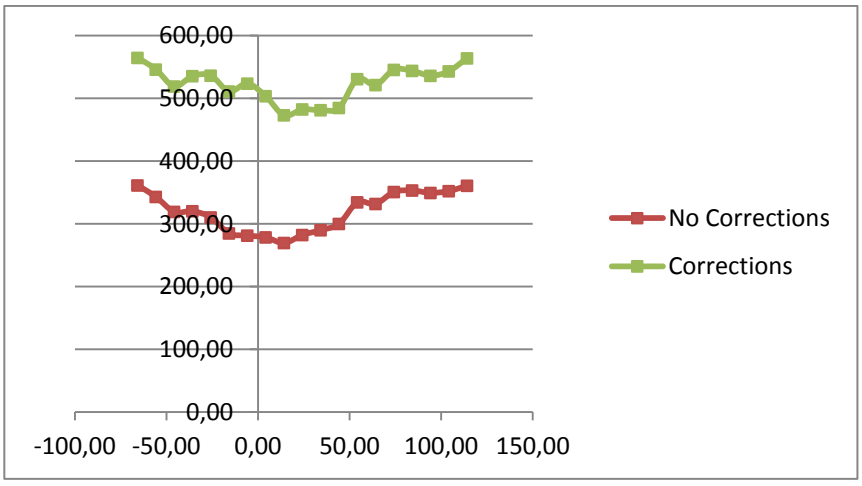

Figure 7.96. *Evolution of the intensity of reflection* ($\bar{\mathbf{2}}$ **4 12**) *used for the REN-scans at 300K.*

For the REN-scans collected at 30, 220, and 300K it is possible to notice a straightening of the reflection intensity profile after the applications of the absorption corrections, whereas the two profiles in the plot at 260K show no significant variation in their trend, indicating that the extent of the absorption effect is minimal and is the same in two normal directions along the $\boldsymbol{\varphi}$ angle.

In Table 7.61, neutron crystallographic data and refinement parameters for a sample of triclinic C3CBA-I at the five collection temperatures are reported.

Name		CYP / 3-chlorobenzoic acid (C3CBA-I) - $C_{14}H_{15}N_3$ $C_7H_5O_2Cl$ - 381.85 g mol^{-1}				
Temperature (K)		30	180	220	260	300
Wavelength (Å)		1.17000				
Crystal system, space group		Triclinic, $P\bar{1}$				
Unit cell dimensions	a (Å) =	7.7343(2)	7.8050(2)	7.8136(4)	7.8612(4)	7.9263(6)
	b (Å) =	16.0426(3)	16.1051(3)	16.1401(6)	16.1636(5)	16.1871(10)
	c (Å) =	16.3434(4)	16.3945(3)	16.4066(7)	16.4040(6)	16.4189(10)
	α (˚) =	63.8400(10)	64.2575(11)	64.522(2)	64.774(2)	64.754(3)
	β (˚) =	85.1630(10)	86.9726(14)	87.922(3)	88.594(2)	88.846(4)
	γ (˚) =	81.6150(10)	83.6534(14)	84.707(3)	85.523(2)	85.656(3)
Volume ($Å^3$)		1800.23(7)	1844.87(7)	1859.88(14)	1879.76(13)	1899.7(2)
Z, calculated density (g cm^{-3})		4, 1.409	4, 1.375	4, 1.409	4, 1.375	4, 1.409
F(000)		456				
Absorption coefficient (mm^{-1})		0.204	0.199	0.204	0.199	0.204
Limiting indices		-11≤ h ≤11, -23≤ k ≤24, -10≤ l ≤23	-11≤ h ≤2, -24≤ k ≤24, -24≤ l ≤24	-11≤ h ≤11, -23≤ k ≤24, -10≤ l ≤23	-11≤ h ≤5, -24≤ k ≤24, -24≤ l ≤24	-11≤ h ≤11, -23≤ k ≤24, -11≤ l ≤23
Reflections collected / unique		16993 / 9929 [R_{int} = 0.0388]	22286 / 11253 [R_{int} = 0.0707]	23247 / 11367 [R_{int} = 0.0731]	32186 / 11807 [R_{int} = 0.0758]	24569 / 11633 [R_{int} = 0.1064]
Data / restrains / parameters		9929 / 0 / 848	11253 / 0 / 848	11367 / 0 / 848	11807 / 0 / 848	11633 / 0 / 848
Goodness-of-fit on F^2		1.111	1.039	1.042	1.085	1.029
Final R indices [I>2sigma(I)]		R_1 = 0.0506, wR_2 = 0.1099	R_1 =0.0925, wR_2 = 0.2323	R_1 = 0.0868, wR_2 = 0.2168	R_1 = 0.1102, wR_2 = 0.2868	R_1 = 0.1076, wR_2 = 0.2634
R indices (all data)		R_1 = 0.0578, wR_2 = 0.1196	R_1 = 0.1442, wR_2 = 0.3035	R_1 = 0.1521, wR_2 = 0.2687	R_1 = 0.1849, wR_2 = 0.3610	R_1 = 0.2281, wR_2 = 0.3457
Largest diff. Peak and hole (fm $Å^{-3}$)		1.14 and -1.33	1.13 and -1.58	1.17 and -1.36	1.58 and -1.41	1.17 and -1.14

Table 7.61. *Neutron crystallographic data and refinement parameters for triclinic C3CBA-I at 30, 180, 220, 260, and 300K.*

7.5.3. Results and discussion

7.5.3.1. Cyprodinil / 2-chlorobenzoic acid (C2CBA)

C2CBA crystallises in the monoclinic system, space group ***P2₁/n***, as thin, colourless rods. The asymmetric unit displays one molecule of protonated cyprodinil and one of the 2-chlorobenzoate anion, as shown in Figure 7.97 for the structure studied with X-ray radiation, indicating the formation of a salt. In Table 7.62 torsion angles and bond lengths of interest are reported.

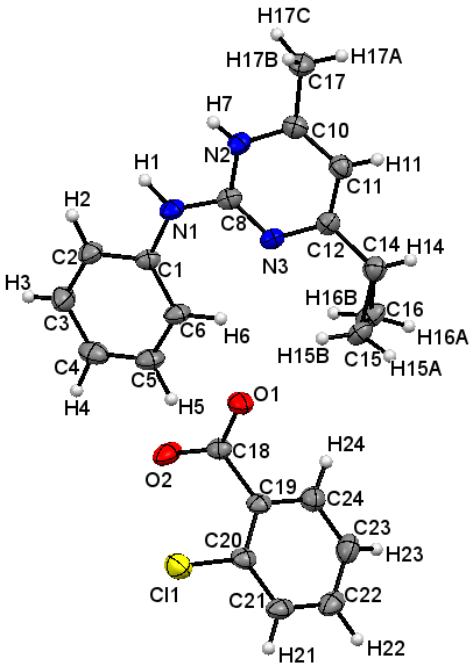

Figure 7.97. *ORTEP representation of the asymmetric unit of C2CBA, viewed along the* ***b****-axis, derived from SXD at 150K. The probability level for all non-hydrogen ellipsoids is 50%, while the hydrogen atoms are drawn as fixed-size spheres of radius 0.15 Å.*

C8-N1-C1-C6	14.3(7)˚
N3-C12-C14-C15	-39.8(6)˚
N3-C12-C14-C16	29.0(6)˚
C8-N3-C12-C14	177.9(4)˚
N2-C8-N1-H1	-2(4)˚
N1-C8-N2-H7	14(6)˚
O2-C18-C19-C20	-58.3(6)˚
C18-C19-C24-C23	-176.1(4)˚
C18-C19-C20-C21	178.4(4)˚
C18-O1	1.247(5) Å
C18-O2	1.257(6) Å

Table 7.62. *Torsion angles and bond lengths of interest at 150K, derived from SXD measurement.*

The benzene and the pyrimidine rings of the cyprodinil molecule are not co-planar, but the former is twisted by 14.3(7)˚ in respect to the latter to avoid hindrance caused by the cyclopropyl substituent, which is positioned below the plane containing the pyrimidine moiety. The two hydrogen atoms, H1 and H7, are rotated from the rest of the molecule in opposite directions by -2(4)˚ and 14(6)˚, respectively, in order to interact with a neighbouring 2-chlorobenzoate anion.

The substituent in the *ortho* position of the acid forces the carboxylic group to rotate by -58.3(6)˚ along the single bond C18-C19 to avoid hindrance by the chlorine atom. The remaining of the acid molecule displays the planarity that is characteristic of aromatic compounds and the intermediate values between a single and a double bond shown by C18-O1 and C18-O2, 1.247(5) Å and 1.257(6) Å, respectively, confirm the presence of the carboxylate anion.

In the three-dimensional structure the molecules of the two components organise in heterogeneous dimers, forming two hydrogen bonds, as shown in Figure 7.98. For both hydrogen bonds, N1-H1···O1 and N2-H7···O2, the two groups that act as donor are on the cyprodinil molecule, while the acceptor is represented by the oxygen atoms of the carboxylate anion. The crystal packing is characterised by the arrangement of the dimers into off-set parallel lines, which allow the formation of π-π interactions between the pyrimidine and benzene rings of two cyprodinil molecules with distances between 3.65(5) Å and 4.11(5) Å. Each dimer is rotated by 180˚ in respect to the one above in order to accommodate the acid molecules. As shown in Figure 7.99, the piles of dimers are shifted from one another along the two unit cell axis ***b*** and ***c***, forming a fishbone motif.

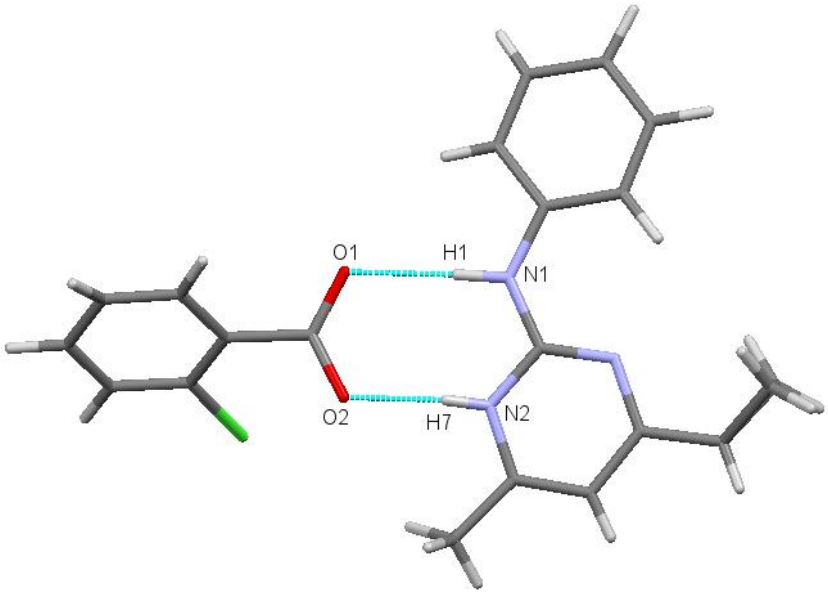

Figure 7.98. *Heterogeneous dimer in the crystal structure of C2CBA at 150K, derived from SXD measurements.*

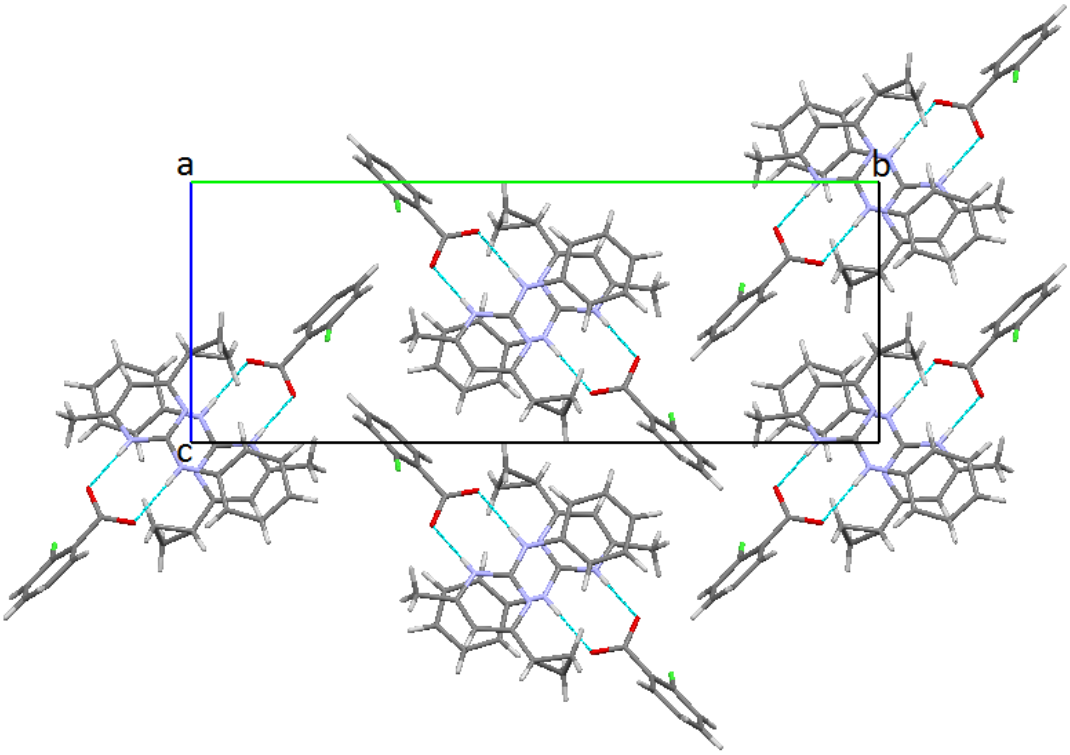

Figure 7.99. *Crystal packing of C2CBA at 150K, viewed along the* ***a****-axis.*

N1-H1	0.91(6) Å
H1···O1	1.98(6) Å
N1-H1···O1	177(5)˚
N1···O1	2.885(5) Å
N2-H7	0.78(7) Å
H7···O2	1.80(7) Å
N2-H7···O2	168(7)˚
O2···N2	2.567(6) Å

Table 7.63 *Hydrogen bond lengths and geometry of interaction for the two hydrogen bonds, N1-H1···O1 and N2-H7···O2, derived from SXD measurements at 150K.*

Considering the hydrogen bond lengths, the donor-acceptor distances and the geometry of interaction, which are listed in Table 7.63, it is possible to classify the two hydrogen bonds as of moderate strength[81]. Investigation of the electron-density maps of the two hydrogen atoms, H1 and H7, excludes the presence of proton migration or disorder in the structure, as shown in Figure 7.100.

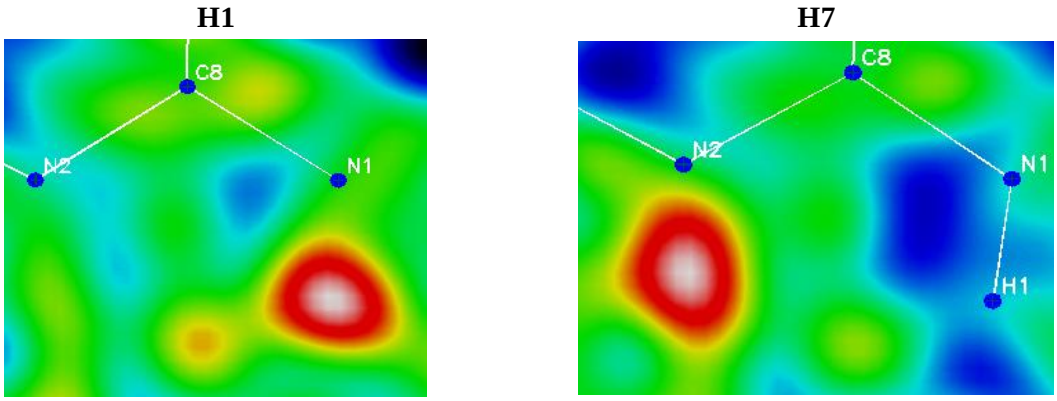

Figure 7.100. *Difference electron-density maps of the hydrogen atoms H1 and H7, which are involved in intermolecular hydrogen bonds.*

7.5.3.2. Cyprodinil / 3-chlorobenzoic acid (C3CBA)

7.5.3.2.1. Triclinic form (C3CBA-I)

The triclinic polymorph of C3CBA crystallises in the space group $\boldsymbol{P\bar{1}}$ and it displays four molecules in the asymmetric unit, one molecule of the fungicide and one of the acid in their neutral state and one molecule of protonated cyprodinil interacting with the 3-chlorobenzoate anion, as shown in Figure 7.101 for the structure studied with neutrons. A variable temperature SND experiment was performed on a sample of triclinic-C3CBA and the unit cell parameters of the crystal under study at the five temperatures are reported in Table 7.64. It is interesting to notice that, while the cell parameters ***a***, ***b***, ***c***, and ***α*** show the expected slight expansion due to the increased temperature, the ***β*** and ***γ*** angles increase both of around 4˚. This is probably caused by changes in the characteristics of the hydrogen bonding network, particularly for the case of the intermolecular interaction N4-H9···O4 between the red and the green molecules (Figure 7.101, bottom).

	30K	180K	220K	260K	300K
a	7.7343(2) Å	7.8050(2) Å	7.8136(4) Å	7.8612(4) Å	7.9263(6) Å
b	16.0426(3) Å	16.1051(3) Å	16.1401(6) Å	16.1636(5) Å	16.1871(10) Å
c	16.3434(4) Å	16.3945(3) Å	16.4066(7) Å	16.4040(6) Å	16.4189(10) Å
α	63.8400(10)˚	64.2570(10)˚	64.522(2)˚	64.774(2)˚	64.754(3)˚
β	85.1630(10)˚	86.9730(10)˚	87.922(3)˚	88.594(2)˚	88.846(4)˚
γ	81.6150(10)˚	83.6530(10)˚	84.707(3)˚	85.523(2)˚	85.656(4)˚
V	1800.23(7) Å	1844.86(7) Å	1859.88(14) Å	1879.76(13) Å	1899.7(2) Å

Table 7.64. *Unit cell parameters of triclinic-C3CBA at the five temperatures of data collection, derived from the SND experiments.*

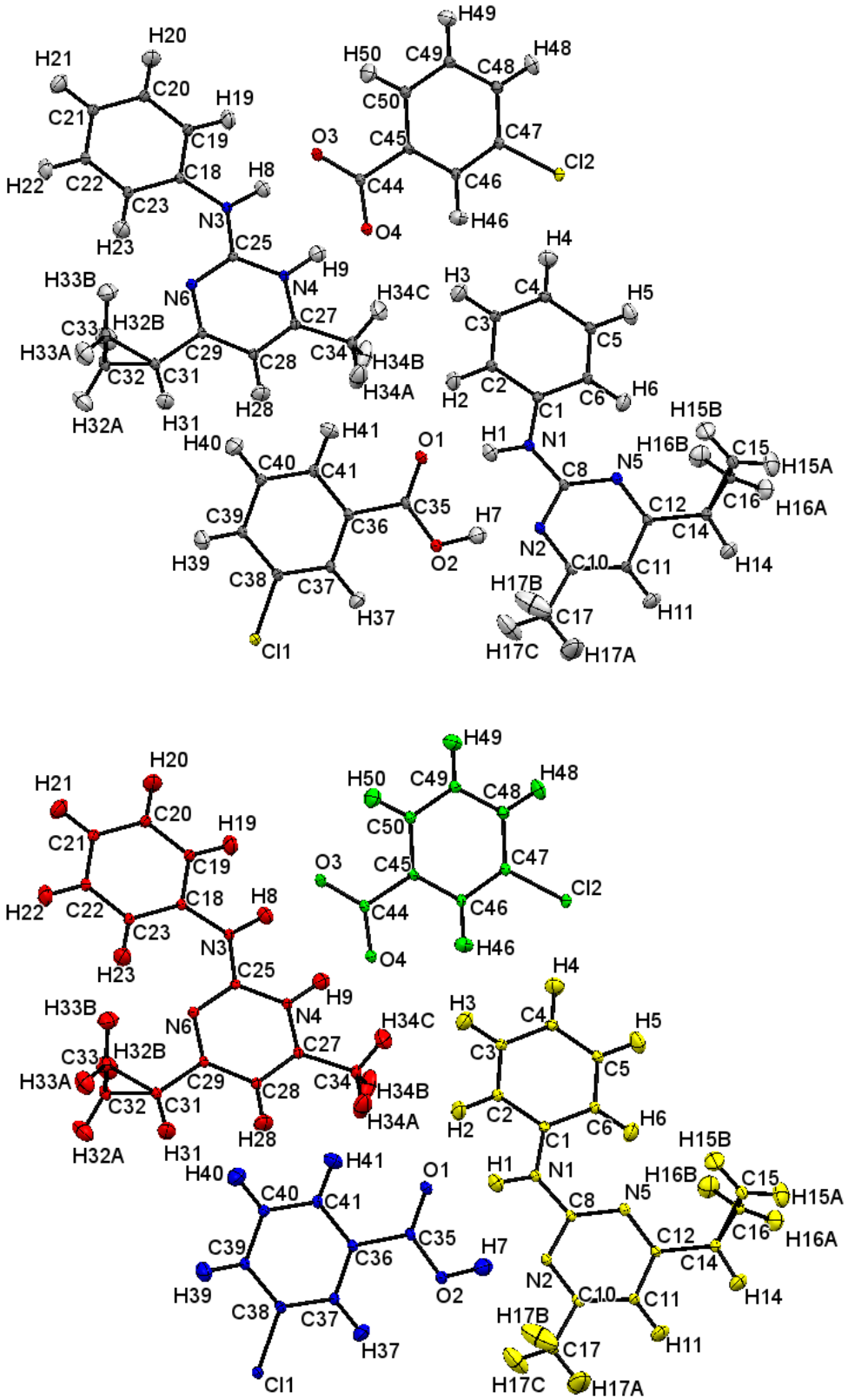

Figure 7.101. *On top: ORTEP representation of the asymmetric unit of triclinic C3CBA-I, viewed along the* ***a****-axis, derived from SND at 30K. On bottom: the molecules are displayed in different colours to facilitate discrimination among them. The probability level for all ellipsoids is 50%.*

	30K	180K	220K	260K	300K
Yellow molecule					
C8-N1-C1-C6	2.6(2)˚	1.3(4)˚	0.6(4)˚	0.6(6)˚	-0.9(6)˚
N5-C12-C14-C15	-26.6(2)˚	-27.2(4)˚	-26.9(4)˚	-27.2(5)˚	-27.9(5)˚
N5-C12-C14-C16	42.6(2)˚	41.5(4)˚	41.9(4)˚	41.5(5)˚	41.4(5)˚
C8-N5-C12-C14	-178.2(1)˚	-178.9(2)˚	-179.7(2)˚	-179.7(3)˚	-179.9(3)˚
N2-C8-N1-H1	7.4(3)˚	5.0(5)˚	5.0(5)˚	2.3(6)˚	2.6(6)˚
Red molecule					
C18-N3-C25-N6	-4.2(2)˚	-2.1(4)˚	-1.2(4)˚	-0.2(5)˚	-0.2(5)˚
N6-C29-C31-C32	-26.4(2)˚	-27.8(4)˚	-29.3(3)˚	-28.9(5)˚	-29.8(5)˚
N6-C29-C31-C33	41.5(2)˚	40.2(4)˚	39.2(3)˚	39.6(5)˚	38.1(5)˚
C25-N6-C29-C31	-177.1(1)˚	-177.9(2)˚	-178.0(2)˚	-178.4(3)˚	-178.0(3)˚
N4-C25-N3-H8	-3.7(3)˚	-2.3(5)˚	-0.9(5)˚	-0.8(6)˚	-0.6(6)˚
N3-C25-N4-H9	-4.4(3)˚	-3.2(6)˚	-2.3(5)˚	-2.7(7)˚	-3.7(7)˚
N4-H9	1.110(3) Å	1.189(9) Å	1.292(9) Å	1.39(1) Å	1.43(1) Å
Blue molecule					
O2-C35-C35-C37	-5.0(2)˚	-5.2(4)˚	-3.7(4)˚	-2.1(6)˚	-2.8(6)˚
C35-C36-C37-C38	177.6(1)˚	178.4(3)˚	179.1(2)˚	179.6(3)˚	179.5(3)˚
C35-C36-C41-C40	-177.9(1)˚	-178.7(3)˚	-178.8(3)˚	-178.9(4)˚	-178.8(4)˚
C35-O1	1.226(2) Å	1.226(4) Å	1.221(4) Å	1.221(5) Å	1.211(6) Å
C35-O2	1.312(3) Å	1.298(6) Å	1.304(6) Å	1.289(7) Å	1.296(8) Å
Green molecule					
O4-C44-C45-C46	10.5(2)˚	8.2(5)˚	7.9(4)˚	6.0(6)˚	5.3(6)˚
C44-C45-C46-C47	-178.5(1)˚	-179.5(3)˚	-179.6(3)˚	-180.0(4)˚	-179.8(4)˚
C44-C45-C50-C49	178.4(1)˚	178.5(3)˚	179.2(2)˚	179.4(4)˚	178.5(4)˚
C44-O3	1.254(3) Å	1.227(7) Å	1.230(6) Å	1.224(8) Å	1.228(9) Å
C44-O4	1.267(2) Å	1.278(5) Å	1.281(5) Å	1.285(6) Å	1.283(6) Å

Table 7.65. *Torsion angles and bond lengths of interest, derived from SND experiments at the five collection temperatures. The colours refer to Figure 7.101.*

The conformation of the two cyprodinil molecules, shown in yellow and red, is similar: the benzene and the pyrimidine rings are not positioned on the same plane, but the former is twisted by 2.6(2)˚ in the yellow molecule and by 4.2(2)˚ in the red one so to avoid hindrance caused by the large dimensions of the cyclopropyl substituent, which is de-centred in respect to the plane containing the pyrimidine moiety. The carbon structure of both molecules is retained without significant variations from 30K to 300K, apart for the position of the hydrogen atoms on the amino groups of two cyprodinil molecules, H1 and H3, which become more in plane with the remainder of the molecule at 300K.

The two molecules of 3-chlorobenzoic acid (shown in blue and green) display an almost perfect planarity and, contrary to the case of C2CBA, the carboxylic groups are only slightly twisted in respect to the benzene ring due to the fact that the chlorine atom is placed in the *meta* position. The two C-O covalent bonds of the carboxylic group on the blue molecule are subjected to a slight apparent shortening caused by the larger thermal vibration of the carbon and oxygen atoms as a result of the increasing temperature and they are reasonable values for a single and a double bond, indicating that the acid is in its neutral state. Conversely, the bond lengths of C44-O3 and C44-O4 in the green molecule change throughout the variable temperature experiment: indeed, at 30K they indicate that the transfer of a proton from the hydroxyl group to the nitrogen atom of a neighbouring cyprodinil molecule occurred, while already in the structure recorded at 180K they appear to be closer in value to a single and a double bond, respectively, suggesting that a migration of the proton H9 back to the hydroxyl group is taking place and that the hydrogen atom position may be tuneable by varying the temperature. The hypothesis of the proton migration is confirmed by the progressive lengthening of the N4-H9 bond that from 1.110(3) Å at 30K becomes 1.43(1) Å at 300K. The behaviour of atom H9 is clearly visible from both electron-density and nucleon-density maps, which are reported in Figures 7.102 and 7.103, and from the size and shape of the anisotropic ADP of atom H9 produced by the treatment of the SND data sets (Figure 7.104).

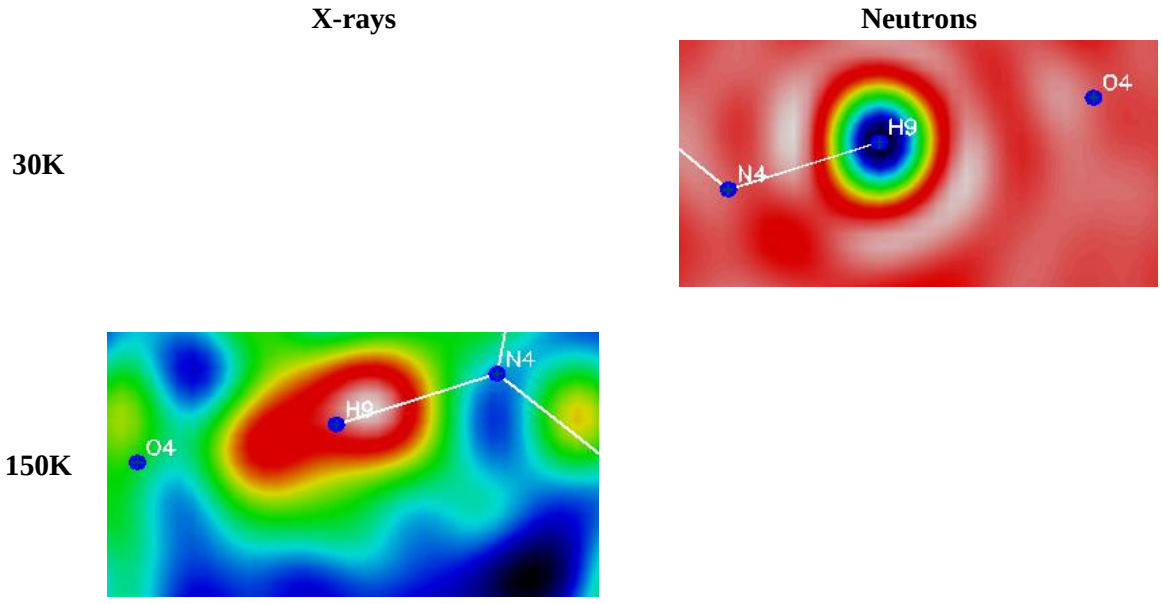

Figure 7.102. *Difference electron-density (left) and nucleon-density (right) maps for the hydrogen bond N4-H9···O4 at 30K and 150K. Atom H9 was excluded from the refinement, but its coordinates were superimposed on the images.*

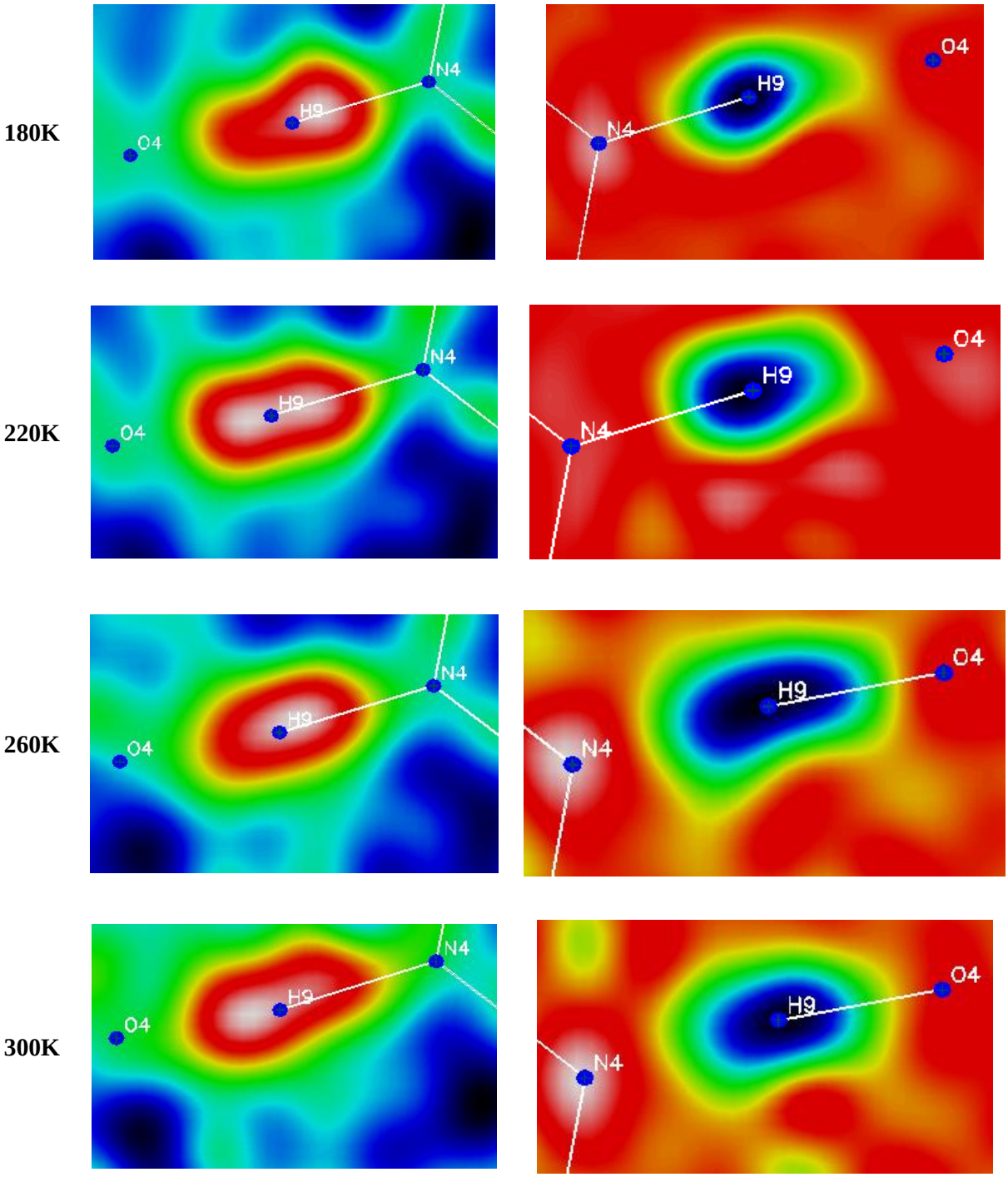

Figure 7.103. *Difference electron-density (left) and nucleon-density (right) maps for the hydrogen bond N4-H9···O4 at 180, 220, 260, and 300K. Atom H9 was excluded from the refinement, but its coordinates were superimposed on the images.*

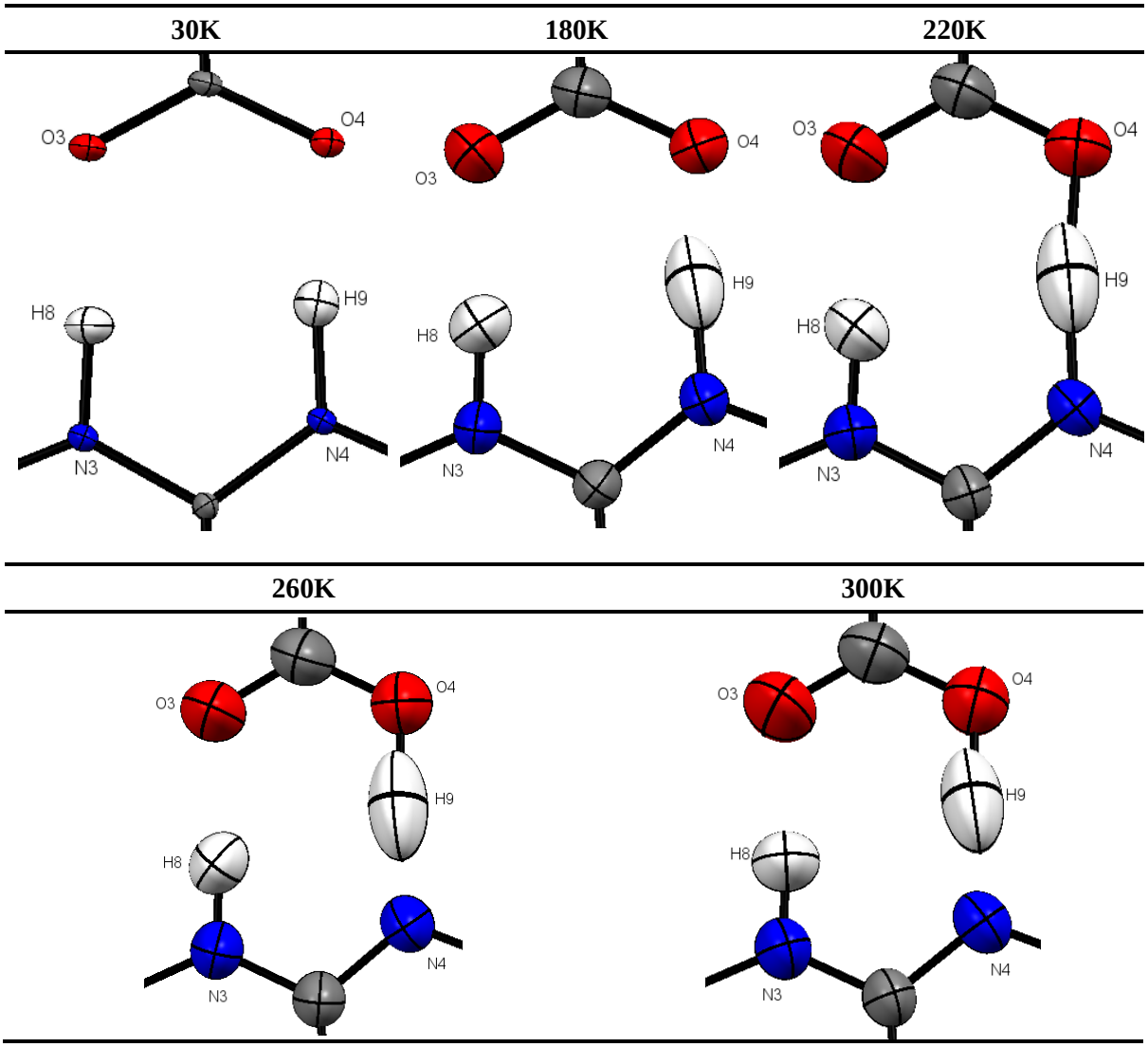

Figure 7.104. *ORTEP representations of the interacting section in a heterogeneous dimer, formed by the red and the green molecules.*

As shown in Figures 7.102, 7.103 and 7.104, at the temperature of 30K the hydrogen atom H9 is bonded to the pyrimidine nitrogen N4 of cyprodinil and the shape and size of its ADP indicate the presence of only one site and the absence of migration. The change in the interatomic connectivity occurs between 220K and 260K, which is in accordance with the results of the DSC analysis that showed an endothermic event around 250K. The elongation of the nucleon density reaches its maximum at 260K and it appears to be more compact at 300K.

The other hydrogen atoms involved in intermolecular hydrogen bonds, H1, H3 and H7, do not show the same behaviour as H9, as displayed in Figure 7.105, probably because of the longer intermolecular distances between nitrogen and oxygen atoms compared to N4···O4.

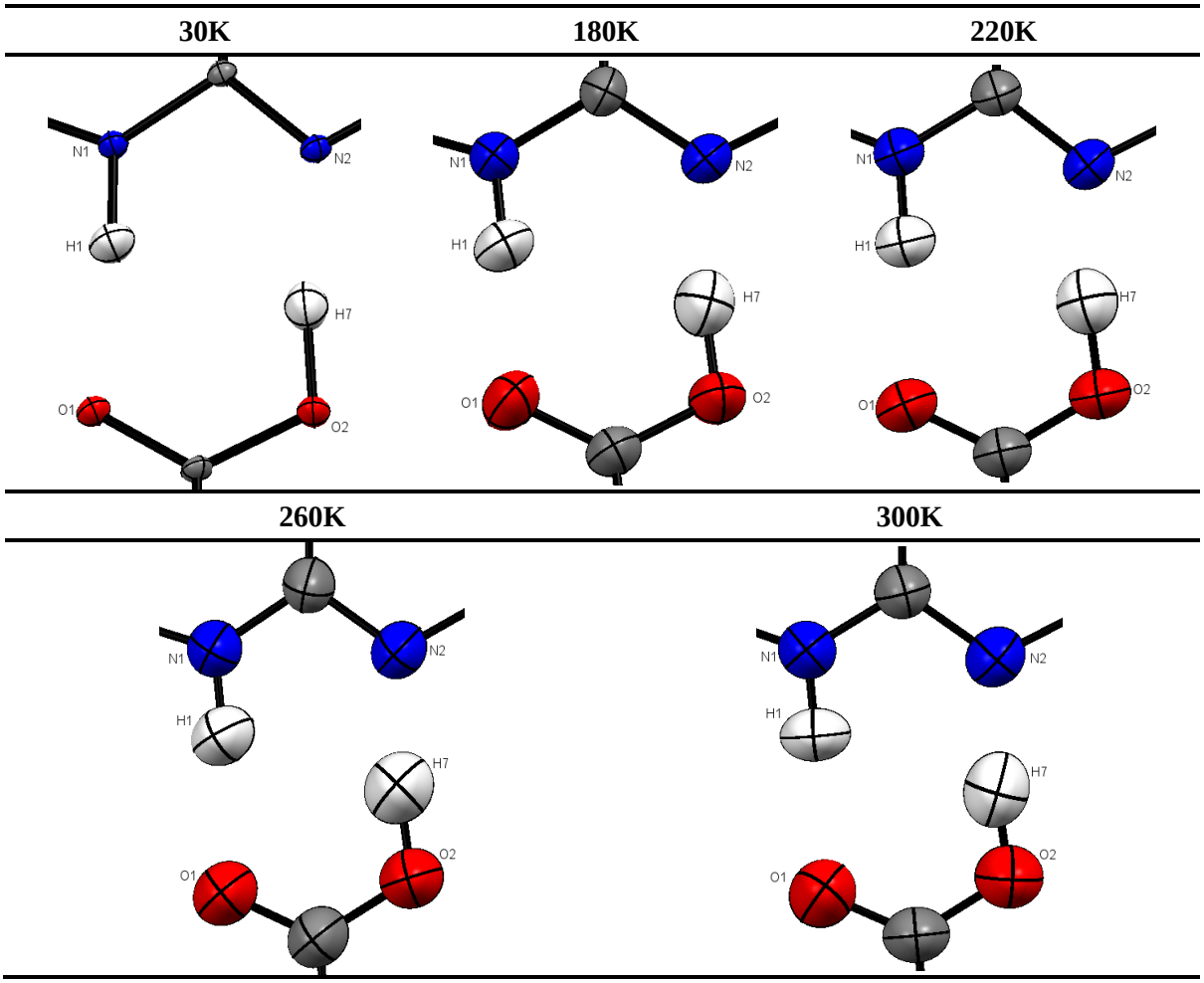

Figure 7.105. *ORTEP representations of the interacting section in a heterogeneous dimer, formed by the yellow and the blue molecules.*

Considering the hydrogen bond lengths, the donor-acceptor distances and the geometry of interaction, which are listed in Table 7.66, it is possible to identify the three hydrogen bonds N1-H1···O1, O2-H7···N2, and N3-H8···O3, as of moderate strength, whereas N4-H9···O4 is a strong hydrogen bond[74].

	30K	180K	220K	260K	300K
N1-H1	1.029(4) Å	1.024(6) Å	1.018(6) Å	1.020(7) Å	1.007(8) Å
H1···O1	1.864(4) Å	1.866(8) Å	1.875(8) Å	1.865(9) Å	1.89(1) Å
N1-H1···O1	171.4(3)˚	172.5(6)˚	174.5(6)˚	173.6(7)˚	174.6(7)˚
N1···O1	2.886(2) Å	2.885(5) Å	2.890(5) Å	2.881(6) Å	2.896(7) Å
O2-H7	1.060(4) Å	1.051(8) Å	1.064(8) Å	1.05(1) Å	1.05(1) Å
H7···N2	1.574(4) Å	1.588(8) Å	1.565(8) Å	1.58(1) Å	1.58(1) Å
O2-H7···N2	171.9(4)˚	171.2(8)˚	171.3(7)˚	171.6(9)˚	172(1)˚
O2···N2	2.628(2) Å	2.632(4) Å	2.621(4) Å	2.626(5) Å	2.621(6) Å
N3-H8	1.050(3) Å	1.046(6) Å	1.016(6) Å	1.012(7) Å	1.006(7) Å
H8···O3	1.666(3) Å	1.707(7) Å	1.747(7) Å	1.765(8) Å	1.786(9) Å
N3-H8···O3	175.4(3)˚	175.8(6)˚	175.4(6)˚	176.5(7)˚	176.2(7)˚
N3···O3	2.714(2) Å	2.752(5) Å	2.760(4) Å	2.776(6) Å	2.790(6) Å
N4-H9	1.110(3) Å	1.189(9) Å	1.292(9) Å	1.39(1) Å	1.43(1) Å
H9···O4	1.531(4) Å	1.42(1) Å	1.32(1) Å	1.21(1) Å	1.18(1) Å
N4-H9···O4	173.6(3)˚	173.4(8)˚	172.6(8)˚	173(1)˚	174(1)˚
O4···N4	2.637(2) Å	2.601(4) Å	2.605(4) Å	2.601(5) Å	2.606(6) Å

Table 7.66. *Hydrogen bond lengths and geometry of interactions. These results derive from SND experiments.*

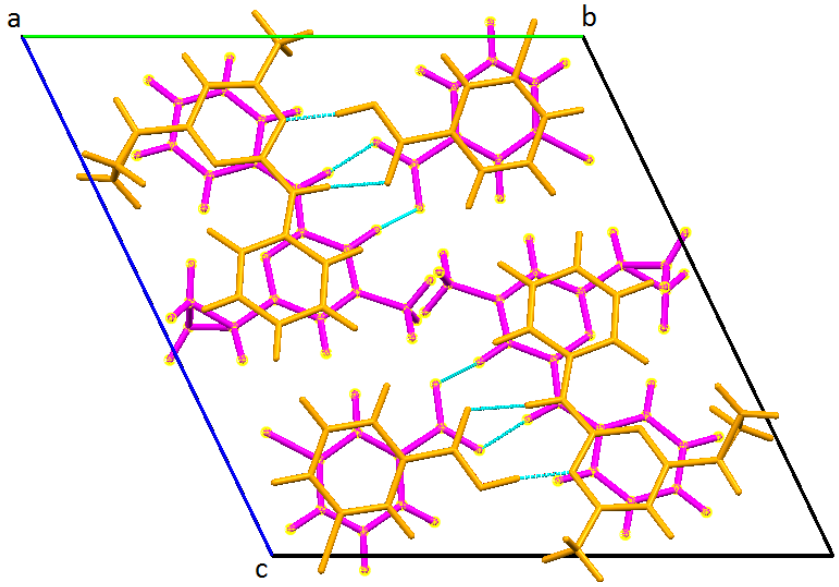

Figure 7.106. *Crystal packing of triclinic-C3CBA at 30K, viewed along the* ***a****-axis.*

The crystal packing of triclinic C3CBA-I is formed by the organisation of the cyprodinil and acid molecules into heterogeneous dimers, interacting *via* circular hydrogen bonds, as shown in Figure 7.106. It is possible to discriminate two types of dimer: one is given by the interaction of cyprodinil and acid molecules in their neutral state (highlighted in orange), while a second type displays the

carboxylate anion and the protonated cyprodinil (in magenta). The dimers arrange into parallel planes so that the neutral dimer coincides with an ionic one on the plane below.

7.5.3.2.2. Monoclinic form (C3CBA-II)

Crystals of monoclinic C3CBA-II grow into the space group ***P2$_1$/c*** and they display two molecules in the asymmetric unit, one of cyprodinil and one of 3-chlorobenzoic acid, forming a dimer, as shown in Figure 7.107 for the structure derived from SXD results. Tables 7.67 and 7.68 report a list of torsion angles and bond lengths of interest at 150, 220, and 300K.

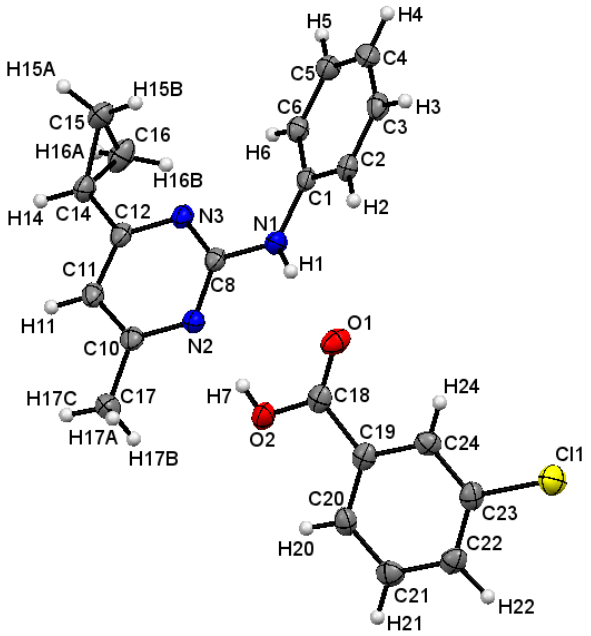

Figure 7.107. *ORTEP representation of the asymmetric unit of monoclinic C3CBA-II, viewed along the* ***b****-axis, derived from SXD at 150K. The probability level for all non-hydrogen ellipsoids is 50%, while the hydrogen atoms are drawn as fixed-size spheres of radius 0.15 Å.*

	150K	**220K**	**300K**
C8-N1-C1-C6	-33.2(4)˚	-32.9(4)˚	-32.0(4)˚
N3-C12-C14-C15	-24.8(3)˚	-24.8(3)˚	-24.9(4)˚
N3-C12-C14-C16	43.5(3)˚	43.5(3)˚	43.3(4)˚
C8-N3-C12-C14	-178.9(2)˚	-178.7(2)˚	-179.0(2)˚
N2-C8-N1-H1	-6(2)˚	-6(2)˚	-6(2)˚
N3-C8-N1-C1	14.6(3)˚	14.0(3)˚	13.5(4)˚
C6-C1-N1-C8	-33.2(4)˚	-32.9(4)˚	-32.0(4)˚

Table 7.67. *Torsion angles and bond lengths of interest of the cyprodinil molecule. The results derive from SXD measurements.*

	150K	220K	300K
O2-C18-C19-C24	-4.8(3)˚	-4.1(3)˚	-3.8(4)˚
C18-C19-C24-C23	-174.5(2)˚	-174.9(2)˚	-175.0(2)˚
C18-C19-C20-C21	174.7(2)˚	175.1(2)˚	175.3(2)˚
C18-O1	1.215(3) Å	1.215(3) Å	1.214(3) Å
C18-O2	1.307(3) Å	1.309(3) Å	1.304(4) Å

Table 7.68. *Torsion angles and bond lengths of interest of the acid molecule. The results derive from SXD measurements.*

The conformation of the cyprodinil molecule is very different from the one displayed in C2CBA and in the triclinic form of C3CBA. Not only is the benzene ring not positioned on the same plane as the pyrimidine ring, but it is also twisted inward with a torsion angle C6-C1-N1-C8 of -33.2(4)˚. The cyclopropyl substituent is not centred in respect to the pyrimidine moiety to avoid hindrance with the benzene ring.

The acid molecule retains the typical planar conformation of all aromatic compounds and the substitution in the *meta* position makes the carboxylic group to be only slightly rotated along the C18-C19 single bond, allowing delocalisation of the electron cloud over the entire molecule. The values for the covalent bonds in the carboxylic group, C18-O1 and C18-O2, indicate the presence of a single and a double bond, respectively, confirming that the acid molecules are in their neutral state. The molecules of both components retain their conformation with the temperature increase.

The three-dimensional arrangement of this co-crystal displays the organisation of cyprodinil and acid molecules in heterogeneous dimer, formed by the interaction of the aminoprymidine moiety of cyprodinil with the carboxylic group of 3-chlorobenzoic acid. Contrary to the case of the triclinic form of C3CBA, the conformation of the dimer is not co-planar, but it is highly twisted, as shown in Figure 7.108. This is reflected in the formation of longer hydrogen bonds compared to the triclinic polymorph, as reported in Table 7.69, which lists hydrogen bond lengths and geometry of interaction. The dimers arrange into alternate, parallel lines, forming a fishbone motif, as reported in Figure 7.109.

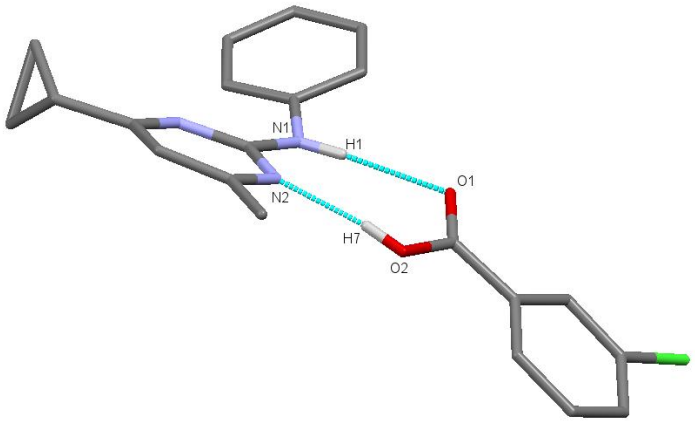

Figure 7.108. *Heterogeneous dimer in a crystal of monoclinic-C3CBA at 150K. The hydrogen atoms, except H1 and H7 , were hidden to allow better visualisation of the dimer conformation.*

	150K	220K	300K
N1-H1	0.84(3) Å	0.81(3) Å	0.80(2) Å
H1···O1	2.06(3) Å	2.11(3) Å	2.12(2) Å
N1-H1···O1	174(3)˚	174(3)˚	175(3)˚
N1···O1	2.893(2) Å	2.910(2) Å	2.922(3) Å
O2-H7	0.78(3) Å	0.82(3) Å	0.75(3) Å
H7···N2	1.82(3) Å	1.81(3) Å	1.90(3) Å
O2-H7···N2	173(4)˚	169(4)˚	165(4)˚
O2···N2	2.601(2) Å	2.622(2) Å	2.631(2) Å

Table 7.69. *Hydrogen bond lengths and geometry of interaction in a crystal of monoclinic-C3CBA.*

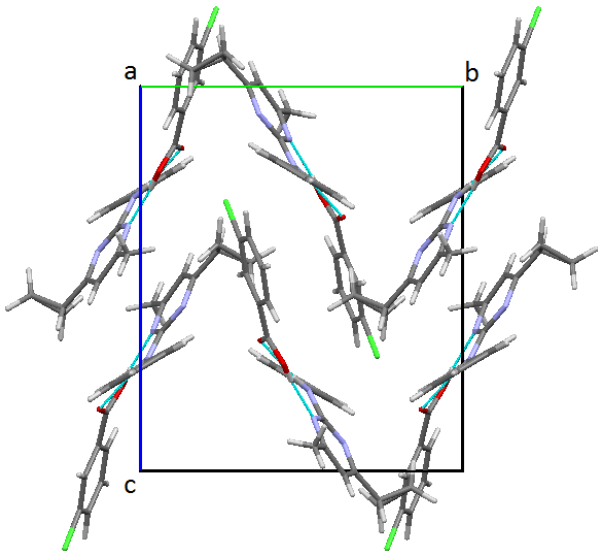

Figure 7.109. *Crystal packing of monoclinic C3CBA-II, viewed along the* ***a****-axis.*

Investigation of the electron-density of the two hydrogen atoms that are involved in the intermolecular interactions, H1 and H7, shows the absence of proton migration or positional disorder in the structure at each data collection temperature. In fact, by observing the electron-density maps reported in Figure 7.110, the size of the electron densities indicates the presence of only one site for each hydrogen atom and the shape is slightly elongated towards the interacting molecule, confirming that an intermolecular hydrogen bond exists.

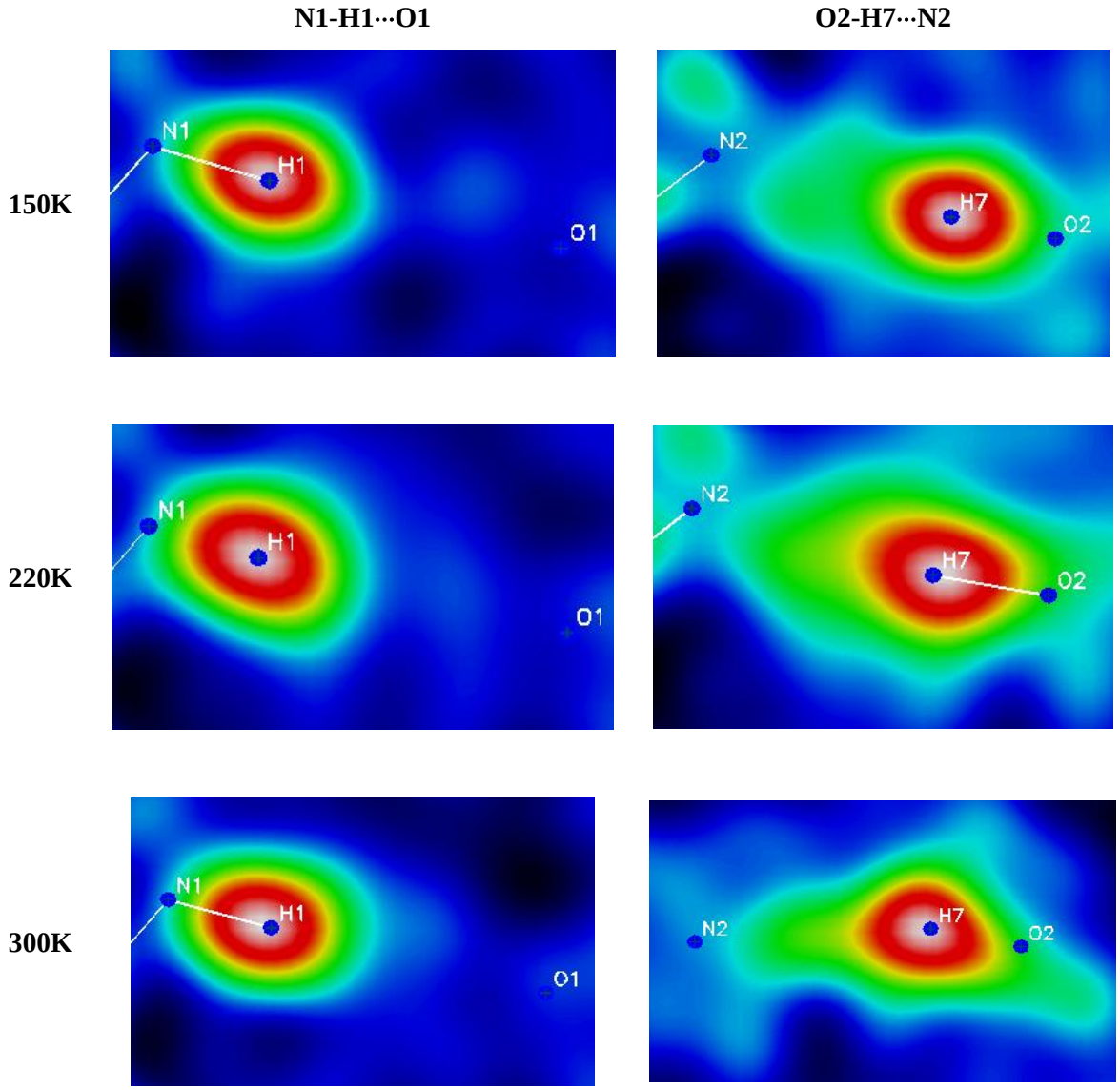

Figure 7.110. *Difference electron-density maps at 150, 220, and 300K for the two hydrogen bonds, N1-H1···O1 and O2-H7···N2. Atoms H1 and H7 were excluded from the refinement, but their coordinates were superimposed on the images.*

7.5.3.3. Cyprodinil / 4-chorobenzoic acid (C4CBA)

The co-crystal C4CBA crystallises in the orthorhombic system, space group ***P2$_1$2$_1$2$_1$***, and it displays two molecules in the asymmetric unit: one of cyprodinil and one of 4-chlorobenzoic acid, as shown in Figure 7.111 for the structure studied with X-ray radiation. Table 7.70 lists torsion angles and bond lengths of interest.

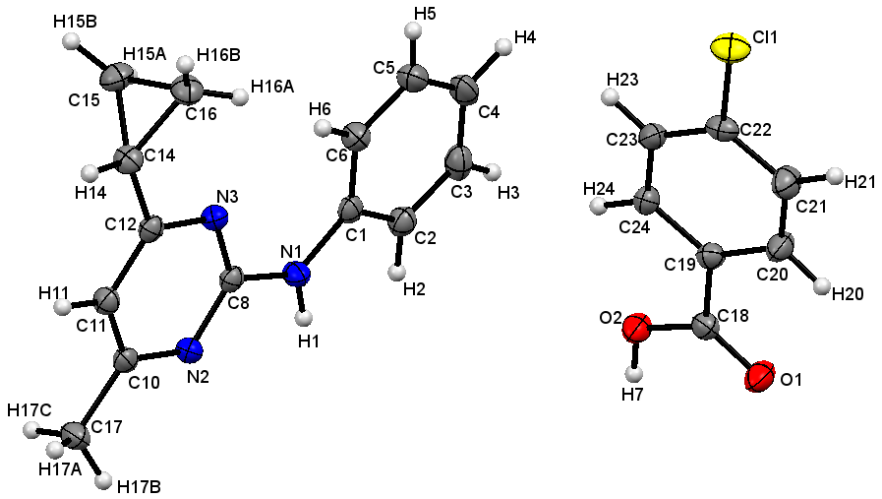

Figure 7.111. *ORTEP representation of the asymmetric unit of monoclinic C4CBA, viewed along the* ***b****-axis, derived from SXD at 150K. The probability level for all non-hydrogen ellipsoids is 50%, while the hydrogen atoms are drawn as fixed-size spheres of radius 0.15 Å.*

C8-N1-C1-C6	10.1(3)˚
N3-C12-C14-C15	50.1(2)˚
N3-C12-C14-C16	-17.6(2)˚
C8-N3-C12-C14	-176.3(1)˚
N2-C8-N1-H1	-3(2)˚
O2-C18-C19-C24	-179.5(2)˚
C18-C19-C24-C23	-179.1(2)˚
C18-C19-C20-C21	179.0(2)˚
C18-O1	1.220(2) Å
C18-O2	1.313(2) Å

Table 7.70. *Torsion angles and bond lengths of interest.*

The conformation of the cyprodinil molecule is similar to that described in the C2CBA crystals: the benzene and the pyrimidine rings are twisted with respect to one another by 10.1(3)˚, which forces the cyclopropyl substituent to be de-centred in respect to the pyrimidine moiety.

The planarity of the acid molecule is almost perfect and the substitution in the *para* position allows the benzene ring and the carboxylic group to be on the same plane. The bond lengths for C18-O1 and C18-O2 are reasonable values for a single, C-O, and a double, C=O, bond, respectively, confirming that the molecules are present in their neutral state.

Intermolecular hydrogen bonds, featuring the amino group on cyprodinil and the hydroxyl on the acid as hydrogen donor and the carbonyl moiety and the nitrogen atom on the pyrimidine ring as acceptors, lead to the formation of heterogeneous dimers, as shown in Figure 7.112. In the three-dimensional crystal structure, the dimers stack themselves into off-set parallel lines with distances of 5.00(2) Å, forming a fishbone motif (Figure 7.113). In each stack, neighbouring molecular-dimers are rotated by 180˚ in respect to the one below so to avoid hindrance between the chlorine atom of one dimer and the cyclopropyl substituent of the adjacent one.

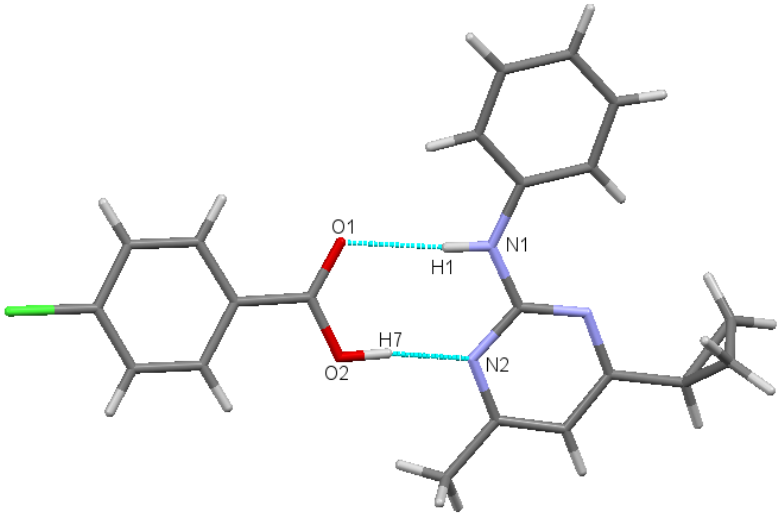

Figure 7.112. *Heterogeneous dimers in a crystal of C4CBA.*

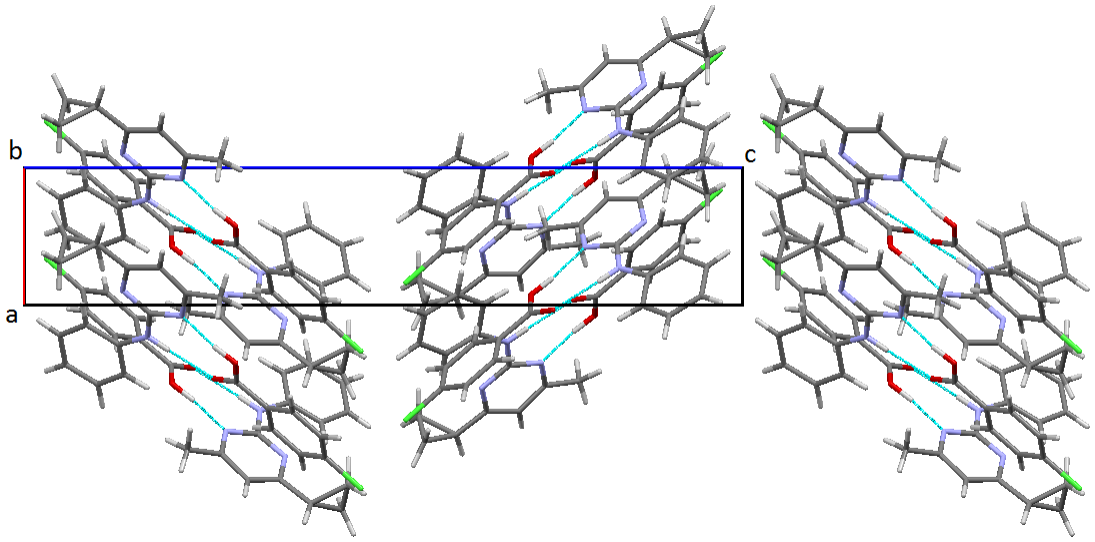

Figure 7.113. *Crystal packing of C4CBA at 150K, viewed along the* ***b****-axis.*

N1-H1	0.87(2) Å
H1···O1	2.06(2) Å
N1-H1···O1	175(2)˚
N1···O1	2.926(2) Å
O2-H7	0.94(2) Å
H7···N2	1.70(2) Å
O2-H7···N2	171(2)˚
O2···N2	2.634(2) Å

Table 7.71. *Hydrogen bond lengths and geometry of interaction in a crystal of C4CBA at 150K. The results derive from SXD measurements.*

Based on the hydrogen bond lengths, the donor-acceptor distances and the geometry of interaction, which are listed in Table 7.71, the two intermolecular interactions, N1-H1···O1 and O2-H7···N2, can be classified as moderate hydrogen bonds[81]. No proton migration or disorder are present in the structure at 150K, as confirmed by the investigation of the electron-density maps of the two hydrogen atoms, H1 and H7, as displayed in Figure 7.114.

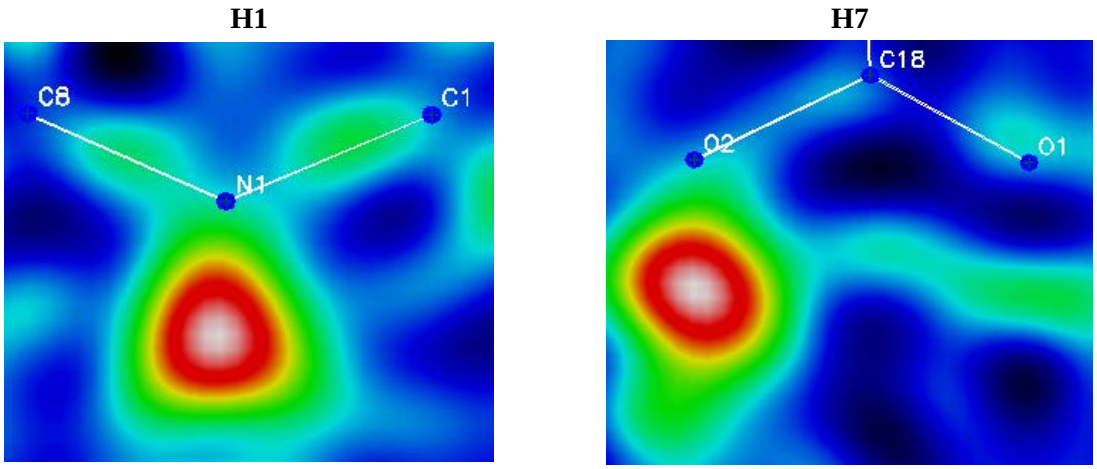

Figure 7.114. *Difference electron-density maps for the two hydrogen atoms, H1 and H7, involved in intermolecular hydrogen bonds.*

7.5.4. Effect of the chlorine substituent on benzoic acid

As explained above (***c.f. 7.5.1***), the chlorine atom exhibits inductive effect ***–I***, which indicates the ability of an electronegative atom to attract electrons. This property is reflected in the acidity of the three isomers of monosubstituted chlorobenzoic acid, 2-CBA, 3-CBA, and 4-CBA, which display pK_a[145] values of 2.90, 3.84, and 4.00, respectively, indicating that they are all more acidic than benzoic acid that has a pK_a of 4.20[145]: the electron-withdrawing power of chlorine subtracts electron density from the carboxylic group of the acid, consequently facilitating the extraction of

the proton on the hydroxyl group by a base. The effect ***–I*** decreases from the *ortho* to the *para* position, which explains the different values of the pK_a of the isomers.

Since SXD experiments at 150K were performed on all co-crystals by single crystal X-ray diffraction, it is possible to compare the crystal structures of C2CBA, triclinic-C3CBA, monoclinic-C3CBA, and C4CBA to assess whether the presence of the chlorine substituent in different positions has an effect on the three-dimensional molecular arrangement. The organisation of the molecules of the two components of each co-crystal in heterogeneous dimers stacked into parallel lines, which are shifted in respect to one another forming a fishbone motif, is similar in all co-crystals. The main differences can be found in the characteristics that the hydrogen bonding network displays in the four molecular complexes. In Table 7.72, a summary of the hydrogen bond lengths and donor-acceptor distances is reported.

	C2CBA	**Triclinic C3CBA-I**	**Monoclinic C3CBA-II**	**C4CBA**
N1-H1	0.91(6) Å	0.88(3) Å	0.84(3) Å	0.87(2) Å
H1···O1	1.97(6) Å	2.01(3) Å	2.06(3) Å	2.06(2) Å
N1···O1	2.885(5) Å	2.892(3) Å	2.893(2) Å	2.926(2) Å
O2-H7	1.80(7) Å	1.05(3) Å	0.78(3) Å	0.94(2) Å
H7···N2	0.78(7) Å	1.58(4) Å	1.82(3) Å	1.70(2) Å
O2···N2	2.567(6) Å	2.625(3) Å	2.601(2) Å	2.634(2) Å
N3-H8		0.90(2) Å		
H8···O3		1.85(2) Å		
N3···O3		2.744(2) Å		
N4-H9		1.19(3) Å		
H9···O4		1.43(3) Å		
O4···N4		2.614(2) Å		

Table 7.72. *Hydrogen bond lengths and donor-acceptor distances in the four co-crystals at 150K, derived from SXD measurements.*

The higher acidity of 2-CBA compared to benzoic acid causes a proton transfer from the hydroxyl group of the acid to the nitrogen atom on the pyrimidine ring of cyprodinil, while in the cases of 3-CBA and 4-CBA there is no sign of proton transfer and the molecules are present in their neutral state. An exception is represent by the triclinic from of C3CBA-I, where half the molecules of 3-CBA are present as carboxylate anions, although the large value for the bond length N4-H9 of 1.19(3) Å suggests that the hydrogen atom H9 might be subjected to partial migration back towards the carboxylic group. This is probably due to the fact that the oxygen-nitrogen distance is shorter in the ionic dimer (N4···O4) than in the neutral one (N3···O3): 2.614(2) Å for the former and 2.625(3) Å for the latter. The lack of proton transfer in the monoclinic modification of C3CBA can be

explained considering the geometry of the heterogeneous dimer: indeed, the high distortion from planarity of the two interacting moieties, the aminopyrimidine part of cyprodinil and the carboxyl of the acid, can prevent the proton extraction by the lone pair of electrons on the basic nitrogen atom, allowing only the formation of a moderate intermolecular hydrogen bond. The hydrogen bonding network in crystals of C4CBA reflects what is expected considering the electronic properties of 4-CBA: in fact, the decreased electron-withdrawing power of chlorine due to the *para* substitution has a minor influence on the electronic density of the carboxylic group, which, in turn, prevent the extraction of the hydrogen atom.

7.5.5. Conclusions

The aim of the study undertaken during this thesis was to assess whether the presence of a chlorine substituent on the benzoic acid had a role to play in the crystal packing of the co-crystals of the fungicide cyprodinil. *Ortho*-, *meta*- and *para*-chlorobenzoic acids were used as co-formers in the synthesis of the three co-crystals with cyprodinil. Single crystals of C2CBA, C3CBA and C4CBA were obtained in ethanol solutions by the method of slow evaporation of the solvent. A triclinic and a monoclinic modification of C3CBA were obtained. Unfortunately, the reproducibility of the synthesis of the monoclinic form was poor: indeed, all subsequent synthesis attempts led to the crystallisation exclusively of the triclinic polymorph. This is probably due to the less favourable crystal packing of the monoclinic C3CBA-II, in which the conformation of the cyprodinil molecules is unusually bent and the heterogeneous dimer highly deviates from planarity.

The crystal structure of all co-crystals was analysed by single crystal X-ray diffraction (SXD) in order to obtain the exact atomic coordinates of all non-hydrogen atoms. The molecular arrangement in the three-dimensional long-range order of the crystal is similar in all four molecular complexes: the cyprodinil and the acid molecules organise into heterogeneous dimers interacting through the formation of intermolecular hydrogen bonds between the aminopyrimidine moiety of cyprodinil and the carboxyl group of the acid. An additional variable temperature (VT) single crystal neutron diffraction (SND) experiment was performed on the triclinic modification of C3CBA-I in order to obtain a better characterisation of the hydrogen bonding network of the material. In fact, by interacting directly with the nuclei of atoms, neutrons allow a ten-fold improvement in the precision of the hydrogen atoms positions and increased accuracy. The VT-SND study showed the transfer of a proton (H9) from the carboxyl group to the cyprodinil molecule at 30K, only to highlight the migration of the same proton back to the 3-chlorobenzoic acid molecule as a function of temperature: the change of atomic connectivity occurs between 220K and 260K, as suggested by the endothermic event at 250K recorded during the DSC analysis.

The effect of the chlorine substituent in different positions of the benzene ring appears to be evident: as expected from the electronic properties of the co-formers, the higher acidity of 2-CBA

causes the formation of a salt, while the minor ***–I*** effect due to the para-substitution in C4CBA results in moderate hydrogen bonds between molecules in their neutral state. Interesting is the behaviour of the hydrogen bonding network when the co-former is 3-CBA, which seem to exhibit electronic properties that are intermediate between those of 2-CBA and 4-CBA.

Chapter 8

8. Conclusions and future work

8.1. Conclusions

The interest towards the phenomenon of polymorphism has grown greatly over the years. The possibility to be able to control the crystal structure of a solid material, so that the material in question may exhibit desired physical properties, opened a new field of research, especially from an industrial and commercial point of view. Investigation of polymorphism in pharmaceuticals is just an example of the applicative potential of this phenomenon. Many other sectors can be highly affected by the presence of polymorphism, such as food industry, explosives, pigments and agrochemicals. The main purpose of the study of polymorphism in an applied field is the recognition of the most stable and, possibly, efficient form. Thinking about pharmaceuticals, it is not hard to understand why: not only must the drug exhibit the function for which it was created in the first place, but it also has to be in a form available to the body, with a minimum number of side effects, and stable over time. The same principles can be extended to the other fields mentioned above: explosives must be stable enough over a range of temperature and pressure to allow a safe handling and manipulation; agrochemicals, once in waters or soil, should follow degradation processes that lead to the formation of non-toxic products and should also be more efficient so to contain the quantities used. All these characteristics and physical properties are strictly related to the arrangement that the molecules in question assume in the long-range order of a crystalline material. Finding the feature responsible for this correlation might enable to direct the creation of a particular crystal structure, which can lead to particular physical properties.

In order to achieve such ability, the right techniques to investigate the solid state must be employed. Various spectroscopies, such as IR and Raman spectroscopy or NMR, are useful instruments for the characterisation of the solid state. However, only by the use of X-ray and neutron diffraction, a plain understanding on how the crystal order is organised and how atoms, molecules or ions obey to that order can be achieved. Fundamental for the recognition and discrimination of polymorphs is powder diffraction, which gives the fingerprint of a certain crystalline material. For a more in depth knowledge about the position of atoms, molecules or ions inside the crystal and of the atomic displacement parameters, which characterise the thermal motion of the compound, single crystal diffraction experiments can be performed; such experiments are able to describe the whole crystal and the symmetry that governs its order.

The work carried out in this thesis is valid proof of what the study of diffraction by crystalline materials can achieve. Not only a valid model for the crystals studied with single crystal X-ray

diffraction can be created, but also comprehension on the feature that governs the structure, that is the hydrogen bonding network, can be reached, and, by using single crystal neutron diffraction, improvement by orders of magnitude in the accuracy and precision in its definition can be obtained. In this context, neutrons really are the best probe to investigate and understand organic materials.

8.1.1. Polymorphism in agrochemicals

Although extensive studies have been undertaken on the research of possible degradation pathways followed by herbicides and fungicides to achieve complete detoxication of these substances by microorganisms or by photolysis processes with the formation of non-toxic products, scarce knowledge on the structure of these active materials, and consequently on the variation of their physical properties upon changes in the crystal structure, is available. A practical problem related to the occurrence of polymorphism in agrochemicals, such as pendimethalin and cyprodinil, is the variation of the particle size distribution during the conversion from one form to another, causing problems related both to the stability of the formulation of these materials, usually prepared as wettable suspensions, and to their application on the field, due to the formation of particle aggregates that obstruct the nozzle of delivery equipment. For this reason the work presented in this thesis focused on the structural characterisation of the key features responsible for the self-assembly of the molecular compounds taken understudy, in this case the hydrogen bond, in order to combine the need of stability of the product over time and storage with the requirement of complete detoxication of these substances in the environment, without altering the agrochemical function of the active molecules.

All performed experiments exhibit encouraging results on the effect that intra- and inter-molecular interactions have on the arrangement of molecules within a crystal structure. Illustrating are, for example, the cases of the herbicide pendimethalin (PDM) and the fungicide cyprodinil (CYP), in which the phenomenon of polymorphism is allowed by the formation of different hydrogen bonding networks. The two polymorphs of PDM display what is usually defined as *conformational polymorphism*, where different crystal structures are the result of a different conformation that the active molecules display in the crystal packing of different polymorphs. In particular, in the case of pendimethalin, the main difference between the molecular conformations exhibited in the two forms is represented by an increase of around 2(1)˚ of the torsion angle of the amino group involved in the intramolecular hydrogen bond in the yellow-PDM. This apparent minor change in the conformation of the PDM molecules is sufficient for the formation of a different crystal structure, which displays a weaker and longer intramolecular hydrogen bond than orange-PDM. This difference is reflected on the physical properties of this material, for example the colour and the temperature of fusion. The different colours for the stable and metastable modifications of PDM, orange and yellow respectively, are a consequence of a different level of planarity of the

intramolecular hydrogen bond between the amino and the nitro groups of the same molecule. The more planar conformation adopted by the PDM molecules in the orange polymorph allows increased delocalisation of the lone-pair of electrons of the nitrogen atom onto the aromatic ring causing a different colour. Computational calculations, based on the experimental single crystal X-ray results, show close values of the internal energy for the two forms, explaining their close melting points, ~54˚C and ~56˚C for the orange and yellow modifications respectively, and validating the occurrence of a polymorphic transformation during storage and transport, where temperature of 50˚-60˚C are easily reached. Unfortunately, time restriction and low availability of the sample did not allow a detailed characterisation of the phase transition temperature that could be achieved by powder neutron diffraction, which would provide important knowledge on the stability of each form in a specific range of temperature, allowing the formulation of strategies that could slow or even prevent the polymorphic transition, such as controlled refrigeration or co-crystallisation routes. However, valuable information can be obtained by single crystal neutron diffraction (SND). Although single crystal neutron data are available only for the yellow-PDM, they show the advantages provided by neutrons in the study of hydrogen bonded compounds in terms of increased accuracy and precision in the definition of the atomic coordinates of the hydrogen atoms, allowing the production of a model that can be used for theoretical studies on energetics and crystal structure prediction, contributing to formalise hypothesis on how to prevent the problems arisen by a polymorphic transformation in these systems.

A combination of single crystal neutron diffraction (SND) and variable-temperature powder neutron diffraction (VT-PND) analyses was undertaken to investigate the crystal structures of the two polymorphs of cyprodinil and to study the relations that define their phase transition. The SND results confirm that the existence of a stable form A and a metastable form B resides in a different arrangement of the cyprodinil molecules, which leads to the formation of different hydrogen bonding networks: in form A, which is the lower melting form, each molecule of cyprodinil is engaged in two intermolecular, linear hydrogen bonds between the hydrogen atom of the amino group and the nitrogen atom on the pyrimidine ring of two neighbouring molecules. On the contrary, the self-assembly in crystals of form B, which display a higher melting point, is characterised by the organisation of the cyprodinil molecules in dimers held together by circular hydrogen bonds formed between the aminopyrimidine functionality. Usually, the formation of a dimeric structure is characteristic of the more stable form, but in the case of modification B of cyprodinil, the dimer is highly twisted from a planar conformation, leading to a less favourable geometry of interaction and destabilising the crystal packing. As for the case of pendimethalin, a polymorphic conversion from form A to form B poses serious inconveniences in the application of the fungicide on the field. Commercial cyprodinil is available as the lower melting form A, which, however, can convert into the metastable form B after reaching a temperature of ~71˚C. The VT-PND analysis on a sample of form A of cyprodinil allowed the accurate description of the phase

transition from form A to form B, which occurred in the solid state, and the consequent re-crystallisation of the metastable form B, which probably is the kinetically favoured form. A temperature-dependent transformation back to form A was not observed during the course of this thesis, either by DSC or PND, suggesting that conversion to the stable form can occur only after a period of storage that can last several weeks. A solution to the problems caused by the polymorphic conversion in samples of cyprodinil was attempted through co-crystallisation processes, the results of which will be discussed later in this chapter (***c.f. 8.2.2.***). PND represented also a useful tool for the observation of the crystallisation *in situ* of the thermodynamically stable form A, which was followed analysing the powder patterns collected on the high-flux powder diffractometer D20, at ILL, on a solution of modification A of cyprodinil in deutereted ethanol, which was chosen to avoid the increase of the background due to the high incoherent scattering of hydrogen. The results highlighted the formation of Bragg peaks, corresponding to form A, from the initial amorphous signal of the d_6-ethanol solution. It is interesting to notice that direct *in situ* heating of the solution already placed on the diffractometer did not lead to crystallisation of the fungicide. In fact, this was achieved only by heating the solution before mounting it to the diffractometer, suggesting that crystallisation of form A occurs by slow evaporation of the solvent.

Neutron radiation was also used for the investigation of the crystal structures of the herbicides, isoproturon (IPU), diflufenican (DFF) and glyphosate (GLY). The reasons that demanded structural studies on these materials are connected with their potential high toxicity, especially in the case of IPU. The suspected carcinogenic effect of IPU arises serious preoccupations in its application as herbicide, since IPU, which has a limited solubility in water, is easily wash out by rain as it is applied directly on the leaves of plants, accumulating in the soil and contaminating the water supplies. A solution to this problem can be found in the discovery of a different crystal form of IPU, which might exhibit higher water solubility, allowing the application of the herbicide as a solution rather than a solid, accelerating the absorption by plants and reducing the contaminated areas. In addition to the screening for unknown polymorphs, the work carried out in this thesis aimed to modify the crystal morphology of active molecule with the goal of facilitating the herbicide absorption by plants. The only SND data set at 20K available for IPU showed the formation of infinite chains of intermolecular hydrogen bonds that can be denoted using the graph-set notation (***c.f. 1.5.***) as $C_1^1(4)$, indicating the presence of one donor and one acceptor of the hydrogen bond over a total of four atoms involved in the intermolecular interaction. In the crystal packing, each molecule of IPU interacts with two neighbouring molecules through hydrogen bonds between the amide functionalities of the herbicide. This type of hydrogen bonding network, alongside π-π interactions between the aromatics rings of IPU molecules, is responsible for the stability of the crystal structure and it can explain the high melting point of ~156˚C detected by the DSC analysis in accordance with the data present in the literature. The stability of the crystal structure of IPU may explain the inconclusive results of the various crystallisation attempts

undertaken to screen for unknown polymorphs of the herbicide, which led always to the formation of the known crystal structure with the same crystal morphology of hexagonal prism. The reluctance showed by IPU in crystallise in different crystal structures is confirmed by the DSC thermal analysis that was performed on a sample of pure IPU, in which the only detected thermal events refer to the melting and re-crystallisation processes of the commercial IPU. The reason behind this behaviour is certainly related to the hydrogen bonding network described above. In fact, as stated by Etter[41], good donors and acceptors will always be used in hydrogen bonding: the amide groups of neighbouring molecules will always organise in infinite chains to create a more favourable structure, independently from the solvent used or the presence of a co-former.

A similar behaviour was observed in the case of DFF, whose crystal packing is characterised by the formation of intramolecular hydrogen bonds between the hydrogen atom of the amino group and the oxygen atom on the phenoxy ring of the same DFF molecule. No phase transition was detected by the DSC analysis in the temperature range 20-200˚C and the attempts undertaken to modify the crystal structure or the crystal morphology were unsuccessful. It is, however, interesting to notice a discrepancy between the experimental SXD structure and the one present in the CCDC database. Both structures belong to the monoclinic system, crystallising in the space group $\boldsymbol{P2_1/c}$, and show the same crystal packing. However, the value of the $\boldsymbol{\beta}$-angle in the experimental structure is 92.61(3)˚, while in the CCDC structure is 90.52(3)˚; both unit cells were collected at room temperature. The SND results showed a $\boldsymbol{\beta}$-angle of 86.761(1)˚ at 20K, increasing to 87.144(2)˚ at 120K and, finally, setting to 89.50(1)˚ at 292K. Although its value is lower than 90˚, the $\boldsymbol{\beta}$-angle found by SND measurements is closer to the CCDC structure, highlighting two possibilities: either a slightly different unit cell can be chosen for the definition of the packing of DFF crystals, or a temperature dependent variation of the crystal structure of DFF might occur, as suggested by the increase of around 3˚ of the $\boldsymbol{\beta}$-angle from 20K to 292K, detected by SND. Powder neutron diffraction (PND) represents a valid option for the study of the behaviour of the $\boldsymbol{\beta}$-angle. Unfortunately, due to unavailability of the instrumentation, it was not possible to assess whether the large variation of the $\boldsymbol{\beta}$-angle with increasing temperature could be an indication of possible hidden temperature-dependent polymorphs of DFF.

All analyses performed on IPU and DFF seem to suggest a significant contribution by the hydrogen bonding networks to the stability of the crystal structures of the two herbicides, preventing the formation of different polymorphs in the experimental conditions used during the work of this thesis. In fact, neither different organic solvents nor the presence of a co-former produce any destabilisation of the structure that could lead to changes in the self-assembly or the crystal habit.

The screening for unknown temperature-dependent polymorphs of glyphosate was undertaken using VT-PND, which allowed the investigation of possible structural changes of a sample of glyphosate and its ammonium salt over a temperature range from 4K to 440K. Interesting results were obtained on pure glyphosate, where the unusual behaviour of the cell parameter $\boldsymbol{a}$ indicates a

strict correlation between the formation of hydrogen bonds and the unit cell dimensions. The linear hydrogen bond between the carboxylic hydrogen and one oxygen atom of the phosphate group is almost perfectly aligned along the ***a***-axis. Data collected between 4K and 200K show a lengthening of the H···O distance accompanied by a gradual increase of the hydrogen bond angle, O-H···O. Since, usually, a bond angle closer to 180° causes a shortening of the hydrogen bond length, it is possible that the two interacting glyphosate molecules slightly change their relative position, sliding one on top of the other, causing a decrease of the value of the unit cell parameter ***a***. The larger thermal motion caused by continuing heating from 200K to 440K causes a relaxation of the ***a***-axis, which resumes the expected expansion at higher temperatures. This is proof that the hydrogen bonding network affects the way in which the glyphosate molecules are arranged in respect to one another, causing a bending of two interacting molecules, leading to changes in the hydrogen bond geometry. The absence of different crystal structures can be explained by the flexibility of the intricate hydrogen bonding network of glyphosate: the level of freedom of the molecules inside the unit cell allows them to change their relative position without breaking any intermolecular interactions.

8.1.2. Co-crystallisation work

As explained above, co-crystallisation work was undertaken on cyprodinil to increase its stability upon storage over longer periods of time, aiming, especially, to prevent the polymorphic conversion into the metastable form B. The choice regarding suitable co-formers followed few simple rules of crystal engineering, using the hydrogen bond as a ***synthon***. The aminopyrimidine functionality displayed by the molecules of cyprodinil directed the research of possible co-formers towards compounds exhibiting functional groups capable of forming 8-membered rings with the molecules of the fungicide. Co-crystals of cyprodinil with 2-aminopyrimidine, maleimide and benzoic acid were promptly obtained and their crystal structures were analysed by single crystal X-ray diffraction (SXD). These co-crystals showed the organisation of cyprodinil and co-former molecules into heterogeneous dimers, interacting through cyclic hydrogen bonds, forming an 8-membered ring; with the graph-set notation, these types of interactions can be written as $R_2^2(8)$, indicating the presence of two hydrogen donors and two hydrogen acceptors over a total of eight atoms involved in the intermolecular interactions. Unfortunately, the poor crystal quality of the molecular complex cyprodinil/maleimide led to a model showing low accuracy in the definition of the hydrogen atom positions. On the contrary, investigation of the difference Fourier maps of the cyclic hydrogen bonds in crystals of cyprodinil/2-aminopyrimidine allowed the classification of these interactions as hydrogen bonds of moderate strength, excluding the presence of proton effects, such as proton migration or disorder. SXD measurements on a sample of the co-crystal cyprodinil/benzoic acid showed the possible presence of proton disorder in the structure and

opened the way for the investigation of the behaviour of the hydrogen atoms in cyclic hydrogen bonds of co-crystals between cyprodinil and a series of differently substituted benzoic acids. The substituted benzoic acids used as co-formers for the co-crystallisation process of cyprodinil were the following (in parentheses, the abbreviation for the name of the molecular complex is reported): o-toluic acid (CoTA), p-toluic acid (CpTA), 2-amino and 4-aminobenzoic acids (C2ABA and C4ABA, respectively); 2-nitro and 3-nitrobenzoic acids (C2NBA and C3NBA, respectively), 2-fluoro, 3-fluoro and 4-flurobenzoic acids (C2FBA, C3FBA and C4FBA), and, finally, 2-chloro, 3-chloro and 4-chlorobenzoic acids (C2CBA, C3CBA, and C4CBA). The different electronic properties, as the inductive effect ***–I*** or ***+I***, of the substituents of the benzene ring were used to induce changes in the hydrogen bonding network of these co-crystals. The inductive effect represents the property of an atom or group of atoms to attract, effect ***–I***, or repulse, effect ***+I***, electrons. In the case of substituted benzoic acids, the higher the ability of a group to attract electrons, the higher the acidity of the derived benzoic acid, expressed in terms of the $\boldsymbol{pK_a}$. Amongst the co-formers listed above, the methyl group in toluic acids shows inductive effect ***+I***, while all other substituents have inductive effect ***–I***, decreasing along the series NO_2 > F > Cl > NH_2. Investigation of the changes in the hydrogen atoms behaviour was undertaken studying the electron-density and, when available, the nucleon-density maps of the cyclic hydrogen bond. Table 8.1 lists a summary of the $\boldsymbol{pK_a}$ values of the co-formers used, the melting point of the co-crystals, when available, and the proton effect caused in the hydrogen bond by the acidity of the co-former.

Co-former	pK_a[145]	Melting point of co-crystal	Proton effect
Benzoic acid	4.20	97˚C	Suspected disorder
2-aminobenzoic acid	4.94	107˚C	-
4-aminobenzoic acid	4.87	-	-
o-toluic acid	3.91	82˚C	-
p-toluic acid	4.36	-	-
2-nitrobenzoic acid	2.16	-	Proton transfer (C2NBA-I)
3-nitrobenzoic acid	3.47	172˚C	-
2-fluorobenzoic acid	3.27	92˚C	-
3-fluorobenzoic acid	3.86	-	-
4-fluorobenzoic acid	4.15	-	-
2-chlorobenzoic acid	2.90	82˚C	Proton transfer
3-chlorobenzoic acid	3.82	72˚C	Proton migration (C3CBA-I)
4-chlorobenzoic acid	3.98	-	-

Table 8.1. *Summary of the acidity of the substituted benzoic acids, reporting also the melting point of the co-crystal and the proton effect in the hydrogen bond (where nothing is specified, a moderate strength-HB is assumed).*

As expected by the values of their pK_a, the high acidity of 2-nitrobenzoic acid and 2-chlorobenzoic acid, caused by the electron-withdrawing properties of the two *ortho*-substituents, produces the transfer of the proton from the carboxylic group of the acid to the nitrogen atom of the pyrimidine ring of cyprodinil. It is, however, interesting to notice that among the two polymorphs of C2NBA only one exhibits the proton transfer: in fact, form II of C2NBA models the hydrogen atom almost perfectly in the middle of the intermolecular interaction, with O-H and N-H bond lengths of 1.26(4) Å and 1.35(4) Å, respectively, at 150K. The hydrogen atom position seems to change at room temperature, where the hydrogen atom is modelled closer to the cyprodinil molecule, having O-H and N-H bond lengths, respectively, of 1.34(5) Å and 1.27(5) Å. The different behaviour of the proton in the two forms can be related to the donor-acceptor distance O···N, which is longer in form I than in form II, specifically 2.642(2) Å in the former and 2.603(3) Å in the latter. It is possible that the hydrogen atom in form II is almost equally affected by the electron lone-pairs of both oxygen and nitrogen atoms. Computational studies showed that the polymorphs of C2NBA have similar energies, which explains the crystallisation of both forms from the same solution.

As shown in Table 8.1, the effect ***+I*** of toluic acids did not induced proton transfer, proton migration or proton disorder in the structure, as confirmed by the SND results on a crystal of CoTA. The SXD analyses on crystals of C2ABA and C4ABA showed residual electron density along the intermolecular hydrogen bond between the hydroxyl group of the acid and the nitrogen atom of the pyrimidine ring of cyprodinil. In addition, the electron density of the hydrogen atom involved in this interaction is elongated and slightly bilobated, indicating the possible presence of a second site for the proton and a disordered structure. However, it is important to underline the limitations that X-ray radiation meets in the detection of light elements, such as hydrogen atoms, leading to incomplete conclusions regarding the nature and properties of the hydrogen bond in these materials. Similar situation was found in the SXD results of the structure of C3NBA collected at room temperature and in the VT-SXD measurements of C2FBA. However, the presence of disorder in crystals of C2FBA was excluded by the VT-SND experiment. In fact, neutrons showed only an increase of the anisotropic atomic displacement parameters (ADPs) of the hydrogen atom involved in the intermolecular interaction suspected to be disordered. The phenomenon of polymorphism was observed in the molecular complex C3CBA, which can crystallise in a triclinic or a monoclinic structure. VT-SND measurements on the triclinic form of C3CBA-I showed an interesting effect of proton migration. At the temperature of 30K half of the heterogeneous cyprodinil/acid dimers showed the transfer of the hydrogen atom from the hydroxyl group to the cyprodinil molecule. The structure at 180K displayed a lengthening of the N-H bond, which continued to increase until 260K, where the hydrogen is modelled bonded back to the carboxylic oxygen. The migration of the proton as a function of temperature can be explained considering the donor-acceptor distances O···N in the different dimers of C3CBA-I. In fact, migration is observed only in dimers showing short O···N distance of 2.601(4) Å opposed to 2.632(4) Å for the dimers

that display a neutral conformation. These findings are consistent with the results on form II of C2NBA, where a short migration of the proton at room temperature was also observed. It is, then, possible to observe that co-crystal synthesis of cyprodinil with differently substituted benzoic acids is valid proof that these co-formers can be used to introduce into the system proton effect, such as proton transfer and proton migration, which are tuneable by temperature.

From the values of the melting points reported in Table 8.1 it is possible to observe that in most cases the presence of a co-former increased the stability of the fungicide. Worthy of notice is the molecular complex C3NBA, which displays the shortest value for the hydrogen bond length and for the donor-acceptor distance, O-H···N = 1.47(2) Å and O···N = 2.579(2) Å, respectively, leading to the formation of what is classified as a strong-HB. It follows that, amongst all co-crystals synthesised, C3NBA exhibits the highest temperature of fusion of ~172˚C. This significant increase of the melting point can make C3NBA a valid solution to the problem of the polymorphic conversion observed for cyprodinil at ~71˚C. However, assessment of the environmental impact and toxicity of 3-nitrobenzoic acid, along with the formulation of degradation pathways, must be considered and evaluated.

8.2. Future work

The work carried out in this thesis contributed to achieve a more in depth understanding of the factors responsible for the occurrence of polymorphism in hydrogen bonded compounds used as agrochemicals, highlighting the advantages of this phenomenon and suggesting possible strategies for the solution of related problems, both from a practical and a toxicological point of view, although additional work still needs to be done on many of the materials taken understudy in order to find methods for the control of the crystal structure and the design of materials with desired physical properties. Future perspective will include VT-PND experiments on both polymorphs of PDM to better characterise the phase transition between the two forms and to screen for possible temperature-dependent unknown polymorphs or even amorphous states, and on a sample of DFF in order to investigate the discrepancy observed in the value of the $\boldsymbol{\beta}$-angle between the structure obtained experimentally and the one present in the literature and assess the presence of possible phase transitions at low temperatures that might be missed in the single crystal analysis. Due to the successful results obtained with cyprodinil, the synthesis of molecular complexes with suitable co-former capable of forming hydrogen bonds with the nitro groups of PDM will be extended to this herbicide, aiming to increase the stability upon storage by the formation of stronger hydrogen bonding networks, preventing the occurrence of the polymorphic transformation.

Due to the problems arisen by the high incoherent scattering of hydrogen atoms in the treatment of the PND data collected on a sample of cyprodinil that did not allow the refinement of the atomic coordinates of the hydrogen atoms involved in the intermolecular hydrogen bonds, high quality X-

ray powder diffraction measurement will be performed, possibly with synchrotron radiation, in order to undertake a joint SND-PXD analysis on both forms of cyprodinil and to produce a model that would be used for computational studies on the energetics of this material. Co-crystallisation of cyprodinil will continue, attempting the process with other derivatives of benzoic acids and other compounds with functional groups capable of forming circular intermolecular interactions. Large crystals of the molecular complexes of cyprodinil with benzoic acid, 2- and 4-aminobenzoic acids, and 3-nitrobenzoic acid will be grown and SND experiments will be carried out to clarify the effect of these co-formers on the hydrogen bond and to corroborate or discredit the hypothesis of disorder suggested by SXD measurements.

Evaluation of the solubility of the molecular complexes of cyprodinil in water and in the most common organic solvents will be undertaken to assess whether the presence of a co-former could allow the preparation of this fungicide in more stable formulations, such as aqueous solutions, which would facilitate the application on the crop field. Finally, the environmental impact of the co-formers needs to be assessed in order to choose the best option balancing the stability of the material with the production of non-toxic compounds.

9. References

(1) Kobayashi Y., Ito S., Itai S., and Yamamoto K. *Int. J. Pharm.*, **193**, 137-146, 2000.

(2) Aguiar A. J., Krc J. Jr., Kinkel A. W., and Samyn J. C. *J. Pharm. Sci.*, **56**, 847-853, 1967.

(3) Ting V. P., Schmidtmann M., Wilson C. C., and Weller M.T. *Angewandte Chemie*, **49,** 9408-9411, 2010.

(4) Berstein J. **Polymorphism in Molecular Crystals**, *Oxford University Press*, 2002.

(5) Jenkins, E. W. **The Polymorphism of Elements and Compounds**, *Methuen Educational Ltd*, 1973.

(6) McCrone W. C. **Polymorphism**. In *Physics and chemistry of the organic solid state*, Vol. 2 (ed. D. Fox, M. M. Labes and A. Weissberger), pp. 725–67. *Wiley Interscience*, New York, U. S. A. 1965.

(7) Marangoni A. G. and McGauley S. E. *Crystal Growth and Design*, **3**, 95-108, 2003.

(8) Herbst W. and Hunger K. **Industrial organic pigments**, 2nd edn. *VCH, Weinheim*, 1997.

(9) Horn D. and Honningman B. **Polymorphism of copper phthalocyanine**. XII. *Fatipec Kongress, Garmisch-Parkinkirchen*, Germany, pp. 181-9, 1974.

(10) Griesser U. J., Weigand D., Rollinger J. M., Haddow M., and E. Gstrein. *Journal of Thermal Analysis and Calorimetry*, **77**, 511-522, 2004.

(11) Alexander M. *Science*, **211**, 132, 1981.

(12) Trask A. V., Motherwell W. D. S, and Jones W., *Chemical Communications*, **7**, 890, 2004.

(13) Davey R. J., Maginn S. J., Andrews S. J., Black S. N., Buckley A. M., Cottler D., Dempsey P., Plowman R., Rout J. E., Stanley D. R. and Taylor A. *J. Chem. Soc., Faraday Trans.*, **90**, 1003–9, 1994.

(14) Jenkins R. and Snyder R. L. **Introduction to X-ray powder diffractometry**. In *Chemical Analysis: A Series of monographs on analytical chemistry and its applications*, Vol. 138, ed. J. Winefordner, *Wiley Interscience, New York*, pp. 324-35, 1996.

(15) Zevin L. S. and Kimmel G. **Quantitative X-ray diffracometry**. *Springer, New York*, 1995.

(16) Stephenson G. A., Forbes R. A., and Rentzel-Edens, S. M. *Adv. Drug Deliv. Revs*, **48**, 67-90, 2001.

(17) Schwarz E. and de Buhr J. Collected applications. Thermal analysis. Pharmaceuticals, Mettler-Toledo GmbH, Schwerzenbach, 1998.

(18) A. Über Haupt- und Nebenvalenzen und die Constitution der Ammoniumverbindungen. *Justus Liebig Ann Chem*, **322**, 261-296, 1902.

(19) Moore T. S. And Winmill T. F. *J. Chem. Soc. Trans.*, **101**, 1635-1676, 1912.

(20) Oddo G. And Puxeddu E. *Gazz. Chim. It.*, **36**, 1-48, 1906.

(21) Pfeiffer P., Fischer Ph., Kunter J., Monti P., and Pros Z. *Justus Liebig Ann Chem*., **398**, 137-196, 1913.

(22) Latimer W. M. And Rodenbush W. H. *J. Am. Chem. Soc.*, **42**, 1419-1433, 1913.

(23) Pauling L. *J. Am. Chem. Soc.*, **53**, 1367-1400, 1931.

(24) Pimentel G. C. and McClellan A. L. **The hydrogen bond**. *Freeman, San Francisco, CA*. 1960.

(25) Vinogradov S. N. And Linnell R. H. **Hydrogen Bonding**. *Van Nostrand-Reinhold, New York*, 1971.

(26) Gilli G. and Gilli P. **The Nature of the Hydrogen Bond**, *Oxford University Press*, 2009.

(27) Jeffrey G. A. and Saenger W. **Hydrogen bonding in biological structures**. *Springer Verlag*, Berlin, D, 1991.

(28) Jeffrey G. A. **An introduction to hydrogen bonding**. *Oxford University Press*, Oxford, UK, 1997.

(29) Childs S. L., Stahly G. P., and Park A. *Mol. Pharm.*, **4**, 323, 2007.

(30) Bhogala B. R., Basavoju S., and Nangia A. *CrystEngComm*, **7**, 551, 2005.

(31) Martins D. M. S., Middlemiss D. S., Pulham C. R., Wilson C. C., Weller M. T., Henry P. F., Shankland N., Shankland K., Marshall W. G., Ibberson R. M., Knight K., Moggach S., Brunelli M., Morrison C. A. *J. Am. Chem. Soc.*, **131**, 3884, 2009.

(32) Steiner T., Majerz I., and Wilson C. C. *Angew. Chem. Int. Ed.*, **40**, 2651, 2001.

(33) Sim G. A., Robertson J. M., Goodwin, T. H. *Acta Crystallogr*., **8**, 157, 1955.

(34) Wilson C. C., Shankland N., Florence A. J. *J. Chem. Soc., Faraday Trans.*, **92**, 5051, 1996.

(35) Cai W. and Katrusiak A. *CrystEngComm*, **14**, 4420, 2012.

(36) Wilson C. C. and Goeta A. E. *Angew. Chem. Int. Ed*., **43**, 2095-2099, 2004.

(37) Moré R., Scholz M., Busse G., Busse L., Paulmann C, Torlkiehn M., and Thechert S. *Phys. Chem. Chem. Phys.*, **14**, 101987-10195, 2012.

(38) Hunter C. A. and Sanders J. K. M. *J. Am. Chem. Soc*., **112**, 5525-5534, 1990.

(39) Loots L. and Barbour L. J. **A rudimentary method for classification of π···π packing motifs for aromatic molecules**. In *The importance of pi-inetractions in crystal engineering: frontiers in crystal engineering, edited by Tiekink E. R. T. and Zukerman-Schpector J., 2nd ed., John Wiley & Sons*, 109-124, 2012.

(40) Desiraju G. R. and Gavezzotti A. *J. Chem. Soc., Chem Commun*, 621-623, 1989.

(41) Lehn J.-M. *Angew. Chem. Int. Ed. Engl.*, **27**, 89, 1988.

(42) J. D. Dunitz. *Pure Appl. Chem.*, **63**, 177, 1991.

(43) Corey E. J. *Pure Appl. Chem*., **14**, 19, 1967.

(44) Desiraju G. R. *Angew. Chem. Int. Ed. Engl*., **34**, 2311-2327, 1995.

(45) Etter M. C. *Acc. Chem. Res.*, **23**, 120, 1990.

(46) Lynch D. E, Latif T., Smith G., Byriel K. A., and Kennard C. H. L. *J. Chem. Crystallogr*., **27**, 567-575, 1997.

(47) Chinnakali K., Fun H.-K., Goswami S., Mahapatra A. K., and Nigam G. D. *Acta Cryst. C*, **55**, 399-401, 1999.

(48) He G., Aitipamula S., Chow P. S., and Tan R. B. H. *Acta Cryst. E*, **67**, o552-o553, 2011.

(49) Jin S., Wang D., Liang S., and Chen S. *J. Chem. Crystallogr*., **42**, 759-766, 2012.

(50) Shan N., Bond A. D., and Jones W. *Tetrahedron Letters*, **43**, 3101-3104, 2002.

(51) Rigault G. **Introduzione alla cristallografia**. *Levrotto & Bella*, 1983.

(52) Waseda Y., Matsubara E., and Shinoda K. **X-ray Diffraction Crystallography**, *Springer*, 2011.

(53) Rhodes G. **Crystallography made crystal clear**. *Academic Press, Elsevier Science*, 1993.

(54) L. J. Farrugia, *Journal of Applied Crystallography*, **32**, 837-838, 1999.

(55) G. Sheldric, *XPREP. Space Group Determination and Reciprocal Space Plots.*, 1991.

(56) G. M. Sheldrick, *Acta Crystallographica Section A*, **46**, 467-473. 1990.

(57) G. M. Sheldrick, *Release 97-2*, University of Göttingen, Germany, 1997.

(58) Pecharsky V. K. and Zavalij P. Y. **Fundamentals of powder diffraction and structural characterization of materials**, *Springer*, 2005.

(59) A. C. Larson and R. B. Von Dreele, *"General Structure Analysis System (GSAS)"*, Los Alamos National Laboratory Report LAUR 86-748, 1994.

(60) Elsasser W. M. *Compt. Rend. Acad. Sci. (Paris)*, **202**, 1029, 1936.

(61) Halban H. and Preiswerk P. *Compt. Rend Seanc. Acad. Sci. (Paris)*, **203**, 73, 1936.

(62) Mitchell D. P and Powers P. N. *Phys Rev.*, **50**, 486, 1936.

(63) Wilson C. C. **Single Crystal Neutron Diffraction from Molecular Materials**, *World Scientific Publishing*, 2000.

(64) *Neutron News*, **Vol. 3**, No. 3, 29-37, 1992.

(65) www.ill.eu

(66) www.ill.eu/en/html/instruments-support/instruments-groups/instruments/d19

(67) www.ill.eu/en/html/instruments-support/instruments-groups/instruments/d20

(68) Kresse G. and Furthmuller J. *Phys. Rev. B: Condens. Matter Mater. Phys*., **54**, 11169–11186, 1996.

(69) Blöchl P. *Phys. Rev. B: Condens. Matter Mater. Phys*., **50**, 17953–17979, 1994.

(70) Perdew J., Ruzsinszky A., Csonka G. and O. Vydrov. *Phys. Rev. Lett*., 2–6, 2008,

(71) Heyd J., Scuseria G. E. and Ernzerhof M. *J. Chem. Phys*., **118**, 8207, 2003.

(72) G. W. Stockton, R. Gogfrey, P. Hitchcock, R. Mendelsohn, p. C. Mowery, S. Rajan, and A. F. Walker, *J. Chem. Soc., Perkin Trans. 2*, pp. 2061-2071, *1998*.

(73) WSSA Herbicide Handbook Committee. Herbicide Handbook of the Weed Science Society of America, 6th Ed. WSSA, Champaign, IL. 1989.

(74) Meister, R.T. Farm Chemicals Handbook '92. *Meister Publishing Company*, Willoughby, OH, 1992.

(75) Copyright © 1981, 1997 International Union of Crystallography.

(76) Warren B. E. X-ray Diffraction. *Dover Publication, INC, New York*, 76, *1990*.

(77) https://www.ill.eu

(78) Campbell J. W., Hao Q., Harding M. M., Nguti N. D., Wilkinson C. *J. Appl. Cryst.*, **31**, 496, 1998.

(79) Wilkinson C., Khamis H. W., Stansfield R. F. D., McIntyre G. J. *J. Appl. Cryst.*, **21**, 471, 1988.

(80) Campbell J. W., Habash J., Helliwell J. R., Moffat K. *Daresbury Inf. Quart. Protein Crystallogr.*, **18**, 23, 1986.

(81) Gilli G., and Gilli P. The Nature of the Hydrogen Bond, *Oxford University Press*, p. 61, 2009.

(82) www.sigmaaldrich.com

(83) G. Pèpe, G. Pfefer, and R. Boistelle. *Acta Cryst. C*, **51**, 2671-2672, 1995.

(84) G. Thodoridis. Fluorine and the Environment. *Advances in Fluorine Science* **2**, 121, 2006.

(85) T. T. Thu Bui, S. Dahaoui, C. Lacomte, G. R. Desiraju, and E. Espinosa. *Angew. Chem. Int. Ed.*, **48**, 3838-3841, 2009.

(86) F. F. Awwadi, R. D. Willett, K. A. Peterson, amd B. Twamley. *Chem. Eur. J.*, **12**, 8952-8960, 2006.

(87) Database code "CCDC 126046"

(88) Worthing C. R. The Pesticide Manual: A World Compendium. pp. 226, 281, 329, 7th ed. *British Crop Protection Council, Hampshire, UK*, 1983.

(89) Peres F., Florin D., Grollier T., Feurtet-Mazel A., Coste M., Ribeyre F., Ricard M., and Boudou A. *Environmental Pollution*, **94**, 141-152, 1996.

(90) Jing Liu. Hayes' Handbook of Pesticide Toxicology, *Elsevier Inc.*, 1725, 2010.

(91) www.monsanto.com

(92) D. S. Sagatys, C. Dalhgren, G. Smith, R. C. Bott, and J. M. White. *J. Chem. Soc., Dalton Trans*., *3404-3410*, 2000.

(93) O'Malley M. Hayes' Handbook of Pesticide Toxicology, *Elsevier Inc.*, **28**, *771-772*, 2010.

(94) Database code "CCDC 152258"

(95) Waechter F., Weber E., Hertner T., and May-Hertl U. Hayes' Handbook of Pesticide Toxicology, *Elsevier Inc.*, 1903, 2010.

(96) WO2010/038008. Cocrystals (of Cyprodinil). Syngenta.

(97) Heye U. J., Speich J., Siegle H., Steinemann A., Forster B., Knauf-Beiter G., Herzog J., and Hubele A. CGA 219417: A novel broad-spectrum fungicide. *Crop. Protection 13*, 541-549, 1994.

(98) Supaphol P. and Spruiell J. E. *J. Applied Polymer Science*, **75**, 337-346, 2000.

(99) WO2010/038008 Cocrystals (of Cyprodinil) Syngenta.

(100) www.ccdc.cam.ac.uk/mercury

(101) Maleimide MSDS (www.sigmaaldrich.com). Direct link produced by Google URL Shortener: http://goo.gl/LR83th

(102) (a) D. E. Lynch, T. Latif, G. Smith, K. A. Byriel, C. H. L. Kennard. *Journal of Chemical Crystallography*, **27**, 567-575, 1997.

(b) K. Chinnakali, H-K. Fun, S. Goswami, A. K. Mahapatra, and G. D. Nigam. *Acta Cryst.*, **C55**, 399-401, 1999.

(c) N. Shan, A. D. Bond, and W. Jones. *Tetrahedron Letters*, **43**, 3101-3104, 2002.

(d) G. He, S. Aitipamula, P. S. Chow, and R. B. H. Tan. *Acta Cryst.*, **E67**, o552-o553, 2011.

(103) C. B, Aakeröy, N. Schultheiss, J. Desper, and C. Moore. *New J. Chem.*, **30**, 1452-1460, 2006.

(104) Z. Li, J. Huang, A. Meng, and B. Zheng. *Journal of Structural Chemistry*, **51**, 53-59, 2010.

(105) S. Jin, D. Wang, S. Liang, and S. Chen. *J. Chem. Crystallogr.*, **42**, 759-766, 2012.

(106) A. Domenicano, A. Vaciago, and C. A. Coulson. *Acta Cryst*., **B31**, 221, 1975.

(107) CCDC deposit number 704847

(108) CCDC deposit number 841392

(109) CCDC deposit number 835730

(110) C. C. Wilson, N. Shankland, and A. J. Florence. *J. Chem. Soc., Faraday Trans.*, **92**, 5051-5057, 1996.

(111) Benzoic acid MSDS (www.sigmaaldrich.com). Direct link produced by Google URL Shortener: http://goo.gl/lffUaR

(112) McCrone W. C., Whitney J., and Corvin I. *Anal. Chem.*, **21**, 1016, 1949.

(113) Brown C. J. *Proc. R. Soc. London Ser. A*, **302**, 185-199, 1968.

(114) CSD code AMBACO01 – CCDC deposit number 1102455

(115) Boone C. D. G., Derissen J. L., and Schoone J. C. *Acta Cryst. B*, **33**, 3205-3206, 1977.

(116) Takazawa H., Ohba S., and Saito Y. *Acta Cryst. C*, **42**, 1880-1881, 1986.

(117) CSD code AMBACO03

(118) CSD code AMBACO08 – CCDC deposit number 1102462

(119) Voogd J., Verzijl B. H. M., and Duisenberg A. J. M. Acta Cryst. B, 36, 2805-2806, 1980.

(120) Lai T. F and Marsh R. E. *Acta Cryst*., **22**, 885, 1967.

(121) CSD code AMBNZA – CCDC deposit number 1102480

(122) CCDC deposit number 661805

(123) Killean R. C. G., Tollin P., Watson D. G., and Young D. W. *Acta Cryst*., **19**, 482, 1965.

(124) 2-Aminobenzoic acid MSDS (www.sigmaaldrich.com). Direct link produced by Google URL Shortener: http://goo.gl/lfMgQT

(125) 3-Aminobenzoic acid MSDS (www.sigmaaldrich.com). Direct link produced by Google URL Shortener: http://goo.gl/8v9Nfh

(126) 4-Aminobenzoic acid MSDS (www.sigmaaldrich.com). Direct link produced by Google URL Shortener: http://goo.gl/R6k0JG

(127) Katayama C., Furusaki A., and Nitta I. *BCSJ*, **40**, 1293, 2006.

(128) Moreno-Fuquen R., De Almeida Santos R., and Kennedy A. R. *Acta Cryst. E*, **67**, o-569-o570, 2011.

(129) Takwale M. G. And Pant L. M. *Acta Cryst. B*, **27**, 1152, 1971.

(130) CCDC deposit number 694061

(131) CCDC deposit number 815522

(132) CCDC deposit number 785064

(133) *o*-Toluic acid MSDS (www.sigmaaldrich.com). Direct link produced with Google URL Shortener: https://goo.gl/jTukiX

(134) *m*-Toluic acid MSDS (www.sigmaaldrich.com). Direct link produced with Google URL Shortener: https://goo.gl/Alpt0p

(135) *p*-Toluic acid MSDS (www.sigmaaldrich.com). Direct link produced with Google URL Shortener: https://goo.gl/vklkdg

(136) Portalone G. *Acta Cryst E*, **65**, o954, 2009.

(137) Dhaneshwar N. N., Tavale S. S., and Pant L. M. *Acta Cryst. B*, **30**, 583, 1974.

(138) Tavale S. S. and Pant L. M. *Acta Cryst. B*, **31**, 1978, 1975.

(139) CCDC deposit number 1212631

(140) CCDC deposit number 1212632

(141) Colapietro M. and Domenicano A. *Acta Cryst. B*, **33**, 2240-2243, 1977.

(142) 2-Nitrobenzoic acid MSDS (www.sigmaaldrich.com). Direct link produced by Google URL Shortener: https://goo.gl/KZskcY

(143) 3-Nitrobenzoic acid MSDS (www.sigmaaldrich.com). Direct link produced by Google URL Shortener: https://goo.gl/vD6etK

(144) 4-Nitrobenzoic acid MSDS (www.sigmaaldrich.com). Direct link produced by Google URL Shortener: https://goo.gl/K50nEr

(145) CRC Handbook of Chemistry and Physics, 91st Edition. Edited by W. M. Haynes. CRC Press. 2010-2011.

(146) Von J. Krausse and H. Dunken. *Acta Cryst.*, **20**, 67, 1966.

(147) Taga T., Yamamoto N., and Osaki K. *Acta Cryst. C*, **41**, 153-154, 1985.

(148) Colapietro M., Domenicano A., and Pela Ceccarini G. *Acta Cryst. B*, **35**, 890-894, 1979.

(149) CCDC deposit number 825370

(150) CCDC deposit number 1130250

(151) CCDC deposit number 1232147

(152) 2-Fluorobenzoic acid MSDS (www.sigmaaldrich.com). Direct ling produced by Google URL Shortener: https://goo.gl/iiPdHL

(153) 3-Fluorobenzoic acid MSDS (www.sigmaaldrich.com). Direct link produced by Google URL Shortener: https://goo.gl/kpmIUN

(154) 4-Fluorobenzoic acid MSDS (www.sigmaaldrich.com). Direct link produced by Google URL Shortener: https://goo.gl/TgFr6g

(155) Ferguson G. and Sim G. A. *Acta Cryst.*, **14**, 1262, 1961.

(156) Zanos Gougoutas J. and Lessinger L. *Journal of Solid State Chemistry*, **12**, 51-62, 1975.

(157) Colapietro M. and Domenicano A. *Acta Cryst. B*, **38**, 1953-1957, 1982.

(158) CCDC deposit number 694059

(159) CCDC deposit number 1210113

(160) CCDC deposit number 1127046

(161) 2-Chlorobenzoic acid MSDS (www.sigmaaldrich.com). Direct link produced by Google URL Shortener: https://goo.gl/Ikrzef

(162) 3-Chlorobenzoic acid MSDS (www.sigmaaldrich.com). Direct link produced by Google URL Shortener: https://goo.gl/Bo5ILN

(163) 4-Chlorobenzoic acid MSDS (www.sigmaaldrich.com). Direct link prodiced by Google URL Shortener: https://goo.gl/QCoH0L